# PERFORMANCE ASSESSMENT OF SHEAR-CRITICAL REINFORCED CONCRETE PLANE FRAMES

by

Serhan Güner

A thesis submitted in conformity with the requirements

for the degree of Doctor of Philosophy

Graduate Department of Civil Engineering

University of Toronto

**Performance Assessment of Shear-Critical Reinforced Concrete Plane Frames**

Degree of Doctor of Philosophy

2008

Serhan Güner

Department of Civil Engineering

University of Toronto

## ABSTRACT

Current analysis procedures for new reinforced concrete structures are typically based on linear-elastic principles. However, under certain conditions, it may be necessary to analyze a structure to more accurately predict its structural behaviour. Such an analysis can be performed using nonlinear analysis procedures which typically require specialized software. This type of software is limited in number and most available programs do not adequately capture shear-related influences, potentially severely overestimating strength and ductility in shear-critical structures.

The purpose of this study is to develop and verify an analytical procedure for the nonlinear analysis of frame structures with the aim of capturing shear-related mechanisms as well as flexural and axial effects. A previously developed analysis program, VecTor5, is further developed for this purpose. Originally formulated in the early 1980s at the University of Toronto, VecTor5 is based on the Modified Compression Field Theory (MCFT) and is capable of performing nonlinear frame analyses under temperature and monotonic loading conditions. Although providing generally satisfactory simulations, there are a number of deficiencies present in its computational algorithms.

This study consists of three major parts: improvement of the original analysis procedure for monotonic loading conditions, expansion of the procedure for general loading conditions including the special cases of cyclic and reversed-cyclic loading, and further development

of the procedure for dynamic loading conditions including time-varying base accelerations, impulse, impact and blast forces, initial mass velocities, and constant mass accelerations. Each part is supported by verification studies performed on a large number and variety of previously tested structures available in the literature. In addition, considerations in nonlinear modelling are discussed with the aim of providing guidelines for general modelling applications.

Analyses of 63 previously tested structures, half of which are shear-critical, demonstrate that the developed analytical procedure is highly successful in simulating the experimental responses in terms of load-deflection response, reinforcement strains, crack widths, failure mode, failure displacement, total energy dissipation, displacement ductility ratio, and post-peak vibrational characteristics.

To My Parents,

Ayten and Hamdi Güner

# ACKNOWLEDGEMENTS

The completion of this study was made possible with the guidance, continuous support and endless patience of Professor Frank J. Vecchio. I have felt privileged to be his student and immensely enjoyed working with him and meeting with him on a regular basis in the last four years. At the same time, I have had the luxury to work independently, provided by his patience and trust. In addition, this report has been benefited greatly by his rigorous editorial reviews and comments. His contributions to my education will be retained throughout my professional life.

I would like to extend my sincere gratitude to Professor Evan C. Bentz for the expert advice and the support he always freely provided throughout my studies at the University of Toronto.

This thesis benefited from the invaluable suggestions of my Ph.D. advisory committee members: Professors Evan C. Bentz, Shamim A. Sheikh and Constantin Christopoulos. I am grateful to all committee members for their feedback and recommendations in the course of this study. I would also like to thank to Professors Michael P. Collins and Paul Gauvreau for their valuable comments at the final stage of this study. Furthermore, I am grateful to Professor Catherine French for her thorough review of this report and for her invaluable technical and editorial comments as the external appraisal of this thesis from the University of Minnesota.

The financial support for this project provided by Professor Frank J. Vecchio and the Department of Civil Engineering of the University of Toronto was gratefully acknowledged.

I would like to thank to my friends and colleagues for their friendship and unconditional support. They include Ana Acevedo, Ciyan Cui, Kien Vinh Duong, Michael Gray, Trevor Hrynyk, Hyunjoon Kim, Nabil Mansour, Gilberto Martinez, Boyan Mihailov, Michael Montgomery, Hossein Mostafaei, Selçuk Saatcı, Gülşah Sağbaş, Mohamed Semelawy, Yunlu Shen, Jimmy Susetyo, Andrew Volt, Lydell Wiebe, Liping Xie, and many others.

Finally, I would like to express my deepest gratitude to my parents, Ayten and Hamdi; my sister, Nilhan; my grandmother, Beria; my grandfather, Nihat; my aunt Ayşe; and my uncle Ali. Their continual support and encouragement throughout my educational life has allowed me to pursue this academic degree.

# TABLE OF CONTENTS

# LIST OF FIGURES

## CHAPTER 1 - INTRODUCTION



## CHAPTER 2 - NONLINEAR ANALYSIS OF RC FRAMES

**CHAPTER 4 - MONOTONIC LOADING: VERIFICATION & APPLICATIONS**

**CHAPTER 5 - GENERAL LOADING: THEORY & IMPLEMENTATION**

**CHAPTER 6 - GENERAL LOADING: VERIFICATION & APPLICATIONS**

**CHAPTER 8 - DYNAMIC LOADING: VERIFICATION & APPLICATIONS**

## APPENDIX A - COMPARISON OF REINFORCEMENT STRAINS OF SAATCI BEAMS

# LIST OF TABLES

**CHAPTER 7 - DYNAMIC LOADING: THEORY & IMPLEMENTATION**



**CHAPTER 8 - DYNAMIC LOADING: VERIFICATION & APPLICATIONS**

# CHAPTER 1

# INTRODUCTION

## 1.1 Need for Advanced Analysis Procedures

### 1.1.1 Analysis of Reinforced Concrete Structures

Over the past few decades, intensive research activity in structural engineering has greatly increased our knowledge of the behaviour of concrete structures under both shear and flexure. As a result, new analysis and design procedures have been developed and incorporated into design codes such as CSA A23.3-04 (Design of Concrete Structures) and NBCC 2005 (National Building Code of Canada).

Occurring at the same time, advancements in computing technology have enabled structural engineers to analyze and design structures according to the new design codes quickly and easily. The analysis procedures are typically based on linear-elastic principles. Even though linear-elastic analyses cannot accurately predict all aspects of structural behaviour, such as cracking of concrete and deformations under service loads, they are deemed sufficient if the structure is designed according to code. As a result, the structure will satisfy strength and serviceability requirements. The reinforcement is detailed so that the structure exhibits ductile behaviour with a flexural failure mode. Currently, there are numerous easy-to-use software programs which can perform such analyses and designs reasonably well.

### 1.1.2 Nonlinear Analysis of Reinforced Concrete Structures

It may be necessary, in some situations, to analyze a structure so as to more accurately predict its structural behaviour. Such an analysis may be required for:

(1) strength, safety and integrity assessment of

   a. damaged or deteriorated structures,

   b. structures which were designed and built 20 to 30 years ago based on previous codes, standards or practices considered deficient today,

(2) performance assessment of planned structures,

(3) accurate assessment of large, atypical or unique structures such as nuclear containment structures and offshore platforms,

(4) assessing the expected behaviour of retrofitted structures,

(5) investigating and selecting a rational retrofit or repair alternative among several alternatives,

(6) addressing questions or problems that arise after construction of a new building, or due to the change of use or function of the existing structure,

(7) forensic analyses in cases of structural failure or collapse.

For these cases, structural engineers may need to assess the maximum load capacity, ultimate displacement capacity, ductility, deficient members/parts and failure mechanism of the structure. Such an analysis can be performed using nonlinear analysis procedures which typically require specialized software.

For a structure whose behaviour is dominated by flexural mechanisms, there are a number of software programs such as SAP2000 (CSI, 2000) that can perform such an analysis with reasonable accuracy in most cases. Therefore, the nonlinear analysis and design of flexure-critical structures is generally considered to be a solved problem in terms of strength calculation. However, for structures whose behaviour is affected by shear-related mechanisms, there is a scarcity of software and the accuracy of the programs that do exist is of great concern. The reason for this is that the shear behaviour of reinforced concrete is still not very well understood; therefore, the accurate modelling of this behaviour remains elusive with many conflicting theoretical approaches and constitutive models being proposed.

### 1.1.3 Case Study – a Clinker Preheater Tower

To further clarify the need for advanced analysis procedures, consider a clinker preheater tower build in a seismically active zone of El Salvador, Central America, in the late 1990s. Designed according to ACI code specifications, the tower spans one bay in each

orthogonal direction in plan and is seven storeys in elevation as shown in Figure 1.1. Following its construction, subsequent design reviews revealed some deficiencies including: inadequate shear reinforcement in some of the beams, as shown in Figure 1.2(b), which may prevent the beams from developing their full flexural capacity, inadequate lateral confining reinforcement in some of the lower storey columns, as shown in Figure 1.2(a), which may lead to the violation of the strong-column and weak-beam seismic design principle, and inadequate penetration of the beam longitudinal reinforcement into the columns, which violates seismic detailing provisions. It was also determined that the behaviour of the frame in the short direction is more critical. It is now desired to analyze this frame structure to assess its safety during a probable earthquake. More specifically, its load and displacement capacity, failure mode, and any deficient members are to be determined.

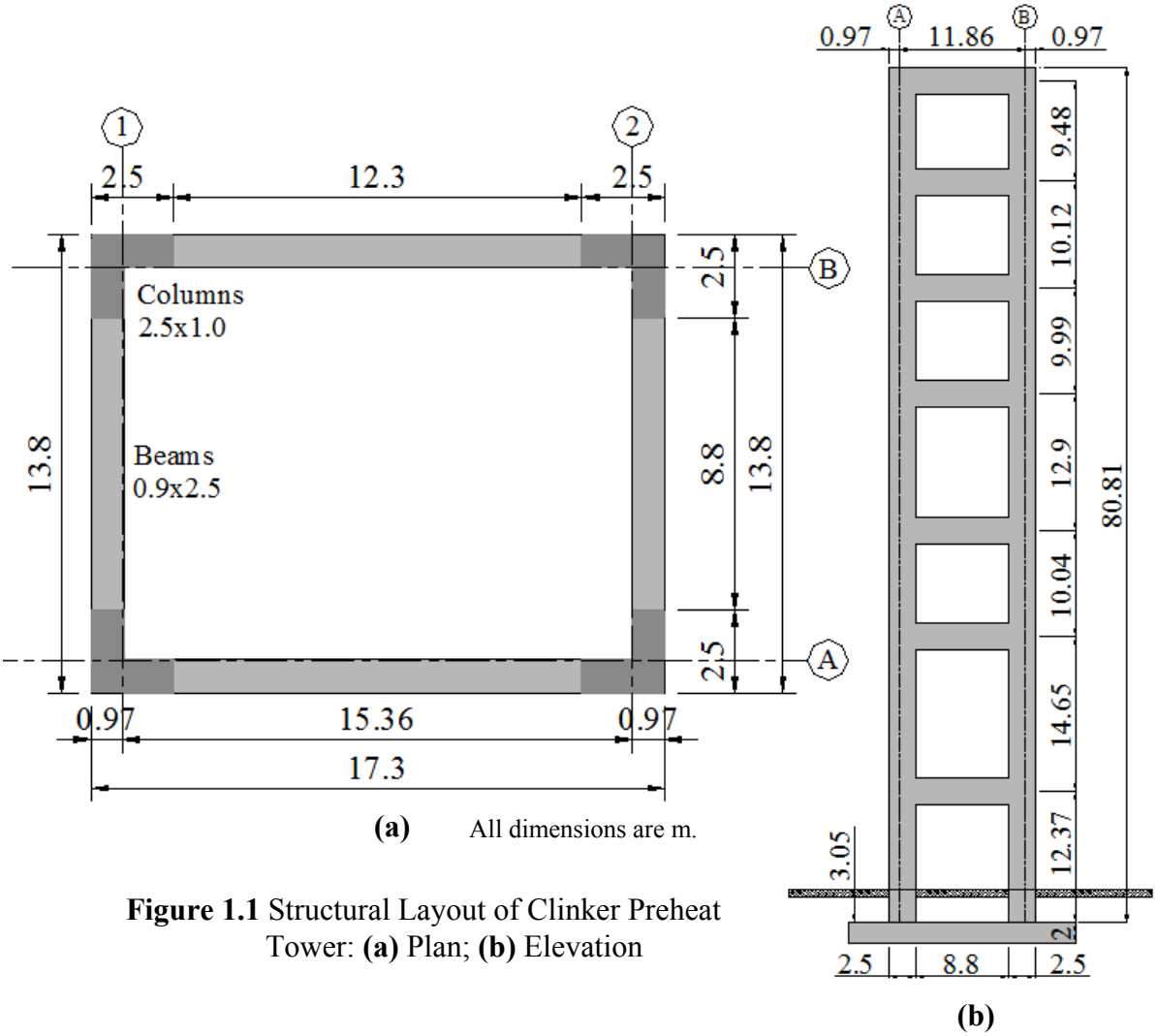


**Figure 1.1** Structural Layout of Clinker Preheat Tower: **(a)** Plan; **(b)** Elevation

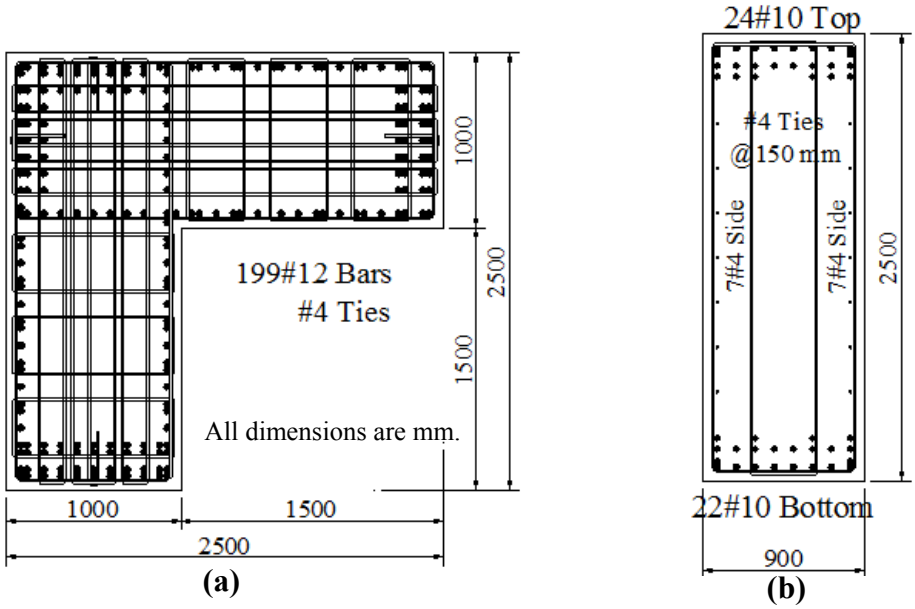


**Figure 1.2** Cross Section Details of Clinker Preheat Tower: **(a)** First Storey Column; **(b)** First Storey Beam

For analysis purposes, three software programs were used: SAP2000 (CSI, 2000), RUAUMOKO (Carr, 2005) and TEMPEST (Vecchio, 1987; Vecchio and Collins, 1988). The frame was modelled using only default options and models which were readily built into the programs, i.e., default hinges and all default material behaviour models. All three models were created using the same geometry, material and support conditions. The analyses were performed in a force-controlled mode under monotonically increasing static storey shear forces which were calculated by the linear dynamic response spectrum method.

As a result of this analysis, unacceptably different results were obtained (Table 1.1). SAP2000 and RUAUMOKO predicted that the frame will fail in flexure, while TEMPEST predicted a sudden shear failure in some of the beams. The largest discrepancy was in the ductility predictions for the frame; SAP2000 predicted approximately 5.6 times greater displacement for the peak load capacity than did TEMPEST (Figure 1.3).

**Table 1.1** Comparison of Analysis Results for Clinker Preheat Tower

| | SAP2000 | RUAUMOKO | TEMPEST |
|---|---|---|---|
| **Failure Load (kN)** | 7343 | 7783 | 7213 |
| **Failure Disp. (m)** | 2.64 | 1.11 | 0.47 |

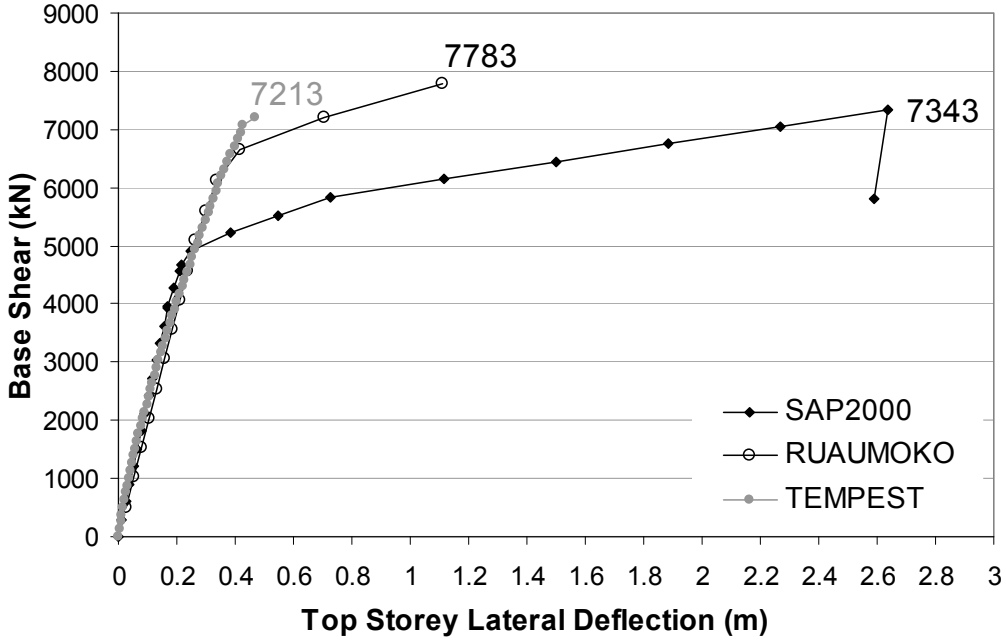


**Figure 1.3** Load-Deflection Responses for Clinker Preheat Tower

In Figure 1.3, the highly ductile load-deflection prediction obtained from SAP2000 resulted from the assumption of purely flexural behaviour. In other words, the influence of shear-related effects was completely neglected in the SAP2000 model by the use of default moment hinges. A similar flexure-dominated behaviour was obtained from the RUAUMOKO model. In the TEMPEST analysis, on the other hand, the default material behaviour models considered inelastic shear-related effects and predicted shear failures for the upper storey beams, thereby providing the least ductile response. During the TEMPEST analysis, however, deteriorating convergence factors and large unbalanced shear forces became apparent beyond a base shear force of 6300 kN. This situation raised questions about the validity of the load-deflection curve at the later load stages. More details of this analysis are presented in Section 4.10.

Anticipating a shear-dominated behaviour *before* the analyses, it is possible to create user-defined custom shear hinges in SAP2000 and RUAUMOKO models as exemplified in Section 2.3.6 when analyzing a shear-critical frame. However, such an analysis requires expert knowledge on the shear-behaviour of reinforced concrete, specialized

supporting software, such as Response-2000 (Bentz, 2000), and may take significant engineering time and effort as discussed in detail in Section 2.3.7.

The apparent difficulty with accurately modelling strength and ductility of this frame exemplifies the need for advanced yet practical analysis procedures which inherently include shear-related influences as well as flexure and axial related ones, thereby capturing all possible failure mechanisms.

## 1.2 Background Development

### 1.2.1 Modified Compression Field Theory (MCFT)

Over the last 30 years at the University of Toronto, research has focused on improving analysis procedures for shear-critical reinforced concrete structures with an emphasis on simple but realistic material behaviour models for reinforced concrete.

Research efforts led to the formulation of the MCFT (Vecchio and Collins, 1986) as a rational model for predicting the response of reinforced concrete under shear and normal stresses. The MCFT is essentially a fully rotating, smeared crack model that represents cracked concrete as an orthotropic material with its own stress and strain characteristics. Equilibrium, compatibility and stress-strain relationships (constitutive relationships) are formulated in terms of average stresses and average strains. Directions of principal stresses and principal strains are assumed to be coincident. The constitutive relationships in the theory resulted from tests of over 200 reinforced concrete panels, using the panel element tester and shell element tester of the University of Toronto as shown in Figure 1.4, under pure shear or combinations of shear and normal stresses.

In the formulation, cracked concrete is treated as fundamentally different from uncracked plain concrete. During the tests of panel elements, it was observed that cracked concrete, when under high tensile strain in the direction normal to the compression, exhibited reduced compression strength and stiffness. As a result, a realistic compression softening relation was incorporated into the theory. In addition, a tension stiffening relation was introduced to take account of the presence of post-cracking tensile stresses in the concrete

between cracks. Finally, consideration was given to the local stress conditions at crack locations to predict reinforcement stresses and strains and shear stresses at the crack interface.

**(a)** Panel Element Tester

**(b)** Shell Element Tester

**Figure 1.4** Concrete Panel Tests at the University of Toronto (Vecchio and Collins, 1986)

Following its formulation, the MCFT was implemented into various design code procedures and advanced analysis tools. The general design method for shear of the 1994 and 2004 Canadian Concrete Design Code was also based on the MCFT. Meantime, various nonlinear finite element computer programs were developed incorporating the MCFT. Over the last 20 years, the MCFT has been applied to the analysis of numerous reinforced concrete structures and found to provide accurate simulations of behaviour. The formulations of the MCFT will be presented in Chapter 3.

### 1.2.2 Computer Program TEMPEST

To apply the MCFT to the analysis of reinforced concrete plane frames, computer program TEMPEST (Vecchio, 1987; Vecchio and Collins, 1988) was developed at the University of Toronto in the late 1980s. The program was able to analyze frame or frame-related structures including single beam and column elements under mechanical (axial load, shear force, bending moment) and temperature loads.

The nonlinear frame analysis procedure in TEMPEST was based on a total load, iterative, secant stiffness formulation. The calculation procedure consisted of two interrelated analyses. First, a global frame analysis was performed to obtain internal member forces; then, *sectional analyses* were performed using the calculated member end actions. An iterative analysis procedure was implemented according to the following sequence: Using uncracked gross section properties, an initial linear-elastic frame analysis was performed to obtain the first estimate of the resultant internal member forces caused by imposed mechanical or thermal loads. Sectional analyses were then performed for each member, at various sections along its length. In this calculation, top and bottom fibre strains were iteratively determined to equilibrate the internal member forces calculated by the global frame analysis. A linear-elastic frame analysis was repeated using the updated section properties and fixed end forces. Convergence factors were calculated from unbalanced forces, effective stiffnesses and effective areas. The iteration was carried on in a similar fashion until adequate convergence was achieved.

The sectional analyses were based on a layered section approach in which a cross section was divided into a number of concrete layers, longitudinal reinforcing bar elements and longitudinal prestressing steel elements. Each concrete layer and steel element was then analyzed individually based on the MCFT, although sectional compatibility and sectional equilibrium was satisfied as a whole. The only sectional compatibility requirement was that plane sections must remain plane, while sectional equilibrium requirements included balancing the axial force, shear force and bending moment calculated by the global frame analysis.

Originally, TEMPEST was able to perform three different types of shear analyses: multi-layer analysis, single-layer analysis, and modified single-layer analysis. All of the options were based on shear-stress-based analysis in force controlled mode. Accordingly, it was only possible to carry out analyses up to the peak load. In other words, it was not possible to obtain the post-peak behaviour of the structure being analyzed.

In a later study (Fulop, 1992), TEMPEST's computational capabilities were expanded to include shear-strain-based analysis and deformation-controlled analysis. The new

formulation allowed for (1) displacement controlled analysis in the post-peak regime, (2) faster execution time, (3) more stable calculations, all of which significantly improved the capability of the program.

In the late 1990s, the name of the program was changed from TEMPEST to VecTor5 in order to be consistent with the other nonlinear analysis programs developed at the University of Toronto (e.g., VecTor1, VecTor2, VecTor3, VecTor4, and VecTor6). While many of the other VecTor programs have undergone further development in the ensuing years, program VecTor5 remained essentially unchanged.

### 1.2.3 Sectional Analysis of Structures

Analysis of structures can be performed using a wide range of approaches. Among them are graphical methods such as strut-and-tie models, nonlinear finite element methods, and sectional methods. Graphical methods provide rational results but they are labour intensive and are therefore limited in the range of applicability. Multi-purpose nonlinear finite element methods are quite powerful but their complexity necessitates a computer, specialized software and experience with finite element modelling. In addition, the complex calculations performed by a computer are difficult if not impossible to check by simple means such as hand calculations.

In the middle ground lie sectional analyses which combine desirable features of both methods. They are simple enough to be understood yet powerful enough to provide acceptably accurate results. Calculations are performed at a specific location along the member for internal forces such as the axial force, shear force and bending moment calculated from the global analysis of the structure. VecTor5 is based on this approach.

### 1.2.4 Assumptions in the Sectional Analysis of TEMPEST and VecTor5

To model a reinforced concrete member with reasonable accuracy using a sectional method, the member should be relatively slender. As the member becomes deeper (i.e. as the span to depth ratio decreases), the longitudinal flexural stress distribution becomes nonlinear which violates the engineering beam assumption made. It can be stated that

sectional analysis should be performed for members with span-to-depth ratios greater than at least 2. If a deeper member is analyzed by sectional procedures, the results will be typically overly conservative.

In the application of sectional analysis techniques in VecTor5, it was assumed that there will be no net stress in the transverse direction. However, it is known that high transverse stresses are present at locations where the load is introduced or where a support is present. These stresses locally increase the strength of the member; therefore, sectional analysis should be performed at a distance away from the load or support. Otherwise, the predictions will be conservative. A more detailed discussion of this assumption can be found in Section 1.5 of Bentz (2000). In VecTor5, this phenomenon is approximately accounted for by the newly implemented shear protection algorithm which artificially increases the shear strengths of sections within a certain distance from applied loads, supports and frame joints. Details of this algorithm are given in Chapter 3.11.

It is assumed that 'plane sections remain plane'. This conveniently permits the calculation of the longitudinal strain in each layer of concrete, reinforcing steel and prestressing steel as a function of the top and bottom fibre strains.

In the shear-strain-based analysis, which is the favoured analysis option throughout this thesis, two simple shear strain distributions were assumed. The first option is a parabolic shear strain distribution which is based on experience that has shown that shear strain through a section often varies in a nearly parabolic fashion, although it is highly dependent on the loading conditions and section details (Vecchio and Collins 1988). The second option is a constant shear strain distribution across the height of the section. Both approaches are approximate and will not exactly reflect the actual shear strain distribution of cracked reinforced concrete section. They are, however, preferred over theoretically more accurate shear-stress-based analysis for the following reasons: (1) they do not require a double iterative procedure and therefore are much faster, (2) they do not possess the inherent instability of shear-stress-based analysis, thereby giving problem-free operation, (3) they can capture post-peak behaviour while shear-stress-based analyses terminate at the peak load, and (4) it is seen that they are able to capture the behaviour of

test specimens reasonably well. Detailed discussions regarding this issue can be found in Vecchio and Collins (1988).

### 1.2.5 Deficiencies in TEMPEST

TEMPEST was a valuable analysis tool for predicting the behaviour of reinforced concrete plane frames under monotonically increasing loads or deformations. The program was capable of capturing shear-related influences as well as several second-order effects. However, there were a number of deficiencies in the computational algorithm and the analytical results.

In terms of predicting load-deflection response:

(1) The program was occasionally producing large unbalanced shear and axial forces especially prior to reaching the load capacity of the structure being analyzed. This situation tended to require the user to check the output files to determine the validity of the load-deflection response around the peak load point.

(2) In the case of a shear-critical structure, the analyses may continue with large unbalanced shear forces into the post-peak regime, providing a response resembling a shear-flexure response.

(3) The program was generally predicting slightly stiffer responses, especially in the initial stages of the analyses, than was typically obtained from experiments and from VecTor2, a nonlinear finite element analysis program for membrane structures based on the MCFT.

(4) The peak load prediction was generally lower than the experimental results for the structures containing little shear reinforcement.

(5) The ultimate displacement predictions tended to be higher than the experimental results especially for shear-critical structures.

(6) The program was incapable of predicting the response of large beams with no transverse reinforcement. It was typically predicting much higher strengths than what was experimentally observed.

(7) The program was incapable of predicting the ductility of flexure-critical structures. The load-deflection responses were typically diminishing after the peak load due to shear-related effects even thought the structure was purely flexure-critical.

In terms of computational capabilities:

(1) The program was only capable of performing analyses under statically increasing deformations or loads.

(2) In the shear-stress controlled mode, the program would occasionally stop the analysis by becoming idle, or stop converging before the peak load was attained.

(3) In the shear-stress controlled mode, the analysis frequently became unstable just at the peak load or shortly afterwards.

(4) In all modes, there was a possibility of termination of analysis because of 'floating point divide by zero' error, which meant there was a zero division somewhere in the computation.

(5) The analysis would occasionally not start due to such input errors as 'bad character in input field" or "end of file". It was difficult to find such input errors.

(6) The maximum number of load stages that could be handled was 99. If 100 or more load stages were specified, the analysis was terminated.

### 1.2.6 Disturbed Stress Field Model (DSFM)

Since its formulation, the MCFT (Vecchio and Collins, 1986) has been found to provide consistently reliable predictions of the response of reinforced concrete with an accuracy that is acceptable in most engineering situations. However, some deficiencies have been revealed for certain structures under specific loading scenarios. In lightly reinforced elements, it is noted that the rotation of principal stress field tends to lag behind the rotation of principal strain field. For such an element, the MCFT generally overestimates the strength and stiffness due to its enforced alignment of principal strain and principal stress fields. Conversely, for heavily reinforced elements, where no or little rotation of

principal strain and principal stress fields occurs, the MCFT underestimates the strength and stiffness due to its overly softened compression response.

The Disturbed Stress Field Model (DSFM) was proposed by Vecchio (2000) to address these two main weaknesses of the MCFT by extending the MCFT in several aspects. Most importantly, in its compatibility relationships, it includes slip deformations at crack locations caused by shear stresses being not necessarily zero at the crack surface. This allows for the deviation of the principal stress field from the principal strain field. In addition, the inclusion of crack slip deformations also removes the complex crack shear check which is required by the MCFT. It also includes refined constitutive relationships for concrete and reinforcement. The formulations of the DSFM will be presented in Chapter 3.

## 1.3 Objectives of this Study

In addition to providing a critical look at the current state-of-the-art, the objectives of this study can be summarized into three main categories: improvement of the original analysis procedure (VecTor5) for monotonic loading conditions, further development of the procedure for general loading conditions, and further development of the procedure for dynamic loading conditions. Each part will be supported by verification studies performed on a large number and variety of structures previously tested. In addition, considerations in nonlinear modelling will be discussed with the aim of providing guidelines for the general modelling applications. A more detailed summary of the research objectives is as follows:

(1) Improve the existing program VecTor5 for monotonic loading conditions:

   a. Completely rewrite the sectional analyses algorithm with an emphasis on shear behaviour based on the MCFT (Vecchio and Collins, 1986).

   b. Include refinements in the underlying theories that have occurred in the past two decades such as the DSFM (Vecchio, 2000).

   c. Correct all the deficiencies listed in Section 1.2.5.

d. Include additional second-order effects such as dowel action, concrete dilatation, concrete prestrains, concrete tension softening, and concrete crack slip check.

e. Implement a shear protection algorithm to approximately account for the increased strengths of D-regions.

f. Implement a shear failure check algorithm to detect sudden shear failures of members in cases where the specified maximum number of iterations is inadequate for the structure being analyzed.

g. Implement a variable crack spacing calculation.

h. Improve the existing dynamic averaging scheme.

i. Include confinement effects in the out-of-plane direction.

j. Include strain hardening behaviour of transverse reinforcement.

k. Include reinforcement stress and strain calculations at a crack.

l. Increase the total number of elements, concrete layers, steel layers, and detailed member output which can be handled by the program.

m. Include a more comprehensive warning mechanism for input errors.

n. Provide a more detailed output for advanced users.

o. Reduce computation time and improve stability and convergence.

(2) Develop analysis capabilities for general loading conditions:

a. Include concrete and reinforcement strain histories for general loading.

b. Implement concrete hysteresis models such as

   i. The Vecchio model with linear unloading (Vecchio, 1999),

   ii. The Vecchio model with nonlinear unloading (Vecchio, 1999),

   iii. The Palermo model with decay (Palermo and Vecchio, 2003).

c. Implement steel hysteresis models such as

i. The Seckin Model with Bauschinger effect (Seckin, 1981),

ii. The elastic-plastic model with strain hardening,

iii. The elastic-plastic model.

(3) Develop analysis capabilities for dynamic loading conditions:

a. Consider masses in the modelling process.

b. Implement direct integration schemes such as

i. Newmark's average acceleration method (1959),

ii. Newmark's linear acceleration method (1959),

iii. Wilson's Theta Method (1976).

c. Include viscous damping mechanisms such as

i. Rayleigh Damping (1878),

ii. Alternative Damping (Clough and Penzien, 1993).

d. Consider strain rate effects for both concrete and reinforcement, to account for the strength gained under dynamic loading conditions, based on

i. CEB-FIP (1988 and 1990) formulations,

ii. Malvar and Crawford (1998) formulations.

e. Consider dynamic loads such as

i. Ground accelerations,

ii. Impulse or blast loads,

iii. Impact loads,

iv. Initial mass velocities,

v. Constant mass accelerations.

f. Implement a modal analysis algorithm to calculate mode shapes and frequencies.

g. Implement algorithms to calculate the mass matrix and dynamic load vectors.

(4) Verify the analytical predictions with a large number and variety of structures which were tested previously and reported in the literature and correct any shortcomings of the developed procedure.

(5) Aim at producing a fast, easy-to-use yet reliable tool which is suitable for everyday use by both researchers and office design engineers:

   a. Use "*default material models"* only to show the applicability of the procedure developed in general modelling of frame structures and shear walls.

   b. Do not require decisions regarding the expected behaviour, failure mode or selection of appropriate parameters prior to the analyses.

(6) Discuss the appropriate use of newly implemented options and appropriate selection of several parameters when necessary.

(7) Discuss important considerations in the nonlinear modelling to provide guidelines for the general modelling process.

## 1.4 Organization of Thesis

This thesis focuses on (1) describing the theory and formulations which were implemented into VecTor5, (2) validating the analytical tool developed through the analyses of structures previously tested, and (3) providing modelling guidelines for frame structures and shear walls with the analytical tool developed.

Chapter 2 contains two main parts: a literature review of previous works on the analysis of reinforced concrete frames; a critical look at the nonlinear analysis capabilities of the current state-of-the-art software related to frame structures.

Chapter 3 describes the theory and formulations for nonlinear analysis of reinforced concrete plane frames subjected to monotonic loading conditions and their implementation into VecTor5.

Chapter 4 discusses the application of the developed nonlinear static analysis procedure to previously tested structures to verify the newly implemented algorithms. Important considerations in nonlinear modelling are also discussed.

Chapter 5 describes the theoretical principles for nonlinear analysis of reinforced concrete frames subjected to general loading conditions and their implementation into the analytical procedure developed for monotonic loading conditions.

Chapter 6 discusses the application of the nonlinear analysis procedure developed for general loading conditions to previously tested structures to verify the newly implemented algorithms. Important considerations in nonlinear modelling are also discussed through the use of practical examples to provide guidelines for general modelling applications.

Chapter 7 describes the theoretical principles for nonlinear analysis of reinforced concrete frames subjected to dynamic loading conditions and their implementation into the analytical procedure developed for general loading conditions.

Chapter 8 discusses the application of the newly implemented nonlinear dynamic analysis algorithms to previously tested structures to verify the new algorithms. In addition, guidelines for modelling of reinforced concrete frame-related structures, particularly those subjected to impact loads, are provided.

Chapter 9 includes the summary of the thesis and discusses the final conclusions and recommendations for future research.

In the appendices, additional comparison graphs for the dynamic analyses performed in Chapter 8 and the introduction to the user's manual of VecTor5 are presented.

# CHAPTER 2

# NONLINEAR ANALYSIS OF REINFORCED CONCRETE FRAMES

## 2.1 Chapter Layout

This chapter is organized in two main parts. In the first part (Section 2.2), a brief review of previous studies on the nonlinear analysis of reinforced concrete frames is presented. The nonlinear models developed to date are categorized into three main groups: global models, discrete finite member models and microscopic finite element models. Several examples of each approach are provided. Discrete finite member models are further divided into two categories: lumped nonlinearity models and distributed nonlinearity models. Limitations of the lumped nonlinearity models are emphasized. Being the main focus of this thesis, distributed nonlinearity models are explored in greater detail. Fibre models and the consideration of shear effects are given particular attention.

In the second part (Section 2.3), three simple structures are analyzed using some currently available software in order to gain some insight into current analysis capabilities. Previously tested at the University of Toronto laboratories, the structures are subjected to monotonically increasing loads until failure. The analysis results are compared to simple hand calculations and experimental results. Deficiencies in the analytical predictions are identified. SAP2000 (CSI, 2000) and RUOUMOKO (Carr, 2005) were selected as the software because of their wide availability and use by office design engineers and researchers. In addition, Response-2000 (Bentz, 2000) was used to check hand calculations and provide additional input required by the software being used.

Section 2.3 starts with introductory information on the software used with an emphasis on their analysis capabilities, ease of use, general modelling steps, and the applicability of analysis results to understanding the failure mechanism. It then follows with details of the structures, analytical modelling, and comparison of the results. The section continues with a discussion of the difficulties and possible courses of action available when modelling reinforced concrete frames. Finally, the section concludes with an emphasis on what is needed for better modelling and analysis of reinforced concrete frames.

## 2.2 Review of Previous Studies

Significant effort has been devoted, in the last several decades, to developing models for accurate simulation of the behaviour of reinforced concrete frame elements. One of the earliest motivations for this was the desire to simulate the behaviour of reinforced concrete elements subjected to seismic excitations. In some cases, it was the desire to assess the remaining capacity of a structure after a strong ground motion. It was known in the 1960s that reinforced concrete structures would not elastically respond to the maximum earthquake expected during the life of the structures (Blume et al., 1961). The determination of the behaviour of structural components was essential for the assessment of the inelastic response of the complete structure. The initial stiffness, ultimate capacity and ductility demand were some of the parameters needed for this purpose. Due to complex interactions between various components of real structures, it was not possible to determine the dynamic characteristics only from dynamic tests of scale models. Furthermore, the cost of such tests was often substantial especially for large-scale specimens (Taucer et al., 1991).

These difficulties have largely been overcome by static tests on structural components (e.g., beams, columns and shear walls) and small-scale structural subassemblies (e.g., beam-column joints) under cyclic load reversals. Results from these tests have been used to develop and calibrate analytical models. These analytical models have then been used to evaluate the nonlinear response of complete structures consisting of similar components for which the models were developed. Since the computational cost for data processing and storage was prohibitive, such analytical assessments could only be done for simple models. However rapid advancements in computing power in the last two decades has permitted the use of more complex nonlinear models, thereby reducing dependence on tests of scale models and simple analytical models.

Several models have been proposed to date for the simulation of the nonlinear behaviour of reinforced concrete frame structures. These range from simple nonlinear springs which lump the behaviour of an entire storey into a one degree-of-freedom system to complex three-dimensional finite element formulations that describe the structural behaviour by

integrating the stress-strain relationships of the constituent materials (Filippou and Issa, 1988). These nonlinear models can be categorized, in a more broad sense, into three categories:

**(1) Global Models**: These models constitute the simplest form of all nonlinear models, requiring the least computational power. In these models, the nonlinear behaviour of the entire structure is concentrated at selected degrees of freedom. For example, a building structure can be modelled with only one lateral degree-of-freedom located at each storey level. In this case, each degree-of-freedom represents the interstorey shear-lateral drift behaviour which is developed and calibrated by tests of small-scale structures with similar details. These models are useful for preliminary analyses and for rough estimates of the interstorey drifts and ductility demands. An accurate representation of the structural response should not be expected through the use these models; the accurate determination of internal member forces from the limited degrees of freedom is practically impossible (Taucer et al., 1991). The accuracy of these models can significantly be improved by considering more degrees of freedom. Some of the analytical tools for nonlinear analysis in this category are SAP2000 (CSI, 2000) and RUAUMOKO (Carr, 2005).

**(2) Discrete Finite Member Models:** These models possess more advanced formulations compared to global models, and require more computational power. In these models, the structure is represented by an assemblage of interconnected elements that describe the nonlinear behaviour of reinforced concrete members. The nonlinearity in the constituent materials is introduced either at the element level in an average sense or at the section level as a more advanced case. Consequently, two types of element formulations are possible with the discrete finite member models: lumped nonlinearity member model, and distributed nonlinearity member model. As an example, SAP2000 (CSI, 2000) and RUAUMOKO (Carr, 2005) can be used as a lumped nonlinearity model; TEMPEST (Vecchio, 1987; Vecchio and Collins, 1988), Response-2000 (Bentz, 2000) and DRAIN2DX (Prakash, 1992) are based on distributed nonlinearity formulations. Being

the main focus of this thesis, discrete finite member models are presented in more detail in Sections 2.2.1 and 2.2.2.

**(3) Microscopic Finite Element Models:** These models possess the most advanced formulations developed to date for nonlinear analyses, requiring significant computational power and analysis time. In these models, members and joints are discretized into a large number of finite elements. Constitutive and geometric nonlinearity are typically accounted for at the stress-strain level or averaged over a finite region. Bond modelling between concrete and reinforcement, interface friction at the cracks, creep, relaxation, thermal effects and geometric crack discontinuities are among the physical nonlinearities usually considered by this class of models. The use of these models is still limited to the analysis of critical regions such as beam-column joints or, at most, small structures consisting of one or two bays and one or two storeys. Some of the analytical tools in this class are VecTor2 (Vecchio et al., 2004), UC-Win/WCOMD (Okamura and Maekawa, 1991), and ATENA (Cervenka, 2000).

Discrete finite member models represent the best compromise between simplicity and accuracy in the nonlinear analysis of reinforced concrete frame structures. They are the simplest class of model allowing significant insight into the nonlinear response at both the member and structure level (Taucer et al., 1991). This thesis concentrates on discrete finite member models; therefore, a brief review of previous studies in this realm is presented below.

### 2.2.1 Lumped Nonlinearity Models

The nonlinear behaviour of reinforced concrete frames tends to be concentrated at the ends of beams or columns in the case of seismic loading conditions and at the midspans in the case of static loading conditions. Therefore, an early means of modelling this behaviour was through the use of zero length plastic hinges as nonlinear springs located at the critical locations and connected by linear-elastic elements. Depending on the formulation, these models may incorporate a number of springs connected in series or in parallel.

Clough and Johnston (1966) introduced the earliest parallel component model allowing for a bilinear moment-rotation (M-φ) relation. As depicted in Figure 2.1(a), this element consists of two parallel elements: one elastic-perfectly plastic to simulate yielding and the other perfectly elastic to represent strain-hardening. Takizava (1976) generalized this model to multilinear monotonic behaviour to take account of the cracking of the concrete.

Giberson (1967) formally introduced the series model although it had been reportedly used earlier. As shown in Figure 2.1(b), this model consists of a linear-elastic element with one equivalent nonlinear rotational spring attached to each end in which the inelastic deformations of the member are lumped. This model is more versatile than the original Clough model because more complex hysteretic behaviour can be described.

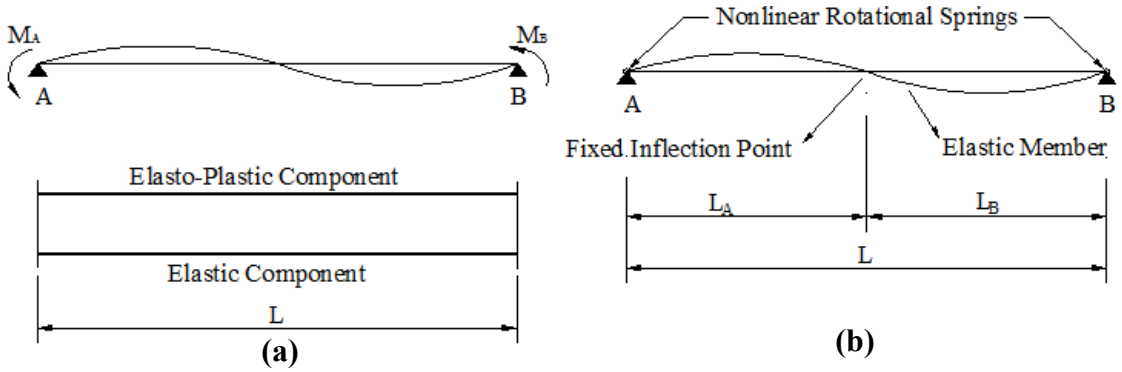


**Figure 2.1** Lumped Plasticity Elements: **(a)** Parallel Model (Clough and Johnston, 1966); **(b)** Series Model (Giberson, 1967) (Figure Adopted from Taucer et al. (1992))

Several lumped plasticity constitutive models have been proposed to date. Such models include cyclic stiffness degradation in flexure and shear (Clough and Benuska, 1967; Takeda et al. 1970; Brancaleoni et al., 1983), pinching under reversal (Banon et al., 1981; Brancaleoni et al., 1983) and fixed-end rotations at the beam-column joint interface due to bar pull-out (Otani, 1974; Filippou and Issa, 1988). Ozdemir (1981) provided continuous hysteretic relations for the nonlinear springs. An extensive discussion of mathematical functions for such models is presented by Iwan (1978). Ciampi and Nicoletti (1986) used an algorithm to ensure a least squares fit between analytical results and experimental data in a formal system identification method; this was done for a selection of parameters for the moment-curvature relation proposed by Brancaleoni et al.

(1983). To overcome some of the limitations of classical plasticity theory for the interaction between axial force and bending moments, Lai et al. (1984) proposed a fibre hinge model. This model is made up of a linear-elastic element spanning through the entire length of the member and one inelastic element at each end. To overcome the limitation of the yield surface of the stress resultant being a function of a reference strain that couples the corresponding displacement component, El-Tawil and Deierlein (2001) developed a bounding surface plasticity model implemented in the stress-resultant space. More details of the above mentioned models and their limitations can be found in Taucer et al. (1991).

Although practical and computationally effective, oversimplification of certain important aspects of hysteretic behaviour of reinforced concrete limits the applicability of the lumped plasticity models proposed to date. Some of the limitations are:

(1) Their inability to consider gradual spread of inelastic deformations into the member as a function of loading history as demonstrated by Charney and Bertero (1982) and Bertero et al. (1984).

(2) Their restrictive assumptions for the determination of the spring parameters prior to the analysis. Anagnostopoulos (1981) demonstrated a strong dependence of model parameters, imposed loading pattern and level of inelastic deformations, all of which are likely to change during a seismic event.

(3) Their inability to adequately consider the deformation softening behaviour typical of reinforced concrete members.

(4) Their applicability to only well-detailed flexure-critical members with large inelastic deformation capacity at the critical regions.

The nonlinear behaviour of reinforced concrete frames can be more accurately simulated through the use of distributed nonlinearity models, which is the focus of this thesis.

### 2.2.2 Distributed Nonlinearity Models

In distributed nonlinearity models, material nonlinearity can take place at any element section. The element behaviour is formulated from weighted integration of the sectional responses. Element integrals are evaluated numerically; therefore, only the behaviour of selected sections along the integration points is monitored. The primary unknowns of the model are either the element deformations or the element forces, which are determined through proper interpolation functions from the global element displacements or forces, respectively. Discrete cracks are treated as smeared over a finite length. The constitutive behaviour of the cross section is either formulated according to classical plasticity theory or is explicitly derived by discretization of the cross section into fibres, as in the case of the spread plasticity models.

Frame models are usually based on either the Hooke-Euler-Bernoulli beam theory (Hooke, 1678 and Bernoulli, 1705) or the Timoshenko beam theory (Gere and Timoshenko, 1991). In the Hooke-Euler-Bernoulli beam theory, plane sections are assumed to remain plane *and* normal to the longitudinal axis of the beam; no shear deformations arise as shown in Figure 2.2(a). In the Timoshenko beam theory, plane sections remain plane *but not* normal to the longitudinal axis; the difference between normal and the plane section rotations is the shear deformation as shown in Figure 2.2(b).

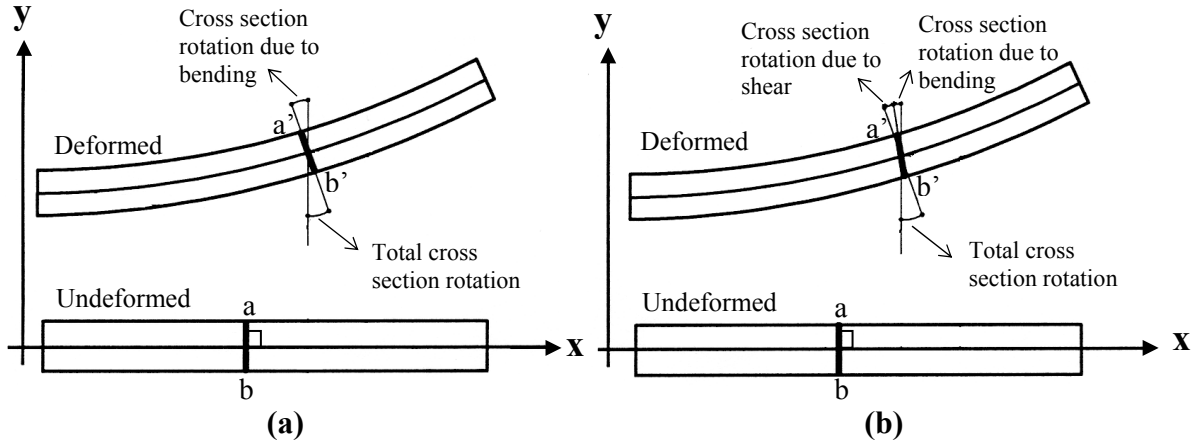


**Figure 2.2** Assumptions: **(a)** Hooke-Euler-Bernoulli Beam Theory; **(b)** Timoshenko Beam Theory (FIB, 2008)

Both Hooke-Euler-Bernoulli beam elements and Timoshenko beam elements can be formulated in the context of either displacement-based or force-based approaches. Defined in terms of the nodal displacements, displacement-based approach uses classical finite element formulations to derive the element stiffness matrix and the element restoring force vector. This approach is used widely as it can be conveniently implemented into a general purpose finite element framework. However, in the case of reinforced concrete frames where material nonlinearities are considered, the displacement-based approach is approximate, requiring refined meshes for satisfactory simulation of the frame response.

Force-based formulations, on the other hand, provide exact solutions regardless of the variations in the beam cross section and material nonlinearity. Computing element resisting forces, however, is a much more complex issue in force-based formulations, arising from the impossibility of directly relating section resisting forces and element resisting forces, as in the case of the displacement-based approach. An iterative method proposed by Spacone et al. (1996) can be used for this purpose. Although there are more computations involved in a force-based approach than in the displacement-based approach, the precision of the force-based approach permits the use of a single element per structural member, thereby giving way to significant reductions in the global degrees of freedom of the structure.

#### 2.2.2.1 Fibre Models Neglecting Shear Effects

Fibre models constitute the most advanced formulation in distributed nonlinearity models. In these models, the element is subdivided into longitudinal fibres as shown in Figure 2.3. The fibre location in the local y, z reference system and the fibre area $A_{fib}$ are geometric characteristics of the cross section. The governing compatibility relationship is based on the “plane sections remain plane” hypothesis (Hooke, 1678; Bernoulli, 1705; Navier, 1826), which forms the basis of the engineering beam theory used in the sectional analysis of concrete members. Equilibrium is satisfied through integrating the responses of the fibres and equating them to the required sectional forces. Appropriate stress-strain

relationships are used for the constituent materials so as to determine the stress distribution on the section for a given strain profile.

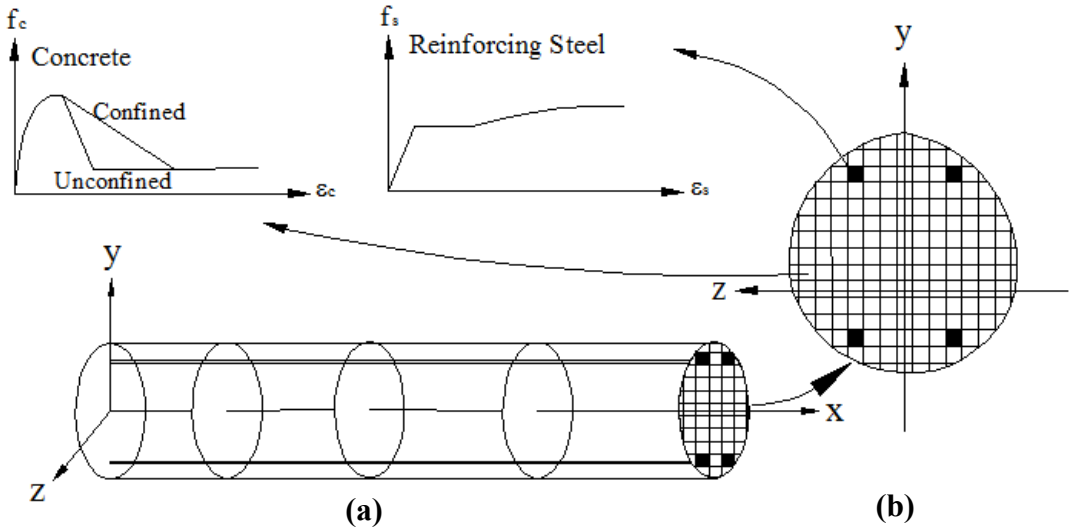


**Figure 2.3** Fibre Element: **(a)** Distribution of Control Sections; **(b)** Section Subdivision into Fibres (Taucer et al, 1991)

The first force-based fibre element model, proposed by Kaba and Mahin (1984), takes into account only uniaxial bending. In this model, the sectional deformations are computed from the element deformations through the use of flexibility-dependent deformation shape functions. Fibre strains are then calculated using sectional deformations, through which fibre stresses and stiffnesses are determined. The section stiffness matrix is assembled and inverted to obtain the flexibility matrix. Although yielding promising results, this model is reported to have convergence problems (Taucer, 1991) and is unable to consider element softening. Zeris and Mahin (1988 and 1991) extended the formulation of Kaba and Mahin (1984) to the biaxial bending case.

The above mentioned models are only able to consider flexural effects. In other words, the accurate simulation of reinforced concrete members dominated by shear or shear-flexure cannot be achieved through these models. It is known, however, that several older structures built according to previous design codes and practices lack sufficient shear reinforcement to guarantee that the flexural capacity of the structure is reached before the shear capacity.

#### 2.2.2.2 Consideration of Shear Effects

Many studies have been carried out to develop analytical models to consider shear effects. Some of the most widely used models are strut-and-tie models and rational theories based on experimental tests.

Strut-and-tie models (Ritter, 1899; and Mörsh 1902) define the flow of forces and stress fields, idealizing a reinforced concrete member as a series of diagonal compression struts (concrete) and tension ties (reinforcement). Although applicable to any structural member, the relative advantage of this method arises only in applications to areas of discontinuity or D-regions, as defined in Section 3.11, where the strain distribution is significantly nonlinear violating the basic assumption (plane sections remain plane) of fibre analysis. Derived from the theory of plasticity, strut-and-tie models represent a design method for complex structural details (FIB, 2008). The strut-and-tie model development for a reinforced concrete member is a subjective and iterative process; different models can be developed for the same member. Following the principles of minimum strain energy, Schlaich et al. (1987) proposed that the model with the least and shortest amount of ties is the most appropriate after cracking, assuming that cracked concrete struts will deform little as compared to the steel-reinforced ties. FIB (1998) stated, however, that this ultimate model may not be valid when evaluating service conditions. As a result, the designer should use his or her judgement in selecting an appropriate geometry when using the strut-and-tie models.

Empirical formulations and rational theories have been developed based on the results of experimental investigations. Arakawa (1969) proposed an empirical approach to determine the ultimate shear strength of reinforced concrete columns and beams. Collins and Mitchell (1980) developed the Compression Field Theory (CFT) for members under torsion and shear, applying Wagner's (1929) tension field approach to reinforced concrete. The CFT treats cracked concrete as a new material with its own stress-strain characteristics, considering cracks as smeared and fully rotating. Equilibrium, compatibility and stress and strain relationships are formulated in terms of average stresses and average strains. Following a comprehensive experimental study, Vecchio and

Collins (1986) proposed the Modified Compression Field Theory (MCFT), which takes into account tensile stresses in the cracked concrete and employs experimentally verified average stress-average strain relationships for cracked concrete. Consideration is also given to the local crack conditions. The MCFT has proven to be a simple yet powerful tool in predicting the load-deformation response of reinforced concrete beams with different amounts of longitudinal and transverse reinforcement (Vecchio, 2000). The formulation of the MCFT is presented in detail in Section 3.2. Okamura and Maekawa (1991) proposed nonlinear models for in-plane shear elements based on similar concepts as the MCFT except for the adoption of the smeared fixed-crack approach. This method has provided successful simulations of the behaviour of reinforced concrete elements as indicated by Mostafaei (2006). Vecchio (2000) proposed the Disturbed Stress Field Model (DSFM) to address the reduced accuracy of the MCFT under specific conditions by extending the MCFT in several aspects. Most importantly, in its compatibility relationships, it includes slip deformations at crack locations caused by shear stresses being not necessarily zero at the crack surface. It also includes refined constitutive relationships for concrete and reinforcement. The Formulation of the DSFM is presented in detail in Section 3.3. Bentz et al. (2005) recently proposed the Simplified Modified Compression Field Theory (SMCFT) to predict the shear strength of reinforced concrete elements for "back of the envelope" calculations.

#### 2.2.2.3 Fibre Models Considering Shear Effects

For considering shear effects, various computation algorithms have been developed based on fibre models. Vecchio and Collins (1988) proposed a fibre model based on the MCFT to predict the response of reinforced concrete beams loaded in combined shear, moment and axial force. In this model, a reinforced or prestressed concrete cross section is discretized into a series of concrete and reinforcing and prestressing steel fibres. A longitudinal strain distribution is assumed for the section based on the engineering beam theory of "plane sections remain plane". A shear stress distribution is assumed for the section such that the sum of the shear stresses in each fibre will be equal to the externally applied shear. Using the longitudinal strain and shear stress present at each fibre, equilibrium and compatibility conditions are satisfied in computing the longitudinal

compressive stress at each fibre. The resultant stresses must balance the applied sectional forces N, M and V, as defined by Eq. 3.103, Eq. 3.104 and Eq. 3.105. Vecchio (1987) implemented this algorithm, as a force-controlled approach into an existing frame analysis procedure resulting in the computational tool TEMPEST. Fulop (1992) expanded the analysis capabilities of TEMPEST by implementing a displacement-controlled approach.

Pentrangeli et al. (1999) proposed a fibre section model incorporating shear deformations. Each fibre in this model has basically three deformations: axial strain, transverse strain (in the direction of stirrups) and shear deformations. Given the section deformations, the axial strain and shear deformations of each fibre are calculated through compatibility. In addition, the stress in the transverse direction is assumed to be zero (i.e., no clamping stresses are considered). The corresponding axial stress, shear stress and vertical deformation are then calculated to find the stiffnesses of each fibre. The sectional stiffness is then determined from the calculated fibre stresses and stiffnesses. The constitutive law for concrete in this force-based model is based on the microplane theory.

Martino et al. (2000) proposed a fibre model incorporating a nonlinear law to describe the shear force-shear deformation response. Although the shear response is decoupled from the axial and bending responses, the implementation of this model into a force-based element permits coupling between axial and bending responses at the element level.

Bentz (2000) proposed a fibre model based on the MCFT to predict the response of reinforced concrete beams, as presented in Section 2.3.2. In this method, he introduced a rigorous longitudinal stiffness method to more accurately determine the nonlinear shear stress distribution on the cross section, as compared to the fibre model of Vecchio and Collins (1988). The full version of the program, Response-2000, is available, free of charge, at www.ecf.utoronto.ca/~bentz.

Bayrak and Sheikh (2001) proposed a plastic hinge analysis technique that can be implemented into a fibre analysis framework to incorporate buckling of longitudinal bars in the analysis. This method includes slightly different displacement compatibility

requirements in addition to equilibrium and constitutive relations to predict the plastic hinge response of tied columns.

Shirai et al. (2001) proposed a macro-element approach to simulate the monotonic and cyclic behaviour of shear-dominated reinforced concrete columns. In this model, the total deformation of the column is decomposed into flexural and shear components. The flexural behaviour is simulated by the fibre element model and the shear behaviour by the so-called shear element model. The model was shown to reproduce the monotonic and cyclic responses of shear-dominated columns tested at the University of California at San Diego (Shirai et al., 2001).

This current study is concerned with the further development and verification of the analytical tool TEMPEST (Vecchio, 1987; Vecchio and Collins, 1988) for the nonlinear analysis of frame structures, with a capability of predicting the post-peak behaviour, based on the DSFM (Vecchio, 2000). The detailed description of the objectives of this study is summarized in Section 1.3.

## 2.3 Review of State-of-the-Art

### 2.3.1 Review of Modelling and Analysis with SAP2000

SAP2000 © (CSI, 2005) is a comprehensive analysis package from Computers and Structures Inc. for structural analysis and design. It is probably the most widely used analysis tool among immediately and easily available analysis software. It can perform linear-elastic static, dynamic and time-history analyses for virtually every material with known engineering properties, as well as nonlinear static and time-history analyses as either a lumped nonlinearity or global model. It possesses a versatile and user-friendly graphical interface as well as a fast and powerful analysis engine. Both structure creation and the result visualization are conveniently done through the graphical interface. Therefore, it is highly suited for practical everyday use by office design engineers.

To perform a nonlinear static analysis of a reinforced concrete frame with SAP2000 v.9.0.3, a model of the structure is first created as if it were a linear-elastic static analysis problem. If automatic hinges are to be used, longitudinal reinforcement details should be

defined including bar sizes, locations, and yield strengths. However, for the shear reinforcement, only the yield stress is required as input; neither the reinforcement ratio nor the tie or stirrup spacing is required.

The next step is to assign hinges to desired locations. This is one of the most critical phases in the nonlinear modelling process with SAP2000. Both hinge locations and selected hinge properties have great influence on the response computed. For the moment hinges, the use of a hinge length in the range of cross section depth, h, is a generally accepted approach (CSI, 2005); therefore, a hinge length of h is used for the moment hinges throughout this study as shown in Figure 2.4. For the selection of the shear hinge length, on the other hand, there is much less information available in the literature. In this study, 1.5 times of the cross section depth is used for the shear hinge lengths. This length is assumed based on CSA A23.3-04 where the term $d_v$ x cot θ is used to determine the length of a shear crack on the longitudinal projection. Assuming an effective shear depth $d_v$ of 0.80 x h, and a shear crack inclination angle of 29 to 35º corresponding to the conditions at ultimate, a shear hinge length of 1.5 x h is found. The selection of larger inclination angles (in the range of 35 to 40º) will result in shorter hinge lengths (in the range of h) and more conservative results. End offsets are also used to account for overlapping cross sections at all connections. The use of rigid or semi-rigid end offsets reduces displacements as they limit rotations of the connecting beams and columns.

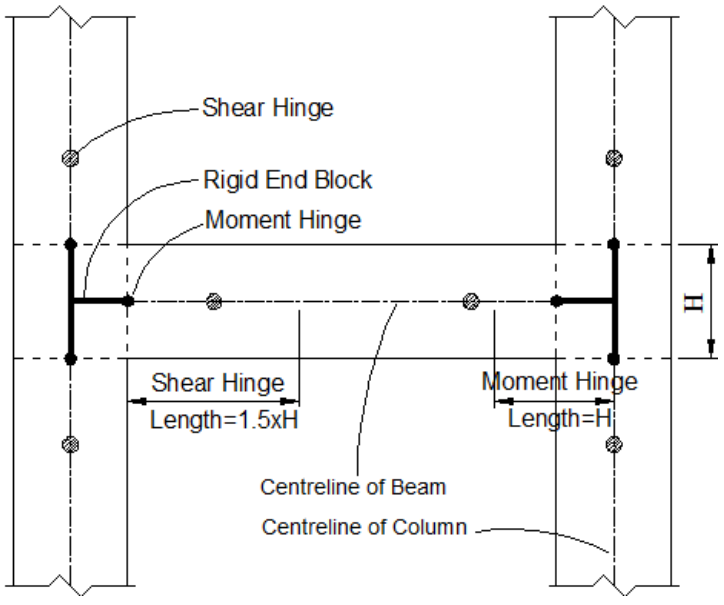


**Figure 2.4** Hinge Locations Assumed in Typical Frame Elements

There are six default hinge options available in version 9.0.3: Axial (P), Torsion (T), Moment (M2 or M3), Shear (V2 or V3), Coupled (P-M2-M3), and Coupled Fibre (P-M2-M3). The hinge properties are calculated by the program for the cross section and reinforcement details provided. For moment hinges, SAP2000 (CSI, 2005) uses Tables 6-7 and 6-8 of FEMA 356 (2000).

The behaviour response assumed by SAP2000 for moment hinges (moment-curvature or moment-rotation relationship) and shear hinges (shear force-shear deformation relationship) is given in Figure 2.5. Based on this curve, no plastic deformation occurs until point B where the hinge yields. This is followed by a yield plateau or strain hardening behaviour until point C which represents the ultimate capacity of the hinge. After point C, the hinge's force capacity immediately drops to point D which corresponds to the residual strength of the hinge. Point E represents the ultimate displacement capacity of the hinge after which total failure of the hinge is reached at point F (CSI, 2005). There are three stages marked between point B and C for information purposes: IO corresponds to immediate occupancy, LS to life safety, and CP to collapse prevention.

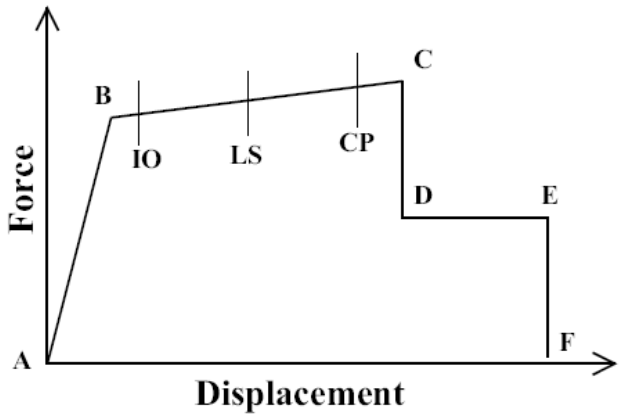


**Figure 2.5** Hinge Behaviour Curve (Figure Adopted from CSI, 2005)

If there is no reinforcement defined and if no design is requested, the program uses the minimum allowable reinforcement ratios for the generation of automatic hinge properties. Generated hinge properties can be explicitly viewed and modified, if desired. For advanced users, user-defined hinges can be created. In this case, the complete flexural or shear hinge behaviour of all hinges defined should be manually supplied to the program.

When using default hinges, the automatically calculated behaviour of the shear hinge raises some questions about its accuracy because no information about the shear reinforcement is required in the modelling process except the yield stress. The shear yield force calculation used by SAP2000 is presented in Eq. 2.1 (CSI, 2005). The notation for this equation is not defined in CSI (2005); the following definitions were provided by the CSI technical support team: $A_s$ is the shear area of the cross section in inch$^2$, typically assumed by SAP2000 as 5/6 times the gross cross-sectional area for rectangular cross sections, $f'_c$ is the compressive strength of concrete in psi, $f_y$ is the yield stress of the shear reinforcement in psi, $A_{sv}$ is the cross-sectional area of the shear reinforcement per unit length in inch, and $d$ is the shear reinforcement spacing in inch. In this case, the resulting shear yield force $V_y$ becomes in psi.

$$V_y = 2 \times A_s \times \sqrt{f'_c} + f_y \times A_{sv} \times d \tag{2.1}$$

The next step is to define the load application procedure and nonlinear parameters. Load application can either be force or displacement-controlled. Nonlinear parameters include the selection of small or large displacements and P-Δ effects. The hinge unloading method is also selected here. The 'unload entire structure' option is recommended by CSI (2005) and thus used in this study. Based on this assumption, when a hinge drops its load (i.e., reaches Point D in Figure 2.5), the entire structure is unloaded until that hinge reaches its load immediately before the load drop (i.e., Point C in Figure 2.5). The program then reverts to increasing the applied load on the whole structure; other parts of the structure may now pick up the load that was removed from the unloaded hinge. There are other options such as 'apply local redistribution' and 'restart using secant stiffnesses', which are recommended by CSI (2005) if the 'unload entire structure' option could not find a solution. This phenomenon was not encountered in this study.

After the analysis, the load versus deflection curve can be visualized through the graphical interface or can be printed out in a data file. In addition, the hinge conditions (B, IO, LS, CP, D, and E) may be seen at each load stage using the graphical interface, which is useful when evaluating the failure mechanism of the structure.

### 2.3.2 Review of Modelling and Analysis with Response-2000

Developed at the University of Toronto as a distributed nonlinearity fibre model specifically for reinforced concrete, Response-2000 (Bentz, 2000) is a nonlinear sectional analysis program for beam-columns based on the MCFT (Vecchio and Collins, 1986). The program allows for axial force, bending moment, shear force, thermal and shrinkage strains, as well as time-dependent creep strains to be applied to the cross section. It is also capable of performing pushover analyses of simply supported beams up to the peak load. The program performs a rigorous dual-section analysis to determine the shear stress distribution on the cross section by the axial stiffness method developed by Bentz (2000). In sectional analysis mode, the program can predict a wide range of responses including moment-curvature, shear force-shear strain and moment-axial force interaction responses, all of which are used herein either to check hand calculations performed or to supply necessary input for SAP2000 and RUAUMOKO. The program has a user-friendly interface for both the model creation and results visualization, which provides ample information, encouraging more detailed investigation of the analysis results. Consequently, it is a convenient tool for both structural engineers and researchers.

In order to perform a sectional analysis, cross section details including both the longitudinal and transverse reinforcement configurations as well as the reinforcement and concrete properties are input using the graphical interface. When the model is finalized, the analysis can be initiated through the solve menu.

When the analysis is complete, the program immediately switches to a display of the analysis results. All relevant graphs can be seen in detail on the screen, and data for desired graphs can be acquired easily for further manipulation, for example, in a spreadsheet program. Also notable is the graphical representation of crack orientation and crack widths which may help the user understand the dominant behaviour of the cross section or beam member.

### 2.3.3 Review of Modelling and Analysis with RUAUMOKO

Developed at the University of Canterbury, RUAUMOKO (Carr, 2005) is an analysis program mainly intended for buildings and bridges subjected to earthquake and other dynamic excitations. Based on either a lumped nonlinearity or a global model, the program is capable of performing nonlinear static and dynamic analyses for a wide range of materials including steel, reinforced concrete, timber, masonry and soil. With the version dated 14 February 2006, the structure creation and result visualization is done using standard text-editors such as Microsoft Windows Notepad.

In order to model a structure for analysis with RUAUMOKO, one input text file is usually required which includes principal analysis options, frame control parameters, output intervals and plotting control parameters, iteration control and wave velocities, nodal points and member incidence list, section properties, lumped nodal weights, external static loads, dynamic load factors, earthquake accelerograms and so on. The text input file has to be prepared from nil based on the structure being analyzed, analysis type, and loading conditions; therefore, the users' manuals should be carefully studied and necessary input parameters should be carefully selected out of a large number of possible values and options. This is a complex process and caution should be exercised.

It is necessary to calculate the complete axial force (N) versus moment (M) interaction diagram for each cross section used and to supply six predetermined (N, M) data points to the program as input. This calculation can be quite laborious; therefore, it usually requires the use of other software such as Response-2000. In addition, if there are forces acting on the span of the members, fixed end forces for each member have to be calculated and supplied to the program manually. As a result, the input text file creation for RUAUMOKO may take considerable time depending on the structure being analyzed.

It is necessary to select one of the fifty-two available hysteresis models for the material used. The more comprehensive the model, the more input related to the selected model is required. In Figure 2.6, one of the complex hysteresis rules and required input parameters is presented.

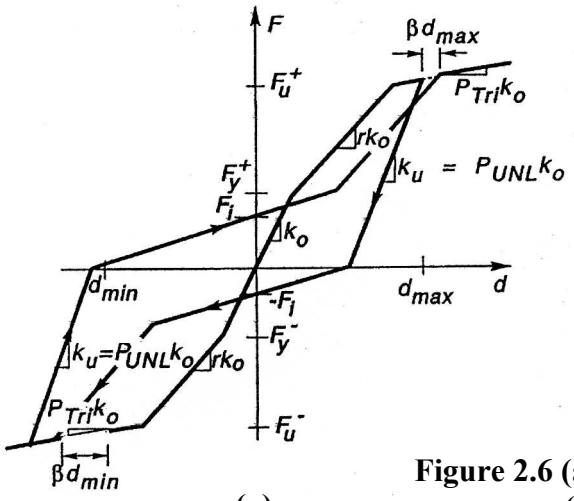


(a)

| | | |
|---|---|---|
| **FU** | Ultimate force or moment | ( > 0.0) |
| **FI** | Intercept force or moment | ( > 0.0) |
| **PTRI** | Tri-linear factor beyond ultimate force or moment | |
| **PUNL** | Unloading stiffness factor | ( > 1.0) |
| **GAP+** | Initial slackness, positive axis | ( > 0.0) |
| **GAP-** | Initial slackness, negative axis | ( < 0.0) |
| **BETA** | Beta or Softening factor | ( ≥ 1.0) |
| **ALPHA** | Reloading or Pinch power factor | ( ≤ 1.0) |
| **LOOP** | = 0 Loop as defined | |
| | = 1 Modified loop | |

**(b)**

**Figure 2.6 (a)** Wayne Stewart Degrading Stiffness Hysteresis, **(b)** Input Parameters Required for this Hysteresis (Carr, 2005)

In this study, one of the simpler models, the elasto-plastic hysteresis, is selected as it does not require any additional input (Figure 2.7).

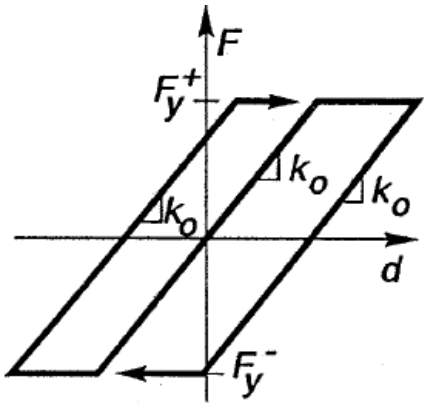


**Figure 2.7** Elasto-plastic Hysteresis (Carr, 2004)

One of the most important decisions in the modelling process is whether to include inelastic shear deformations or not. This decision is directly related to the structural behaviour and if shear-dominated behaviour is expected, inelastic shear deformations should be included. However, such an inclusion requires additional input as shown in Figure 2.8 and Table 2.1. There are several uncertainties and difficulties associated with the calculation of the required values. One relates to the interaction of axial force and shear yield force. It is known that the presence of axial compression force generally increases the shear yield force and therefore should be considered in such a calculation.

Another is that the shear yield force may be dependent on the ratio of bending moment to shear, depending on the theory used for the consideration of shear strength. Therefore, dependent on the applied load, the shear hinge properties should change which will require an iterative process until the peak load is reached. In addition, the SINA hysteresis required (Figure 2.8) will likely be different at each hinge location (at each end of each member used) due to the changing M/V ratio and axial forces, which may require significant pre-calculations for the definition of the SINA hysteresis. For these reasons, it is very difficult and laborious to consider inelastic shear behaviour in the model.

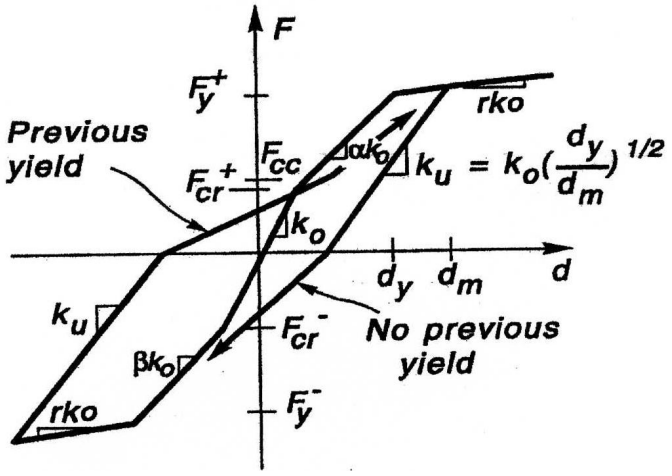


**Figure 2.8** SINA Hysteresis for the Consideration of Inelastic Shear Behaviour (Carr, 2005)

**Table 2.1** Input Parameters for the Consideration of Inelastic Shear Behaviour (Carr, 2005)

| | | |
|---|---|---|
| **Vy** | Shear yield strength | ( > 0.0) |
| **Vcr** | Shear cracking strength | (> 0.0) |
| **Vee** | Shear crack closing coree | (> 0.0) |
| **Alfa** | Bi-linear factor, cracking to yield | ( R < Alfa < 0.0) |
| **R** | Tri-linear factor after yield | (> 0.01) |
| **Duct1** | Shear ductility where strength degradation starts<br>If less than 1.0 then no shear strength degradation | |
| **Duct2** | Shear ductility where shear strength degradation stops | (> Duct1) |
| **Vres** | Residual shear strength as proportion of Vy | (0.01 < Vres < 1.0) |
| **Phi1** | Flexural ductility where shear strength degradation starts<br>If less than 1.0 then no shear strength degradation | |
| **Phi2** | Flexural ductility where shear strength degradation stops | (>Phi1) |
| **Pres** | Residual shear strength as proportion of Vy<br>(Note: Vres*Pres*Vy must be somewhat greater than Vcr) | (0.01 < Pres < 1.0) |
| **Ido** | =0 In-elastic shear yield may occur (default)<br>=1 Retrofit assumed, message printed, shear remains elastic.<br>=2 Failure assumed, message printed, analysis terminated. | |

Another important consideration in the modelling process is whether to include degrading material strengths. It was shown by Vecchio and Collins (1986) that the compression response of cracked concrete is characterized by significant degrees of softening arising from the effects of transverse cracking. This behaviour will likely be an important mechanism when loading the structure to failure or when performing a cyclic or reversed cyclic analysis. Therefore, modelling of the degrading strength should be included in the model. However, such an inclusion requires additional input as shown in Figure 2.9 and Table 2.2.

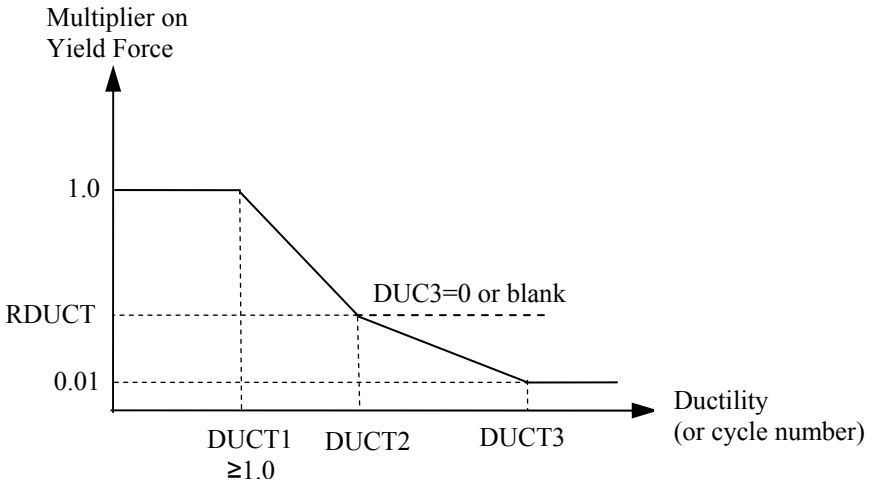


**Figure 2.9** Strength Reduction Variation (Carr, 2005)

**Table 2.2** Input Parameters for the Consideration of Strength Reduction (Carr, 2005)

| | | |
|---|---|---|
| **DUCT1** | Ductility at which degradation begins | ( > 1.0) |
| **DUCT2** | Ductility at which degradation stops | ( > DUCT1) |
| **RDUCT** | Residual strength as a fraction of the initial yield strength | |
| **DUCT3** | Ductility at 0.01 initial strength | ( blank or> DUCT2) |
| **RCYC** | % reduction of strength per cycle of inelastic behaviour (ILOS =4, 5, 6 or 7 only) | |

There are uncertainties and difficulties in the calculation of the strength reduction parameters. One of them is that the principal tensile strain in the concrete affects this degradation and should be considered. For this reason, it is very difficult, if not impossible, to consider degrading material strength behaviour in the model as it depends on the strain state.

In this study, due to the reasons mentioned above, neither inelastic shear behaviour nor strength degradation is considered in the RUAUMOKO models used.

When the input file is complete, an analysis can be initiated by running RUAUMOKO2D.exe and answering additional questions interactively. When the analysis is complete, the deflected shape of the structure is displayed momentarily on the screen. The program creates a single text file which includes member end actions and maximum member ductilities for each of the load stage considered. Other than member end forces and ductilities, however, the program does not provide information on member conditions which may help in understanding the failure mechanism of the structure. Load versus deflection curves can be obtained by help of the data extraction program provided.

In the author's view, to perform a pushover analysis of a reinforced concrete frame, RUAUMOKO requires a certain level of experience in nonlinear modelling of frame structures and a good understanding of material behaviour so that the appropriate behaviour models can be selected. The user will probably need secondary software to obtain the input values required by RUAUMOKO.

To illustrate the use of the software described above and to compare the analytical results to hand calculations, three simple structures, previously tested at the laboratories of the University of Toronto, are examined in the following sections.

### 2.3.4 Nonlinear Analysis of a Flexure-Critical Beam

The beam in consideration was taken from an experimental study which was carried out at the University of Toronto in 2003 to investigate the long term structural performance of shear- and flexure-critical reinforced concrete beams (Aguilera, 2003). Having a 270 x 400 mm cross section, Beam B1 was simply supported and spanned a clear distance of 3.65 m between two roller supports, leaving 350 mm overhang on each side (Figure 2.10). The loading involved the application of two point loads in a displacement-controlled mode. The concrete strength was determined from standard cylinders. The

longitudinal and transverse reinforcem ent properties were found fr om standard coupon tests, as shown in Table 2.3.

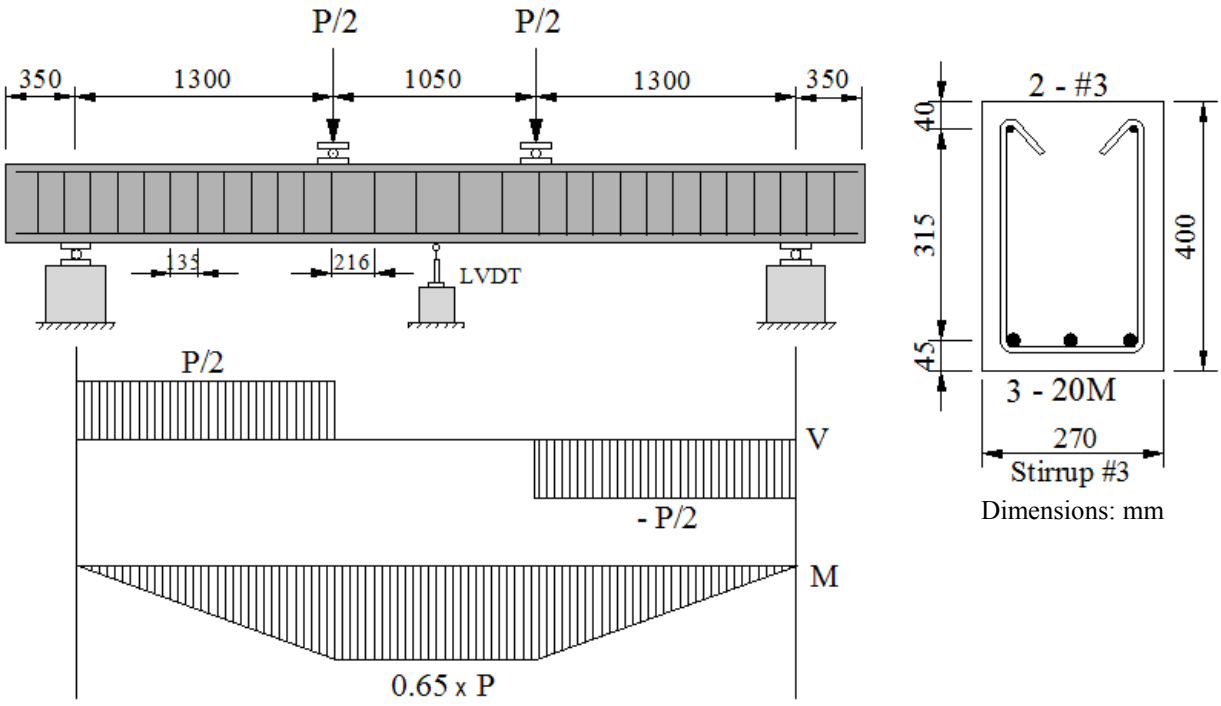


**Figure 2.10** Details of Beam B1

**Table 2.3** Material Properties of the Beam B1

| | Reinforcement | | | | | | | | Concrete | | | | |
|---|---|---|---|---|---|---|---|---|---|---|---|---|---|
| | $A_s$ ($mm^2$) | $d_b$ (mm) | $f_y$ (MPa) | $f_u$ (MPa) | $E_s$ (MPa) | $E_{sh}$ (MPa) | $\varepsilon_{sh}$ ($x10^{-3}$) | $\varepsilon_u$ ($x10^{-3}$) | $f'_c$ (MPa) | $\varepsilon_0$ ($x10^{-3}$) | $E_c$ (MPa) | $G_c$ (MPa) | μ |
| **20M** | 300 | 19.5 | 429 | 621 | 206000 | 1605 | 9.3 | 128.9 | 33.8 | 2.00* | 26200* | 10917* | 0.2* |
| **#3** | 71 | 9.5 | 507 | 779 | 199000 | 2433 | 9.5 | 121.3 | | | | | |

*assumed

### 2.3.4.1 Hand Calculation

*Cracking Load*

The load w hich caus es first crack ing at the bo ttom face of the beam at the m idspan was calculated b ased on tran sformed section properties ($A_t$ and $I_t$). The crac king s tress was assumed to be $f_{cr} = 0.33 \times \sqrt{f_c'} = 1.92\ MPa$ as suggested by CSA A23.3-04. Based on this calculation, the cracking load w as found to be 24.6 kN, while the cracking curvature was 0.76 x $10^{-6}$ /mm based on an effective stiffness value of 0.5x$EI_t$ as suggested by Table 6.5 of FEMA 356 (2000).

*Moment-Curvature Relationship*

The moment-curvature relationship was calculated through the use of rectangular stress blocks, with the assumption of a parabolic stress-strain curve, in Eq. 2.2 and Eq. 2.3, where $\varepsilon_t$ is the strain at the top of the cross section and $\varepsilon_o$ is the strain corresponding to the peak stress of concrete (Collins and Mitchell, 1991).

$$\beta_1 = \frac{4 - \varepsilon_t / \varepsilon_o}{6 - 2 \times \varepsilon_t / \varepsilon_o} \tag{2.2}$$

$$\alpha_1 \times \beta_1 = \frac{\varepsilon_t}{\varepsilon_t} - \frac{1}{3} \times \left( \frac{\varepsilon_t}{\varepsilon_o} \right)^2 \tag{2.3}$$

In order to verify the calculations, Response-2000 was used. A similar response was obtained up to the yield strain of the tensile steel; afterwards, Response-2000 predicted higher moment values (Figure 2.11). This difference was caused by the assumption of a parabolic stress strain curve in the rectangular stress block approach. However, based on a layer-by-layer sectional analysis approach, Response-2000 uses a more general stress-strain response for concrete, which keeps the analysis continuing with the strain hardening behaviour of steel (Bentz, 2000). For consistency, the hand-calculated moment-curvature response is used in the following calculations.

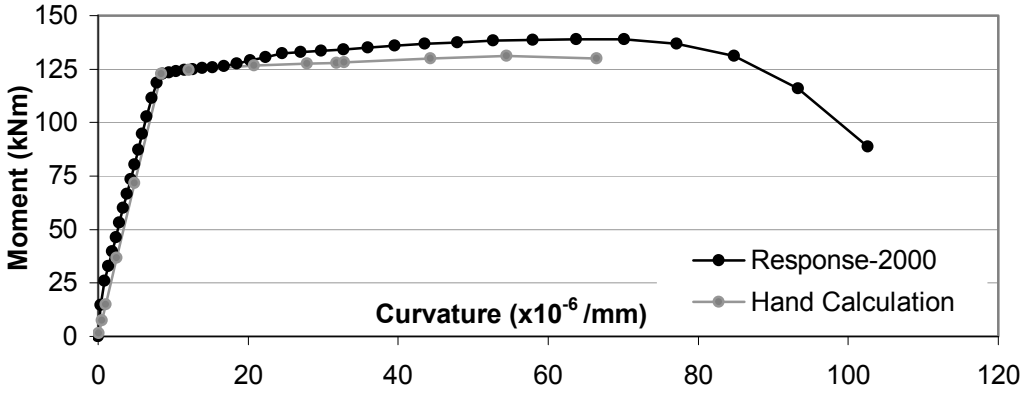


**Figure 2.11** Moment-Curvature Response of Beam B1

Based on the response shown on Figure 2.11 (hand calculation), the yield moment and yield curvature are 122.9 kNm and 8.4 x $10^{-6}$ /mm, while ultimate moment and ultimate curvature are 131.2 kNm and 54.4 x $10^{-6}$ /mm.

*Midspan Deflection*

The midspan deflection, $\delta$, calculation was carried out using the elastic formula of Eq. 2.4, based on the effective stiffness value of 0.5 xEI as suggested by Table 6.5 of FEMA 356 (2000). In Eq. 2.4, $P$ is the load in N, $E$ is the modulus of elasticity of concrete in MPa and I is the moment of inertia of the beam section in mm$^4$. For the ultimate load of P = 201.8 kN, the ultimate deflection was calculated to be 9.75 mm.

$$\delta = \frac{0.90 \times P}{0.5 \times E \times I} \times 10^9 \quad (mm) \tag{2.4}$$

### 2.3.4.2 Analysis with SAP2000

In the SAP2000 modelling of the beam, the cross section was defined with exactly the same material properties as used in the hand calculation. The concrete shear area was input as 0.09 m$^2$, being 5/6 times the gross-sectional area as recommended by CSI (2005). One default moment hinge was placed at the midspan of the beam and the analysis was performed in the displacement-controlled mode (Figure 2.12). It should be noted that neither the spacing or the percentage of the shear reinforcement nor the strain hardening properties of the longitudinal reinforcement are required by the program.

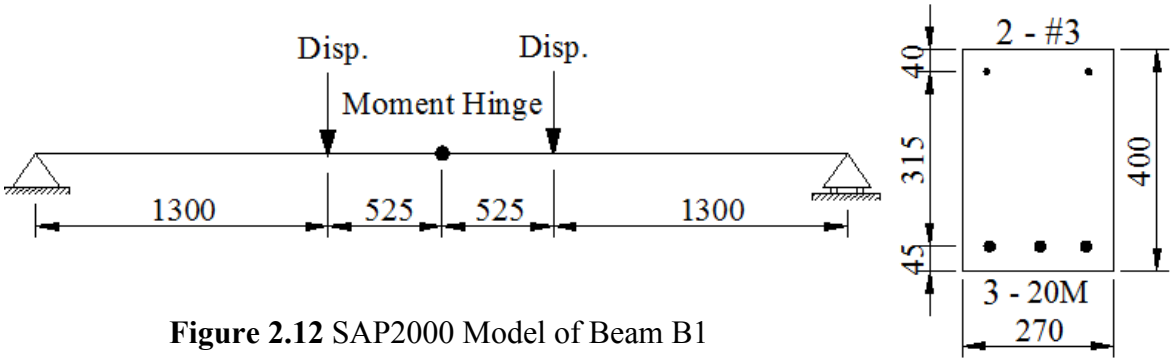


**Figure 2.12** SAP2000 Model of Beam B1

At the end of analysis, the SAP2000 output indicated that the default hinge properties were calculated to be $M_y = 127.5\,kNm$ and $M_u = 127.6\,kNm$.

### 2.3.4.3 Analysis with RUAUMOKO

For the RUAUMOKO model, a bending moment - axial force interaction diagram is required for the cross section of the beam, for which Response-2000 was used. The resultant graph is presented in Figure 2.13.

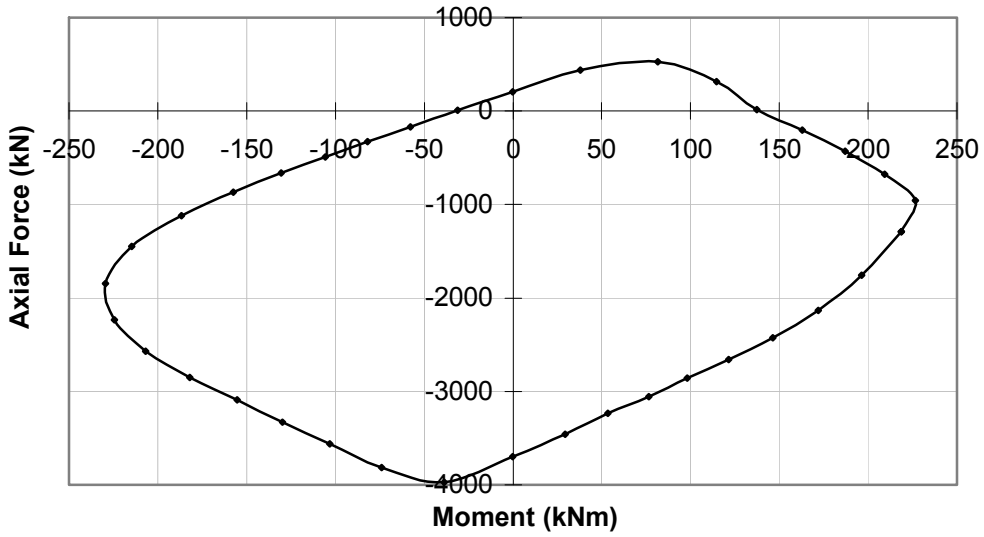


**Figure 2.13** Moment-Axial Force Interaction Response of Beam B1

The model used for the RUAUMOKO analysis was essentially the same as the SAP2000 model (Figure 2.12). The only difference was that three members were used with a moment hinge at each end. The hinge length was assumed to be the same as the depth of the cross section; that is, 400 mm. It was noted that changing the hinge length had no influence on the results.

From the RUAUMOKO analysis, the beam's ultimate moment capacity was calculated to be 137.5 kNm, which was obvious from the input interaction diagram for zero axial load.

### 2.3.4.4 Comparison of the Analytical and Experimental Results

As seen in Table 2.4, the cracking load of the beam was predicted reasonably well by hand calculation. However, it was not possible to determine the cracking load by either SAP2000 or RUAUMOKO, as these programs use linear-elastic calculations until the yield point of the hinge is reached without considering the cracking of concrete.

Both computer programs and hand calculations produced similar yield loads for the beam with a maximum deviation of 6% from the experimental value for the hand calculation. As for the ultimate load, similar predictions were obtained with a maximum deviation of 11% from the experimental value in the SAP2000 calculation.

The stiffness of the beam was overestimated even though an effective stiffness value of 0.5 x EI was used; the yield displacement was predicted by all three calculations to be slightly more than half of the experimental value.

The failure modes were found to be reasonably consistent with the experimental observations. As defined in the modelling process, both programs predicted flexural yielding of the hinges.

**Table 2.4** Comparison of Analytical and Experimental Results for Beam B1

| | | Hand Calc. | SAP2000 | Ruaumoko | Experiment |
|---|---|---|---|---|---|
| Cracking | Load (kN) | 26.4 | n/a | n/a | 31.0+ |
| | Curvature (rad/km) | 0.76 | n/a | n/a | n/r |
| | Midspan Disp. (mm) | 0.6 | n/a | n/a | 1.0+ |
| Yielding | Load (kN) | 189.1 | 196.1 | 211.5 | 200.0 |
| | Curvature (rad/km) | 8.4 | n/a | n/a | n/r |
| | Midspan Disp. (mm) | 9.1 | 9.5 | 10.2 | 17.2 |
| Ultimate | Load (kN) | 201.8 | 196.2 | 211.5 | 218.0 |
| | Curvature (rad/km) | 54.4 | n/a | n/a | 48.0 |
| | Midspan Disp. (mm) | 9.8 | 32.3 | n/a | >50 |
| | Behaviour | Flexure | Flexure | Flexure | Flexure |

n/a: not available n/r: not reported + estimated

Based on Figure 2.14, neither of the programs was able to predict the displacement capacity of the beam with reasonable accuracy. SAP2000 estimated the failure of the beam occurring at a significantly less midspan displacement than that of the experiment. As for the RUAUMOKO analysis, it was not possible to determine the ultimate displacement; the same load was returned by the program while midspan displacement was increasing. This behaviour occurred due to the elastic-plastic hinge assumption made. It should be noted that the experimental graph reported in Aguilera (2003) was

terminated at a 50 mm lateral displacement; the experimental failure displacement of the beam was likely higher than 50 mm.

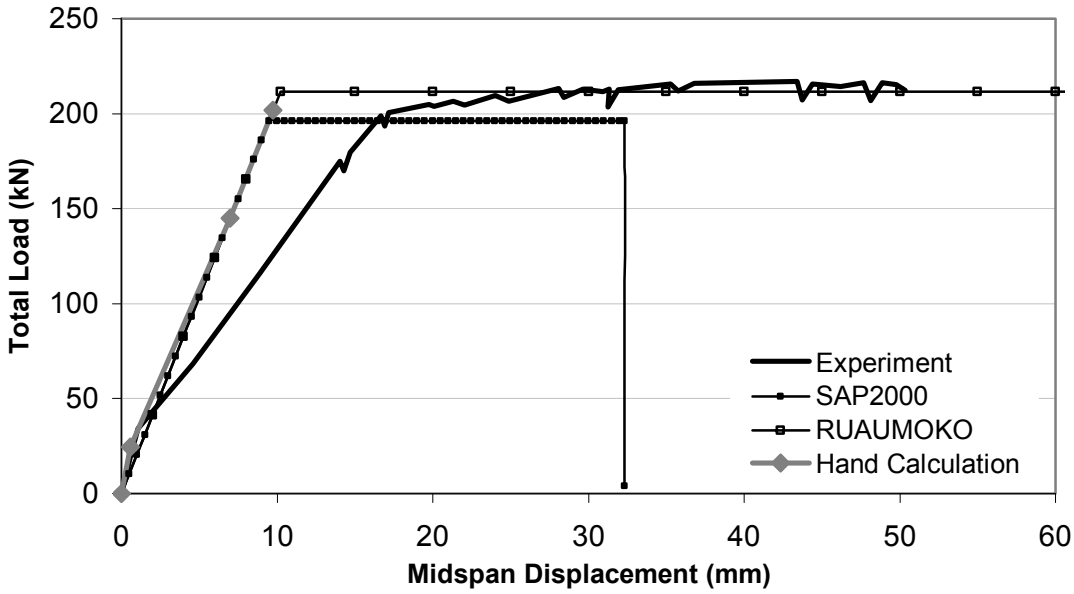


**Figure 2.14** Comparison of Load-Deflection Responses for Beam B1

It is obvious from Figure 2.14 that both SAP2000 and RUAUMOKO performed a linear-elastic analysis until the yielding of the midspan hinge. After that point, SAP2000 conservatively neglected the strain hardening effects of the reinforcement and returned the same load value until the plastic deformation capacity of the hinge was reached and the hinge dropped load (Point F in Figure 2.5). RUAUMOKO, on the other hand, continued with the analysis, predicting the same yield load under increasing midspan displacement.

In conclusion, both the first yielding and the ultimate load capacity of this flexure-critical simply supported beam were predicted accurately. As for the failure displacement, a reasonable estimate was not achieved.

### 2.3.5 Nonlinear Analysis of a Flexure-Critical Frame

A one-span, two-storey, flexure-critical reinforced concrete frame was tested by Vecchio and Emara (1992) to gain further insight into the magnitude and influence of shear deformations in flexure-critical frame structures and to assess the accuracy of analytical procedures developed.

The frame was constructed with a centre-to-centre span of 3500 mm, a storey height of 2000 mm and an overall height of 4600 mm as shown in Figure 2.15. All beams and columns were 300 mm wide and 400 mm deep, while the base was 800 mm wide and 400 mm deep. The frame was built integral with a large, heavily reinforced concrete base to create an essentially fixed foundation. The base was fixed to the lab floor using ten pairs of bolts which were post-tensioned to prevent slip. Material properties were determined from concrete cylinder tests and steel coupon tests, as summarized in Table 2.5.

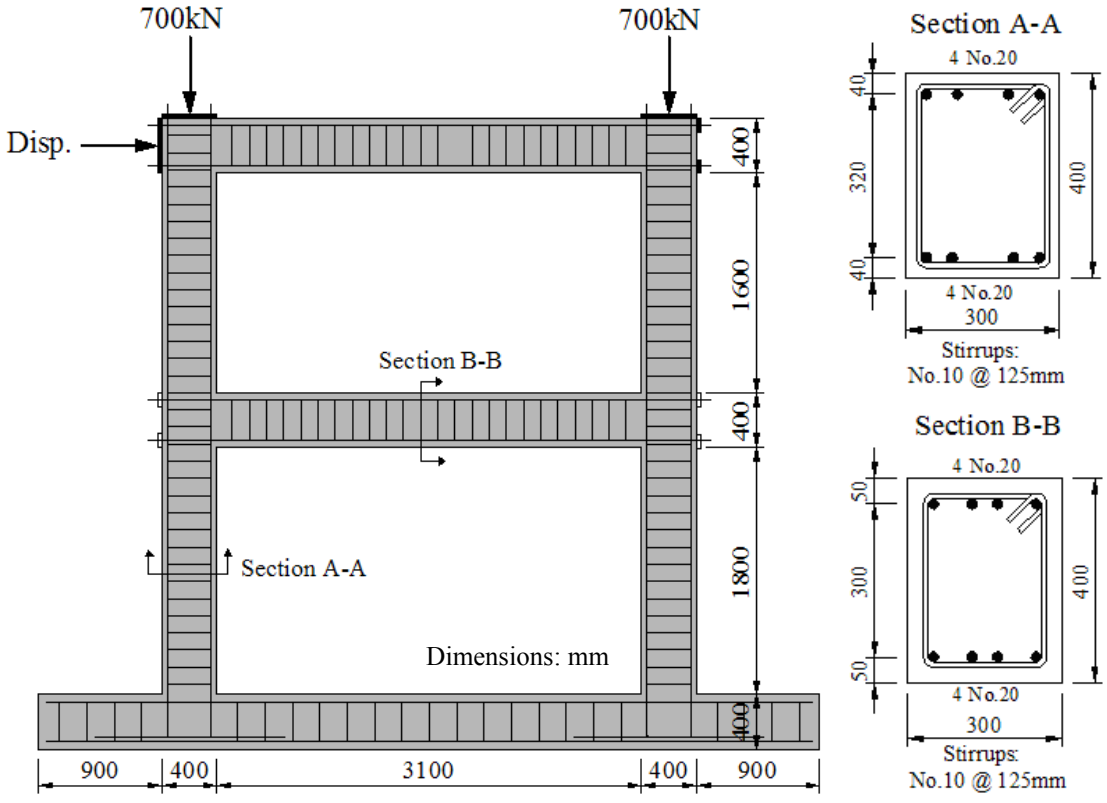


**Figure 2.15** Details of Vecchio and Emara Frame

**Table 2.5** Material Properties of Vecchio and Emara Frame

| | Reinforcement | | | | | | | | Concrete | | | | |
|---|---|---|---|---|---|---|---|---|---|---|---|---|---|
| | $A_s$ ($mm^2$) | $d_b$ (mm) | $f_y$ (MPa) | $f_u$ (MPa) | $E_s$ (MPa) | $E_{sh}$ (MPa) | $\varepsilon_{sh}$ ($x10^{-3}$) | $\varepsilon_u$ ($x10^{-3}$) | $f'_c$ (MPa) | $\varepsilon_0$ ($x10^{-3}$) | $E_c$ (MPa) | $G_c$ (MPa) | μ |
| **No.20** | 300 | 19.5 | 418 | 596 | 192500 | 3100 | 9.5 | 66.9 | 30 | 1.85 | 23674 | 9864* | 0.2* |
| **No.10** | 100 | 11.3 | 454 | 640 | 200000* | 3100* | 9.5* | 69.5 | | | | | |

* estimated

The testing of the frame involved applying an axial load of 700 kN to each column, maintained constant throughout the test, while monotonically applying a lateral load to the second storey beam until the ultimate capacity of the frame was reached. The column loads were provided by two pairs of 450 kN capacity hydraulic jacks, applied through two transverse beams in the force-controlled mode. The lateral load was provided by a 1000 kN capacity actuator, mounted laterally against a reacting strong wall, in a displacement mode.

### 2.3.5.1 Hand Calculation

As there were significant axial forces acting, the hand calculation was done in an iterative manner in order to take account of the change in the axial force values as the lateral force on the frame increased. First, the ultimate moment capacities of cross sections were determined using stress block factors. In this calculation, the initial axial forces of members were used; that is, 700 kN axial compression for the columns and no axial force for the beams. The beam ultimate moment capacity was calculated to be 174 kNm by hand calculation and 206 kNm by Response-2000. As Response-2000 includes strain hardening of steel and considers a more general concrete stress-strain response, its prediction of 206 kNm is used as the ultimate capacity. Then, using linear-elastic frame analyses, a lateral load was determined which would cause the acting moment inside the clear span of one of the members to reach the corresponding calculated flexural capacity. In this calculation, the effective stiffness values recommended by FEMA 356 (2000) were used as shown in Figure 2.16. Corresponding to that lateral load, the axial force values for each member were determined and the ultimate moment capacities of the cross sections were re-calculated accordingly. A new estimate of lateral load was determined and the same procedure was carried on in an iterative manner.

### 2.3.5 Nonlinear Analysis of a Flexure-Critical Frame

A one-span, two-storey, flexure-critical reinforced concrete frame was tested by Vecchio and Emara (1992) to gain further insight into the magnitude and influence of shear deformations in flexure-critical frame structures and to assess the accuracy of analytical procedures developed.

The frame was constructed with a centre-to-centre span of 3500 mm, a storey height of 2000 mm and an overall height of 4600 mm as shown in Figure 2.15. All beams and columns were 300 mm wide and 400 mm deep, while the base was 800 mm wide and 400 mm deep. The frame was built integral with a large, heavily reinforced concrete base to create an essentially fixed foundation. The base was fixed to the lab floor using ten pairs of bolts which were post-tensioned to prevent slip. Material properties were determined from concrete cylinder tests and steel coupon tests, as summarized in Table 2.5.

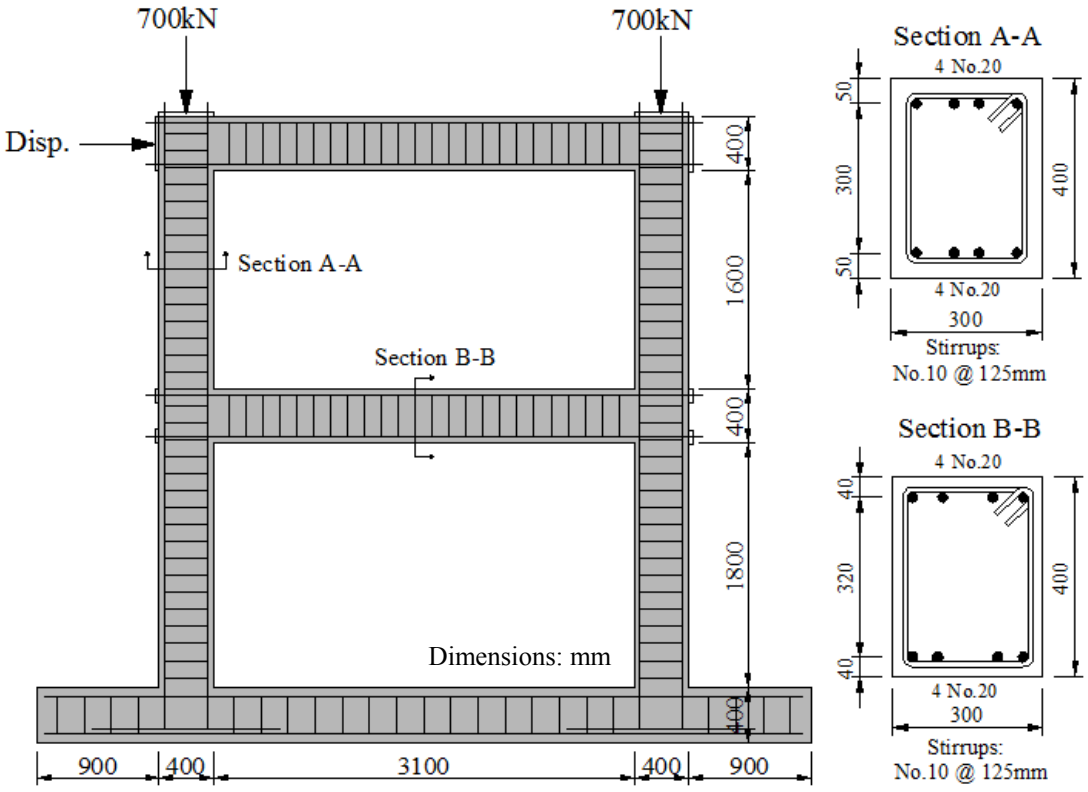


**Figure 2.15** Details of Vecchio and Emara Frame

corresponding PM interaction surface in the plane of the frame. The automatic hinge calculations performed by SAP2000 are mainly based on FEMA 356 (2000).

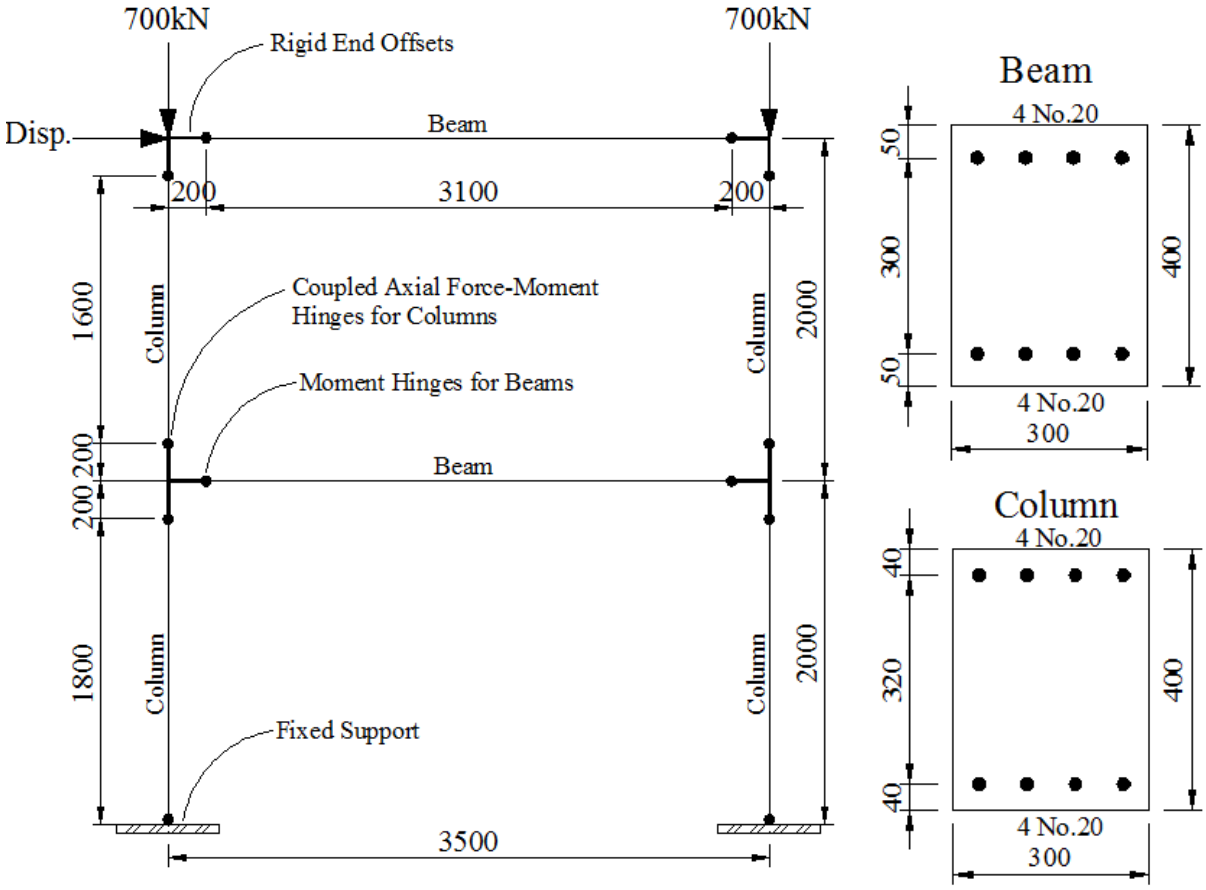


**Figure 2.17** SAP2000 Model of Vecchio and Emara Frame

As coupled automatic PM hinges were not available for the beams, default moment hinges were defined similar to those of the columns. The output indicated that SAP2000 calculated the yield moment for the cross section based on the longitudinal reinforcement details provided and assumed almost the same moment capacity for the ultimate condition.

Rigid end offsets with rigid end factors of 1.0, which correspond to a fully rigid connection, were used in order to account for the overlapping portions of the beam-column connections as suggested by FEMA 356 (2000) Clause 6.5.2.

Neither the transverse reinforcement spacing or ratio nor the strain hardening properties of the longitudinal steel were required by the program as input.

### 2.3.5.3 Analysis with RUAUMOKO

The analytical model used in the RUAUMOKO analysis is shown in Figure 2.18. To be consistent with the other analyses, fully rigid end zones were used and the analysis was performed with the assumption of small displacements. Hinge lengths were also assumed to be the same as the section height; namely, 400mm. It was later noted that the use of different hinge length did not affect the results.

As mentioned previously, RUAUMOKO requires complete M-N interaction responses for all of the cross sections used. For simplicity, only one cross section with 25 mm clear cover was used, rather than two cross sections with 20 mm and 30 mm clear covers. The interaction diagram to be supplied to RUAUMOKO was calculated by both hand and Response-2000. The two responses were found to be quite similar.

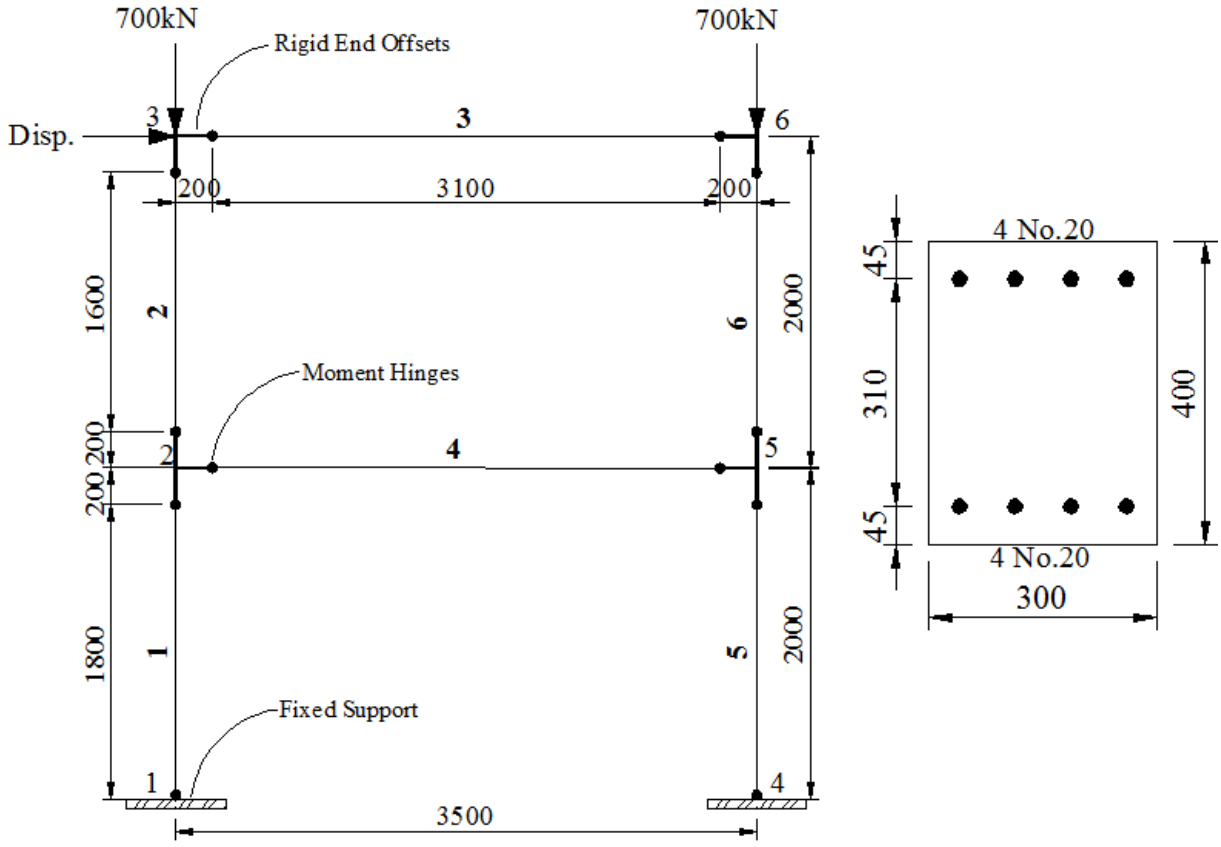


**Figure 2.18** RUAUMOKO Model of Vecchio and Emara Frame

### 2.3.5.4 Comparison of the Analytical and Experimental Results

As seen in Table 2.6, both programs and the hand calculation predicted similar yield loads for the frame with a maximum deviation of 11 percent from the experimental value in the SAP2000 calculation. Similarly, the peak load capacity of the frame was predicted with good accuracy with a maximum deviation of 7 percent from the experimental value in the SAP2000 calculation. This underestimation was expected because SAP2000 neglects the strain hardening of the longitudinal reinforcement, thereby providing a lower bound estimate.

**Table 2.6** Comparison of Analytical and Experimental Results for Vecchio and Emara Frame

| | | Hand Calc. | SAP2000 | RUAUMOKO | Experiment |
|---|---|---|---|---|---|
| Yielding | Load (kN) | 252 | 238 | 265 | 264 |
| | Disp. (mm) | 18.7 | 18.9 | 22.0 | 30.2 |
| Ultimate | Load (kN) | 312 | 309 | 339 | 332 |
| | Max Disp. (mm) | 23.1 | 80.6 | n/a | >154 |
| | Behaviour | Flexure | Flexure | Flexure | Flexure |
| | Failure Mode | 1 Plastic Hinge | 6 Plastic Hinges | 4 Plastic Hinges | 6 Plastic Hinges |

n/a: not available

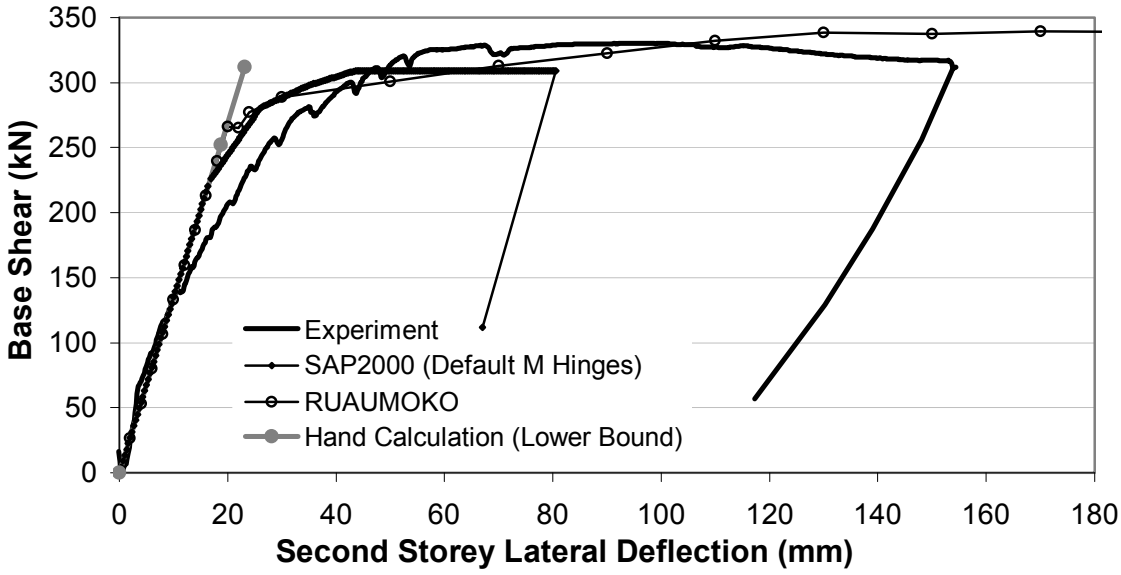


**Figure 2.19** Comparison of Load-Deflection Responses for Vecchio and Emara Frame

As seen in Figure 2.19, the lateral stiffness of the frame was predicted reasonably well with the use of effective stiffness values of 0.5 x E I in all three calculations.

The failure modes were also found to be consistent with the experimental observations. As defined in the modelling process, both programs predicted flexural yielding of the hinges. The final condition of the hinges is presented in Figure 2.20 based on the hinge behaviour given in Figure 2.5. It should be noted that, in the RUAUMOKO model, after the yielding point B, the hinge continues carrying the same load without any drop in its capacity due to the elastic-plastic hysteresis assumption made. In the hand calculation, the failure was assumed to be caused by the first yielding of B1 R hinge in Figure 2.16.

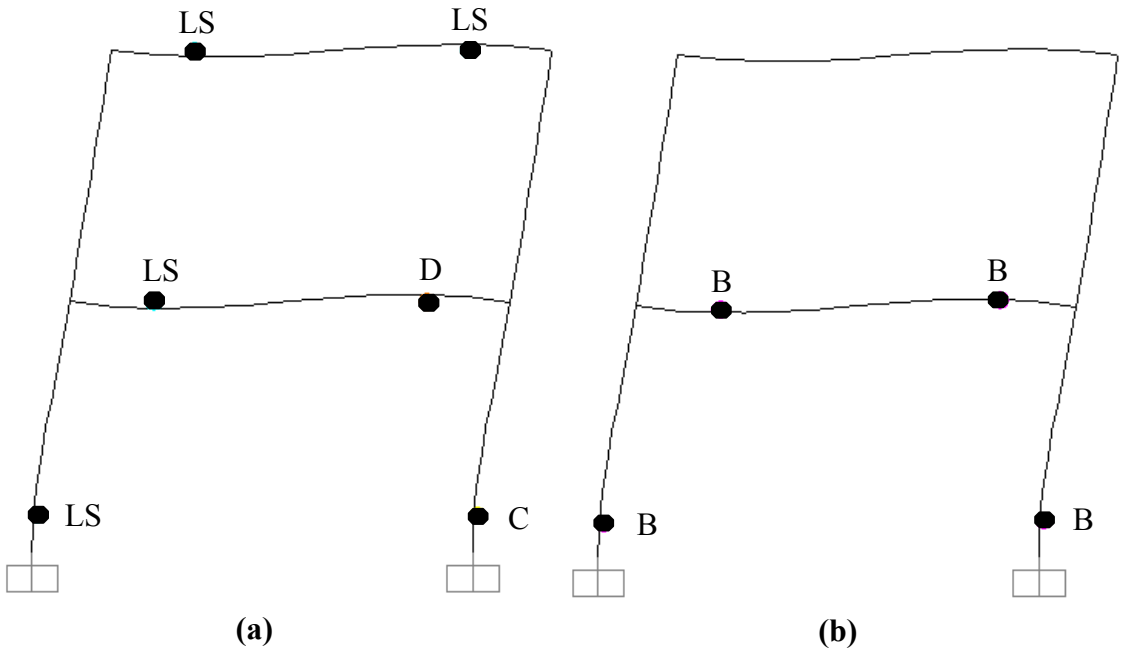


**Figure 2.20** Final Conditions of Hinges for Vecchio and Emara Frame: **(a)** SAP2000; **(b)** RUAUMOKO

However, inspection of Figure 2.19 reveals that neither of the programs could predict the displacement capacity of the frame with reasonable accuracy. SAP2000 provided an overly conservative estimate of less than half of the experimental displacement capacity. RUAUMOKO did not provide any indication of the ultimate displacement; the analysis carried on sustaining the ultimate load based on the elastic-plastic hinge behaviour. It should be noted that the experiment was terminated at a 154 mm lateral displacement due

to stroke limitations; the experimental failure displacement of the beam would likely have been higher than 154 mm.

In conclusion, both the first yielding and ultimate load capacity of this flexure-critical frame were estimated accurately. As for the failure displacement, a reasonable estimate was not achieved.

### 2.3.6 Nonlinear Analysis of a Shear-Critical Frame

A one-span, two-storey, shear-critical reinforced concrete frame was tested by Duong et al. (2007) to study the behaviour of shear-critical reinforced concrete frames under seismic loading conditions and to corroborate analytical procedures.

The frame was constructed with a centre-to-centre span of 1900 mm, a storey height of 2100 mm and an overall height of 4600 mm (Figure 2.21). All beam and columns were nominally 300 mm wide and 400 mm deep, while the base was 800 mm wide and 400 mm deep. The frame was built integral with a large, heavily reinforced concrete base to create an essentially fixed foundation. The base was fixed to the lab floor using six pairs of bolts which were post-tensioned to prevent slip. The material properties, determined from concrete cylinder tests and steel coupon tests, are summarized in Table 2.7.

Testing of the frame consisted of two phases. In Phase A, the test program involved applying an axial load of 420 kN to each column, maintained constant throughout the test, while monotonically applying a lateral displacement to the second storey beam until the ultimate capacity of the frame was reached. The column loads were provided by two 450 kN capacity hydraulic jacks through two transverse beams in a force-controlled mode. The horizontal load was provided by a 1000 kN capacity actuator mounted laterally against a reacting strong wall in a displacement-controlled mode.

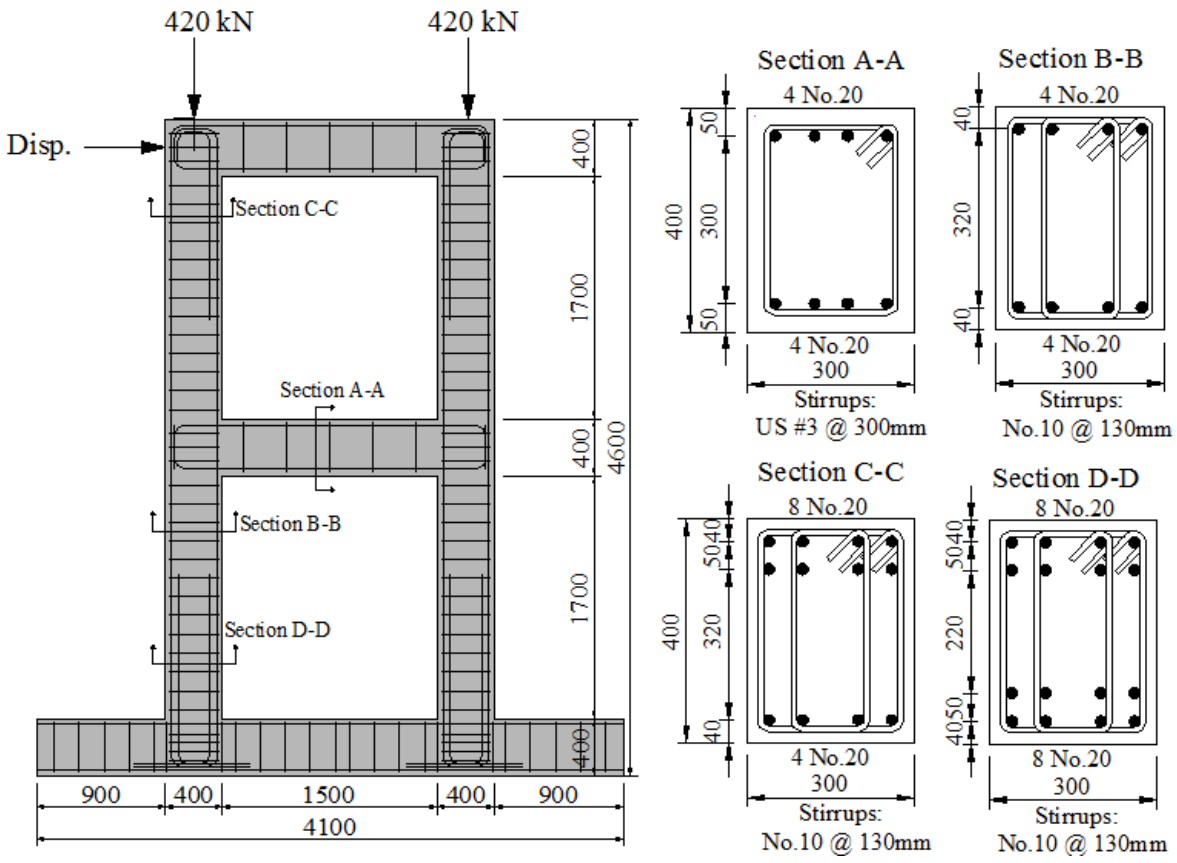


**Figure 2.21** Details of Duong Frame

**Table 2.7** Material Properties of Duong Frame

| | Reinforcement | | | | | | | | Concrete | | | | |
|---|---|---|---|---|---|---|---|---|---|---|---|---|---|
| | $A_s$ ($mm^2$) | $d_b$ (mm) | $f_y$ (MPa) | $f_u$ (MPa) | $E_s$ (MPa) | $E_{sh}$ (MPa) | $\varepsilon_{sh}$ ($x10^{-3}$) | $\varepsilon_u$ ($x10^{-3}$) | $f'_c$ (MPa) | $\varepsilon_0$ ($x10^{-3}$) | $E_c$ (MPa) | $G_c$ (MPa) | $\mu$ |
| **No.20** | 300 | 19.5 | 447 | 603 | 198400 | 1372 | 17.1 | 130.8 | 42.9 | 2.31 | 30058 | 13069* | 0.2* |
| **No.10** | 100 | 11.3 | 455 | 583 | 192400 | 1195 | 22.8 | 129.9 | | | | | |
| **US #3** | 71 | 11.3 | 506 | 615 | 210000 | 1025 | 28.3 | 134.6 | | | | | |

* estimated

### 2.3.6.1 Hand Calculation

Similar to the frame analyzed in the preceding section, hand calculation of this frame's response was performed in an iterative manner in order to consider axial force and axial restraint effects. The model used for hand calculation is presented in Figure 2.22, where the effective stiffness values of 0.5xEI were used for all members as recommended by Table 6.5 of FEMA (2000). Note that the effective stiffness values smaller than 0.5xEI for members in tension and larger than 0.5xEI for member in compression, as suggested by Paulay and Priestley (1992), may lead to better prediction of the frame's response.

First, a linear-elastic analysis of the frame was performed for 100 kN lateral load. The shear force and bending moment values for both ends of each member, at $d_v = 0.9 \times 350 = 315$ mm away from the face of the columns, were determined. Then, based on the General Method of the CSA A23.3-04, Clause 11, the shear capacities of the members were calculated and found to be less than the acting shear at the predetermined locations shown in Figure 2.22. The moment capacities were also calculated using rectangular stress blocks and were found to be less than the acting moment at the predetermined locations shown in Figure 2.22.

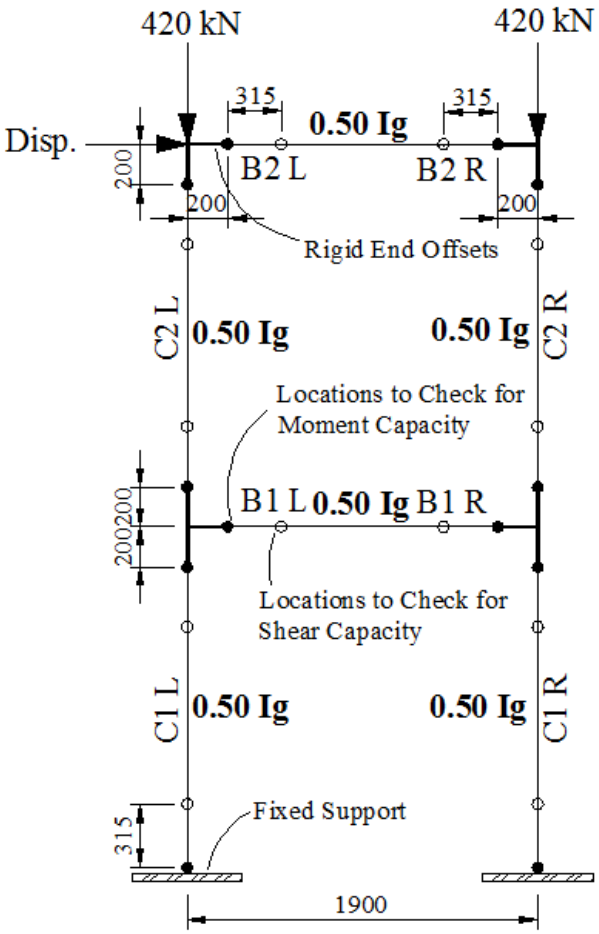


**Figure 2.22** Model of Duong Frame for Hand Calculation

Lateral load was gradually increased until the moment or shear capacity of one of the members was reached at the locations shown on Figure 2.22. When the lateral load reached 245 kN, the corresponding bending moment and shear force diagram for this beam were found to be as follows:

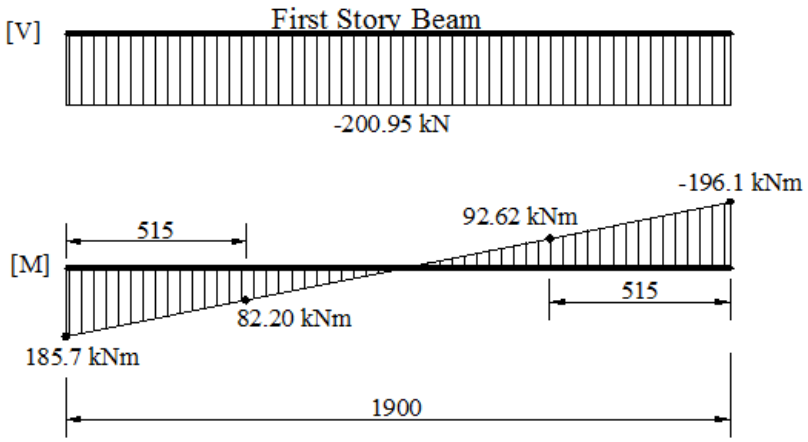


**Figure 2.23** Shear Force (V) and Moment (M) Diagram for Lateral Load of 240 kN for Duong Frame

According to Figure 2.23, the bending moment acting at the face of the column (i.e., 200 mm away from the joint) at B1 R was 155.9 kN. The moment capacity of the beam was calculated to be $M_r = 176.4\,kNm$. As $M_r = 176.4\,kNm > M_f = 151.5\,kNm$, the beam had not yet reached its flexural capacity.

The shear capacity of the beam was calculated as 199.2 kN based on the General Method of CSA A23.3-04, Clause 11. As the shear force on the first storey beam B1 R became approximately equal to its shear capacity, it was confirmed that at a lateral load of 245 kN, the first storey beam would have reached its shear capacity.

There is also another important mechanism in the behaviour of this frame which should be considered. Subjected to bending, reinforced concrete sections typically develop flexural cracks resulting in average tensile strains on the tension face being much larger than the compressive strains on the compression face. This results in a *tensile* average strain at the mid-height of the section giving, when integrated over the depth of the section, a net elongation. However, when the member is restrained from freely elongating, as in this case by the columns, an axial compressive force is induced in the member. This axial compression force increases both the flexural and shear capacities of the member. This mechanism, known as *membrane action*, should be considered when estimating the shear capacity of this frame.

With the help of Response-2000, the elongation of the first storey beam under its ultimate condition was calculated to be 1.17 mm. Due to the columns on each sides of the beam, this elongation will cause axial compression on the beam which can be calculated as

$$C = \frac{12 \times (\mathrm{E} \times \mathrm{I})}{h^3} \times \Delta \tag{2.6}$$

$$C = \frac{12 \times (0.5 \times 30058 \times 1.60 \times 10^9)}{1700^3} \times (1.17 \times 0.5) = 35 \text{ kN extra compression}$$

In the calculation above, the effective flexural stiffness of the columns was assumed to be half of its uncracked value, at the ultimate condition, based on Table 6.5 of FEMA 356 (2000). Using the additional compression value of 35 kN, the shear capacity of the beam was calculated to be 211.4 kN and the corresponding lateral load value to be 252 kN. This load corresponds to the yielding of the beam B1 R in shear and therefore can be accepted to be a lower bound estimate of this frame's failure load.

#### 2.3.6.2 Analysis with SAP2000

Using the same material properties and geometry, the SAP2000 model of the structure was created (Figure 2.24). The bases of the columns were modelled as fixed without including the base beam. For simplicity, only two cross sections were used in the model: one for the beams and one for the columns.

For each column and beam, two default bending moment hinges were defined as automatic hinges at each end of the elements just inside their clear spans. The automatic hinge properties were found by SAP2000 by calculating the yield moment for the cross section based on the longitudinal reinforcement details provided and assuming almost the same moment capacity for the ultimate condition. In other words, no strain hardening of the longitudinal reinforcement was considered by SAP2000. The ultimate rotation capacity for this calculation is typically taken by SAP2000 from Table 6.7 or Table 6.8 of FEMA 356 (2000). Inspection of the hinge behaviour calculated by SAP2000 revealed that the yield moment of the beam was calculated as 174.6 kNm, which is somewhat greater than the hand-calculated value of 167.2 kNm.

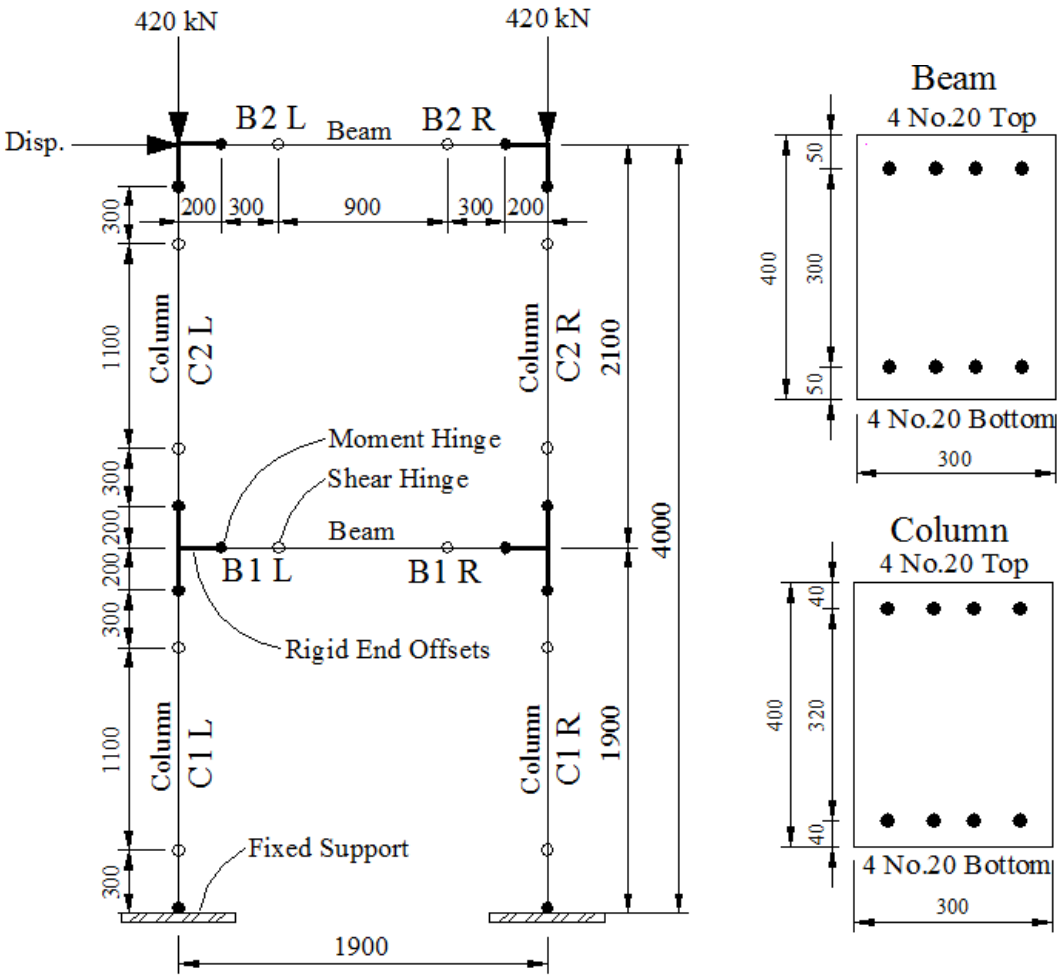


**Figure 2.24** SAP2000 Model of Duong Frame

As the structure is known to be shear-critical, default shear hinges were assigned to each end of all members. In order to determine the location of the hinges, it was assumed that the hinge length would be approximately 1.5 times the height of the cross section (1.5×400 = 600 mm) and the hinge was placed at the centre of the hinge length as described in Section 2.3.1. Similar inspection of the hinge behaviour calculated by SAP2000 revealed that the yield shear force for the beam was calculated to be 87.2 kN which is quite contrary to the hand-calculated value of 211.4 kN. This unreasonably low estimation of shear strength for the beams is expected to lower the peak load capacity of the frame in the SAP2000 analysis.

Rigid end offsets with rigid end factors of 1.0 were used in order to account for the overlapping portions of the beam-column connections as suggested by FEMA 356 Clause 6.5.2. Neither the transverse reinforcement spacing or ratio nor the strain hardening properties of longitudinal reinforcement were defined as they are not demanded by the program.

### 2.3.6.3 Analysis with RUAUMOKO

The analytical model used in the RUAUMOKO analysis is shown in Figure 2.25. To be consistent with other analyses, rigid end zones were used and the analysis was performed with the assumption of small displacements. The hinge lengths were also assumed to be the same as the section height; namely, 400mm. It was also noted that the use of different hinge lengths did not change the results. The axial force and bending moment interaction responses for both cross sections were calculated with the help of Response-2000 and supplied to RUAUMOKO.

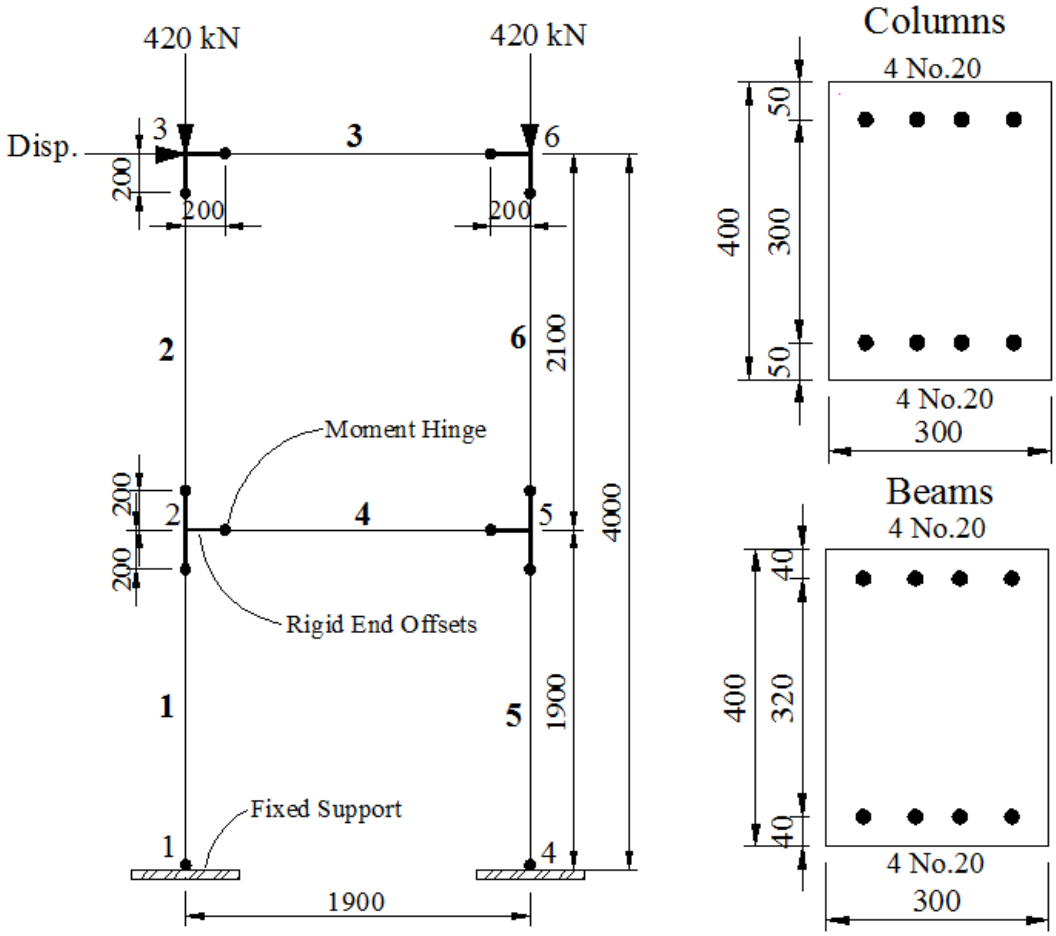


**Figure 2.25** RUAUMOKO Model of Duong Frame

### 2.3.6.4 Comparison of the Analytical and Experimental Results

As seen in Table 2.8, RUAUMOKO predicted the first yielding of the reinforcement with an excellent accuracy. This was, however, caused by the flexural behaviour assumed in the model. In other words, there were no shear hinges defined in the RUAUMOKO analysis which could have yielded prior to the flexural hinges. In both the hand calculation and the SAP2000 prediction, no yielding of flexural hinges was predicted; the yielding of the shear hinge caused failure.

The peak load capacity of the frame was poorly predicted. SAP2000 *under*estimated the strength by 70%; while RUAUMOKO *over*estimated it by 27%. RUAUMOKO predicted a failure load which corresponded to the flexural capacity of the frame. The erroneous prediction of SAP2000 was caused by the use of the automatic shear hinges built into the program. Inspection of the generated hinge properties of SAP2000 revealed that the shear capacity of the first storey beam was estimated as 87.2 kN while the general method of CSA A23.3-04 predicted a value of approximately 210 kN. The actual beam shear failure load from the test was reported in Duong (2006) to be around 210 kN.

As for the hand calculation, the strength was calculated to be 252 kN which corresponded to the yield shear force of beam B1 R in Figure 2.22. This value, therefore, can be accepted to be the lower bound estimate of the peak load capacity of the frame.

**Table 2.8** Comparison of Analytical and Experimental Results for Duong Frame

| | | Hand Calc. | SAP2000 | Ruaumoko | Experiment |
|---|---|---|---|---|---|
| Yielding | Load (kN) | no yielding | no yielding | 288 | 295 |
| | Disp. (mm) | | | 12.0 | 26.6 |
| Ultimate | Load (kN) | 252.0 | 100.0 | 408.9 | 323.0 |
| | Max Disp. (mm) | 10.0 | 4.0 | n/a | 44.7 |
| | Behaviour | Shear | Shear | Flexure | Flexural-Shear |
| | Damage Mode | Shear Failure of B1 R | Shear Failure of B1 L and B1 R | n/a | Shear Damage of B1 L and Extensive Flexural Cracking |

n/a: not available

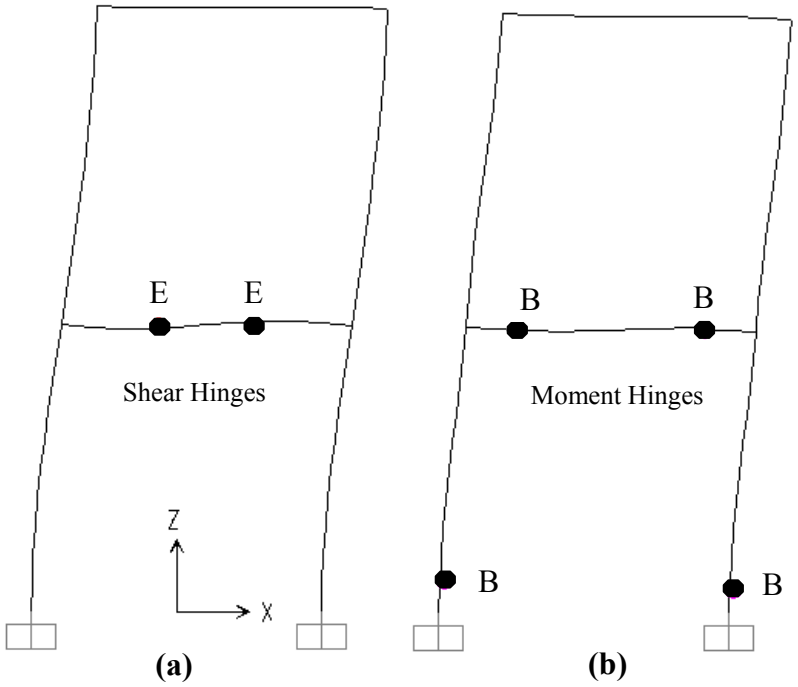


**Figure 2.26** Final Conditions of Hinges for Duong Frame: **(a)** SAP2000; **(b)** RUAUMOKO

The failure mode of the frame was also predicted with a varying degree of success. Failure was caused by shear yielding of the first storey shear hinges in the SAP2000 model. However, RUAUMOKO returned a flexural failure mechanism with yielding of four moment hinges as shown in Figure 2.26.

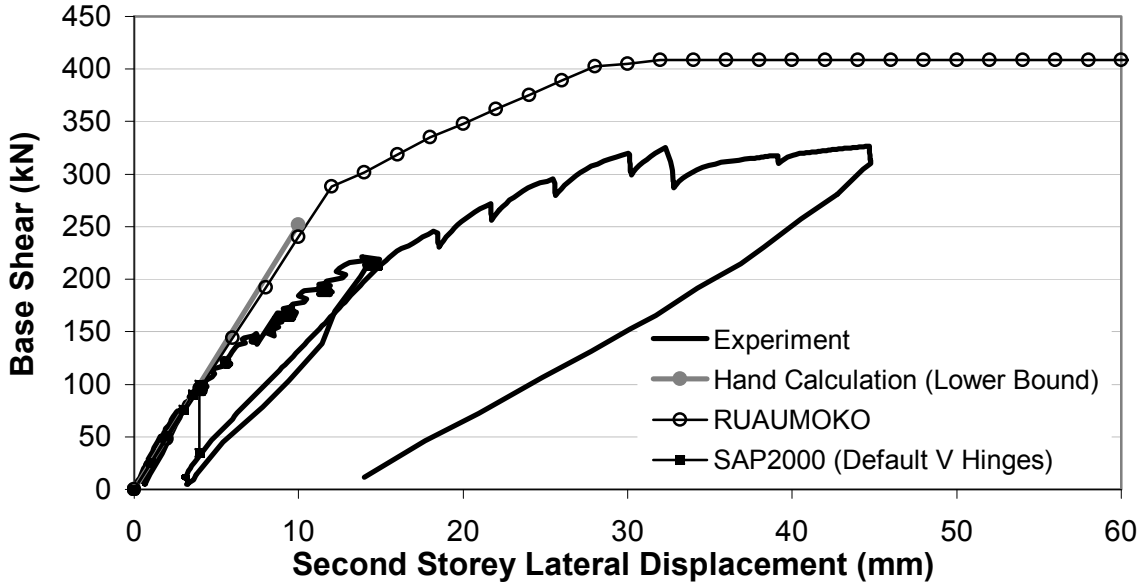


**Figure 2.27** Comparison of Load-Deflection Responses for Duong Frame

Inspection of Figure 2.27 reveals that neither program was able to produce an acceptable ultimate displacement capacity for the frame. SAP2000 predicted an unreasonable 4.0 mm. The RUAUMOKO analysis did not provide any indication of the ultimate displacement; the analysis carried on sustaining the ultimate load based on the elastic-plastic hinge behaviour. The actual failure displacement in the test was expected to be only slightly more than the 44.8 mm attained (Duong, 2006); the loading was stopped to prevent a catastrophic shear failure of the beam because repair of the beam was to take place.

In conclusion, neither the strength nor the ductility of this shear-critical frame was calculated with acceptable accuracy by the use of default hinges of SAP2000 and RUAUMOKO. In fact, highly contradictory and misleading responses were obtained.

#### 2.3.6.5 Analysis with SAP2000 (User-Defined Hinges)

As the prediction of SAP2000 with default shear hinges was unacceptable, it was decided to create user-defined moment and shear hinges and repeat the same analysis.

For this purpose, exactly the same model of the structure was used (Figure 2.24). With the help of Response-2000, the moment-curvature (M - Ø) responses for both the beam and column sections were calculated. In this calculation, the axial forces were assumed to be zero and the moment hinge lengths were assumed to be equal to the height of the cross sections, h. As a result, the rotation values were calculated as

$$Rotation = \phi \times h \tag{2.5}$$

The shear hinge behaviour was also calculated with Response-2000. For this calculation, the ratios of bending moment to shear force were required for all shear hinges. Thus, an initial linear-elastic analysis of the frame was performed to find the required ratios. Then, the shear force-shear strain (V - $\gamma$) responses were obtained from Response-2000 assuming zero axial loads for all members. The shear hinge lengths were assumed to be

equal to 1.5 times the depth of the cross sections as defined in Section 2.3.1, and the shear displacements were calculated using Eq. 2.6.

$$Shear\ Displacement = \gamma \times (1.5 \times h) \tag{2.6}$$

The results of these calculations were then idealized as the hinge behaviour given in Figure 2.5 for SAP2000 input. It was important not to assign a negative slope for any branch of Figure 2.5 in order to avoid stability problems during the analysis (CSI, 2005). For information purposes, the IO, LS and CP points were approximately determined and supplied to SAP2000.

#### 2.3.6.6 Analysis with SAP2000 (User-Defined Hinges, Refined Model)

As the axial force effects were not included in the analytical model previously, it was decided to consider them to determine their influence on the predicted response. This inclusion, however, required an iterative solution procedure as the axial forces are dependent on the lateral loads acting on the structure. For this reason, first, the axial forces of all members were obtained corresponding to the failure load found in the analysis in Section 2.3.6.5. Then, both the shear and moment hinge calculations were repeated by Response-2000 and the results were input into SAP2000 to get a second estimate of the failure load of the frame. Then, using the new estimate of the failure load, the same procedure was repeated until convergence was achieved. It should be noted that this calculation was quite laborious and took a significant amount of time.

#### 2.3.6.7 Comparison of SAP2000 Predictions

As shown in Table 2.9, the models with user-defined moment and shear hinges provided acceptable estimates of the major occurrences in the behaviour of the frame. The model with user defined hinges underestimated the first flexural yielding load by 20 percent, while the refined model which also included axial force effects predicted the same event with only 4 percent overestimation.

One of the most important values, the load capacity of the frame, was predicted successfully. The model with user defined hinges underestimated the peak load by 15 percent, while the refined model which also includes axial force effects accurately predicted the load capacity with only 2 percent deviation from the experimental value.

**Table 2.9** Comparison of Analytical and Experimental Results for Duong Frame

| | | Automatic M and V Hinges | User Defined M and V Hinges | User Defined M and V Hinges (Refined) | Experiment |
|---|---|---|---|---|---|
| Flexure Yielding | Load (kN) | no yielding | 244.0 | 278.6 | 295.0 |
| | Disp. (mm) | - | 14.9 | 18.5 | 26.6 |
| Ultimate | Load (kN) | 100.0 | 266.7 | 314.6 | 323.0 |
| | Max Disp. (mm) | 4.0 | 19.2 | 26.4 | 44.7 |
| | Behaviour | Shear | Flexural-Shear | Flexural-Shear | Flexural-Shear |
| | Damage Mode | Shear Failure of B1 L and B1 R | Shear Failure of B1 R | Shear Failure of B1 R | Shear Damage of B1 L and Extensive Flexural Cracking |

The failure mode of the frame was also predicted successfully. Both models predicted the shear failure of B1R and the flexural yielding of both column bases (Figure 2.28). The only differences in the prediction of the two models were the final conditions of the shear hinges. As the axial force effects were considered in the refined model, the shear hinge B1R carried more shear force and, under increasing applied horizontal force, the other shear hinges moved into more advanced levels of plastic deformations as seen in Figure 2.5.

As seen in Figure 2.29, the lateral stiffness of the frame was predicted very well with the use of effective stiffness values of 0.5 x EI in all three calculations. However, the ultimate displacement capacity of the frame was not predicted successfully; both models underestimated the failure displacement significantly.

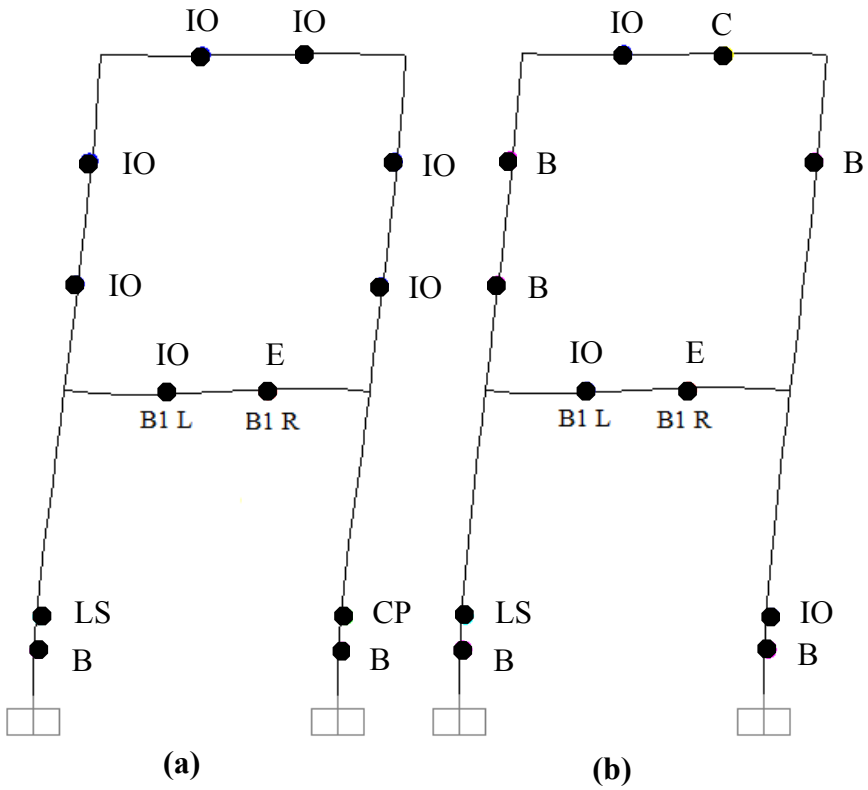


**Figure 2.28** Final Conditions of Hinges for Duong Frame: **(a)** Model with User-Defined Hinges; **(b)** Refined Model with User-Defined Hinges

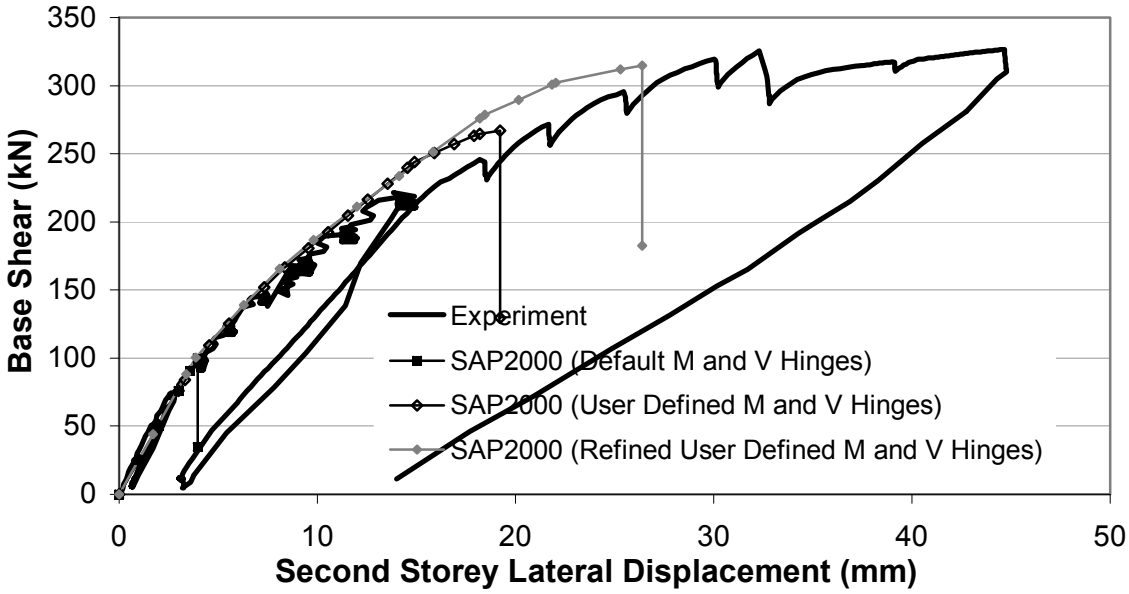


**Figure 2.29** Comparison of Load-Deflection Responses for Duong Frame (Including SAP2000 Models with User-Defined Hinges)

In conclusion, with the use of user-defined shear hinges, the strength of this shear-critical frame was calculated reasonably well. The ductility was not predicted with similar success; nonetheless, the prediction was not misleading as it was with the use of default shear hinges. Note that the creation of user-defined hinges required expert knowledge and was quite laborious, taking significant time to develop even for such a small frame.

### 2.3.7 Discussion

Based on the analysis results, both computer programs provided estimates of the peak load capacity of flexure-critical structures which were well within the margins of accuracy one can expect to achieve with nonlinear analysis of reinforced concrete. However, the ultimate displacements corresponding to the failure conditions of the structures were not calculated with same degree of accuracy. Ultimate displacements are an important parameter when evaluating the seismic performance of structures including ductility ratios and energy absorption capacities. Seismic design provisions in modern design codes are not based on the actual lateral loads that a structure must resist and remain elastic, but rather on the lateral displacement level that it can withstand without collapsing (Christopoulos and Filiatrault, 2006).

In the case of a reinforced concrete frame with dominant shear behaviour, reliable and reasonable predictions of neither the peak load nor the ultimate displacement could be achieved.

It was clearly seen, in this chapter, that modelling simple structures, as simple as a simply supported beam, requires a certain amount of experience and expertise in behaviour and modelling of reinforced concrete structures. Previous knowledge of the failure mode of the structure is required so that the appropriate hinges are used – shear or moment. If the expected failure mode is shear, there is a daunting task awaiting the analyst.

It was realized during this study that, when modelling a reinforced concrete frame structure, there are usually three courses of action available, one of which should be taken.

The first one is the use of default or automatic consideration of shear behaviour available in some of the analysis software presently in use. However, there is usually insufficient information available on the theoretical basis on which those calculations are performed. The assumed shear behaviour may be based on empirical formulations for a certain type of system or there may be several assumptions made which may not be valid for the problem at hand. The output generated by the programs tends to be difficult to verify. Therefore, it is usually necessary to take it on trust that the program works properly.

This course of action was taken when modelling and analyzing the Duong frame by SAP2000. Both the modelling and analysis processes went without any problem or warning. The program predicted the shear failure at the end, but the result was unacceptable in terms of both strength and ductility; less than one third of the experimental failure load was predicted. This clearly shows that using generic or unknown models to simulate the behaviour of reinforced concrete in shear can easily lead to grossly inaccurate results.

The second course of action, when modelling a reinforced concrete frame, is to calculate the shear behaviours of the structural components and to supply the results to the software being used. In this way, the analyst has full control of the assumptions and theories used. However, this calculation requires expert knowledge on the shear behaviour of concrete and can be quite laborious. For example, for the General Method of the CSA A23.3-04, Clause 11, knowledge of the axial forces and ratios of bending moment to shear force are required for all of the shear hinges used; these values change when the load on the structure is increased. Because the failure load is not known, an iterative solution process is required. As a result, the complexity and repetition involved will most likely require the use of other software such as Response-2000. After calculation of the necessary values, the process of inputting them into a text file, one by one, inherently involves a high risk for input errors. It may also take significant time depending on the scale of the structure being modelled.

This course of action was taken when modelling and analyzing the Duong frame for a second time using SAP2000. Based on the frame properties, user-defined hinges were

created for consideration of both shear and flexure. As a result, an acceptable estimate of the load capacity of the structure was achieved. However, even for such a small frame (only one bay and two storeys), the level of expertise required and the magnitude of pre-calculations performed were significant with considerable time and effort spent.

The third course of action is to ignore shear behaviour and assume the structure is flexure-critical. Such an approach is often taken when the analyst does not have sufficient knowledge of the structural behaviour, or is intimidated by the amount of work required to consider shear behaviour. In this case, if the structure happens to be shear-critical, the analyst usually ends up with a large overestimation of both the ultimate load and the ultimate displacement capacity of the frame. Such an analysis was performed in this study for demonstrative purposes. The shear-critical Duong frame was modelled using RUAUMOKO without considering inelastic shear behaviour. At the end of analysis, the program overestimated the strength of the structure by 26 percent even if the structure was not purely shear-critical; there were significant flexural influences in the test. This clearly shows that ignoring shear related mechanisms may lead to grossly unconservative results.

### 2.3.8 Conclusion

These apparent difficulties with accurately modelling the strength and ductility of reinforced concrete frames led to this thesis study. It is believed that the tools needed for such an analysis should not require previous knowledge of the failure mechanism of the structure and should not require expert knowledge on the selection of material models and assumptions in the analysis. It is also desired that these tools only require basic material and sectional properties and do not need previously calculated values as input, such as axial force-moment or shear force-shear deformation relations for the cross sections used.

# CHAPTER 3

## MONOTONIC LOADING: THEORY AND IMPLEMENTATION

### 3.1 Chapter Layout

This chapter describes theoretical principles for the nonlinear analysis of reinforced concrete frames subjected to monotonic loading conditions and their implementation into the analytical framework of VecTor5 (Vecchio, 1987; Vecchio and Collins, 1988) for monotonic loading conditions. Throughout the chapter, the existing formulations that were modified and the new algorithms that were added are described in detail. For the sake of completeness, the unaltered formulations of the original procedure are briefly described.

The chapter starts with a detailed summary of the Modified Compression Field Theory (MCFT) and the Disturbed Stress Field Model (DSFM), on which the sectional analyses of the developed procedure were based. It is then followed by the general description of the nonlinear analysis procedure employed. The chapter continues with the formulations of the global frame analysis and the nonlinear sectional analysis procedures. Finally, the chapter ends with the newly implemented algorithms and second-order mechanisms. In addition, when necessary, the appropriate use of the different formulations and options implemented are discussed.

### 3.2 Modified Compression Field Theory (MCFT)

The MCFT (Vecchio and Collins, 1986) is an analytical model for predicting the response of two-dimensional reinforced concrete structures subjected to in-plane shear and normal stresses. The MCFT considers cracked concrete as a new orthotropic material using a smeared rotating crack approach. In this approach, as dictated by the loading or material response, the crack direction reorients gradually as opposed to the fixed crack approach where the crack orientation remains fixed in the direction of first cracking. Central to the theory is the assumption that the directions of principal stress and principal strain remain coincident. Even though cracks are smeared, and stress and strain values are averaged, consideration is also given to the local stresses and strains at cracks. The theory

consists of three sets of relationships: compatibility, equilibrium, and constitutive relationships. The stress-strain relationships (constitutive relationships) were derived empirically from tests of 30 reinforced concrete panels subjected to uniform in-plane normal and shear stresses as shown in Figure 3.1. Since then, the constitutive relationships of the theory have been validated by more than 200 reinforced concrete panel element tests.

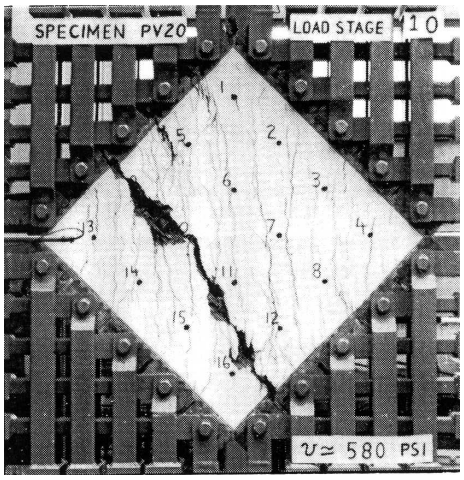


**Figure 3.1** Panel Element PV20 Tested at the University of Toronto (Vecchio and Collins, 1986)

### 3.2.1 Assumptions

Key assumptions made in the MCFT include:

(1) Reinforcement is uniformly distributed across the element.

(2) Cracks are smeared and able to rotate.

(3) Loads are applied uniformly on the element.

(4) Formulations are based on average stresses and strains over a distance that includes several cracks.

(5) The direction of principal strain is the same as the direction of principal stress.

(6) Independent of loading history, there is a unique stress state for each strain state.

(7) Perfect bond between the reinforcement and the concrete exists.

(8) Shear stresses on the reinforcement are negligible.

(9) Average tensile stress in the concrete is limited to the reserve strength of the reinforcement at the cracks.

(10) Independent constitutive relationships are considered for concrete and reinforcement.

### 3.2.2 Compatibility Relations

Under external loads, the concrete component may experience normal and shear strains as shown in Figure 3.2.

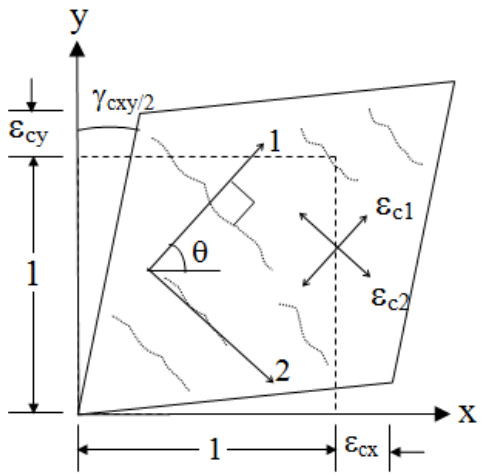


**Figure 3.2** Average Concrete Strains (Wong and Vecchio, 2002)

Compatibility requires that any deformation experienced by the concrete must be identical to the deformation experienced by the reinforcement, as perfect bond between the reinforcement and the concrete is assumed. Therefore, for non-prestressed reinforcement, the average strain in the reinforcement is equal to the average strain in the concrete. Although the MCFT can handle any number of reinforcement components and orientations, in the formulation of the proposed procedure, only two orthogonal directions are considered: x (longitudinal) and y (transverse). Thus, the compatibility equations become as follows:

$$\varepsilon_x = \varepsilon_{cx} = \varepsilon_{sx} \tag{3.1}$$

$$\varepsilon_y = \varepsilon_{cy} = \varepsilon_{sy} \tag{3.2}$$

where $\varepsilon_x$ and $\varepsilon_y$ are element total strains, $\varepsilon_{cx}$ and $\varepsilon_{cy}$ are concrete total strains, and $\varepsilon_{sx}$ and $\varepsilon_{sy}$ are reinforcement total strains.

If the average element total shear strain is also known, with the aid of a Mohr's circle of strain (Figure 3.3), the total average principal tensile and compressive strains can be calculated as follows:

$$\varepsilon_{c1} = \frac{\varepsilon_x + \varepsilon_y}{2} + \frac{1}{2} \times \sqrt{(\varepsilon_x + \varepsilon_y)^2 + \gamma_{xy}^2} \qquad (3.3)$$

$$\varepsilon_{c2} = \frac{\varepsilon_x + \varepsilon_y}{2} - \frac{1}{2} \times \sqrt{(\varepsilon_x + \varepsilon_y)^2 + \gamma_{xy}^2} \qquad (3.4)$$

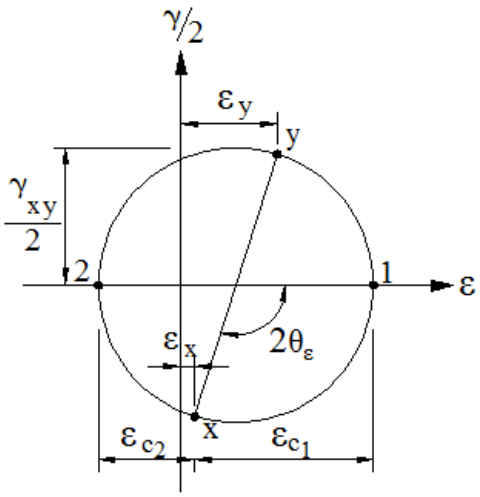


**Figure 3.3** Mohr's Circle of Average Strains

From the Mohr's circle of strain, the orientation of the average principal tensile strain is

$$\theta_\varepsilon = \frac{1}{2} \times \tan^{-1}\left[\frac{\gamma_{xy}}{\varepsilon_x - \varepsilon_y}\right] \qquad (3.5)$$

It should be remembered that, in the MCFT, the inclination of the principal strain field, $\theta_\varepsilon$ is assumed to be equal to the inclination of the principal stress field, $\theta_\sigma$. Thus,

$$\theta = \theta_\varepsilon = \theta_\sigma \qquad (3.6)$$

### 3.2.3 Equilibrium Relations

Under externally applied stresses, the concrete and reinforcement components may experience stresses as shown in Figure 3.4.

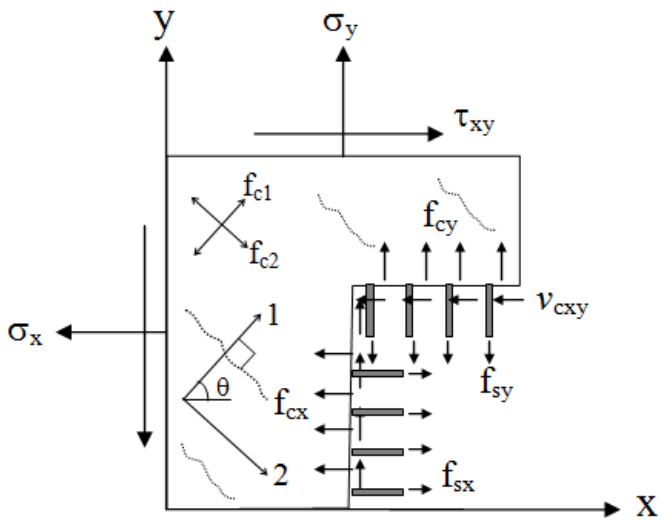


**Figure 3.4** Free Body Diagram of a Reinforced Concrete Element Showing Average Stresses (Wong and Vecchio, 2002)

Equilibrium of forces requires that the resultant of the externally applied normal stresses in the x-and y-direction, ($\sigma_x$, $\sigma_y$), be resisted by average concrete stresses ($f_{cx}$, $f_{cy}$) and average reinforcement ($f_{sx}$, $f_{sy}$) stresses in the x- and y-directions. Equilibrium of moment requires that the externally applied shear stress ($\tau_{xy}$) be entirely balanced by an average shear stress ($v_{cxy}$) in the concrete. No dowel action is taken into account in this equilibrium. It will be added explicitly into the global frame analysis algorithm of analysis procedure developed.

These equilibrium conditions can be summarized as follows:

$$\sigma_x = f_{cx} + \rho_x \times f_{sx} \tag{3.7}$$

$$\sigma_y = f_{cy} + \rho_y \times f_{sy} \tag{3.8}$$

$$\tau_{xy} = v_{cxy} \tag{3.9}$$

where $\rho_x$ and $\rho_y$ are the smeared reinforcement ratios in the x- and y-directions.

The average concrete stresses can be calculated by making use of the Mohr's circle of stress as shown in Figure 3.5.

$$f_{cx} = f_{c1} - v_{cxy} \times \cot(90 - \theta) \qquad (3.10)$$

$$f_{cy} = f_{c1} - v_{cxy} \times \tan(90 - \theta) \qquad (3.11)$$

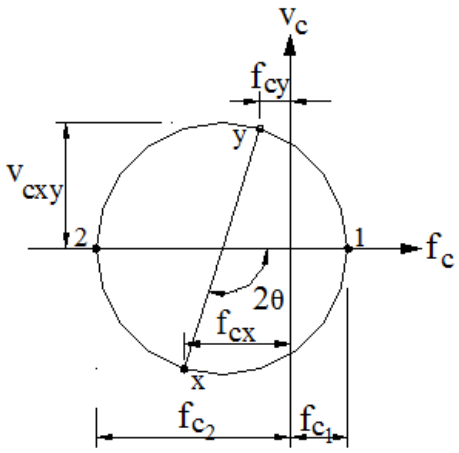


**Figure 3.5** Mohr's Circle of Average Stresses

### 3.2.4 Constitutive Relations

Constitutive relations are required to associate average stresses with average strains for both the concrete and the reinforcement. They were derived from a comprehensive series of panel element tests (Vecchio and Collins, 1986).

#### 3.2.4.1 Concrete in Compression

During the panel element tests (Vecchio and Collins, 1986), it was found that the average stress-strain relations in cracked reinforced concrete are substantially different than those obtained from uniaxial element tests. That is, when simultaneously subjected to high tensile strains in the direction normal to the compression, cracked concrete exhibited softer and weaker response compared to uncracked uniaxially compressed concrete. This led to the so-called *compression softening* formulation (Figure 3.6).

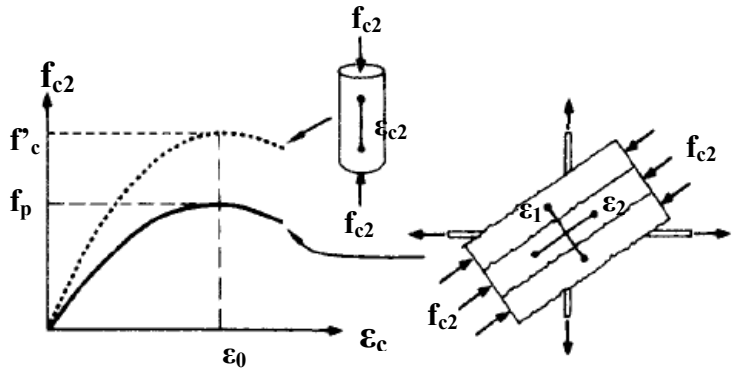


**Figure 3.6** Stress-Strain Relationship for Cracked Concrete in Compression (Vecchio and Collins, 1986)

In the original 1982 formulation, based on 30 panel tests, both the strength and strain were softened as follow:

$$\beta_d = \frac{1}{0.8 - 0.34 \times \frac{\varepsilon_{c1}}{\varepsilon_0}} \leq 1 \qquad (3.12)$$

where $f_p = \beta_d \times f_c'$ (3.13)

and $\varepsilon_p = \beta_d \times \varepsilon_0$ (3.14)

The MCFT uses the Hognestad parabola to relate strains with stresses as follows:

$$f_{c2} = f_p \times \left[ 2 \times \left( \frac{\varepsilon_{c2}}{\varepsilon_p} \right) - \left( \frac{\varepsilon_{c2}}{\varepsilon_p} \right)^2 \right] \qquad (3.15)$$

In the equations above, $f'_c$ is the concrete cylinder compressive strength and $\varepsilon_0$ is the strain corresponding to $f'_c$.

### 3.2.4.2 Uncracked Concrete in Tension

The pre-cracking response of concrete is modeled as a linear response.

$$f_{c1} = \mathrm{E}_c \times \varepsilon_{c1} \qquad \text{for} \quad 0 \leq \varepsilon_{c1} \leq \varepsilon_{cr} \qquad (3.16)$$

where $\varepsilon_{cr} = \frac{f_{cr}}{E_c}$ ; $E_c = 2 \times \frac{f'_c}{\varepsilon_0}$ and $f_{cr} = 0.33 \times \sqrt{f'_c}$ (3.17; 3.18 and 3.19)

In the equations above, $E_c$ is the initial tangent modulus of the concrete in compression, and $f_{cr}$ and $\varepsilon_{cr}$ are the cracking stress and strain, respectively.

### 3.2.4.3 Cracked Concrete in Tension

As observed from the panel element tests, significant tensile stresses were carried by the concrete between the cracks even at very high values of average tensile strain. This observation led to the so-called *tension stiffening* formulation (Figure 3.7).

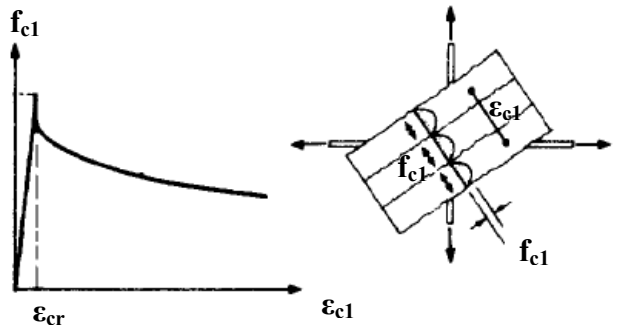


**Figure 3.7** Stress-Strain Relationship for Concrete in Tension (Vecchio and Collins, 1986)

$$f_{c1} = \frac{f_{cr}}{1+\sqrt{200 \times \varepsilon_{c1}}} \quad \text{for relatively small elements.} \quad \varepsilon_{c1} > \varepsilon_{cr} \tag{3.20}$$

$$f_{c1} = \frac{f_{cr}}{1+\sqrt{500 \times \varepsilon_{c1}}} \quad \text{for larger elements.} \quad \varepsilon_{c1} > \varepsilon_{cr} \tag{3.21}$$

### 3.2.4.4 Reinforcement in Tension or Compression

The reinforcement response in compression or tension is represented by a bilinear relationship between the average strains and stresses as follows:

$$f_{si} = E_{si} \times \varepsilon_{si} \qquad \text{for} \quad 0 \le \varepsilon_{si} \le \varepsilon_{yi} \tag{3.22}$$

$$f_{si} = f_{yi} \qquad \text{for} \quad \varepsilon_{yi} \le \varepsilon_{si} \tag{3.23}$$

where the subscript i refers to either the x- or y-component of reinforcement, $f_{si}$ is the stress, and $f_{yi}$ is the yield stress. Figure 3.8 depicts the resulting reinforcement response.

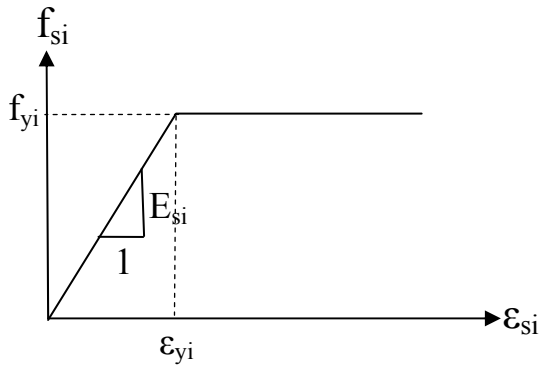


**Figure 3.8** Stress-Strain Relationship for Reinforcement (Vecchio and Collins, 1986)

### 3.2.5 Local Crack Conditions

As described above, compatibility, equilibrium and constitutive relations were derived using average stress and strain values. However, it must be ensured that the average stresses are compatible with the condition of the cracked concrete.

In Figure 3.9(a), the average stresses at a section between cracks perpendicular to the tensile principal strain are depicted, while in Figure 3.9(b), the local stresses on a free crack surface are shown.

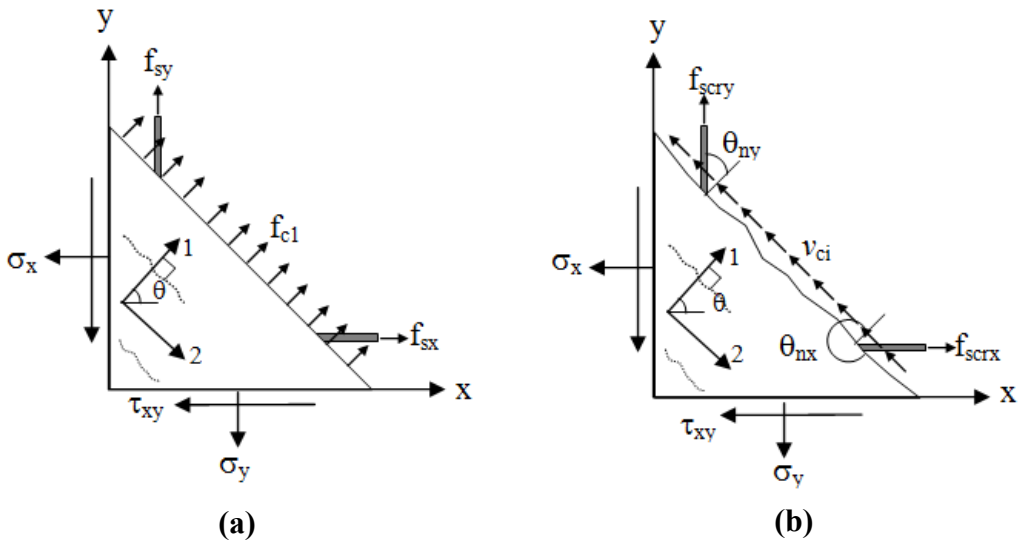


**Figure 3.9** Stresses of a Reinforced Concrete Element: **(a)** Average Stresses; **(b)** Local Stresses at Crack (Wong and Vecchio, 2002)

Tension stiffening mechanisms allow cracked concrete to carry average tensile stresses. It is assumed that concrete carries no tensile stress at the crack; therefore, the average tensile stress must be carried by an increase in the reinforcement stresses at the crack. This is limited by the reserve capacity of the reinforcement, i.e., $(f_{yi} - f_{si})$, for which the following equation must be satisfied:

$$f_{c1} \le \rho_x \times \left( f_{yx} - f_{sx} \right) \times \cos^2 \theta + \rho_y \times \left( f_{yy} - f_{sy} \right) \times \sin^2 \theta \qquad (3.24)$$

where $\rho_x$ and $\rho_y$ are the reinforcement ratios, $f_{yx}$ and $f_{yy}$ are the yield stresses, $f_{sx}$ and $f_{sy}$ are the stresses in the reinforcement in the x- and y-directions, and $\theta$ is the inclination of the principal tensile stress.

Local increases in the reinforcement stresses, which are required by the above equation, can be calculated by static equilibrium in the direction normal to the crack surface (Figure 3.9(b)). The resulting equation becomes

$$f_{c1} = \rho_x \times \left( f_{scrx} - f_{sx} \right) \times \cos^2 \theta + \rho_y \times \left( f_{scry} - f_{sy} \right) \times \cos^2 \left( \theta - 90^\circ \right) \qquad (3.25)$$

Local increases in the reinforcement stresses usually cause interface shear stresses to develop on the crack surface because the reinforcement is generally crossed by a crack at a skew angle. These shear stresses can be statically determined from Figure 3.9(b), as follows:

$$v_{ci} = \rho_x \times \left( f_{scrx} - f_{sx} \right) \times \cos\theta \times \sin\theta + \rho_y \times \left( f_{scry} - f_{sy} \right) \times \cos\left( \theta - 90^\circ \right) \times \sin\left( \theta - 90^\circ \right) \qquad (3.26)$$

where $v_{ci}$ is the shear stress along the crack surface, and $f_{scrx}$ and $f_{scrx}$ are the local stresses in the reinforcement in the x- and y-directions.

The amount of interface shear stress that can be carried by the concrete is limited to the so-called *aggregate interlock* mechanism which loses its efficiency as the crack width, $w$, increases or the maximum aggregate size, $a$, decreases (Figure 3.10).

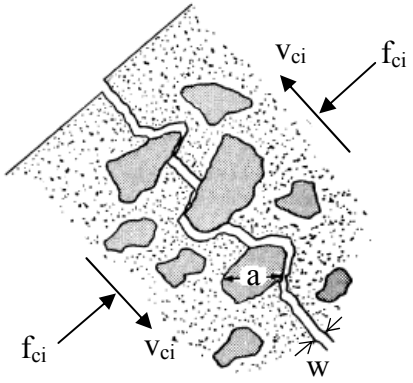


**Figure 3.10** Transmitting Shear Stresses across Crack by Aggregate Interlock (Vecchio and Collins, 1986)

Based on the analysis of aggregate interlock by Walraven (1981), the MCFT limits the interface shear stress to the following value:

$$v_{ci} \le \frac{0.18 \times \sqrt{f'_c}}{0.31 + \frac{24 \times w}{a + 16}} \qquad (in\ mm\ and\ MPa) \tag{3.27}$$

If this value is exceeded, shear slip along the crack surface occurs; this deformation component is not explicitly considered by the MCFT. For this reason, in case of exceedance, the principal tensile stress is reduced until $v_{ci}$ equals its maximum value.

The average crack width, $w$, can be taken as the product of the average concrete tensile stress and the average crack spacing perpendicular to cracks, $S_{m\theta}$.

$$w = \varepsilon_{c1} \times s_{m\theta} \tag{3.28}$$

The average crack spacing depends on the crack control characteristics of both the longitudinal (x) and transverse (y) reinforcement, which can be taken as

$$s_{m\theta} = \frac{1}{\frac{\cos\theta}{s_{mx}} + \frac{\sin\theta}{s_{my}}} \tag{3.29}$$

where $s_{mx}$ is the average crack spacing that would result if the element was subjected to longitudinal tension, while $s_{my}$ is the average crack spacing that would result if the element was subjected to transverse tension.

### 3.3 Disturbed Stress Field Model (DSFM)

The Disturbed Stress Field Model (Vecchio, 2000) is an advanced reformulation of the MCFT that was specifically developed to address reduced accuracy encountered in the MCFT under specific circumstances by extending the MCFT in several aspects. Experience with the MCFT for over 20 years has shown that the MCFT underestimates the shear strength and stiffness of panels containing heavy amounts of reinforcement in both directions when subjected to biaxial compression and shear (e.g., Panel PV23 shown in Figure 3.11(a)). In addition, the shear strength and stiffness of panels containing light amounts of transverse reinforcement are overestimated by the MCFT (e.g., Panel PB20 shown in Figure 3.11(b)).

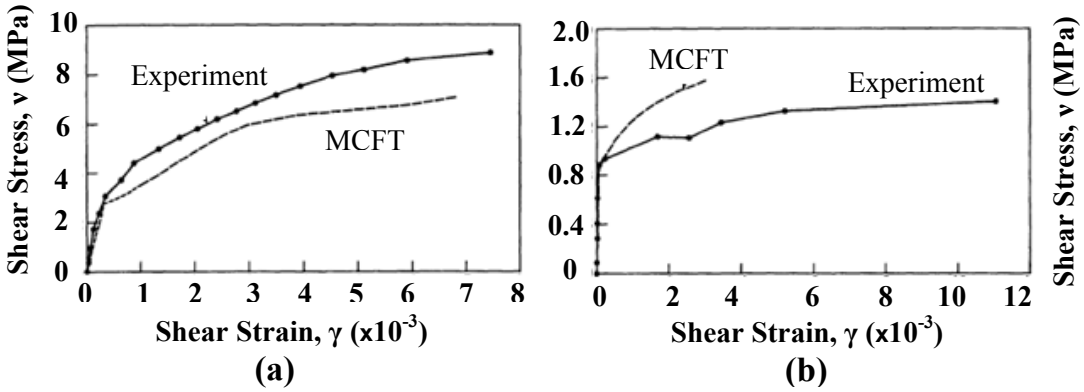


**Figure 3.11** Shear Stress and Strain Responses from Two Tests: **(a)** Panel PV23; **(b)** Panel PB20 (Vecchio, 2000)

These inaccuracies were believed to be partly connected to the assumption of the principal stress and strain axes being collinear. Examination of test data revealed that the direction of principal stress lags behind the direction of principal strain in some cases

(Figure 3.12). This observation led to the removal of the restriction found in the MCFT that the principal stress and strain directions must be coincident. This was achieved by the explicit inclusion of crack slip deformations in the compatibility relations of the DSFM. Through the consideration of these crack slip deformations, it also became possible to eliminate the complex crack slip check required by the MCFT.

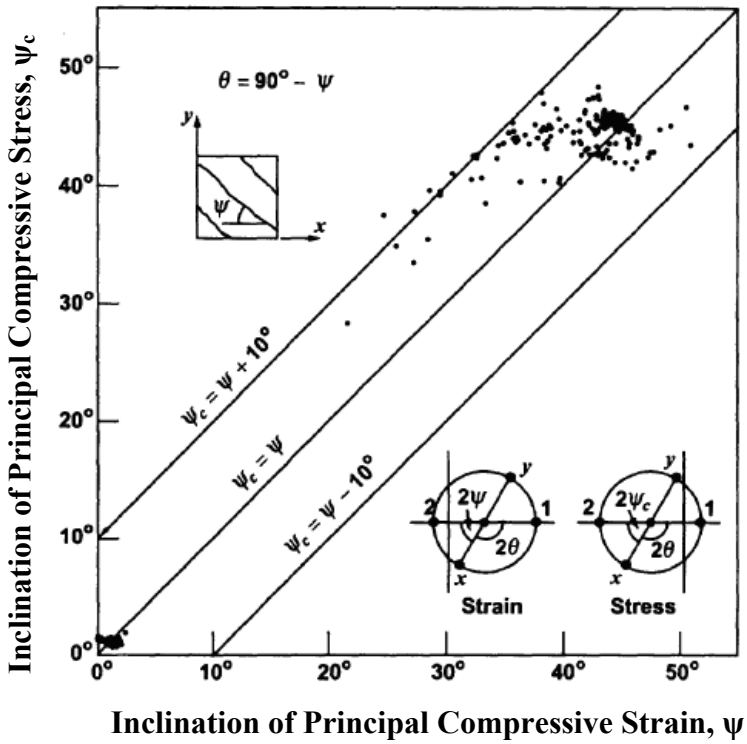


**Figure 3.12** Deviation of Principal Stress and Principal Strain Directions (Vecchio, 2000)

In addition, the DSFM incorporated improved constitutive relations for both concrete and reinforcement.

### 3.3.1 Compatibility Relations

Based on the panel element tests, the change in the principal stress direction was usually observed to lag behind the change in the principal strain direction (Figure 3.12). This is attributed to the way that the stress and strain fields developed. The total or apparent strains emerge as a response to both continuum strains (Figure 3.2) and discontinuous

shear slip (Figure 3.13), while the concrete stresses emerge as a response to only continuum strains caused by applied stresses.

To take this phenomena into account, the DSFM decomposes the total strains into net concrete strains, $\varepsilon_{cx}, \varepsilon_{cy}$ and $\gamma_{cxy}$, and concrete crack slip strains, $\varepsilon_x^s, \varepsilon_y^s$ and $\gamma_{xy}^s$. Therefore,

$$\varepsilon_x = \varepsilon_{cx} + \varepsilon_x^s \tag{3.30}$$

$$\varepsilon_y = \varepsilon_{cy} + \varepsilon_y^s \tag{3.31}$$

$$\gamma_{xy} = \gamma_{cxy} + \gamma_{xy}^s \tag{3.32}$$

With the help of the Mohr's circle of strain, the principal strains are calculated as follows:

$$\varepsilon_{c1} = \frac{\varepsilon_{cx} + \varepsilon_{cy}}{2} + \frac{1}{2} \times \sqrt{(\varepsilon_{cx} + \varepsilon_{cy})^2 + \gamma_{cxy}^2} \tag{3.33}$$

$$\varepsilon_{c2} = \frac{\varepsilon_{cx} + \varepsilon_{cy}}{2} - \frac{1}{2} \times \sqrt{(\varepsilon_{cx} + \varepsilon_{cy})^2 + \gamma_{cxy}^2} \tag{3.34}$$

It should be noted that the principal strains are obtained using *net* concrete strains in the DSFM as opposed to total strains in the MCFT.

From the Mohr's circle of strain (Figure 3.3), the orientation of the average principal tensile strain is

$$\theta_\sigma = \frac{1}{2} \times \tan^{-1}\left[\frac{\gamma_{cxy}}{\varepsilon_{cx} - \varepsilon_{cy}}\right] \tag{3.35}$$

Calculated using *net* concrete strains, $\theta_\sigma$ corresponds to the inclination of the stress field as opposed to the strain field in the MCFT. Therefore,

$$\theta = \theta_\sigma \tag{3.36}$$

The concrete crack slip strains, $\varepsilon_x^{\ s}, \varepsilon_y^{\ s}$ and $\gamma_{xy}^{\ s}$ are calculated from the average crack slip strain, $\delta_s$, which is defined by

$$\gamma_s = \frac{\delta_s}{s_{m\theta}} \tag{3.37}$$

where $s_{m\theta}$ is the average crack spacing defined by Eq. 3.29.

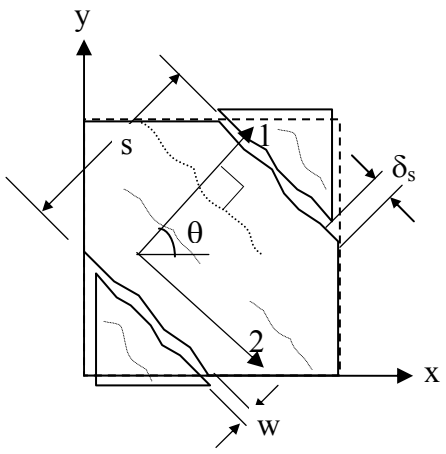


**Figure 3.13** Deformations due to Crack Shear Slip (Vecchio and Wong, 2002)

The average crack slip strain, $\delta_s$, can be calculated by the expression of Walraven (1981) as follows:

$$\delta_s = \frac{v_{ci}}{1.8 \times w^{-0.8} + (0.234 \times w^{-0.707} - 0.20) \times f_{cc}} \tag{3.38}$$

where $v_{ci}$ is the interface shear stress as defined by Eq. 3.27, $w$ is the average crack width as defined by Eq. 3.28, and $f_{cc}$ is the concrete cube strength which may be taken as

$$f_{cc} = 1.2 \times f_c' \qquad \text{where } f_c' \text{ is the concrete cylinder strength.} \tag{3.39}$$

Although the DSFM can handle any number of reinforcement components and orientations, in the formulation of the proposed analysis procedure, only two orthogonal directions are considered: x-direction (longitudinal) and y-direction (transverse). Thus, the compatibility equations become as follows:

$$\varepsilon_{sx} = \varepsilon_x \tag{3.40}$$

$$\varepsilon_{sy} = \varepsilon_y \tag{3.41}$$

where $\varepsilon_x$ and $\varepsilon_y$ are the element total strains, and $\varepsilon_{sx}$ and $\varepsilon_{sy}$ are the reinforcement total strains in the x- and y-directions.

### 3.3.2 Equilibrium Relations

As with the MCFT (Figure 3.4), the equilibrium conditions can be summarized as follows:

$$\sigma_x = f_{cx} + \rho_x \times f_{sx} \tag{3.7}$$

$$\sigma_y = f_{cy} + \rho_y \times f_{sy} \tag{3.8}$$

$$\tau_{xy} = v_{cxy} \tag{3.9}$$

where $\rho_x$ and $\rho_y$ are the smeared reinforcement ratios, $f_{sx}$ and $f_{sy}$ are the reinforcement stresses in the x- and y-directions, $\tau_{xy}$ is the applied shear stress and $v_{cxy}$ is the average shear stress in the concrete.

As with the MCFT, there is no dowel action taken into account in this equilibrium. It will be added explicitly into the global frame analysis algorithm of the analytical procedure developed.

The average concrete stresses can be calculated by making use of the Mohr's circle of stress (Figure 3.5) as follows:

$$f_{cx} = f_{c1} - v_{cxy} \times \cot\left(90° - \theta\right) \tag{3.10}$$

$$f_{cy} = f_{c1} - v_{cxy} \times \tan\left(90° - \theta\right) \tag{3.11}$$

### 3.3.3 Constitutive Relations

The constitutive relations of the DSFM are a revised and refined version of those of the MCFT, as explained in the following section.

#### 3.3.3.1 Concrete in Compression

The compression softening relation used in the DSFM is similar to that in the MCFT, but is softened to a lesser degree.

The Vecchio-A formulation, which is mainly used in the finite element programs, is as follow:

$$\beta_d = \frac{1}{0.1925 \times \left( -\frac{\varepsilon_{c1}}{\varepsilon_{c2}} - 0.28 \right)^{0.8}} \leq 1 \tag{3.42}$$

For easier implementations in design procedures, it was reported that accuracy is not much reduced when using the Vecchio-B formulation which only requires principal compressive tensile strain as follows:

$$\beta_d = \frac{1}{0.1285 \times \left( \frac{\varepsilon_{c1}}{\varepsilon_0} - 0.37 \right)} \leq 1 \tag{3.43}$$

The DSFM softens both the compressive strength and corresponding peak strain as follows:

$$f_p = \beta_d \times f_c' \tag{3.13}$$

$$\varepsilon_p = \beta_d \times \varepsilon_0 \tag{3.14}$$

### 3.3.3.2 Uncracked Concrete in Tension

The pre-cracking response of concrete is modeled as a linear response.

$$f_{c1} = \mathrm{E}_{c1} \times \varepsilon_{c1} \qquad \text{for} \quad 0 \le \varepsilon_{c1} \le \varepsilon_{cr} \tag{3.16}$$

$$\text{where } \varepsilon_{cr} = \frac{f_{cr}}{E_c} \;\; ; \;\; E_c = 2 \times \frac{f_c'}{\varepsilon_0} \text{ and } f_{cr} = 0.33 \times \sqrt{f_c\,'} \tag{3.17; 3.18 and 3.19}$$

In the above equations, $E_c$ is the initial tangent modulus of concrete in compression, and $f_{cr}$ and $\varepsilon_{cr}$ are the cracking stress and strain, respectively.

### 3.3.3.3 Cracked Concrete in Tension

The DSFM considers post-cracking tensile stresses as a result of two independent mechanisms; namely, tension stiffening and tension softening.

*Tension stiffening* refers to the presence of average tensile stresses in cracked concrete as a result of load transfer between concrete and reinforcement via bond stresses. Tension stiffening in the DSFM is based on the formulation of Bentz (2000 and 2005) who showed that the reinforcement ratio and bar diameter affect the degree of tension stiffening. His formulation was modified by Vecchio (2000) to account for multi-directional reinforcement, as follows:

$$f_{c1}{}^{a} = \frac{f_{cr}}{1 + \sqrt{c_t \times \varepsilon_{c1}}} \tag{3.44}$$

$$\text{where } \; c_t = 3.6 \times t_d \times m \;\text{ and }\; t_d = 0.6 \tag{3.45) and (3.46}$$

$$\frac{1}{m} = \frac{4 \times \rho_x}{d_{bx}} \times \left|\cos\theta\right| + \frac{4 \times \rho_y}{d_{by}} \times \left|\sin\theta\right| \tag{3.47}$$

It should be noted that $f_{c1}{}^{a}$ is limited to the amount which can be transmitted across cracks as defined by Eq. 3.25.

*Tension softening* refers to fracture-associated mechanisms. This phenomenon may be significant in lightly reinforced concrete members such as beams containing no transverse reinforcement. The tension softening formulation used in the DSFM is as follows:

$$f_{c1}{}^{b} = f_{cr} \times \left( 1 - \frac{\varepsilon_{c1} - \varepsilon_{cr}}{\varepsilon_{ch} - \varepsilon_{cr}} \right) \geq 0 \tag{3.48}$$

$$\text{where } \varepsilon_{ch} = \frac{2 \times G_f}{L_r \times f_{cr}} \tag{3.49}$$

where $G_f$ is the facture energy of concrete taken as $G_f = 75 \times 10^{-3}$ N / *mm*, and $L_r$ is the reference length taken as $S_{m\theta}$ of Eq. 3.29.

The resulting *average tensile principal stress* is the larger of the tension stiffening and tension softening stresses:

$$f_{c1} = \max \left( f_{c1}{}^{a}, f_{c1}{}^{b} \right) \tag{3.50}$$

### 3.3.3.4 Reinforcement in Tension or Compression

As shown in Figure 3.14, the reinforcement response in compression or tension is represented by a trilinear relationship between average strains and stresses as follows:

$$f_{si} = E_{si} \times \varepsilon_{si} \qquad \text{for} \quad 0 \leq \varepsilon_{si} \leq \varepsilon_{yi} \tag{3.51}$$

$$f_{si} = f_{yi} \qquad \text{for} \quad \varepsilon_{yi} \leq \varepsilon_{si} \leq \varepsilon_{shi} \tag{3.52}$$

$$f_{si} = f_{yi} + E_{shi} \times (\varepsilon_{si} - \varepsilon_{shi}) \qquad \text{for} \quad \varepsilon_{shi} < \varepsilon_{si} < \varepsilon_{u} \tag{3.53}$$

$$f_{si} = 0 \qquad \text{for} \qquad \varepsilon_{si} \geq \varepsilon_u \tag{3.54}$$

where the subscript i refers to either the x- or y-component of reinforcement, $f_{si}$ is the stress, $f_{yi}$ is the yield stress, $f_{ui}$ is the ultimate stress, $\varepsilon_{si}$ is the strain, $\varepsilon_{yi}$ is the yield strain, $\varepsilon_{shi}$ is the strain at the onset of strain hardening, and $\varepsilon_{ui}$ is the ultimate stress.

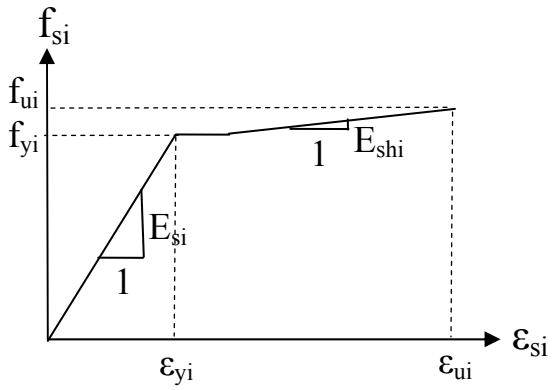


**Figure 3.14** Stress-Strain Relationship for Reinforcement

### 3.3.4 Local Crack Conditions

As in the MCFT, it is assumed that the average tensile stress in the concrete must be carried by an increase in the reinforcement stresses at the crack, and is limited to the reserve capacity of the reinforcement for which Eq. 3.24 must be satisfied.

$$f_{c1} \leq \rho_x \times \left( f_{yx} - f_{sx} \right) \times \cos^2 \theta + \rho_y \times \left( f_{yy} - f_{sy} \right) \times \sin^2 \theta \tag{3.24}$$

The local reinforcement stresses can be calculated by static equilibrium in the direction normal to the crack surface (Figure 3.9(b)). The resulting equation becomes

$$f_{c1}{}^a - f_{c1}{}^b = \rho_x \times \left( f_{scrx} - f_{sx} \right) \times \cos^2 \theta + \rho_y \times \left( f_{scry} - f_{sy} \right) \times \cos^2 \left( \theta - 90^\circ \right) \tag{3.25}$$

In Eq. 3.25, $f_{c1}{}^a$ refers to the concrete tensile stress due to the tension stiffening mechanism (Eq. 3.44), and $f_{c1}{}^b$ refers to the concrete tensile stress due to the tension softening mechanism (Eq. 3.48). If the tension softening mechanism is governing (i.e.,

$f_{c1}^{\ b} > f_{c1}^{\ a}$), the left-hand side of Eq. 3.25 is taken as zero, thereby yielding $f_{scrx} = f_{sx}$ and $f_{scry} = f_{sy}$.

Unlike MCFT, there is no need to limit the interface shear stress because the crack slip deformations are explicitly incorporated into the DSFM formulations. Elimination of this complex calculation gives the DSFM an advantage when implementing it into finite element programs.

Defined by Eq. 3.26, the interface shear stress, $v_{ci}$, is still calculated and used in the slip strain calculations.

$$v_{ci} = \rho_x \times \left(f_{scrx} - f_{sx}\right) \times \cos\theta \times \sin\theta + \rho_y \times \left(f_{scry} - f_{sy}\right) \times \cos\left(\theta - 90^\circ\right) \times \sin\left(\theta - 90^\circ\right) \qquad (3.26)$$

## 3.4 Brief Description of the Nonlinear Analysis Procedure

### 3.4.1 Overview of the Proposed Analysis Procedure

The nonlinear frame analysis procedure involves a total load, iterative, secant stiffness formulation. It is capable of performing analyses for the combined effects of both mechanical (axial load, shear force, bending moment) and thermal loads while considering several second-order effects: geometric nonlinearity, concrete dilatation, concrete confined strength and reinforcement dowel action. In addition, based on the MCFT or the DSFM, realistic constitutive relations are utilized which include such mechanisms as compression softening, tension stiffening, tension softening, crack slip check and element slip distortions.

The calculation procedure consists of two interrelated analyses. First, a *global frame analysis* is performed to obtain the member end forces and displacements which are used to calculate member deformations. Using the calculated member deformations, *sectional analyses* are then performed to determine the sectional member forces. Both the global frame analysis and the sectional analyses are performed iteratively, thereby resulting in a

double iterative procedure. The analysis is carried on until the member end forces obtained from the global analysis and from the sectional analysis converge.

### 3.4.2 Unbalanced Force Approach

The nonlinear analysis procedure is based on the concept of *unbalanced forces*. In this approach, gross member properties are used (i.e., $I_g$, $E_g$ and $A_g$) throughout the analysis. The basic analysis steps of the global frame analysis are listed below for a particular load stage:

**(1)** Determine all the forces acting on the structure including mechanical loads, temperature loads, and compatibility restoring forces.

**(2)** Perform a global linear-elastic frame analysis of the structure to determine the member end-actions, i.e., M, N and V.

**(3)** Determine the axial and shear strain distributions for each member.

**(4)** Perform sectional analysis iterations for each member to calculate the sectional forces.

**(5)** Calculate the unbalanced forces (i.e., the differences between sectional and global forces) for each member.

**(6)** Add the unbalanced forces to the compatibility restoring forces to be applied to the structure.

**(7)** Return to step (1) until all unbalanced forces become zero.

The analytical procedures summarized above are explained in detail in the following sections.

### 3.4.3 Compatibility Restoring Forces

Compatibility restoring forces can be defined as virtual static loads which are used to force member deformations in the frame analysis to match those in the nonlinear sectional analysis. This procedure is performed through global frame analysis iterations during which the unbalanced forces are added to the compatibility restoring forces until

no additional unbalanced forces are produced by the members. Compatibility restoring forces are applied to the ends of each member in a self-equilibrating manner (Figure 3.15). As a result, they do not affect reactions.

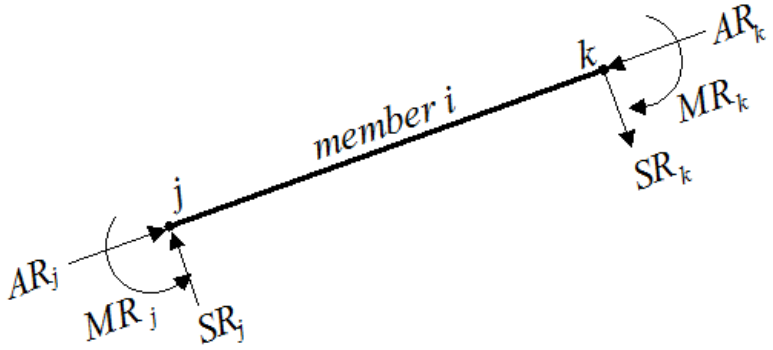


**Figure 3.15** Compatibility Restoring Forces in Element-Oriented Axes

### 3.5 Nonlinear Thermal Analysis

One of the most important analysis capabilities of TEMPEST was its ability to analyze reinforced concrete frames subjected to thermal loads. The analytical model used in this calculation was not restricted by any particular set of simplifying assumptions. The sectional analysis procedure used for this purpose could account for nonlinear material response and time- and temperature-dependent effects (Vecchio, 1987).

At elevated temperatures, strength, stiffness and other mechanical properties of concrete and reinforcing steel are significantly affected. Therefore, strength-temperature dependence must be taken into account in determining a section's response to load. In TEMPEST, eight modification factors were used for that purpose. Based on Eurocode 2, Part 1.2, Section 3 (1992), they were all built into the program as presented in Figure 3.16.

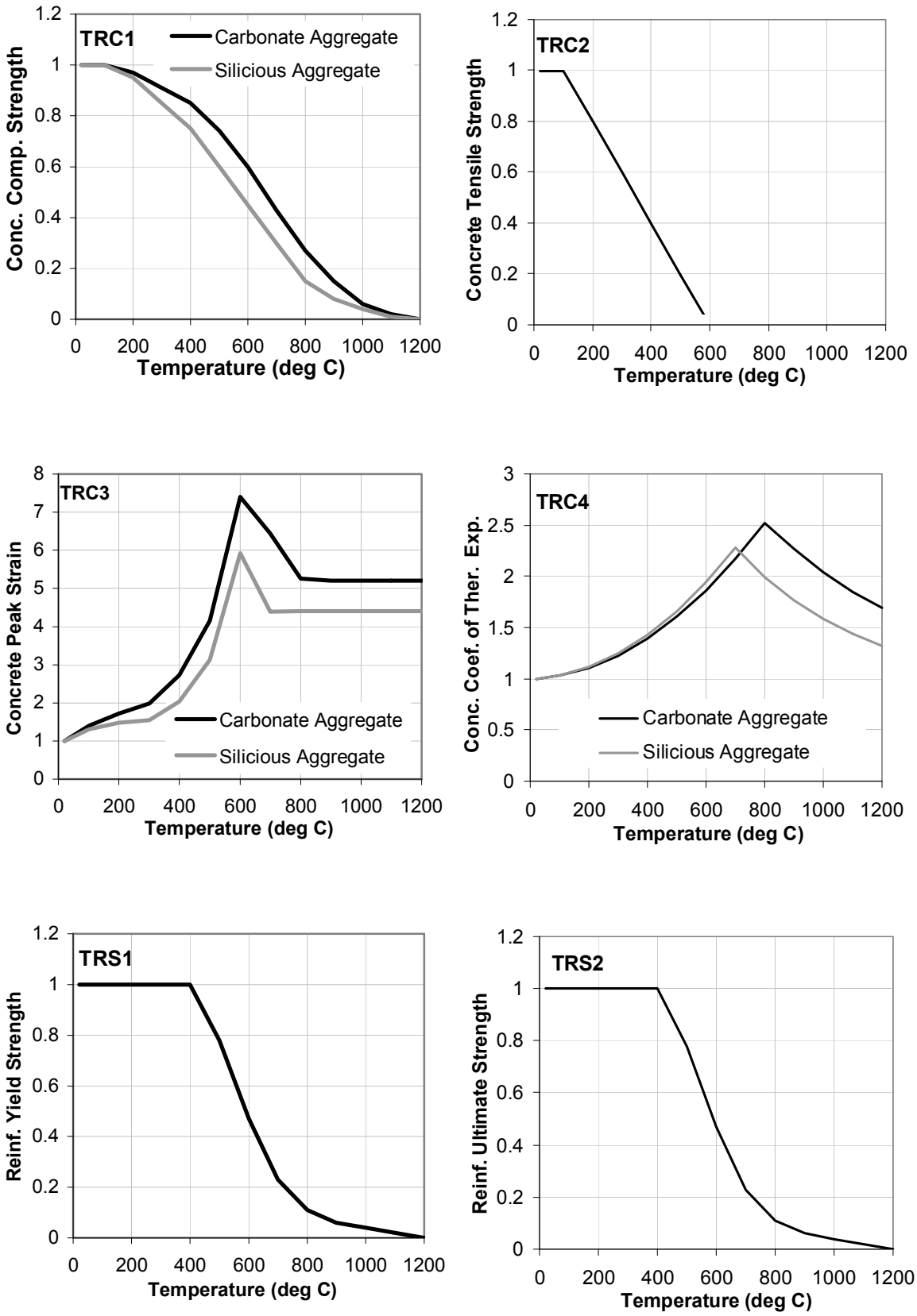


**Figure 3.16** Modification Factors due to Elevated Temperatures

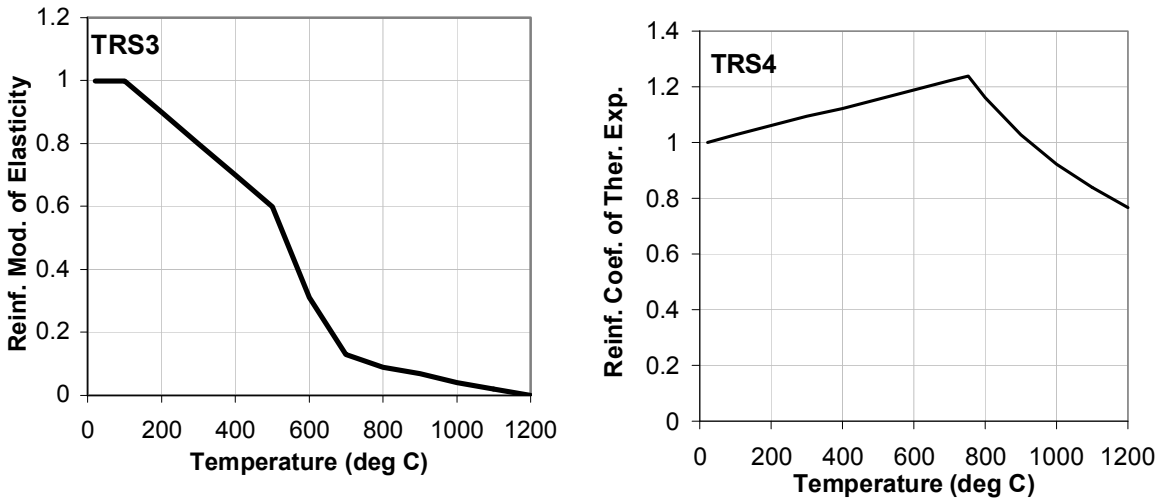


**Figure 3.16** Modification Factors due to Elevated Temperatures (continued)

For members under thermal load, TEMPEST determined nonlinear temperature profiles for each layer using standard one-dimensional heat flow principles. The temperature at the mid-depth of each concrete layer, reinforcing bar and prestressing steel component was determined using the following equation (Eq. 3.55). (3-55)

$$T_i = T_1 + \frac{(T_2 - T_1) \times x}{h_s} + \frac{2}{\pi} \sum_{n=1}^{\infty} \left\{ \frac{\left[T_2 \times \cos(n\pi) - T_1\right] - \left[T_2' \times \cos(n\pi) - T_1'\right]}{n} \times \sin\left(\frac{n\pi x}{h}\right) \times e^{\frac{-k \times n^2 \times \pi^2 \times t}{h_s^2}} \right\}$$

where $T_i$ is the temperature (°C) at midpoint of component *i*, $T_1$ is the temperature at the bottom surface, $T_2$ is the temperature at the top surface, $T_1'$ is the initial temperature at the bottom surface, $T_2'$ is the initial temperature at the top surface, $x$ is the distance $(mm)$ from the bottom surface to the midpoint of element *i*, $t$ is the time elapsed $(hr)$, and k is the coefficient of thermal conductivity $\left(mm^2/hr\right)$ of concrete (Vecchio, 1987). An example of the resulting temperature gradient based on Eq. 3.55 is given in Figure 3.17.

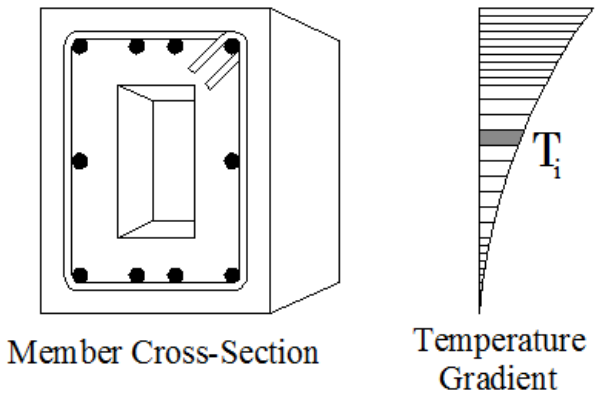


**Figure 3.17** Nonlinear Temperature Gradient across Cross Section Depth

The thermal calculations presented above were retained in VecTor5 and the resulting thermal analysis procedure was verified through several simple applications. Having determined the temperature of the concrete layers and the reinforcing and prestressing bar layers, the newly implemented sectional calculations are performed with the thermally induced prestrains added to the elastic concrete and steel prestrains as explained in Section 3.7.

### 3.6 Global Linear-Elastic Frame Analysis

A typical plane frame member is shown in Figure 3.18. The nodes at the ends of the member are denoted as j and k. The degrees of freedom of the typical *member i* are indicated relative to the member-oriented local coordinate system axes, $X_M$, $Y_M$ and $Z_M$ in Figure 3.18. The member axes are rotated from global coordinate system axes, x, y, z about $Z_M$ axis by the angle γ.

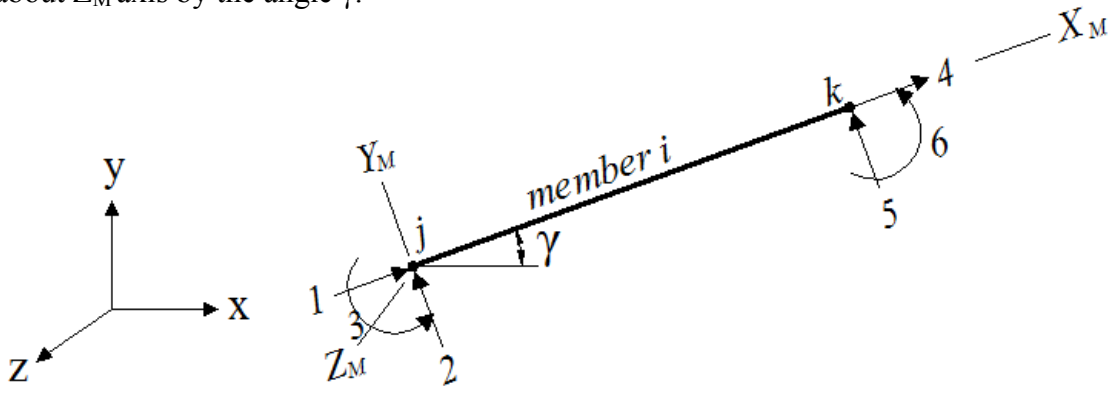


**Figure 3.18** Degrees of Freedom of a Typical Frame Member in Element-Oriented Axes

The elastic plane frame analysis routine used as the basis for the procedure is that described by Weaver and Gere (1990) with some additions (Vecchio, 1987). As in most elastic frame analysis programs, fixed-end forces are determined to define a load vector. A global stiffness matrix is assembled and inverted, and final deflections and force distribution are then calculated directly.

The only significant difference is in the handling of fixed-end forces. In most elastic frame analyses, fixed-end forces are determined solely from the magnitude of the applied loads and from the properties of members on which they act. However, this direct approach cannot be used in a nonlinear analysis procedure based on the concept of unbalanced forces where the compatibility restoring forces must be added to the fixed-end forces. As explained above, the compatibility restoring forces change based on the unbalanced forces calculated. As a result, the elastic frame analysis should be performed iteratively until the compatibility restoring forces converge (i.e., all unbalanced forces became zero). A flowchart indicating the global frame analysis steps is presented in Figure 3.19, where the newly added steps are shown with bold type and the modified steps with dotted lines.

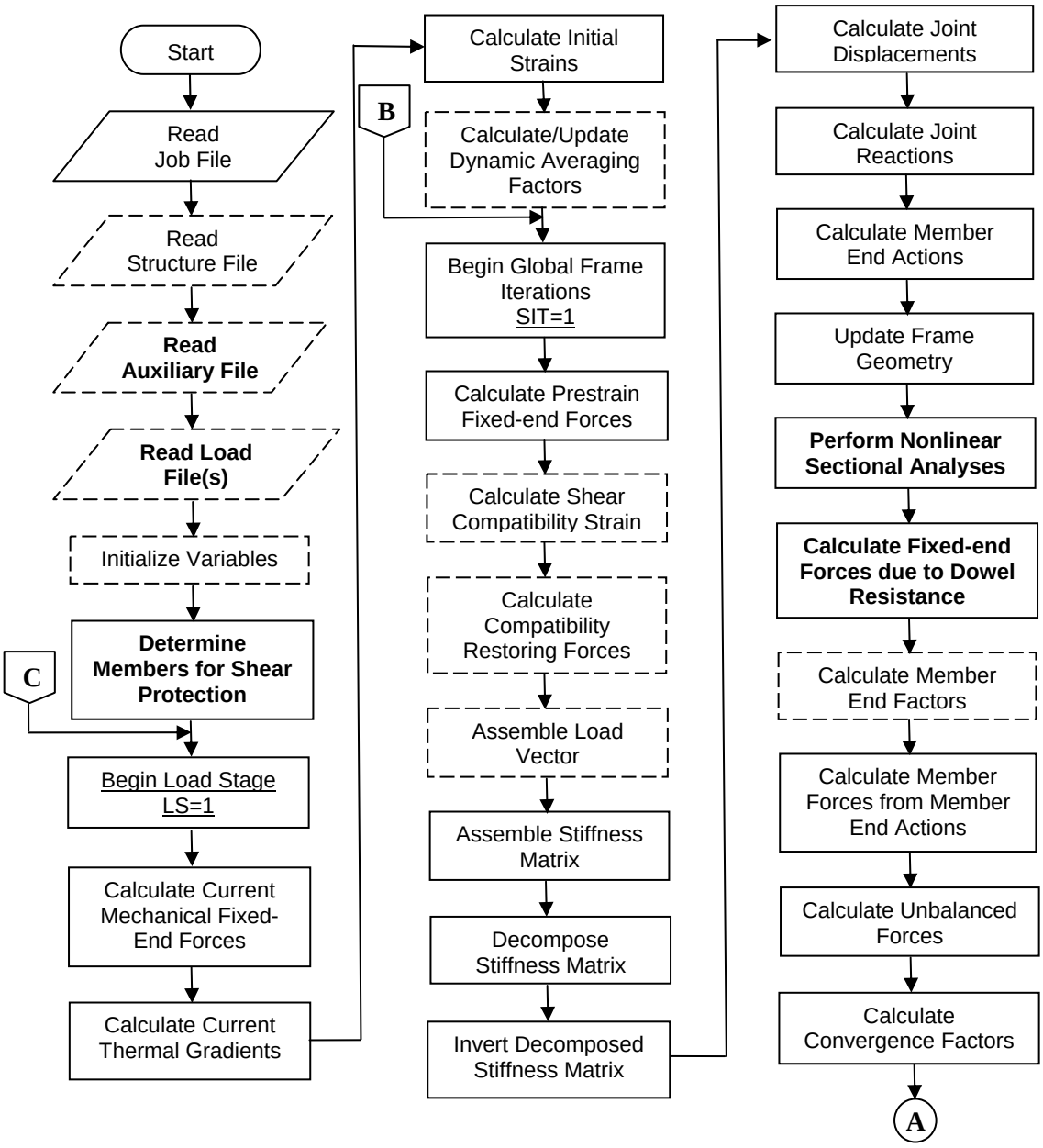


**Figure 3.19** Flow Chart for the Global Frame Analysis

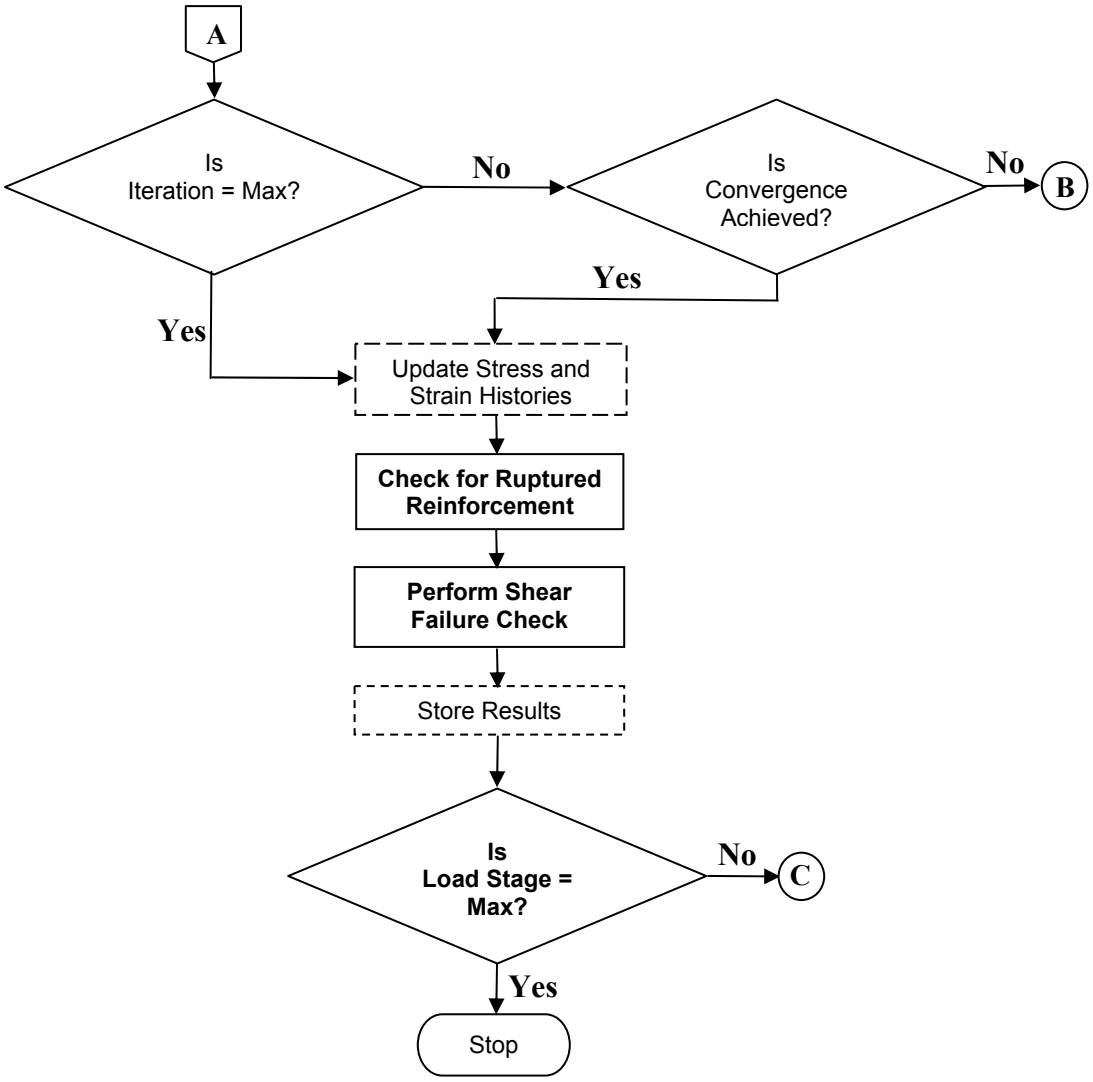


**Figure 3.19** Flow Chart for the Global Frame Analysis (continued)

### 3.6.1 Read Input Data

A nonlinear frame analysis starts with reading input text files which include structure, load, job and auxiliary data files.

### 3.6.2 Determination of Members for Shear Protection

This algorithm is described in Section 3.11.

### 3.6.3 Calculation of Current Mechanical Fixed-end Forces

The algorithm used to calculate the mechanical fixed-end forces is as described by Weaver and Gere (1990). The fixed-end forces must be recalculated at each load stage as the loads usually change from one load stage to another.

### 3.6.4 Calculation of Thermal Gradients

Thermal gradients are time-dependent and are calculated based on Eq. 3.55 for each concrete layer, reinforcing bar and prestressing steel component. When performing a temperature analysis, a time step is defined rather than a load step. At each time step, the nonlinear thermal gradients must be re-evaluated.

### 3.6.5 Calculation of Initial Strains

The initial strains for each reinforcing bar and prestressing steel component are calculated with Eq. 3.56.

$$\varepsilon_{slp} = \Delta\varepsilon_p + \alpha_s \times TRS4 \times \Delta t \tag{3.56}$$

where $\Delta\varepsilon_p$ is the locked-in prestrain for prestressing steel bars, $\alpha_s$ is the coefficient of thermal expansion of the reinforcement $(1/°C)$, *TRS4* is the modification factor for $\alpha_s$ as shown in Figure 3.16, and $\Delta t$ is the temperature change.

### 3.6.6 Calculation of Dynamic Averaging Factors

Averaging factors are used for averaging the unbalanced forces to increase computational speed. This calculation is described in detail in Section 3.10.

### 3.6.7 Calculation of Shear Compatibility Strain

A shear compatibility strain, $\gamma_{ltc}$, as defined by Eq. 3.57, is calculated for each member based on the unbalanced shear force for the member determined from the previous global

frame iteration. For the first two global frame iterations, the unbalanced shear force is assumed to be zero.

$$\gamma_{ltc} = \gamma_{ltc}^{pre} + 1.15 \times \frac{FUS}{G_c \times A_t} \times DAVG_3 \tag{3.57}$$

where $\gamma_{ltc}$ is the shear compatibility strain to be used in the current global frame iteration, $\gamma_{ltc}^{pre}$ is the shear compatibility strain of the previous global frame iteration, FUS is the unbalanced shear force, $G_c$ is the elastic shear modulus as defined by Eq. 3.58, $A_t$ is the transformed cross-sectional area, and *DAVG3* is the dynamic averaging factor for the shear compatibility strain as explained in Section 3.10. As the shear area factor for a solid rectangular section is 1.2 and for a solid circular section 1.11, a factor of 1.15 is assumed in Eq. 3.57 for general cross sections. The shear modulus is calculated as

$$G_c = \frac{E_c}{2 \times (1 + \nu)} \tag{3.58}$$

where $E_c$ is the modulus of elasticity of concrete, and ν is the Poisson's ratio which is initially assumed to be 0.15.

### 3.6.8 Calculation of Compatibility Restoring Forces

The axial, moment and shear compatibility restoring forces are determined for each frame member as follows:

$$AR = AR^{pre} + FUA \times DAVG_1 \times TURBO \tag{3.59}$$

$$MR = MR^{pre} + FUM \times DAVG_2 \tag{3.60}$$

$$SR = SR^{pre} + (\gamma_{ltc} \times \frac{12 \times \mathrm{E}_c \times \mathrm{I}_z}{L_x^{\,2}} - SR^{pre}) \times DAVG_3 \tag{3.61}$$

where $AR^{pre}$, $MR^{pre}$ and $SR^{pre}$ are the axial, moment and shear compatibility restoring forces from the previous global frame iteration, *FUA* and *FUM* are the unbalanced axial force and bending moment, *DAVG1*, *DAVG2* and *DAVG3* are the dynamic averaging

factor described in Section 3.10, $I_z$ is the moment of inertia of the cross section, and $L_x$ is the length of the member. The term *TURBO* is used to increase the stability and speed of the unbalanced axial force calculation. It assumes a minimum value of 0.5 when the axial strain is in the range of zero. As the axial strain of the member increases or decreases, the value of *TURBO* increases to a predefined maximum value. The default maximum value is set to 2.0. $SR \times L_x / 2$ is also added to fixed-end moments to satisfy equilibrium (Figure 3.20).

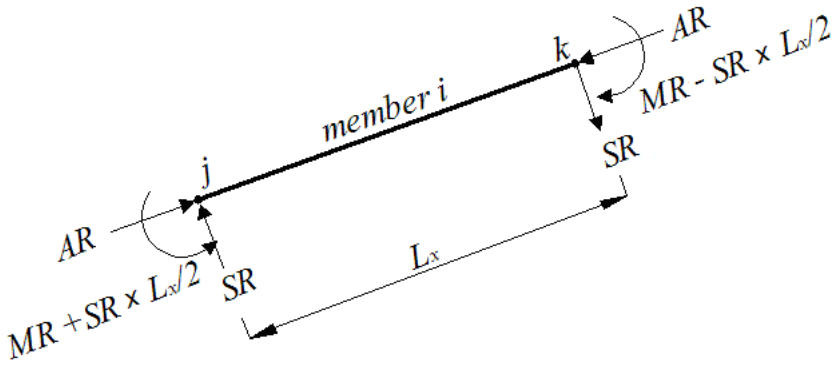


**Figure 3.20** Compatibility Restoring Forces in Element-Oriented Axes

### 3.6.9 Calculation of Joint Displacements, Reactions and Member End-Actions

A load vector $\{p\}$, consisting of fixed-end forces due to both applied mechanical loads and fictitious compatibility restoring forces, first is assembled. A structural stiffness matrix $[k]$ is then created and assembled based on the procedure described by Weaver and Gere (1990). Decomposition and inversion is carried out according to the Gauss elimination procedure. Joint displacements $\{u\}$ are determined through the partitioned matrix approach. Support reactions and member end-actions relative to the elemental axes are calculated based on Weaver and Gere (1990). This calculation procedure was taken directly from the original formulation of TEMPEST.

$$[k] \times \{u\} = \{p\} \quad \text{and} \quad \{u\} = [k]^{-1} \times \{p\} \tag{3.62}$$

### 3.6.10 Update of Frame Geometry

Based on the calculated displacements of the nodes, the new coordinates of all nodes are determined and new member lengths and direction cosines are calculated. This update is

performed at each global frame iteration in order to consider geometric nonlinearity. More details of this calculation are presented in Section 3.13.1.

### 3.6.11 Perform Nonlinear Sectional Analyses

This is one of the most important new algorithms implemented into the proposed analytical tool. The purpose of this calculation is to determine the nonlinear response of each section to imposed sectional deformations; that is, to find the resulting sectional forces M, N and V. This calculation can be performed using either of two different shear analysis modes: (1) shear-strain-based and (2) shear-stress-based. In both approaches, the longitudinal strain distribution is determined from the global frame analysis results. Using the updated nodal displacements and the initial member lengths, the change in the lengths of the members is calculated to find the axial strains at the mid-depths of the members, $\varepsilon_{cl}$ , as defined in Eq. 3.63 (Figure 3.21). The curvatures of the members, $\phi$ , are calculated from the two end rotations, $\varphi_i$ and $\varphi_{i+1}$ ,and the updated member lengths, $L$, as defined by Eq. 3.64.

$$\varepsilon_{cl} = \frac{L - L_o}{L_o} \qquad (3.63)$$

$$\phi = \frac{\varphi_{i+1} - \varphi_i}{L} \qquad (3.64)$$

$$\varepsilon_{x,top} = \varepsilon_{cl} - \frac{h_s}{2} \times \phi \qquad (3.65)$$

$$\varepsilon_{x,bot} = \varepsilon_{cl} + \frac{h_s}{2} \times \phi \qquad (3.66)$$

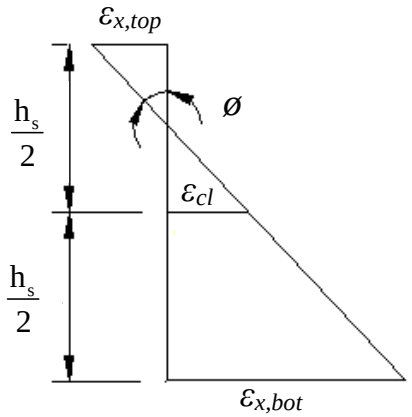


**Figure 3.21** Longitudinal Strain Distribution across Cross Section Depth

where $L_o$ is the initial length of the member, and $h_s$ is the cross section height.

In the shear-strain-based analysis, the average shear strain for each member is calculated by Eq. 3.57 and is distributed across the cross section depth based on either of two different assumptions. The first available assumption is that the calculated $\gamma_{ltc}$ is uniform

throughout the cross section depth, while the second one is that the calculated $\gamma_{ltc}$ varies parabolically with $\gamma_{ltc}$ being the value at the mid-depth of the cross section. In this approach, the strain in the transverse direction, $\varepsilon_y$, must converge to find the required axial stresses in the concrete layers, $\sigma_{cx}$, at the end of the sectional calculations.

In the shear-stress-based analysis, a uniform shear flow is assumed across the cross section depth based on Eq. 3.67 and the corresponding shear strains of the layers are calculated through sectional calculations. This approach is more demanding in terms of computation as both $\gamma_{ltc}$ and $\varepsilon_y$ for each concrete layer must be determined to find the required axial stress in each concrete layer, $\sigma_{cx}$.

$$q = \frac{V}{y_c} \tag{3.67}$$

By default, the shear-strain-based analysis (parabolic distribution) is selected due to its ability to continue the analysis into the post-peak regime and its fast and numerically stable execution. Both approaches are usable with either the MCFT or the DSFM (by default), as desired.

Sectional analyses are performed iteratively for each concrete and steel layer present in each member. The purpose of the iterations performed for the concrete layers is to determine the axial and shear stresses in the shear-strain-based analysis as formulated in Section 3.7.2, or to determine the axial stresses in the shear-stress-based analysis as formulated in Section 3.7.4. At the same time the stresses in the reinforcing or prestressing bars are calculated as formulated in Section 3.7.5, and superimposed on the concrete response to obtain the sectional forces (i.e., N, V, M) as defined in Section 3.7.7. In addition, the local crack calculations are performed as defined in Section 3.7.6 These iterative calculations are performed during each global frame analysis iteration, creating a double iterative solution technique.

### 3.6.12 Calculation of Fixed-End Forces due to Dowel Resistance

The dowel resistance provided by the reinforcing bars may be significant in some cases, for example, in beams or columns with low percentages of shear reinforcement. Therefore, this resistance is taken into account in the analysis calculation and is added to the fixed-end forces. Details of this implementation are given in Section 3.13.2.

### 3.6.13 Calculation of End Factors and Member Forces

End factors are used to average the end actions of members to determine one axial force, one shear force and one bending moment value for each member. In order to account for a possible concentration of deformations at one particular end of the member, the end with higher actions is typically given a higher weighting in this averaging process. Details of this implementation are given in Section 3.8.

### 3.6.14 Calculation of Unbalanced Forces

Unbalanced forces are the differences between member forces calculated by the global frame analysis and those obtained from the nonlinear sectional analysis, as follows:

$$N_{unbal_i} = N_i - N_{\sec_i} \tag{3.68}$$

$$M_{unbal_i} = M_i - M_{\sec_i} \tag{3.69}$$

$$V_{unbal_i} = V_i - V_{\sec_i} \tag{3.70}$$

In the case of a shear-stress-based analysis, there are no unbalanced shear forces produced as the shear force calculated by the global frame analysis is directly used to calculate shear flow in the sectional analyses.

### 3.6.15 Calculation of Convergence Factors

There are three options available for this purpose. The default option is '*weighted displacements'*. Details of this calculation are given in Section 3.9.

### 3.6.16 Update stress and Strain Histories

Information such as the stresses and strains in the concrete layers and reinforcing and prestressing steel layers, concrete crack conditions, and parameters required for cyclic models are stored to the computer memory. This information is especially useful when performing cyclic, reversed cyclic or dynamic analysis with the developed analysis tool. However, in the case of monotonic loading, they are also used as some parts of the structure may be unloading or the neutral axes of the member sections may be shifting which may cause some layers to unload.

### 3.6.17 Check for Ruptured Reinforcement

All reinforcement strains are checked with their rupture strains to determine bar fractures. If a bar fracture is encountered, the stress in that bar is taken as zero for all subsequent load stages.

### 3.6.18 Storage of Results

The analysis results pertaining the current load stage are stored in an ASCII file which then can be viewed with a text editor such as Microsoft Windows Notepad. This file contains detailed information regarding structure deformations, reactions and concrete and reinforcement conditions. It is also possible to store the analysis results in a binary file. This file can be used as a seed file when starting an analysis from the damaged condition of the structure at the end of a previous analysis and applying a new load condition on the structure.

## 3.7 Sectional Analysis

The response of each reinforced or prestressed concrete section to thermal and mechanical loads is determined using a layered section approach in which the cross section is divided into a number of concrete layers, longitudinal reinforcing bar layers and longitudinal prestressing steel layers (Figure 3.22). The procedure requires supply of the concrete layer widths, $b_i$ and heights, $h_i$, reinforcing and prestressing steel areas, $A_{sj}$, and basic mechanical properties of concrete, reinforcing steel (longitudinal and transverse) and prestressing steel (longitudinal) as shown in Figure 3.22.

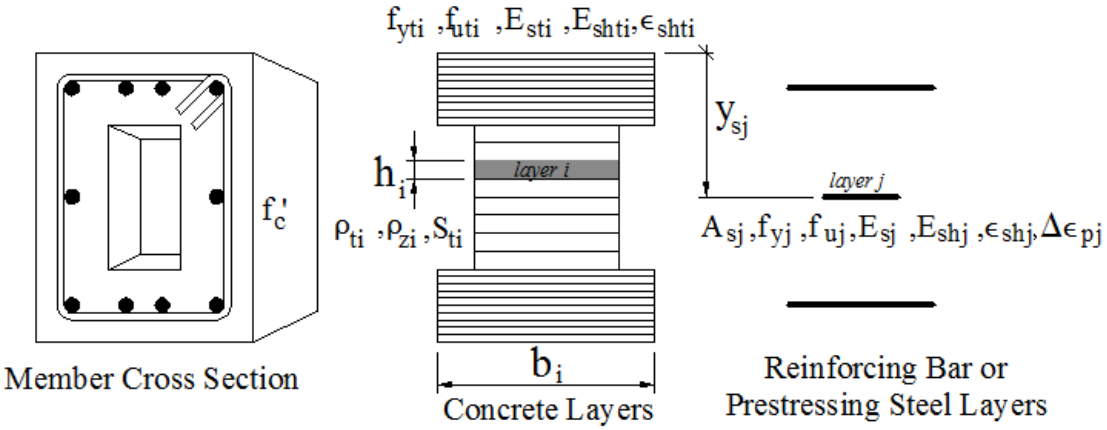


**Figure 3.22** Input Parameters for Sectional Analysis of VecTor5

In Figure 3.22, $f'_c$ is the concrete compressive strength, $\rho_{ti}$ and $\rho_{zi}$ are the transverse and out-of-plane reinforcement ratios respectively, $S_{ti}$ is the spacing of the transverse reinforcement in the longitudinal direction, $f_{yi}$ and $f_{ui}$ are the yield and ultimate stresses of the transverse reinforcement respectively, $E_{sti}$ and $E_{shti}$ are the Young's and the strain hardening moduli of the transverse reinforcement, $\varepsilon_{shti}$ is the strain at the onset of strain hardening, $A_{sj}$ is the total cross-sectional area of the longitudinal reinforcement, and $\Delta\varepsilon_{pj}$ is the locked-in strain for a prestressing steel layer.

Each concrete layer and steel element is then analyzed individually based on the MCFT or the DSFM, although sectional compatibility and sectional equilibrium conditions are satisfied as a whole. The main sectional compatibility requirement enforced is that plane sections must remain plane, while the sectional equilibrium requirements include balancing the axial force, shear force and bending moment which are calculated by the global frame analysis. An assumption regarding the shear strain or shear flow distribution is also made as explained below. In addition, the clamping stresses in the transverse direction are assumed to be zero, which permits the calculation of the total concrete strains in the transverse direction in a shear-strain-based analysis as explained in Section 3.7.2, or the axial concrete stresses in a shear-strain-based analysis as explained in Section 3.7.4. It should be noted that the assumption of zero clamping stresses is not always true as explained in Section 1.2.4.

In this layered representation of a cross section, the 'plane sections remain plane' hypothesis permits the calculation of the longitudinal strain in each layer of concrete,

reinforcing steel and prestressing steel as a function of the top and bottom fibre strains (Figure 3.21). It is further assumed that the strains in each layer are uniform and equal to the strains at the centre of the layer (Figure 3.23). Therefore, the longitudinal strain distribution (Figure 3.21) can simply be determined from the axial deformation and curvature values calculated by the global frame analysis as defined by Eq. 3.63 to 3.66.

As for the consideration of shear, there are basically two different procedures available, as previously indicated: a shear-stress-based analysis, and a shear-strain-based analysis. Based on these two procedures, five different shear analysis options are available. They are: (0) Shear not Considered, (1) Uniform Shear Flow Distribution (Multi-Layer Analysis), (2) Uniform Shear Strain Distribution (Multi-Layer Analysis), (3) Parabolic Shear Strain Distribution (Multi-Layer Analysis), and (4) Parabolic Shear Strain Distribution (Single-Layer Analysis) (Figure 3.23).

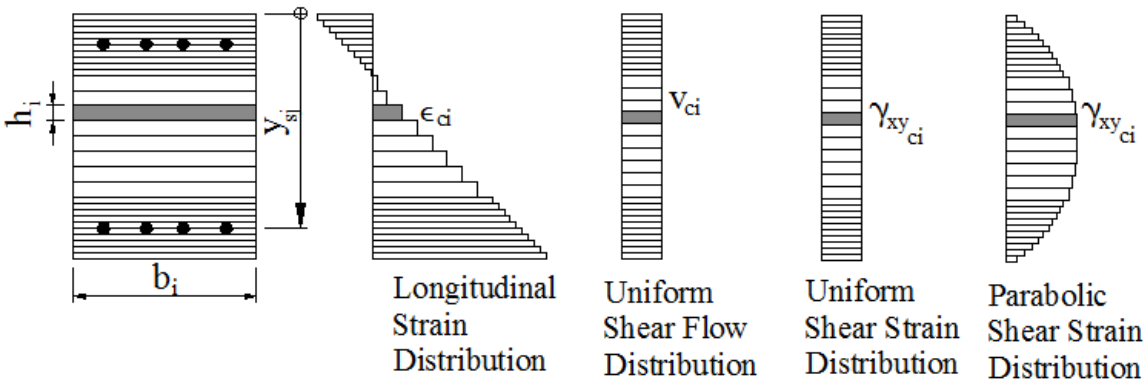


**Figure 3.23** Longitudinal and Shear Strain Distribution across Cross Section Depth

With option (0), the shear-related effects are neglected: that is, $\gamma_{xy} = 0$ for all layers of all members. This will significantly simplify and speed up the calculations. This option may be useful when analyzing a structure which is clearly flexure-dominated or evaluating the effects of shear deformations after running one of the other options.

### 3.7.1 Calculation of Longitudinal Reinforcement Ratios for Sectional Calculations

In the application of the MCFT or the DSFM to the sectional analysis, smeared reinforcement ratios should be known for each concrete layer in order to form the

composite material stiffness matrix. Transverse reinforcement ratios are assigned to each concrete layer; therefore, no calculation is required to determine them. However, as the longitudinal reinforcement is defined as discrete bars for each cross section, it should be smeared within the concrete layer as a percentage.

To smear the defined longitudinal reinforcement within the concrete layers, the reinforcement layers are assumed to be effective for each member in a tributary area of 7.5 times the bar diameters as suggested by CEB-FIB (1990). Based on this approach, the effective concrete areas for each reinforcement are calculated and the smeared reinforcement ratios are then determined as the quotient of the total reinforcement area divided by the effective concrete area. The resulting reinforcement ratio is used directly in the sectional analyses when analyzing the related concrete layer. If there is a layer in which more than one layer of reinforcement is contributing, the reinforcement ratios are added for that particular layer and the material properties of the two contributing reinforcement layers are averaged based on their total areas.

For clarification purposes, consider a cross section with three layers of reinforcement as shown in Figure 3.24. Assume the following properties: $d_{b1} = d_{b2} = 10$ mm and $d_{b3} = 20$ mm, $A_1 = 314$ mm$^2$, $A_2 = 157$ mm$^2$ and $A_3 = 1257$ mm$^2$, $f_{y1} = f_{y2} = 400$ MPa and $f_{y3} = 500$ MPa.

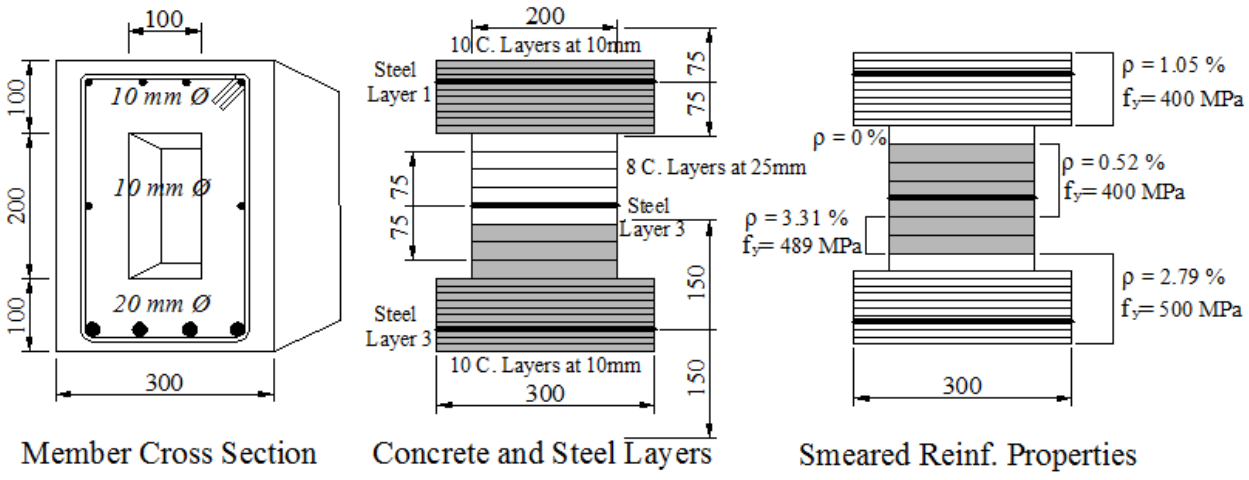


**Figure 3.24** Determination of Smeared Reinforcement Properties for Each Concrete Layer

Based on the given properties, the smeared reinforcement ratios and averaged steel properties are calculated as follows:

$$\rho_{eff\,1} = \frac{A_1}{A_{trb1}} = \frac{314}{100 \times 300} = 1.05\%$$

$$\rho_{eff\,2} = \frac{A_2}{A_{trb2}} = \frac{157}{150 \times 200} = 0.52\%$$

$$\rho_{eff\,3} = \frac{A_3}{A_{trb3}} = \frac{1257}{100 \times 300 + 75 \times 200} = 2.79\%$$

$f_{yeff} = \dfrac{157 \times 400 + 1257 \times 500}{157 + 1257} = 489$ MPa for the overlapping reinforcement ratios.

### 3.7.2 Shear-Strain-Based Analysis

In the shear-strain-based analysis, the shear strain at the mid-depth of the cross section is determined from the global frame analysis based on the unbalanced shear force as defined by Eq. 3.57.

The distribution of this strain to the concrete layers must be determined before starting the sectional calculations. For this purpose, one of two assumptions can be made: a uniform shear strain distribution, or a parabolic shear strain distribution (Figure 3.25).

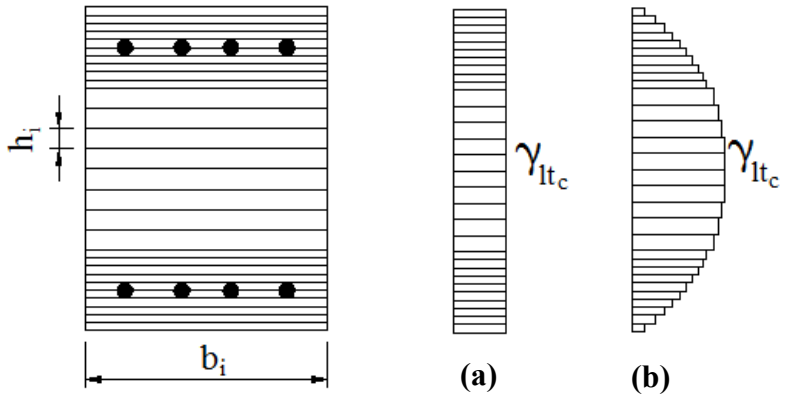


**Figure 3.25** Available Assumptions for Shear Strain Distribution: **(a)** Uniform Shear Strain; **(b)** Parabolic Shear Strain

The purpose of the shear-strain-based analysis is to calculate the longitudinal stress $\sigma_{cx}$ and shear stress $\tau_{xy}$ of each concrete layer. Known from the global frame analysis are $\varepsilon_x$ and $\gamma_{xy}$, while required is $\varepsilon_y$. After finding $\varepsilon_y$, the unknowns, $\sigma_{cx}$ and $\tau_{xy}$ can be found directly.

In its most general form, the total strains are assumed to consist of: (1) concrete net strains (the strains that cause stress), (2) concrete elastic offset strains (due to lateral expansion, thermal, shrinkage and prestrain effects), (3) concrete plastic offset strains (due to cyclic loading and damage), and (4) concrete crack slip offset strains (due to shear slip as considered by the DSFM). The resulting vector becomes

$$\left[\varepsilon\right] = \left[\varepsilon_{\mathrm{c}}\right]+\left[\varepsilon_{\mathrm{c}}^{\mathrm{o}}\right]+\left[\varepsilon_{\mathrm{c}}^{\mathrm{p}}\right]+\left[\varepsilon_{c}^{\mathrm{s}}\right]=\begin{bmatrix}\varepsilon_x\\ \varepsilon_y\\ \gamma_{xy}\end{bmatrix} \tag{3.71}$$

As perfect bond between concrete and reinforcement is assumed, the total strain of the reinforcement equals the total strain of concrete, and consists of: (1) reinforcement net strains (the strains that cause stress), (2) reinforcement elastic offset strains (due to thermal and prestrain effects), and (3) reinforcement plastic offset strains (due to cyclic loading and yielding). The resulting vector becomes

$$\left[\varepsilon\right] = \left[\varepsilon_{s}\right]+\left[\varepsilon_{s}^{o}\right]+\left[\varepsilon_{s}^{p}\right]=\begin{bmatrix}\varepsilon_x\\ \varepsilon_y\\ \gamma_{xy}\end{bmatrix} \tag{3.72}$$

In order to calculate the principal strains in this layer, $\varepsilon_y$ should be determined as both $\varepsilon_x$ and $\gamma_{xy}$ are known. Any value can be assumed for $\varepsilon_y$ to start the iterative calculation process. In the analytical tool developed, for faster execution, the starting value of $\varepsilon_y$ is taken from the previous sectional iteration. If this is the first sectional iteration, it is taken

from the previous load stage. If this is the first load stage, it is taken as zero. The principal strains, $\varepsilon_{c1}$ and $\varepsilon_{c2}$, can be calculated conveniently by means of a Mohr's circle (Figure 3.5). The corresponding principal stresses, $f_{c1}$ and $f_{c2}$, are calculated based on the MCFT or the DSFM as described in Section 3.2 and Section 3.3.

The concrete material secant moduli are then calculated based on Figure 3.26(a) as follows:

$$\overline{E}_{c1} = \frac{f_{c1}}{\varepsilon_{c1}} \tag{3.73}$$

$$\overline{E}_{c2} = \frac{f_{c2}}{\varepsilon_{c2}} \tag{3.74}$$

$$\overline{G}_c = \frac{\overline{E}_{c1} \times \overline{E}_{c2}}{\overline{E}_{c1} + \overline{E}_{c2}} \tag{3.75}$$

As the MCFT and the DSFM consider reinforced concrete as an orthotropic material in the principal stress directions, it is necessary to formulate the concrete material stiffness matrix, $[D_c]$', relative to those directions as follows:

$$[D_c]' = \begin{bmatrix} \overline{E}_{c1} & 0 & 0 \\ 0 & \overline{E}_{c2} & 0 \\ 0 & 0 & \overline{G}_c \end{bmatrix} \tag{3.76}$$

The concrete material stiffness matrix can then be transformed to the global x and y axes as follows:

$$[T_c] = \begin{bmatrix} \cos^2\theta & \sin^2\theta & \cos\theta \times \sin\theta \\ \sin^2\theta & \cos^2\theta & -\cos\theta \times \sin\theta \\ -2\times\cos\theta\times\sin\theta & 2\times\cos\theta\times\sin\theta & \cos^2\theta - \sin^2\theta \end{bmatrix} \tag{3.77}$$

$$[D_c] = [T_c]^T \times [D_c]' \times [T_c] \tag{3.78}$$

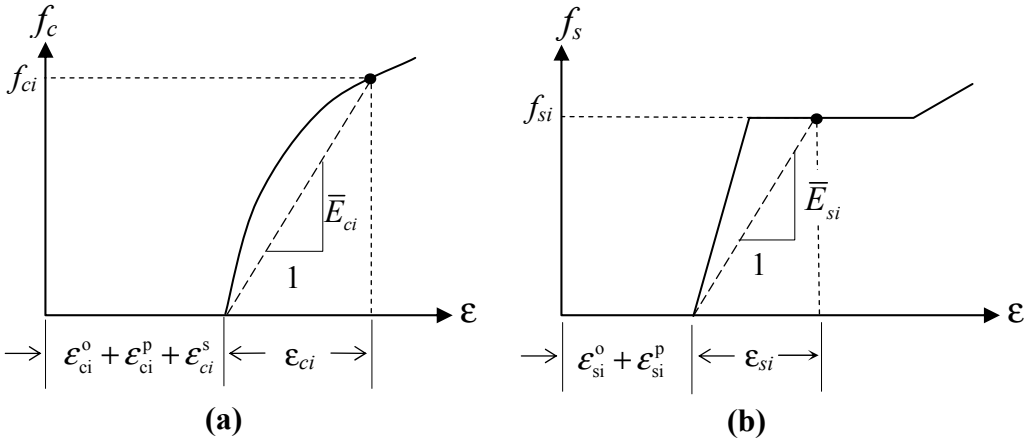


**Figure 3.26** Determination of Secant Moduli: **(a)** Concrete; **(b)** Reinforcement

Reinforcement secant moduli are calculated based on Figure 3.26(b) as follows:

$$\overline{E}_{sx} = \frac{f_{sx}}{\varepsilon_{sx}} \tag{3.79}$$

$$\overline{E}_{sy} = \frac{f_{sy}}{\varepsilon_{sy}} \tag{3.80}$$

Because the reinforcement components lie in two orthogonal directions, the global x and y axes, the reinforcement stiffness matrix becomes as shown below.

$$[D_s] = \begin{bmatrix} \rho_x \times \overline{E}_{sx} & 0 & 0 \\ 0 & \rho_y \times \overline{E}_{sy} & 0 \\ 0 & 0 & 0 \end{bmatrix} \tag{3.81}$$

The resulting composite material stiffness matrix is calculated as

$$[D] = [D_c] + [D_s] \tag{3.82}$$

$$[\sigma] = [D] \times [\varepsilon] - [\sigma^o] \tag{3.83}$$

In the equation above, both the $[D]$ matrix and the $[\varepsilon]$ vector are based on *total* strains, necessitating the deduction of $[\sigma^o]$ which is a pseudo stress matrix arising from the strain offsets shown in Figure 3.26:

$$[\sigma^o] = [\sigma_c{}^o] + \sum_{i=1}^{n} [\sigma_s{}^o]_i = \begin{bmatrix} S_{01} \\ S_{02} \\ S_{03} \end{bmatrix} \tag{3.84}$$

$$[\sigma_c{}^o] = [D_c] \times \left( [\varepsilon_c{}^o] + [\varepsilon_c{}^p] + [\varepsilon_c{}^s] \right) = [D_c] \times \left( \begin{bmatrix} \varepsilon_{cx}{}^o \\ \varepsilon_{cy}{}^o \\ \gamma_{cxy}{}^o \end{bmatrix} + \begin{bmatrix} \varepsilon_{cx}{}^p \\ \varepsilon_{cy}{}^p \\ \gamma_{cxy}{}^p \end{bmatrix} + \begin{bmatrix} \varepsilon_{cx}{}^s \\ \varepsilon_{cy}{}^s \\ \gamma_{cxy}{}^s \end{bmatrix} \right) \tag{3.85}$$

$$\sum_{i=1}^{n} [\sigma_s{}^o]_i = \sum_{i=1}^{n} [D_s]_i \times \left( [\varepsilon_s{}^o] + [\varepsilon_p{}^o] \right) = [D_s] \times \begin{bmatrix} \varepsilon_{sx}{}^o + \varepsilon_{sx}{}^p \\ 0 \\ 0 \end{bmatrix} + [D_s] \times \begin{bmatrix} 0 \\ \varepsilon_{sy}{}^o + \varepsilon_{sy}{}^p \\ 0 \end{bmatrix} \tag{3.86}$$

The layer stresses can then be calculated as follows:

$$\begin{bmatrix} \sigma_x \\ \sigma_y \\ \tau_{xy} \end{bmatrix} = \begin{bmatrix} D_{11} & D_{12} & D_{13} \\ D_{21} & D_{22} & D_{23} \\ D_{31} & D_{32} & D_{33} \end{bmatrix} \times \begin{bmatrix} \varepsilon_x \\ \varepsilon_y \\ \gamma_{xy} \end{bmatrix} - \begin{bmatrix} S_{01} \\ S_{02} \\ S_{03} \end{bmatrix} \tag{3.87}$$

Taking advantage of the assumption that there are no clamping stresses in the transverse direction, Eq. 3.87 can be expanded as

$$\sigma_y = D_{21} \times \varepsilon_x + D_{22} \times \varepsilon_y + D_{23} \times \gamma_{xy} - S_{02} = 0 \tag{3.88}$$

This assumption permits the calculation of the total strain in the transverse direction, which is the basic unknown in the procedure.

$$\varepsilon_y = \frac{-D_{21} \times \varepsilon_x - D_{23} \times \gamma_{xy} + S_{02}}{D_{22}} \tag{3.89}$$

Using the calculated $\varepsilon_y$ value, the new principal stresses are determined and the above calculations are repeated until the $\varepsilon_y$ value converges or the specified maximum number of iterations is reached (100 iterations by default). At the end of these calculations, the required stress values are calculated as follows:

$$\sigma_x = D_{11} \times \varepsilon_x + D_{12} \times \varepsilon_y + D_{13} \times \gamma_{xy} - S_{01} \tag{3.90}$$

$$\tau_{xy} = D_{31} \times \varepsilon_x + D_{32} \times \varepsilon_y + D_{33} \times \gamma_{xy} - S_{03} \tag{3.91}$$

### 3.7.3 Approximate Single-Layer Analysis

A new approximate analysis procedure was developed for very fast execution to get an estimate of the structural behaviour by considering shear-related influences only approximately. According to this analysis option, the above calculations including full shear effects are only performed for the concrete layer located at the mid-depth of the cross section where the shear strain is $\gamma_{ltc}$. The longitudinal reinforcement properties of the mid-depth layer are calculated by uniformly smearing all longitudinal reinforcement present in the cross section to all concrete layers in order to avoid a mid-depth layer with no smeared longitudinal reinforcement. The shear stress, $\tau_{xy}$, is calculated in exactly the same manner as explained above for the mid-depth layer. All layers are then analyzed based on flexural effects only (i.e., $\gamma_{ltc} = 0$), and the shear stresses of all layers are assumed to be equal to the value calculated for the mid-depth layer.

This analysis option runs very quickly and is useful when analyzing a model for the first time to adjust load steps and to check the model and structural behaviour for input errors.

A second analysis with full shear consideration is recommended for a more thorough consideration of shear-related effects.

### 3.7.4 Shear-Stress-Based Analysis

In a shear-stress-based analysis, the shear flow, $q$, acting on a cross section is determined from the global frame analysis based on the shear force, $V$, calculated as below.

$$q = \frac{V}{y_c} \tag{3.67}$$

where $y_c$ equals the section depth in which the transverse reinforcement is assigned; that is, the clear cover is assumed to not carry any shear flow. If the cross section does not contain transverse reinforcement, $y_c$ is assumed to be two thirds of the section depth (Figure 3.27).

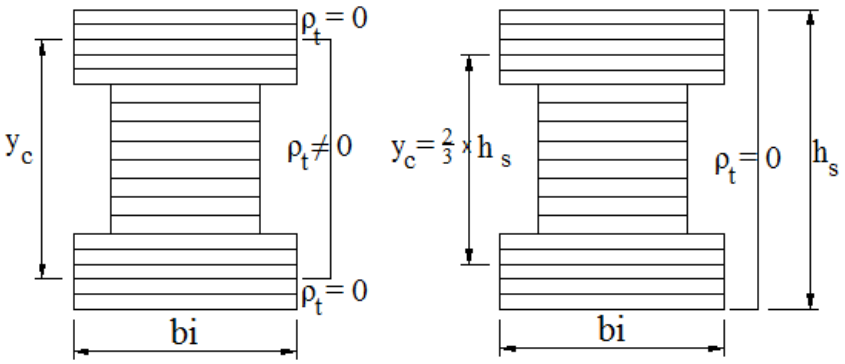


**Figure 3.27** Determination of Shear Flow for Concrete Layers

The shear stress $\tau_{xy}$ is calculated, for concrete layers carrying shear stress, as follows:

$$\tau_{xy} = \frac{q}{b_i} \tag{3.92}$$

The purpose of the shear-stress-based analysis is to calculate the longitudinal stress, $\sigma_{cx}$, within each concrete layer. Known from the global frame analysis are $\varepsilon_x$ and $\tau_{xy}$ while

required are $\gamma_{xy}$ and $\varepsilon_y$. After finding $\gamma_{xy}$ and $\varepsilon_y$, the unknown, $\sigma_x$ can be calculated directly. This procedure requires more iterations than the shear-strain-based procedure as two unknowns are evaluated iteratively. It also includes a matrix inversion at each iteration, which further increases the computational demand.

Consider again a single concrete layer which has a certain percentage of longitudinal and transverse reinforcement (Figure 3.23, shaded layer). In order to calculate the principal strains in this layer, both $\varepsilon_y$ and $\gamma_{xy}$ are needed. Any values can be assumed to start the iterative calculation process. In the analytical tool developed, for faster execution, they are taken from the previous sectional iteration as explained in the shear-strain-based analysis.

The principal stresses are found and the composite material stiffness matrix is assembled in the same way as formulated for the shear-strain-based analysis.

The layer stresses can be evaluated by Eq. 3.83. However, the total strains have to be determined first, requiring the inverse of composite material stiffness matrix $[D]$.

$$[\varepsilon] = [D]^{-1} \times [\sigma + \sigma^o] = [C] \times [\sigma + \sigma^o] \tag{3.93}$$

$$\begin{bmatrix} \varepsilon_x \\ \varepsilon_y \\ \gamma_{xy} \end{bmatrix} = \begin{bmatrix} C_{11} & C_{12} & C_{13} \\ C_{21} & C_{22} & C_{23} \\ C_{31} & C_{32} & C_{33} \end{bmatrix} \times \begin{bmatrix} \sigma_x + S_{01} \\ \sigma_y + S_{02} \\ \tau_{xy} + S_{03} \end{bmatrix} \tag{3.94}$$

From the matrix above, $\varepsilon_x$ can be expressed as follows:

$$\varepsilon_x = C_{11} \times (\sigma_x + S_{01}) + C_{12} \times (\sigma_y + S_{02}) + C_{13} \times (\tau_{xy} + S_{03}) \tag{3.95}$$

Taking advantage of the assumption that there are no clamping stresses in the transverse direction (i.e., $\sigma_y = 0$), the axial stress of the concrete can be easily found rearranging Eq. 3.95 as follows:

$$\sigma_x = \frac{\varepsilon_x - C_{12} \times (S_{02}) - C_{13} \times (\tau_{xy} + S_{03})}{C_{11}} - S_{01} \tag{3.96}$$

Using the calculated $\sigma_x$ value, the two unknown values can now be calculated as

$$\varepsilon_y = C_{21} \times (\sigma_x + S_{01}) + C_{22} \times (S_{02}) + C_{23} \times (\tau_{xy} + S_{03}) \tag{3.97}$$

$$\gamma_{xy} = C_{31} \times (\sigma_x + S_{01}) + C_{32} \times (S_{02}) + C_{33} \times (\tau_{xy} + S_{03}) \tag{3.98}$$

Using the calculated $\varepsilon_y$ and $\gamma_{xy}$ values, the new principal stresses are determined and the above calculations are repeated until convergence of $\varepsilon_y$ and $\gamma_{xy}$ are achieved or the specified maximum number of iterations is reached (100 iterations by default). At the end of these calculations, the $\sigma_x$ value can then be taken as the resulting longitudinal stress of the concrete layer.

### 3.7.5 Reinforcement Response

The reinforcement response must be superimposed on the concrete response to determine the necessary nonlinear sectional forces. For this purpose, the reinforcement strains should first be determined. Two reinforcement components are considered in the analysis procedure developed: longitudinal and transverse reinforcement.

In the most general case, the longitudinal reinforcement strain is composed of: (1) net strain $\varepsilon^{net}$ (i.e., the strain that causes stress), (2) prestrain offset strains $\Delta \varepsilon p$ (due to prestressing), (3) elastic offset strains $\alpha_s \times \Delta T \times \mathrm{T}RS4$ (due to thermal effects), and (4)

plastic offset strains $\varepsilon_s^{\ p}$ (due to cyclic loading and yielding). The resulting strain becomes

$$\varepsilon_{si} = \varepsilon^{net} - \Delta\varepsilon_p + \alpha_s \times \Delta T \times \mathrm{T}RS4 + \varepsilon_s^{\ p} \tag{3.99}$$

where *TRS4* is the modification factor for $\alpha_s$ as shown in Figure 3.16. The total strain $\varepsilon_{si}$ for each reinforcing or prestressing bar can be conveniently determined from the longitudinal strain distribution given in Figure 3.23. In this calculation, the strain values corresponding to the centre of the bar are considered.

As for the transverse reinforcement, the total strain is similarly decomposed into its components. The only difference is that no prestrains are considered for the transverse reinforcement.

$$\varepsilon_{yi} = \varepsilon_{yi}^{\ net} + \alpha_s \times \Delta T \times TRS4 + \varepsilon_{yi}^{\ p} \tag{3.100}$$

After determining the *net* strains for the reinforcement components, the corresponding stresses are calculated using the tri-linear reinforcement response described in Figure 3.14.

### 3.7.6 Local Crack Calculations

As explained in Sections 3.2.5 and 3.3.4, the MCFT and the DSFM require the consideration of local crack conditions. The purpose of this calculation is to determine the reinforcement stress and strain values at the cracks and to make sure that the average concrete stresses can be transmitted across the cracks by the reserve capacity of the reinforcement. In addition, the shear stresses $v_{ci}$ developed at the crack interface are calculated.

The local crack calculations are performed using a newly implemented subroutine during each sectional analysis iteration for each concrete layer. A flow chart of this subroutine is presented in Figure 3.28.

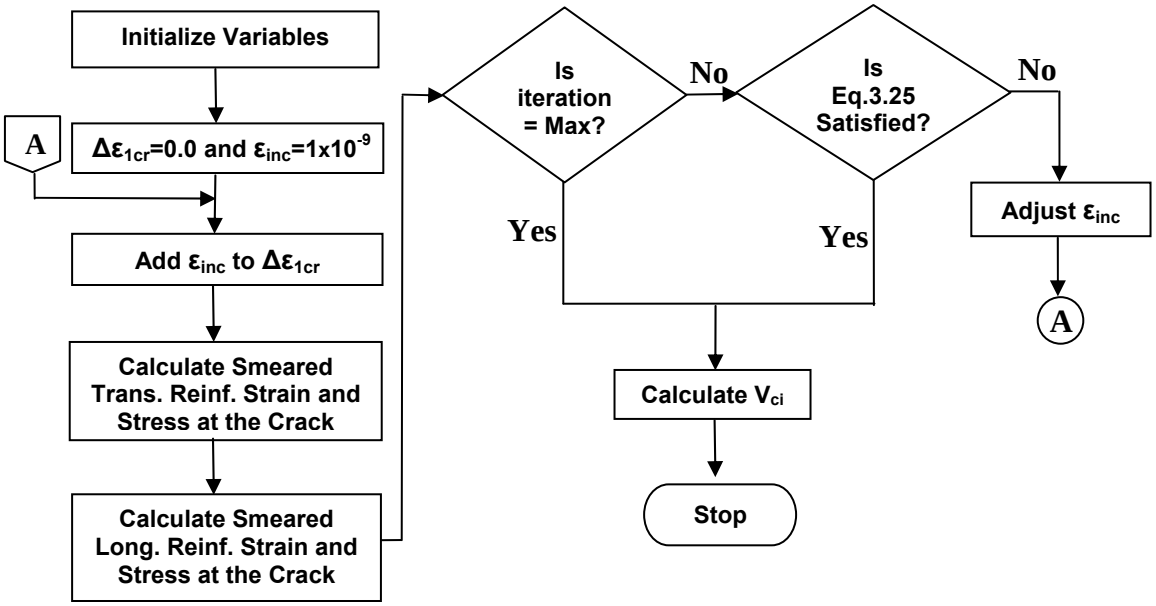


**Figure 3.28** Flow Chart for the Local Crack Calculation Algorithm of VecTor5

As indicated by Figure 3.28, the local crack calculations start by assuming a small value ($1x10^{-9}$) for the incremental strain, $\Delta\varepsilon_{1cr}$. The smeared longitudinal and transverse reinforcement strains at the crack are then calculated by Eq. 3.101 and Eq. 3.102, respectively.

$$\varepsilon_{scri} = \varepsilon^{net} - \Delta\varepsilon_p + \alpha_s \times \Delta T \times \mathrm{T}RS4 + \varepsilon_s{}^p + \Delta\varepsilon_{1cr} \times \cos^2\theta \tag{3.101}$$

$$\varepsilon_{ycri} = \varepsilon_{yi}{}^{net} + \alpha_s \times \Delta T \times TRS4 + \varepsilon_{yi}{}^p + \Delta\varepsilon_{1cr} \times \sin^2\theta \tag{3.102}$$

Through use of the calculated strains, the corresponding longitudinal and transverse reinforcement stresses are calculated as described in Sections 5.4.4.1 and 5.4.4.2, respectively. If Eq. 3.25 is not satisfied, the incremental strain value is adjusted and the same calculations are repeated until satisfactory convergence is achieved or the maximum number of iterations (currently 300) is reached. As the final step, the interface shear stress $v_{ci}$ is calculated through the use of Eq. 3.26.

Because the local crack calculations are performed for each concrete layer in each member at each sectional analysis iteration based on an iterative formulation as explained

above, the execution of this subroutine at each global frame analysis iteration increases the overall computation time significantly. Therefore, this calculation is performed once for every 20 global frame analysis iterations. For the iterations in which this calculation is not performed, the previously determined local crack calculation values are used. Considering a maximum number of 100 global frame analysis iterations, which is the default value, this calculation will be performed up to five times for each load stage.

It is also necessary to make sure that the reserve capacity of the reinforcement is sufficient to transfer the average concrete tensile stresses, $f_{c1}$, across cracks. This calculation is performed based on Eq. 3.24 for each concrete layer in each sectional analysis iteration of each global frame analysis iteration. If the reserve reinforcement capacity is found to be insufficient, the average principal tensile stress, $f_{c1}$, is reduced accordingly.

Moreover, the reserve capacity of each discrete reinforcing and prestressing steel layer is checked based on Eq. 3.24. This calculation is performed for each concrete layer during each sectional analysis iteration of each global frame analysis iteration. For the concrete layer in consideration, the contributing discrete steel layers are determined considering a tributary distance of 7.5 times the bar diameter as explained in Section 3.7.1. For the contributing steel layers, the right-hand side of Eq. 3.24 is calculated and the principal tensile stress of the concrete layer in consideration is limited to that value.

### 3.7.7 Resultant Sectional Member Forces

After determining both the concrete and reinforcement responses, the resultant sectional forces are obtained as follows:

$$N_{\text{sec}} = \sum_{i=1}^{ncl} \sigma_{xi} \times b_i \times h_i + \sum_{j=1}^{nsl} f_{sxi} \times A_{sj} \tag{3.103}$$

$$M_{\text{sec}} = \sum_{i=1}^{ncl} \sigma_{xi} \times b_i \times h_i \times y_{ci} + \sum_{j=1}^{nsl} f_{sxi} \times A_{sj} \times y_{sj} \tag{3.104}$$

$$V_{\text{sec}} = \sum_{i=1}^{ncl} \tau_{xy} \times b_i \times h_i \tag{3.105}$$

The calculated forces are returned to the global frame analysis algorithm where they are checked with the member forces obtained from the global linear-elastic frame analysis. The differences between the sectional and global calculated forces are the *unbalanced forces;* these are used to define the compatibility restoring forces. The objective of the global frame analysis is to ideally make all unbalanced forces zero before proceeding to a new load or time stage.

### 3.7.8 Discussion of Shear-Stress- and Shear-Strain-Based Analysis Options

One of the most rigorous and theoretically accurate procedures for determination of the sectional shear force is to perform a *dual section analysis* where two adjacent sections are selected and analyzed iteratively for the assumed shear stress distribution (Vecchio and Collins, 1988). The analysis ends when the assumed and calculated shear stress distributions converge. Although theoretically accurate, this approach takes significant computation time and has some stability issues as reported by Bentz (2000). As a result, this approach is not used in the analytical procedure developed here where two iterative analysis algorithms (global frame analysis and sectional analyses) are present and another double iterative procedure is not desired.

Analyses conducted using the rigorous dual layer analysis (e.g., in programs SMAL and VecTor1) have often shown the shear flow distribution to be fairly uniform across the area between the top and bottom reinforcement (Vecchio and Collins, 1988). This observation led to the constant shear flow assumption of VecTor5 for much quicker computation. In this way the analysis of second section, and therefore the double iteration is not required, increasing the computation speed significantly.

Experience has also shown that the shear strain through the section often varies in a nearly parabolic fashion, although it is somewhat dependent on the loading conditions and sectional details (Vecchio and Collins, 1988). This led to the assumption of a

parabolic shear strain distribution in the VecTor5 analysis. In this way, the computation intensity and computation time decrease significantly as compared to the uniform shear flow assumption. The other, and perhaps the biggest, advantage of this method is that the analysis is very stable and continues into the post-peak regimes. Post-peak behaviour is necessary when determining the ductility of the structures and, therefore, one of the most important outputs which is sought as a result of a nonlinear analysis.

For the reasons noted above, the shear-stress-based analysis option is more suitable for force-controlled analyses until the load capacity of the structure is reached. In the force controlled analysis, post-peak behaviour cannot be determined whether using either the shear-stress or strain-based analyses; therefore, the disadvantage of termination at the peak load level in the shear-stress-based analysis disappears. As for shear-strain-based analyses, they are recommended for deformation-controlled analyses where post-peak behaviour is needed.

### 3.7.9 Average Crack Spacing Formulation

An estimate of the average crack spacing is needed in the MCFT for the crack slip check and in the DSFM for the crack slip calculation. Therefore, a reasonable estimate of the average crack spacing for each reinforced concrete layer is essential for the sectional analyses.

In the analytical procedure developed, a variable crack spacing formulation is newly adapted from Collins and Mitchell (1991) based on the CEB-FIB Code (1978). In contrast to the constant crack spacing, the variable crack spacing model considers the fact that the crack spacing becomes larger as the distance from the reinforcement increases. Thus, for uniform tensile straining (i.e., $k_2 = 0.25$), the average crack spacing in the longitudinal and transverse directions can be estimated as follows:

$$s_{mx} = 2 \times \left( c_x + \frac{s_x}{10} \right) + 0.25 \times k_1 \times \frac{d_{bx}}{\rho_x} \tag{3.106}$$

$$s_{my} = 2 \times \left( c_y + \frac{s}{10} \right) + 0.25 \times k_1 \times \frac{d_{by}}{\rho_y} \tag{3.107}$$

where $d_{bx}$ and $d_{by}$ are the diameters of the reinforcing bars in the x- and y-directions, $k_1$ is 0.4 for deformed bars and 0.8 for plain bars or bonded strands; other variables are defined in Figure 3.29.

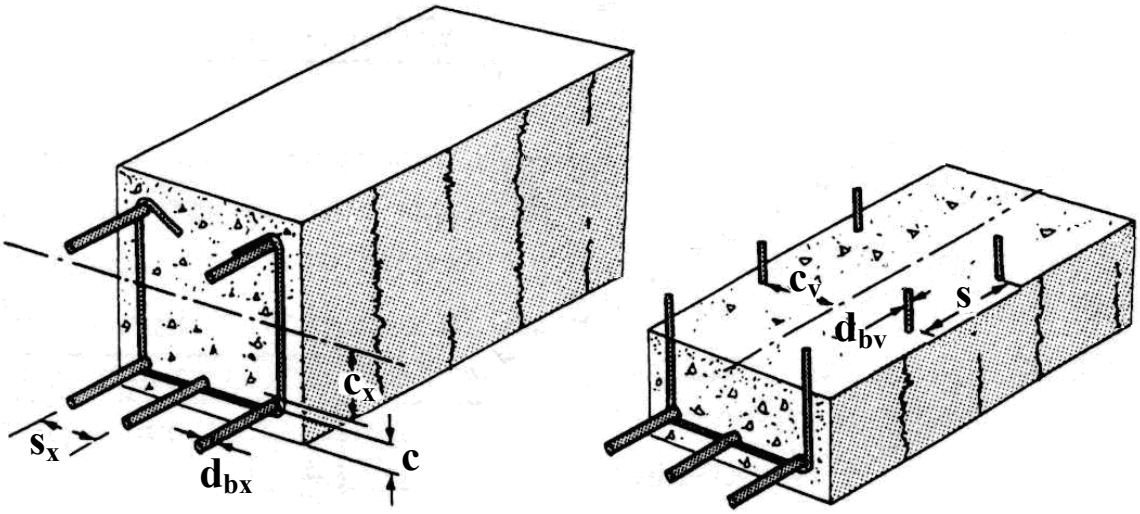


**Figure 3.29** Parameters Influencing Crack Spacing (Collins and Mitchell, 1991)

Based on the formulation above, each concrete layer may have different crack spacings in the longitudinal and transverse directions based on the reinforcement quantity and configuration. For analytical purposes, a maximum limit equal to the section depth, *h,* is applied to the transverse crack spacing. The resulting spacing for each concrete layer is printed out in the expanded structure data file for verification purposes.

### 3.8 Member End Factors

Average member forces are determined from the member end-actions calculated by the global frame analysis and used in the sectional calculations. If both ends of a member have the same end-actions, those values can directly be used for that member. However, the ends of a member usually have different values of bending moments. In this case, an appropriate averaging scheme for those two values is required. In this averaging, it is

important to conservatively account for the end with the higher value as local plastic hinging may be forming at that end.

For this reason, two end factors ($EF_j$ and $EF_k$) for each member are calculated for averaging purposes: one for *end j* and one for *end k* (Figure 3.30). In the proposed analysis procedure, the resultant member moment is calculated as follows:

$$BM = EF_j \times BM_j + EF_k \times BM_k \tag{3.108}$$

$$EF_i + EF_k = 1.00 \tag{3.109}$$

To clarify the determination of the end factors, consider a member with end j and end k and assume that the bending moment at end j is higher than at end k.

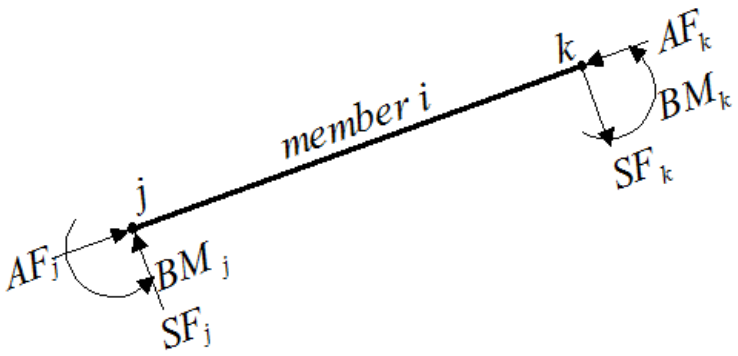


**Figure 3.30** Member i with End Actions

If all layers of *member i* are uncracked, the end factors are initially taken as 0.5. Under increased compressive straining, however, concrete damage due to crushing may be occurring at the end with higher bending moment. To take this into account, it is assumed that after a maximum compressive strain of -2.0 x $10^{-3}$, end factor $EF_j$ is gradually increased to 0.75 while end factor $EF_k$ is gradually reduced to 0.25 with increasing compressive strains up to -3.0 x $10^{-3}$. Afterwards, the 0.75 and 0.25 end factors are held constant (Figure 3.31). The assumed compressive strain values are selected so that when the CSA A23.3 Clause 10.1.3 stipulated concrete crushing strain of -3.5 x $10^{-3}$ is reached, the end factor of 0.75 will be in use for the end with the higher moment value.

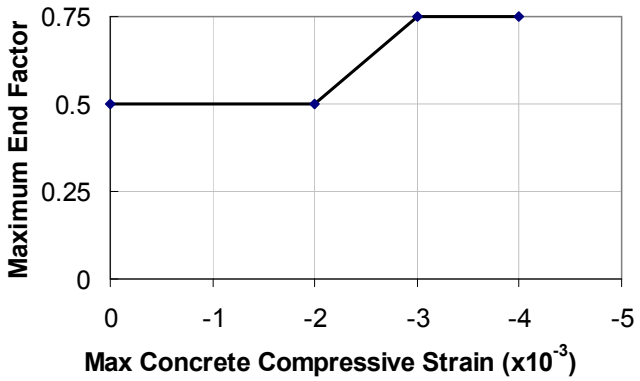


**Figure 3.31** Variation of Maximum End Factor for Uncracked Members

For cracked members, independent of the maximum concrete compressive strain, an end factor of 0.75 is assumed for the end with the higher bending moment while an end factor of 0.25 is used for the other end.

Exactly the same calculation is performed for axial forces. For shear forces, an averaging factor of 0.5 is assumed at both ends.

### 3.9 Convergence Factors

Convergence factors are needed at the end of the global frame analysis and are determined based on the selected criterion. The first available criterion is *unbalanced forces.* According to this criterion, the convergence factor is calculated as follows:

$$CF = 1 + \sqrt{\frac{1}{3 \times n} \times \sum_{i=1}^{n} \left( \left( \frac{N_{unbal_i}}{N_{\sec_i}} \right)^2 + \left( \frac{V_{unbal_i}}{V_{\sec_i}} \right)^2 + \left( \frac{M_{unbal_i}}{M_{\sec_i}} \right)^2 \right)} \tag{3.110}$$

where $N_{unbal_i}$, $V_{unbal_i}$ and $M_{unbal_i}$ are the unbalanced forces defined in Eq. 3.68 to 3.70, n is the total number of members.

The second option is *weighted displacements.* This criterion is the default option used in the analytical tool developed. Here, the convergence factor is determined as

$$CF = 1 + \sqrt{\frac{1}{3 \times n} \times \sum_{i=1}^{3 \times n} \left( Di - Di^{pre} \right)^2} \tag{3.111}$$

where $D_i$ is the nodal displacements and n is the total number of nodes.

The third option is *maximum displacements,* which is not suitable for deformation-controlled analysis as the maximum displacement may be the one which is applied to the structure. This criterion calculates the convergence factor as follows:

$$CF = 1 + \left( \frac{D_{\max} - D_{\max}^{pre}}{D_{\max}^{pre}} \right) \tag{3.112}$$

In the formulations above, the subscript *pre* signifies that the value obtained from the previous global frame iteration.

When the specified convergence limit is achieved or the maximum number of iterations is reached, the global frame analysis completes the calculations related to the current load stage and moves on to the next load stage.

### 3.10 Dynamic Averaging Factors

In iterative numerical analyses, it is common to use an averaging scheme to ensure a gradual and stable convergence to the exact result. In most schemes, the value calculated in the previous iteration is averaged with the value calculated in the current iteration. In this averaging scheme, the factor used for averaging purposes must be selected. In general applications, a factor of 0.5 can be assumed to weight the two iteration outcomes equally.

The smaller the averaging factor, the more weight is assumed for the previous value. For example, consider the calculation of a secant stiffness value, $\overline{E}_{c2}$, in a particular reinforced concrete layer and assume that a second iteration is being performed. At the end of this iteration, the resulting value of $\overline{E}_{c2}$ is calculated as

$$\bar{E}_{c2}^{\,current} = AVGF \times \bar{E}_{c2}^{\,ite2} + (1 - AVGF) \times \bar{E}_{c2}^{\,ite1} \tag{3.113}$$

Smaller values for the averaging factor ($0.1 \le AVGF < 0.5$) typically result in more stable convergence to the final result but tend to increase the number of iterations required, thereby increasing the computation time. Averaging factors greater than 0.5 provide faster convergence but the analyses may be numerically less stable as the factor increases. As both stability and fast execution are main concerns, the optimum selection of this factor should be based on the convergence characteristics experienced in the current iteration. In other words, an ideal averaging factor would be the one that has the ability to change at each iteration depending on how smoothly the exact result is being approached. Based on this, if the exact result is approached gradually, the averaging factor would be increased for faster convergence. However, if the solution keeps overshooting and undershooting the exact result, the averaging factor would be reduced.

To take this phenomenon into account, a dynamic averaging factor is used in the analysis procedure developed when averaging the *unbalanced forces*. In this calculation, each member has three averaging factors stored in the computer memory. Those factors are used when calculating: (1) unbalanced axial forces, (2) unbalanced bending moments, and (3) unbalanced shear forces, all of which should ideally have an exact value of zero at the end of the load stage. With the dynamic averaging scheme, if the unbalanced force is gradually decreasing, the averaging factor is increased for that member. If the unbalanced force keeps changing its sign, then the averaging factor is reduced. It is assumed that dynamic averaging factor can assume values between 0.1 and 1. By default, the dynamic averaging scheme is used in the proposed analysis tool. Examples of variation of unbalanced forces are presented in Figure 3.32(a) for the members critical in flexure and in Figure 3.32(b) for the members critical in shear.

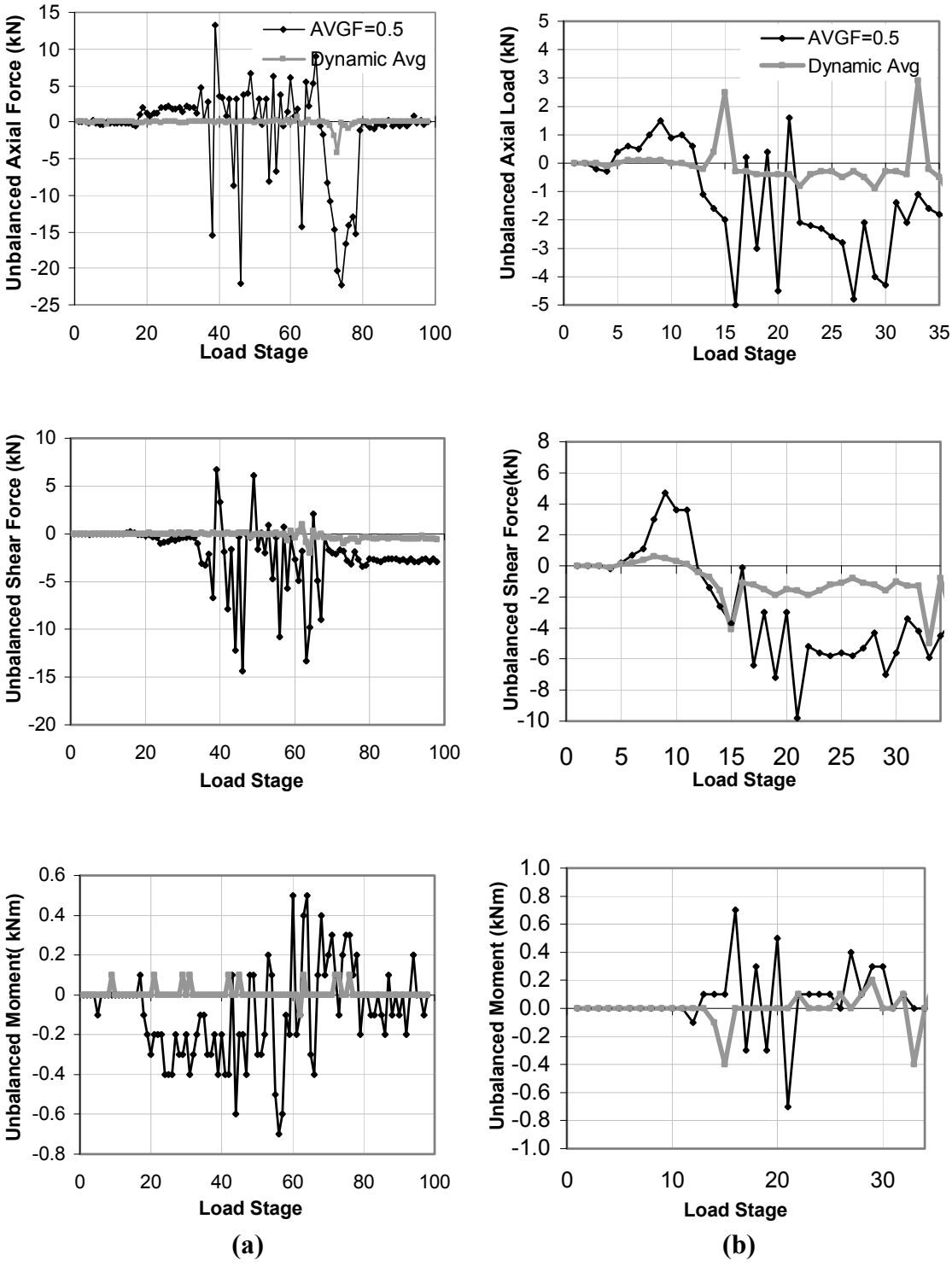


**Figure 3.32** Unbalanced Forces **(a)** Vecchio and Emara Frame in Section 4.7, Member 74; **(b)** Duong Frame in Section 4.8, Member 61

### 3.11 Shear Protection Algorithm

The regions of a structure where the hypothesis of plane strain distribution (Hooke, 1678 and Bernoulli, 1705) is valid are commonly referred to as B-regions (where B refers to beam) (Schlaich et al., 1987). B-regions can be analyzed by sectional calculations such as those employed in the analytical tool developed. However, this method is not directly applicable to other regions where the strain distribution is significantly nonlinear; that is, near concentrated loads, corners, supports and other discontinuities. Such regions are commonly called D-regions (where D refers to discontinuity, disturbance, or detail). Modelling of D-regions with sectional analysis procedures typically produces overly conservative results. This deficiency is typically a result of direct strut action in the concrete, in the case of a support or a joint, where the load goes directly into the support or connecting beam or column without causing additional stresses in the stirrups or ties. In the case of a point load, significant compressive clamping stresses emerge under and adjacent to the point load, which significantly increase the shear strength of those regions. As examples, B- and D-regions are shown in Figure 3.33(a) for a reinforced concrete frame and in Figure 3.34 for a simply supported beam. It also happens that those disturbed regions usually have high sectional forces as shown in Figure 3.33(b).

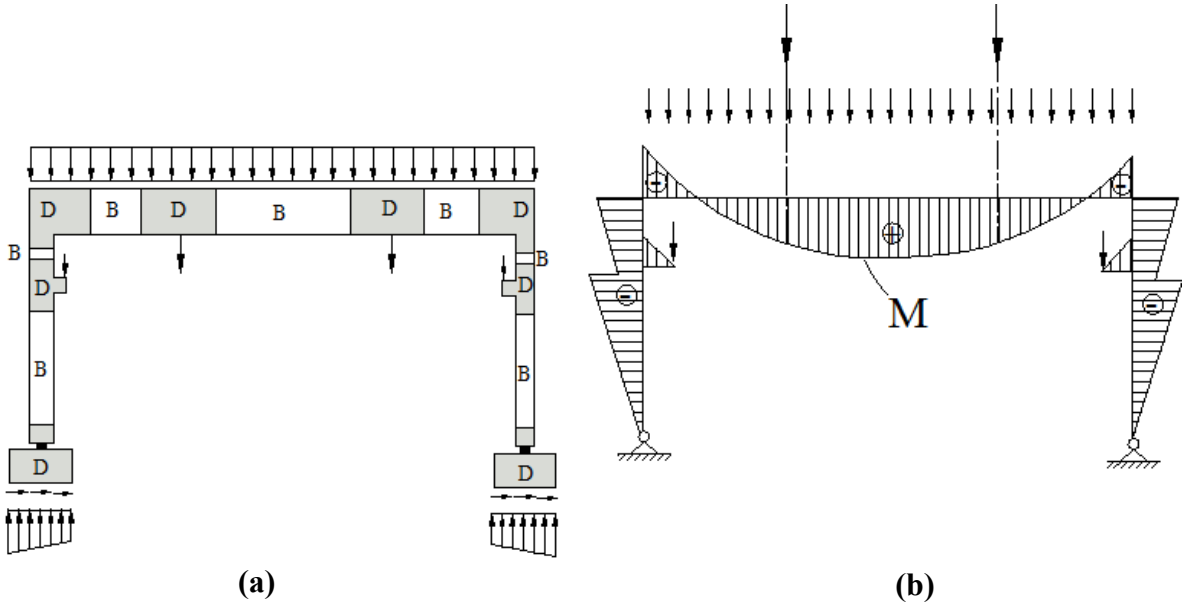


**Figure 3.33** A Reinforced Concrete Frame: **(a)** B- and D-Regions; **(b)** Bending Moment Distribution (Schlaich et al., 1987)

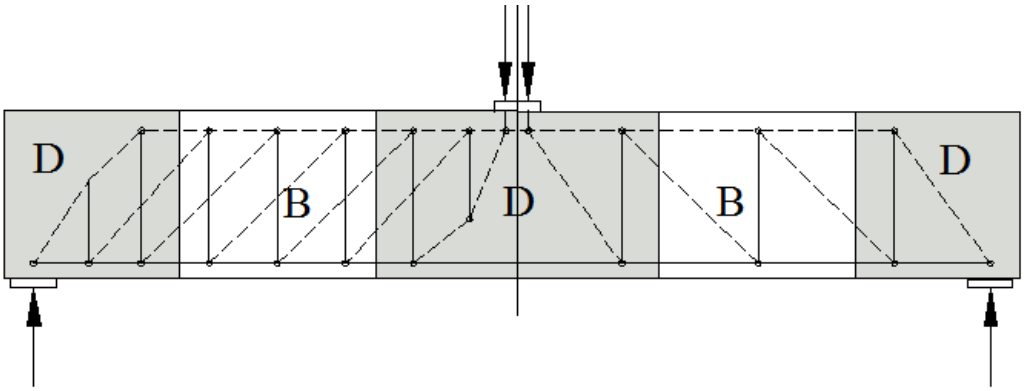


**Figure 3.34** B- and D-Regions of a Simply Supported Beam (Schlaich et al., 1987)

Experience with VecTor5 has shown that D-regions are vulnerable to premature shear failures because both concrete strut action and clamping stresses are neglected in the sectional calculations. As a result, to account for this phenomenon in D-regions, an algorithm called *shear protection* was introduced into the proposed analysis procedure.

This algorithm first determines the frame joints (i.e., connection of beams and columns) by checking the direction cosines of the members, and then locates the faces of the columns and beams. Starting from the face, the members which fall within distance 0.7 x h are then determined. Finally, the algorithm reduces the calculated shear forces of those members by 50 percent. In this calculation, the distance in which the shear force reduction is assumed (0.7 x h) is based on CSA A23.3-04 Clause 11.3. This shear force reduction is applied when the shear strains are calculated in the case of a shear-strain-based analysis and when the shear flow is calculated in the case of a shear-stress-based analysis. In other words, this reduction does not change the static member end-actions; rather, it is used to reduce the shear strains or the shear flows in the sectional calculations so that a premature shear failure can be prevented. The reduction factor of 0.5 was determined as a result of a parametric study where different reduction ratios were used to simulate the experimental behaviour of a set of structures. It was first observed that a reduction factor of 0.75 works reasonably well. However, in later analyses, premature shear failures of D-regions were experienced in some of the analyses which were contrary to the experimental behaviour. Therefore, the reduction ratio was changed to 0.5 in response to the observation that it better simulates the experimental behaviour.

The same reduction is performed for members near supports and point loads. As an example, a simple frame structure is shown in Figure 3.35. In this structure, the shear protection algorithm automatically determines the members marked with an asterisk (*) as suitable for shear force reduction.

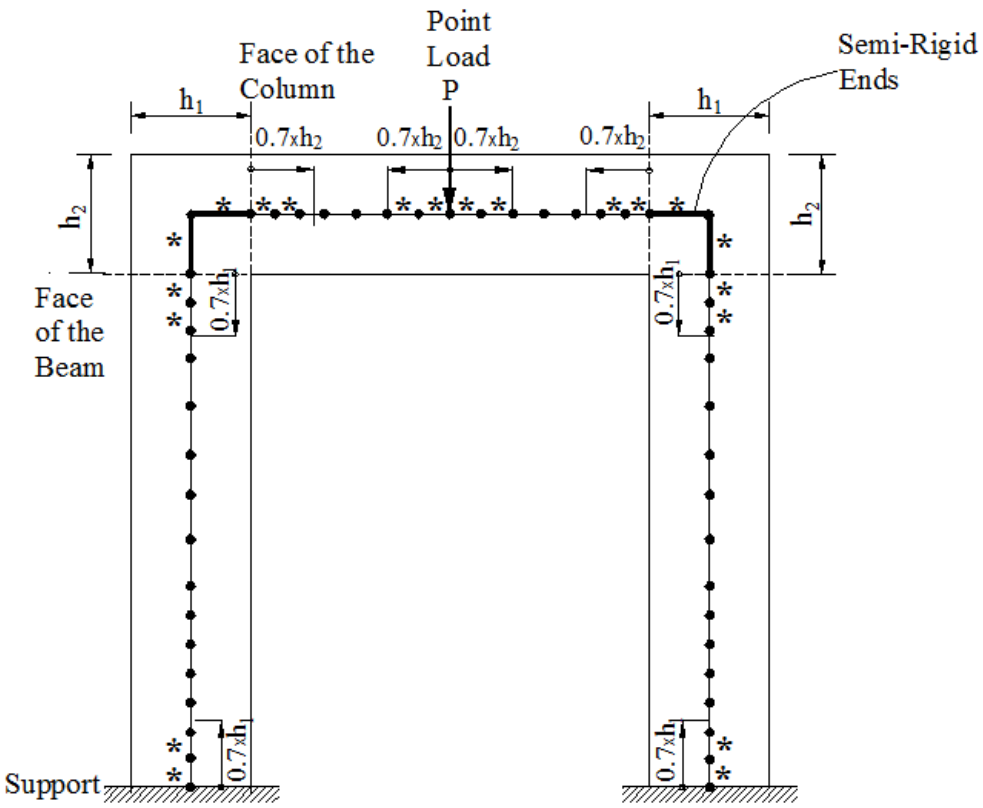


**Figure 3.35** A Reinforced Concrete Frame with Shear Force Reduced Members (shown with an asterisk)

For verification purposes, the automatically determined members for shear protection are printed out in the expanded structure data file of VecTor5. Even though the shear protection is a default feature of the program, it can be turned off if so desired by the user. When using the shear protection feature, the reduction factor of 0.5 cannot be modified by the user to be consistent in all analytical predictions.

## 3.12 Shear Failure Check

One of the most important aspects of the analysis procedure developed is the use of *unbalanced forces* in calculating nonlinear frame deformations. Based on this approach,

unbalanced forces are calculated and added to the *compatibility restoring forces* which are then applied to the structure as if they were static joint forces. Self-equilibrating restoring forces cause member deformations in frame analysis to match those in the nonlinear sectional analysis. This procedure is performed through global frame analysis iterations during which unbalanced forces are ideally reduced to zero while both restoring forces and frame deformations increase.

For a flexure-critical structure, under monotonically increasing applied deformations, the unbalanced force approach works as expected until the failure of the structure. In other words, in the post-peak regime, under increasing deformations, the members which are reaching their moment capacity start experiencing difficulty in carrying the current acting moment. In this case, greater unbalanced forces are produced, causing the frame deformations to increase resulting in more bending moment for the members in difficulty. Increased deformations may eventually cause the longitudinal tension reinforcement to rupture or the concrete in the compression zone to crush. When this happens, the member drops its load, failing under flexure.

In case of a shear-critical structure, a similar calculation procedure is employed, using unbalanced shear forces found through the global frame analysis to impose more shear deformations until no more unbalanced shear forces are produced for the current load stage. In some cases, however, it was noticed that after the shear capacity of one of the members was reached, significant unbalanced shear forces were present at the end of each load stage, instead of ideally being zero. This phenomenon is closely related to the maximum number of global frame analysis iterations permitted because the specified convergence is not usually achieved before the maximum number of iterations is reached in such a situation.

For clarification purposes, the analysis of the shear-critical frame tested by Duong et al. (2007) was repeated specifying a different maximum number of iterations (i.e., 100, 200 and 400). The details of this frame and loading were presented in Section 2.3.6. The load-deflection responses obtained are shown in Figure 3.36.

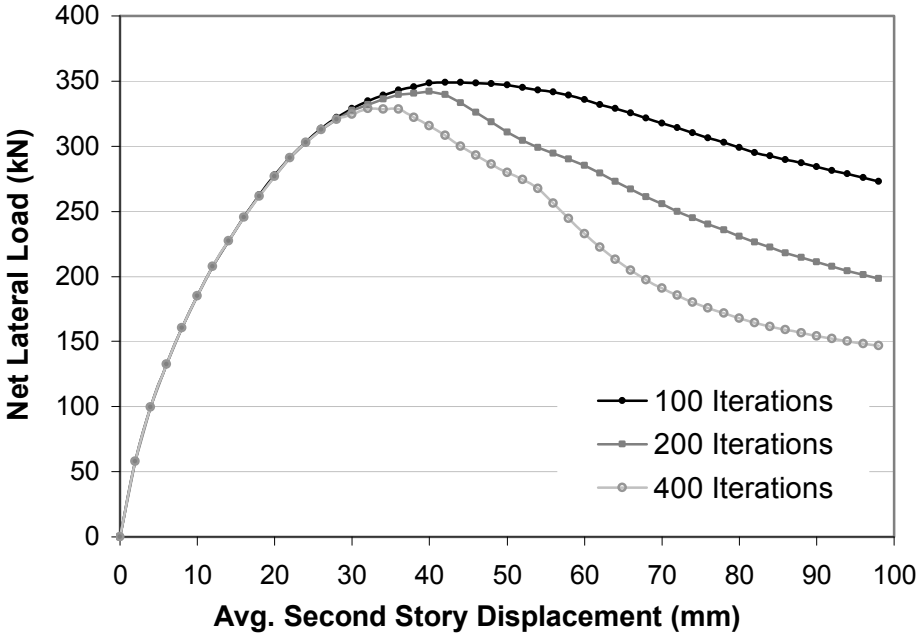


**Figure 3.36** Load-Deflection Responses for Duong Frame
(Before the Implementation of Shear Failure Check)

Consider the response for the analysis with 100 maximum iterations, which is the value used for the maximum number of iterations throughout this thesis. After the peak load, the gradually decreasing branch suggests that shear-related mechanisms are playing a significant role. Inspection of the output files revealed that both the left and right end of the first storey beam were critical in shear. Consider the right end of the beam which was slightly more critical. In Figure 3.37, the unbalanced shear and bending moment values are shown with respect to the acting shear force and moment values.

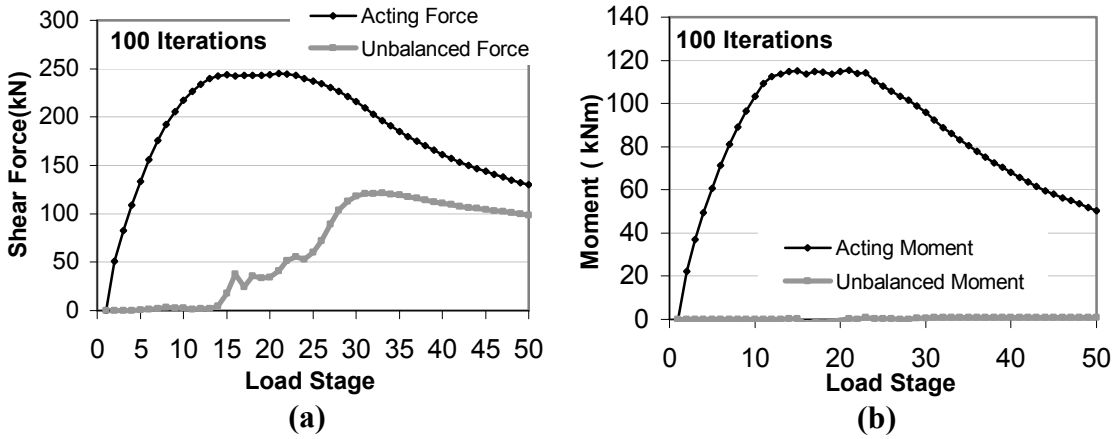


**Figure 3.37** Forces for Member 62 for Duong Frame in Figure 4.25 for 100 Global Frame Analysis Iterations: **(a)** Shear Force; **(b)** Bending Moment
(Note: Second Storey Disp. = 2 x Load Stage - 2 (mm))

It is obvious that, around load stage 14, this member had reached its shear force capacity. In such a situation, the global frame analysis should have reduced the acting shear force on the frame making sure that no significant unbalanced shear force was returned for all members at the end of each load stage. However, due to the insufficient maximum number of iterations specified, the reduction in the shear force acting on the frame took place rather gradually with unbalanced shear forces reaching up to 75 percent of the total shear force for Member 62. Such behaviour is obviously unacceptable.

Consider now the responses obtained for maximum number of iterations 200 and 400 in Figure 3.38. As the maximum number of iterations increases, the faster reduction in the shear force acting on the frame and the unbalanced shear force were realized.

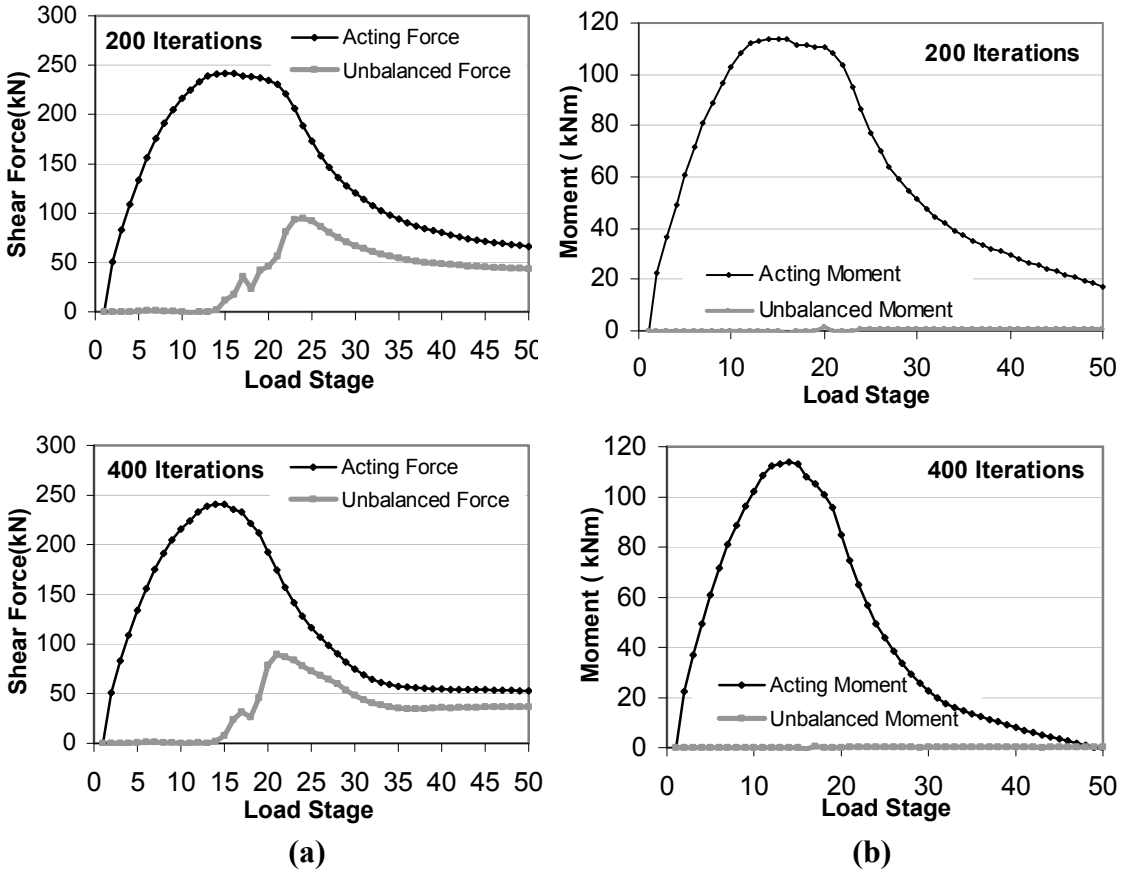


**Figure 3.38** Forces for Member 62 for Duong Frame, in Figure 4.25, for 200 and 400 Global Frame Analysis Iterations: **(a)** Shear Force; **(b)** Bending Moment (Note: Second Storey Disp. = 2 x Load Stage - 2 (mm))

However, the increase in the specified maximum number of iterations increases the computation time significantly (Figure 3.39). For the purpose of solely dealing with such a situation, the specification of a large number of maximum iterations may be unnecessary for general analyses. In addition, even when using the maximum number of iterations of 400, considerable unbalanced shear still exists around the load stage 20 as shown in Figure 3.38(a). It should be noted that the response investigated here was one of the most extreme cases in which the structure showed a shear-dominated behaviour with significant flexural effects encouraging the frame to carry loads flexurally into the post-peak regime.

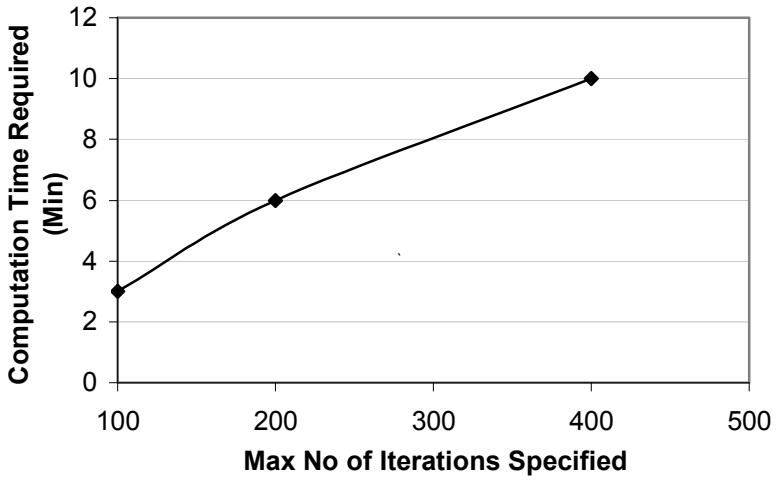


**Figure 3.39** Computation Time Required for Duong Frame for Different Maximum Number of Iterations Specified

To deal with such situations, a *shear failure check* was introduced into the analytical procedure developed. Based on this calculation, if there is an unbalanced shear force on a member greater than a certain percentage of the acting shear force at the end of more than one load stage, that member is intentionally failed by reducing its moment of inertia to essentially zero. The frame, however, may still continue to carry load based on the conditions of the other members. This check was introduced to provide conservative estimates in the post-peak ductilities of shear-critical structures in the cases where the specified maximum number of iterations turns out to be insufficient for the structure being analyzed.

The specification of different percentages (i.e., percentage of unbalanced shear force relative to the total acting shear force) to initiate the failure was determined to produce similar responses with slightly different failure displacements as shown in Figure 3.40. In such a situation, as the unbalanced shear force is expected to increase, the use of larger percentages will typically cause the failure to occur at a later load stage. It was deemed appropriate to use the value of 25% to be conservative in the cases where the specified maximum number of iterations becomes insufficient for the problem at hand.

As is clear from Figure 3.40, two sudden shear failures were experienced in this analysis with the use of shear failure check algorithm. The first one occurred at the right end of the first storey beam (Figure 3.41). After that failure, all members of the first storey beam dropped their internal forces to zero as expected. The analysis carried on as the second storey beam was still resisting the acting forces. A second shear failure was then observed at the right end of the second storey beam after which only one cantilever column remained in resisting the applied displacement at the top (Figure 3.42). Throughout the analysis, the stability of the computation was not lost and the analysis carried on with acceptable convergence and minimal unbalanced forces.

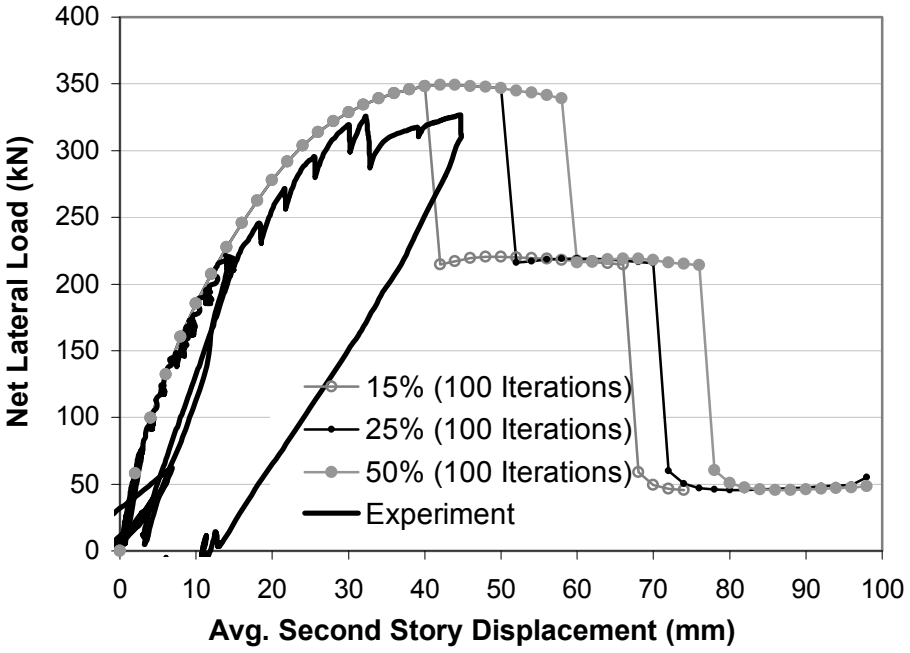


**Figure 3.40** Load-Deflection Responses for Duong Frame
(After the Implementation of Shear Failure Check)

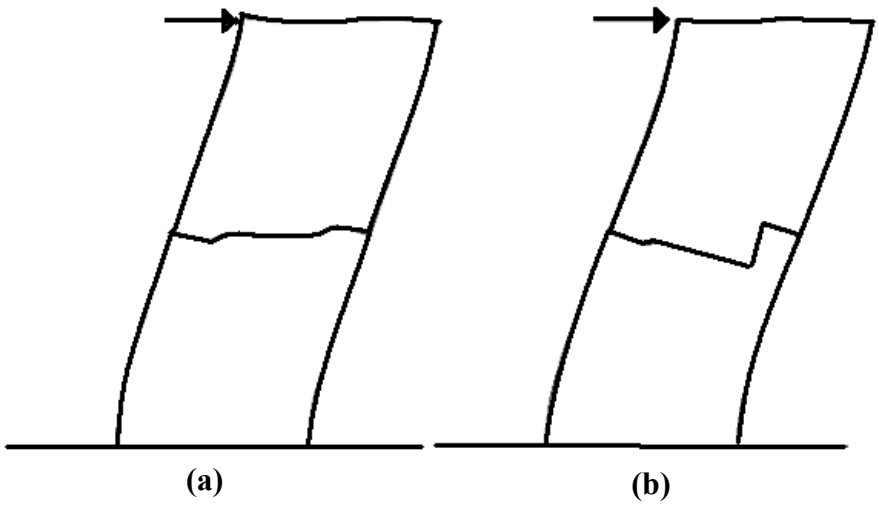


**Figure 3.41** Deflected Shape of Duong Frame during the First Shear Failure: **(a)** Before the Failure; **(b)** After the Failure

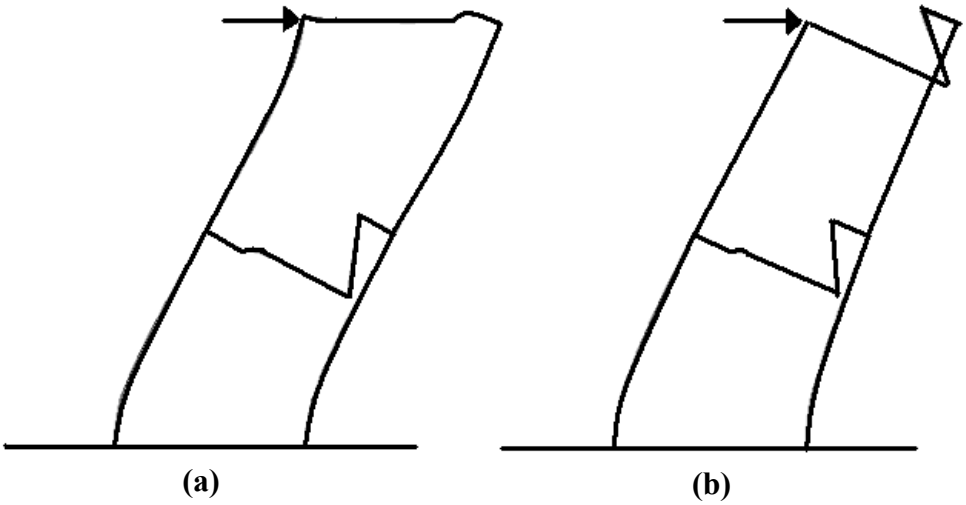


**Figure 3.42** Deflected Shape of Duong Frame during the Second Shear Failure: **(a)** Before the Failure; **(b)** After the Failure

In the following chapters which discuss the application of the analytical procedure developed, the shear failure check algorithm detected the shear failures of some specimens that would have gone unnoticed with large unbalanced forces and gradually diminishing responses otherwise. The beneficial effects of this algorithm were particularly realized when analyzing shear-critical structures with flexural influences (e.g., DB0.53M in Section 4.6, Duong Frame in Section 4.8, Vecchio and Balopoulou Frame in Section 4.9, and Clinker Preheat Tower in Section 4.10).

## 3.13 Second-Order Mechanisms

### 3.13.1 Geometric Nonlinearity

Changes in the geometry of a structure may significantly affect structural response. The geometry changes are caused by the loads acting on the structure and may lead to secondary moment effects, especially for slender structures (Figure 3.43). Also known as *P-Δ effects* or *second-order effects*, geometric nonlinearities may significantly reduce the load capacity of the structure while significantly increasing the deformations. Therefore, they are considered in the frame analyses performed by VecTor5.

Based on the calculated displacements of the nodes, the new coordinates of all nodes are determined and new member lengths and direction cosines are calculated during each global frame analysis iteration. In the iterations following, the updated geometry of the structure is used taking into account the geometric nonlinearities.

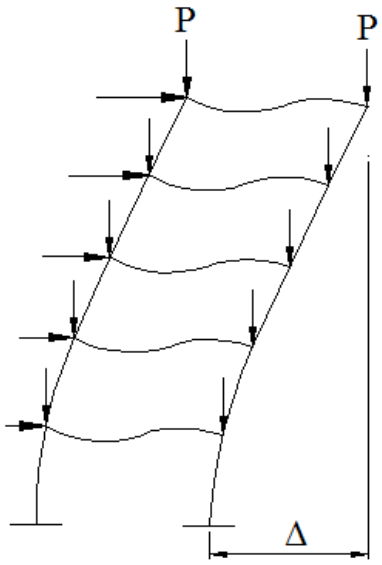


**Figure 3.43** A Frame Structure under Gravity and Lateral Loads

### 3.13.2 Reinforcement Dowel Action

Dowel action refers to the resistance provided by reinforcing bars crossing a crack as the crack slips transversely. This resistance can significantly increase the shear strength and

post-peak ductility of some members such as beams with little or no transverse reinforcement.

Dowel action is taken into account for each member through the introduction of resisting fixed-end moments. Consider a member with a reinforcing bar crossed by one perpendicular crack (Figure 3.44). The resisting moment, $M_d$ can be calculated as

$$M_d = V_d \times L \tag{3.114}$$

where $V_d$ is the dowel force, and L is the length of the element in consideration.

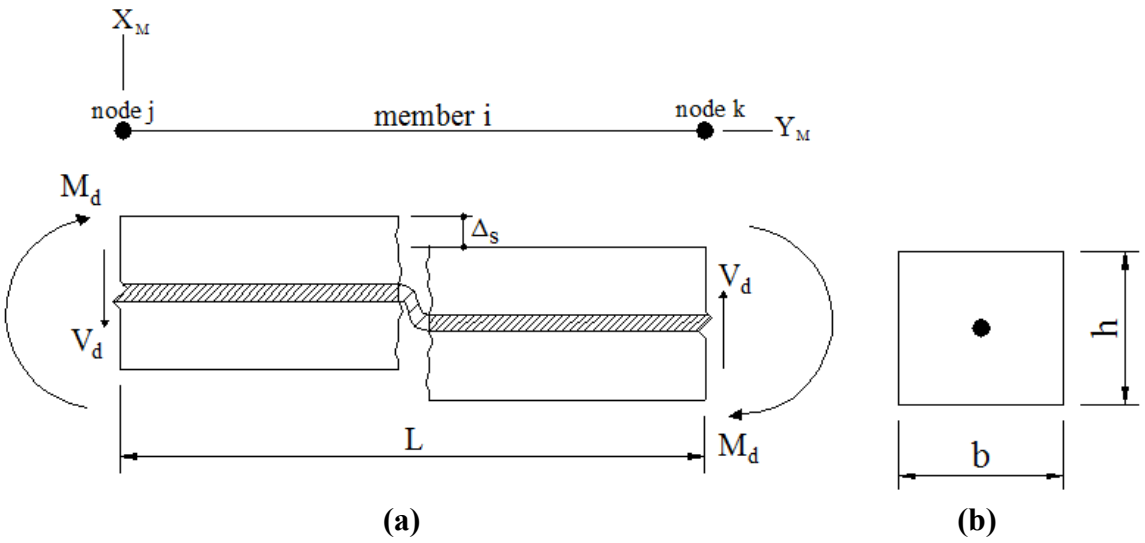


**Figure 3.44** Dowel Resistance Mechanism: **(a)** Member Longitudinal View; **(b)** Member Cross Section

The dowel force is calculated by taking the stiffness portion of the dowel force-dowel displacement formulation proposed by He and Kwan (2001). As a result, the dowel force, $V_d$, is found to be

$$V_d = \left(E_s \times I_z \times \lambda^3\right) \times \Delta_s \;\leq\; V_{du} \tag{3.115}$$

$$I_z = \frac{\pi \times d_b^{\,4}}{64} \tag{3.116}$$

$$\lambda = \sqrt[4]{\frac{k_c \times d_b}{4 \times \mathrm{E}_s \times I_z}} \tag{3.117}$$

$$k_c = \frac{127 \times c \times \sqrt{f_c'}}{{d_b}^{2/3}} \text{ where } c = 0.8 \tag{3.118}$$

where $\Delta_s$ is the dowel displacement, $E_s$ is the stiffness of the reinforcing bar, $d_b$ is the bar diameter, $I_z$ is the moment of inertia of the reinforcing bar, $\lambda$ is a parameter comparing the stiffness of concrete to that of the reinforcing bar, $k_c$ is the stiffness of the notional concrete foundation, and $c$ is an empirical parameter reflecting bar spacing.

$V_d$ is limited to the reserve capacity of the reinforcing bar defined by the following equation.

$$V_{du} = 1.27 \times {d_b}^2 \times \sqrt{f_c'} \times \sqrt{f_{s\,rem}} \tag{3.119}$$

$$f_{s\,rem} = f_y - f_s \tag{3.120}$$

where $f_{s\,rem}$ is the remaining stress capacity of reinforcing bar, $f_y$ is the yield stress, and $f_s$ is the current stress of the reinforcing bar.

The dowel displacement is determined through the use of shear strains calculated by the sectional analysis algorithm. In this calculation, it is assumed that each reinforcing bar is affected by shear strains within its tributary area, i.e., $7.5 \times d_b$. Therefore, the average values of the shear strains ($\gamma_{xy_{avg}}$) and crack spacing ($S_{mx_{avg}}$) in the longitudinal (x) direction are calculated in the tributary area for each of the reinforcing bars present. As a result, the dowel displacement is calculated to be

$$\Delta_s = \left(\frac{\pi}{\lambda}\right) \times \gamma_{xy_{avg}} \tag{3.121}$$

In a more general implementation that considers several reinforcing bars and several cracks perpendicularly crossing those bars, the equation for resisting dowel fixed-end moments becomes

$$M_d = \sum_{i=1}^{nsl} (V_d) \times L \times \frac{S_{mx_{avg}}}{L} \tag{3.122}$$

where *nsl* is the number of steel layers present in the cross section under consideration.

In the equation above, the term $S_{mx_{avg}} / L$ was used to account for the number of cracks crossing the reinforcing bars in each member.

### 3.13.3 Concrete Dilatation (Poisson's Effect)

Under biaxial stress conditions, it is common to assume that Poisson's effects are negligible for cracked concrete. However, if the concrete is uncracked or if the tensile straining in the cracked concrete is relatively small, the lateral expansion of concrete due to Poisson's effects can account for a significant portion of the total strains. Therefore, these effects need to be taken into account.

Poisson's ratio, $v_{ij}$, refers to expansion of concrete in the principal *i*-direction under compressive straining due to stress in the principal-*j* direction. Due to internal micro-cracking, $v_{ij}$ increases as the acting compressive stress increases, which causes concrete to expand. When confined by transverse or out-of plane reinforcement, the lateral expansion results in passive confining stresses that considerably improve the strength and ductility of the reinforced concrete under compression.

In VecTor5, adjustable by the user, the default value for $v_{ij}$ is taken as 0.15, while the default model for lateral expansion is adopted from Kupfer et al. (1969). As a result, the Poisson's ratio under compression becomes as follows:

$$v_{ij} = v_o \qquad if \quad -0.5 \times \varepsilon_p < \varepsilon_{cj} < 0 \tag{3.123}$$

$$v_{ij} = v_o \times \left[ 1 + 1.5 \times \left( \frac{-2 \times \varepsilon_{cj}}{\varepsilon_p} - 1 \right)^2 \right] \leq 0.5 \quad if \quad \varepsilon_{cj} < -0.5 \times \varepsilon_p \tag{3.124}$$

In the calculation, an upper limit of 0.5 was assumed for numerical stability reasons (Figure 3.45).

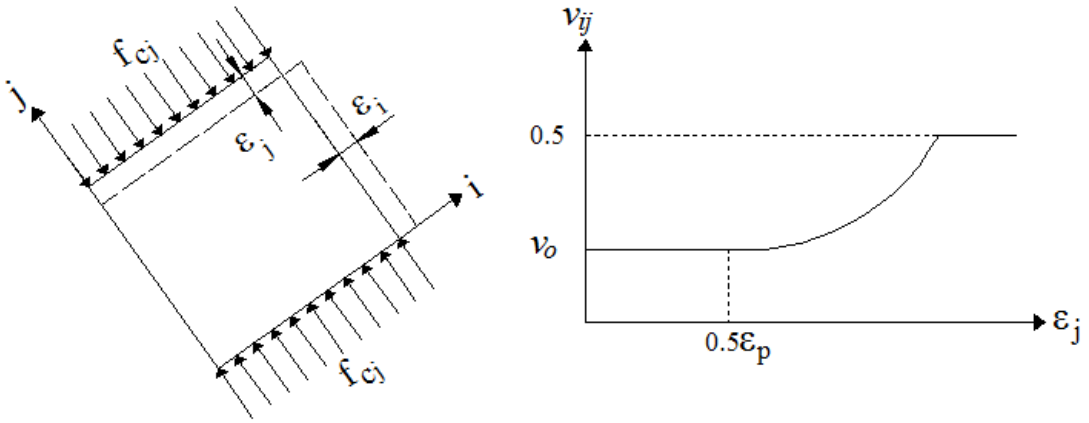


**Figure 3.45** Variation of Poisson's Ratio under Compressive Straining

As shown in Figure 3.46, under tension, Poisson's ratio, $v_{ij}$ decreases linearly to zero from its initial value, $v_o$, as follows:

$$v_{12} = v_{21} = v_o \qquad if \quad 0 < \varepsilon_{c1} < \varepsilon_{cr} \tag{3.125}$$

$$v_{12} = v_{21} = v_o \times \left( 1 - \frac{\varepsilon_{c1}}{2 \times \varepsilon_{cr}} \right) \geq 0 \qquad if \quad \varepsilon_{cr} < \varepsilon_{c1} \tag{3.126}$$

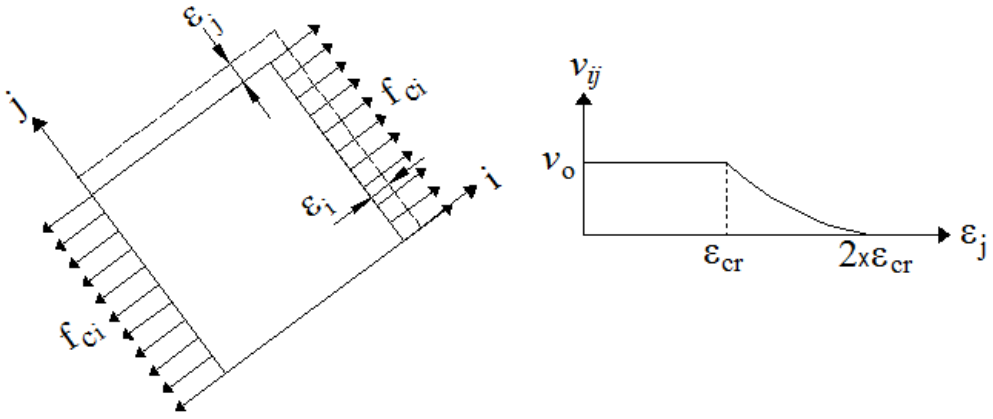


**Figure 3.46** Variation of Poisson's Ratio under Tensile Straining

In the analysis procedure developed, concrete dilatation is treated in the sectional calculations as concrete elastic offset strains as proposed by Vecchio (1992). In the principal directions, these strains become

$$\varepsilon_{c1}{}^{o} = -\nu_{12} \times \varepsilon_{c2} \qquad (3.127)$$

$$\varepsilon_{c2}{}^{o} = -\nu_{21} \times \varepsilon_{c1} \qquad (3.128)$$

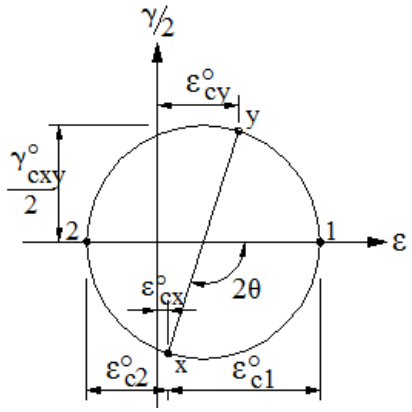


**Figure 3.47** Mohr's Circle of Strain for Determination of Elastic Strains

Through the use of a Mohr's circle of strain (Figure 3.47), the concrete elastic strains due to dilatation relative to the x- and y-axes can be found as

$$\varepsilon_{cx}{}^{o} = \frac{1}{2} \times \varepsilon_{c1}{}^{o} \times (1 + \cos 2\theta) + \frac{1}{2} \times \varepsilon_{c2}{}^{o} \times (1 - \cos 2\theta) \qquad (3.129)$$

$$\varepsilon_{cy}{}^{o} = \frac{1}{2} \times \varepsilon_{c1}{}^{o} \times (1 - \cos 2\theta) + \frac{1}{2} \times \varepsilon_{c2}{}^{o} \times (1 + \cos 2\theta) \qquad (3.130)$$

$$\gamma_{cxy}{}^{o} = \varepsilon_{c1}{}^{o} \times \sin 2\theta - \varepsilon_{c2}{}^{o} \times \sin 2\theta \qquad (3.131)$$

These elastic strains due to lateral expansion are explicitly included in the sectional analyses and explained in detail in Section 3.7.

### 3.13.4 Concrete Prestrains

Concrete prestrains, such as shrinkage strains, are also considered as a load case and can be assigned to desired members. These prestrains are treated as elastic concrete offsets, i.e., $\varepsilon_{cx}{}^{o} = \varepsilon_{sh}$ and $\varepsilon_{cy}{}^{o} = \varepsilon_{sh}$ while $\gamma_{cxy}{}^{o} = 0$, and are included in the sectional analyses explained in Section 3.7.

### 3.13.5 Out-of-Plane (Confinement) Reinforcement Calculations

As mentioned above, lateral expansion causes passive confining pressures in the transverse and out-of-plane reinforcement which may considerably improve the strength and ductility of the concrete under compression.

In the analytical procedure developed, the stress in the transverse reinforcement due to lateral expansion is inherently taken into account by the use of concrete elastic offset strains as explained above.

However, as sectional calculations only consider in-plane reinforcement and loading conditions, stresses in the out-of-plane reinforcement must be calculated separately and supplied to the sectional analysis.

In the most general form, the total strain in the out-of-plane direction is assumed to be generated by: (1) concrete elastic offset strains (due to lateral expansion, thermal and shrinkage effects), and (2) out-of-plane reinforcement elastic offset strains (due to thermal effects). The resulting total strain in the out-of-plane direction becomes

$$\varepsilon_z = \frac{1}{E_c + \rho_z \times E_s} \times \left( \varepsilon_{c1}{}^{o} + \varepsilon_{c2}{}^{o} + E_{sz} \times \rho_z \times \Delta t \times \alpha_s \times TRS4 \right) + \varepsilon_{csh} + \Delta t \times \alpha_c \times TRC4 \quad (3.132)$$

The *net* out-of-plane reinforcement strain can then be found as

$$\varepsilon_{zs} = \varepsilon_z - \Delta t \times \alpha_s \times TRS4 \quad (3.133)$$

The stress corresponding to the *net* strain is calculated by a bilinear stress-strain relation as follows:

$$f_{sz} = \varepsilon_z \times E_{sz} \le f_{yz} \quad (3.134)$$

$$f_{c3} = -f_{sz} \times \rho_z \quad (3.135)$$

where $E_c$ is the initial tangent modulus of elasticity of concrete, $\varepsilon_{c1}{}^{o}$ and $\varepsilon_{c2}{}^{o}$ are defined by Eq. 3.127 and Eq. 3.128, $\rho_z$ is the ratio of out-of-plane reinforcement, $E_{sz}$ is the modulus of elasticity of the out-of-plane reinforcement, *TRS4* is the modification factor for $\alpha_s$ as shown in Figure 3.16, $f_{yz}$ is the yield strength of the out-of-plane reinforcement, and $f_{c3}$ is the resulting confining pressure.

For simplicity of input, the modulus of elasticity of the out-of-plane reinforcement is assumed to be the same as that of transverse reinforcement. In addition, the strain hardening behaviour of the out-of-plane reinforcement is neglected.

The resulting stress in the out-of-plane direction is taken into account in the sectional analyses when the concrete response is evaluated in compression depending on the confined strength criteria selected. The default criterion is based on the formulations of Kupfer et al. (1969) and Richart et al. (1928). Detailed information regarding this model can be found in Vecchio (1992).

---

# CHAPTER 4

## MONOTONIC LOADING: VERIFICATION & APPLICATIONS

### 4.1 Chapter Layout

This chapter discusses the application of the proposed nonlinear static analysis procedure to previously tested structures, with the aim of verifying the newly implemented algorithms. The main focus in these applications is to verify the accuracy of the analytical procedures for shear-critical structures. Important considerations in nonlinear modelling are also discussed through the use of practical examples, with the aim of providing guidelines for general modelling applications.

The structures considered include: two sets of twelve beams tested by Vecchio and Shim (2004) and Angelakos et al. (2001), three large-scale frame structures tested by Vecchio and Emara (1992), Duong et al. (2007) and Vecchio and Balopoulou (1990), and six large-scale shear walls tested by Lefas et al. (1990). Moreover, the clinker preheat tower, introduced in Section 1.1.3, is analyzed with the newly developed VecTor5, to ascertain any improvement over the old analysis procedure of TEMPEST.

The chapter starts with a short discussion on the use of different material behaviour models and analysis options; the default options, used for all VecTor analyses programs, are listed. It is then followed by recommendations for the selection of an appropriate member length for use in the frame models and an appropriate displacement increment.

The coverage of each experimental study considers the following steps. The test structure is first introduced, giving the structural details required for the modelling. This is then followed by the modelling and analyses of the structures. Afterwards, the resulting responses are compared to the experimental responses for load-deflection response, reinforcement strains, and crack widths. Discussions regarding the comparisons are finally presented. In addition, the difficulties encountered or expected with respect to the modelling and simulation of the behaviour of the structures are discussed.

## 4.2 Analysis Parameters and Material Behaviour Models Used

When performing a nonlinear analysis with any software program, there are usually a number of parameters or models which must be selected by the user. These may include material models, such as the concrete tensile or compressive response models, or nonlinear analysis options, such as large displacements or hinge unloading methods.

While these options are useful for researchers, for example, when investigating a particular material behaviour or an analysis option, there are a number of disadvantages inherent in the choosing of suitable analysis parameters or models.

The first difficulty is that the selection of appropriate models for the problem at hand may require expert knowledge on the behaviour of reinforced concrete and on the application of nonlinear analyses. This presents a difficult challenge to the users who desire a reasonable estimate of the structural behaviour with a reasonable effort. In other words, repeated analyses with different analysis options and significant engineering effort to decide the appropriate models are not generally desired for practical applications of nonlinear analysis software.

The other issue regarding a large number of different analysis options appears when the developed nonlinear analysis procedure is being verified with previously tested structures, as in the studies that follow in this chapter. As the selected analysis parameters may have a significant effect on the computed responses, they may be used to adjust the analytical predictions to obtain a better correlation with the experimental results. In other words, it becomes possible for the analyst to have more than one answer for each problem at hand. Such a situation is certainly not desired.

For these reasons, the material behaviour models which will always provide reasonable solutions were defined as *default* models. These default models are common to all VecTor programs and were predefined prior to this work, as listed in Table 4.1. The other material behaviour models were also retained as available options; they are useful for advanced applications and for various special situations involving atypical structural details and loading conditions. Consequently, the use of these non-default models are not

recommended for general analyses unless a specific issue regarding the use of a default option arises.

**Table 4.1** Default Material Behaviour Models for VecTor Programs

| Concrete Behaviour | Model | Reinforcement Behaviour | Model |
|---|---|---|---|
| Compression Base Curve | Hognestad (Parabola)* | Hysteresis | Seckin with Bauschinger |
| Compression Post-Peak | Modified Park-Kent | Dowel Action | Tassios (Crack Slip) |
| Compression Softening | Vecchio 1992-A | Strain Rate Effects | Malvar and Crawford |
| Tension Stiffening | Modified Bentz | | |
| Tension Softening | Linear | **Analysis Options** | **Model** |
| Tension Splitting | Not Considered | Geometric Nonlineartity | Considered |
| Confinement Strength | Kupfer / Richart | Shear Analysis Mode | Parabolic Shear Strain |
| Dilatation | Variable - Kupfer | Shear Protection | On |
| Cracking Criterion | Mohr-Coulomb (Stress) | Convergence Limit | 1.00001 |
| Crack Width Check | Crack Limit (Agg/5) | Maximum No of Iterations | 100 |
| Hysteresis | NL (Vecchio) | | * See the text below. |
| Slip Distortion | Vecchio-Lai | | |

Among them, only the concrete compression base curve is varied here, selected on the basis of the concrete strength $f'_c$ used. Two options are available for normal strength concrete: Hognestad (Parabola) and Popovics (NSC). The implementation in VecTor5 was done such that the Hognestad model requires only the concrete strain $\varepsilon_0$, corresponding to the peak stress, while the Popovics (NSC) model requires both $\varepsilon_0$ and the modulus of elasticity of concrete, $E_c$. Thus, if both $\varepsilon_0$ and $E_c$ are known, the use of Popovics (NSC) is recommended rather than the default Hognestad model. Two options are available for high strength concrete: Popovics (HSC) and Hoshikuma (HSC). Note that it was found that the analytical responses do not change significantly if the default Hognestad model is used for all concrete strengths. More information on the formulations of these models is found in the User's Manual of VecTor5 (see Appendix B).

In addition, when performing the nonlinear dynamic analyses in Chapter 8, the elastic-plastic-with-strain-hardening hysteresis model for the reinforcement was used. This was deemed necessary because of the unusual behaviour demonstrated by the default Seckin model under low strain reversals. This phenomenon is reported in Section 8.4.

All analyses performed in this study were multi-layer analyses with shear effects considered, assuming a parabolic shear-strain distribution and using the shear protection and shear failure algorithms as described in Chapter 3. Moreover, throughout this study,

the tensile strength of concrete was taken as defined by Eq. 4.1, which is recommended by CSA A23.3-04 as a lower bound value.

$$f_t' = 0.33 \times \sqrt{f_c'} \tag{4.1}$$

Experience with the MCFT and the DSFM has shown that the use of Eq. 4.1 provides better simulations than the use of experimentally determined tensile strength for the structure being analyzed due to the uncertainties in the experimental determination of the tensile strength of concrete. Further discussion of this issue is presented in Section 4.5.3.

## 4.3 Selection of an Appropriate Member (Segment) Length for Frame Models

When performing a nonlinear analysis with the finite element method, the general approach is to discritize the entire structure into smaller elements. The accuracy of the results is directly dependent on the element sizes used; in general, the smaller the members used, the more accurate the results barring localization effects.

Similar to finite element analyses, the frame analysis procedure employed in VecTor5 requires that frame members be divided into *reasonably* small segments. Average forces for each segment are calculated through the use of member end actions as described in Section 3.8. The use of smaller segments ensures that the average segment forces are calculated more precisely, as required for the nonlinear sectional analyses. Consequently, the nonlinear behaviour of the segments is simulated more accurately.

However, it was found that the use of excessively small segments may cause deterioration in accuracy for shear-critical structures. This anomaly arises from the calculation of the shear compatibility restoring forces, as described in Section 3.6.7. The term used in Eq. 3.61, $\gamma_{ltc} \times (12 \times \mathrm{E}_c \times \mathrm{I}_z) / L_x^{\,2}$, is dependent on the segment sizes used. Consequently, using excessively smaller segments increases the compatibility restoring forces and may cause less ductile responses especially for shear-dominated structures.

To obtain a sense for the optimum segment lengths, a parametric study was carried out in which several previously tested shear- and flexure-critical structures were analyzed with

differing segment lengths. As an example of the shear-critical case, consider the computed responses of Beam VS-A1, introduced in Section 4.5, with varying segment lengths as a function of the cross section depth, h.

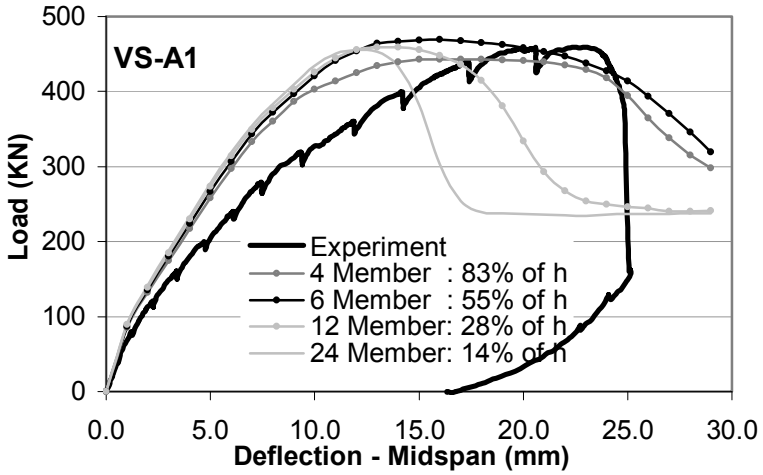


**Figure 4.1** Comparison of Responses for Four Different Segment Lengths (Beam VS-A1)

As seen from Figure 4.1, the selected segment lengths significantly affected the computed post-peak responses of this shear-critical beam. These responses should be regarded as an extreme case, in which the structure showed a shear-dominated behaviour with significant post-peak response, both analytically and experimentally. It is clear that neither the stiffness nor the strength of the beam is affected considerably.

Consider now the computed responses of flexure-critical Beam SS3, introduced in Section 8.2, with varying segment lengths as a function of the cross section depth, h.

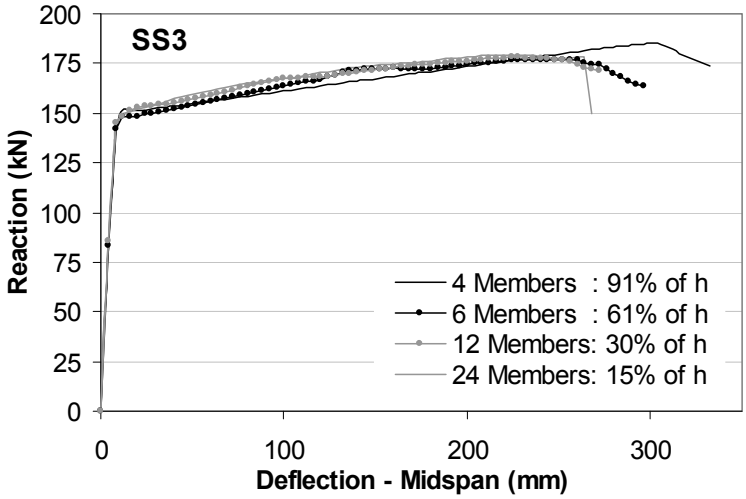


**Figure 4.2** Comparison of Responses for Four Different Segment Lengths (Beam SS3)

As seen from Figure 4.2, the selected segment lengths did not significantly affect the computed responses of this flexure-critical beam. The use of 4 segments provided slightly more ductile response. However, this occurrence is directly related to the smaller average member forces calculated as a result of the averaging of end actions of excessively long members, rather than as a result of amplified shear compatibility restoring forces. As explained before, to adequately account for the localized plasticity, relatively small members should be used. Longer members will typically yield lower average member forces and result in more ductile responses. The use of 6, 12 and 24 members essentially provided the same load deflection responses, failing at the same displacement in flexure. Therefore, contrary to the shear-critical case, the use of smaller segment lengths for the flexure-critical beam did not affect the computed response noticeably.

As a result of the parametric study, it was concluded that the segment lengths in the range of 50% of the cross section depth should provide reasonable simulations of the post-peak behaviour of *frame-related structures* in both shear- and flexure-dominated cases.

A total number of 12 flexure-critical large-scale shear walls, tested previously, are examined in this thesis (Sections 4.11 and 6.7). Half of the walls had a height-to-width ratio of 2.4; the remaining walls had a height-to-width ratio of 2.0. In order to determine the optimum segment lengths to be used in the analyses, a parametric study was conducted in which the walls were analyzed with differing segment lengths. As an example, consider the computed responses of PCA Wall B7 (Oesterle et al, 1976), introduced in Section 6.7, with varying segment lengths as a function of the cross section depth, h. In the first series of analyses, a variable segment length scheme was employed in which the segment lengths were reduced towards the base of the wall as shown in Figure 6.28(a).

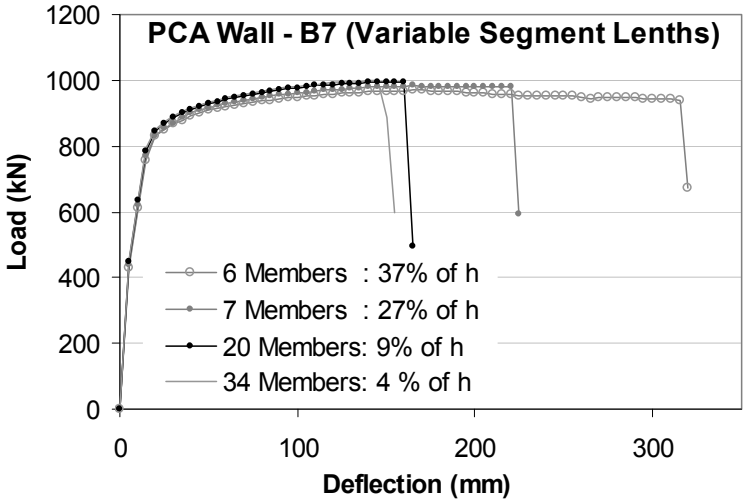


**Figure 4.3** Comparison of Responses for Four Different Varying Segment Lengths (PCA Wall B7) Note: Segment lengths specified were used towards the base.

As seen from Figure 4.3, the selected segment lengths significantly affected the computed post-peak responses of this flexure-critical shear wall. This phenomenon, however, was directly caused by the smaller average member forces obtained from the averaging algorithm in the longer members, rather than as a result of a shear-related effect. In all four cases, the failure was caused by flexural mechanisms. Similar to the previous case, the use of differing segment lengths affected neither the stiffness nor the strength of the wall significantly.

In the second series of analyses, constant segment lengths were used throughout the wall.

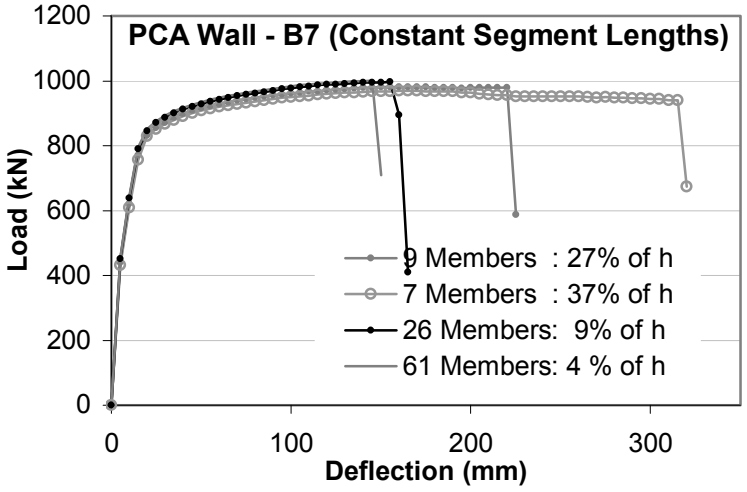


**Figure 4.4** Comparison of Responses for Four Different Constant Segment Lengths (PCA Wall B7)

As seen from Figure 4.4, the responses obtained using constant segment lengths throughout the wall were almost identical to the responses obtained using variable segment lengths. As the concentration of plastic deformations and the ensuing flexural failures occurred in the members adjacent to the bases, the use of more members with the constant segment lengths did not produce any benefits. In fact, it increased the computation time significantly. For example, the analysis with 61 members required 70% more computation time than the analysis with 34 members; they both provided almost identical responses. In conclusion, it is advisable to use varying segment lengths with the shortest segments located at the expected plastic deformation regions.

As a result of this parametric study, segment lengths in the range of 10% of the cross section depth were deemed appropriate in terms of both post-peak behaviour and computational demand for the analysis of the 12 flexure-critical *shear-wall structures* examined in this thesis. This suggestion is also in agreement with the recommendations by Kurama and Jiang (2008) for the analytical modelling of flexure-critical shear walls with a sectional analysis procedure. It should be noted, however, that investigation of shear-critical shear walls are needed in order to reach a more conclusive recommendation. For this purpose, shear walls reported by Sittipunt and Wood (1995) or Wood (1990) may be used in future work.

## 4.4 Selection of an Appropriate Displacement Increment

At the beginning of a nonlinear monotonic displacement controlled-analysis, used extensively in this study, the selection of a displacement increment is required. Unlike tangent stiffness formulations, the secant stiffness formulation, implemented in Chapter 3, does not require sufficiently small displacement increments for accurate simulations of the behaviour. In other words, the selected displacement increment does not have a direct impact on the accuracy of the calculations.

However, in order to capture nuances in the nonlinear behaviour, such as the cracking of concrete and yielding of reinforcement, in a precise manner, an appropriate displacement increment is needed. This selection depends on the problem under consideration. For

example, for a structure that is expected to fail under an imposed displacement of 20 mm, 0.5 mm displacement increment may be sufficient. But for a structure failing at a 200 mm displacement, the use of a 0.5 mm increment will probably be unnecessarily small, increasing the computation time significantly.

To avoid such a situation, an initial analysis of the structure is recommended using a faster analysis procedure such as the single-layer analysis, which was specifically developed for this purpose in Section 3.7.3. At the end of this analysis, depending on the ultimate condition of the structure, an appropriate displacement increment can be selected and the analysis can be repeated using the rigorous multi-layer procedures such as the parabolic shear-strain-based calculation.

## 4.5 Vecchio and Shim Beams

The series of beams tested by Bresler and Scordelis (1963) is often used as a benchmark for verifying analytical procedures. The beams were designed and loaded such as to be critical in shear, with heavy amounts of flexural reinforcement and light amounts of shear reinforcement ranging from 0.0% to 0.2%. These tests represent a difficult challenge in modelling with many nonlinear analyses formulations failing to provide accurate simulations of the behaviour exhibited by these beams (Vecchio and Shim, 2004).

A test program was undertaken by Vecchio and Shim (2004) at the University of Toronto to recreate the Bresler-Scordelis test beams, with an aim to determine the repeatability of the test results. In addition, the Toronto tests also aimed at providing information on the post-peak responses of the beams, which were not reported in the Bresler-Scordelis beams. The test program involved 12 beams subjected to point loads monotonically increasing until failure.

Due to the challenges involved in the simulation of the behaviour of these beams, all 12 beams were modelled with VecTor5 to verify the formulations implemented, especially with respect to shear-critical beams.

The tested 12 beams consisted of four sets (OA, A, B, and C) of three beam series (1, 2, and 3), all of which were supported by simple rollers in a symmetrical test setup. Three different span lengths, *L*, were used for the three beam series. Series 1 had a span length of 3.66 m; Series 2 had a span length of 4.57 m; and Series 3 had a span length of 6.4 m. A typical experimental setup is shown in Figure 4.5.

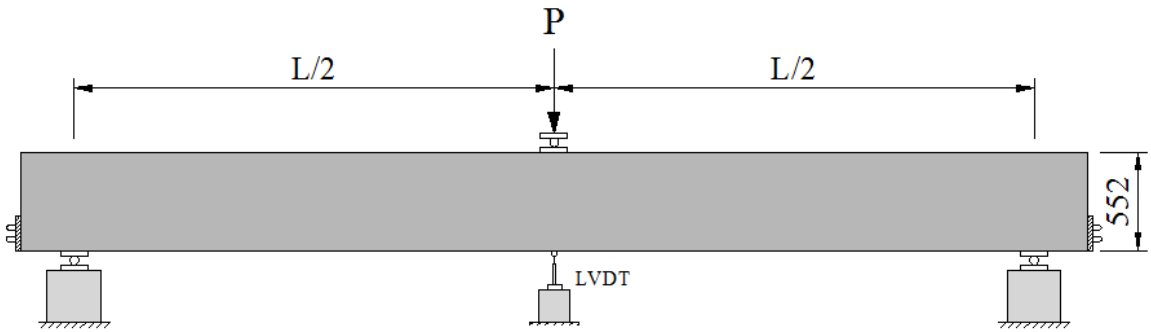


**Figure 4.5** Experimental Setup for Vecchio and Shim Beams

The cross section of each set differed in the amount of longitudinal reinforcement and amount of shear reinforcement as shown in Figure 4.6. All 12 beams had a cross section depth of 552 mm with varying widths. The material properties were determined, in the experimental study, from concrete cylinder tests and steel coupon tests and are summarized in Table 4.2. The maximum aggregate size used was reported to be 20 mm for all beams.

**Table 4.2** Material Properties of Vecchio and Shim Beams

| | Reinforcement | | | | | | |
|---|---|---|---|---|---|---|---|
| | $d_b$ (mm) | $f_y$ (MPa) | $f_u$ (MPa) | $E_s$ (MPa) | $E_{sh}$ (MPa) | $\varepsilon_{sh}$ (x $10^{-3}$) | $\varepsilon_u$ (x $10^{-3}$) |
| **D-5** | 6.4 | 600 | 649 | 200000 | 1530 | 3 | 35 |
| **D-4** | 5.7 | 600 | 651 | 200000 | 1460 | 3 | 38 |
| **10M** | 11.3 | 315 | 460 | 200000 | 730 | 7.7 | 207 |
| **30M** | 29.9 | 436 | 700 | 200000 | 1610 | 11.4 | 175 |
| **25M**[1,3] | 25.2 | 445 | 680 | 220000 | 1130 | 8.5 | 216 |
| **25M**[2] | 25.2 | 440 | 615 | 210000 | 910 | 7.5 | 200 |

[1]: Series 1

| | Concrete | | |
|---|---|---|---|
| | $f'_c$ (MPa) | $\varepsilon_0$ (x $10^{-3}$) | $E_c$ (MPa) |
| **Series 1** | 22.6 | 1.6 | 36500 |
| **Series 2** | 25.9 | 2.1 | 32900 |
| **Series 3** | 43.5 | 1.9 | 34300 |

All beams were subjected to monotonically increasing point loads applied at their midspans, in a displacement-controlled mode, until the final failure of the beams occurred. Additional details regarding these tests can be found in Shim (2002).

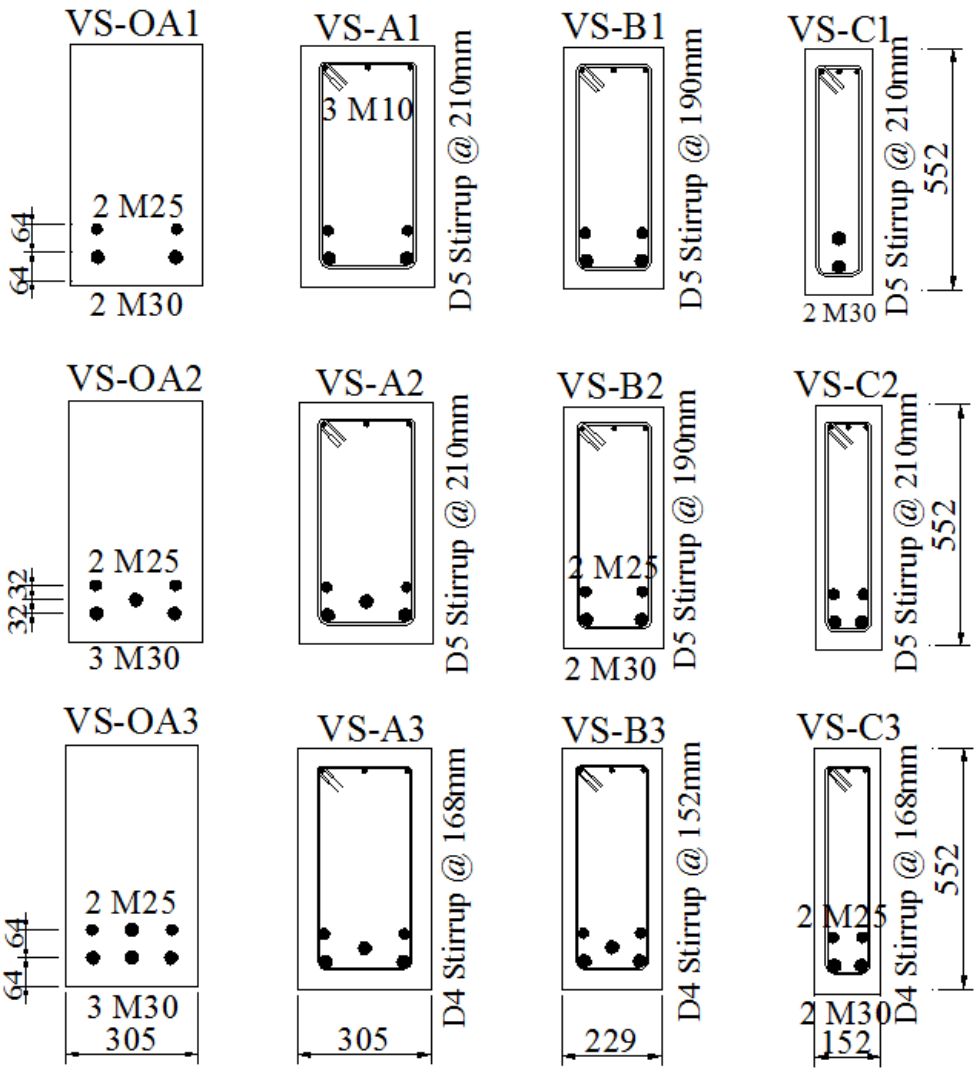


**Figure 4.6** Cross Section Details of Vecchio and Shim Beams

### 4.5.1 Analytical Modelling

Taking advantage of the symmetry of the beams and the test setup, only one-half of each beam was modelled (Figure 4.7). In the model, half of the main span of the beam was typically divided into 6 segments. As a result, 305 mm long members (segments) were used for the Series 1 beams; 380 mm long members were used for the Series 2 beams; and 533 mm long members were used for the Series 3 beams.

The cross sections of the beams were divided into either 34 or 35 concrete layers and into a number of steel layers depending on the longitudinal reinforcement configuration of the particular beam under consideration.

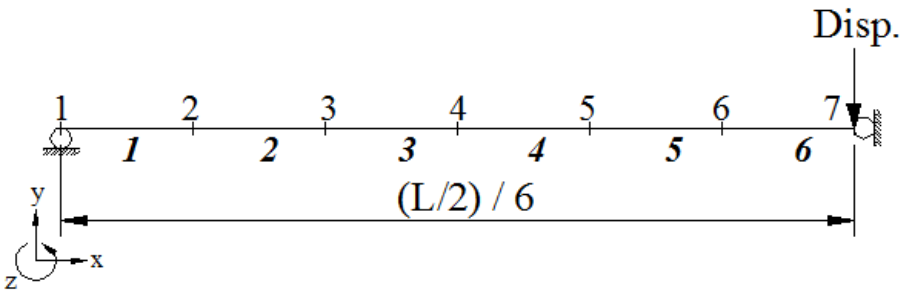


**Figure 4.7** Analytical Model for Vecchio and Shim Beams

### 4.5.2 Creation of the Sectional Model

For general applications, 30 to 40 concrete layers are recommended for use in the sectional models. Because the longitudinal strain distribution reaches maximum values at the top and the bottom of the cross section (Figure 3.23), concrete layer thicknesses should be reduced in these regions, especially for the compression zone layers. If the compression side of the cross section is not known or may change during the analysis due to load reversals, a symmetrical layout for the concrete layer thicknesses can be used (e.g., Figure 4.9(b)).

Determination of the concrete layer thicknesses requires particular attention to the clear cover thickness and the out-of-plane reinforcement configuration. As an example application, consider Beam VS-A1, which has a clear cover of 38 mm and a closed stirrup fabricated from a 6.4 mm diameter bar. The legs of the stirrups extending in the out-of-plane direction constitute the out-of-plane reinforcement, which enhances concrete strength and, more importantly, ductility for the layers in which they are assigned. Consideration of out-of-plane reinforcement is particularly important for the layers under compression. Therefore, an appropriate determination of the tributary area for the out-of-plane reinforcement is needed.

For reinforcing bars in the tension zone, the CEB-FIP model code (1990) suggests a tributary area of 7.5 times the bar diameter. As the definition of a tributary area in the compression zone is needed, approximately 5.5 times the bar diameter was assumed due to the fact that compression zone generally extends over a smaller portion of the cross section than does the tension zone (Figure 4.8(a)). Based on this assumption, for Beam VS-A1, a $6.4\,\text{mm} \times 5.5 = 35\,\text{mm}$ tributary area is engaged. As the concrete thickness

above the centerline of the out-of-plane reinforcement is 41 mm, it is more convenient to assume a tributary area of 41 mm for this particular beam (Figure 4.8(b)). As a result, the number and width of the concrete layers should be defined such as to cover a depth of $41+41=82$ mm at both the top and bottom of the cross section. After determining the distance in which the out-of-plane reinforcement is to be smeared, the out-of-plane reinforcement ratio can be calculated as follows:

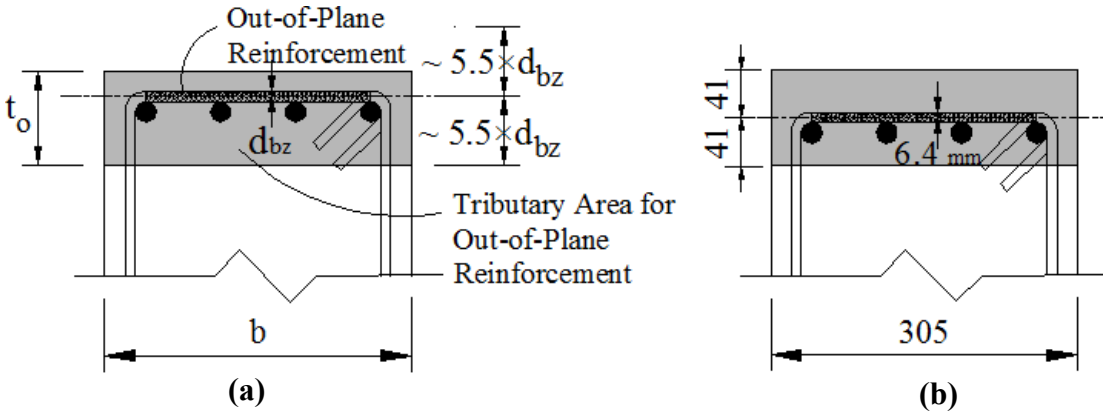


**Figure 4.8** Determination of the Out-of-Plane Reinforcement Tributary Area: **(a)** General Case; **(b)** for Beam VS-A1

$$\rho_z = \frac{A_b}{s_t \times t_0} = \frac{(\pi \times 6.4^2)/4}{210 \times 82} = 0.18\,\% \tag{4.2}$$

where $A_b$ is the cross-sectional area of the out-of-plane reinforcement, $s_t$ is the spacing of the out-of-plane reinforcement in the longitudinal direction, and $t_o$ is the distance, in the transverse direction, in which the out-of-plane reinforcement is to be assigned (Figure 4.8(a)).

Moreover, due to a clear-cover thickness of 38 mm, a number of layers adding up to 38 mm should be created in which no smeared transverse reinforcement is assigned. As a result, the concrete layers and the assigned smeared transverse ( ρt ) and out-of-plane (ρz) reinforcement ratios are determined as shown in Figure 4.9. Note that contrary to the compression zone, fine concrete layers towards the extreme tension fibre are not required although fine layers are used at the bottom of Figure 4.9(b) for ease of modelling with a symmetrical cross section. In addition, three layers of discrete longitudinal reinforcement

reinforcement layers does not affect the selection of the concrete layers. In other words, the reinforcement layers can be defined independently at any desired depth within the cross section.

| Dc (mm) | $\rho_t$ (%) | $\rho_z$ (%) | Nx |
|---|---|---|---|
| 8 | 0 | 0.19 | 1 |
| 10 | 0 | 0.19 | 3 |
| 14 | 0.10 | 0.19 | 2 |
| 16 | 0.10 | 0.19 | 1 |
| 19.4 | 0.10 | 0 | 20 |
| 16 | 0.10 | 0.19 | 1 |
| 14 | 0.10 | 0.19 | 2 |
| 10 | 0 | 0.19 | 3 |
| 8 | 0 | 0.19 | 1 |

**(a)**

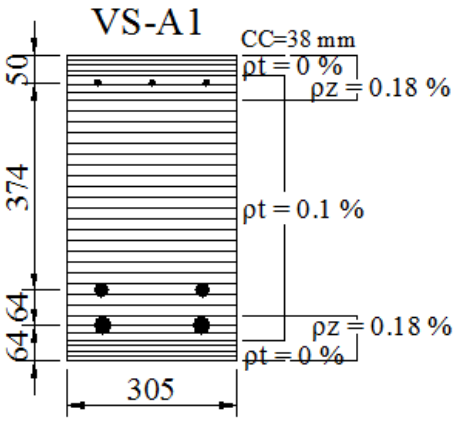


**(b)**

**Figure 4.9** Sectional Model Details for Beam VS-A1: **(a)** Assigned Smeared Reinforcement Ratios; **(b)** Concrete Layers

Sectional models for the remaining beams were created in a similar manner with the smeared reinforcement ratios given in Table 4.3.

**Table 4.3** Assigned Smeared Reinforcement Ratios for Vecchio and Shim Beams

| | $\rho_t$ (%) | $\rho_z$ (%) |
|---|---|---|
| **VS-OA1** | 0 | 0 |
| **VS-OA2** | 0 | 0 |
| **VS-OA3** | 0 | 0 |
| **VS-A1** | 0.10 | 0.19 |
| **VS-A2** | 0.10 | 0.19 |
| **VS-A3** | 0.10 | 0.27 |

| | $\rho_t$ (%) | $\rho_z$ (%) |
|---|---|---|
| **VS-B1** | 0.15 | 0.20 |
| **VS-B2** | 0.15 | 0.20 |
| **VS-B3** | 0.15 | 0.30 |
| **VS-C1** | 0.20 | 0.19 |
| **VS-C2** | 0.20 | 0.19 |
| **VS-C3** | 0.20 | 0.27 |

A simple roller was defined at Node 1, by restraining the vertical degree-of-freedom of Node 1. In addition, to satisfy the condition of symmetry, both the horizontal and rotational degrees of freedom were restrained at Node 7 (Figure 4.7). A monotonically increasing vertical displacement was imposed at Node 7 and the analyses were propagated until failure of the beams occurred.

### 4.5.3 Comparison of the Analytical and Experimental Responses

The analytically and experimentally obtained midspan load-deflection responses are compared in Figure 4.10.

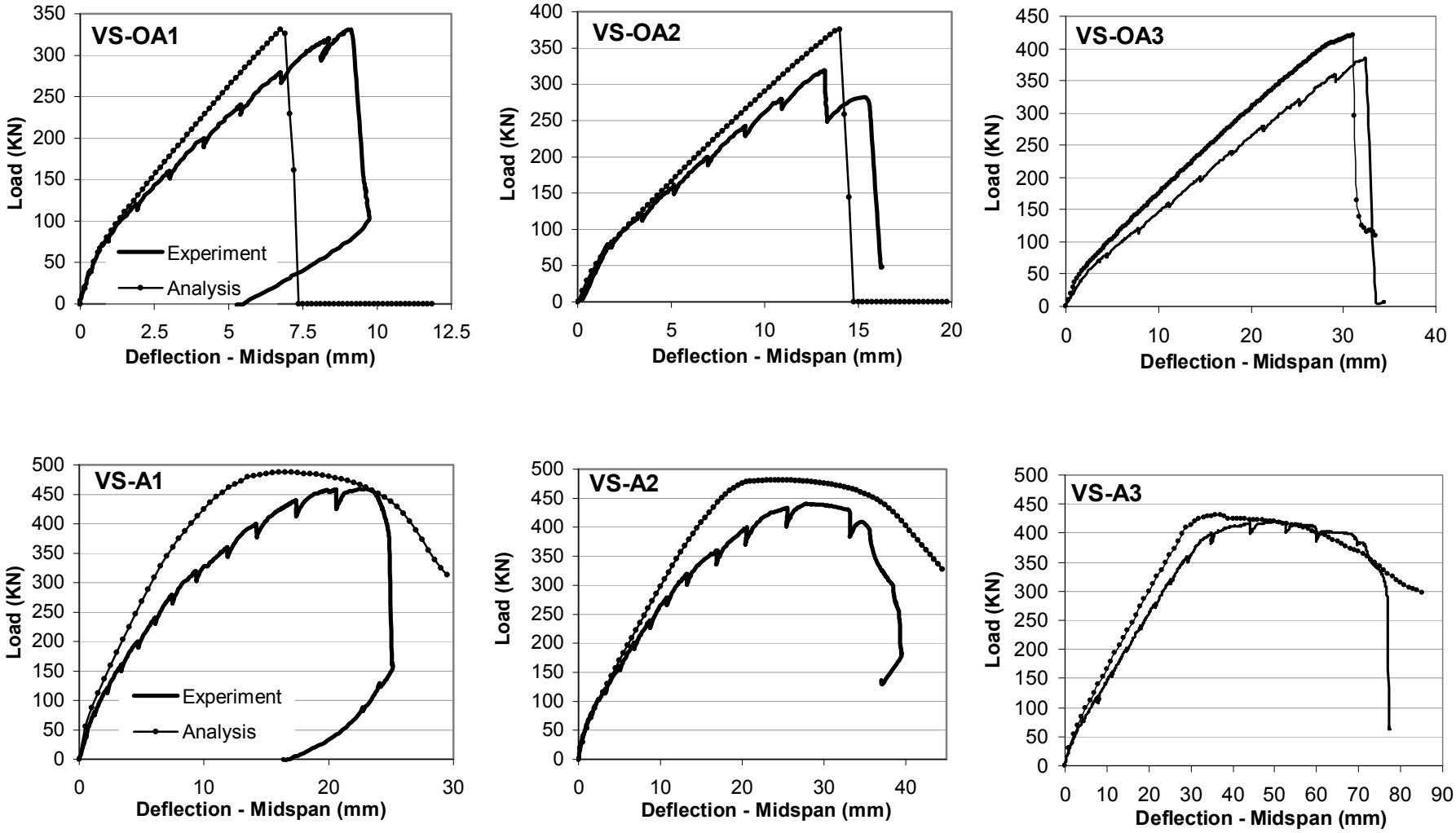


**Figure 4.10** Comparison of the Midspan Load-Displacement Responses for Vecchio and Shim Beams

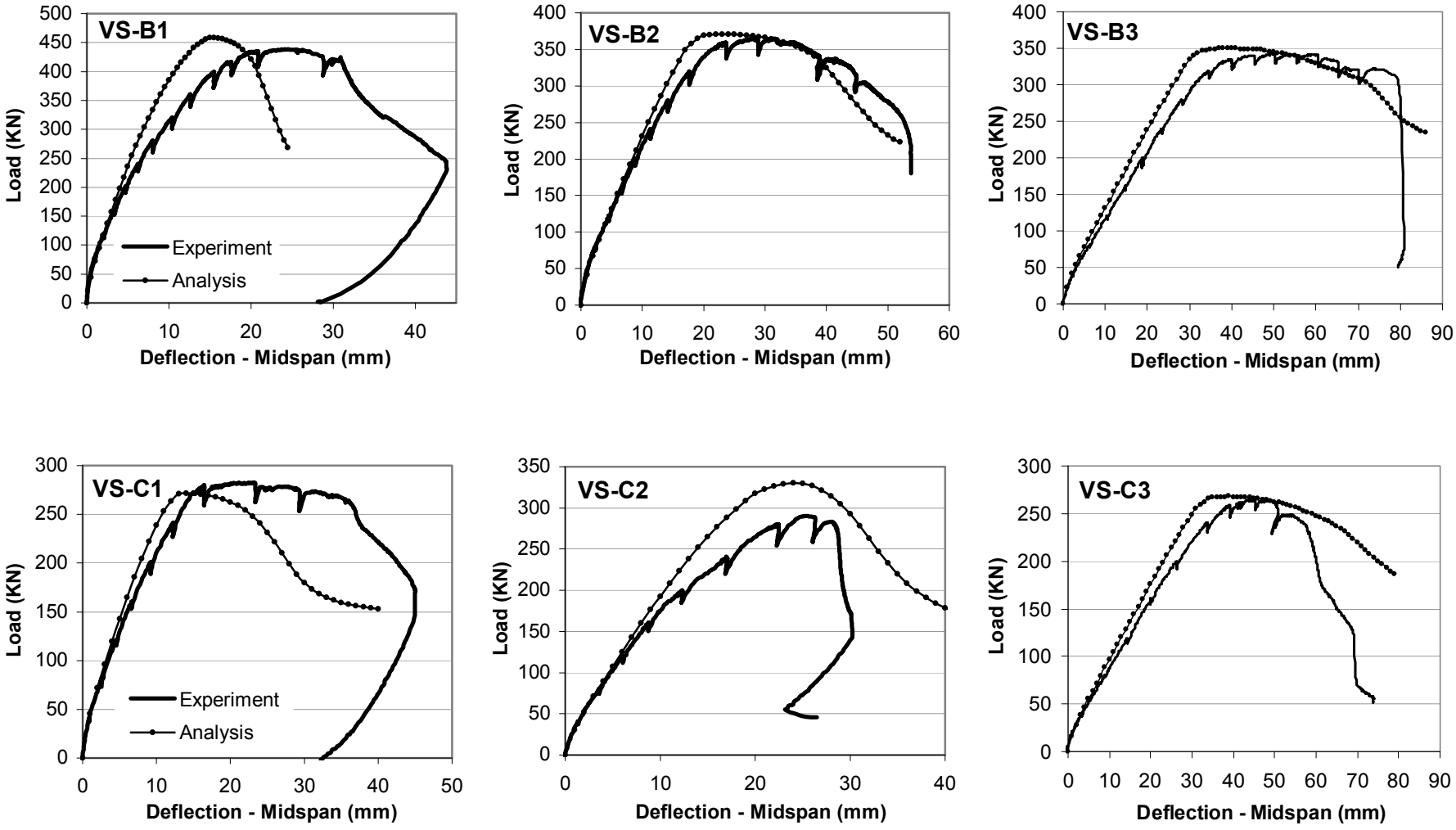


**Figure 4.10** Comparison of the Midspan Load-Displacement Responses for Vecchio and Shim Beams (continued)

The comparisons of the maximum loads and the corresponding midspan displacements, as well the midspan displacements attained prior to the beams dropping their load significantly, as obtained analytically and experimentally, are summarized in Table 4.4.

**Table 4.4** Comparison of Load and Displacement Results for Vecchio and Shim Beams

| | Peak Load (kN) | | | Corresponding Disp. (mm) | | | Failure Disp. (mm) | | |
|---|---|---|---|---|---|---|---|---|---|
| | VecTor5 | Test | Ratio | VecTor5 | Test | Ratio | VecTor5 | Test | Ratio |
| **VS-OA1** | 331 | 331 | 1.00 | 7 | 9 | 0.74 | 7 | 9 | 0.74 |
| **VS-OA2** | 376 | 320 | 1.17 | 14 | 13 | 1.06 | 14 | 16 | 0.90 |
| **VS-OA3** | 420 | 385 | 1.09 | 31 | 32 | 0.96 | 31 | 32 | 0.96 |
| **VS-A1** | 487 | 459 | 1.06 | 17 | 19 | 0.90 | 28 | 25 | 1.12 |
| **VS-A2** | 481 | 439 | 1.10 | 25 | 29 | 0.84 | 43 | 39 | 1.09 |
| **VS-A3** | 430 | 420 | 1.02 | 36 | 51 | 0.71 | 81 | 78 | 1.05 |
| **VS-B1** | 459 | 434 | 1.06 | 15 | 22 | 0.68 | 25 | 44 | 0.56 |
| **VS-B2** | 371 | 365 | 1.02 | 24 | 32 | 0.76 | 49 | 54 | 0.91 |
| **VS-B3** | 351 | 342 | 1.03 | 39 | 60 | 0.65 | 81 | 81 | 1.00 |
| **VS-C1** | 272 | 282 | 0.96 | 15 | 21 | 0.71 | 30 | 45 | 0.67 |
| **VS-C2** | 331 | 290 | 1.14 | 24 | 26 | 0.93 | 34 | 30 | 1.13 |
| **VS-C3** | 268 | 265 | 1.01 | 39 | 44 | 0.88 | 72 | 74 | 0.98 |
| | | **Mean** | **1.05** | | **Mean** | **0.82** | | **Mean** | **0.93** |
| | | **COV (%)** | **6.1** | | **COV (%)** | **12.8** | | **COV (%)** | **18.3** |

The peak load capacities of the beams were calculated with good accuracy. The ratio of the predicted-to-observed ultimate load for all 12 beams had a mean of 1.05 with a coefficient of variation (COV) of 6.1%. Considering the shear-dominated behaviour of the beams, these ratios can be regarded as highly satisfactory.

In terms of the peak load capacity predictions, the least accuracy with a predicted-to-observed mean ratio of 1.17 was encountered in the specimen containing no stirrups; namely, VS-OA2. It is known that the behaviour of reinforced concrete elements which do not contain any shear reinforcement is intrinsically associated with mechanisms heavily dependent on the concrete tensile strength (Vecchio, 2000). However, the tensile strength of concrete is not constant for a particular concrete but varies with a number of parameters such as the volume of concrete, gradient of longitudinal strain, and the presence of restrained shrinkage strains (Collins and Mitchell, 1991). As a result, due to the uncertainties in the determination of the tensile strength of concrete, a lower-bound value defined by Eq. 4.1 is recommended by CSA A23.3-04, which is used throughout this study as discussed in Section 4.2. Consequently, when analyzing a specimen with no shear reinforcement, more scattered predictions should typically be anticipated.

The midspan deflections at maximum loads were predicted with a reasonable mean ratio ($\delta_{theo}/\delta_{test}$) of 0.82 and a COV of 12.8%. The general tendency in the analytical predictions was to underestimate deflections, giving stiffer responses than the experimental responses. The analyses of these beams with a more rigorous finite element tool also provided similarly stiffer responses than the experimental responses (Vecchio and Shim, 2004). These softer experimental behaviours may be attributable to the flexibility of the loading machine or irregularities in the test set-up.

The failure displacements, which are particularly important when determining the ductility of structures, of the beams were calculated with a mean of 0.93 and a COV of 18.3%. These more scattered predictions should be expected in the prediction of the post-peak ductility of beams containing no or as little as 0.1% of shear reinforcement due to the mechanisms heavily dependent on the concrete tensile strength.

The comparisons of the maximum crack widths and the failure mechanisms, as obtained analytically and experimentally, are presented in Table 4.5.

**Table 4.5** Comparison of Crack Widths and Failure Modes for Vecchio and Shim Beams

| | | $W_{cr}$* for P=200 kN | | $W_{cr}$* prior to Failure | | Failure Mode | |
|---|---|---|---|---|---|---|---|
| | | VecTor5 | Test | VecTor5 | Test | VecTor5 | Test |
| VS-OA1 | Flexure | 0.24 | 0.25 | 0.43 | 0.40 | D-T | D-T |
| | Shear | - | - | 0.15 | 0.25 | | |
| VS-OA2 | Flexure | 0.23 | 0.20 | 0.50 | 0.30 | D-T | D-T |
| VS-OA3 | Shear | 0.21 | 0.25 | 0.58 | 0.40 | D-T | D-T |
| VS-A1 | Flexure | 0.24 | 0.20 | 1.00 | 0.50 | S-C | S-C |
| | Shear | - | - | 1.90 | 2.00 | | |
| VS-A2 | Flexure | 0.22 | 0.20 | 1.16 | 1.40 | S-C | S-C |
| VS-A3 | Shear | 0.21 | 0.20 | 0.83 | 1.60 | F-C | F-C |
| VS-B1 | Flexure | 0.21 | 0.20 | 0.68 | 0.75 | S-C | S-C |
| | Shear | - | - | 2.00 | 0.90 | | |
| VS-B2 | Flexure | 0.28 | 0.30 | 1.10 | 1.60 | S-C | S-C |
| VS-B3 | Shear | 0.21 | 0.25 | 0.94 | 1.20 | F-C | F-C |
| VS-C1 | Flexure | 0.35 | 0.40 | 1.00 | 1.80 | S-C | S-C |
| | Shear | - | - | 0.65 | 0.50 | | |
| VS-C2 | Flexure | 0.25 | 0.20 | 0.60 | 0.35 | S-C | S-C |
| VS-C3 | Shear | 0.33 | 0.35 | 0.74 | 0.90 | F-C | F-C |

* crack widths in mm.

As seen from Table 4.5, the crack widths were predicted with excellent accuracy for the applied load of 200 kN, and with a mostly reasonable accuracy just prior to the failure.

Three different failure modes were reported in the experimental study. Diagonal tension failures (D-T) were observed for all three beams containing no shear reinforcement in which a sudden shear-failure mechanism occurred with little prior cracking (see the crack widths in Table 4.5 prior to failure). Shear-compression (S-C) failures were observed for the intermediate-length beams containing shear reinforcement, which can be characterized as shear-flexural in nature. These beams exhibited extensive diagonal-tension cracking in the later load stages with a final failure occurring by crushing of the concrete in the compression zone. Flexure-compression (F-C) failures were observed for the long-span beams containing shear reinforcement. These beams exhibited extensive flexural cracking with a final failure occurring by crushing of the concrete in the compression zone. Diagonal tension cracking was minor, if present at all, in these beams. In all cases, the failure modes were predicted correctly in the analyses (Table 4.5).

### 4.5.4. Determination of Damage or Failure Modes

The developed analytical tool provides ample output including analysis results for nodes, members and concrete and steel layers. The output is especially useful when evaluating the dominant mechanism and the damage or failure mode of the structure. To illustrate the interpretation of the damage mode, consider the analysis result for Beam VS-A1 at a midspan displacement of 25 mm where the beam load capacity dropped significantly (see Figure 4.10). It is advisable to first inspect the member deformations to determine the critical members.

**Table 4.6** Output for Member Deformations at Load Stage 51 (Beam VS-A1)

| M | ECL ($x10^{-3}$) | GXY ($x10^{-3}$) | PHI ($10^{-3}$/m) | ESL-MAX ($x10^{-3}$) | ESL-MIN ($x10^{-3}$) | EST-MAX ($x10^{-3}$) | WCR-MAX (mm) |
|---|---|---|---|---|---|---|---|
| 1 | -0.003 | -0.07 | 0.212 | 0.042 | -0.051 | 0.009 | |
| 2 | 0.21 | -1.028 | 1.612 | 0.551 | -0.155 | 0.951 | 0.49 |
| 3 | 0.299 | -1.297 | 2.697 | 0.87 | -0.311 | 1.304 | 0.65 |
| 4 | 0.369 | -1.429 | 3.882 | 1.192 | -0.508 | 1.561 | 0.77 |
| **5** | 0.446 | **-2.366** | 5.529 | 1.619 | -0.803 | 3.672 | 1.62 |
| **6** | 0.789 | -1.288 | **35.628** | 8.342 | -7.262 | 2.446 | 2.55 |

In Table 4.6, M is the member number, ECL is the axial concrete strain at the mid-depth of the cross section, GXY is the shear strain of the concrete at the mid-depth, PHI is the curvature, ESL-MAX is the maximum longitudinal reinforcement strain, ESL-MIN is the

minimum longitudinal reinforcement strain, EST-MAX is the maximum transverse reinforcement strain and WCR-MAX is the maximum average crack width for the related member. All reinforcement strains are average values.

Inspection of Table 4.6 reveals that Member 5 is the most critical member in terms of shear deformations; Member 6 is the most critical member in terms of flexural deformations. To investigate the conditions of these members, the detailed member output should be utilized. First, consider some of the detailed member output calculated for Member 5 as presented in Table 4.7.

**Table 4.7** Detailed Output for Concrete Layers of Member 5 (Beam VS-A1)

| NC | WCR (mm) | SLIP (mm) | FCX (MPa) | FCY (MPa) | VC (MPa) | FC1 (MPa) | FC2 (MPa) | FC2/FP (MPa) | BETA | E1 ($x10^{-3}$) | E2 ($x10^{-3}$) | THETA1 (Deg) |
|---|---|---|---|---|---|---|---|---|---|---|---|---|
| 1 | 0 | 0.0 | -15.05 | 0.00 | -0.64 | 0.02 | -15.07 | 0.7 | 1.0 | 0.001 | -0.596 | -87.6 |
| 2 | 0 | 0.0 | -14.84 | 0.00 | -2.09 | 0.29 | -15.13 | 0.7 | 1.0 | 0.01 | -0.586 | -82.1 |
| 3 | 0.69 | 0.0 | -12.29 | 0.00 | -0.94 | 0.01 | -12.36 | 0.7 | 0.8 | 1.484 | -0.474 | -85.6 |
| 4 | 1.48 | -0.3 | -9.41 | 0.00 | -1.23 | 0.01 | -9.57 | 0.7 | 0.6 | 3.599 | -0.425 | -82.6 |
| 5 | 0.4 | 0.0 | -12.91 | -0.22 | -2.35 | 0.20 | -13.34 | 0.7 | 0.8 | 1.099 | -0.517 | -79.8 |
| 6 | 0.6 | 0.0 | -12.04 | -0.32 | -2.28 | 0.11 | -12.47 | 0.7 | 0.8 | 1.624 | -0.479 | -79.4 |
| 7 | 1.09 | 0.0 | -10.44 | -0.24 | -1.66 | 0.02 | -10.70 | 0.7 | 0.7 | 2.693 | -0.422 | -81.0 |
| 8 | 1.16 | 0.0 | -9.92 | -0.27 | -1.80 | 0.05 | -10.25 | 0.7 | 0.6 | 2.842 | -0.396 | -79.8 |
| 9 | 1.19 | 0.0 | -9.39 | -0.31 | -1.95 | 0.09 | -9.79 | 0.7 | 0.6 | 2.91 | -0.372 | -78.4 |
| 10 | 1.51 | 0.0 | -8.71 | -0.25 | -1.68 | 0.08 | -9.04 | 0.7 | 0.5 | 3.536 | -0.334 | -79.2 |
| 11 | 1.57 | 0.0 | -7.74 | -0.48 | -1.94 | 0.01 | -8.23 | 0.7 | 0.5 | 3.456 | -0.301 | -75.9 |
| 12 | 1.62 | 0.0 | -6.89 | -0.48 | -1.84 | 0.01 | -7.38 | 0.7 | 0.5 | 3.596 | -0.266 | -75.1 |
| 13 | 1.62 | 0.0 | -6.03 | -0.49 | -1.73 | 0.01 | -6.52 | 0.7 | 0.4 | 3.636 | -0.234 | -74.0 |
| 14 | 1.58 | 0.0 | -5.14 | -0.49 | -1.61 | 0.01 | -5.65 | 0.6 | 0.4 | 3.584 | -0.201 | -72.6 |
| 15 | 1.5 | 0.0 | -4.27 | -0.50 | -1.48 | 0.01 | -4.79 | 0.6 | 0.4 | 3.452 | -0.17 | -70.9 |
| 16 | 1.25 | -0.4 | -2.24 | -0.54 | -1.48 | 0.31 | -3.09 | 0.5 | 0.3 | 3.093 | -0.11 | -59.9 |
| 17 | 1.02 | -0.3 | -1.89 | -0.47 | -1.59 | 0.56 | -2.92 | 0.4 | 0.3 | 2.822 | -0.103 | -57.1 |
| 18 | 0.9 | -0.2 | -1.44 | -0.42 | -1.44 | 0.60 | -2.48 | 0.4 | 0.3 | 2.649 | -0.087 | -54.7 |
| 19 | 0.79 | -0.2 | -1.01 | -0.37 | -1.28 | 0.63 | -2.02 | 0.4 | 0.3 | 2.488 | -0.071 | -52.1 |
| 20 | 0.68 | -0.2 | -0.64 | -0.32 | -1.12 | 0.65 | -1.61 | 0.3 | 0.2 | 2.337 | -0.057 | -49.1 |
| 21 | 0.59 | -0.1 | -0.33 | -0.27 | -0.96 | 0.66 | -1.27 | 0.3 | 0.2 | 2.202 | -0.045 | -45.9 |
| 22 | 0.49 | -0.1 | -0.08 | -0.23 | -0.81 | 0.66 | -0.97 | 0.2 | 0.2 | 2.083 | -0.035 | -42.4 |
| 23 | 0.41 | -0.1 | 0.12 | -0.19 | -0.68 | 0.66 | -0.73 | 0.2 | 0.2 | 1.98 | -0.026 | -38.6 |
| 24 | 0.32 | -0.1 | 0.27 | -0.15 | -0.56 | 0.65 | -0.54 | 0.1 | 0.2 | 1.894 | -0.019 | -34.6 |
| 25 | 0.26 | -0.1 | 0.38 | -0.12 | -0.45 | 0.64 | -0.38 | 0.1 | 0.2 | 1.826 | -0.014 | -30.3 |
| 26 | 0.24 | 0.0 | 0.46 | -0.09 | -0.36 | 0.63 | -0.27 | 0.1 | 0.2 | 1.779 | -0.009 | -26.1 |
| 27 | 0.28 | 0.0 | 0.51 | -0.07 | -0.28 | 0.62 | -0.18 | 0.0 | 0.2 | 1.753 | -0.006 | -21.9 |
| 28 | 0.28 | 0.0 | 0.54 | -0.05 | -0.21 | 0.61 | -0.11 | 0.0 | 0.2 | 1.745 | -0.004 | -17.9 |
| 29 | 0.27 | 0.0 | 0.54 | -0.03 | -0.15 | 0.58 | -0.07 | 0.0 | 0.2 | 1.754 | -0.002 | -14.1 |
| 30 | 0.27 | 0.0 | 0.19 | -0.02 | -0.04 | 0.19 | -0.03 | 0.0 | 0.2 | 1.782 | -0.001 | -11.5 |
| 31 | 0.31 | 0.0 | 0.01 | 0.00 | 0.00 | 0.01 | -0.01 | 0.0 | 0.2 | 1.816 | 0.000 | -9.5 |
| 32 | 0.36 | 0.0 | 0.01 | 0.00 | 0.00 | 0.01 | -0.01 | 0.0 | 0.2 | 1.85 | 0.000 | -6.9 |
| 33 | 0.41 | 0.0 | 0.01 | 0.00 | 0.00 | 0.01 | -0.01 | 0.0 | 0.2 | 1.893 | 0.000 | -4.1 |
| 34 | 0.47 | 0.0 | 0.01 | 0.00 | 0.00 | 0.01 | -0.01 | 0.0 | 0.2 | 1.944 | 0.000 | -1.3 |

In Table 4.7, NC is the concrete layer number starting from the top of the cross section, WCR is the average crack width, SLIP is the crack slip displacement as defined by Eq. 3.38, FCX is the axial stress of the concrete as defined by either Eq. 3.90 or Eq. 3.96, FCY is the transverse stress of the concrete as defined by Eq. 3.8, VC is the shear stress of the concrete as defined by Eq. 3.9, FC1 and FC2 are the concrete principal stresses as defined in Sections 3.2.4 and 3.3.3, FP is the concrete softened compressive strength as defined by Eq. 3.13, BETA is the coefficient for the concrete compression softening as defined by Eq. 3.12 when using the MCFT or Eq. 3.42 when using the DSFM, E1 and E2 are the net concrete principal strains as defined by Eq. 3.3 and Eq. 3.4 when using the MCFT or Eq. 3.33 and Eq. 3.34 when using the DSFT, THETA1 is the inclination of principal tensile stress field as defined by Eq.3.5 when using the MCFT or Eq. 3.35 when using the DSFM. By default, the DSFM formulations were used.

In Table 4.7, a crack width of 0.47 mm is calculated for the extreme tension layer (Layer 34) with almost zero degree angle from the vertical plane indicating that this is a flexural crack. While extending towards the top of the cross section (i.e., compression zone), the crack widens significantly and takes a diagonal form reaching a maximum width of approximately 1.6 mm, indicating shear cracking. There is also an almost horizontal splitting crack occurring at layer 4. The FC2/FP values indicate that the concrete layers in the compression zone have reached 70% of their peak strengths, indicating that concrete compression crushing or failure has not yet occurred but may occur in the following load stages. Strain in the tension reinforcement is approximately $1.6 \times 10^{-3}$ (not shown on Table 4.7) indicating that the member is far from reaching the reinforcement rupture strain of $175 \times 10^{-3}$. As a result, a damage mode of significant diagonal cracking can be concluded for this member.

Consider now some of the detailed member output calculated for Member 6 as shown in Table 4.8.

**Table 4.8** Detailed Output for Concrete Layers of Member 6 (Beam VS-A1)

| NC (mm) | WCR (mm) | SLIP | STATE | FCX (MPa) | FCY (MPa) | VC (MPa) | FC1 (MPa) | FC2 (MPa) | FC2/FP (MPa) | BETA | E1 ($x10^{-3}$) | E2 (Deg) | THETA1 |
|---|---|---|---|---|---|---|---|---|---|---|---|---|---|
| 1 | 0 | 0.0 | 0 | -4.52 | 0.00 | 0.00 | -0.04 | -4.52 | 0.20 | 1.00 | 0.00 | -1.77 | -89.982 |
| 2 | 0 | 0.0 | 0 | -4.52 | 0.00 | -0.01 | -0.05 | -4.52 | 0.20 | 1.00 | 0.00 | -1.77 | -89.936 |
| 3 | 0 | 0.0 | 0 | -4.52 | 0.00 | -0.01 | -0.07 | -4.52 | 0.20 | 1.00 | 0.00 | -1.77 | -89.873 |
| 4 | 0 | 0.0 | 0 | -4.52 | 0.00 | -0.02 | -0.07 | -4.52 | 0.20 | 1.00 | 0.00 | -1.76 | -89.798 |
| 5 | 0 | 0.0 | 0 | -7.95 | -0.19 | -0.05 | -0.28 | -7.95 | 0.34 | 1.00 | -0.01 | -1.88 | -89.627 |
| 6 | 0 | 0.0 | 0 | -10.15 | -0.19 | -0.10 | -0.35 | -10.15 | 0.42 | 1.00 | -0.01 | -1.90 | -89.418 |
| 7 | 0 | 0.0 | 0 | -11.61 | -0.18 | -0.17 | -0.36 | -11.61 | 0.49 | 1.00 | -0.01 | -1.89 | -89.147 |
| 8 | 0.00 | 0.0 | 1 | -7.71 | -0.16 | -0.16 | -0.30 | -7.71 | 0.34 | 1.00 | -0.01 | -1.62 | -88.801 |
| 9 | 0.00 | 0.0 | 1 | -9.74 | -0.15 | -0.34 | -0.28 | -9.75 | 0.43 | 1.00 | -0.01 | -1.58 | -87.976 |
| 10 | 0.00 | 0.0 | 1 | -11.82 | -0.14 | -0.67 | -0.18 | -11.86 | 0.52 | 1.00 | 0.00 | -1.53 | -86.719 |
| 11 | 0.00 | 0.0 | 1 | -14.02 | -0.14 | -1.33 | -0.02 | -14.14 | 0.63 | 1.00 | 0.00 | -1.48 | -84.579 |
| 12 | 0.23 | 0.0 | 1 | -17.20 | -0.22 | -2.00 | 0.01 | -17.43 | 0.77 | 1.00 | 0.46 | -1.45 | -83.366 |
| 13 | 0.49 | 0.0 | 1 | -19.48 | -0.32 | -2.58 | 0.03 | -19.82 | 0.91 | 0.96 | 1.00 | -1.34 | -82.459 |
| 14 | 0.74 | 0.0 | 1 | -19.54 | -0.39 | -2.96 | 0.06 | -19.99 | 1.00 | 0.89 | 1.52 | -1.14 | -81.405 |
| 15 | 0.94 | 0.1 | 1 | -16.92 | -0.40 | -3.07 | 0.15 | -17.47 | 0.98 | 0.79 | 1.99 | -0.84 | -79.801 |
| 16 | 1.14 | -0.1 | 3 | -8.77 | -0.49 | -2.35 | 0.13 | -9.39 | 0.73 | 0.57 | 2.52 | -0.41 | -75.183 |
| 17 | 0.47 | -0.1 | 3 | -0.54 | -0.19 | -0.78 | 0.43 | -1.16 | 0.20 | 0.25 | 1.33 | -0.04 | -51.516 |
| 18 | 0.46 | 0.0 | 1 | -0.02 | -0.08 | -0.06 | 0.02 | -0.12 | 0.03 | 0.20 | 1.43 | 0.00 | -30.77 |
| 19 | 0.6 | 0.0 | 1 | 0.01 | -0.05 | -0.02 | 0.02 | -0.06 | 0.01 | 0.20 | 1.94 | 0.00 | -19.86 |
| 20 | 0.73 | 0.0 | 1 | 0.01 | -0.03 | -0.01 | 0.01 | -0.04 | 0.01 | 0.20 | 2.54 | 0.00 | -14.20 |
| 21 | 0.83 | 0.0 | 1 | 0.01 | -0.02 | -0.01 | 0.01 | -0.03 | 0.01 | 0.20 | 3.16 | 0.00 | -10.78 |
| 22 | 0.88 | 0.0 | 1 | 0.01 | -0.02 | 0.00 | 0.01 | -0.02 | 0.00 | 0.20 | 3.80 | 0.00 | -8.47 |
| 23 | 0.89 | 0.0 | 1 | 0.01 | -0.01 | 0.00 | 0.01 | -0.02 | 0.00 | 0.20 | 4.45 | 0.00 | -6.79 |
| 24 | 0.85 | 0.0 | 1 | 0.01 | -0.01 | 0.00 | 0.01 | -0.01 | 0.00 | 0.20 | 5.10 | 0.00 | -5.50 |
| 25 | 0.78 | 0.0 | 1 | 0.01 | -0.01 | 0.00 | 0.01 | -0.01 | 0.00 | 0.20 | 5.75 | 0.00 | -4.46 |
| 26 | 0.87 | 0.0 | 1 | 0.01 | -0.01 | 0.00 | 0.01 | -0.01 | 0.00 | 0.20 | 6.41 | 0.00 | -3.56 |
| 27 | 1.17 | 0.0 | 1 | 0.01 | 0.00 | 0.00 | 0.01 | -0.01 | 0.00 | 0.20 | 7.07 | 0.00 | -2.71 |
| 28 | 1.25 | 0.0 | 1 | 0.01 | 0.00 | 0.00 | 0.01 | -0.01 | 0.00 | 0.20 | 7.68 | 0.00 | -2.40 |
| 29 | 1.28 | 0.0 | 3 | 0.01 | 0.00 | 0.00 | 0.01 | -0.01 | 0.00 | 0.20 | 8.25 | 0.00 | -1.91 |
| 30 | 1.37 | 0.0 | 3 | 0.01 | 0.00 | 0.00 | 0.01 | -0.01 | 0.00 | 0.20 | 8.81 | 0.00 | -1.41 |
| 31 | 1.66 | 0.0 | 2 | 0.01 | 0.00 | 0.00 | 0.01 | -0.01 | 0.00 | 0.20 | 9.29 | 0.00 | -1.01 |
| 32 | 1.94 | 0.0 | 2 | 0.01 | 0.00 | 0.00 | 0.01 | -0.01 | 0.00 | 0.20 | 9.67 | 0.00 | -0.71 |
| 33 | 2.23 | 0.0 | 2 | 0.01 | 0.00 | 0.00 | 0.01 | 0.00 | 0.00 | 0.20 | 10.05 | 0.00 | -0.42 |
| 34 | 2.55 | 0.0 | 2 | 0.01 | 0.00 | 0.00 | 0.01 | 0.00 | 0.00 | 0.20 | 10.43 | 0.00 | -0.14 |

In Table 4.8, the maximum crack width of 2.55 mm is calculated for the extreme tension layer (Layer 34) with almost zero degree angle from the vertical plane indicating a flexural cracking. Diagonal shear cracking is calculated for Layer 16 with a crack width of 1.14 mm. Compared to the flexural cracking, the shear cracking is not significant.

The FC2/FP values indicate that concrete layers in the compression zone sustain 20% of their peak strengths. BETA values of 1.00 indicate that the sustained stress values correspond to the maximum strength of the concrete, thereby indicating compression crushing for those layers. In the default concrete post-peak base curve of Modified Park-

Kent model (Park, Kent and Gill, 1982), there is 0.20 x $f'_c$ residual stress present as shown in Figure 4.11. Therefore, the stress values of 0.20 x $f'_c$ (0.20 x 22.6 = 4.52 MPa for Beam VS-A1) indicate concrete crushing if they are calculated in the post-peak regime. More details on this model can be found in Wong and Vecchio (2002). The strain in the tension reinforcement is approximately 8.3 x $10^{-3}$ indicating that the member is far from reaching the reinforcement rupture strain of 175 x $10^{-3}$.

Note that FC2/FP and BETA values reported for the tension layers in Table 4.7 and Table 4.8 do not have any significance in the interpretation of damage or failure modes.

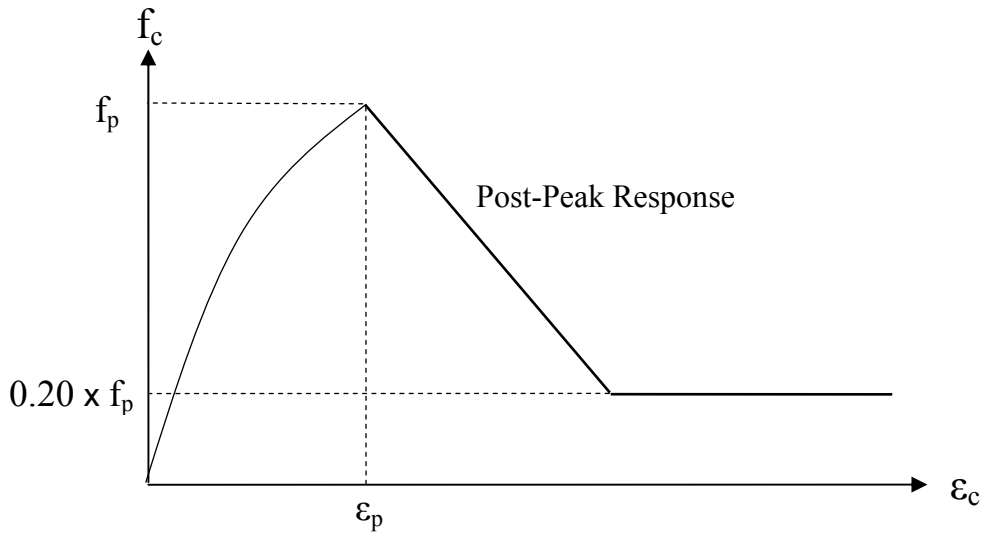


**Figure 4.11** Concrete Post-Peak Response: Modified Park-Kent (Park, Kent and Gill, 1982)

As a result, the damage mode of Beam VS-A1 can clearly be interpreted as shear-compression. If there were no crushing of the concrete in Member 6, the damage mode would be diagonal-tension. If there were no significant diagonal shear cracking in Member 5, the damage mode would be flexure-compression.

In addition, fracture of the transverse and longitudinal reinforcement is considered by the analytical procedure developed. If such a failure occurs, the load capacity of the structure suddenly drops noticeably in most of cases; the ruptured reinforcement and the member it belongs to are written clearly in the output file.

When investigating the detailed output for the concrete layers, the STATE output may provide useful information on the state of the concrete (see Table 4.8). There are currently five states available as shown in Table 4.9, which are defined in Sections 3.2 and 3.3.

**Table 4.9** Available Concrete States Output for Concrete Layers

| STATE | MEANING |
|---|---|
| 0 | Layer Uncracked |
| 1 | Tension Stiffening Governs |
| 2 | Tension Softening Governs |
| 3 | Reinf Reserve Capacity Limited FC1 |
| 4 | Crack Width Check Limited FC2 |
| 5 | VCImax Limited FC1 (MCFT) |

## 4.6 Angelakos Beams

A test program was conducted at the University of Toronto to investigate the influence of the concrete compressive strength and the minimum transverse reinforcement ratio on the shear response of large lightly reinforced concrete members (Angelakos et al., 2001). The test program involved twelve 1.0 m deep beams with concrete strengths ranging from 21 to 80 MPa. All 12 beams were supported by simple rollers in a symmetrical test setup with a typical span length of 5.4 m as shown in Figure 4.12.

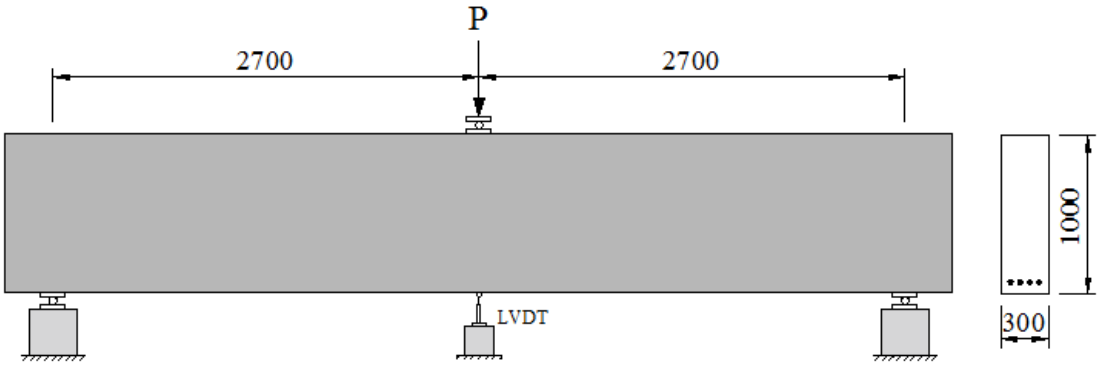


**Figure 4.12** Experimental Setup for Angelakos Beams

All beams had a 1.0 m deep and 0.3 m wide cross section with varying amounts of longitudinal and shear reinforcement as shown in Figure 4.13. The material properties were experimentally determined through concrete cylinder tests and steel coupon tests

and are summarized in Table 4.10 and Figure 4.13. The maximum aggregate size used was reported as 10 mm for all beams.

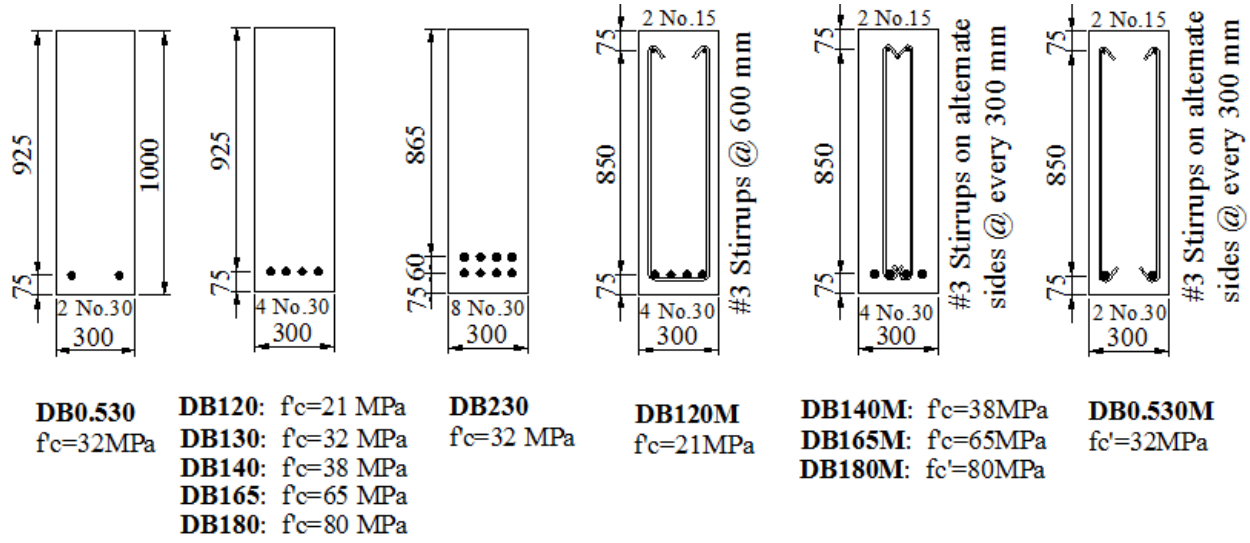


**Figure 4.13** Cross Section Details and Concrete Strengths for Angelakos Beams

**Table 4.10** Material Properties of Angelakos Beams

| | Reinforcement | | | | | | |
|---|---|---|---|---|---|---|---|
| | $d_b$ (mm) | $f_y$ (MPa) | $f_u$ (MPa) | $E_s$ (MPa) | $E_{sh}$ (MPa) | $\varepsilon_{sh}$ (x $10^{-3}$) | $\varepsilon_u$ (x $10^{-3}$) |
| **#3** | 9.5 | 508 | 778 | 200000 | 2578 | 9.25 | 114 |
| **15M** | 16 | 435 | 640 | 174000 | 1095 | 8.75 | 196 |
| **30M** | 29.9 | 550 | 710 | 200000 | 573 | 17 | 291 |

During the curing process, concrete shrinkage strains were measured by strain gauges placed on the longitudinal reinforcement and were reported to be -0.18 x $10^{-3}$ for DB140 and DB140M, -0.19 x $10^{-3}$ for DB165 and DB165M, and -0.35 x $10^{-3}$ for DB180 and DB180M.

All beams were subjected to monotonically increasing point loads applied at their midspan in a displacement-controlled mode until the final failure occurred.

Additional details regarding these tests can be found in Angelakos (1999).

### 4.6.1 Analytical Modelling

Taking advantage of the symmetry of the beams and the test setup, only one-half of each beam was modelled (Figure 4.14). In the model, half of the main span of the beam was typically divided into 6 segments, resulting in 450 mm long members.

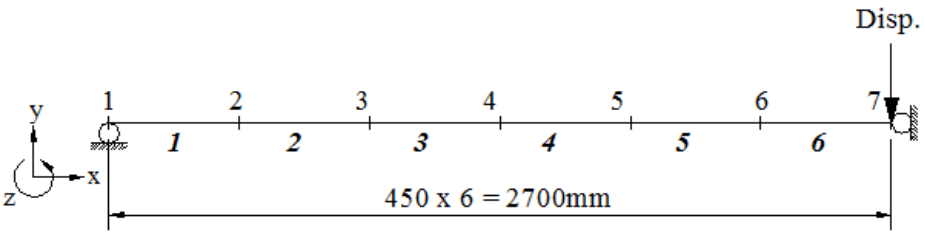


**Figure 4.14** Analytical Model for Angelakos Beams

The sectional model was created by using 40 concrete layers (25 mm thick) for the beams containing no shear reinforcement, and using 52 concrete layers for the beams containing shear reinforcement. This difference was purely caused by the need to consider the clear cover present in the beams containing transverse reinforcement. In addition, the out-of-plane reinforcement in the beam DB120M was considered in a similar way to that described in the Section 4.5.2. The resulting sectional models are presented in Figure 4.15.

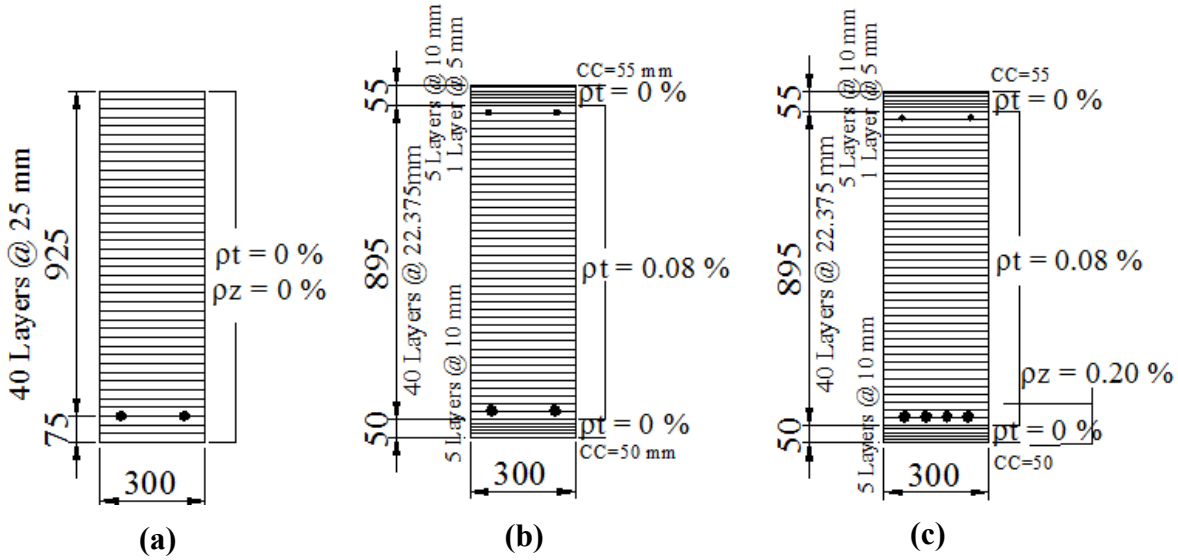


**Figure 4.15** Sectional Models for Angelakos Beams **(a)** All Beams Containing no Transverse Reinf.; **(b)** Beams Containing Transverse Reinforcement; **(c)** Beam DB120M

*Support Restraints*

A simple roller was defined at Node 1 by restraining the vertical degree-of-freedom of the node. In addition, to satisfy the condition of symmetry, both the horizontal and rotational degrees of freedom were restrained at Node 7 (Figure 4.14).

*Loading*

A monotonically increasing load involving a vertical displacement applied at Node 7 was assigned to all beams. A constant load case of uniform shrinkage strains assigned to all members was defined for the beams with reported shrinkage strains. The newly implemented consideration of shrinkage strains was used in these analyses.

All default material behaviour models were used except for the concrete base curve. For concrete strengths up to 40 MPa, the default base curve of Hognestad was used. For concrete strengths of 65 and 80 MPa, the Popovics (HSC) model was selected as described in Section 4.2.

In members made from high strength concrete, cracks pass through, rather than going around, the aggregate and, hence, the maximum aggregate size does not have the same effect on the crack roughness. It was recommended by Lubell et al. (2004) to take the maximum aggregate as zero for concrete strengths in excess of 70 MPa. Consequently, the maximum aggregate size was taken as zero for the concrete strengths of 65 and 80 MPa (Beams DB165, DB165M, DB180 and DB180M).

*Difficulties Expected in the Analyses*

The simulation of the behaviour of these beams was expected to be particularly challenging due to the following reasons.

The beams contained very small amounts of shear reinforcement with two ratios employed: 0.0% and 0.08%. In addition, the longitudinal reinforcement was mainly provided in one layer in the tension zone. Thus, for the beams containing no shear reinforcement, more than half of the concrete layers were unreinforced in both the x- and

y-directions. An example output file for beam DB120, listing the calculated reinforcement ratios and crack spacings, is presented in Table 4.11.

For the beams containing transverse reinforcement, a large number of layers were unreinforced in the x-direction due to the lack of distributed reinforcement through the depth of the beams.

As a result, the behaviour of these beams was expected to be significantly influenced by the tensile strength of concrete, estimated by Eq. 4.1, which intrinsically causes scattered predictions. In addition, the tension softening mechanism would most likely be dominant in the calculation of the concrete tensile principal stresses as defined in Section 3.3.3.3.

**Table 4.11** Output Values Showing the Smeared Reinforcement Ratios for Angelakos Beams

| Layer No | $D_c$ (mm) | ρt (%) | ρz (%) | $\rho_L$ (mm) | $S_{mx}$ (mm) | $S_{mv}$ (mm) |
|---|---|---|---|---|---|---|
| 1 to 28 | 25 | 0 | 0 | 0 | 1000 | 1000 |
| 29 | 25 | 0 | 0 | 3.111 | 501.2 | 1000 |
| 30 | 25 | 0 | 0 | 3.111 | 451.2 | 1000 |
| 31 | 25 | 0 | 0 | 3.111 | 401.2 | 1000 |
| 32 | 25 | 0 | 0 | 3.111 | 351.2 | 1000 |
| 33 | 25 | 0 | 0 | 3.111 | 301.2 | 1000 |
| 34 | 25 | 0 | 0 | 3.111 | 251.2 | 1000 |

| Layer No | $D_c$ (mm) | ρt (%) | ρz (%) | $\rho_L$ (mm) | $S_{mx}$ (mm) | $S_{mv}$ (mm) |
|---|---|---|---|---|---|---|
| 35 | 25 | 0 | 0 | 3.111 | 201.2 | 1000 |
| 36 | 25 | 0 | 0 | 3.111 | 151.2 | 1000 |
| 37 | 25 | 0 | 0 | 3.111 | 106.1 | 1000 |
| 38 | 25 | 0 | 0 | 3.111 | 106.1 | 1000 |
| 39 | 25 | 0 | 0 | 3.111 | 151.2 | 1000 |
| 40 | 25 | 0 | 0 | 3.111 | 201.2 | 1000 |

In Table 4.11, $D_c$ is the concrete layer thickness, $\rho_t$ is the transverse reinforcement ratio, $\rho_z$ is the out-of-plane reinforcement ratio, and $s_{mx}$ and $s_{mv}$ are the crack spacing in the x- and y-directions, respectively.

### 4.6.2 Comparison of the Analytical and Experimental Responses

The analytically and experimentally obtained midspan load-deflection responses are presented in Figure 4.16.

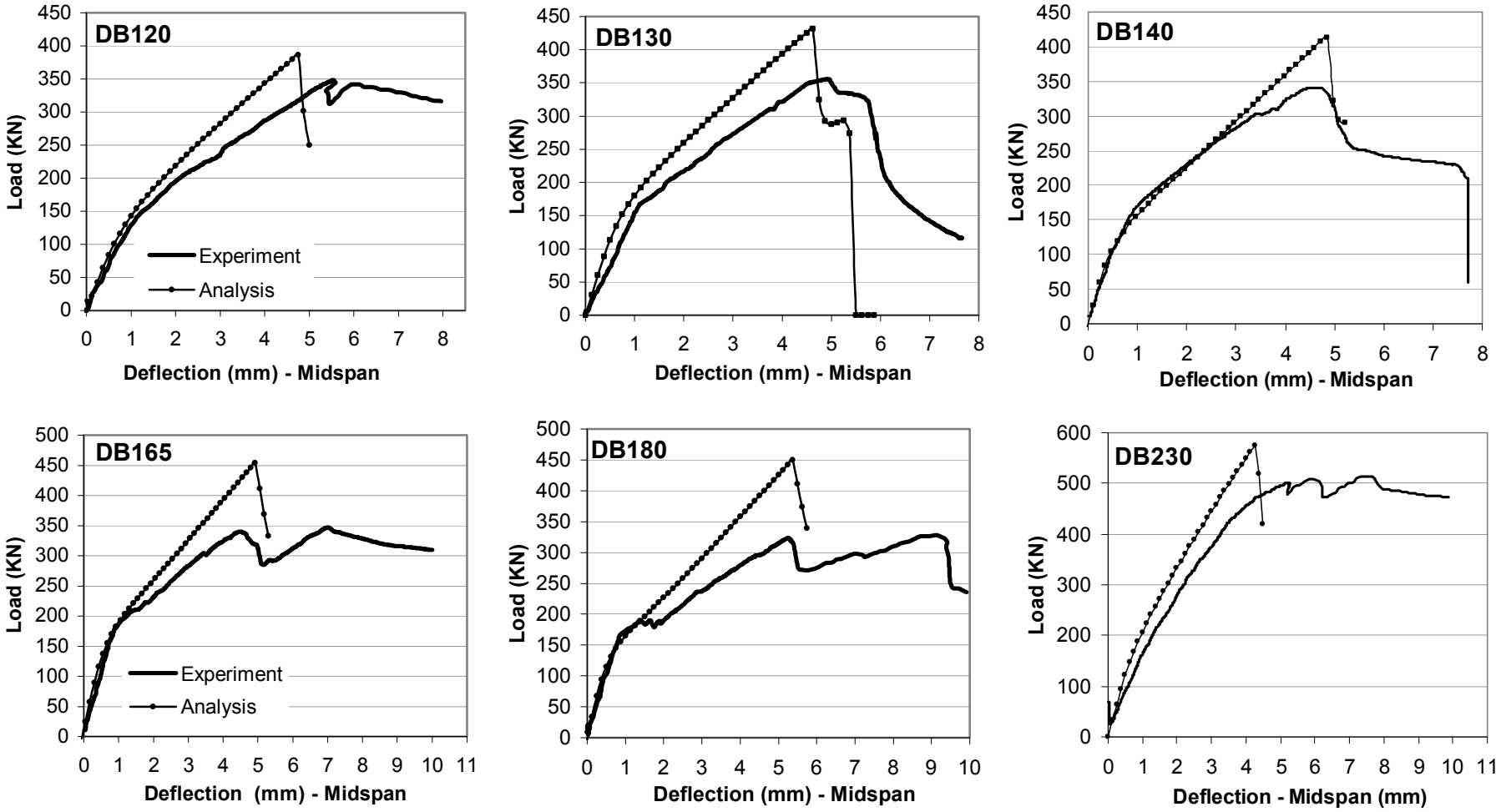


**Figure 4.16** Comparison of the Midspan Load-Displacement Responses for Angelakos Beams

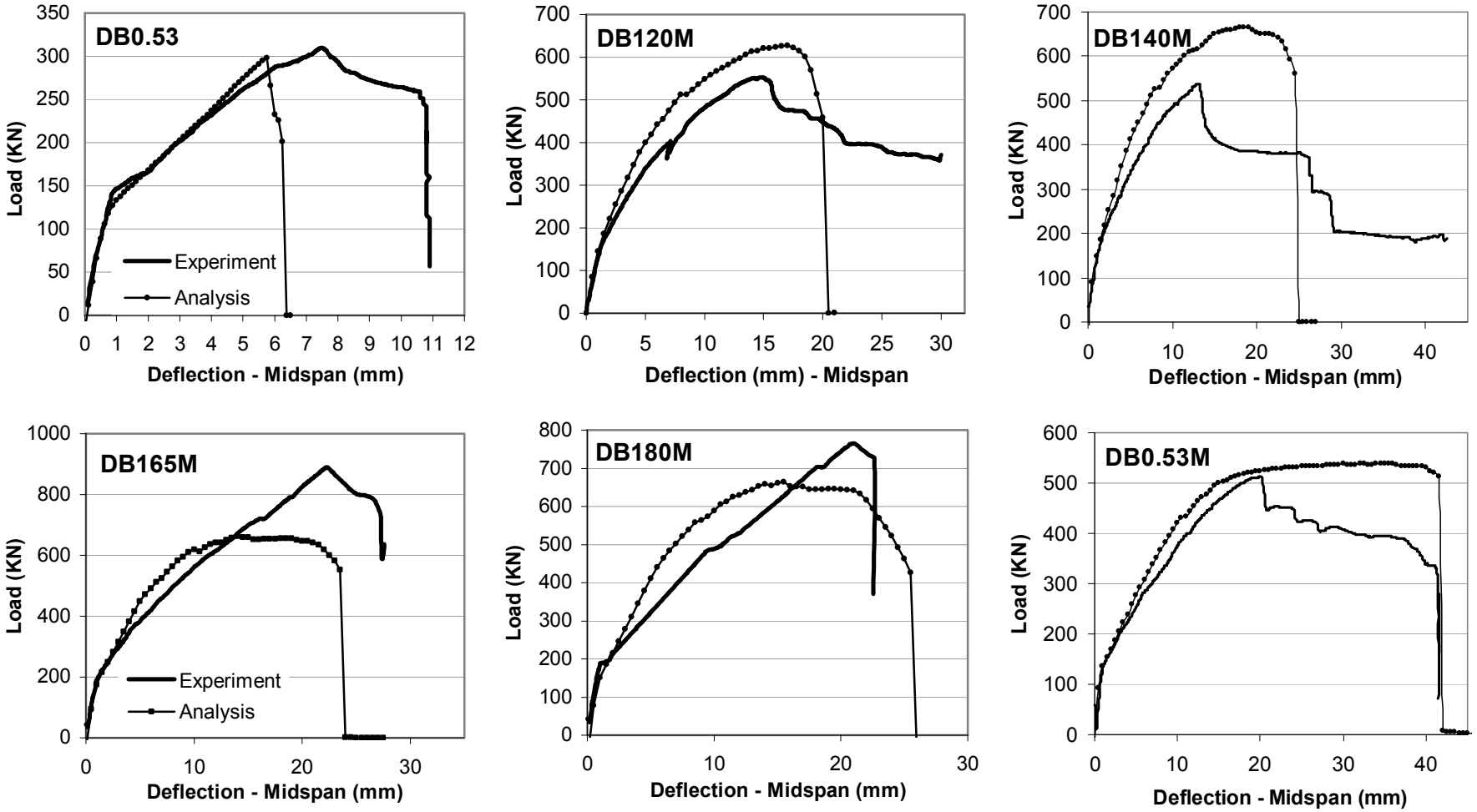


**Figure 4.16** Comparison of the Midspan Load-Displacement Responses for Angelakos Beams

The comparisons of several parameters, as obtained analytically and experimentally, are summarized in Table 4.12.

**Table 4.12** Comparison of Loads and Displacements for Angelakos Beams

| | $P_{cracking}$ (kN) | | Peak Load, $P_{max}$ (kN) | | | Disp. for $P_{max}$ (mm) | | | Failure Disp. (mm) | | |
|---|---|---|---|---|---|---|---|---|---|---|---|
| | VecTor5 | Test | VecTor5 | Test | Ratio | VecTor5 | Test | Ratio | VecTor5 | Test | Ratio |
| DB120 | 137 | 150 | 387 | 358 | 1.08 | 4.8 | 5.6 | 0.86 | 5.0 | 8.0 | 0.63 |
| DB130 | 154 | 170 | 431 | 370 | 1.17 | 4.6 | 4.9 | 0.94 | 5.5 | 6.0 | 0.92 |
| DB140 | 104 | 142 | 412 | 360 | 1.15 | 4.9 | 4.6 | 1.05 | 5.0 | 7.7 | 0.65 |
| DB165 | 130 | 186 | 454 | 370 | 1.23 | 4.9 | 4.5 | 1.09 | 5.3 | 10.0 | 0.53 |
| DB180 | 100 | 170 | 450 | 344 | 1.31 | 5.4 | 5.2 | 1.03 | 5.8 | 9.6 | 0.60 |
| DB230 | 215 | 200 | 575 | 514 | 1.12 | 4.3 | 5.4 | 0.79 | 6.4 | 10.9 | 0.59 |
| DB0.53 | 106 | 144 | 304 | 330 | 0.92 | 5.8 | 7.5 | 0.77 | 4.5 | 9.9 | 0.45 |
| DB120M | 139 | 148 | 628 | 564 | 1.11 | 17.0 | 14.8 | 1.15 | 20.5 | 30.0 | 0.68 |
| DB140M | 106 | 154 | 664 | 554 | 1.20 | 18.0 | 13.2 | 1.36 | 25.5 | 29.8 | 0.86 |
| DB165M | 118 | 182 | 660 | 904 | 0.73 | 15.0 | 22.2 | 0.68 | 23.5 | 27.5 | 0.85 |
| DB180M | 85 | 176 | 666 | 790 | 0.84 | 15.5 | 20.8 | 0.75 | 25.5 | 22.5 | 1.13 |
| DB0.53M | 108 | 140 | 539 | 526 | 1.02 | 35.5 | 20.2 | 1.76 | 42.5 | 41.4 | 1.03 |
| | | | | Mean | 1.07 | | Mean | 1.02 | | Mean | 0.74 |
| | | | | COV (%) | 16.7 | | COV (%) | 30.6 | | COV (%) | 21.0 |

In Table 4.12, the loads causing the first flexural cracking are compared, where it was assumed that the analytical first cracking takes place when the crack widths reach 0.05 mm. The decrease in the analytical cracking loads as the concrete strength increased was caused by the consideration of shrinkage strains for the higher strength beams as defined in Section 4.6.

The peak load capacities of the beams were calculated with reasonable accuracy. The coefficient of variation (COV) of the predicted-to-observed ratio was 16.7%, which is somewhat higher than the results normally expected with nonlinear analyses. The reason for the scattered response is that the majority of the concrete layers used for the beams with no transverse reinforcement consisted of unreinforced plain concrete as described in Section 4.6.1. In the case of beams with transverse reinforcement, approximately half of the layers were only reinforced in the transverse direction with a small amount of reinforcement (0.08%). The strength and ductility of beams containing little or no reinforcement is extremely sensitive to the tensile stresses permitted in the concrete, which were taken into account by the cracking, tension softening and tension stiffening mechanisms. These formulations depend heavily on the tensile strength of concrete,

which is difficult to determine. Due to similar reasons, displacements corresponding to the peak loads and the failure conditions were estimated with somewhat large COVs.

For the beams analyzed, the tension softening mechanism was found to be particularly important. As an example of the influence of the tension softening formulations, the analyses of beam DB120 and DB140M were repeated using a bilinear tension softening formulation (Yamamoto, 1999) rather than the default linear formulation (Yamamoto, 1999). In the analyses, the tensile strengths used were 1.51 MPa and 2.03 MPa for DB102 and DB140M, respectively. Comparisons of the responses are shown in Figure 4.17.

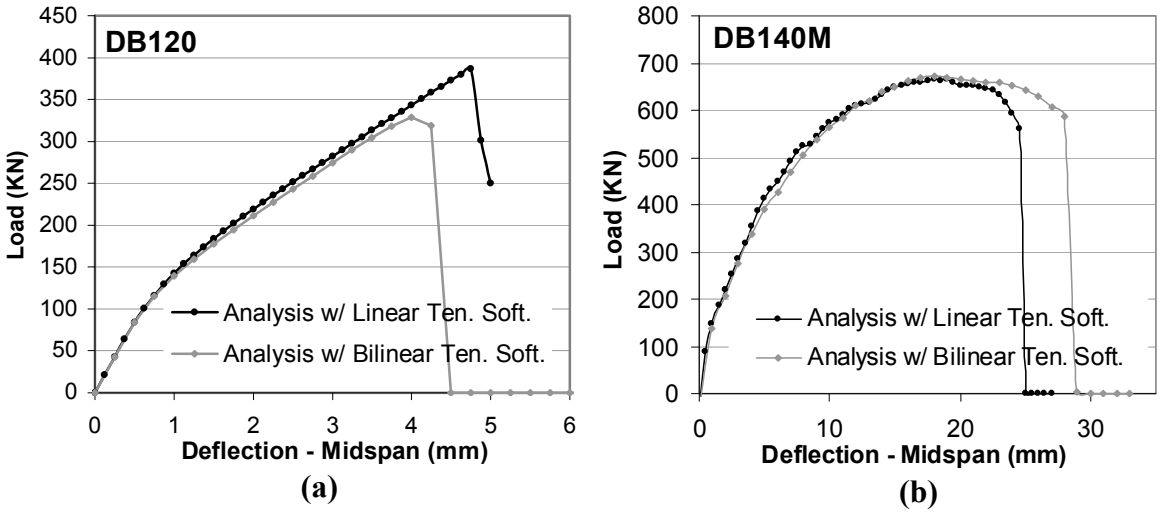


**Figure 4.17** Comparison of the Analytical Responses for Two Different Tension Softening Formulations: **(a)** Beam DB120; **(b)** Beam DB140M

As seen from Figure 4.17, the use of two different tension softening formulations changed the predictions noticeably. The responses of beams with no shear reinforcement (e.g., DB120) were significantly more affected by this mechanism than the beams with minimum shear reinforcement (e.g., DB140M). The sensitivity of the responses to the two different tension softening formulations suggests the need for a more comprehensive tension softening model. More experimental and analytical study is required in this respect to better understand and address this issue.

One of the main findings of this experimental study, as reported by Angelakos et al. (2001), is that changing the concrete strength by a factor of 4 had almost no influence on the experimental shear strengths of these large beams. Note the roughly similar

experimental peak loads of Beams DB120 ($f'_c$=21 MPa) to DB180 ($f'_c$=80 MPa), all of which were identically reinforced for flexure and contained no stirrups. The reason for this behaviour was not entirely understood, although it can be attributed to the crack spacing formulations. In the analytical predictions, the strengths of beams increased with the increasing concrete strength, thereby yielding the least accurate prediction for DB180, which had the highest concrete strength of 80 MPa.

Comparisons of the average shear strain of concrete, $\gamma_{xy}$, average strain of the bottom longitudinal reinforcement, $\varepsilon_{long}$, and average strain of the transverse reinforcement, $\varepsilon_{trans}$ are presented in Table 4.13. In most cases, a reasonable estimate was obtained.

**Table 4.13** Comparison of Analytical and Experimental Strains for Angelakos Beams

| | $\gamma_{xy}$ (x10$^{-3}$) for $P_{max}$ | | $\varepsilon_{long}$ (x10$^{-3}$) for $P_{max}$ | | $\varepsilon_{trans}$ (x10$^{-3}$) for $P_{max}$ | |
|---|---|---|---|---|---|---|
| | VecTor5 | Test | VecTor5 | Test | VecTor5 | Test |
| DB120 | 0.31 | 0.38 | 0.96 | 0.94 | n/a | n/a |
| DB130 | 0.35 | 0.34 | 0.83 | 1.02 | n/a | n/a |
| DB140 | 0.36 | 0.50 | 0.95 | 1.00 | n/a | n/a |
| DB165 | 0.32 | 0.37 | 0.94 | 0.95 | n/a | n/a |
| DB180 | 0.34 | 0.54 | 0.90 | 1.14 | n/a | n/a |
| DB230 | 0.26 | 1.18 | 0.70 | 0.82 | n/a | n/a |
| DB0.53 | 0.40 | 0.55 | 1.30 | 1.53 | n/a | n/a |
| DB120M | 4.20 | 2.72 | 1.60 | 1.49 | 6.3 | 6.2 |
| DB140M | 5.50 | 2.50 | 1.60 | 4.59 | 5.5 | 7.3 |
| DB165M | 3.30 | 3.85 | 1.60 | 3.40 | 3.8 | 8 |
| DB180M | 3.80 | 4.15 | 1.50 | 3.15 | 3.5 | 8.5 |
| DB0.53M | 4.90 | 3.70 | 11.90 | 2.45 | 6.2 | 10.8 |

In Table 4.13, the discrepancies in the analytical predictions DB0.53M were mainly caused by the near flat-top nature of the analytical response, which reached the peak load at a larger displacement than the experimental response, thereby providing larger analytical strain values at the peak load level (Figure 4.16).

The failure modes of all the beams were accurately predicted as being diagonal-tension failures. For the specimens containing no shear reinforcement, the analytical failures occurred suddenly in the compression zone of Member 5. Typically, one load stage before the failure, Member 5 had a maximum flexural crack width of approximately 0.4 mm and a practically uncracked compression zone. In the following load stage, the layers

towards the top of the beam cracked suddenly with large strains resulting in the transverse direction. As there was no transverse reinforcement, extensive horizontal cracking occurred within layers in the top half of the beam. As a result, the member load capacity dropped, and the beam failed completely. A similar failure mechanism was observed in the experimental program.

The analytically determined failure of the beams containing shear reinforcement typically involved the failure of Member 2. In the analytical model, these beams experienced more diagonal cracking compared to the beams containing no shear reinforcement, up to 4.0 mm in width before the failure occurred. Under increasing cracking, Member 2 started to return unbalanced shear force at the end of load stages as the specified maximum number of iterations (100) started to be insufficient. The failure was detected by the newly implemented *shear failure check* due to excessive unbalanced shear force. A diagonal-tension failure mode was also observed in the experiment with diagonal cracks extending between the point load at the midspan and the support.

## 4.7 Vecchio and Emara Frame

An experimental program was conducted at the University of Toronto to investigate the magnitude and influence of shear deformations in flexure-critical frame structures and to verify the accuracy of the analytical procedures developed (Vecchio and Emara, 1992). The experiment involved the testing of a one-bay, two-storey frame under increasing lateral load levels applied to the second storey beam. Two column axial forces of 700 kN were applied to simulate the effects of loads coming from the storeys above the second floor. The details of the frame, material properties and the loading conditions were described in Section 2.3.5, where this frame was analyzed using several other software programs and hand calculation procedures. Additional details regarding this experiment can be found in Emara (1990).

### 4.7.1 Analytical Modelling

The beams and columns were divided into a number of segments to create the frame model of the structure (Figure 4.18). Segment lengths were selected to be approximately

half the cross section depth of 400 mm. Three member types were used for the sectional models of the beams, columns and base: MT1, MT2 and MT3, respectively.

As the frame model of the structure is based on the centreline dimensions, the stiffening effects of the overlapping portions of the beams and columns should be considered; this is achieved, in this study, by increasing the reinforcement amounts of those portions. For this purpose, a study was carried out for two frame structures by increasing the reinforcement ratios for the members in the overlapping portions and repeating the nonlinear frame analyses. It was determined that the multiplication of the reinforcement amount by a factor of greater than approximately 2 essentially gives the same stiffness in the load-deflection response with insignificant curvature values calculated for those overlapping members. Therefore, the amounts of all reinforcement components (discrete longitudinal, smeared transverse and smeared out-of-plane) were doubled to create members within the beam-column joints of the frame. This approach is used throughout this study. Therefore, member types MT4, MT5, and MT6 were created by doubling the reinforcement amounts of MT1, MT2, and MT3, respectively (see Figure 4.20). The concrete layers and out-of-plane reinforcement ratios for the sectional models (member types) were determined in the manner explained in Section 4.5.2. The transverse reinforcement ratios were assigned to all layers except the clear-cover layers. The resulting sectional models are presented in Figure 4.19(a).

The bolts used in the experiment to fix the base beam to the strong floor were represented by restraining both the x- and y-degrees of freedom of the nodes approximately corresponding to the bolt locations as shown in Figure 4.20.

All default material behaviour models were used except the concrete compression base curve. As both the modulus of elasticity and peak strain corresponding to the peak stress were known, the Popovics (NSC) formulation was used as explained in Section 4.2.

Two load cases were defined for this analysis: a monotonically increasing displacement applied to Node 39 in the x-direction, and two constant column axial forces applied to Nodes 39 and 55 in the y-direction. The frame was loaded to a lateral displacement of 155 mm, and then unloaded to a net lateral load of zero as it was in the experiment.

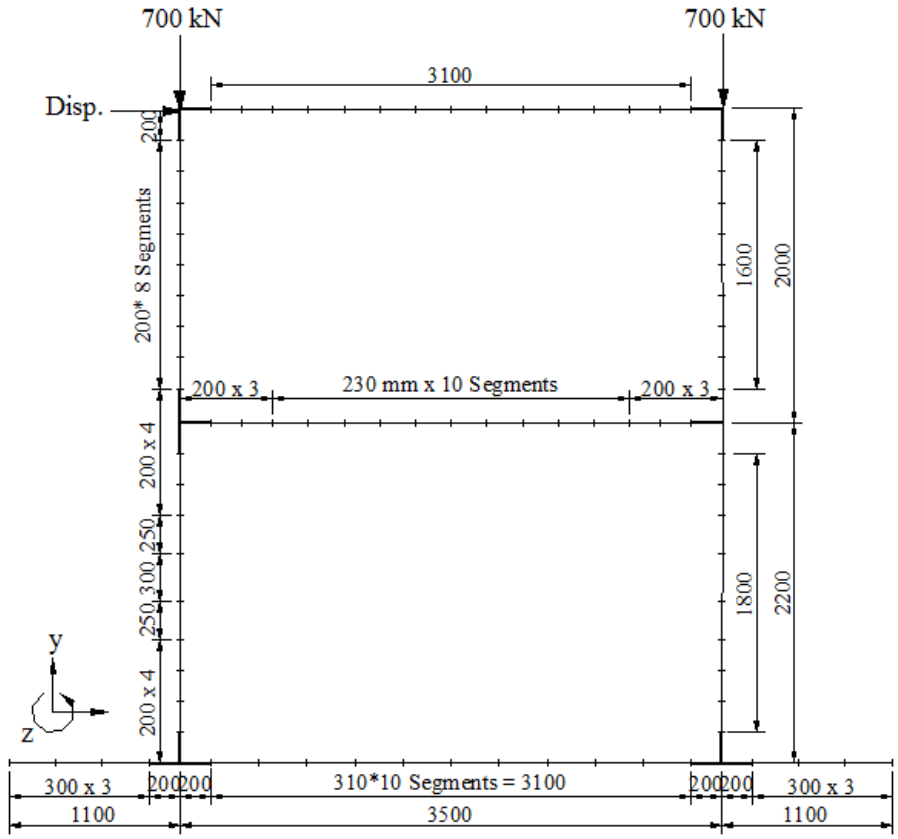


**Figure 4.18** Analytical Model Showing Segment Lengths and Loading for Vecchio and Emara Frame

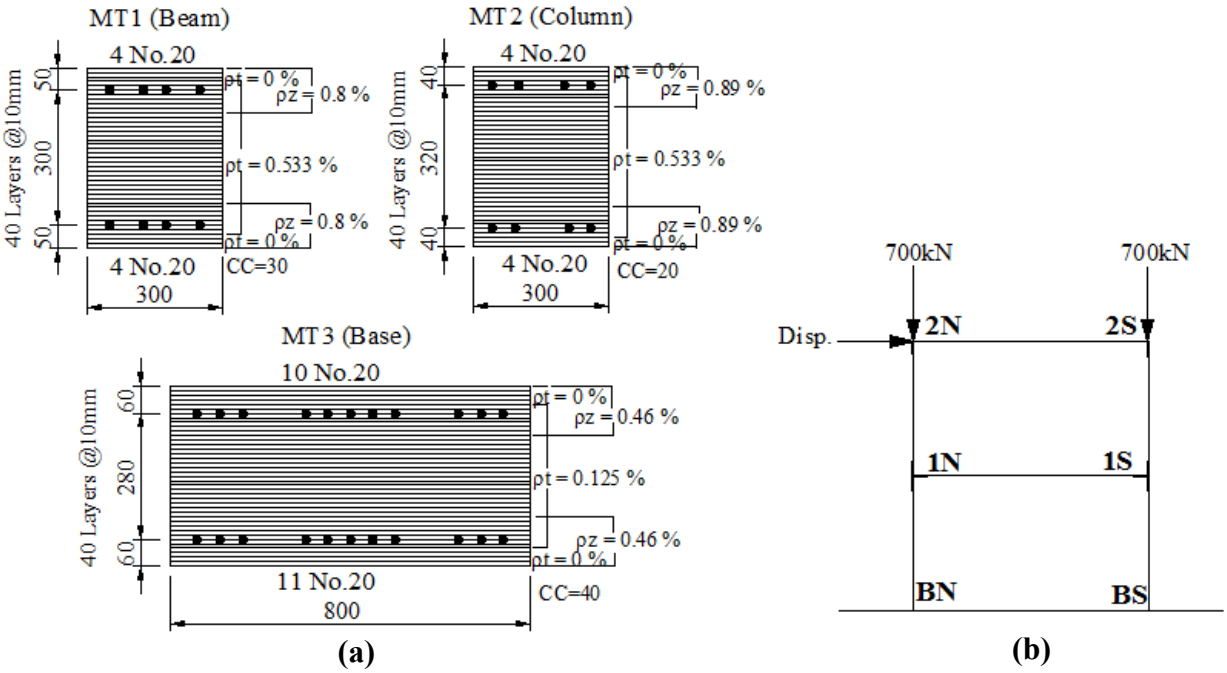


**Figure 4.19 (a)** Sectional Models for Vecchio and Emara Frame; **(b)** Name Convention Adopted

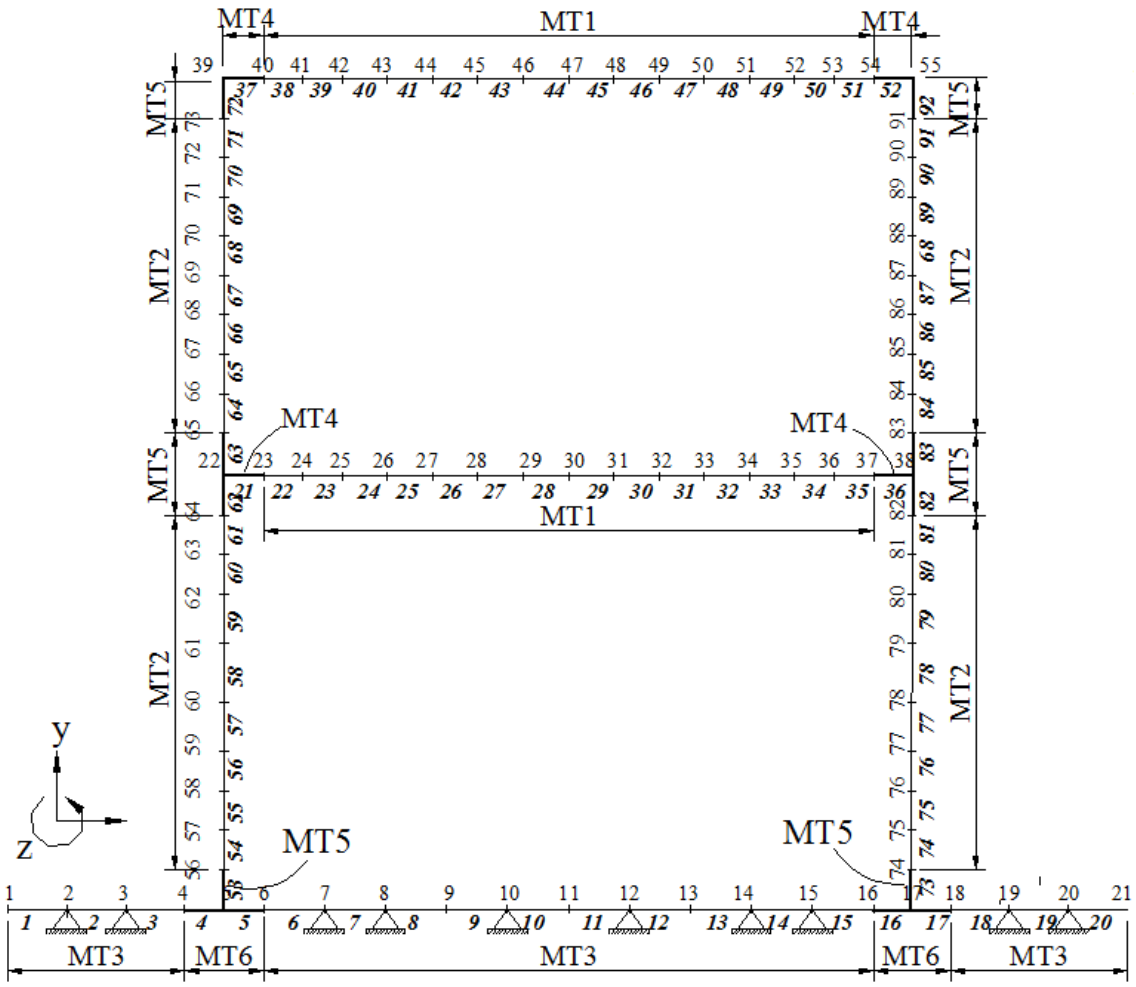


**Figure 4.20** Analytical Model Showing Member Types and Support Restraints for Vecchio and Emara Frame

In the following discussion, a name convention was adopted as shown in Figure 4.19(b). The ends of the beams and the column bases were denoted by their North or South orientation. As the shear protection algorithm was used by default, the VecTor5 output indicated that first storey beam Members 21, 22, 35 and 36 were protected members with their shear forces being reduced. As a result, possible shear damage will be diverted to the adjacent members. Therefore, 1N and 1S refer to Member 23 and Member 34, respectively, when discussing shear-related mechanisms such as shear crack widths. Similarly 2N and 2S refer to the Members 39 and 50, respectively. However, when flexure-related behaviour is discussed, 1N and 1S refer to Members 22 and 35, and 2N and 2N refer to Members 38 and 51. Similarly, BN and BS refer to Members 54 and 74 in flexure.

### 4.7.2 Comparison of the Analytical and Experimental Responses

The analytically and experimentally obtained applied net lateral load-second storey beam lateral deflection responses are compared in Figure 4.21.

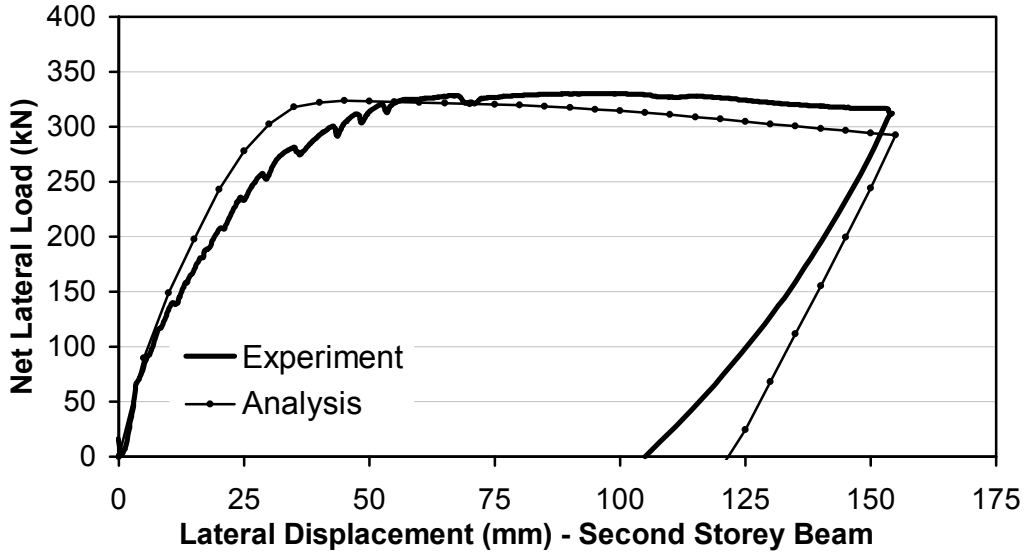


**Figure 4.21** Comparison of Load-Deflection Responses for Vecchio and Emara Frame

As apparent from Figure 4.21, the frame's maximum load capacity was estimated with excellent accuracy, having a predicted-to-observed ratio of 0.98.

The lateral stiffness of the frame was predicted with very good accuracy as well. A slight underestimation of the displacements was observed in the initial stages of the loading. After achieving the peak lateral load of 324 kN, in the analytical model, the net lateral load decreased gradually although the total lateral load applied was being increased. This decrease in the net lateral load was caused by the second-order effects considered in the analysis. As the columns deflected laterally, the axial forces deviated from the vertical axes creating countering lateral forces, which reduced the applied lateral load. This behaviour was also observed in the experiment to a lesser extend.

Upon entirely unloading the frame, the residual displacement was predicted with a 14% overestimation. However, the total energy dissipated by the frame (i.e., the area under the

load-deflection curve) was predicted with excellent accuracy to be 44.6 kNm as compared to the experimental value of 44.4 kNm.

For information purposes, the experimental effective lateral stiffness of the frame was calculated, using the secant stiffness of the load-deflection curve at the complete yielding point (approximately 319 kN lateral load), as approximately 6.1 kN/mm. As the linear-elastic lateral stiffness of the frame was approximately 25.7 kN/m, an effective stiffness value of 0.25 times the uncracked gross stiffness value of the frame was determined.

The first storey midspan displacements in the y-direction, as determined analytically and experimentally, are compared in Figure 4.22. The initial vertical displacement of the first storey beam was accurately calculated to be approximately 0.5 mm. The overall response showed a strong agreement with the experimental response. The residual displacement value, however, is overestimated significantly.

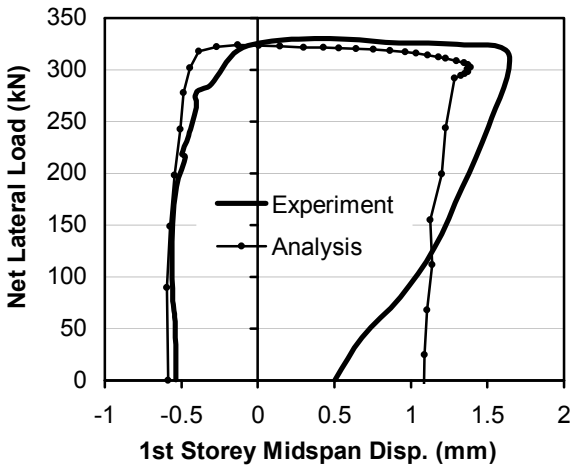


**Figure 4.22** Comparison of First Storey Midspan Displacement Responses for Vecchio and Emara Frame (Downward displacements are shown as negative.)

As shown in Table 4.14, the lateral loads causing the first yielding of the reinforcement were predicted accurately. A strong correlation in terms of crack widths was also obtained.

**Table 4.14** Comparison of Analytical and Experimental Results for Vecchio and Emara Frame

| | Analysis | Test |
|---|---|---|
| Lateral Load (kN) causing **First Flexural Cracking** | 50.0 | 52.5 |
| Crack Widths (mm) | | |
| Beam 1N | 0.03 | 0.05 |
| Beam 1S | 0.03 | 0.05 |
| Lateral Load (kN) causing **First Yielding of Reinf.** | | |
| Beam 1N Longitudinal | 267 | 264 |
| $W_{cr}$ (mm) | 0.45 | 0.60 |
| Beam 1S Longitudinal | 267 | 287 |
| $W_{cr}$ (mm) | 0.45 | 0.60 |
| Column BN Longitudinal | 318 | 323 |
| Column BS Longitudinal | 318 | 323 |
| Beam 2S Longitudinal | 318 | 329 |
| Column BS Long. in Comp* | 332 | 320 |
| Column BN Long. in Comp* | 332 | 310 |

*post-peak

| | Analysis | Test |
|---|---|---|
| **Crack Widths (mm)** for Lateral Load (kN) | 90 kN | 97 kN |
| Beam 2N | 0.06 | 0.05 |
| Beam 2S | 0.05 | 0.05 |
| | 150 kN | 145 kN |
| Column BN | 0.06 | 0.05 |
| Column BS | 0.05 | 0.05 |
| Beam 1 | 0.05-0.20 | 0.05-0.15 |
| | 200 kN | 193 kN |
| Column TS | 0.03 | hairline |
| | 304 kN | |
| Beam 1N | 1.1 | 1.3 |
| Column BN | 0.30 | 0.45 |
| Column BS | 0.30 | 0.45 |
| | 320 kN | 329 kN |
| Beam 1N | 2.3 | 2.2 |

The experimentally observed damage mode of the frame involved ductile plastic hinging of both beam ends (Beam 1N, 1S, 2N and 2S) and both column bases (BN and BS), including yielding of both the tension and compression reinforcement and some concrete crushing. The analytical damage mode was mainly caused by the plastic hinging of the column bases including yielding of both tension and compression reinforcement and crushing of concrete, especially in the BS area. The first and second storey beams ends were predicted to be extensively damaged with crack widths as high as 9.0 mm and tensile reinforcement strains reaching 47 x $10^{-3}$. The compression reinforcement at the beam ends, however, did not yield but typically reached 80% of their yield strain. As two typical examples, the reinforcement strain responses for Beam 1S and for the column bases are presented in Figure 4.23.

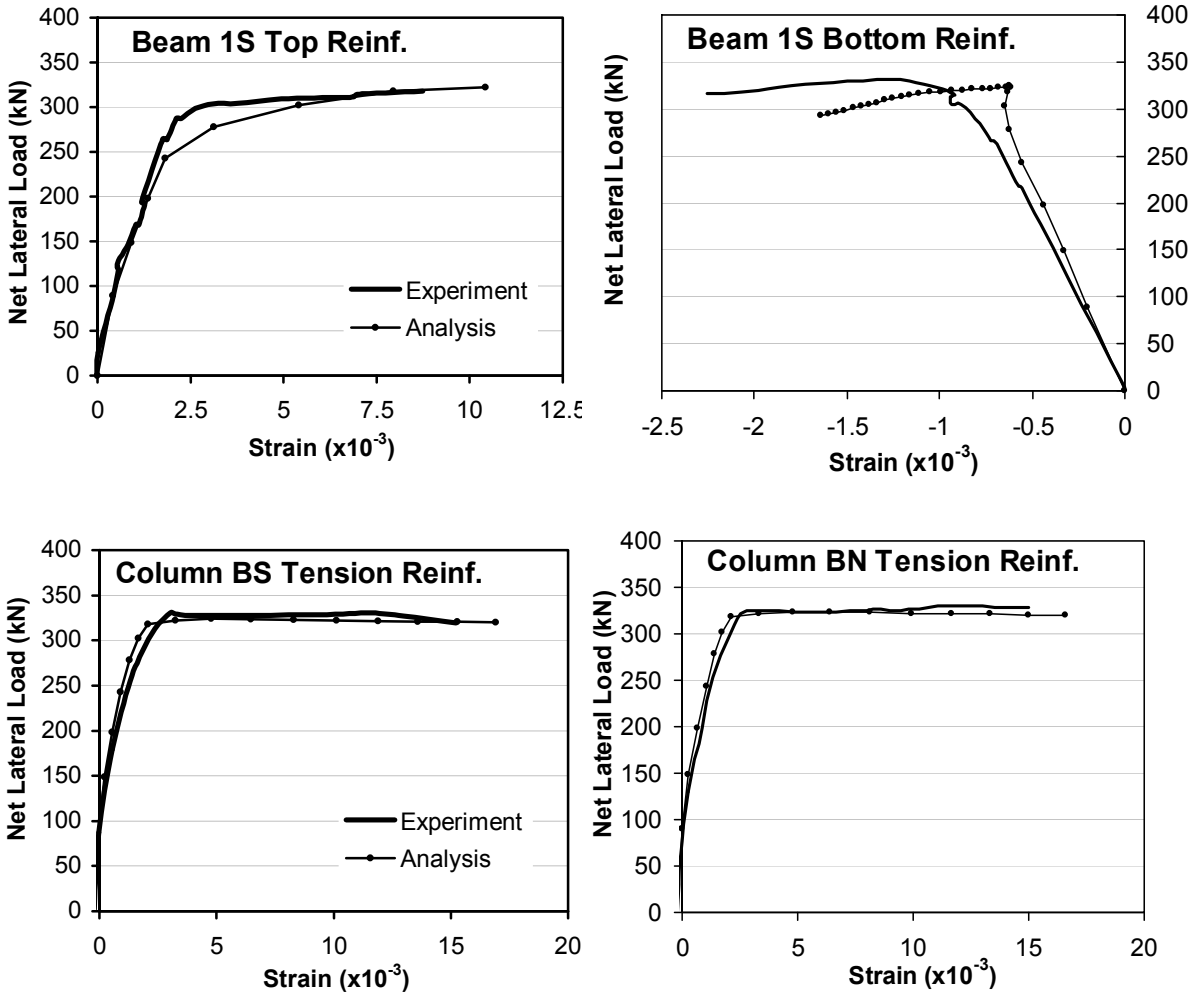


**Figure 4.23** Comparison of Reinforcement Strains for Vecchio and Emara Frame

Of particular interest in the behaviour of this frame is the influence of the second-order effects (i.e., P-Δ effects), which accounted for 12% of the total overturning moment acting on this frame at ultimate. To investigate the second-order influences on the analytical behaviour, the same analysis was repeated without considering geometric nonlinearity. In other words, the initial frame geometry and loading was considered throughout this analysis based on small displacements assumption. As shown in Figure 4.24, the net lateral load continued increasing with the increased lateral displacement, causing an overestimation of the frame's strength.

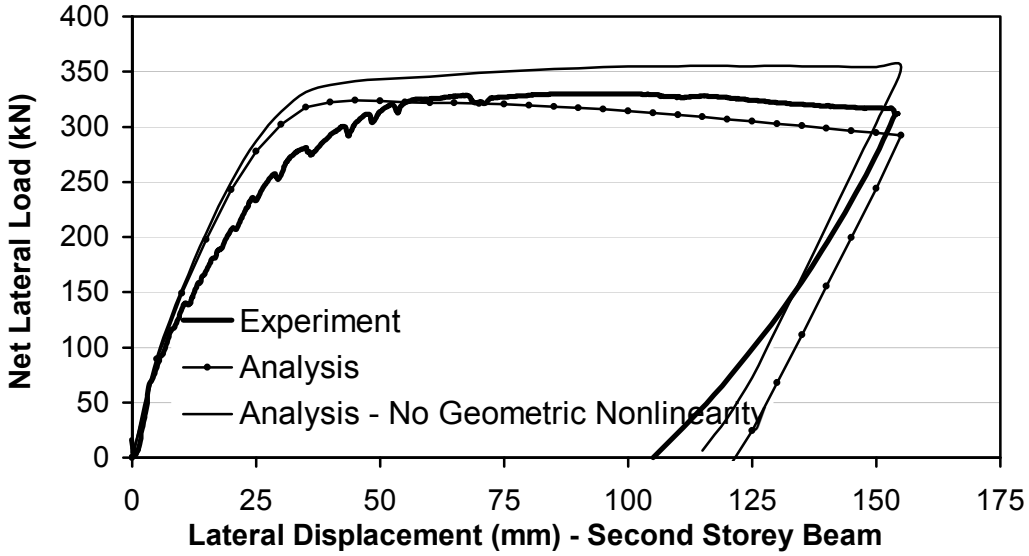


**Figure 4.24** Influence of Geometric Nonlinearity on Load-Deflection Responses for Vecchio and Emara Frame

## 4.8 Duong Frame

An experimental program was carried out at the University of Toronto to investigate the behaviour of shear-critical reinforced concrete frames under seismic loading conditions and to corroborate analytical procedures (Duong et al., 2007). The experiment involved testing of a one-bay, two-storey frame under increasing lateral load levels applied at the second storey beam. Two 420 kN axial column forces were applied to simulate the effects of loads coming from the storeys above the second floor.

The experiment consisted of two phases. In Phase A, the frame was laterally loaded until significant damage took place in the shear-critical beams and then was unloaded completely. The frame was then loaded in the reverse direction to the same displacement attained in the forward cycle. The frame was finally unloaded. In Phase B testing, the damaged frame was repaired and then tested under reversed cyclic loading conditions.

Details of the frame, material properties and loading conditions were described in Section 2.3.6, where this frame was analyzed by several other software programs and by hand calculation procedures. More details regarding this experiment can be found in Duong (2006).

### 4.8.1 Analytical Modelling

The beams and columns are divided into a number of segments to generate the frame model of the structure (see Figure 4.25(a)). The segment lengths were selected to be approximately half of the cross section depth of 400 mm.

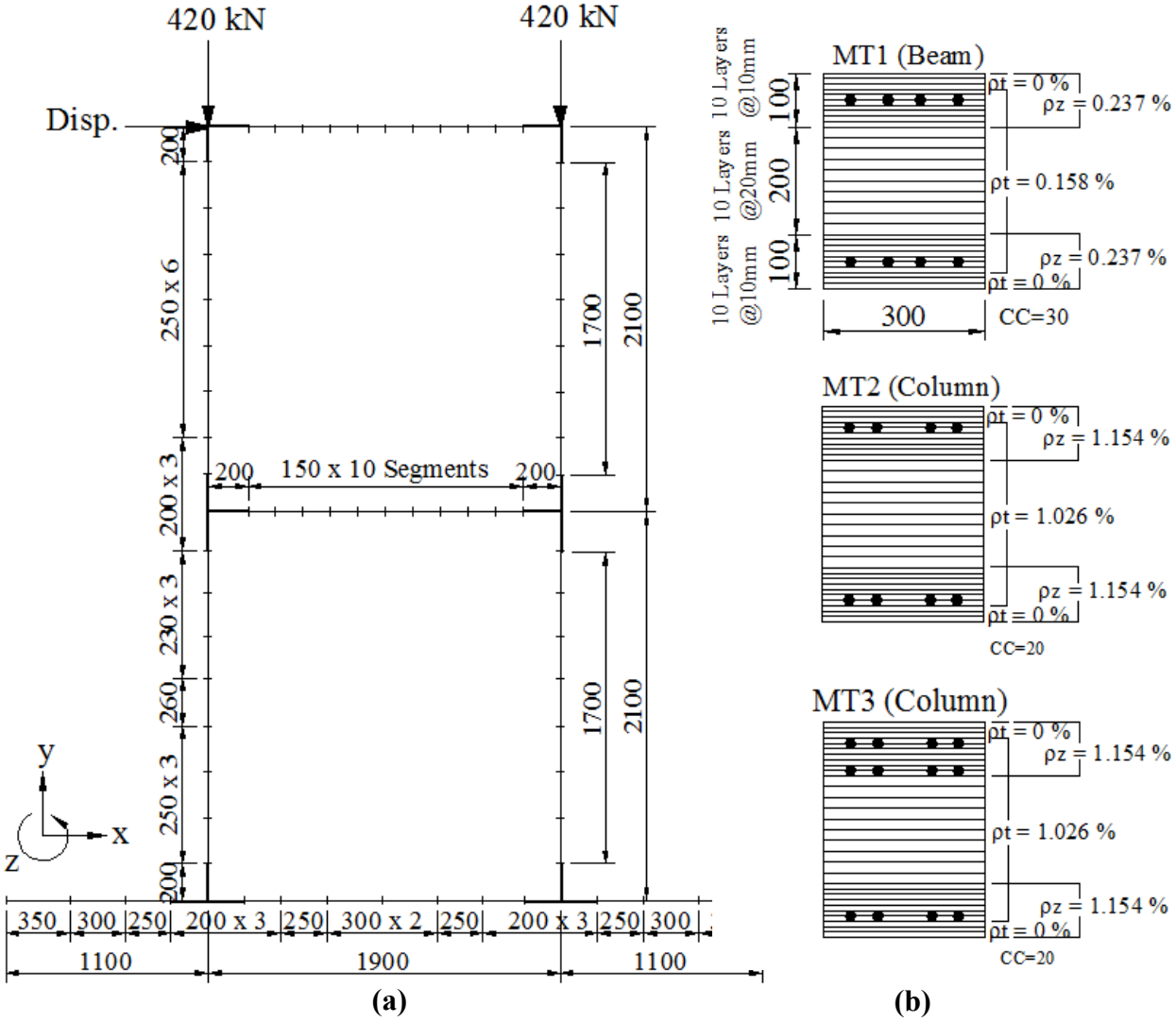


**Figure 4.25 (a)** Analytical Model of Duong Frame**; (b)** Sectional Models for Member Types MT1, MT2 and MT3 of Duong Frame

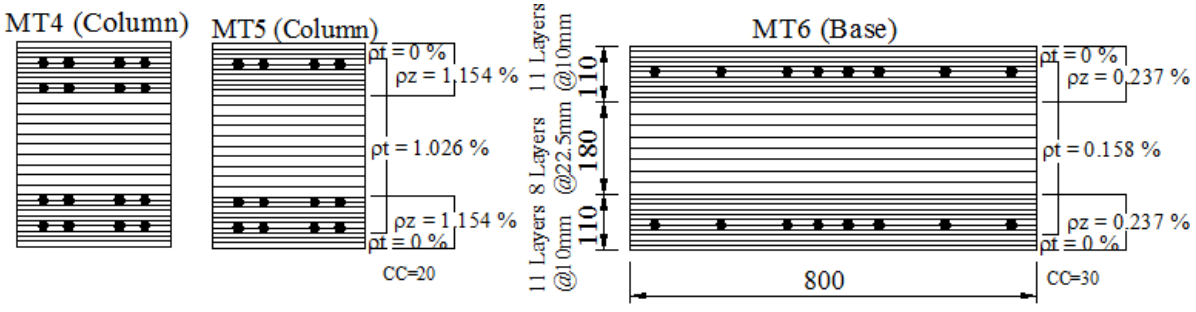


**Figure 4.26** Sectional Models for Member Types MT4, MT5 and MT6 of Duong Frame

Six member types were used for the sectional models of the beam, column and base; these were MT1, MT2, MT3, MT4, MT5 and MT6 as shown in Figures 4.25(b) and 4.26. To represent the members within the beam-column joints of the frame, six additional member types were created (MT 7 to MT 12) by multiplying the reinforcement amounts of MT1 to MT6 by a factor of 2 (see Figure 4.27(a)). The concrete layers and smeared reinforcement ratios for the sectional models (member types) were determined in the manner explained in Section 4.5.2.

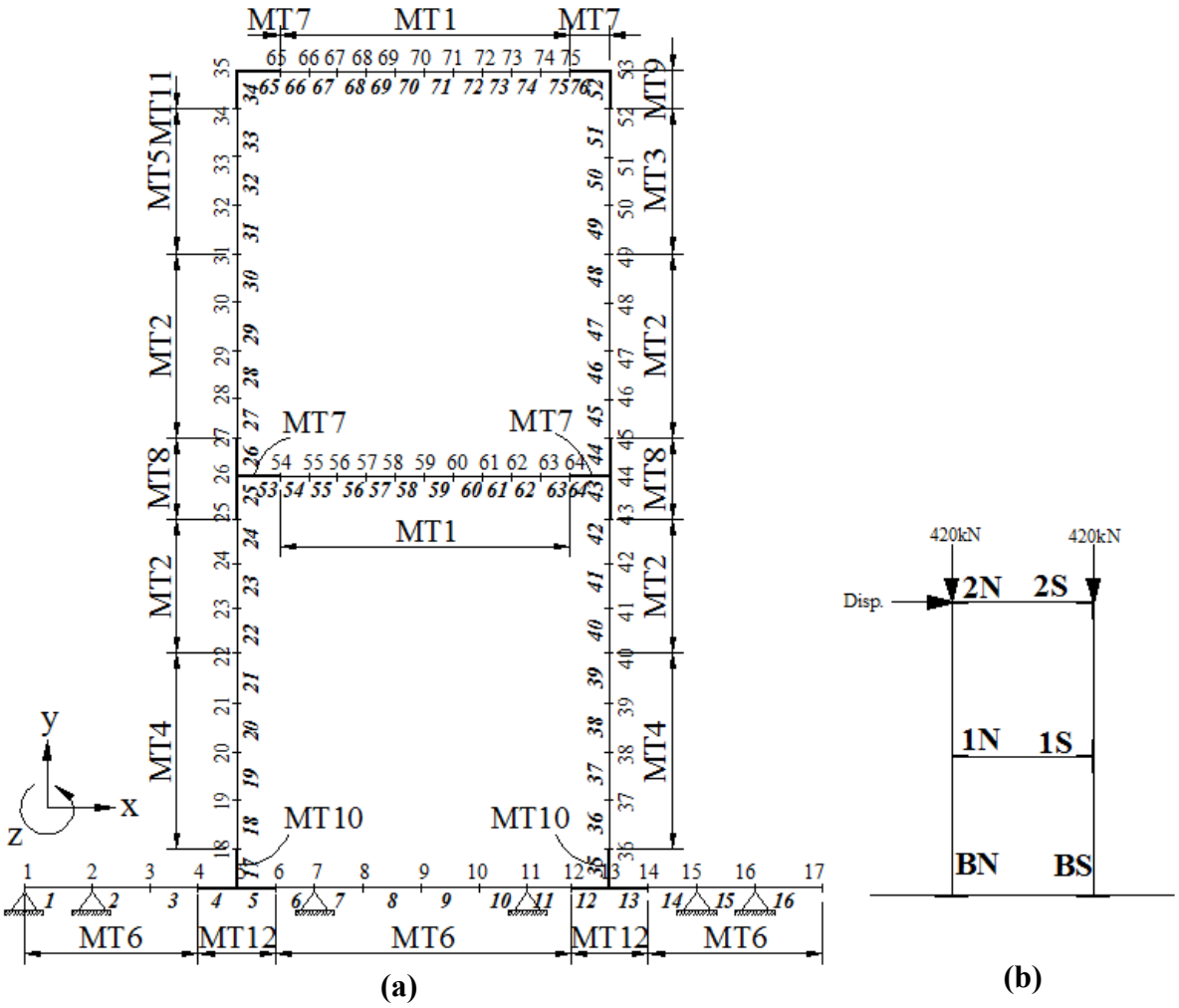


**Figure 4.27 (a)** Analytical Model Showing Member Types and Support Restraints of Duong Frame; **(b)** Name Convention Adopted

The bolts used in the experiment to fix the base beam to the strong floor were represented by restraining the x- and y-degrees of freedom of Nodes 1, 2, 7, 11, 15, and 16.

Default material models were used except for the concrete compression base curve for which the Popovics (NSC) formulation was selected as described in Section 4.2.

Two load cases were defined for the analysis. The first was with monotonically increasing displacement applied to Node 35 in the x-direction; the second was with the two constant column axial forces applied at the Nodes 35 and 53 in the y-direction. In the experimental study, the frame was unloaded once significant shear damage took place to prevent the total failure of the frame because Phase B of the test program was to be performed. However, because the determination of the total failure condition of the frame was desired in this study, the frame was loaded with increasing lateral displacement to failure. A reversed cyclic analysis of this frame, similar to the experiment, is presented in Section 6.4.

In the following discussion, similar to the convention adopted in Section 4.7.1, the naming convention shown in Figure 4.27(b) was used. Due to the shear protection algorithm used, some of the members were considered with a reduced shear force, thereby diverting the possible shear damage to adjacent members. As a result, the notations 1N and 1S refer to Member 55 and 62, respectively, when discussing the shear-related behaviour. Similarly 2N and 2S refer to Members 67 and 74, respectively. However, when flexure-related behaviour is discussed, 1N and 1S refer to Members 54 and 63; and 2N and 2N refer to Members 66 and 75, which will likely be critical in flexure. Similarly, BN and BS refer to Members 18 and 36 in flexure.

### 4.8.2 Comparison of the Analytical and Experimental Responses

The analytically and experimentally obtained applied net lateral load-second storey beam lateral deflection responses are compared in Figure 4.28.

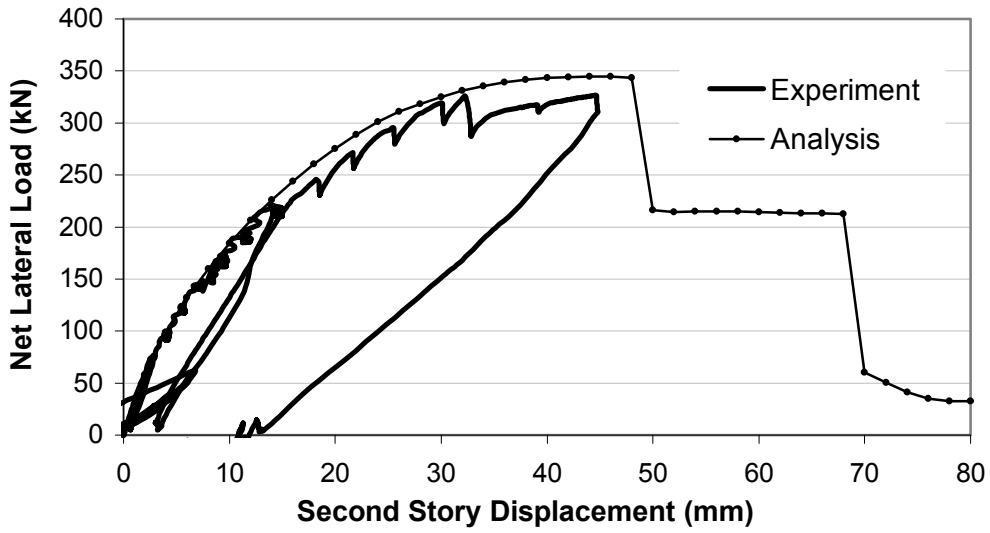


**Figure 4.28** Comparison of Load-Deflection Responses for Duong Frame

The frame's maximum load capacity was estimated with good accuracy, having a predicted-to-observed ratio of 1.06. In addition, the gradual decrease in the lateral stiffness was captured accurately.

For information purposes, the experimental lateral effective stiffness of the frame was calculated to be approximately 12 kN/mm. Similar to the Vecchio and Emara Frame, an effective stiffness value of 0.25 times the uncracked gross stiffness value of the frame was determined.

As shown in Table 4.15, the lateral load levels causing the first yielding of several reinforcement components were estimated reasonably. The predictions of the crack width also showed a strong correlation to the experimental crack widths.

**Table 4.15** Comparison of Analytical and Experimental Results for Duong Frame

| | Analysis | Test |
|---|---|---|
| **Column Shortening (mm)** (No Lateral Load) | 0.48 | 0.58 |
| Lateral Load (kN) causing **First Flexural Cracking** | 80 | 75 |
| Lateral Load (kN) causing **First Yielding of Reinf.** | | |
| 1S Longitudinal | 285 | 295 |
| 1N Longitudinal | 300 | 295 |
| 2S Longitudinal | 340 | 320 |
| 2N Longitudinal | never | 320 |
| | (reached 85% of yield) | |
| 1S Transverse | 285 | 320 |
| 2S Transverse | 340 | 327 |

| | Analysis | Test |
|---|---|---|
| **Crack Widths (mm)** for Lateral Load (kN) | 115 kN | 100 kN |
| Column NB | 0.05 | 0.05 |
| | 150 kN | |
| Beam 1N | 0.18 | 0.15 |
| Beam 1S | 0.18 | 0.15 |
| Column SB | 0.05 | Hairline |
| | 325 kN | |
| 1N Shear Crack Width (mm) | 2.2 | 4.0 |
| 1S Shear Crack Width (mm) | 2.8 | 1.6 |

The damage mode of the frame was experimentally classified as flexure-shear with significant shear damage of beam 1N accompanied by flexural mechanisms involving flexural cracking and reinforcement yielding. A similar failure mechanism was determined analytically. The first drop in the load capacity of the frame, at 48 mm displacement, was caused by the shear failure of beam 1S. As the top storey beam was intact, the frame continued carrying increased deformations until the shear failure of beam 2S, at 68 mm displacement, caused the second drop in Figure 4.29. After this, the only remaining load resisting mechanism was a cantilever column. The frame also showed significant flexural behaviour with flexural cracking and reinforcement yielding. The deflected shapes of the frame before and after the shear failures of the beams were presented in Figure 3.41 and 3.42.

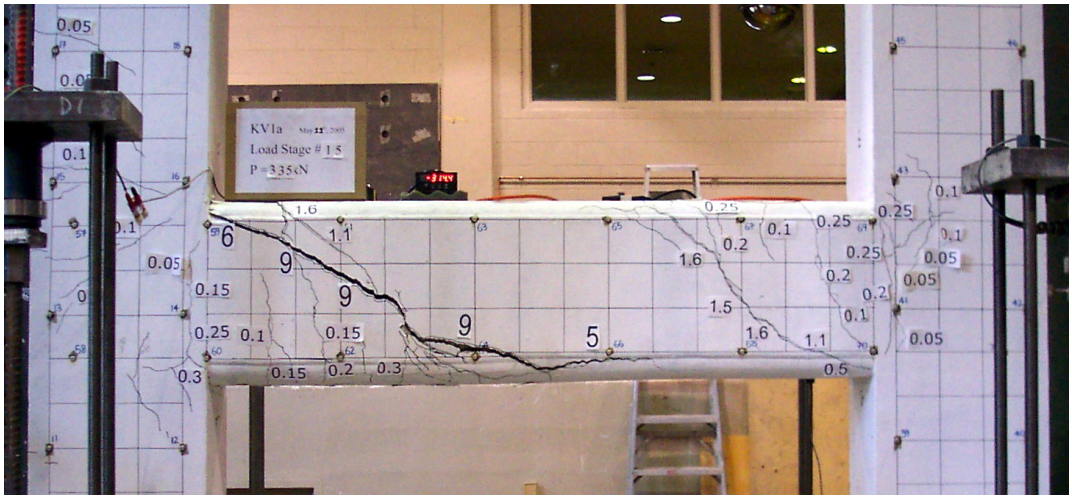


**Figure 4.29** Condition of the First Storey Beam at a Lateral Deflection of 44mm for Duong et al. Frame (Duong, 2006)

Additional comparisons of the analytical and experimental responses of this frame, in terms of reinforcement strains and column and beam axial deformations, are given in Section 6.4 where this frame was analyzed for the reverse half-cycle.

## 4.9 Vecchio and Balopoulou Frame

An experimental investigation was performed at the University of Toronto to study the factors contributing to the nonlinear behaviour of frame structures under short-term loading conditions (Vecchio and Balopoulou, 1990). The factors investigated included second-order mechanisms such as material nonlinearities, geometric nonlinearities, concrete shrinkage effects, and shear deformations. The experiment involved testing of a one-bay, two-storey frame under increasing load levels applied to the midspan of the first storey beam. Significant shrinkage strains were also reported for this frame.

*Details of Frame and Test Setup*

The test frame was constructed with a centre-to-centre span of 3500 mm, a storey height of 2000 mm and an overall height of 4600 mm (Figure 4.30). All beams and columns were 300 mm wide and 400 mm deep, while the base was 800 mm wide and 400 mm deep. The first storey beam top reinforcement was cut back to two No.20 bars in the central 500 mm length of the first storey beam. The frame was built integral with a large, heavily reinforced concrete base, bolted to the laboratory strong-floor, to create an essentially fixed base. The material properties were determined through concrete cylinder and steel coupon tests and are summarized in Table 4.16.

**Table 4.16** Material Properties of Vecchio and Balopoulou Frame

| | Reinforcement | | | | | | | Concrete | | |
|---|---|---|---|---|---|---|---|---|---|---|
| | $d_b$ (mm) | $f_y$ (MPa) | $f_u$ (MPa) | $E_s$ (MPa) | $E_{sh}$ (MPa) | $\varepsilon_{sh}$ (x $10^{-3}$) | $\varepsilon_u$ (x $10^{-3}$) | $f'_c$ (MPa) | $\varepsilon_0$ (x $10^{-3}$) | $E_c$ (MPa) |
| **No.20** | 19.5 | 418 | 596 | 192600 | 3100 | 9.25 | 66 | 29 | 2.15 | 22400 |
| **No.10** | 11.3 | 454 | 640 | 200000* | 4000* | 5* | 72* | | | |

* estimated

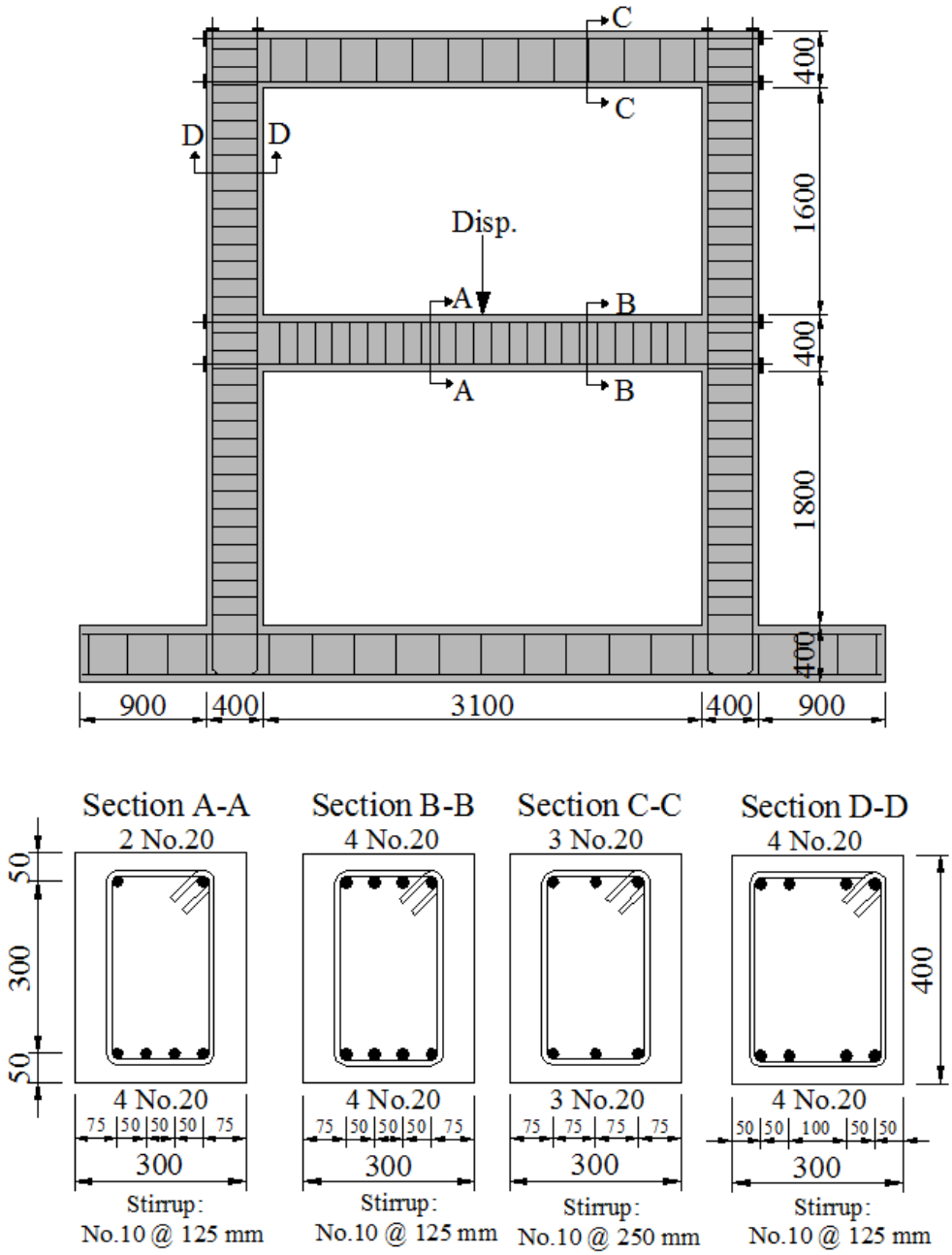


**Figure 4.30** Structural Details of Vecchio and Balopoulou Frame

The testing of the frame involved a simple case of monotonically increasing point load applied to the midspan of the first storey beam in a displacement-controlled mode.

Additional details regarding this experiment can be found in Balopoulou (1988).

### 4.9.1 Analytical Modelling

Taking advantage of the symmetry of the test setup, only one half of the frame was modelled. The beams and columns were divided into segments with lengths in the range of half of the cross section depth of 400 mm (Figure 4.31(a)).

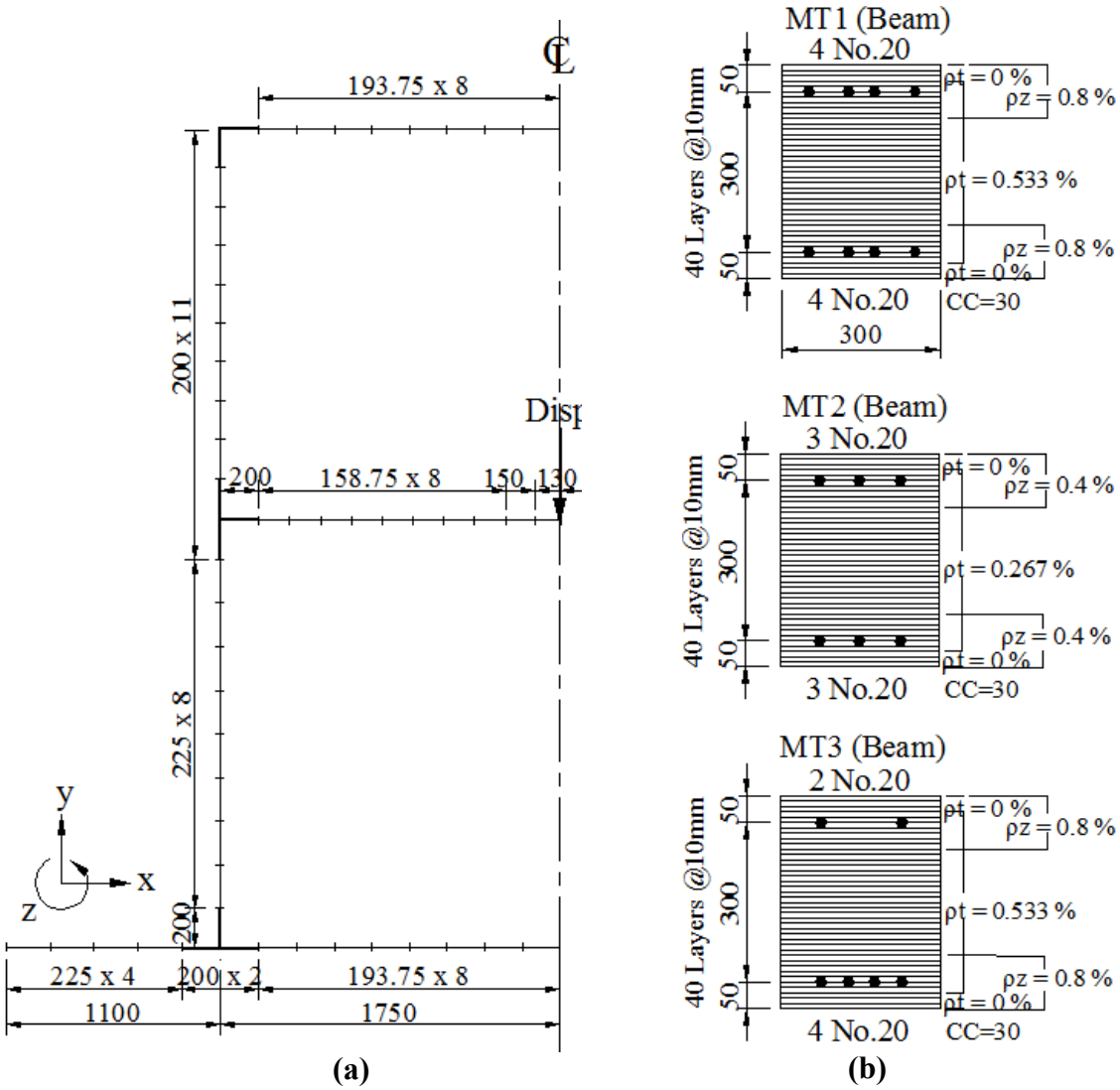


**Figure 4.31 (a)** Analytical Model Showing Segment Lengths and Loading for Vecchio and Balopoulou Frame; **(b)** Sectional Models for the Member Types 1, 2 and 3

Four member types were used for the sectional models of the beams, columns and base: MT1, MT2, MT3 and MT4 (see Figure 4.32(a)). To create the members within the beam-column joints of the frame, three additional member types were defined (MT5, MT6 and MT7) by multiplying the reinforcement amounts of MT1, MT2 and MT3 by a factor of 2.

The concrete layers and the smeared reinforcement ratios for the sectional models were determined in a way similar to that explained in Section 4.5.2 and shown in Figures 4.31(b) and 4.32(b).

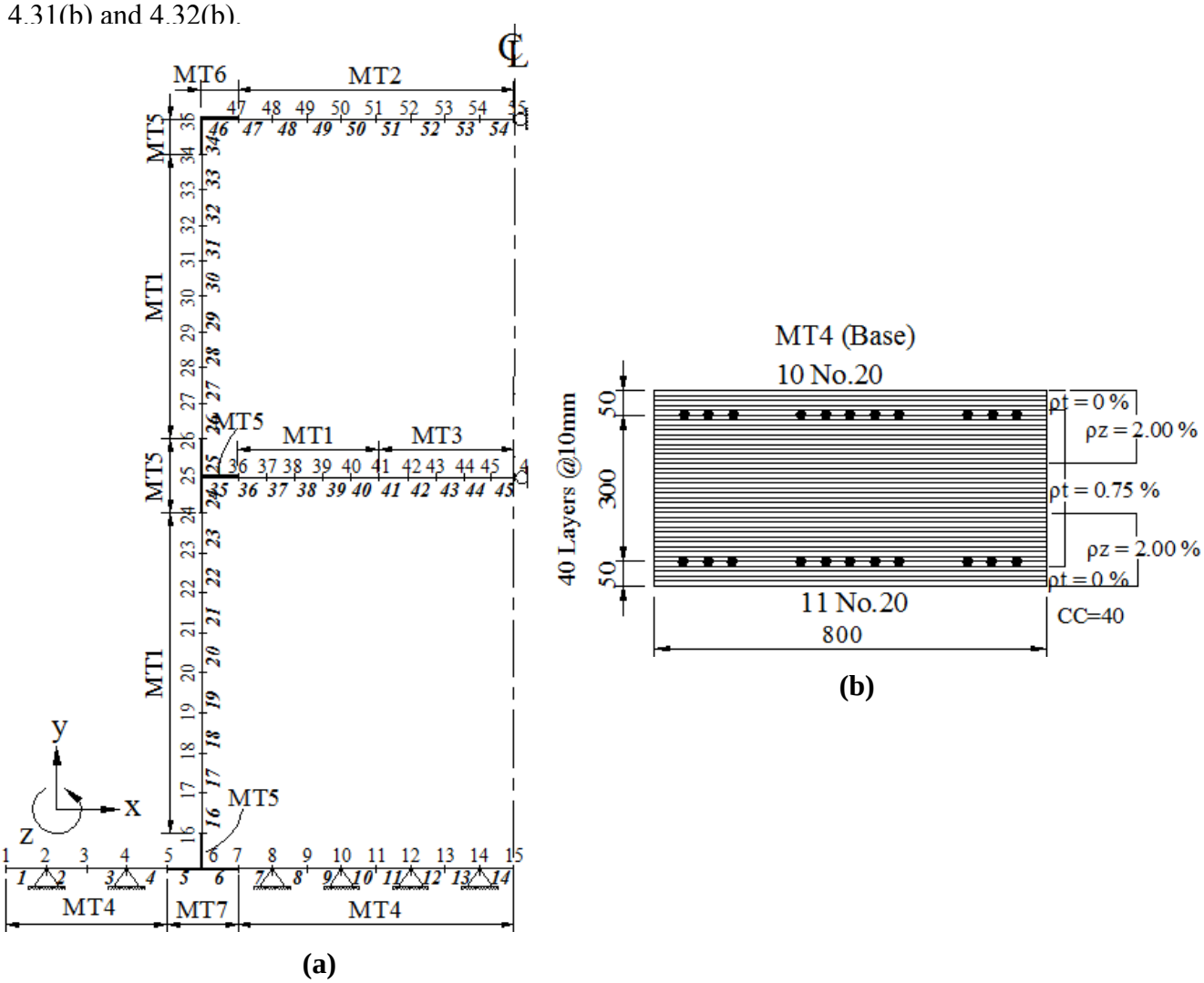


**Figure 4.32 (a)** Analytical Model Showing Member Types and Support Restraints for Vecchio and Balopoulou Frame; **(b)** Sectional Model of the Base

As for the support restraints, 6 pin supports were defined to represent the bolts that were used in the experiment to fix the base to the strong floor. Default material models were used except for the concrete base curve being the Popovics (NSC) formulation, as described in Section 4.2. Two load cases were defined in the analysis. The first was with monotonically increasing displacement applied to Node 46 in the y-direction; the second involved the concrete shrinkage strains. In the experimental study, it was estimated that

the shrinkage strains were in the range of -0.5 x $10^{-3}$. Consequently, a uniform shrinkage strain of -0.5 x $10^{-3}$ was applied to all members as the second load case.

### 4.9.2 Comparison of the Analytical and Experimental Responses

The analytically and experimentally obtained first storey midspan load-deflection responses are compared in Figure 4.33. Because the load-deflection response reported by Vecchio and Balopoulou (1990) was terminated before the failure of the frame, the load-stroke response for the complete test, as measured by the loading machine including the flexibility of the machine, was also compared to the analytical load-deflection response.

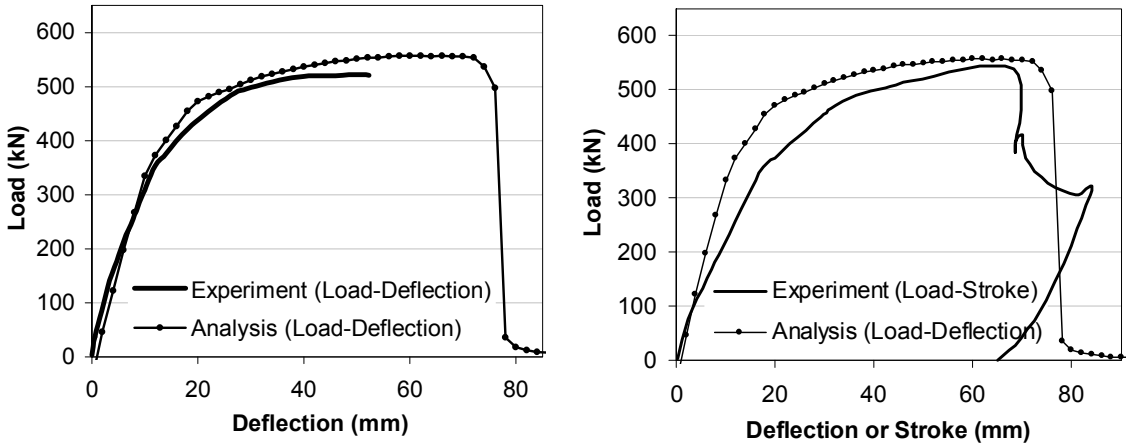


**Figure 4.33** Comparison of Responses for Vecchio and Balopoulou Frame

The analytical load-deflection response showed excellent agreement with the experimental response. The frame's strength, stiffness and failure deflection, which is particularly important when calculating the frame's ductility, were calculated accurately.

For information purposes, the experimental effective stiffness of the frame was calculated, using the secant stiffness of the load-deflection curve at the complete yielding point, to be approximately 6.5 kN/mm. Considering that the uncracked gross stiffness of the frame was approximately 25 kN/mm, an effective stiffness value of approximately 0.25 times the uncracked gross stiffness was found to be appropriate for this frame.

The maximum flexural crack widths were predicted with reasonable accuracy as indicated in Table 4.17.

The maximum flexural crack widths were predicted with reasonable accuracy as indicated in Table 4.17.

**Table 4.17** Comparison of Crack Widths for Vecchio and Balopoulou Frame

**Initial Shrinkage Crack Widths (mm)**

| | Analysis | Test |
|---|---|---|
| **Base** | 0.16 - 0.20 | 0.20 - 0.25 |
| **Column** | 0.10 - 0.11 | |
| **Beams** | 0.10 - 0.18 | |

**Crack Widths (mm) for P = 300 kN**

| | Analysis | Test |
|---|---|---|
| **Column** | 0.20 | 0.25 |
| **Beam** | 0.51 | 0.75 |

The experimental failure mode of the frame involved a combination of a flexural collapse mechanism (i.e., a three-hinge mechanism formed at the ends and the midspan of the first storey beam) and a shear failure near the midspan of the first storey beam. A similar failure mechanism was calculated analytically with the plastic hinges forming under somewhat larger applied loads as shown in Table 4.18.

**Table 4.18** Comparison of Hinging Loads for Vecchio and Balopoulou Frame

| | Applied Load (kN) for Beam-End Plastic Hinging |
|---|---|
| Analysis | 460 |
| Test | 370 |

| | Applied Load (kN) for Midspan Plastic Hinging |
|---|---|
| Analysis | 510 |
| Test | 430 |

The final failure of the frame in the analysis involved the shear failure of Member 44. When this failure occurred, the strain of the midspan tensile reinforcement ($50 \times 10^{-3}$) was close to the rupture strain of $66 \times 10^{-3}$. The reinforcement strain responses for the first storey beam are presented in Figure 4.34.

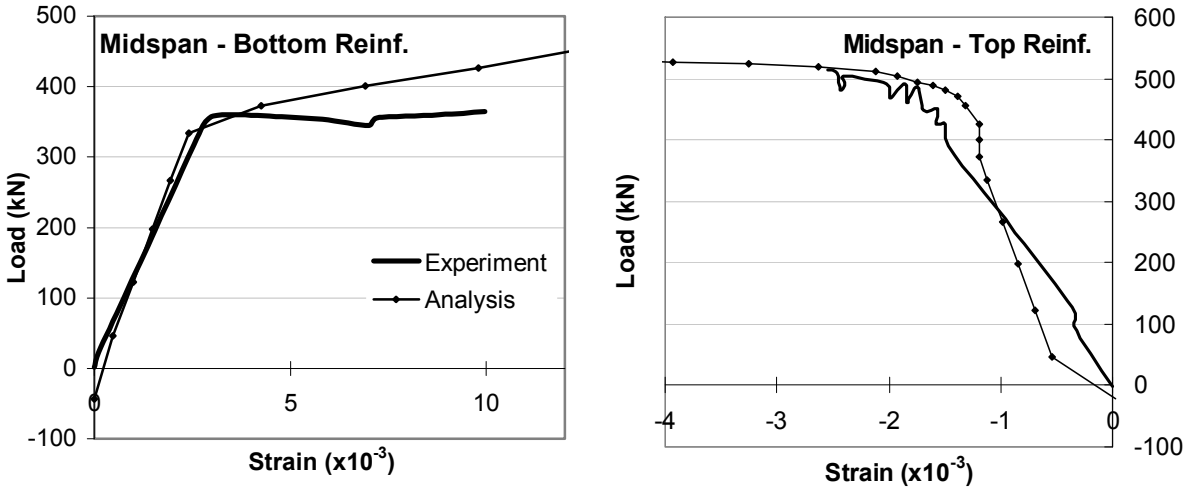


**Figure 4.34** Comparison of Reinforcement Responses for Vecchio and Balopoulou Frame

Of particular interest in the behaviour of this frame is the *membrane action mechanism*. As explained in Section 2.3.6.1, the first storey beam of the frame had a tendency to elongate due to the average tensile strains on the tension face being much larger than the compressive strains on the compression face. However, the columns acted as an axial restraint, thereby inducing axial force in the beam. The accurate determination of this axial force is essential for accurate simulation of the frame behaviour, as the axial force can significantly increase the shear and flexural strength of the beam.

To show the significance of this effect, a plastic analysis of the frame was performed with a simple three-hinge mechanism assumed for the first storey beam (Figure 4.35). For $P_u$ = 380 kN, using a linear-elastic frame analysis, the axial force in the beam was determined as -12 kN, the shear force as 190 kN, and the bending moment at the midspan (Node 45) as 190 kNm. A nonlinear sectional analysis was then performed for the beam to calculate the shear and moment capacities for the midspan section as 220 kN and 186 kNm, respectively. Therefore, a flexural failure of the mid-span was predicted for $P_u$ = 380 kN, which is 30% less than the actual failure load of the frame. This underestimation of the failure load occurred due to the linear-elastic frame analysis performed, which calculated the axial compression force in the beam to be much less than the value determined experimentally. In addition, the failure mechanism was determined incorrectly to be a flexural failure of the midspan section; in fact, a shear failure was observed near the midspan.

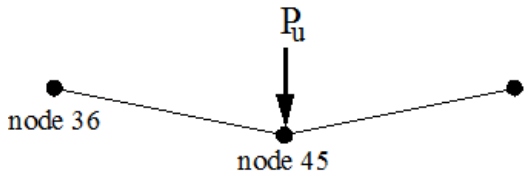


**Figure 4.35** A Simple Three-Hinge Mechanism for the First Storey Beam

As a result, nonlinear frame analysis procedures which incorporate the second-order effects such as membrane action are required for the accurate simulation of the frame behaviour. As experienced above, even if a nonlinear sectional analysis procedure is employed for the first storey beam of the frame, the use of linear-elastic frame analyses may lead to significant errors in the determination of the strength of a frame.

## 4.10 Clinker Preheat Tower

For the comparison of the developed analytical procedure to the previous procedure of TEMPEST, the clinker preheat tower introduced in Section 1.1.3 was reanalyzed using the newly developed program VecTor5. The details of the structure are given in Figure 1.1 and 1.2. The loading on the frame included monotonically increasing static storey shear forces, calculated using the linear dynamic response spectrum method, and the constant dead load of the structure as shown in Figure 4.36(a).

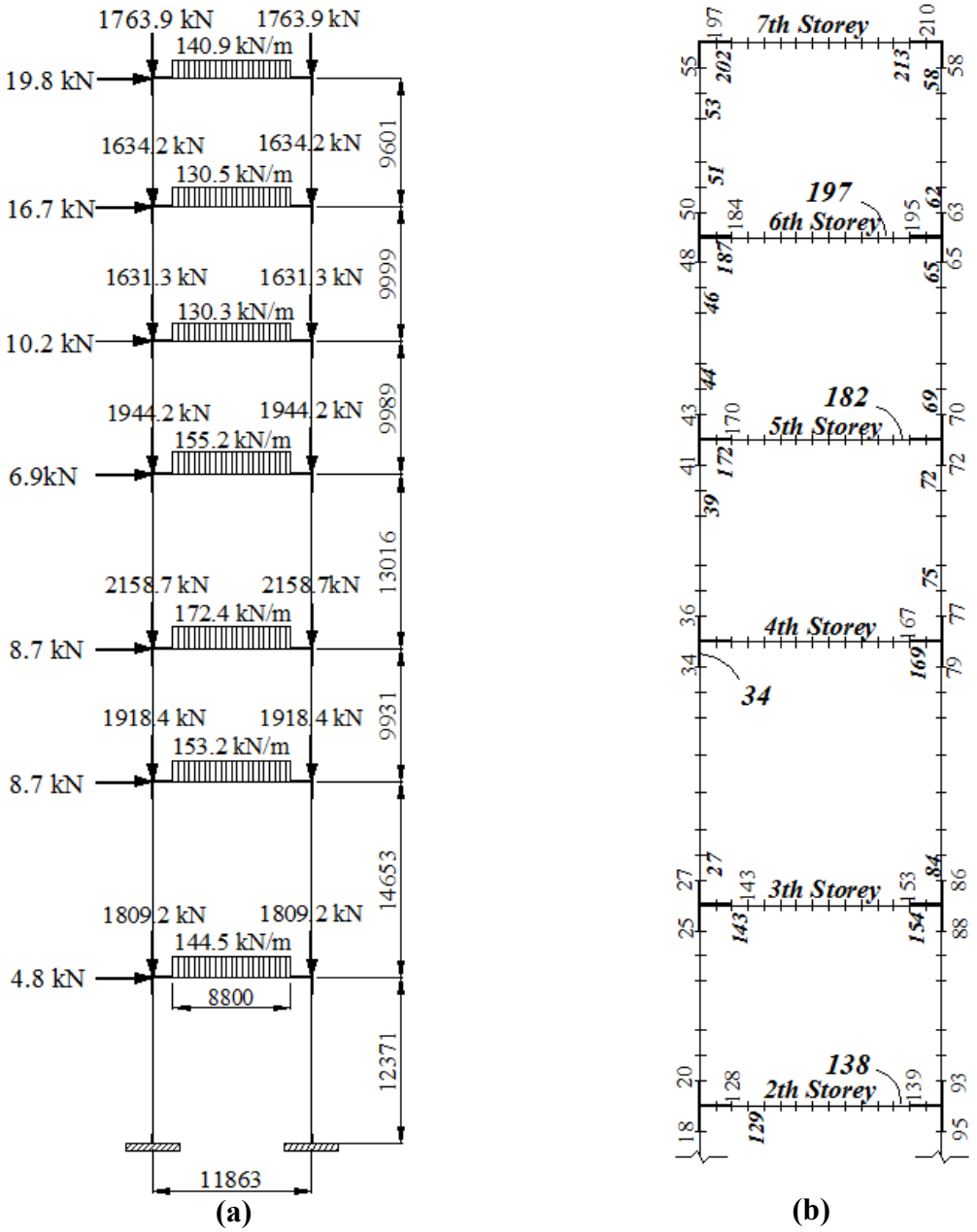


**Figure 4.36** Clinker Preheat Tower: **(a)** Loading; **(b)** Analytical Model

A part of the analytical model of the structure is shown in Figure 4.36(b), where the bold numbers refer to the members and the regular numbers to the nodes.

### 4.10.1 Comparison of Analytical Responses

The load deflection responses obtained are compared in Figure 4.37.

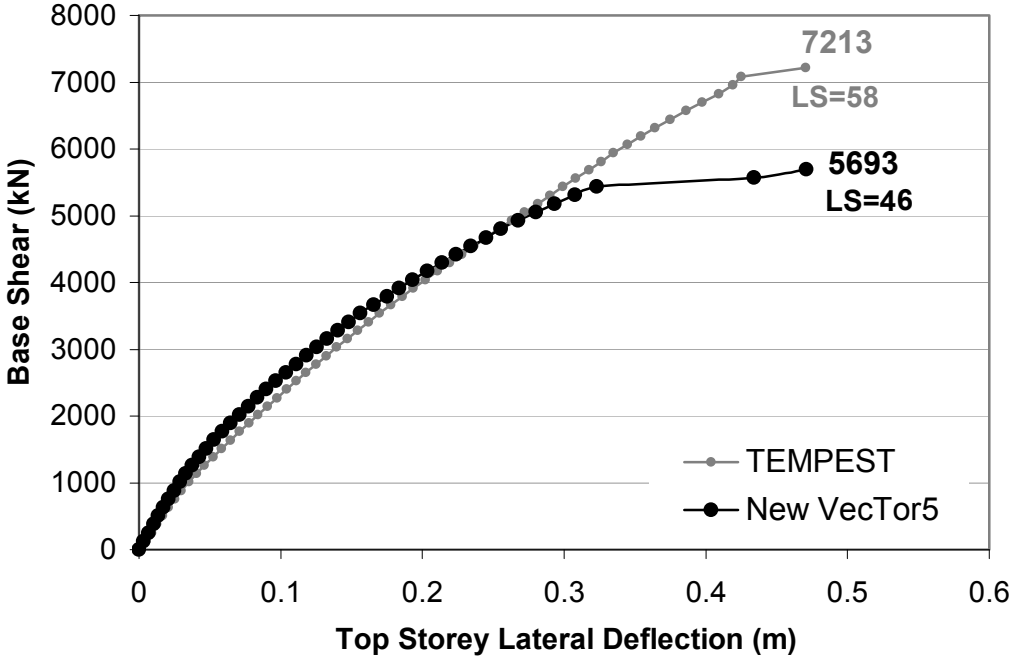


**Figure 4.37** Comparison of Load-Deflection Responses for Clinker Preheat Tower (Note: LS = Load Stage)

Both procedures predicted shear failures of some of the upper storey beams and identical displacements for the peak load capacity of the structure. The strength of the frame, however, was predicted differently. Performing 58 load stages before encountering a loss of stability of the structure, TEMPEST predicted 27% higher strength than did the new VecTor5 which achieved 46 load stages before stability loss. Detailed inspection of the output files revealed that towards the end of the analysis, large unbalanced forces were present in some of the members in the TEMPEST analysis. As an example, the comparisons of unbalanced forces are presented in Figure 4.38(a) for Member 34 and Figure 4.38(b) for Member 138, where the unacceptably large unbalanced forces are clearly visible especially for the last 8 load stages in the TEMPEST analysis.

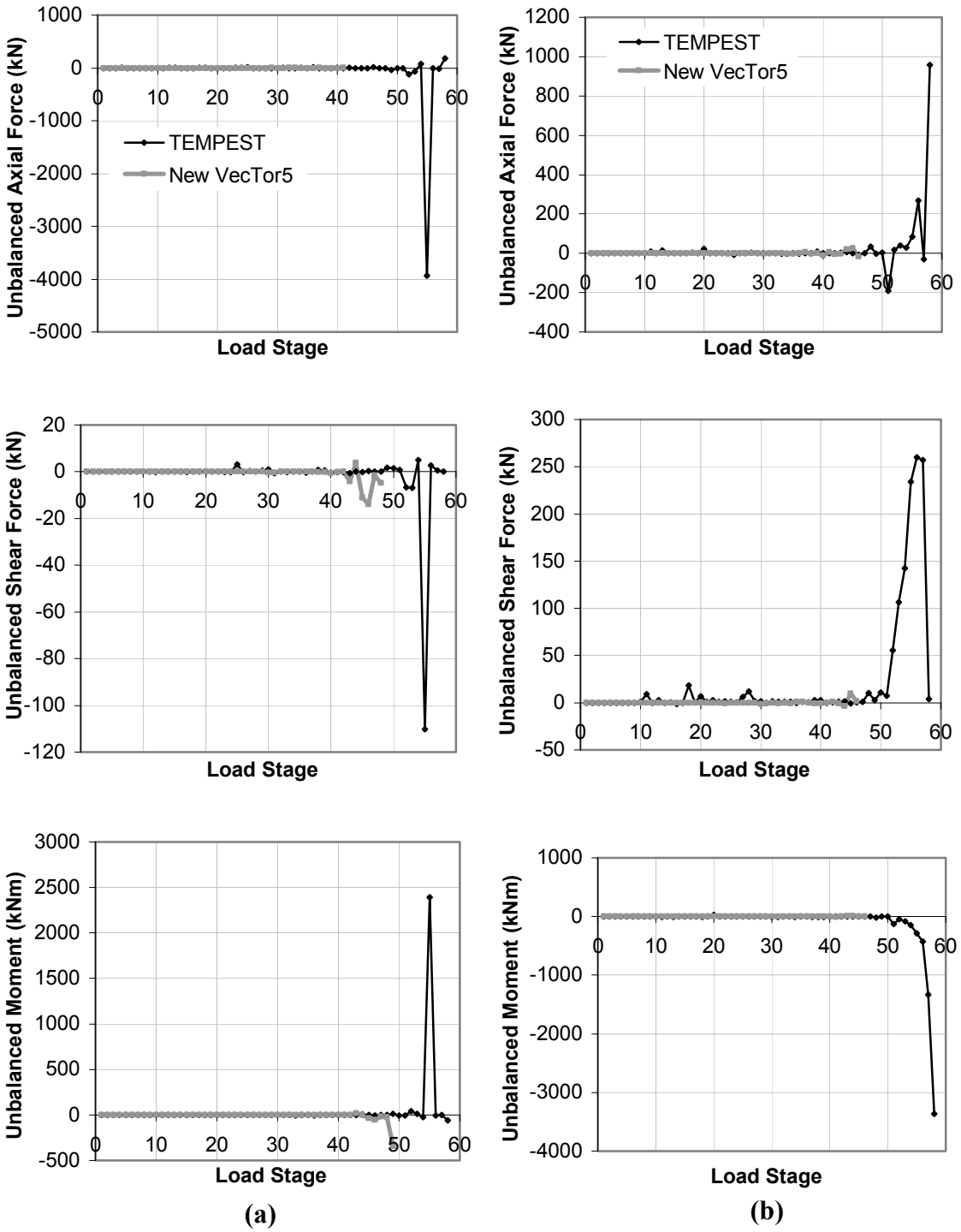


**Figure 4.38** Comparison of Unbalanced Forces as Predicted by TEMPEST and VecTor5 for Clinker Preheat Tower: **(a)** Member 34; **(b)** Member 138

Moreover, during the TEMPEST analysis, deteriorated convergence factors were noticed at some of the load stages (i.e., at the end of 100 global frame analysis iterations). As described in Section 3.9, a new load stage is started when the default convergence factor of 1.00001 is achieved or the default maximum number of iterations of 100 is reached in both procedures. A comparison of the convergence factors is presented in Figure 4.39.

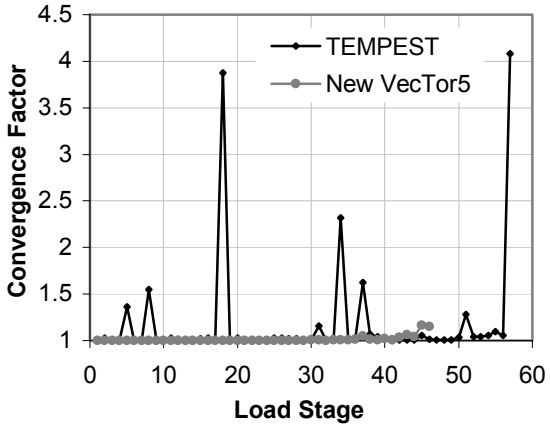


**Figure 4.39** Comparison of Convergence Factors at the End of Load Stages for Clinker Preheat Tower

Unacceptably high convergence factors reaching as high as 4.0 during the early stages of the TEMPEST analysis are clearly visible in Figure 4.39.

In the new VecTor5 analysis, the failure of the frame was initiated by a shear failure in the fifth storey beam (Member 182 in Figure 4.36(b)), followed by a shear failure of the sixth storey beam (Member 197) as shown in Figure 4.40. Finally, the shear failure of the seventh storey beam resulted in the complete loss of stability of the structure, thereby indicating a total failure condition (i.e., the collapse of the structure). Because the tower is an existing structure built in El Salvador, Central America, in the late 1990s, the experimental failure mechanism is not available for comparison purposes.

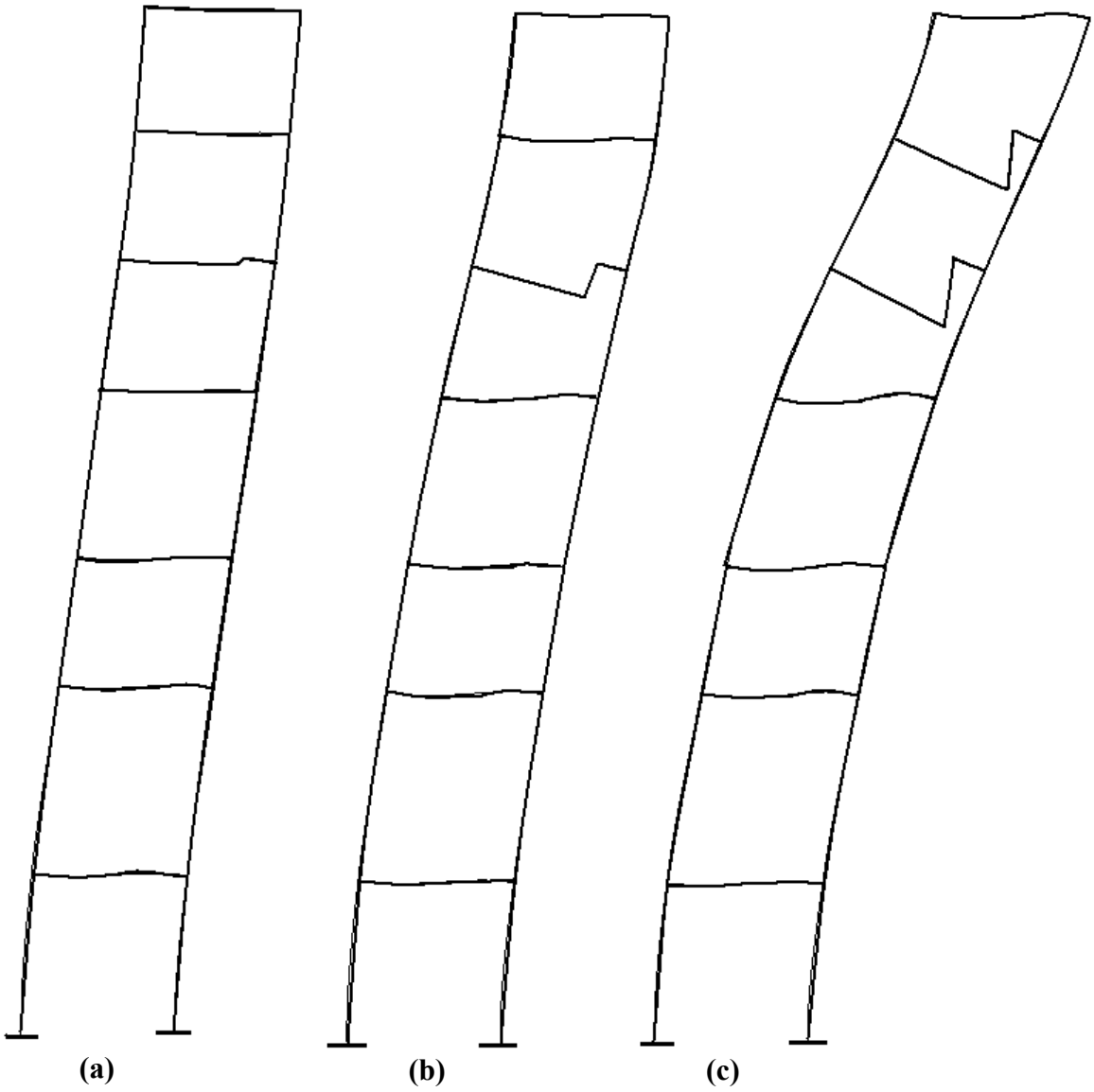


**Figure 4.40** Failure Stages of the Clinker Preheat Tower as Predicted by VecTor5: **(a)** Load Stage 44; **(b)** Load Stage 45; **(c)** Load Stage 47

Sudden shear failures were initiated by the newly implemented shear failure check algorithm, which detected large unbalanced shear forces present at the end of some of the load stages ($100^{th}$ global frame analysis iteration). As an example, the comparison of the unbalanced forces and acting forces for Member 182, which was the first member to fail, are presented in Figure 4.41, where it is clear that the shear capacity of Member 182 is exceeded around load stage 40.

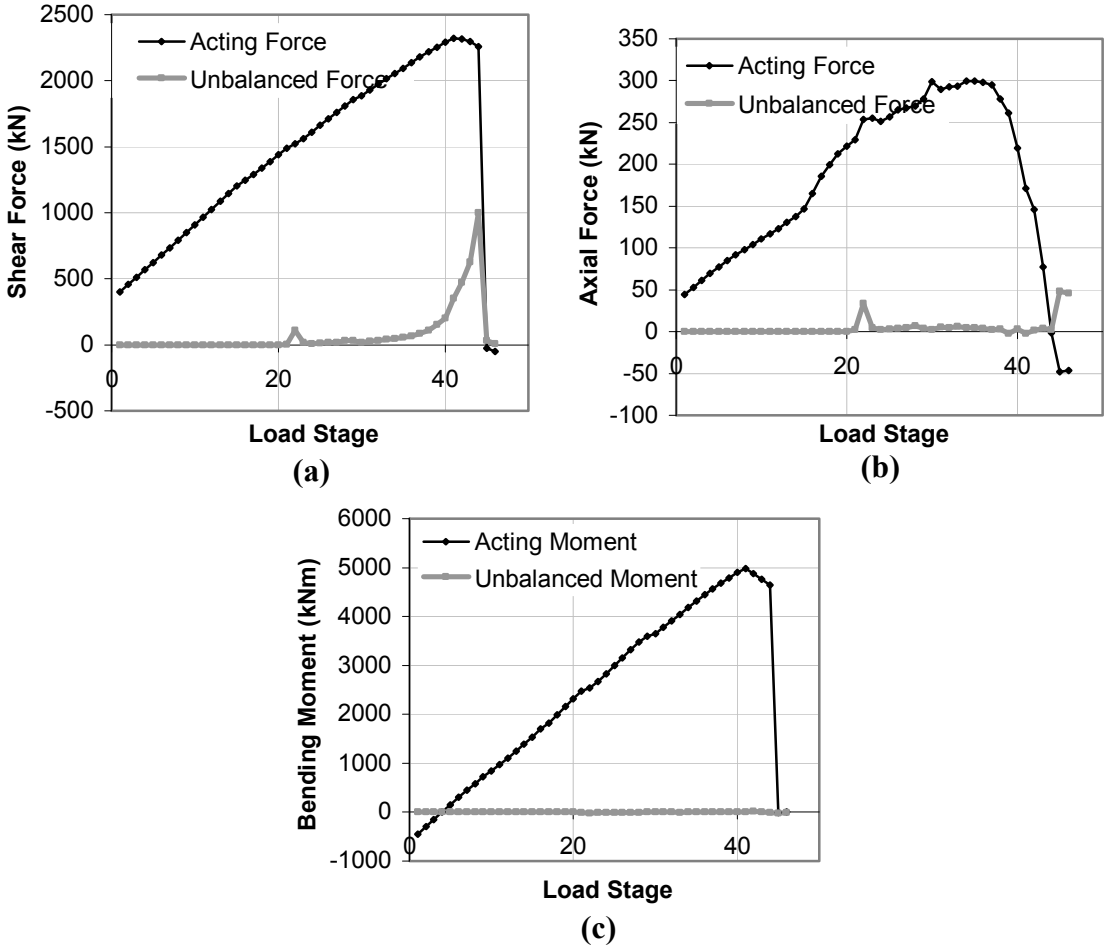


**Figure 4.41** Forces for Member 182 of the Clinker Preheat Tower as Predicted by VecTor5: **(a)** Shear Force; **(b)** Axial Force; **(c)** Bending Moment

In conclusion, the newly developed analytical procedure provided a more conservative estimate of the strength of the frame as compared to the previous procedure of TEMPEST. Throughout the analyses using the new VecTor5, excellent convergence factors and negligible unbalanced forces were realized, which supported the validity of the calculated load-deflection response.

## 4.11 Lefas Shear Walls

Two sets of large-scale shear walls were tested to failure by Lefas et al. (1990), under the combined action of constant axial loads and monotonically increasing horizontal loads, to investigate the effects of a number of parameters on wall behaviour. These parameters included the height-to-width ratio, the axial load, the concrete strength and the amount of

wall horizontal reinforcement. Two height-to-width ratios were used for the walls: 1.0 for Type I walls and 2.0 for Type II walls.

As discussed in Section 4.11.2, elements with shear span-to-depth ratios greater than 2.0 are suitable for analysis with sectional procedures because direct strut mechanisms become significant at ratios less than 2.0 to 2.5 (Collins and Mitchell, 1991). For this reason, the Type II walls were considered in the following analytical study.

All six Type II walls consisted of a 650 mm wide and 65 mm thick cross section extending vertically 1300 mm between the two beams which were monotonically connected to the walls (Figure 4.42(a)). The wall sections typically included concealed columns at each side. The reinforcement ratios reported are summarized in Figure 4.42(b), where the transverse reinforcement ratios $\rho_t$ were calculated considering the gross sectional area of the wall, and the out-of-plane reinforcement ratios $\rho_z$ were determined considering the gross sectional area of the concealed columns. The vertical and horizontal reinforcement consisted of high-tensile deformed steel of 8 and 6.25 mm diameters with the properties summarized in Table 4.19.

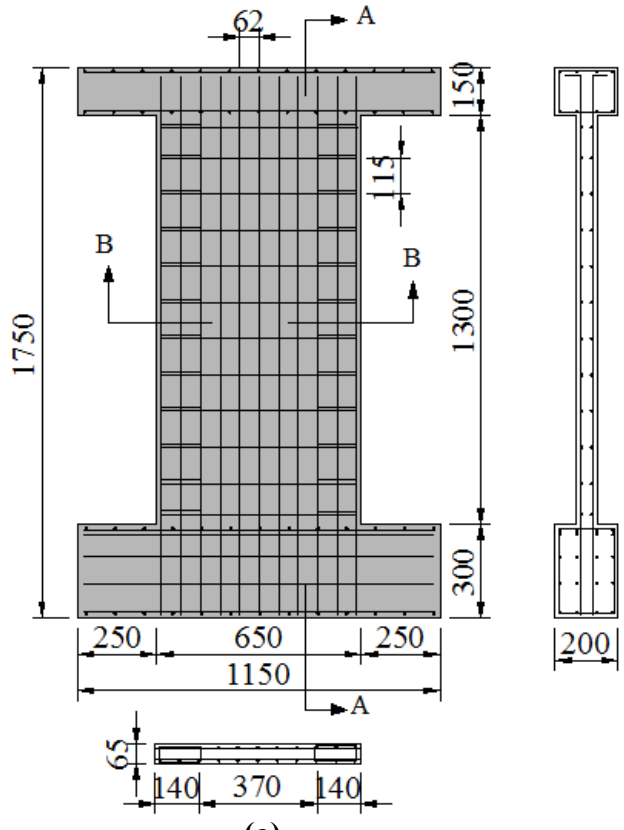


(a)

| | $\rho_t$ (%) | $\rho_z$ (%) | N (kN) |
|---|---|---|---|
| **SW21** | 0.8 | 0.9 | 0 |
| **SW22** | 0.8 | 0.9 | 182 |
| **SW23** | 0.8 | 0.9 | 343 |
| **SW24** | 0.8 | 0.9 | 0 |
| **SW25** | 0.8 | 0.9 | 325 |
| **SW26** | 0.4 | 0.9 | 0 |

**(b)**

**Figure 4.42 (a)** Structural Details of the Lefas Type II Walls; **(b)** Reinforcement Ratios

**Table 4.19** Material Properties of Lefas Type II Walls

| | Concrete | | | |
|---|---|---|---|---|
| | $f_{cc}$ (MPa) | $f'_c$ * (MPa) | $\varepsilon_0$ * ( x $10^{-3}$) | $E_c$ * (MPa) |
| **SW21** | 42.8 | 35.7 | 2.61 | 26710 |
| **SW22** | 50.6 | 42.2 | 2.13 | 28250 |
| **SW23** | 47.8 | 39.8 | 2.10 | 27850 |
| **SW24** | 48.3 | 40.3 | 2.10 | 28000 |
| **SW25** | 45.0 | 37.5 | 2.06 | 27230 |
| **SW26** | 30.1 | 25.1 | 1.90 | 23500 |

| | Reinforcement | | | | | |
|---|---|---|---|---|---|---|
| | $d_b$ (mm) | $f_y$ (MPa) | $f_u$ (MPa) | $E_s$ (MPa) | $E_{sh}$ (MPa) | $\varepsilon_{sh}$ ( x $10^{-3}$) |
| **ø8** | 8 | 470 | 565 | 200000* | 2000* | 2.5* |
| **ø6.25** | 6.25 | 520 | 610 | 200000* | 2000* | 2.7* |

* estimated

The testing of the walls involved the application of a monotonically increasing lateral load and a constant axial load applied through the top beam (Figure 4.42(a)). Axial load values were varied from 0 to 325 kN as shown in Figure 4.42(b).

### 4.11.1 Analytical Modelling

The walls were modelled with varying lengths of segments. A segment length of 58.5 mm (approximately 10% of the wall width) was used towards the base of the walls, where a concentration of plastic deformation was expected. The segment lengths were gradually increased towards the top of the walls. The beam at the base of the walls was not modelled; rather, the walls were assumed to be fixed at the base (Figure 4.43(a)).

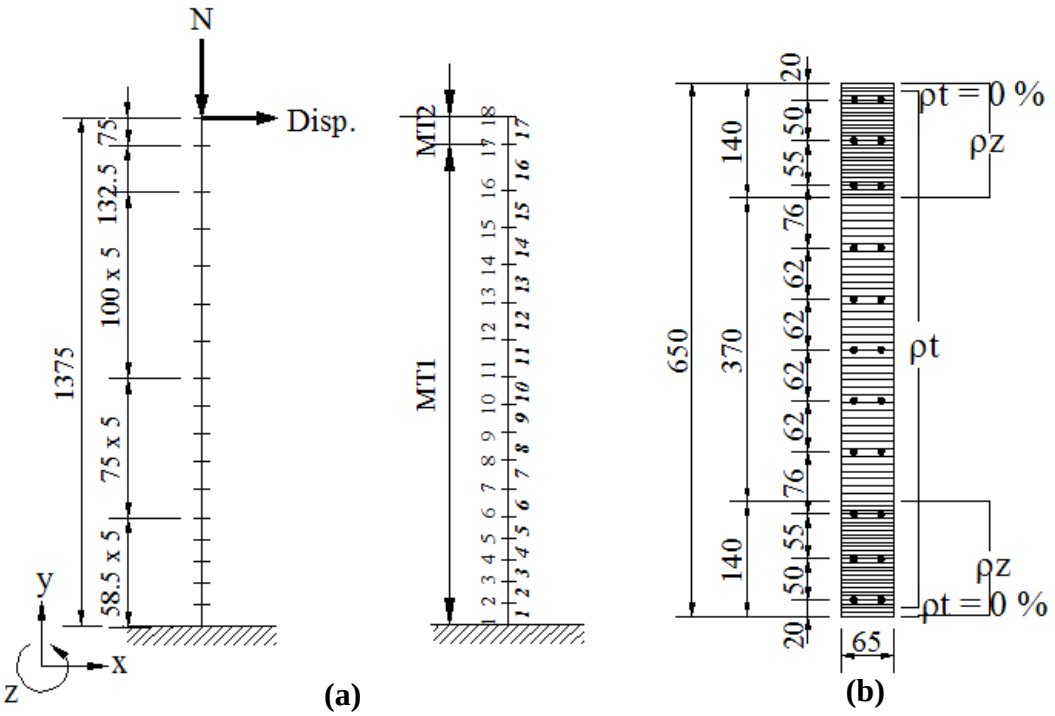


**Figure 4.43 (a)** Frame Model for Lefas Walls; **(b)** Sectional Model

One member type was used for the sectional model of the walls: MT1. To simulate the top loading beam, an artificial member type, MT2, was created by multiplying the reinforcement ratios of MT1 by a factor of 2. As the local conditions of the region through which the load is introduced was not particularly important in the sectional calculations, the top loading beam was modelled superficially.

The sectional model for MT1 is presented in Figure 4.43(b); 96 concrete layers were typically used (5.0 mm x 28 layers, 9.25 mm x 40 layers and, 5.0 mm x 28 layers). Out-of-plane reinforcement was assigned to the layers constituting the concealed columns, and transverse reinforcement was assigned to all layers except the 10 mm thick clear-cover layers as defined in Figure 4.43(b).

Default material models were used except for the concrete base curve for which the Popovics (NSC) formulation was adopted as described in Section 4.2. Because the only the cube strengths of the concrete, $f_{cc}$, were reported, the cylinder strengths were determined approximately as follows:

$$f_c' = f_{cc} / 1.20 \tag{4.3}$$

In addition, the modulus of elasticity of concrete $E_c$, and the strain $\varepsilon_o$ corresponding to the peak stress $f'_c$ were estimated based on Eq. 4.4 and 4.5 (Collins and Mitchell, 1991).

$$E_c = 3320 \times \sqrt{f_c'} + 6900 \ \ (MPa) \tag{4.4}$$

$$\varepsilon_o = \frac{f_c}{E_c} \times \frac{n}{n-1} \quad \text{where} \quad n = 0.8 + \frac{f_c'}{17} \tag{4.5}$$

The resulting values for all six different concrete types used are listed in Table 4.19

### 4.11.2 Comparison of the Analytical and Experimental Responses

The analytical and experimental lateral load- deflection responses are compared in Figure 4.44. It should be noted that as the tests were performed in a force-controlled mode, the following graphs and discussion consider the behaviour up to the peak load levels only. In other words, the post-peak responses of the walls are not considered.

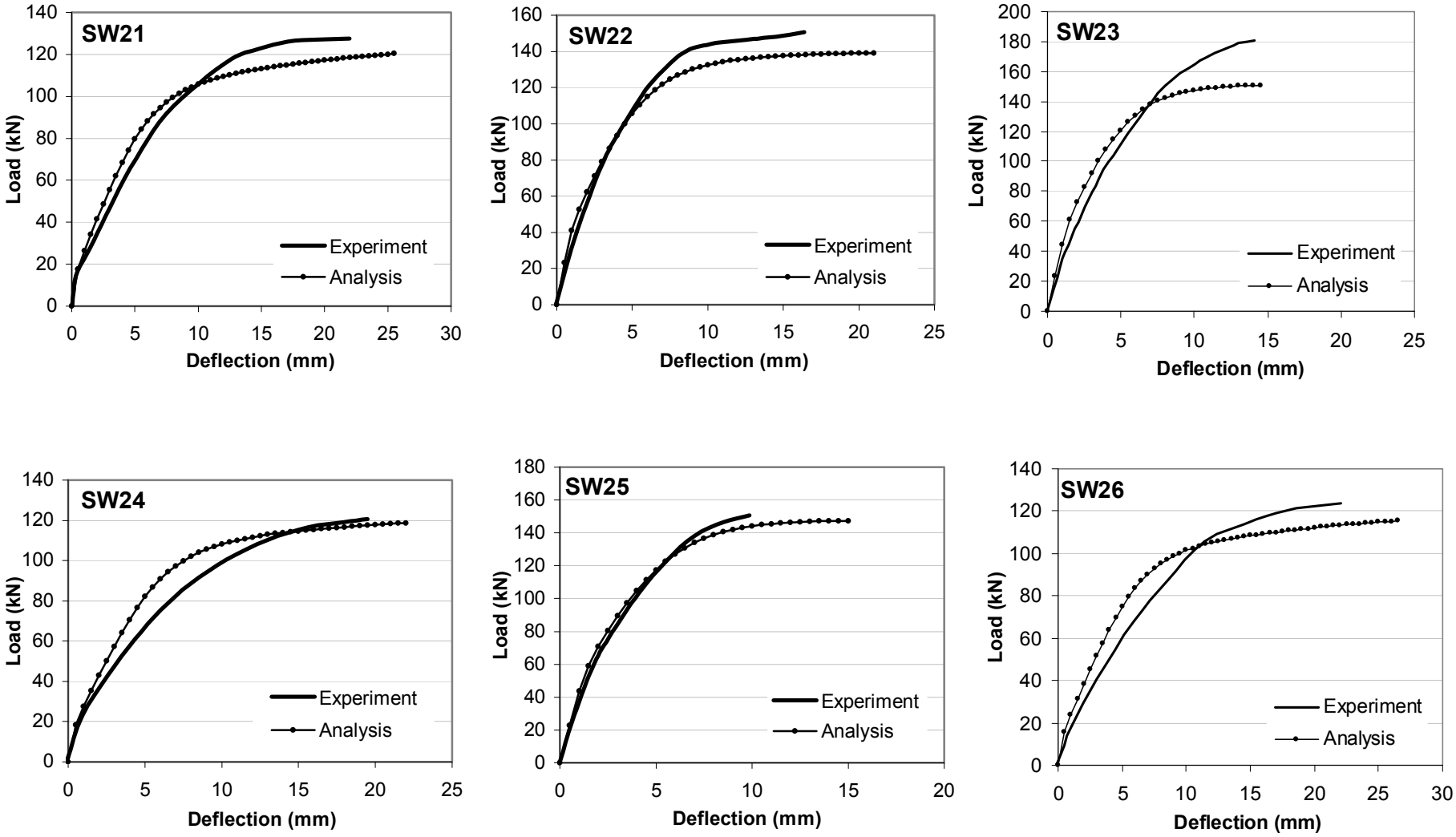


**Figure 4.44** Comparison of the Lateral Load-Displacement Responses for Lefas Walls

The analytical results, as shown in Figure 4.44, predicted the lateral stiffnesses of the walls reasonably well. The general tendency was to slightly underestimate the experimental deflections, thereby giving slightly stiffer responses. It should be noted that, in the experiment, strain penetration into the wall bases may have noticeably affected the lateral stiffnesses of the walls. In the analyses, the base beams were not included in the model; a fixed base assumption was made. Note that for the walls with constant axial forces (i.e., SW22, SW23 and SW25), the analytical underestimations of the deflections are minimal. This can be attributed to less strain penetration into the bases in these experiments, providing a base condition more similar to the analytical base condition.

The comparisons of several parameters, as obtained analytically and experimentally, are summarized in Table 4.20.

**Table 4.20** Comparison of Analytical and Experimental Results for Lefas Walls

| | Initiation of Cracking | | | First Long. Reinf. Yielding | | | Peak Load | | |
|---|---|---|---|---|---|---|---|---|---|
| | VecTor5 | Test | Ratio | VecTor5 | Test | Ratio | VecTor5 | Test | Ratio |
| **SW21** | 8.7 | 10 | 0.87 | 70 | 80 | 0.88 | 120.4 | 128 | 0.94 |
| **SW22** | 23.3 | 14 | 1.66 | 95 | 110 | 0.86 | 139 | 150 | 0.93 |
| **SW23** | 36.7 | 20 | 1.84 | 114 | 120 | 0.95 | 150.6 | 180 | 0.84 |
| **SW24** | 9.0 | 10 | 0.90 | 74 | 80 | 0.93 | 119 | 120 | 0.99 |
| **SW25** | 35.9 | 25 | 1.44 | 111.5 | 130 | 0.86 | 147.4 | 150 | 0.98 |
| **SW26** | 7.8 | 10 | 0.78 | 72 | 68 | 1.06 | 114.5 | 123 | 0.93 |
| | | **Mean** | **1.25** | | **Mean** | **0.92** | | **Mean** | **0.93** |
| | | **COV (%)** | **45.5** | | **COV (%)** | **7.7** | | **COV (%)** | **5.5** |

The strengths of the walls were predicted reasonably well with a mean of 0.93 and a coefficient of variation (COV) of 5.5% for the predicted-to-observed strength ratio. The slight underestimation of the strengths is likely associated with direct strut action in the walls being developed because the shear-span-to depth ratios were 2.0.

Beams with shear-span-to depth ratios less than about 2.5 carry load largely by direct strut action, as classified by D-regions in Section 3.11. The analyses of such members with sectional analysis procedures typically produce conservative results depending on the depth of the member. The smaller the shear span-to-depth ratio from the limiting value 2.5, the more conservative the sectional analysis predictions become. A detailed discussion of this behaviour can be found in Collins and Mitchell (1991). Consequently,

the strength predictions of the walls, analyzed here, with a shear-span-to depth ratio of 2.0, was understandably underestimated but surprisingly not by a significant degree.

The lateral loads causing the first yielding of the longitudinal reinforcement were predicted with a reasonable mean of 0.92 and a COV of 7.7%. The typical calculation of the first yielding at lower lateral load levels in the analytical study was most likely caused by the modelling of the base as perfectly fixed. In the experiment, a lower beam was utilized to create an essentially fixed base (see Figure 4.42(a)) and the longitudinal reinforcement of the walls extended into the base beams. Consequently, due to cracking of the wall bases and perhaps some bond slip, the longitudinal reinforcement could rationally yield at a greater lateral load level than the analyses estimated.

The lateral loads causing the first flexural cracking of the walls are also compared in Table 4.20 for information purposes only, as the methodology used in determining the experimental first cracking loads is not known. In the analytical predictions, first cracking was assumed to take place when the crack widths reached 0.05 mm, as it would be difficult to observe crack widths smaller than 0.05 mm in an experimental study. In addition, the experimentally determined crack widths are usually measured at discrete load stages; therefore, first cracking occurring between two load stages may not be noted during the experiments.

The experimental behaviour of the walls typically involved the following stages. In the earlier stages of the experiments, the bottom one-third of the walls, in the vertical plane, experienced horizontal flexural cracking. Under increasing lateral load levels, the cracks started to incline towards the compression toe of the walls. The final failures were caused by crushing of concrete in the compression toe of the walls, which was initiated by near vertical cracks reaching the base of the compression toe.

A similar flexure-dominated behaviour was obtained for all of the walls in the analytical study. The final failure modes of the walls were predicted to be caused by rupturing of the longitudinal reinforcement in the tension zone, rather than the crushing of the concrete in the compression zone. This can be associated with the assumed value of the

rupture strain of the longitudinal reinforcement. As the experimental rupture strains of the high-tensile reinforcement were not reported, a value of 50 x $10^{-3}$ was assumed in the analytical study. The use of larger rupture strains would increase the deformation levels, causing the crushing of concrete in the compression zone. However, in order to demonstrate the applicability of the procedure in practical situations involving several unknowns in the concrete and steel properties, these walls were analyzed with conservatively assumed material properties (i.e., weaker than actual) and default analysis options.

Of particular interest in the behaviour of these walls is the influence of shear-related mechanisms. In the analyses above, the shear protection algorithm was used, which reduced the shear forces and strains in the first 7 members, as indicated by the program output (i.e., within a distance 0.7 x h from the base). It was decided to investigate the influence of this reduction as well as the total contribution of the shear deformations to the behaviour of the walls. For this purpose, two additional analyses were performed: considering full shear effects without the use of the shear protection, and neglecting shear effects all together. As two typical examples, the load-deflection curves obtained for SW24 and SW25 are shown below.

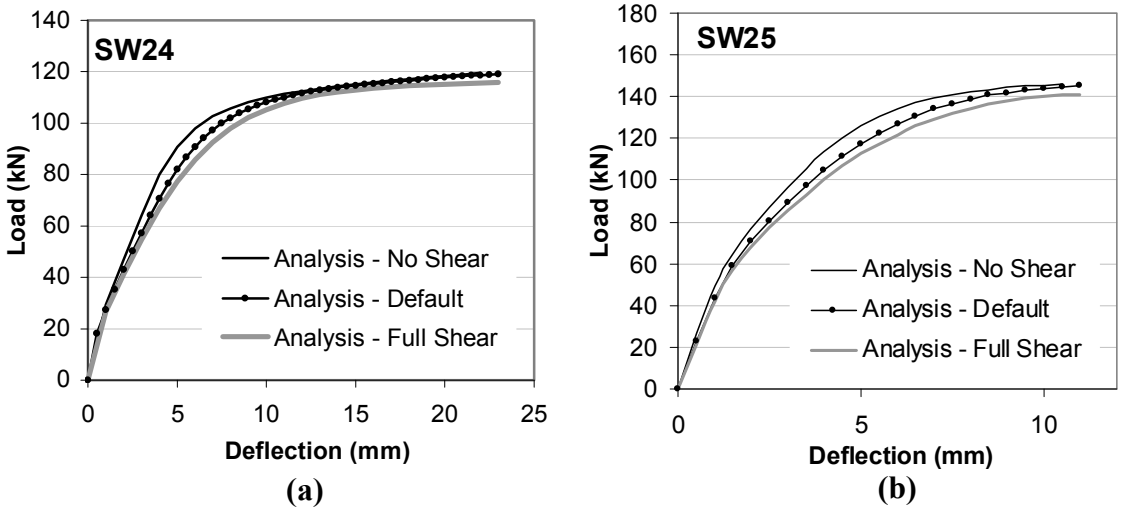


**Table 4.45** Comparison of the Analytical Responses for Different Shear Considerations: **(a)** Wall SW24; **(b)** Wall SW25

As seen in Figure 4.45, shear-related influences did not play a significant role in the overall responses of these walls. The inclusion of full shear (i.e., deactivating the shear protection feature) increased the deflections slightly without changing the peak loads considerably. However, it should be noted that, in these comparisons, the behaviour only *up to* the peak load was considered due to the force-controlled nature of the loading. Significantly different responses may be obtained in the post-peak response of the walls. Such a comparison involving the post-peak responses of another wall series tested under reversed cyclic loads is presented in Section 6.7.2 (see Figure 6.37).

## 4.12 Summary, Conclusions and Recommendations

In this chapter, the analytical procedure developed in Chapter 3 for monotonic loading condition was verified with two sets of beams, three large-scale frames and six large-scale shear walls, all of which were previously tested. The experimental behaviours of the structures were carefully compared to the analytical behaviours in terms of load-deflection responses, reinforcement strain responses and crack widths. The failure conditions of the structures, as obtained experimentally and analytically, were compared in terms of failure modes and failure displacements. Important in the seismic assessment of the structures, the analytical post-peak responses were compared to the experimental responses and the energy dissipation characteristics were discussed.

As the main focus of the analytical procedure developed was to accurately simulate the shear behaviour of reinforced concrete, most of the structures examined in this chapter were selected from the available literature to exhibit shear-critical behaviour. In addition, several flexure-critical structures were also examined, comprising one-thirds of the structures considered in this chapter.

Considering all 33 structures, a mean of 1.03 and a coefficient of variation (COV) of 11.9% were achieved for the predicted-to-observed strength ratio. As for the complete failure displacements, a mean of 0.85 with a COV of 20.7% was realized. Considering the challenges involved in modelling shear-critical structures, these ratios can be regarded as satisfactory. The failure modes of the structures were predicted accurately. In addition,

computed parameters such as reinforcement strain responses, member elongation responses and crack widths showed strong correlations with the experimental results.

In conclusion, the nonlinear sectional analysis procedure implemented for the monotonic loading condition provided reasonable simulations of the responses of the previously tested structures. Shear-related mechanisms were captured well.

Also notable is that all analyses were performed with the use of default material behaviour models and analysis options. No decisions regarding the expected behaviour, failure mode or selection of appropriate parameters were made prior to the analyses. No additional calculations, such as interaction responses or moment-curvature responses of the cross sections, were performed in the modelling process. In addition, the analyses required little computation time. For the beams analyzed, approximately 1 minute was required; the longest analysis time of approximately 6 minutes was required for the Duong frame*. Therefore, the aim of reasonable simulations with reasonable engineering effort was achieved.

The newly implemented shear protection algorithm, which approximately takes into account the increased strengths of D-regions, performed well. Premature shear failures of sections adjacent to beam-column panel zones, point load application areas and support areas were prevented.

The newly implemented shear failure check algorithm performed well also. Sudden shear failures of several structures were detected that would otherwise have gone unnoticed with significant unbalanced shear forces and gradually diminishing responses.

The need for improvements in some of the material behaviour models used was pointed out. The use of two different tension softening formulations was found to significantly affect the computed responses of beams containing very little amounts of shear reinforcement. Consequently, the need for a more comprehensive tension softening formulation was emphasized.

*On a Laptop computer with an Intel ® Dual Core 2 Due® T7500 (2.2 GHz) Processor®, a 2 GB DDR2, 677MHz RAM and a 7200 RPM hard disk drive.

Two recommendations were made for the selection of optimum segment lengths for use in the frame models. A segment length in the range of 50% of the cross section depth was suggested for frame-related structures (i.e., beams, columns and frames); a segment length in the range of 10% of the cross section depth was suggested for shear walls. It should be noted that a limited number of flexure-critical shear walls were considered to determine the optimum segment lengths for shear walls; more analytical study should be conducted on shear-critical shear walls to reach a more definitive conclusion.

Considering the experimental load-deflection behaviour of the three frames examined, effective stiffness values were typically found to be approximately 0.25 times the uncracked gross stiffness values.

---

# CHAPTER 5

## GENERAL LOADING: THEORY AND IMPLEMENTATION

### 5.1 Chapter Layout

This chapter describes the theoretical principles needed for nonlinear analysis of reinforced concrete frames subjected to general loading conditions and their implementation into the analytical procedure developed for monotonic loading conditions.

The chapter starts with a discussion of the need for the nonlinear analysis capability under general loading conditions and a short overview of the analysis procedures for reinforced concrete under general loading conditions. It is then followed by the methodology adopted to consider the general loading conditions in the context of the smeared rotating crack approach. The chapter concludes with the formulations for the concrete and reinforcement hysteresis models implemented. Each implementation is supported by a verification example including a simple axial element. In addition, the appropriate selection of the implemented models is discussed.

### 5.2 Need for Nonlinear Analysis Procedures for General Loading

As formulated in Chapter 3, nonlinear static analysis of reinforced concrete frame structures under primarily static loads serves various purposes; it can be used for: (1) the determination of the failure mode of the structure (this may reveal undesirable mechanisms such as shear-critical behaviour which may cause premature failure of the structure), (2) the estimation of the strength of the structure (this may be useful when determining whether the structure meets code required strength levels), and (3) the determination of any deficient parts or members (this may be useful when deciding on an appropriate retrofitting scheme).

In the case of an evaluation of a structure in a seismically active area, nonlinear static analysis procedures may provide some useful information for: the estimation of the maximum deformation capacity of the structure (this may help, for example, when

checking if the structure meets the FEMA 356 (2000) stipulated target displacement criteria), and for the estimation of the ductility ratio of the structure (this may help, for example, to verify if the selected force reduction factor, according to NBCC (2005), is appropriate). However, structural failures sustained during major earthquakes such as the 1994 Northridge, California and the 1995 Kobe, Japan events demonstrated that load reversals play a major role in the structural behaviour. Many of the collapses involved structural elements subjected to reversed lateral shears, placing high strength and ductility demands on cracked reinforced concrete (Vecchio, 1999). In such a situation, a static analysis procedure which is based on the strength envelope of the structure does not capture the cyclic behaviour that is expected under seismic loading (Christopoulos and Filiatrault, 2006). Therefore, the capability for analysis of reinforced concrete structures under general loading conditions including cyclic and reversed-cyclic loads is needed.

For the reasons described above, in this chapter, the formulations established for monotonic loading conditions in Chapter 3 are expanded to include analysis capabilities under general loading conditions.

## 5.3 Overview of Nonlinear Analysis of Reinforced Concrete under General Loading Conditions

Analysis of reinforced concrete structures subjected to general loading conditions requires realistic constitutive models and analytical procedures in order to achieve reasonably accurate simulations of the behaviour (Palermo and Vecchio, 2003). However, successful models available in the literature for the general loading are limited in number as compared to those available for monotonic loading. Usually based on the smeared crack approach, fixed crack models have demonstrated good correlation to experimental results under general loading conditions as documented by Okamura and Maekawa (1991), Sittipunt and Wood (1995) and others. However, in some fixed crack approaches, separate formulations have been used to model the hysteretic behaviour of normal and shear stresses which is at odds with test observations (Vecchio, 1999). An alternative method of analysis was developed by Vecchio (1999) for general loading which assumed smeared rotating cracks consistent with a compression field approach. Characterized by

the excellent convergence and numerical stability afforded by the secant stiffness approach, this alternative formulation eliminated the need to model the shear and normal stresses separately. This formulation was implemented into a finite element software program, VecTor2, to successfully model the response of structures under cyclic and reversed-cyclic loading, addressing the criticism that the secant stiffness formulation could not effectively be used to model general loading conditions (Vecchio, 1999). This procedure was based on an iterative, secant stiffness formulation treating concrete as an orthotropic material modelled according to the MCFT (Vecchio and Collins, 1986) or the DSFM (Vecchio, 2000). It included simple unloading and reloading rules for concrete based on a plastic offset formulation.

In a later study, built on the preliminary constitutive formulations of Vecchio, Palermo and Vecchio (2003) developed a more comprehensive constitutive model for concrete, which additionally included a degradation in strength in the reloading curves, calculation of plastic offsets in *both* the tension and compression domains, and consideration of partial unloading and reloading in both the tension and compression domains.

## 5.4 Implementations in the Analytical Procedure Developed

Both formulations proposed by Vecchio (1999) and Palermo and Vecchio (2003) were implemented into the sectional and global frame analysis algorithms of the analytical procedure developed, giving it the capability to consider general loading conditions. The vast majority of the implementations were performed in the sectional analysis algorithm, where stress and strain calculations were carried out for each concrete, reinforcing and prestressing steel layers as explained in the Section 3.7. The only addition to the global frame analysis subroutine was in the updating process for the concrete and steel strain and stress histories at the end of each load stage as shown in the flowchart of Figure 3.19.

### 5.4.1 Consideration of Concrete Plastic Offset Strains

In the formulation of the sectional calculations in Chapter 3, concrete plastic offset strains were incorporated into the total strains experienced by a concrete layer as defined by Eq. 3.71, and both the shear-stress and shear-strain-based sectional calculation procedures

were developed accordingly. The remaining task was to implement a plastic offset formulation for concrete.

In the implementation, plastic offset strains for concrete are defined and retained based on the formulations proposed by Vecchio. As a rotating crack approach is used, the principal strain directions are free to rotate; therefore, plastic offset strains should be defined with respect to the elemental axes (x and y in VecTor5) so that the previous damage does not rotate with the rotation of the principal strain directions. This requires an *incremental formulation* for plastic offset strains. Based on this approach, in each sectional analysis iteration performed for each concrete layer, previously stored concrete plastic offset strains $\varepsilon_{cx}{}^{p}, \varepsilon_{cy}{}^{p}, \varepsilon_{cxy}{}^{p}$ are transformed into principal concrete plastic offset strains $\varepsilon_{c1}{}^{p}, \varepsilon_{c2}{}^{p}$ based on the *current* inclination angle through the use of a Mohr's circle of strain as follows:

$$\varepsilon_{c1}^{p} = \frac{\varepsilon_{cx}^{p} + \varepsilon_{cy}^{p}}{2} + \frac{\varepsilon_{cx}^{p} - \varepsilon_{cy}^{p}}{2} \times \cos 2\theta + \frac{\gamma_{cxy}^{p}}{2} \times \sin 2\theta \tag{5.1}$$

$$\varepsilon_{c2}^{p} = \frac{\varepsilon_{cx}^{p} + \varepsilon_{cy}^{p}}{2} - \frac{\varepsilon_{cx}^{p} - \varepsilon_{cy}^{p}}{2} \times \cos 2\theta - \frac{\gamma_{cxy}^{p}}{2} \times \sin 2\theta \tag{5.2}$$

It should be noted that the *current* inclination, $\theta$, corresponds to the inclination of the strain field (same as stress field) when using the MCFT, and to the inclination of stress field when using the DSFM.

During each sectional iteration performed for the concrete layer under consideration, the *instantaneous* concrete plastic offset strains are then calculated based on the selected concrete hysteresis model.

The Vecchio model considers the instantaneous concrete plastic offsets in the compression domain as defined by Eq. 5.3 and Eq. 5.4.

$$\varepsilon_c^{\,p} = \varepsilon_c + \varepsilon_p \times \left[ 0.29 \times \left( \frac{\varepsilon_c}{\varepsilon_p} \right)^2 - 0.87 \times \left( \frac{\varepsilon_c}{\varepsilon_p} \right) \right] \quad if\ \varepsilon_c > 1.5 \times \varepsilon_p \tag{5.3}$$

$$\varepsilon_c^{\,p} = \varepsilon_c - 0.001305 \times \left( \frac{\varepsilon_p}{0.002} \right) \quad if\ \varepsilon_c < 1.5 \times \varepsilon_p \tag{5.4}$$

where $\varepsilon_c$ is the principal compressive strain, and $\varepsilon_p$ is the strain corresponding to peak stress in the base curve.

As shown in Figure 5.1, in the tension domain, the Vecchio model does not fully consider positive plastic offset strains. The unloading branch (arrows 2 and 7) of the compression response passes through a negative plastic offset strain when going into the tensile domain (arrows 3 and 8), eventually reaching the tensile base response. The unloading branch of the tensile responses (arrows 4 and 9) follows a linear path towards a positive plastic offset strain until it essentially reaches the positive offset. The branch then progresses linearly towards the origin virtually parallel to the horizontal axis. It eventually passes through the origin before becoming the reloading branch (arrows 5 and 10) in compression.

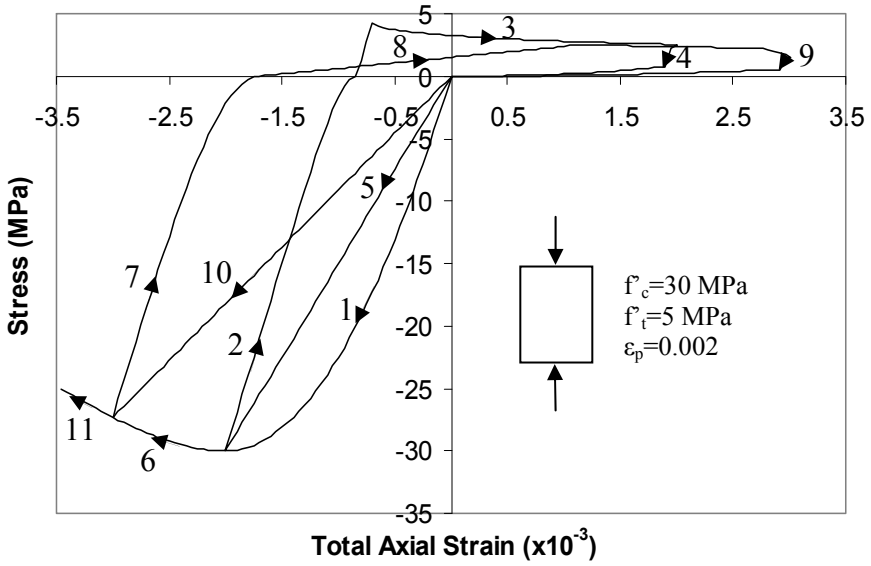


**Figure 5.1** Vecchio Model: Response for an Element under Uniaxial Strain Reversals

The Palermo model formulates the concrete plastic offset strains in the compression domain as defined by Eq. 5.5.

$$\varepsilon_c^{\ p} = \varepsilon_p \times \left[ 0.166 \times \left( \frac{\varepsilon_{2c}}{\varepsilon_p} \right)^2 + 0.132 \times \left( \frac{\varepsilon_{2c}}{\varepsilon_p} \right) \right] \tag{5.5}$$

As for the tension domain, the Palermo model uses the Eq. 5.6 to calculate the tensile plastic offset strains.

$$\varepsilon_c^{\ p} = 146 \times \varepsilon_{1c}^{\ 2} + 0.523 \times \varepsilon_{1c} \tag{5.6}$$

where $\varepsilon_c^{\ p}$ is the instantaneous plastic offset strain, and $\varepsilon_{1c}$ *and* $\varepsilon_{2c}$ are the principal unloading strain from the backbone curve.

It should be noted that the current implementation of the Palermo model into the VecTor analysis programs does not fully consider the positive plastic offsets due to numerical difficulties encountered. As shown in Figure 5.2, the unloading branch (arrows 4, 8 and 12) of the tensile responses follows a nonlinear path until they reach a positive plastic offset strain. The responses then progress along the horizontal axis, passing through the origin before becoming the reloading branch (arrows 5 and 9) in compression.

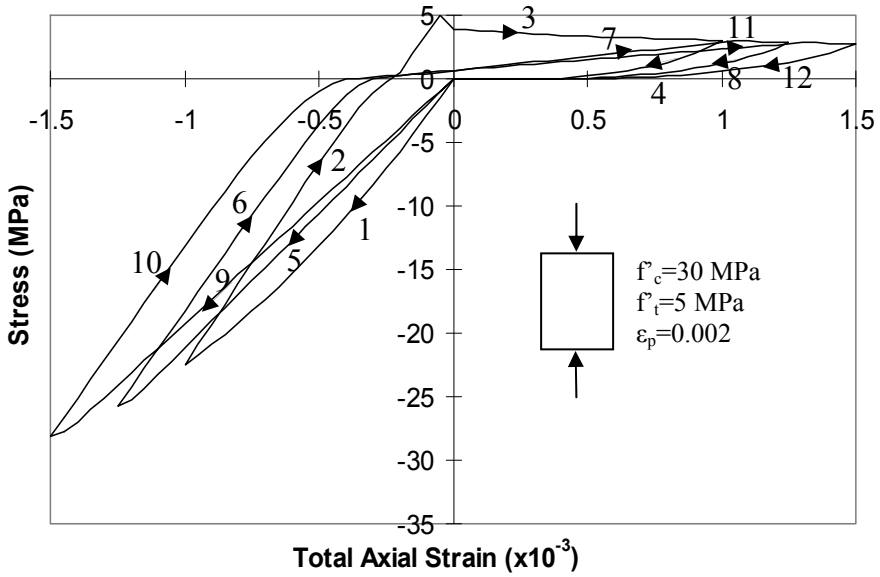


**Figure 5.2** Palermo Model: Response for an Element under Uniaxial Strain Reversals

After the calculation of the instantaneous plastic offset strains, a check is made to determine whether the instantaneous plastic offset strains exceed the stored plastic offset strains. If that is the case, incremental plastic offset strains are generated in the principal directions as follows:

$$\Delta\varepsilon_{c1}{}^{p} = \varepsilon_1 - \varepsilon_{c1}{}^{p} \tag{5.7}$$

$$\Delta\varepsilon_{c2}{}^{p} = \varepsilon_2 - \varepsilon_{c2}{}^{p} \tag{5.8}$$

As shown in the flowchart of Figure 3.19, at the end of each load stage of the global frame analysis, previously stored concrete plastic offset strains are updated for all concrete layers as follows:

$$\varepsilon_{cx}{}^{p'} = \varepsilon_{cx}{}^{p} + \frac{\Delta\varepsilon_{c1}{}^{p}}{2} \times (1+\cos 2\theta) + \frac{\Delta\varepsilon_{c2}{}^{p}}{2} \times (1-\cos 2\theta) \tag{5.9}$$

$$\varepsilon_{cy}{}^{p'} = \varepsilon_{cy}{}^{p} + \frac{\Delta\varepsilon_{c1}{}^{p}}{2} \times (1-\cos 2\theta) + \frac{\Delta\varepsilon_{c2}{}^{p}}{2} \times (1+\cos 2\theta) \tag{5.10}$$

$$\gamma_{cxy}{}^{p'} = \gamma_{cxy}{}^{p} + \Delta\varepsilon_{c1}{}^{p} \times \sin 2\theta + \Delta\varepsilon_{c2}{}^{p} \times \sin 2\theta \tag{5.11}$$

### 5.4.2 Consideration of Maximum Concrete Strains

Both hysteresis models developed by Vecchio and Palermo require the knowledge of previously attained maximum and minimum concrete strains. This is to due to the fact that, in both hysteresis models, concrete stresses are calculated from a set of rules linked to the backbone curve which corresponds to the monotonic response of the concrete.

Analogous to the plastic offset formulation, as cracks are free to rotate, an *incremental formulation* should be adopted for the calculation of maximum and minimum concrete strains attained. Consider first the maximum concrete strains in the concrete. In each sectional analysis iteration performed for each concrete layer, previously stored maximum *total* concrete strains $\varepsilon_{cmx}, \varepsilon_{cmy}, \varepsilon_{cmxy}$ are transformed into principal directions

as $\varepsilon_{cm1}$ *and* $\varepsilon_{cm2}$ based on the *current* inclination angle through the use of a Mohr's circle of strain as defined by Eq. 5.12 and Eq. 5.13.

$$\varepsilon_{cm1} = \frac{\varepsilon_{cmx} + \varepsilon_{cmy}}{2} + \frac{\varepsilon_{cmx} - \varepsilon_{cmy}}{2} \times \cos 2\theta + \frac{\gamma_{cmxy}}{2} \times \sin 2\theta \tag{5.12}$$

$$\varepsilon_{cm2} = \frac{\varepsilon_{cmx} - \varepsilon_{cmy}}{2} - \frac{\varepsilon_{cmx} - \varepsilon_{cmy}}{2} \times \cos 2\theta - \frac{\gamma_{cmxy}}{2} \times \sin 2\theta \tag{5.13}$$

It should be noted that the *current* inclination, $\theta$, correspond to the inclination of the strain field when using the MCFT, and to the inclination of the stress field when using the DSFM.

During the sectional iterations for the concrete layer under consideration, if the current concrete total compressive strain exceeds the stored maximum compressive strain, $\varepsilon_{cm2}$, incremental concrete total strains are generated as follows:

$$\Delta\varepsilon_{cm2} = \varepsilon_2 - \varepsilon_{cm2} \tag{5.14}$$

As shown in the flowchart of Figure 3.19, at the end of each load stage of the global frame analysis, previously stored concrete maximum compressive strains are updated for all concrete layers as follows:

$$\varepsilon'_{cmx} = \varepsilon_{cmx} + \frac{\Delta\varepsilon_{cm1}}{2} \times (1 + \cos 2\theta) + \frac{\Delta\varepsilon_{cm2}}{2} \times (1 - \cos 2\theta) \tag{5.15}$$

$$\varepsilon'_{cmy} = \varepsilon_{cmy} + \frac{\Delta\varepsilon_{cm1}}{2} \times (1 - \cos 2\theta) + \frac{\Delta\varepsilon_{cm2}}{2} \times (1 + \cos 2\theta) \tag{5.16}$$

$$\gamma'_{cmy} = \gamma_{cmxy} + \Delta\varepsilon_{cm1} \times \sin 2\theta + \Delta\varepsilon_{cm2} \times \sin 2\theta \tag{5.17}$$

The maximum tensile strains ($\varepsilon_{tmx}, \varepsilon_{tmy}$ *and* $\varepsilon_{tmxy}$) are calculated and stored in computer memory in a similar manner.

### 5.4.3 Stress-Strain Models for Concrete

Three stress-strain models for concrete were implemented into the analytical procedure developed. The implementations were made through the use of the model subroutines, which are common to all VecTor programs and which were created prior to this work. The detailed formulations of the models considered are presented below.

#### 5.4.3.1 Vecchio Model with Linear Unloading

Compressive Response

*Unloading* to a compressive strain of $\varepsilon_c$ results in the concrete stress $f_c$ as follows:

$$f_c = E_{cm} \times (\varepsilon_c - \varepsilon_c^{\,p}) \tag{5.18}$$

where $E_{cm}$ is the unloading modulus as defined by

$$E_{cm} = \frac{f_{cm}}{(\varepsilon_{cm} - \varepsilon_c^{\,p})} \tag{5.19}$$

where $f_{cm}$ is the stress corresponding to maximum concrete strain previously stored as $\varepsilon_{cm}$, and $\varepsilon_c^{\,p}$ is the concrete plastic offset strain as defined in Section 5.4.2 and 5.4.1.

*Reloading* to a compressive strain of $\varepsilon_c$ produces the concrete stress $f_c$ as follows:

$$f_c = 0 \qquad \text{if } \varepsilon_c > \varepsilon_c^{\,p} \quad \text{or} \quad \varepsilon_c > 0 \tag{5.20}$$

$$f_c = \frac{(\varepsilon_c - \varepsilon_c^{\,p}) \times f_{cm}}{\varepsilon_{cm} - \varepsilon_c^{\,p}} \qquad \text{if} \quad \varepsilon_c^{\,p} > \varepsilon_c > \varepsilon_{cm} \tag{5.21}$$

$$f_c = f_{bc} \qquad \text{if} \quad \varepsilon_c < \varepsilon_{cm} \tag{5.22}$$

where $f_{bc}$ is the stress calculated from the base curve corresponding to concrete strain $\varepsilon_c$, and $\varepsilon_c^{\,p}$ is the concrete plastic offset strain.

Tensile Response

*Unloading* to a tensile strain of $\varepsilon_c$ returns the concrete stress $f_c$ as follows:

$$f_c = E_{tm} \times (\varepsilon_c - \varepsilon_{cp}) \tag{5.23}$$

where unloading modulus $E_{tm}$ is defined by

$$E_{tm} = \frac{f_{tm}}{\varepsilon_{tm} - \varepsilon_{cp}} \tag{5.24}$$

*Reloading* to a tensile strain of $\varepsilon_c$ returns the concrete stress $f_c$ as follows:

$$f_c = \frac{(\varepsilon_c - \varepsilon_c^{\,p}) \times f_{tm}}{\varepsilon_{tm} - \varepsilon_c^{\,p}} \qquad if \quad \varepsilon_c^{\,p} < \varepsilon_c < \varepsilon_{tm} \tag{5.25}$$

$$f_c = f_{bt} \qquad if \quad \varepsilon_c > \varepsilon_{tm} \tag{5.26}$$

where $f_{bt}$ is the stress calculated from the base curve corresponding to concrete strain $\varepsilon_c$, and $\varepsilon_c^{\,p}$ is the concrete plastic offset strain.

### 5.4.3.2 Vecchio Model with Nonlinear Unloading

This model is similar to the previous model except that the unloading branch follows a nonlinear path defined by a Ramberg-Osgood function.

Compressive Response

*Unloading* to a compressive strain of $\varepsilon_c$ results in the concrete stress $f_c$ as follows:

$$f_c = f_{cm} + E_c\left(\varepsilon_c - \varepsilon_{cm}\right) + \frac{E_c\left(\varepsilon_c - \varepsilon_{cm}\right)^{N_c}}{N_c\left(\varepsilon_c^{p} - \varepsilon_{cm}\right)^{N_c - 1}} \qquad \text{for } 1 \le N_c \le 20 \tag{5.27}$$

where $E_c$ is the initial tangent stiffness of concrete, and $N_c$ is the power term that defines the deviation from the linear unloading branch as follows:

$$N_c = \frac{E_c \times \left(\varepsilon_c{}^p - \varepsilon_{cm}\right)}{f_{cm} + E_c \times \left(\varepsilon_c{}^p - \varepsilon_{cm}\right)} \tag{5.28}$$

If $N_c$ is less than 1 or greater than 20, a linear unloading branch is used as defined by

$$f_c = E_c \times \left(\varepsilon_c - \varepsilon_c{}^p\right) \quad for \;\; N_c \le 1 \; or \; 20 \le N_c \tag{5.29}$$

The reloading response in compression is the same as that defined for the preceding model.

Tensile Response

*Unloading* to a tensile strain of $\varepsilon_c$ returns the concrete stress $f_c$ as follows:

$$f_c = f_{tm} - E_c\left(\varepsilon_{tm} - \varepsilon_c\right) + \frac{E_c\left(\varepsilon_{tm} - \varepsilon_c\right)^{N_t}}{N_t\left(\varepsilon_{tm} - \varepsilon_c^p\right)^{N_t - 1}} \qquad \text{for } 1 \le \mathrm{N_t} \le 20 \tag{5.30}$$

where $N_t$ is the power term that introduces the nonlinearity in the unloading branch as follows:

$$N_t = \frac{E_c \times \left(\varepsilon_{tm} - \varepsilon_c{}^p\right)}{E_c \times \left(\varepsilon_{tm} - \varepsilon_c{}^p\right) - f_{tm}} \tag{5.31}$$

If $N_t$ is less than 1 or greater than 20, a linear unloading branch is used as defined below:

$$f_c = E_c \times \left(\varepsilon_c - \varepsilon_c{}^p\right) \quad for \quad N_t \le 1 \; or \; 20 \le N_t \tag{5.32}$$

The *reloading* response in tension is the same as that defined for the preceding model.

### 5.4.3.3 Palermo Model

Proposed by Palermo and Vecchio (2002), this model is similar to the preceding models, but includes more comprehensive stress-strain relationships which consider modelling of the degradation in the reloading stiffness based on the amount of strain recovered during the unloading phase, calculation of plastic offsets for both the tension and compression regimes, and consideration of partial unloading and reloading. Note that the plastic offsets in the tension domain are not fully considered in the formulation of the VecTor analysis programs as explained in Section 5.4.1 (Figure 5.2).

Compressive Response

*Unloading* to a compressive strain of $\varepsilon_c$ results in the concrete stress $f_c$ as follows:

$$f_c = f_{cm} + E_c \times \left(\varepsilon_c - \varepsilon_{cm}\right) - \frac{0.929 \times E_c \times \left(\varepsilon_c - \varepsilon_{cm}\right)^{N_c}}{N_c \times \left(\varepsilon_c{}^{p} - \varepsilon_{cm}\right)^{N_c - 1}} \tag{5.33}$$

where $f_{cm}$ is the stress corresponding to maximum concrete strain previously stored as $\varepsilon_{cm}$, $E_c$ is the tangent modulus of` concrete, and $N_c$ is a Ramberg-Osgood formulation to describe the nonlinear unloading branch of concrete similar to that used by Seckin (1981) as follows:

$$N_c = \frac{0.929 \times E_c \times \left(\varepsilon_c{}^{p} - \varepsilon_{cm}\right)}{f_{cm} + E_c \times \left(\varepsilon_c{}^{p} - \varepsilon_{cm}\right)} \tag{5.34}$$

$N_c$ is defined in a way that the unloading modulus equals to the initial tangent modulus $E_c$ at the beginning of the unloading branch and to 0.071 x $E_c$ at the end of the unloading branch as shown in Figure 5.3(a).

*Reloading* to a compressive strain of $\varepsilon_c$ yields the concrete stress $f_c$ as follows:

$$f_c = f_{ro} + E_{cm}^{+} \times \left(\varepsilon_c - \varepsilon_{ro}\right) \tag{5.35}$$

where $f_{ro}$ is the stress corresponding to the strain $\varepsilon_{ro}$ at the load reversal in the current loop, and $E_{cm}^{+}$ is the reloading modulus as defined by Eq. 5.36 (Figure 5.3(b))

$$E_{cm}^{+} = \frac{\beta_c \times f_{cm} - f_{ro}}{\varepsilon_{cm} - \varepsilon_{ro}} \tag{5.36}$$

where $\beta_c$ is a damage indicator which degrades $E_{cm}^{+}$ so that additional straining is required to reach the monotonic backbone curve.

$$\beta_c = \frac{1}{1 + 0.10 \times \left( \frac{\varepsilon_{rec}}{\varepsilon_p} \right)^{0.5}} \qquad for \left| \varepsilon_c \right| < \left| \varepsilon_p \right| \tag{5.37}$$

$$\beta_c = \frac{1}{1 + 0.175 \times \left( \frac{\varepsilon_{rec}}{\varepsilon_p} \right)^{0.6}} \qquad for \left| \varepsilon_c \right| > \left| \varepsilon_p \right| \tag{5.38}$$

where $\varepsilon_{rec} = \varepsilon_{cm} - \varepsilon_{ro}$ (5.39)

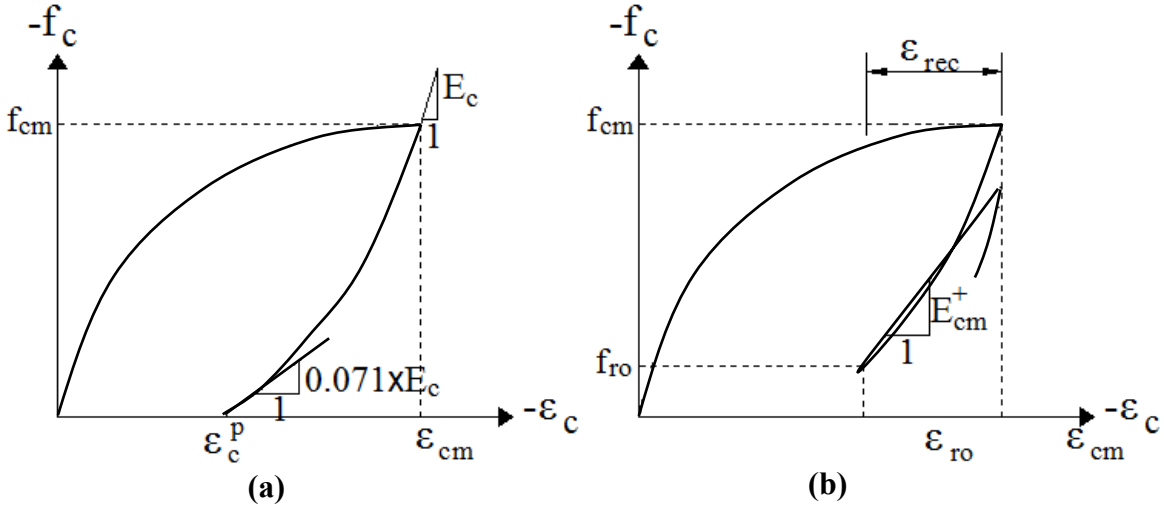


**Figure 5.3** Palermo Model, Compression Domain: **(a)** Unloading; **(b)** Reloading (Palermo and Vecchio, 2003)

Tensile Response

*Unloading* to a tensile strain of $\varepsilon_c$ yields the concrete stress $f_c$ as follows:

$$f_c = f_{tm} - E_c \times \left(\varepsilon_{tm} - \varepsilon_c\right) + \frac{\left(E_c - E_c{}^f\right) \times \left(\varepsilon_{tm} - \varepsilon_c\right)^{N_t}}{N_t \times \left(\varepsilon_{tm} - \varepsilon_c{}^p\right)^{N_t - 1}} \tag{5.40}$$

where $f_{tm}$ is the stress corresponding to the maximum concrete tensile strain previously stored as $\varepsilon_{tm}$, $E_c^f$ is the unloading modulus of` elasticity of the concrete, and $N_t$ is a power term that describes the degree of nonlinearity as follows:

$$N_t = \frac{\left(E_c - E_c{}^f\right) \times \left(\varepsilon_{tm} - \varepsilon_c{}^p\right)}{E_c \times \left(\varepsilon_{tm} - \varepsilon_c{}^p\right) - f_{tm}} \tag{5.41}$$

where

$$E_c{}^f = 0.071 \times E_c \times \left(\frac{0.001}{\varepsilon_{tm}}\right) \quad \text{for } \varepsilon_{tm} \le 0.001 \tag{5.42}$$

$$E_c{}^f = 0.053 \times E_c \times \left(\frac{0.001}{\varepsilon_{tm}}\right) \quad \text{for } \varepsilon_{tm} > 0.001 \tag{5.43}$$

$N_t$ is defined in a way that the unloading modulus equals the initial tangent modulus $E_c$ at the beginning of the unloading branch and to $E_c^f$ at the end of the unloading branch as shown in Figure 5.4(a).

Reloading to a tensile strain of $\varepsilon_c$ produces the concrete stress $f_c$ as follows:

$$f_c = \beta_t \times f_{tm} - E_{tm}{}^+ \times \left(\varepsilon_{tm} - \varepsilon_c\right) \tag{5.44}$$

where $E_{tm}{}^+$ is the reloading stiffness as defined by Eq. 5.45 (Figure 5.4(b)).

$$E_{tm}^{+} = \frac{\beta_t \times f_{tm} - f_{ro}}{\varepsilon_{tm} - \varepsilon_{ro}} \tag{5.45}$$

where $\beta_t$ is a tensile damage indicator which degrades $E_{tm}^{+}$ so that additional straining is required to intersect the base curve as defined below.

$$\beta_t = \frac{1}{1 + 1.15 \times \left(\varepsilon_{rec}\right)^{0.25}} \tag{5.46}$$

where

$$\varepsilon_{rec} = \varepsilon_{tm} - \varepsilon_{ro} \tag{5.47}$$

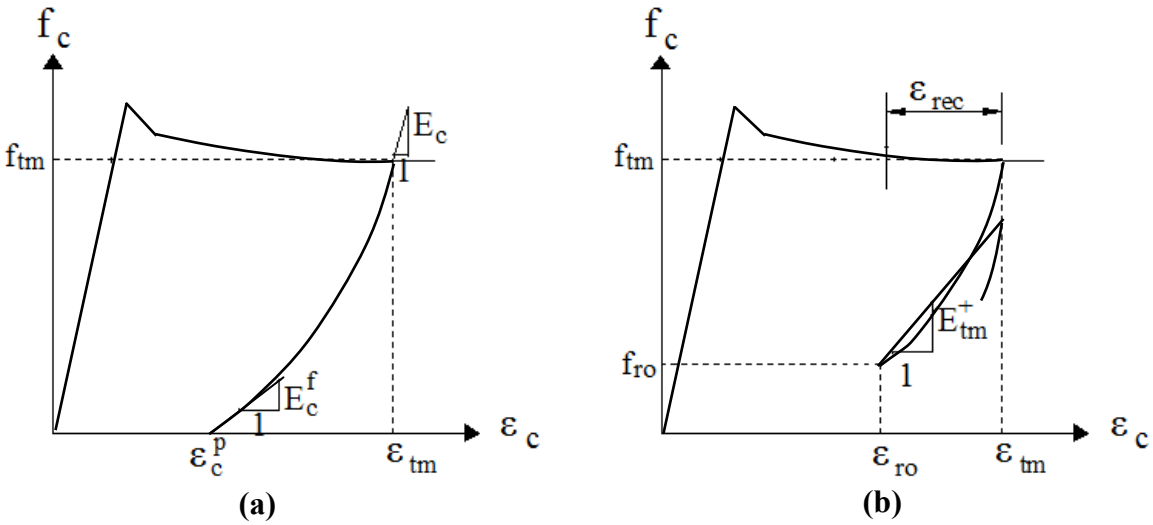


**Figure 5.4** Palermo Model, Tension Domain: **(a)** Unloading; **(b)** Reloading (Palermo and Vecchio, 2003)

Partial Unloading and Reloading in Compression

In Figure 5.5, Curves 1 and 2 represent full unloading and reloading as defined above. Curve 3 is the case of a partial unloading from a reloading curve at a strain less than the previously attained unloading strain $\varepsilon_{cm}$. In this case, full unloading rules are applied except that the unloading stress and strain, $f_{c\max 1}$ *and* $\varepsilon_{c\max 1}$, are substituted for the maximum unloading stress and strain $f_{cm}$ *and* $\varepsilon_{cm}$. Curve 4 represents a partial reloading from a partial unloading. In this case, the unloading stiffness becomes

$$E_{c1} = \frac{f_{c\max 1} - f_{ro}}{\varepsilon_{c\max 1} - \varepsilon_{ro}} \tag{5.48}$$

and the corresponding stress is calculated as

$$f_c = f_{ro} + E_{c1} \times (\varepsilon_c - \varepsilon_{ro}) \tag{5.49}$$

Following the partial reloading of Curve 4, Curve 5 connects the response to the back-bone curve including the $\beta_c$ damage indicator which accounts for the strength degradation in compression. In this case, the reloading stiffness becomes

$$E_{c2} = \frac{\beta_c \times f_{c\mathrm{m}} - f_{c\max 1}}{\varepsilon_{cm} - \varepsilon_{c\max 1}} \tag{5.50}$$

and the corresponding stress is found to be

$$f_c = f_{c\max 1} + E_{c2} \times (\varepsilon_c - \varepsilon_{c\max 1}) \tag{5.51}$$

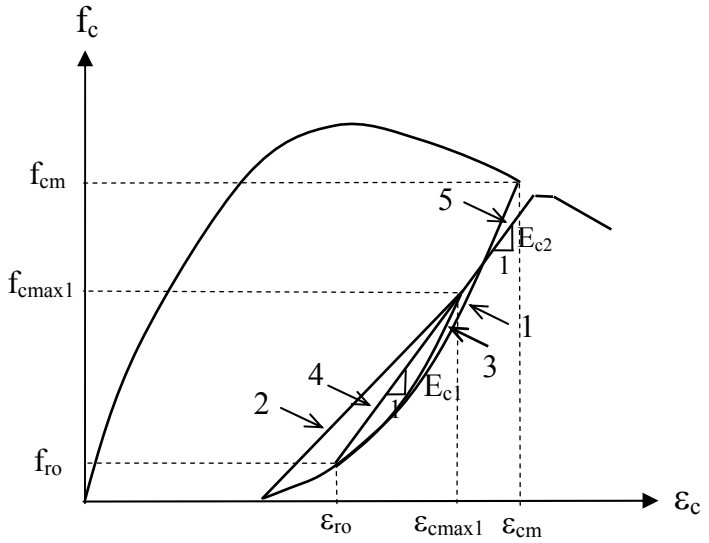


**Figure 5.5** Palermo Model, Compression Domain: Partial Unloading and Reloading (Palermo and Vecchio, 2003)

Partial Unloading and Reloading in Tension

In Figure 5.6, Curves 1 and 2 represent full unloading and reloading as explained before. Curve 3 is the case of a partial unloading from a reloading curve at a strain less than the previously attained unloading strain $\varepsilon_{tm}$. In this case, full unloading rules are applied except that the unloading stress and strain, $f_{t\max 1}$ *and* $\varepsilon_{t\max 1}$, are substituted for maximum unloading stress and strain $f_{t\mathrm{m}}$ *and* $\varepsilon_{t\mathrm{m}}$. Curve 4 represents a partial reloading from a partial unloading. In this case, the unloading stiffness becomes

$$E_{c3} = \frac{f_{t\max 1} - f_{ro}}{\varepsilon_{t\max 1} - \varepsilon_{ro}} \tag{5.52}$$

and the corresponding stress is calculated by Eq. 5.53.

$$f_c = f_{ro} + E_{c3} \times (\varepsilon_c - \varepsilon_{ro}) \tag{5.53}$$

Following the partial reloading of Curve 4, Curve 5 connects the response to the back-bone curve including the $\beta_t$ damage indicator which accounts for the strength degradation in tension. In this case, the reloading stiffness becomes

$$E_{c4} = \frac{\beta_t \times f_{c\mathrm{m}} - f_{t\max 1}}{\varepsilon_{cm} - \varepsilon_{t\max 1}} \tag{5.54}$$

and the corresponding stress is found to be

$$f_c = f_{t\max 1} + E_{c4} \times (\varepsilon_c - \varepsilon_{t\max 1}) \tag{5.55}$$

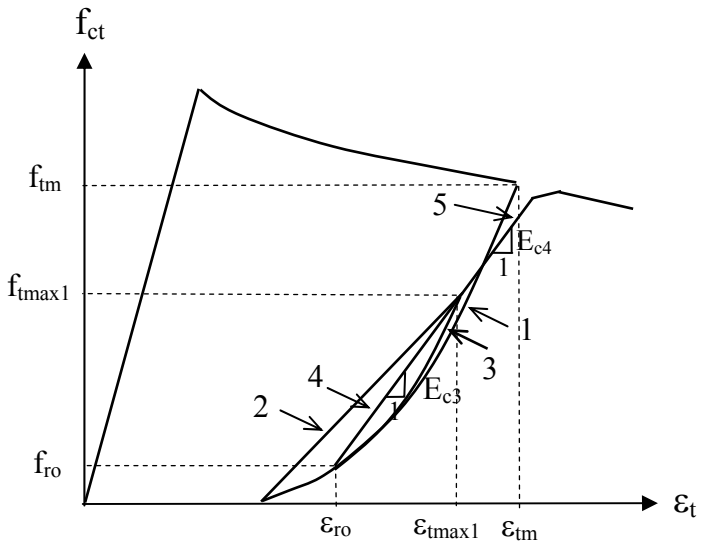


**Figure 5.6** Palermo Model, Tension Domain: Partial Unloading and Reloading (Palermo and Vecchio, 2003)

### 5.4.3.4 Verification Example

To illustrate the concrete responses produced by the three hysteresis models implemented, an example analysis was carried out. The structure analyzed consisted of a one-member cantilevered reinforced concrete column with the geometric details given in Figure 5.7. Axial loading was applied at the top node of the column in a displacement-controlled mode. The purpose of the analyses was to obtain the stress-*total* strain and the stress-*net* strain responses of the concrete under cyclic and reversed-cyclic loading conditions as shown in Figure 5.8.

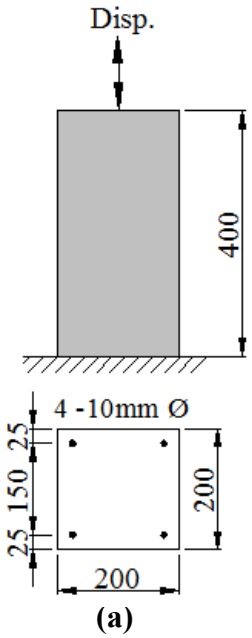


(a)

| Concrete | | | |
|---|---|---|---|
| $f'_c$ (MPa) | $f_t$ (MPa) | $\varepsilon_0$ (x $10^{-3}$) | $E_c$ (MPa) |
| 30 | 5 | 2 | 30000 |

| Reinforcement | | | | | |
|---|---|---|---|---|---|
| | $A_s$ ($mm^2$) | $d_b$ (mm) | $f_y$ (MPa) | $f_u$ (MPa) | $E_s$ (MPa) |
| **10m Ø** | 78.5 | 10 | 500 | 600 | 200000 |

**(b)**

**Figure 5.7** A Cantilever Column: **(a)** Model; **(b)** Material Properties

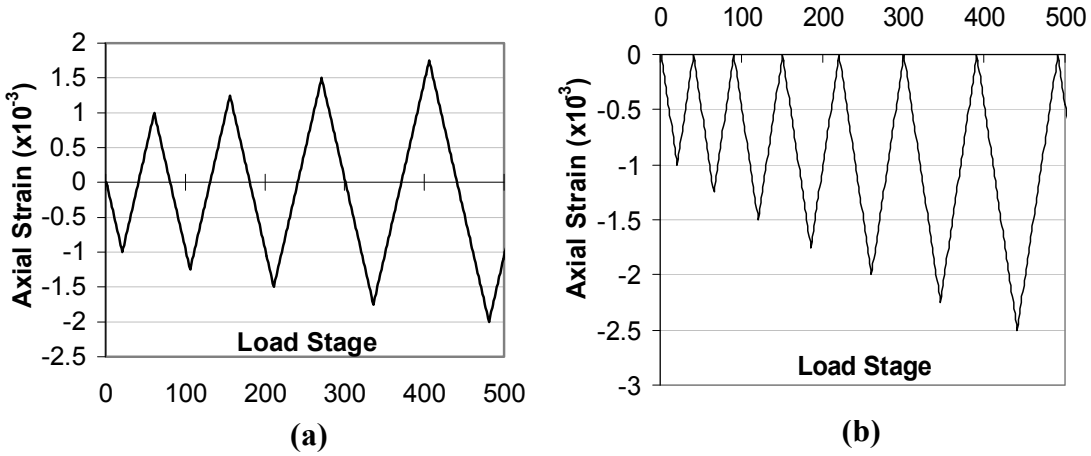


**Figure 5.8** Applied Loading for the Cantilever Column: **(a)** Reversed-Cyclic**; (b)** Cyclic

The responses produced by the Vecchio model are presented in Figure 5.9 to Figure 5.12 for the cyclic and reversed-cyclic loading conditions. The only difference between the responses is the unloading branches; in Figure 5.9 and 5.10, the unloading responses are linear while, in Figure 5.11 and 5.12, the unloading responses are nonlinear.

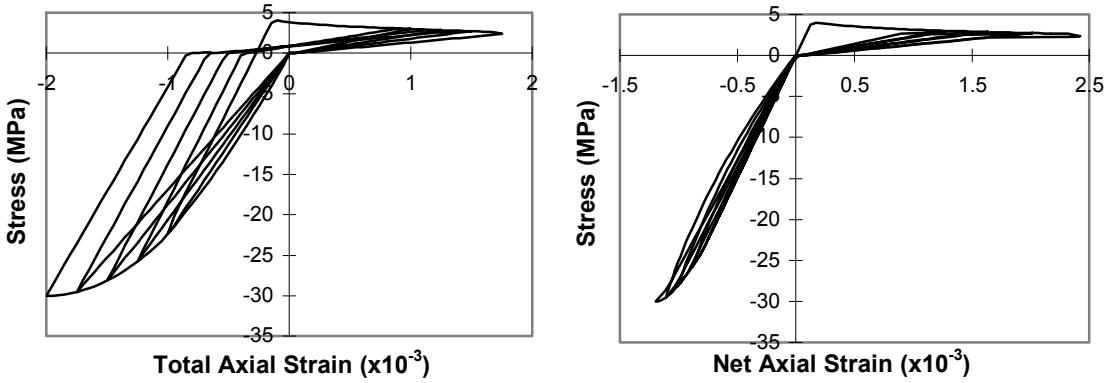


**Figure 5.9** Concrete Response of the Cantilever Column using Vecchio Model with Linear Unloading under Reversed-Cyclic Loading

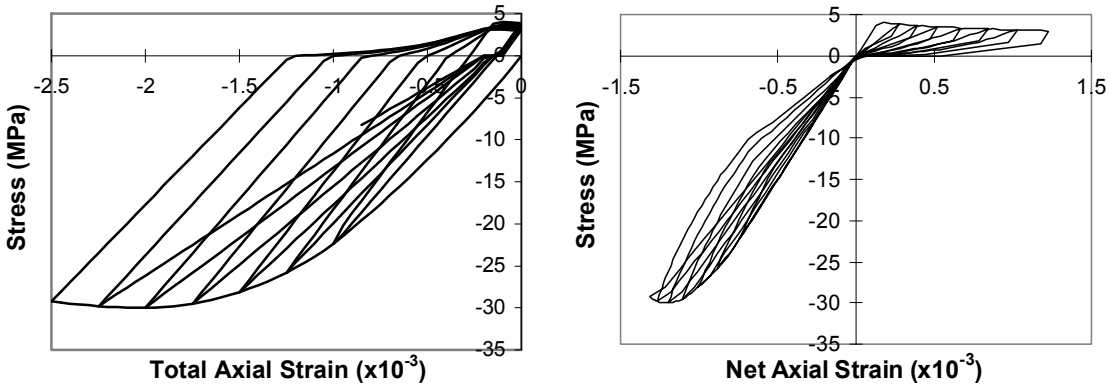


**Figure 5.10** Concrete Response of the Cantilever Column using Vecchio Model with Linear Unloading under Cyclic Loading

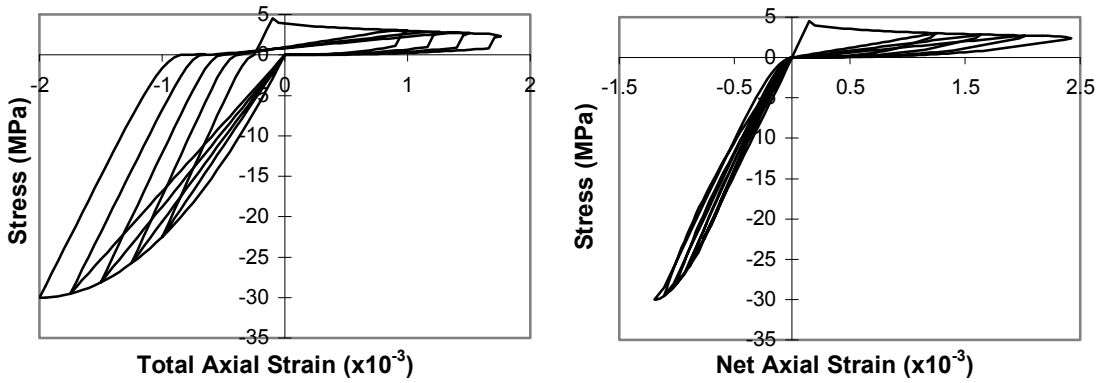


**Figure 5.11** Concrete Response of the Cantilever Column using Vecchio Model with Nonlinear Unloading under Reversed-Cyclic Loading

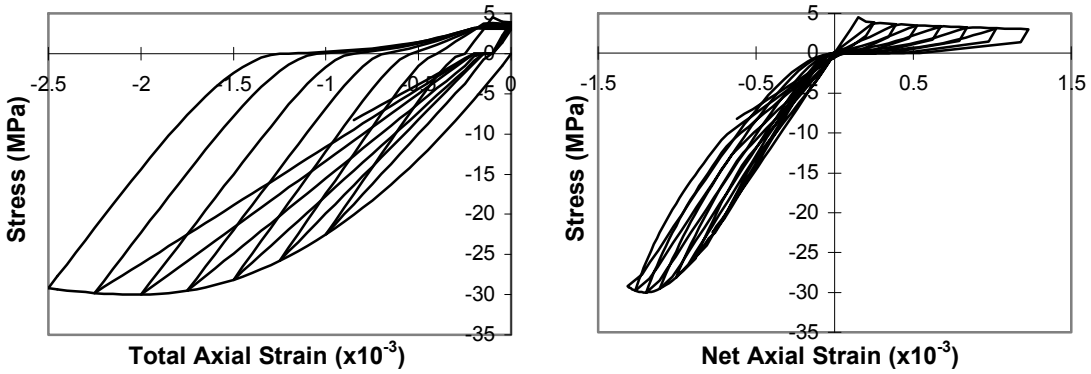


**Figure 5.12** Concrete Response of the Cantilever Column using Vecchio Model with Nonlinear Unloading under Cyclic Loading

The responses produced by the Palermo model are presented in Figure 5.13 and 5.14 for the cyclic and reversed-cyclic loading conditions. Not included in the preceding model, strength degradation in the reloading stiffnesses is clearly visible in both the tension and compression domains; that is, more straining is necessary to reach the backbone curve when reloading from a strain less than the previously attained maximum strain. Also visible from the figures below, this model includes more nonlinearity in the unloading branches than do the preceding models.

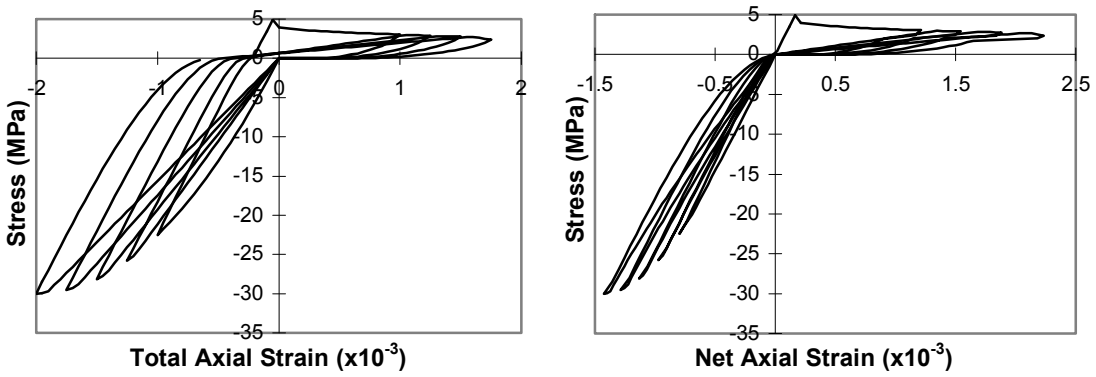


**Figure 5.13** Concrete Response of the Cantilever Column using Palermo Model under Reversed-Cyclic Loading

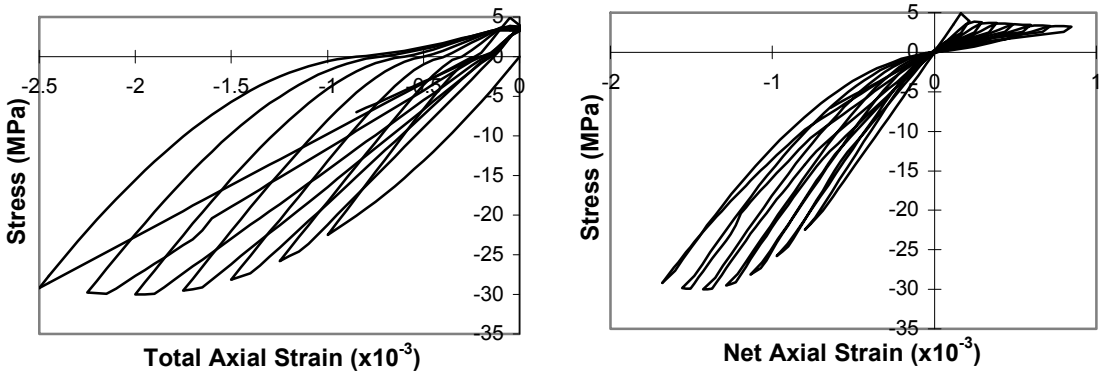


**Figure 5.14** Concrete Response of the Cantilever Column using Palermo Model under Cyclic Loading

### 5.4.4 Stress-Strain Models for Reinforcement

Under monotonic loading conditions, a tri-linear response is implemented for both the longitudinal and transverse reinforcement as described in Chapter 3. These responses are expanded in this section to allow for general loading conditions as explained below.

#### 5.4.4.1 Stress-Strain Models for Longitudinal Reinforcement

In the formulation of the sectional calculations in Chapter 3, the plastic offset strains $\varepsilon_s^{\,p}$ were incorporated into the total strains experienced by each reinforcing or prestressing bar layers as defined by Eq. 3.99. The remaining task is to introduce a formulation which calculates reinforcement stresses based on the *net* reinforcement strain, $\varepsilon_{si}$ .

For this purpose, three models were implemented for the hysteretic response calculations of longitudinal reinforcement: the Seckin model with Bauschinger effect, the elastic-plastic model with strain hardening, and the elastic-plastic model (bilinear). The implementations were made through the use of the model subroutines, which are common to all VecTor programs and which were created prior to this work. The detailed formulations of the models considered are presented below.

### Seckin Model with Bauschinger Effect

The default and the most comprehensive hysteretic response model for the longitudinal reinforcement is based on the formulation of Seckin (1981) with some minor simplifications by Vecchio (1999). The Bauschinger effect, which lowers the yield stress under stress reversals, was represented by a Ramberg-Osgood formulation as illustrated in Figure 5.15. The detailed formulations of this model are given below.

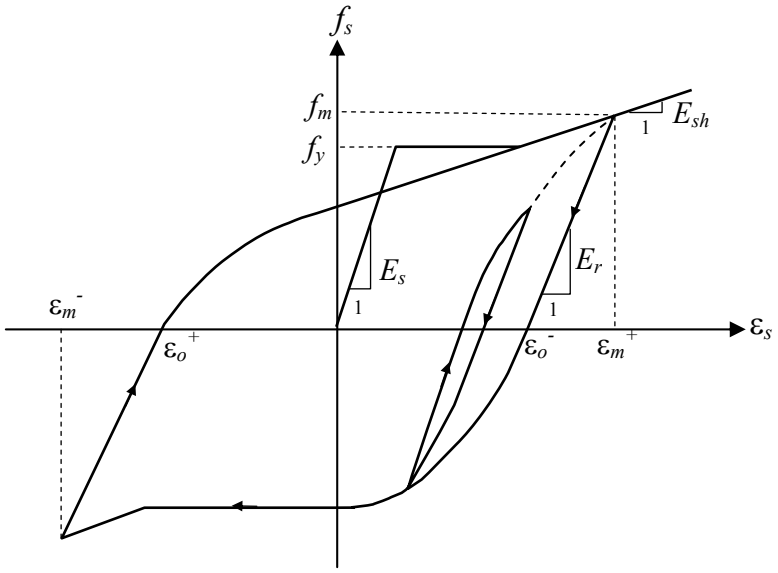


**Figure 5.15** Seckin Model with Bauschinger Effect (Vecchio, 1999)

$$f_{si} = f_{si-1} + E_r \times (\varepsilon_i - \varepsilon_{i-1}) \tag{5.56}$$

where $E_r$ is the linear unloading modulus as defined below:

$$E_r = E_s \quad if \quad (\varepsilon_m - \varepsilon_o) < \varepsilon_y \tag{5.57}$$

$$E_r = E_s \times \left( 1.05 - 0.05 \times \frac{\varepsilon_m - \varepsilon_o}{\varepsilon_y} \right) \quad if \ \ \varepsilon_y < \left( \varepsilon_m - \varepsilon_o \right) < 4 \times \varepsilon_y \tag{5.58}$$

$$E_r = 0.85 \times E_s \quad if \ \left( \varepsilon_m - \varepsilon_o \right) > 4 \times \varepsilon_y \tag{5.59}$$

$f_{si-1}$ and $\varepsilon_{i-1}$ are the stress and strain in the bar at the previous load step, $\varepsilon_m$ is the maximum strain attained during previous cycles, and $\varepsilon_s^{\ p}$ is the plastic offset strain.

Following a nonlinear path, *reloading* to a strain of $\varepsilon_i$ results in reinforcement stress $f_{si}$ as follows:

$$f_{si} = E_r \times (\varepsilon_i - \varepsilon_o) + \frac{E_m - E_r}{N \times \left( \varepsilon_m - \varepsilon_o \right)^{N-1}} \times \left( \varepsilon_i - \varepsilon_o \right) \tag{5.60}$$

where *N* is a power term which defines the degree of nonlinearity as follows:

$$N = \frac{\left( E_m - E_r \right) \times \left( \varepsilon_m - \varepsilon_s^{\ p} \right)}{f_m - E_r \times \left( \varepsilon_m - \varepsilon_s^{\ p} \right)} \tag{5.61}$$

where $f_m$ is the maximum stress corresponding to $\varepsilon_m$, and $E_m$ is the tangent stiffness at $\varepsilon_m$. For the first reversed cycle, $\varepsilon_m$ is taken as zero. Afterwards the formulations are given below are used.

$$E_m = 0 \quad if \ f_m = f_y \tag{5.62}$$

$$E_m = E_s \quad if \ f_m < f_y \tag{5.63}$$

$$E_m = E_{sh} \quad if \ f_m > f_y \tag{5.64}$$

In a negative cycle, the same formulations apply except that $\varepsilon_m$ is the maximum negative strain previously attained. The stress $f_m$ and the stiffness $E_m$ are calculated accordingly.

In the implementation of this model into VecTor5, five parameters were required to be stored in computer memory for each longitudinal reinforcing and prestressing layer present. These were the maximum positive and negative strains attained $\varepsilon_m^+$ and $\varepsilon_m^-$, the reinforcement stress and strain in the previous load or time step $f_{s_{i-1}}$ *and* $\varepsilon_{s_{i-1}}$, and the plastic offset strain corresponding to zero stress $\varepsilon_s^p$ which is redefined whenever the stress passes through zero.

In Chapter 8, a number of previously tested reinforced concrete beams were analyzed under the free-falling drop-weights to verify the developed analytical tool for the dynamic loading conditions. It was noted, during these analyses, that the bottom reinforcement plastic offset strains, at the midspan, recovered under low strain reversals when the Seckin model with Bauschinger effect was used. This caused the residual midspan displacement of the beams to recover slightly, which was not observed during the experimental study of Saatci (2007). Details of this occurrence are presented in Section 8.4.

**Elastic-Plastic Hysteresis Models**

Neglecting the Bauschinger effect, two elastic-plastic reinforcement hysteresis models are implemented into the sectional calculation algorithm as alternative options. The first one includes strain hardening effects while the second one considers a bilinear response only. These options are not generally recommended for cyclic and reversed-cyclic analysis purposes as neglecting the Bauschinger effect may lead to the overestimation of the stress in the reinforcement. However, for special investigative purposes, those options may be useful.

### 5.4.4.2 Stress-Strain Model for Transverse Reinforcement

In the sectional calculations formulated in Chapter 3, the plastic offset strains $\varepsilon_{yi}^p$ were incorporated into the total strains experienced by each smeared transverse reinforcement component present in each concrete layer as defined by Eq. 3.100.

As explained in Chapter 3, in the both shear-stress and shear-strain-based calculation procedures, the strain $\varepsilon_y$ in the transverse direction is the unknown which is determined iteratively during the sectional calculations performed for each layer in each global frame analysis iteration. In these iterations, the transverse reinforcement stresses are also needed. Therefore, implementation of the Seckin Model with Bauschinger effects would increase computational intensity, thereby increasing the analysis time. The Bauschinger effect in the transverse direction is usually not a significant mechanism as the strain reversals for members primarily occur along their longitudinal axis. Therefore, the elastic-plastic hysteresis model with strain hardening effect is implemented for the stress calculation of the smeared transverse reinforcement, i.e. stirrups or ties.

### 5.4.4.3 Verification Example

To illustrate the reinforcement responses produced by the three models implemented, an example analysis was carried out. The structure analyzed consisted of a one-member cantilever reinforced concrete column with the geometric details given in Figure 5.16. Inducing axial effects only, loading was applied at the top node of the column in a displacement-controlled mode as shown in Figure 5.8. The purpose of the analysis was to obtain the stress-*total* strain response of the longitudinal reinforcement under cyclic and reversed-cyclic loading conditions.

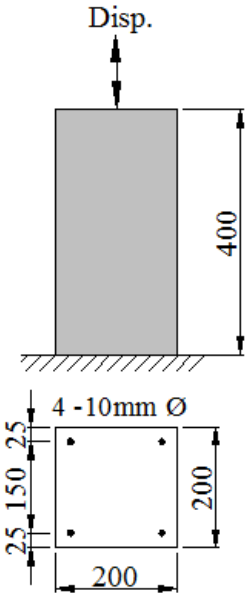


**(a)**

| Concrete | | | |
|---|---|---|---|
| $f'_c$ (MPa) | $f_t$ (MPa) | $\varepsilon_0$ (x $10^{-3}$) | $E_c$ (MPa) |
| 30 | 5 | 2 | 30000 |

| | Reinforcement | | | | | | |
|---|---|---|---|---|---|---|---|
| | $A_s$ ($mm^2$) | $d_b$ (mm) | $f_y$ (MPa) | $f_u$ (MPa) | $E_s$ (MPa) | $E_{sh}$ (MPa) | $\varepsilon_{sh}$ (x $10^{-3}$) |
| **10m Ø** | 78.5 | 10 | 400 | 550 | 200000 | 3000 | 4.0 |

**(b)**

**Figure 5.16** A Cantilever Column: **(a)** Model; **(b)** Material Properties

The responses produced by the Seckin model with Bauschinger effect are presented in Figure 5.17 for the cyclic and reversed-cyclic loading conditions. The significance of the Bauschinger effect is clearly visible especially in the cyclic loading response of Figure 5.17(b). At each strain reversal, the yield stress of the bar decreases significantly. This decrease becomes more pronounced as the maximum total strain previously attained by the reinforcement increases. Therefore, the Bauschinger effect should be expected to be a significant mechanism for flexure-dominated structures subjected to large strain excursions within a cyclic loading condition.

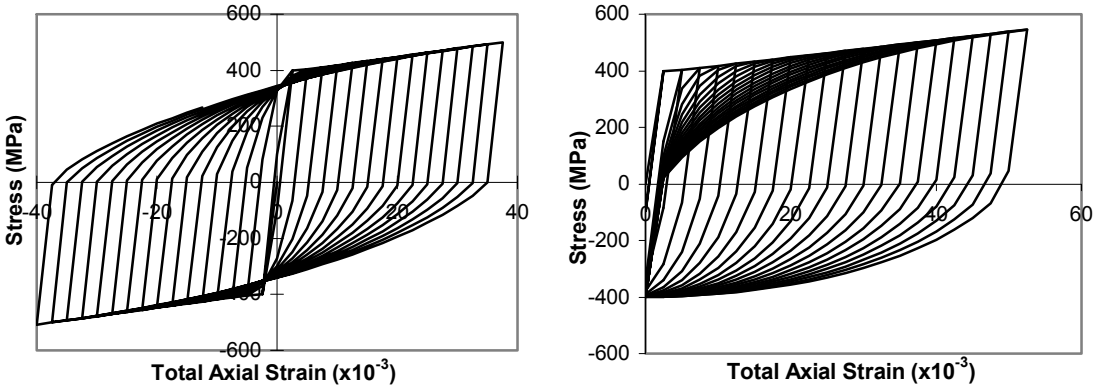


**Figure 5.17** Reinforcement Response of the Cantilever Column using Seckin Model with Bauschinger under **(a)** Reversed-Cyclic; **(b)** Cyclic Loading

The responses produced by the elastic-plastic model with strain hardening are presented in Figure 5.18 for the cyclic and reversed-cyclic loading conditions. As compared to the responses of Figure 5.17, it is clear that larger reinforcement stresses are returned upon unloading from the tensile backbone or compressive backbone. Therefore, overestimation of reinforcement stresses should be anticipated when using this model.

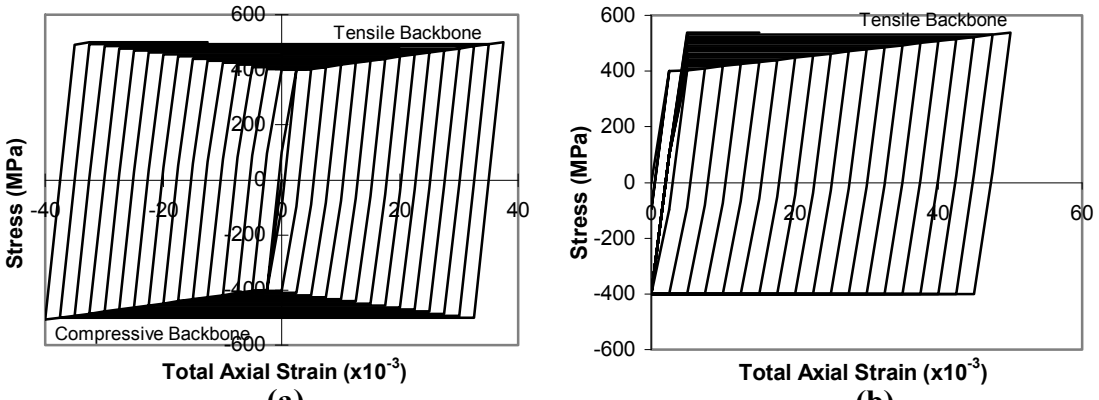


**Figure 5.18** Reinforcement Response of the Cantilever Column using Elastic-Plastic Model with Strain Hardening under **(a)** Reversed-Cyclic; **(b)** Cyclic Loading

The responses produced by the elastic-plastic model are presented in Figure 5.19 for the cyclic and reversed-cyclic loading conditions. As expected, after the yielding strain, the same yield stress is returned until the rupture strain of the reinforcement is reached.

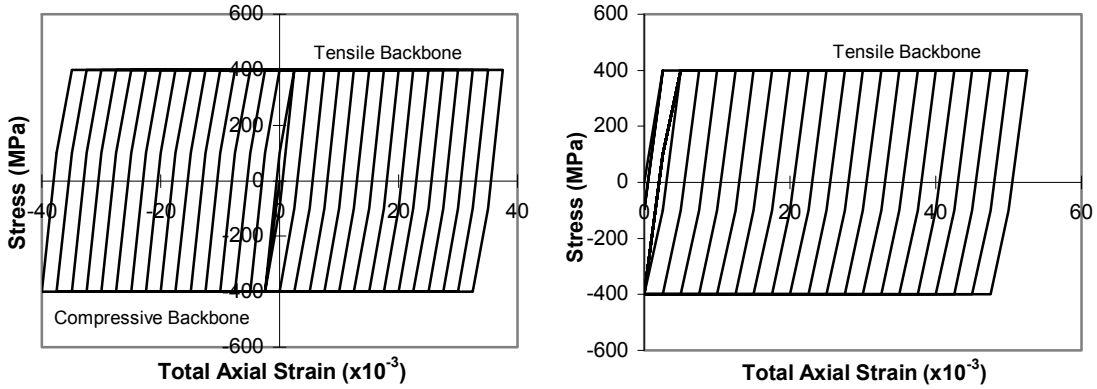


**(a)** **(b)**

**Figure 5.19** Reinforcement Response of the Cantilever Column using Elastic-Plastic Model under **(a)** Reversed-Cyclic; **(b)** Cyclic Loading

# CHAPTER 6

## GENERAL LOADING: VERIFICATION & APPLICATIONS

### 6.1 Chapter Layout

This chapter discusses the application of the nonlinear analysis procedure developed for general loading conditions to previously tested structures with the aim of verifying the newly implemented algorithms. Important considerations in the nonlinear modelling are also discussed through the use of practical examples, with the aim of providing guidelines for general modelling applications.

The structures considered include one large-scale frame structure tested by Duong et al. (2007), two full-scale exterior beam-column subassemblies tested by Seckin (1981), two 1/2-scale interior beam-column subassemblies tested by Shiohara and Kusuhara (2006), and six 1/3-scale shear walls tested by Oesterle at al. (1976). All of the tests were performed under a prescribed reversed-cyclic loading regime.

The chapter starts with a short discussion on the limitations of the analytical procedure, especially regarding the detailed local analyses of beam-column subassemblies. It is then followed by a description of the modelling of the test specimens.

The coverage of each experimental study considers the following steps. The test structure is first introduced, giving the structural details required for the modelling. This is then followed by the modelling and analysis details of the structures. Afterwards, the resulting responses are compared to the experimental responses for load-deflection response, axial deformation response, reinforcement strains, crack widths, displacement ductility and total energy dissipation. Discussions regarding the comparisons are finally presented.

## 6.2 Limitations of the Analytical Procedure

As discussed in detail in Chapter 3, the nonlinear analysis procedure developed depends on two interrelated analyses: global frame analyses and sectional analyses. The main framework of the calculation is performed through the global frame analysis, which assumes 1D frame members. As is established for frame analyses of this type, the structural model is created using the centreline dimensions of the structure. However, in a typical beam-column connection of a reinforced concrete frame structure, a significant 2D overlapping of the beam and column members occurs (see shaded area in Figure 6.1(a)). This overlapping region is generally called the beam-column joint panel zone, which in general exhibits stiffer behaviour as compared to the connecting beams and columns.

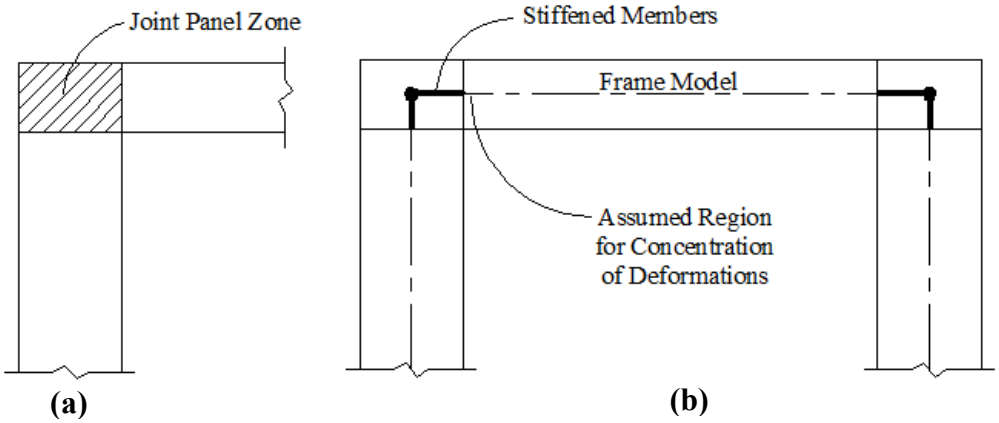


**Figure 6.1 (a)** A Beam-Column Connection; **(b)** Frame Model of a Structure Consisting of 1D Frame Members

Because it is not possible to simulate such a 2D zone with 1D frame members, the assumption of stiffened joint members is usually made to account for the stiffening effects of the joint panel zone (Figure 6.1(b)). Through such an assumption, the deformations are diverted to the adjacent beam and column ends with the stiffened members behaving rigidly. Consequently, when performing nonlinear analyses based on this approach, the cracking and damage, whether shear or flexural in nature, occurs at the faces of the beams and columns rather than in the joint panel zone. This approach is generally in agreement with the behaviour of well-designed structures which have joints with sufficient confinement and proper reinforcement detailing stipulated by modern

design codes. However, for structures with improper reinforcement detailing or insufficient confinement in the joint panel zone, significant joint deformations and resulting damage may occur. The analysis of such a structure with the analytical procedure developed will most likely predict damage occurring at the face of the joint panel zone with stiffer and less pinched behaviour compared to the real behaviour.

In this sense, the analytical tool developed is more suitable for the global analyses of large frame structures, rather than detailed local analyses of beam-column joints. It is advisable to inspect the reinforcement detailing in the joint panel zone to make sure that the detailing practice used is appropriate. In the case of unusual or improper detailing, or in cases where analysis results indicate possible joint distress, a detailed nonlinear finite element analysis (NLFEA) of the joint should be undertaken. The sectional forces determined by VecTor5 are an important asset for such analyses. A detailed discussion of such analyses can be found in Sagbas (2007).

In this chapter, detailed local analyses of four previously tested beam-column subassemblies are undertaken using VecTor5, even though such analyses are not the intended use of the analytical procedure developed. The motivation of those analyses is to thoroughly verify the cyclic analysis formulations implemented into the program because the behaviour of subassemblies under reversed cyclic conditions represents a challenge to nonlinear analyses. For this purpose, four specimens were selected from the literature, all of which experimentally sustained damage occurring predominantly at the face of the joint panel zone. In some of the specimens, however, there was considerable joint cracking present. A discussion of the effect of this cracking in the specimen behaviour is presented in Section 6.5.2 and 6.6.2.

Another limitation of the analytical procedure developed is the assumption of perfect bond between the reinforcement and the concrete. However, in beam-column joints under load reversals, there is the possibility of bond slip occurring depending on the reinforcement detailing of the joint panel zone. This phenomenon is reported to be common for exterior connections having inadequately confined joint panel zones (Seckin, 1981). This behaviour is also linked to the cracking of the joint panel zone, which usually

allows for the loss of bond between the reinforcement and the concrete. Analysis of a beam-column subassembly exhibiting bond-slip mechanisms with the analytical procedure developed will most likely overestimate the reinforcement strains of the slipped bars, with a stiffer and less pinched load-deformation response, compared to the experimental response.

Another limitation of the analytical procedure developed is the assumption that the longitudinal reinforcement continues to carry compressive stress until the failure of the member occurs due to the crushing of concrete. However, for members under large compressive strains, there is the possibility of longitudinal reinforcement buckling depending primarily on the confining reinforcement details. A detailed discussion of this mechanism can be found in Bayrak (1998). Analysis of a compression member exhibiting longitudinal reinforcement buckling mechanisms with the analytical procedure developed will most likely overestimate the ductility of the structure compared to the experimental response. Significant overestimation of the strength is not expected as the buckling usually takes place under compressive strains larger than the yield strain.

### 6.3 Analysis Parameters and Material Behaviour Models Used

The default material models and analysis options, which were defined prior to this study and common to all VecTor programs as discussed in Section 4.2, were used throughout this chapter except for the concrete compression base curve. Based on the concrete strength of the tested structure, the concrete compression base curve was selected to be either the default Hognestad formulation or the Popovics formulation. However, if all the analyses were performed with the default Hognestad (Parabola) model, the results would not change noticeably. Such a comparison is given in Section 8.4 (Figure 8.9).

Particularly important for simulations under reversed-cyclic loading conditions is the concrete hysteresis model used. Herein the default option, the Vecchio model with nonlinear unloading is used, even though the Palermo model was reported to be superior in some respects such as energy dissipation (Sagbas, 2007). As the focus of this chapter is to provide reasonable simulations with the use of default material behaviour models and

analysis options, the use of Palermo model was not undertaken. The reason for Palermo model not being the default concrete hysteresis rule is that it usually requires longer computation times owing to its relatively complex calculations. In addition, in some instances, some numerical instability was observed which may reflect on the calculated load-deflection responses. Note the slight numerical instabilities in Figure 5.14 for Palermo model as compared to Figure 5.10 for the default Vecchio model with linear unloading.

## 6.4 Duong Frame

An experimental program was carried out on a large-scale, one-bay and two-storey frame at the University of Toronto to investigate the behaviour of shear-critical reinforced concrete frames under seismic loading conditions and to corroborate analytical procedures (Duong et al., 2007). The experiment consisted of two phases. In Phase A, the frame was laterally loaded until significant damage took place in the shear-critical beams and was then unloaded completely. The frame was then loaded in the reverse direction to the same lateral displacement (44 mm) attained in the forward half-cycle. The frame was finally unloaded. In Phase B, the damaged frame was repaired and then tested under reversed cyclic loading conditions.

In Section 4.8, this frame was analyzed under monotonically increasing lateral displacement applied at the second storey beam until the failure of the frame took place. In this section, the same frame model was analyzed under a reversed cyclic loading in a displacement-controlled mode to simulate the loading protocol used in the experiment.

### 6.4.1 Comparison of the Analytical and Experimental Responses

The analytical and experimental net lateral load-deflection responses for the second storey beam are compared in Figure 6.2.

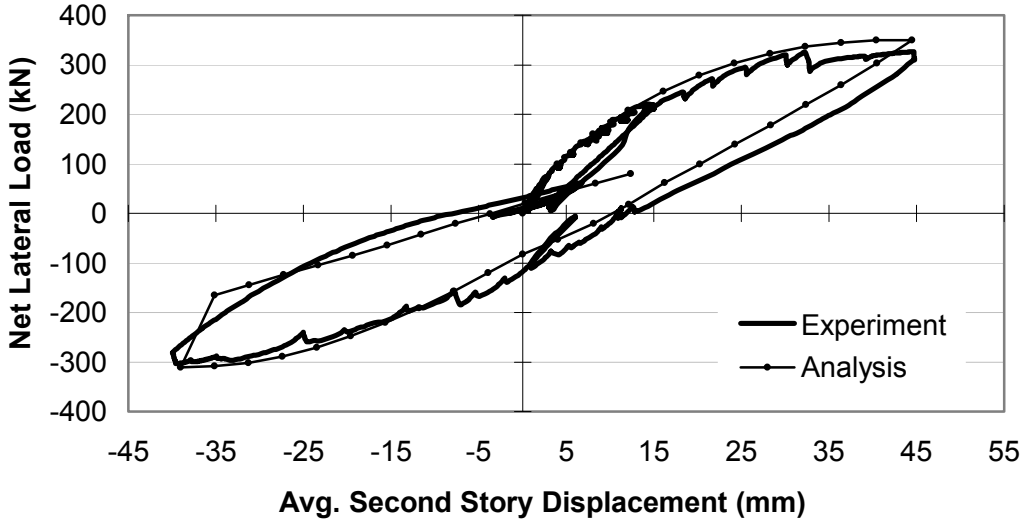


**Figure 6.2** Comparison of Load-Deflection Responses for Duong Frame

As seen in Figure 6.2, the overall response of the frame under cyclic loading was predicted with excellent accuracy. The strength of the frame in the reverse cycle was estimated well at approximately 311 kN. Upon unloading, the residual displacement was calculated with a reasonable 8% underestimation. The total energy dissipated by the frame (i.e., the area under the load-deflection curve) was predicted with excellent accuracy to be 20.9 kNm as compared to the experimental value of 21.0 kNm.

**Table 6.1** Comparison of Analytical and Experimental Results for Duong Frame:
**(a)** Sequence of Events; **(b)** Crack Widths at Ultimate Condition

**(a)**

| | Analysis | Test |
|---|---|---|
| **Residual Disp. (mm)** | 10.5 | 11.3 |
| Lateral Load (kN) causing **First Flexural Cracking** | -30 | -32 |
| Lateral Load (kN) causing **Zero Displacement** | -83 | -111 |
| Lateral Load (kN) causing **First Yielding of Reinf.** | | |
| Beam 1N Longitudinal | 300 | 304 |
| | (96% of yield) | |
| Beam 1N Longitudinal | 300 | 304 |
| | (96% of yield) | |
| Beam 1S Transverse | -230 | -260 |
| Beam 1N Transverse | -250 | -260 |

**(b)**

| | VecTor5 | Test |
|---|---|---|
| **Peak Load (kN)** | -311.4 | -304 |
| **Shear Crack Widths (mm) at the Peak Load** | | |
| Beam 1 Centre | 0.9 | 7.0 |
| Beam 2 Centre | 1.0 | 5.0 |
| Beam 1N | 4.7 | 1.8 |
| Beam 1S | 4.8 | 3.0 |
| Beam 2N | 1.4 | 0.3 |
| Beam 2S | 1.1 | 0.5 |

As shown in Table 6.1(a), the lateral load levels causing the first yielding of several reinforcement components were estimated reasonably well.

The axial deformations of both columns, as determined experimentally and analytically at the top of the columns (second storey level), are compared in Figure 6.3. The first and second storey beam axial deformation responses are presented in Figure 6.4.

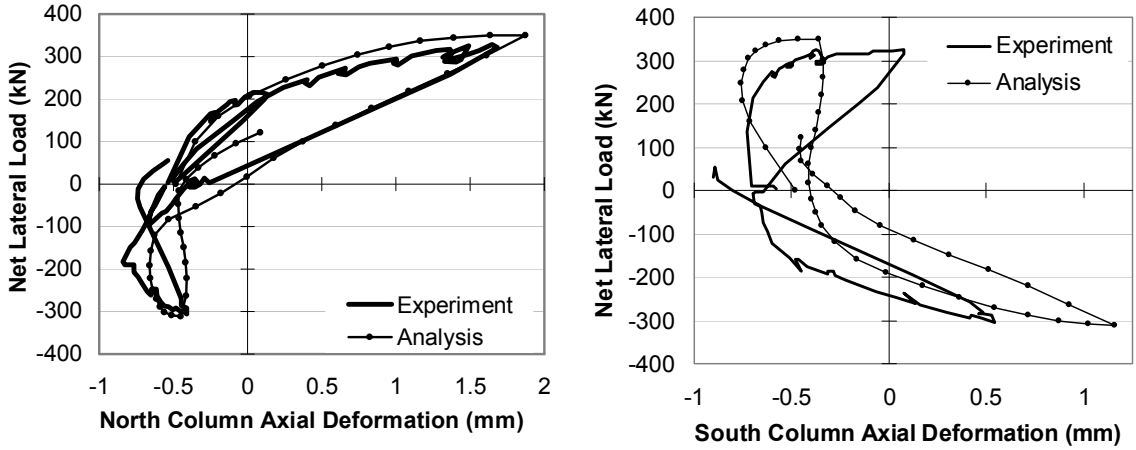


**Figure 6.3** Comparison of Axial Deformation Responses for Duong Frame

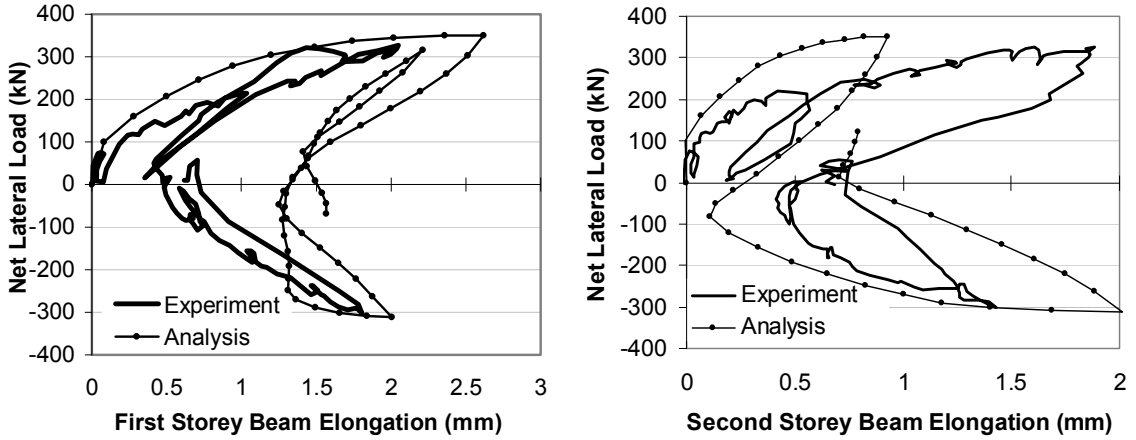


**Figure 6.4** Comparison of Beam Elongation Responses for Duong Frame

As seen from the graphs above, the predicted column and beam axial deformation responses showed reasonably good agreement with the experimental responses. It should be noted, however, that the accurate predictions of such secondary responses are extremely difficult.

As two typical examples, the reinforcement strain responses for Beam 1N and Beam 2S are presented in Figure 6.5 and 6.6.

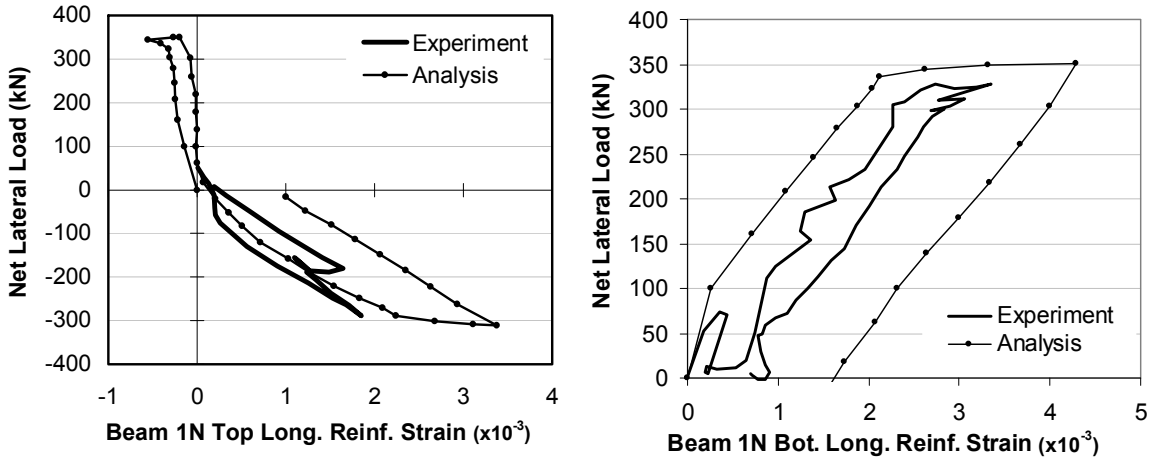


**Figure 6.5** Comparison of First Storey Reinforcement Strain Responses for Duong Frame

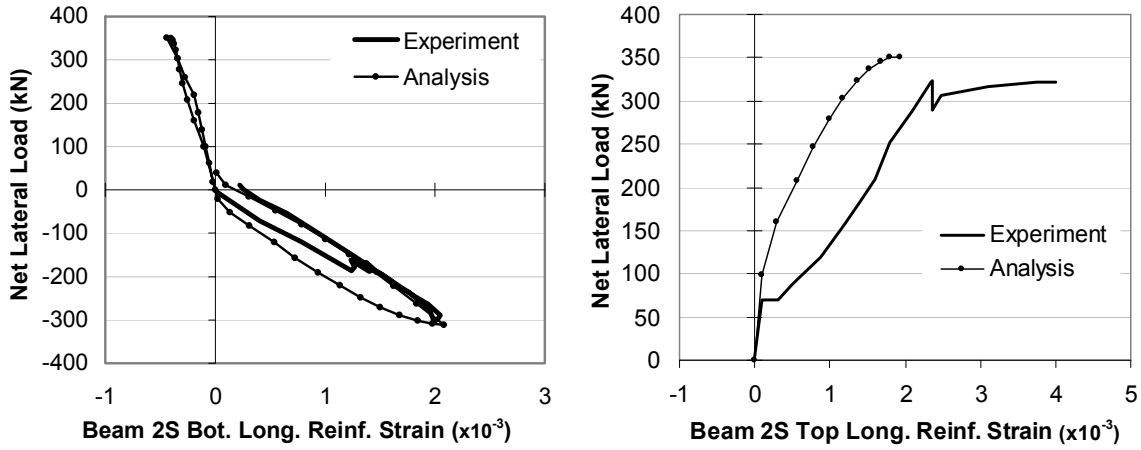


**Figure 6.6** Comparison of Second Storey Reinforcement Strain Responses for Duong Frame

In the experiment, the damage mode of the frame in the reverse half-cycle was shear-dominated, with significant damage to the *central* portion of the first storey beam as shown in Figure 6.7.

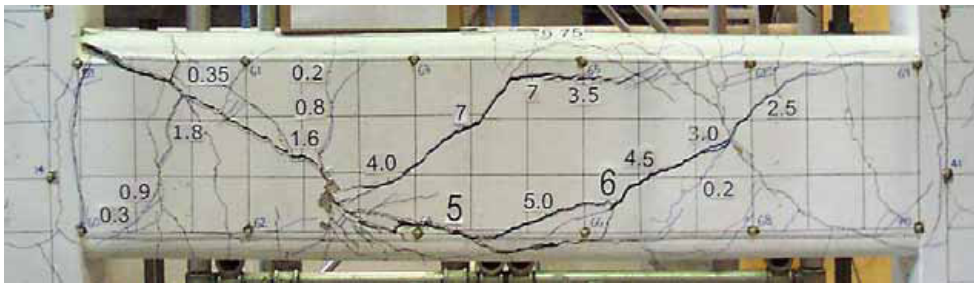


**Figure 6.7** View of the First Storey Beam at a Lateral Deflection of -40 mm (Duong, 2006)

In the analytical study, shear failures at *both ends* of the first storey beam (beam 1N and beam 1S in Figure 4.27(b)) occurred at a lateral displacement of -40 mm. In Figure 6.2, the drop in the load capacity from 311 kN to 165 kN occurred due to these failures. Shear cracking in the central portion of the first storey beam was insignificant in the analytical study as compared to the cracking of the beam ends (Table 6.1(b)). In this regard, the crack widths corresponding to the failure condition of the frame showed discrepancies as compared to the experimental crack widths.

## 6.5 Seckin Exterior Beam-Column Subassemblies

A test program was carried out at the University of Toronto, involving full-scale exterior beam-column subassemblies, to investigate the influence of a number of parameters on the subassembly behaviour. These parameters included the amount and placement of the confining reinforcement inside and outside the joint panel region, load protocol, physical properties of the materials, and geometric proportions of the connecting beams and columns. The subassemblies were dimensioned to represent exterior beam-column joints of a moment resisting frame having spans of 6.10 m (20 ft) with a storey height of 3.05 m (10 ft). Specimens SP6 and SP7, with damage modes occurring outside the joint panel regions, were selected for analysis with the developed analytical procedure.

### *Details of Specimens and Test Setup*

Specimen SP6 and SP7 had identical details, as shown in Figure 6.8, with two exceptions: the amount of tie reinforcement inside the joint panel region, and the material properties. The tie spacing in the joint panel region was 44.5 mm (1.75 in) for Specimen SP6 and 76.3 mm (3 in) for Specimen SP7. The material properties are listed in Table 6.2.

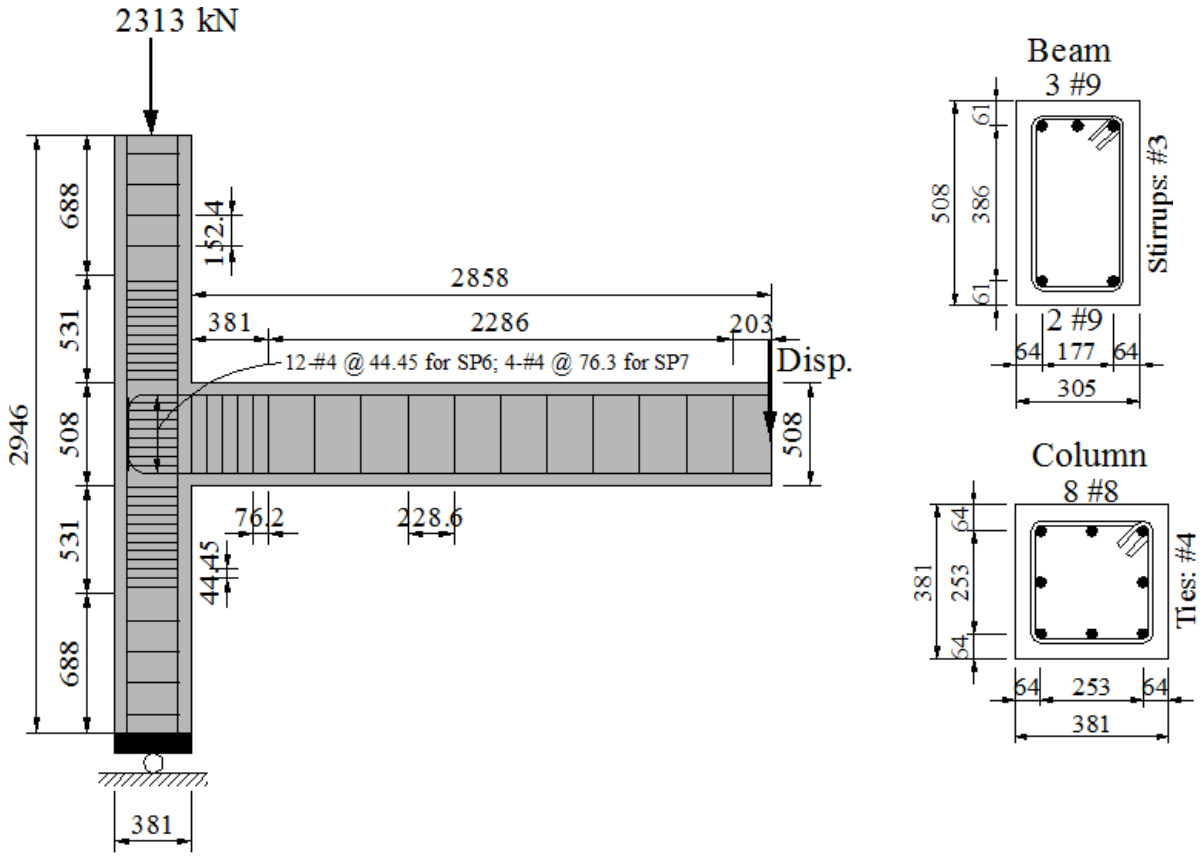


**Figure 6.8** Structural Details of Subassemblies SP6 and SP7

**Table 6.2** Material Properties of Subassemblies SP6 and SP7

| | Reinforcement | | | | | | |
|---|---|---|---|---|---|---|---|
| | $d_b$ (mm) | $f_y$ (MPa) | $f_u$ (MPa) | $E_s$ (MPa) | $E_{sh}$ (MPa) | $\varepsilon_{sh}$ (x $10^{-3}$) | $\varepsilon_u$ (x $10^{-3}$) |
| **#3** | 9.5 | 427 | 759 | 170000 | 7814 | 2.51 | 45 |
| **#4** | 12.7 | 362 | 552 | 170000 | 1199 | 12.5 | 171 |
| **#8** | 25.4 | 335 | 552 | 170000 | 3191 | 6 | 74 |
| **#9** | 28.7 | 350 | 621 | 170000 | 3031 | 11 | 100 |

| | Concrete | | |
|---|---|---|---|
| | $f'_c$ (MPa) | $\varepsilon_0$ * (x $10^{-3}$) | $E_c$ * (MPa) |
| **SP6 Beam &Joint** | 36.2 | 2.69 | 26875 |
| **SP6 Column** | 37.7 | 2.76 | 27285 |
| **SP7** | 30.8 | 2.43 | 25325 |

* estimated

In Table 6.2, the reinforcement properties shown were estimated from the steel coupon test results reported by Seckin (1981). As only the concrete strengths $f'_c$ were reported, the elastic modulus of the concrete $E_c$ was calculated using Eq. 4.4, and the strain $\varepsilon_o$ was determined based on the Hognestad (Parabola) using Eq. 6.1.

$$\varepsilon_0 = \frac{2 \times f'_c}{E_c} \tag{6.1}$$

The testing of the subassemblies involved the application of a vertical force at the tip of the beams in a displacement-controlled mode, and a constant axial force of 2313 kN at the top of the columns. No attempts were reportedly made to follow a prescribed loading program in terms of the applied beam tip force. Decisions about the loading were made on the basis of the specimen behaviour and appearance. The resulting beam tip deflection histories are presented in Figure 6.9.

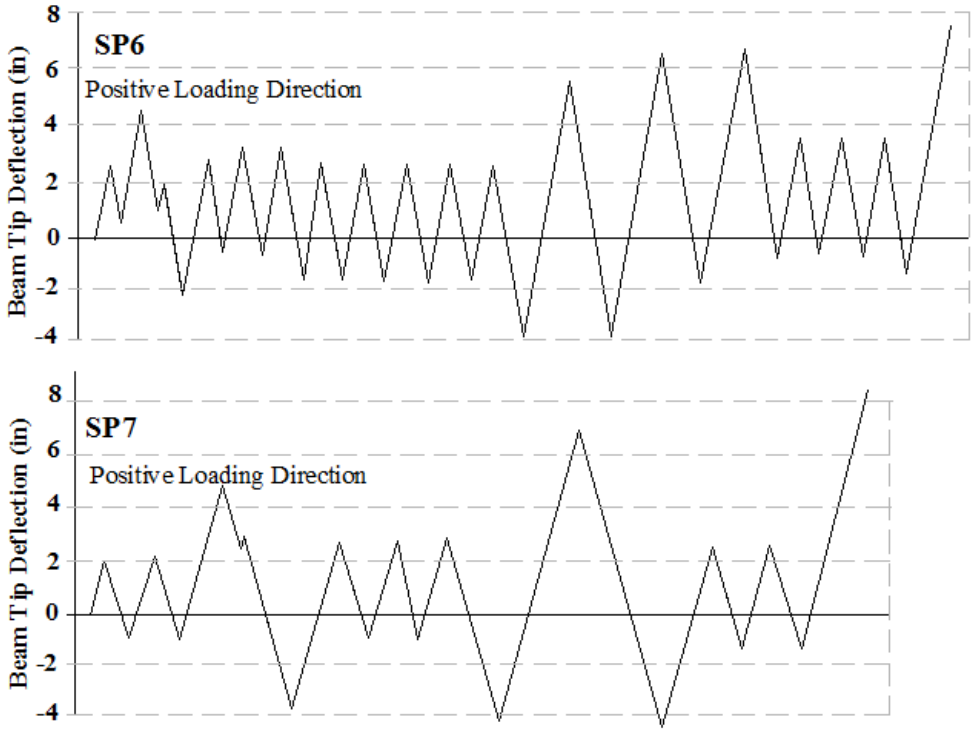


**Figure 6.9** Loading Program Applied to Subassemblies SP6 and SP7 (Seckin, 1981)

### 6.5.1 Analytical Modelling

The specimens were modelled with varying lengths of segments in the range of one half of the cross section depths, as shown in Figure 6.10(a). Three member types were used to represent the beam sections: MT1, MT2 and MT3. Two member types were defined for the column sections: MT4 and MT5. To create members within the beam-column joint zone, MT6 and MT7 were defined by doubling the reinforcement ratios of MT5 and MT1, respectively (Figure 6.12). As mentioned before, due to the use of one-dimensional frame members, the accurate modelling of joint panel zones is not possible; therefore,

joint-panel zone members were created with stiffer sections to represent the relatively stiff behaviour of the joint.

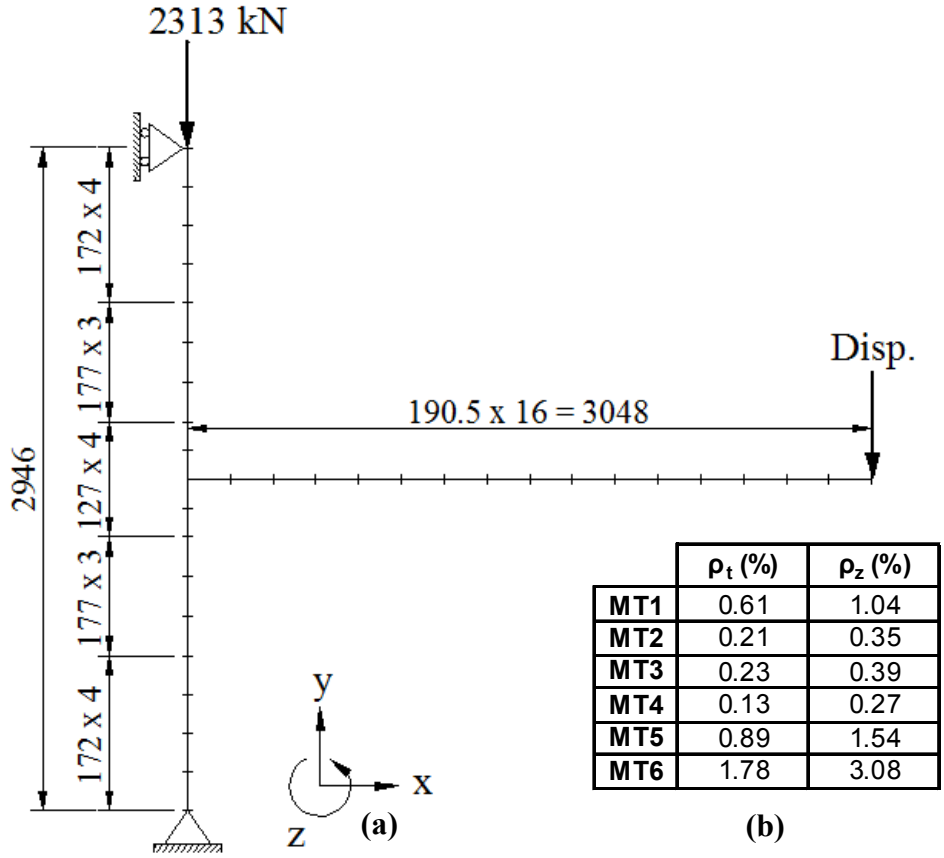


| | $\rho_t$ (%) | $\rho_z$ (%) |
|---|---|---|
| **MT1** | 0.61 | 1.04 |
| **MT2** | 0.21 | 0.35 |
| **MT3** | 0.23 | 0.39 |
| **MT4** | 0.13 | 0.27 |
| **MT5** | 0.89 | 1.54 |
| **MT6** | 1.78 | 3.08 |

**Figure 6.10 (a)** Analytical Model Showing Segment Lengths, Loading and Support Restraints for Subassemblies SP6 and SP7; **(b)** Smeared Reinforcement Ratios for the Member Types Used

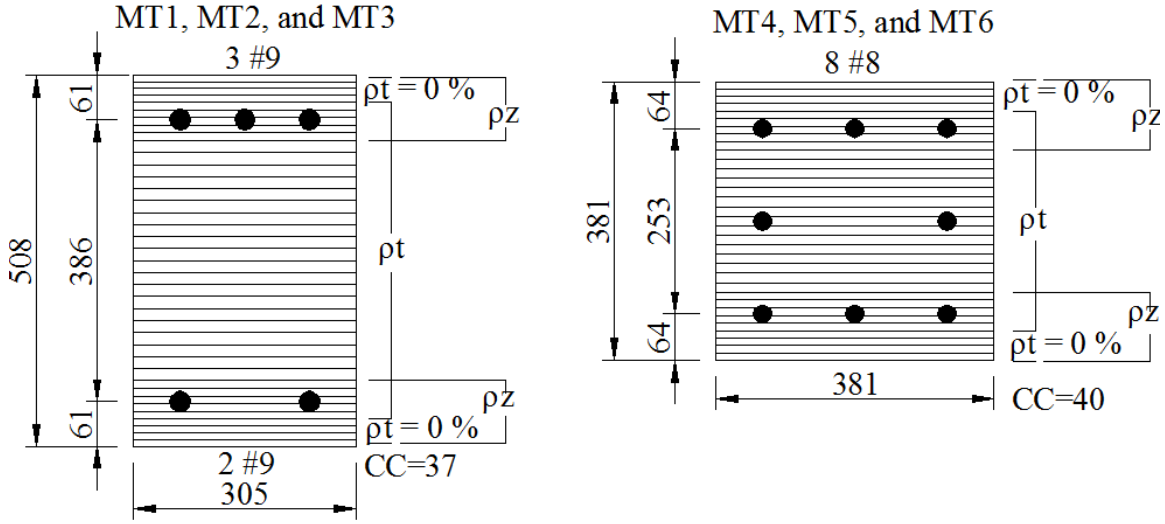


**Figure 6.11** Sectional Models for Member Types of Subassemblies SP6 and SP7

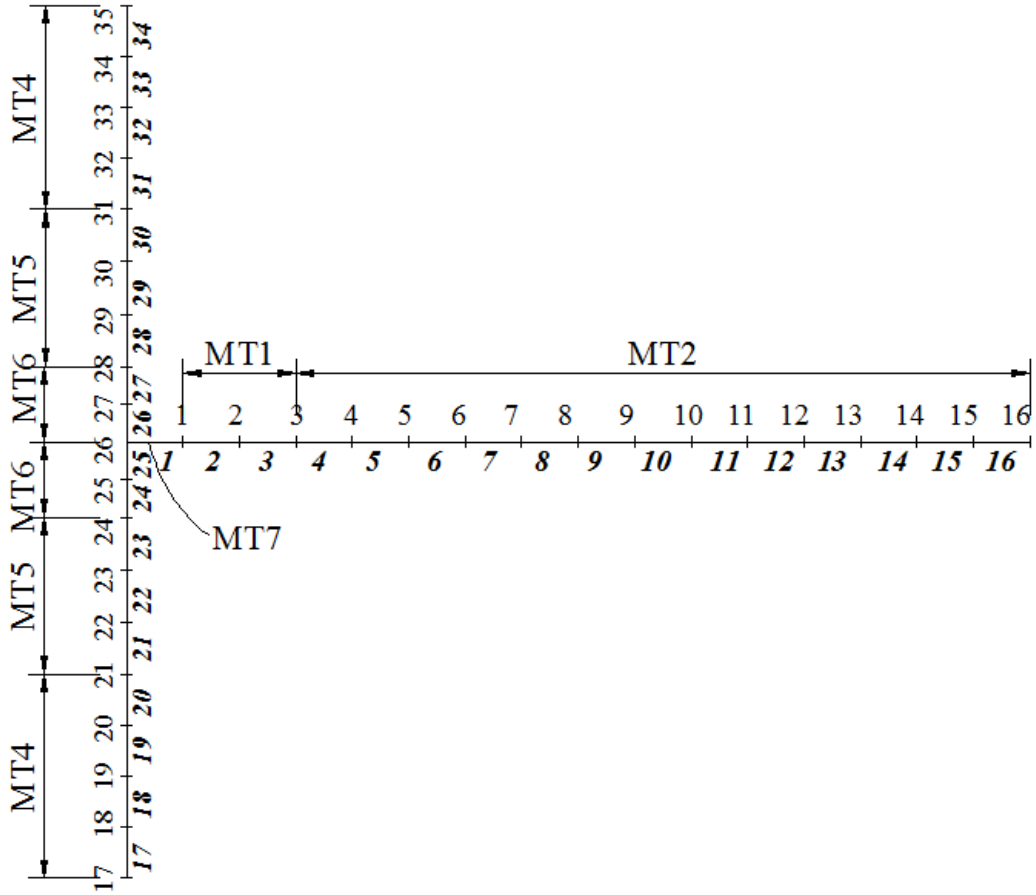


**Figure 6.12** Analytical Model Showing Member Types for Subassemblies SP6 and SP7

As presented in Figure 6.11, 38 concrete layers (9.25 mm x 4, 10.6 mm x 5, 16.4 mm x 20, 10.6 mm x 5, and 9.25 mm x 4) were used for MT1, MT2 and MT 3 with the reinforcement ratios listed in Figure 6.10(b). Similarly, 36 concrete layers (10 mm x 11, 11.5 mm x 14, and 10 mm x 11) were used for MT4, MT5 and MT6.

All default material behaviour models were used in the analysis including the default concrete compression base curve (Hognestad) as described in Section 6.3. The support conditions were represented by restraining both the x- and y-degrees of freedom of Node 17 and by restraining only the x-degree-of-freedom of Node 35. Two load cases were defined: a constant axial load applied at Node 35, and a beam tip displacement applied at Node 16. The highly irregular beam tip displacement history was handled through the use of seed files, in which the analyses had to be stopped several times to redefine the beam tip displacement required for the next cycle.

### 6.5.2 Comparison of the Analytical and Experimental Responses

The analytical and experimental beam tip load-beam tip deflection responses are compared in Figure 6.13.

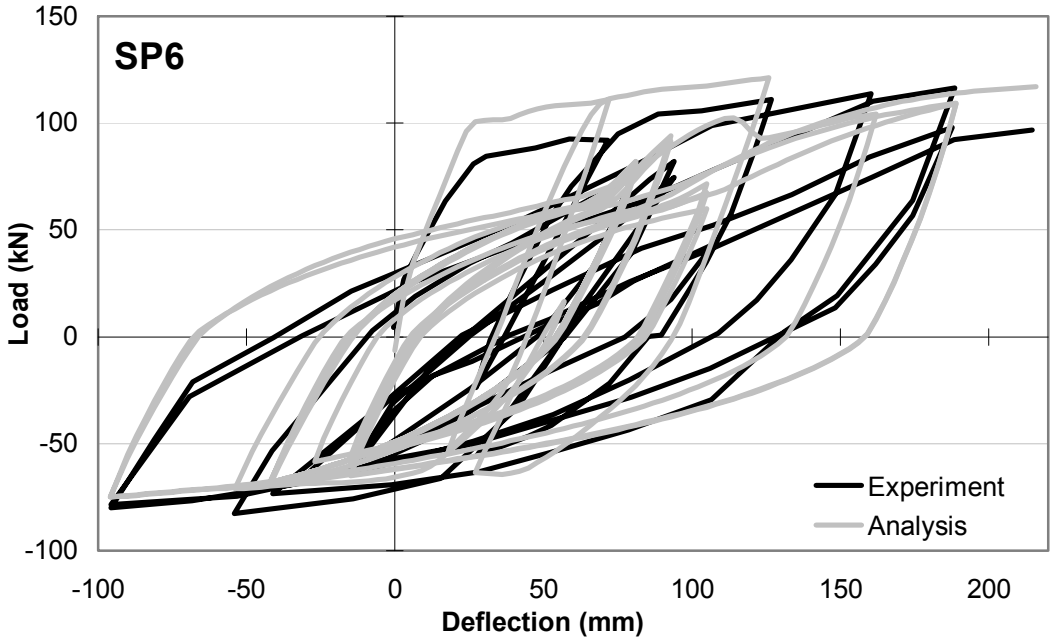


**Figure 6.13** Comparison of Load-Deflection Responses for Subassembly SP6

As seen from Figure 6.13, the overall behaviour of the subassembly was predicted well. The degradation of the strength under large displacement reversals was captured reasonably well. Note the degradation of the analytical response after a deflection of 126 mm; this degradation occurred even though the default concrete hysteresis rule (Vecchio model with nonlinear unloading), which does not consider strength degradation, was used. The strength degradation was caused by excessive flexural crack widths being reached. It is known that the compressive strength of concrete is adversely affected by transverse cracking. To take this behaviour into account, a material behaviour model, termed the crack width limit, is embodied into the VecTor programs as a default behaviour model (Vecchio, 2000). This algorithm reduces the strength of concrete based on the cracks widths. In this analysis, with the crack widths of Member 2 reaching approximately 5.0 mm, the strength was reduced, causing a noticeable degradation in the overall response of the subassembly.

The pinching characteristics of the experimental response were also captured reasonably well with a slight underestimation. The reduction in the reloading stiffness of the subassembly under increasing strain reversals is apparent from Figure 6.13. A more detailed comparison of the predicted and observed parameters is listed in Table 6.3.

**Table 6.3** Comparison of Analytical and Experimental Results for Subassembly SP6

| | Analysis | | Test | | |
|---|---|---|---|---|---|
| **SP6 Positive Loading** | **Disp (mm)** | **Shear (kN)** | **Disp (mm)** | **Shear (kN)** | **Ratio** |
| Beam Reinf. First Yielding | 24.4 | 101.0 | 25.7 | 84.0 | |
| Max Story Shear | 126.0 | **121.4** | 188.6 | **116.5** | **1.04** |
| Displacement Ductility | 7.7 | | 7.3 | | 1.05 |
| Energy Dissipation (kNm) | 119.6 | | 93.8 | | 1.27 |
| **SP6 Negative Loading** | | | | | |
| Beam Reinf. First Yielding | 28.2 | -61.0 | 33.3 | -60.0 | |
| Max Story Shear | -96.0 | **-75.0** | -54.0 | **-82.6** | **0.91** |
| Displacement Ductility | 3.4 | | 2.9 | | 1.18 |
| Energy Dissipation (kNm) | 81.7 | | 78.3 | | 1.04 |

As is apparent from Table 6.3, the loads causing the first yielding of the beam reinforcement, the strengths, and the ductilities in both the positive and negative loading directions are all predicted reasonably well. The displacements at the maximum storey shears were predicted with some discrepancies. This was mainly caused by the near flat-top of the load deflection response, thus making it prone to large errors in estimating the displacements at the peak load. The total energy dissipated, analytically and experimentally, was calculated as the area under the load-deflection curves. A relatively large predicted-to-observed ratio of 1.27 was obtained for the positive loading direction. This is mainly caused by the overestimation of strength in the first two positive cycles by approximately 18% (16 kN), which translated into large areas in the energy dissipation calculation. Note that the self-weight of the subassembly was neglected in the analysis. Consideration of the approximately 11 kN self-weight of the beam would reduce this overestimation significantly. The total energy dissipated in the negative loading direction, on the other hand, was calculated accurately.

In the experiment, the primary damage mode involved flexural plastic hinging in the beam section close to the joint panel region. A similar damage mode involving Member 2 was predicted analytically. At the last load stage (+125 mm), the member suffered flexural cracks of widths as great as 10 mm, with tensile straining in the longitudinal

reinforcement reaching +35.5 x $10^{-3}$. Due to high compression forces, the members forming the column were essentially uncracked.

Displacement ductilities were calculated as the ratio of the maximum displacement attained by the structure to the yield displacement, $\delta_y$. The yield displacements were consistently estimated through the use of the effective yield point approach of Christopoulos and Filiatrault (2006). An example showing the determination of the effective yield displacements under positive and negative loading is given in Figure 6.14.

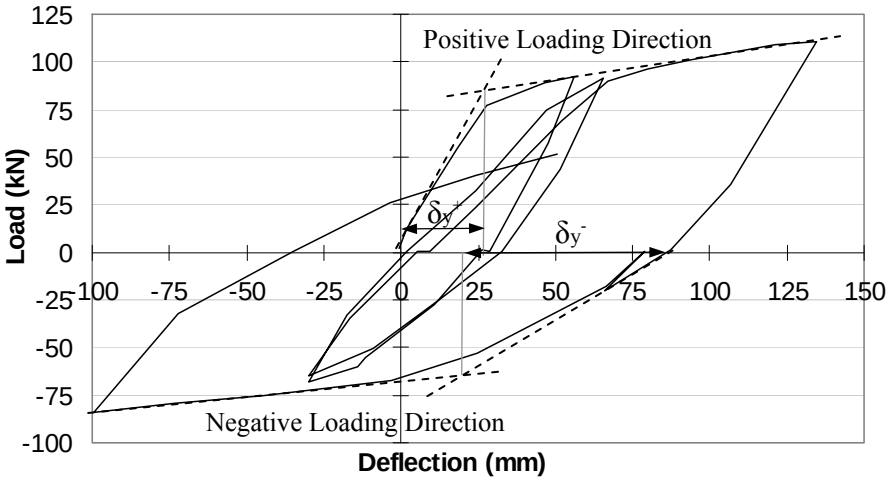


**Figure 6.14** Determination of Effective Yield Displacements

The comparison of the load-deflection responses for SP7 is presented in Figure 6.15.

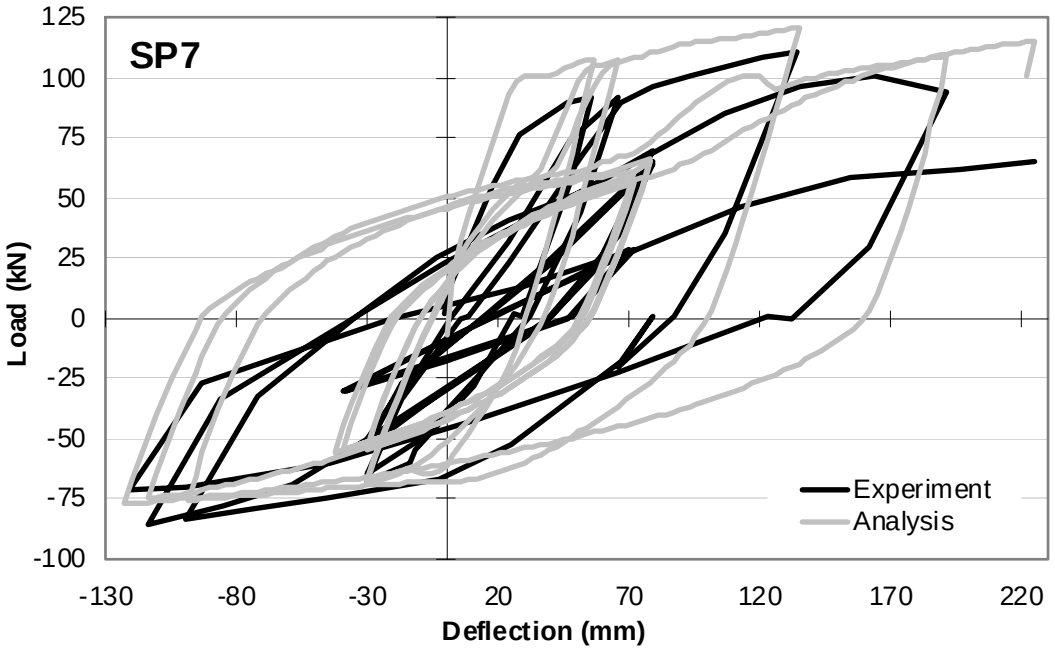


**Figure 6.15** Comparison of Load-Deflection Responses for Subassembly SP7

The overall behaviour of this subassembly was predicted less accurately as compared to Specimen SP6. The same discussion applies to this specimen regarding the strength degradation which was mainly caused by the excessive flexural crack widths sustained. The pinching behaviour observed in the experiment was predicted only marginally well. The reasons for this relate to the joint damage and, more importantly, to bond slip of the top longitudinal beam reinforcement as reported by Seckin (1981). In the analytical model, perfect bond is assumed, resulting in stiffer responses under load reveals compared to the experimental response. Joint cracking in the experiment also contributed to this underestimation (Figure 6.16). A more detailed comparison of the several parameters is listed in Table 6.4.

**Table 6.4** Comparison of Analytical and Experimental Results for Subassembly SP7

| **SP7 Positive Loading** | **Analysis** | | **Test** | | |
|---|---|---|---|---|---|
| | **Disp (mm)** | **Shear (kN)** | **Disp (mm)** | **Shear (kN)** | **Ratio** |
| Beam Reinf. First Yielding | 26.1 | 102.0 | 32.6 | 87.7 | |
| Max Story Shear | 135.0 | **121.6** | 135.0 | **110.5** | **1.10** |
| Displacement Ductility | 7.3 | | 5.9 | | 1.25 |
| Energy Dissipation (kNm) | 79.7 | | 59.4 | | 1.34 |
| **SP7 Negative Loading** | | | | | |
| Beam Reinf. First Yielding | 53.2 | -61 | 61.1 | -60 | |
| Max Story Shear | -123.0 | **-77.4** | -114.4 | **-86.0** | **0.90** |
| Displacement Ductility | 2.3 | | 2.0 | | 1.15 |
| Energy Dissipation (kNm) | 52.6 | | 39.8 | | 1.32 |

The peak load capacity of the subassembly was predicted with reasonable accuracy in both loading directions. The beam reinforcement in the modelled structure typically yielded at a lower displacement than it did in the experiment. This was again caused by the bond slip, which seemingly reduced the deformation of the reinforcement. The total energy dissipation estimates showed some discrepancies stemming from the overestimation of strength in the first two positive cycles by approximately 14% (13 kN) and the less pinched behaviour of the analytical model. Note that the self-weight of the subassembly was neglected in the analysis. Consideration of the approximately 11 kN self-weight of the beam would reduce the overestimation in the first two positive cycles significantly.

Similar to Specimen SP6, a damage mode involving flexural plastic hinging of the beam close to the beam-column panel zone was obtained both in the analysis and in the experiment.

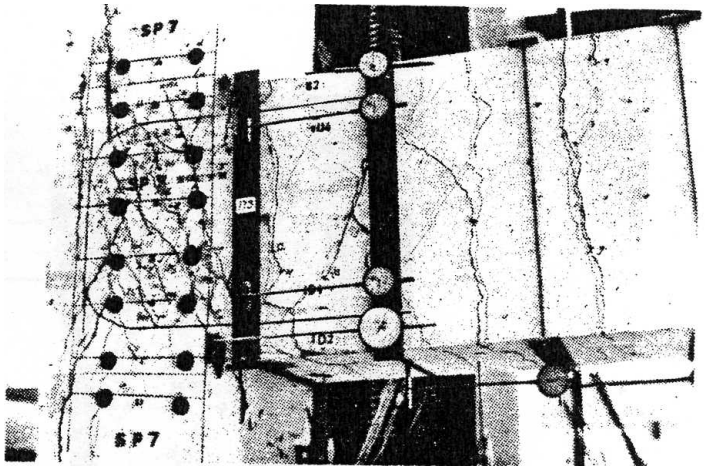


**Figure 6.16** Condition of Specimen SP7 at the End of the Experiment (Seckin, 1981)

### 6.6 Shiohara and Kusuhara Interior Beam-Column Subassemblies

A test program was conducted at the University of Tokyo, involving six half-scale beam-column joint subassemblies, as a benchmark test series intended to provide researchers and engineers with reliable test data for validating models and design tools. Specimens A2 and A3, with damage modes occurring outside the joint panel regions, were selected for analysis with the developed analytical procedure.

*Details of Specimens and Test Setup*

Specimen A2 and A3 had identical details except for the application points of the loading as described below (Figures 6.17 and 6.18). It should be noted that half of the beam longitudinal reinforcement was grooved to 75% of its original cross-sectional area for the installation of state-of-the-art measurement devices. The grooved reinforcement was used inside the joint panel zone as well as in the beam at locations within 450 mm from the face of the column. The material properties are listed in Table 6.5, where the reinforcement properties were estimated from the steel coupon test results reported by Shiohara and Kusuhara (2006).

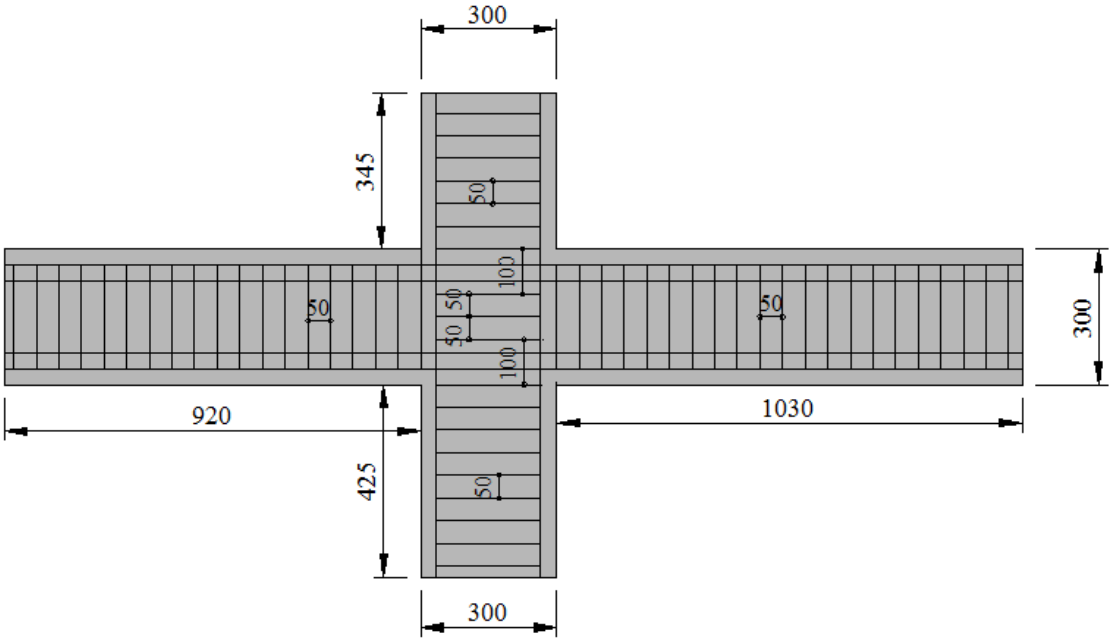


**Figure 6.17** Structural Details of Subassemblies A2 and A3

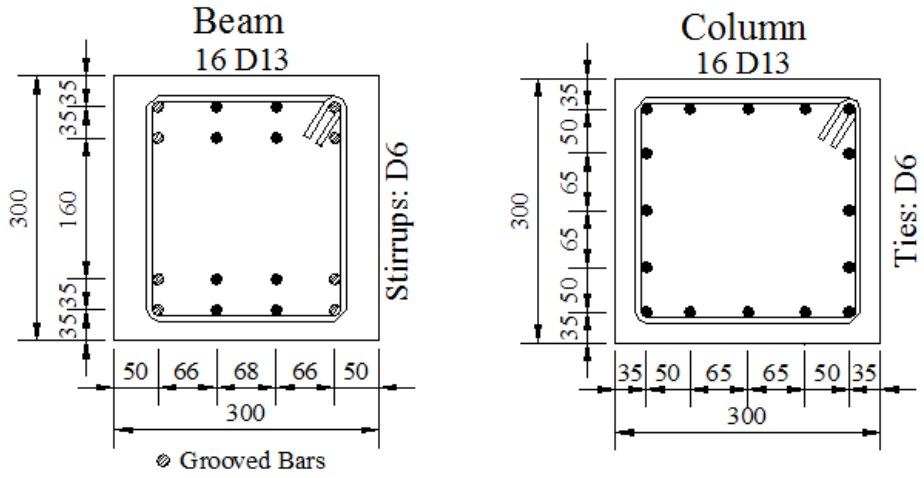


**Figure 6.18** Cross Section Details of Subassemblies A2 and A3

**Table 6.5** Material Properties of Subassemblies A2 and A3

| | $d_b$ (mm) | $f_y$ (MPa) | $f_u$ (MPa) | $E_s$ (MPa) | $E_{sh}$ (MPa) | $\varepsilon_{sh}$ ($x10^{-3}$) | $\varepsilon_u$ ($x10^{-3}$) |
|---|---|---|---|---|---|---|---|
| **D13 Beam** | 12.7 | 456 | 582 | 176000 | 962 | 29 | 160 |
| **D13 Column** | 12.7 | 357 | 485 | 176300 | 962 | 27 | 160 |
| **D6** | 6.4 | 326 | 383 | 151300 | 3775 | 2.2 | 17.3 |

| | Concrete | | |
|---|---|---|---|
| | $f'_c$ (MPa) | $\varepsilon_0$ * ($x10^{-3}$) | $E_c$ (MPa) |
| **A2** | 28.3 | 2.20 | 25700 |
| **A3** | | | |

*estimated

The testing of the subassemblies involved the application of a force in a displacement controlled mode and a constant axial force of 216 kN at the top of the columns. The

horizontal reversed cyclic load was applied at the top of the column for Specimen A2, and at the end of left beam for Specimen A3, as shown in Figure 6.20. The loading history used for both specimens is shown in Figure 6.19.

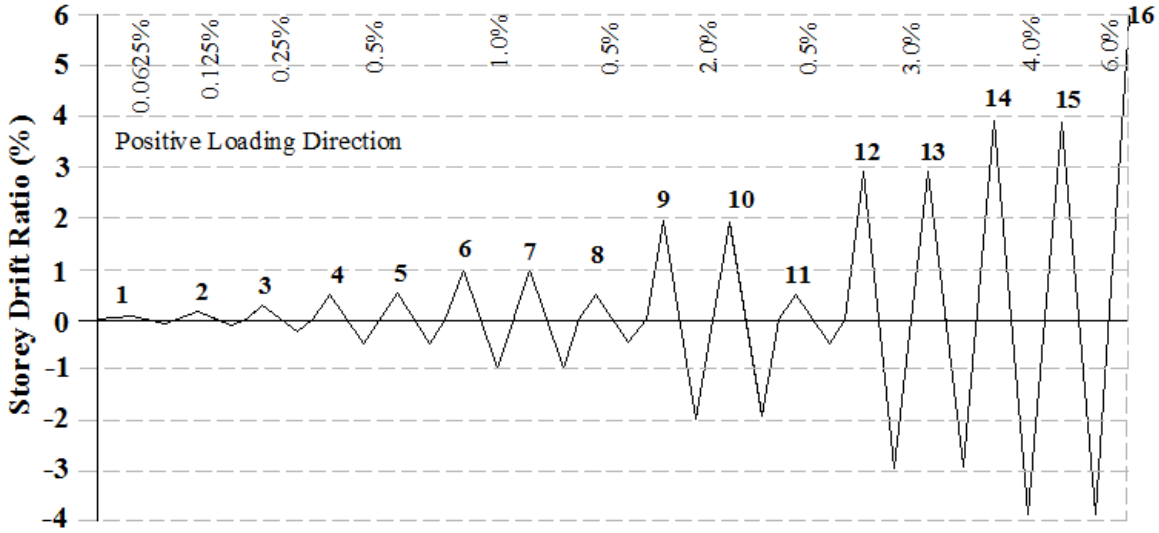


**Figure 6.19** Loading Program Applied to the Subassemblies A2 and A3 (Shiohara and Kusuhara, 2006)

The storey drift ratio corresponds to $\delta_{applied}$ / 1470 (in mm) for Specimen A2 and $\delta_{applied}$ / 735 (in mm) for Specimen A3, where $\delta_{applied}$ is the applied displacement shown in Figure 6.20.

### 6.6.1 Analytical Modelling

The specimens were modelled with varying lengths of segments in the range of one half of the cross section depths as shown in Figure 6.20. Two member types, MT1 and MT2, were used to represent the beam and column sections, respectively (Figure 6.22). MT3 and MT4 were created by doubling the reinforcement ratios of MT1 and MT2, respectively, to simulate the relatively stiffer behaviour of members within the beam-column panel region (Figure 6.21).

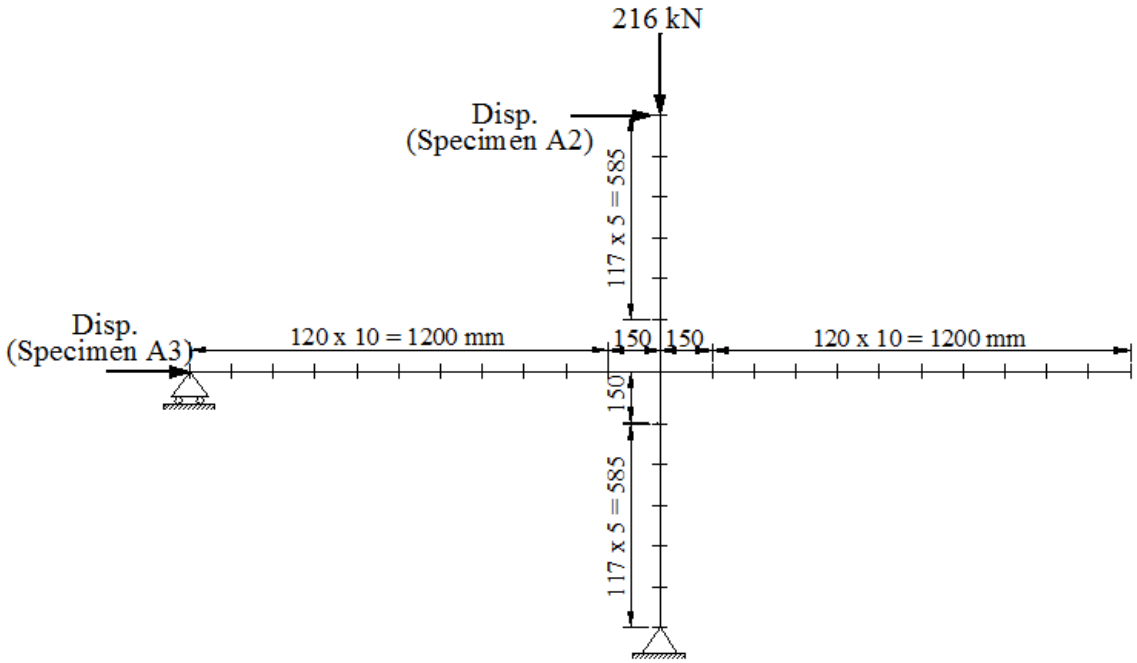


**Figure 6.20** Analytical Model Showing Segment Lengths, Loading and Support Restraints for Subassemblies A2 and A3

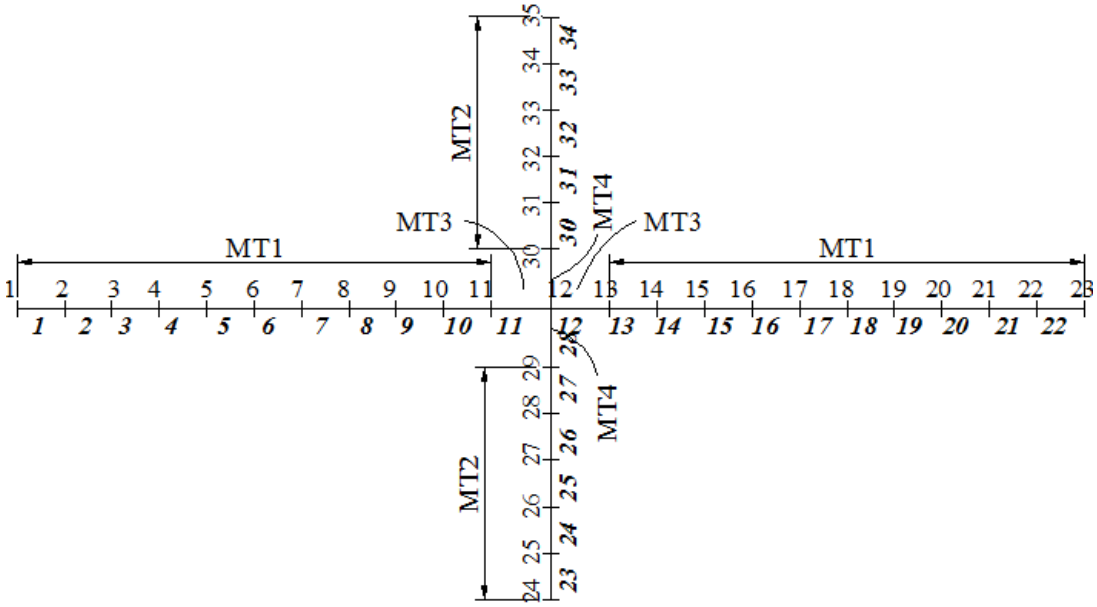


**Figure 6.21** Analytical Model Showing Member Types for Subassemblies A2 and A3

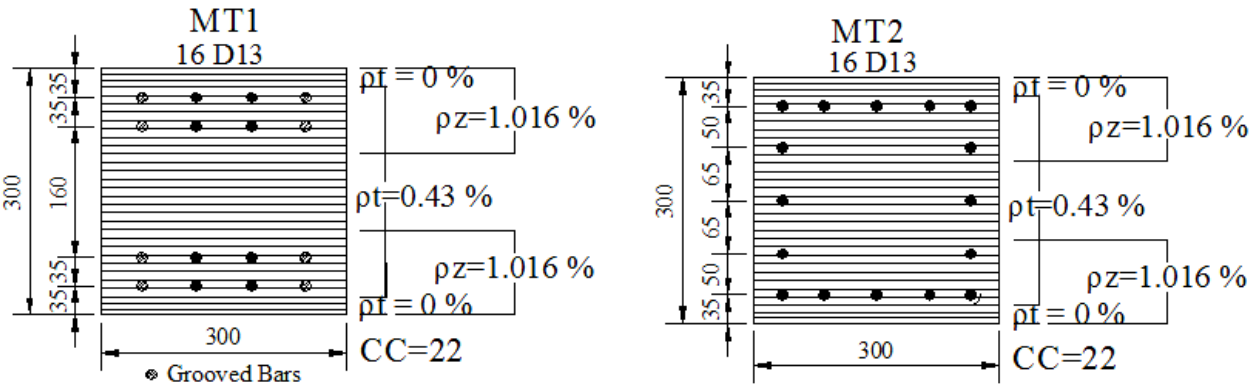


**Figure 6.22** Sectional Models for the Member Types of Subassemblies A2 and A3

As presented in Figure 6.22, 31 concrete layers (7.00 mm x 2, 8 mm x 1, 10.24 mm x 25, 8 mm x 1, and 7 mm x 2) were used for all four member types. All default material behaviour models were used in the analysis including the default concrete compression base curve (Hognestad) as described in Section 6.3. The support conditions were represented by restraining both the x- and y-degrees of freedom of Node 24 and by restraining only the y-degree-of-freedom of Node 1. Two load cases were defined: a constant axial load applied at Node 35, and a lateral displacement applied at Node 35 for Specimen A2 and at Node 1 for Specimen A3.

### 6.6.2 Comparison of the Analytical and Experimental Responses

The analytical and experimental beam tip load-deflection responses obtained are compared in Figure 6.23.

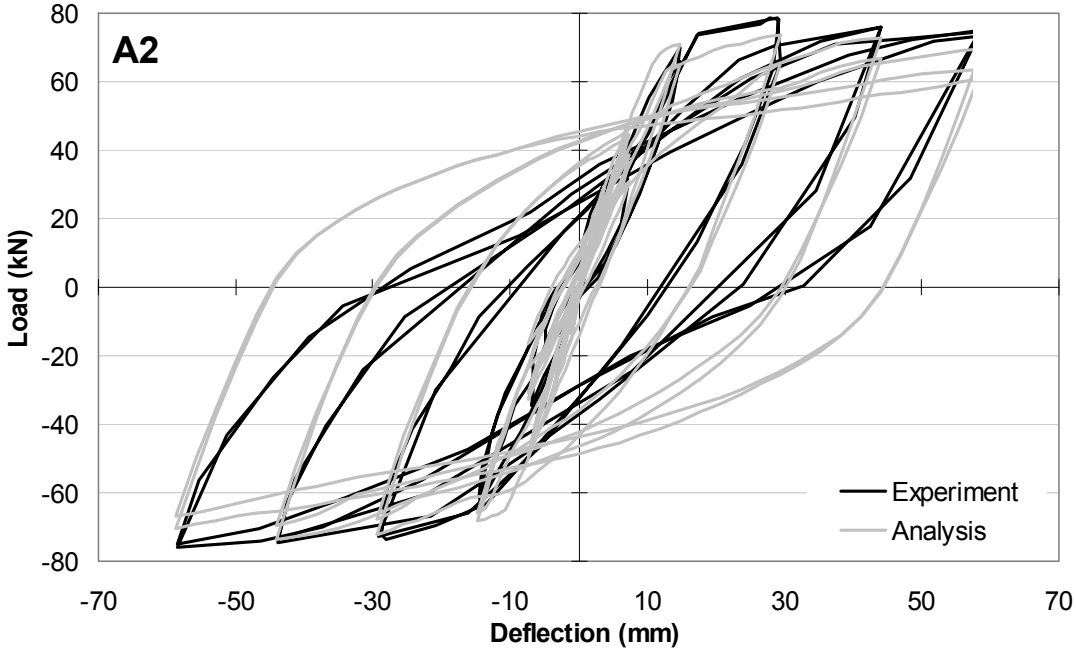


**Figure 6.23** Comparison of Load-Deflection Responses for Subassembly A2

As seen from Figure 6.23, the overall behaviour of the subassembly was predicted reasonably well. The strength degradation of the specimen under repeated cycles at the same displacement amplitude was predicted to be slightly more than the experimental degradation. Note the reduction in the load capacity in the second cycle at each displacement amplitude. This degradation was primarily caused by the excessive shear straining that occurred, particularly in Member 9. Notice too the decrease in strength and stiffness at a displacement of 58 mm.

The pinching behaviour of the experimental load-deflection response was simulated only marginally well with considerable underestimation. This is likely related to the cracking in the joint panel zone that was observed in the experimental behaviour (Figure 6.24) and a possible bond slip of the longitudinal reinforcement.

Detailed comparisons of other response parameters are given in Table 6.6.

**Table 6.6** Comparison of Analytical Experimental Results for Subassembly A2

| | VecTor5 | | Test | | |
|---|---|---|---|---|---|
| **A2 Positive Loading** | Disp (mm) | Shear (kN) | Disp (mm) | Shear (kN) | **Ratio** |
| Beam Reinf. First Layer Yielding | 12.2 | 66.4 | 12.6 | 63.6 | |
| Beam Reinf. Second Layer Yielding | 12.7 | 69.7 | 17.3 | 74.1 | |
| Column Reinf. Yielding | No Yielding | | No Yielding | | |
| Max Story Shear | 29.4 | **73.6** | 29.3 | **77.9** | **1.01** |
| Displacement Ductility | 4.8 | | 4.7 | | 1.04 |
| Energy Dissipation (kNm) | 25.3 | | 22.2 | | 1.14 |
| **A2 Negative Loading** | | | | | |
| Beam Reinf. First Layer Yielding | -10.0 | 62.0 | -14.3 | -60.9 | |
| Beam Reinf. Second Layer Yielding | -11.0 | 65.0 | -14.3 | -60.9 | |
| Column Reinf. Yielding | No Yielding | | No Yielding | | |
| Max Story Shear | -44.0 | **-73.5** | -58.5 | **-77.1** | **0.95** |
| Displacement Ductility | -5.9 | | -4.1 | | 1.43 |
| Energy Dissipation (kNm) | 22.4 | | 18.9 | | 1.19 |

As apparent from Table 6.6, the strength and energy dissipation characteristics of the subassembly were captured reasonably well. The displacement ductility in the negative loading direction was the least accurately predicted value due to the yielding of the beam longitudinal reinforcement at lower displacements than observed in the experiment. This is probably associated with cracking of the joint panel zone and a possible bond slip of the reinforcement in the experiment, which may have softened the response and caused less straining in the longitudinal beam reinforcement.

The damage mode of the specimen was accurately predicted to be flexure-shear. Significant flexural damage was predicted for Member 10 with the tensile beam reinforcement strains reaching $45 \times 10^{-3}$ with 6 mm crack widths. More importantly, Member 9 suffered intensive diagonal shear cracking with widths up to 9 mm. An attempt to perform the third cycle of 58.8 mm displacement caused the failure of Member 9 in shear (not shown in Figure 6.23). The experimental crack pattern of the specimen at the end of the second cycle (+58.8 mm) is shown in Figure 6.24.

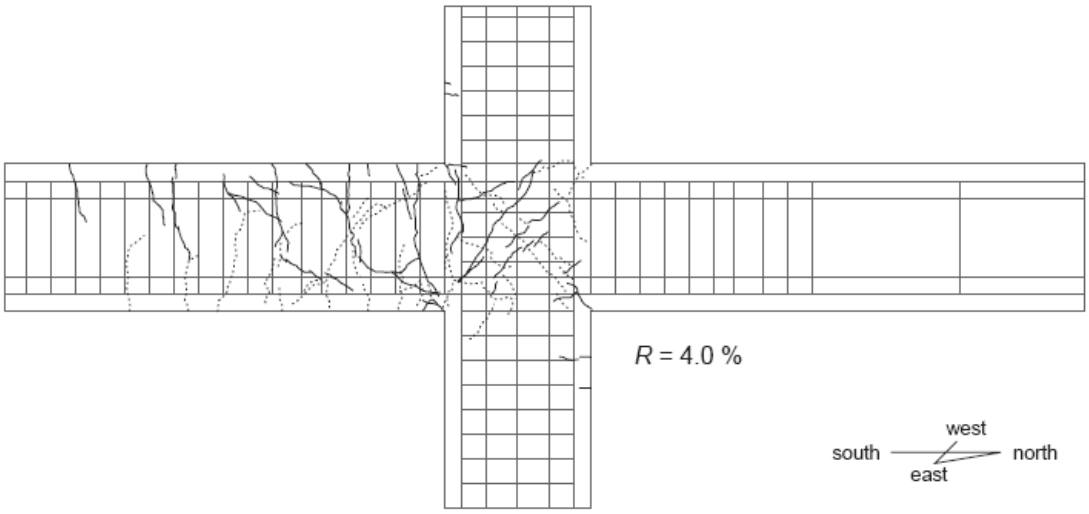


**Figure 6.24** Crack Pattern of Subassembly A2 at the End of the Test (Shiohara and Kusuhara, 2006)

The comparison of the load-deflection responses for Specimen A3 is shown in Figure 6.25.

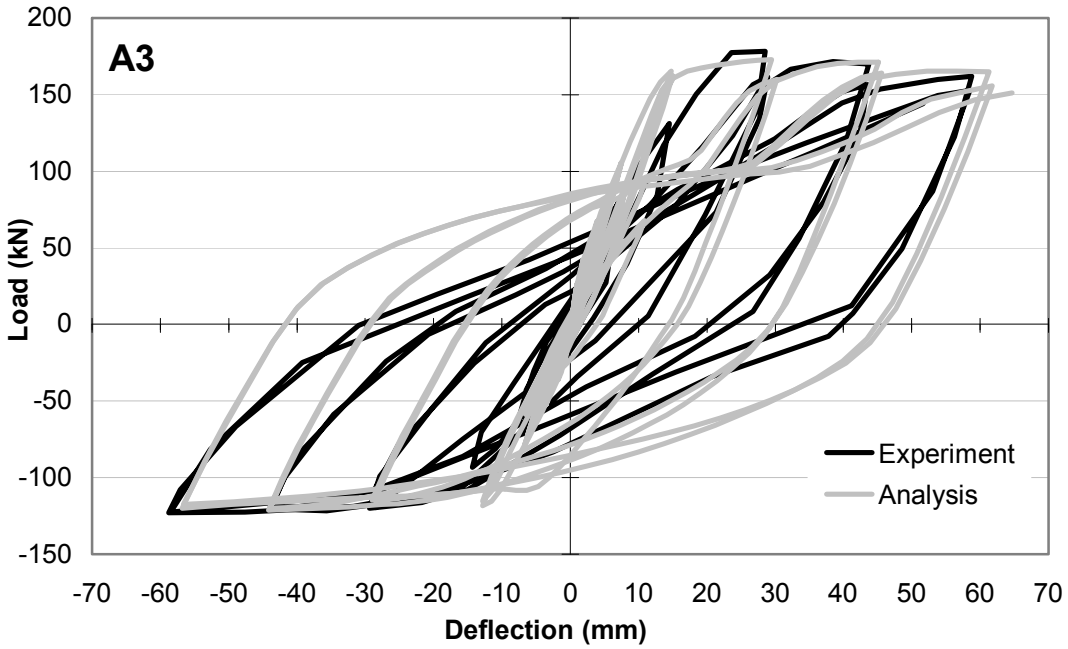


**Figure 6.25** Comparison of Load-Deflection Responses for Subassembly A3

The overall behaviour of the specimen was predicted successfully. Most notably, the strength degradation characteristics were simulated accurately. Note the decrease in strength in the second cycle of each displacement excursion. Almost identical behaviour

was present in the experimental response. Pinching of the response was predicted with a considerable underestimation possibly due to the joint cracking observed in the experiment (Figure 6.26) and a possible bond slip of the reinforcement.

**Table 6.7** Comparison of Analytical and Experimental Results for Subassembly A3

| | VecTor5 | | Test | | |
|---|---|---|---|---|---|
| **A3 Positive Loading** | Disp (mm) | Shear (kN) | Disp (mm) | Shear (kN) | **Ratio** |
| Beam Reinf. First Layer Yielding | 12.5 | 153.0 | 19.7 | 158.3 | |
| Beam Reinf. Second Layer Yielding | 14.0 | 161.8 | 23.8 | 176.4 | |
| Column Reinf. Yielding | No Yielding | | 26.9 | 156.1 | |
| Max Story Shear | 29.5 | **173.0** | 28.5 | **176.4** | **1.03** |
| Displacement Ductility | 4.7 | | 3.0 | | 1.58 |
| Energy Dissipation (kNm) | 52.1 | | 39.9 | | 1.30 |
| **A3 Negative Loading** | | | | | |
| Beam Reinf First Layer Yielding | -10.9 | -111.6 | -12.5 | -93.4 | |
| Beam Reinf Second Layer Yielding | -12.2 | -117.0 | -14.3 | -100.9 | |
| Column Yielding | No Yielding | | -44.5 | -123.0 | |
| Max Story Shear | -44.0 | **-120.0** | -58.5 | **-122.5** | **0.98** |
| Displacement Ductility | 5.4 | | 4.7 | | 1.15 |
| Energy Dissipation (kNm) | 40.3 | | 33.4 | | 1.21 |

As presented in Table 6.7, the strength of the specimen was calculated with excellent accuracy in both the positive and negative loading directions. The total energy dissipated by the specimen was predicted with a slight overestimation caused by the underestimation of the pinching in the load deflection response. The least accurately predicted value was the displacement ductility in the positive cycle. This occurred due to earlier yielding of the beam longitudinal reinforcement in the analytical study.

Similar to Specimen A2, a flexure-shear damage mode was predicted for Specimen A3. As compared to the damage mode obtained for Specimen A2, less shear damage of Member 9, with shear crack widths of 6 mm, and more flexural damage of Member 10, with 7 mm flexural crack widths, was found. The experimental crack pattern of the specimen at the end of the second cycle (+58.8 mm) is shown in Figure 6.26.

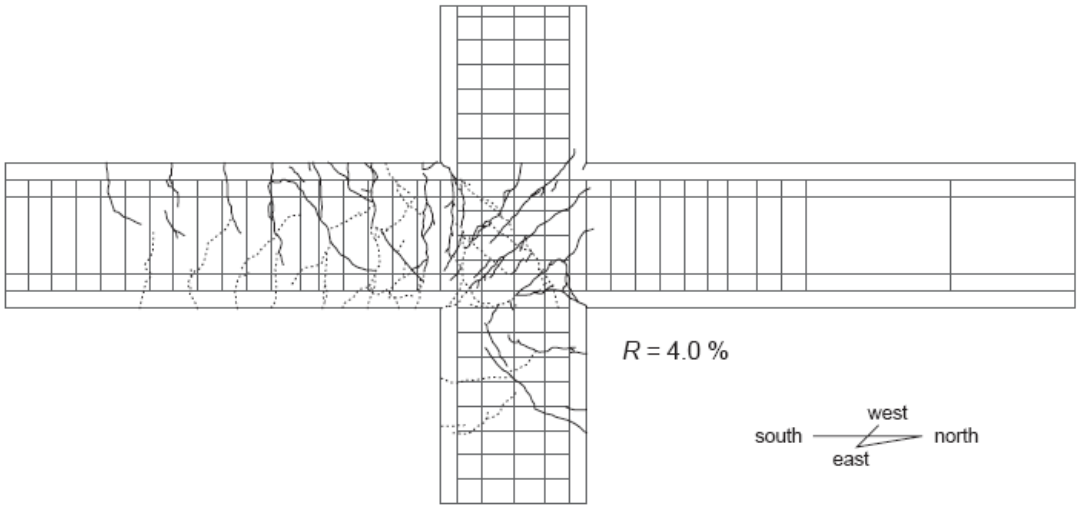


**Figure 6.26** Crack Pattern of the Specimen A3 at the End of the Test (Shiohara and Kusuhara, 2006)

## 6.7 PCA Shear Walls

An experimental program was carried out by Portland Cement Association (PCA) (Oesterle et al., 1976) involving several barbell-, flange- and rectangular-shaped shear walls to investigate the influence of a number of parameters on wall behaviour. The walls were dimensioned to represent a 1/3-scale model of a five storey shear wall. Six specimens (B1, B2, B7, B8, R1, and F1) were selected for analysis with the developed analytical procedure. This selection was made on the basis of the availability of the experimental results. Some shear walls were omitted due to deficiencies in the experiment. For example, for Wall R2, out-of-plane displacements were reported, which may invalidate the experimental results.

*Details of Specimens and Test Setup*

All walls extended 4.57 m (15 ft) between the top loading beam and the base beam. A typical view of the walls is shown in Figure 6.27. Cross section details of the walls are presented in the following section. Reinforcement properties were estimated from the reported steel coupon test results. For some reinforcing bars, when the experimental results were unavailable, conservative estimates (i.e., small values) were made for the reinforcement properties. Concrete strength and modulus of elasticity were taken as

reported; the strain $\varepsilon_o$ corresponding to peak stress $f'_c$ was estimated with Eq. 4.5. The resulting values are listed Table 6.8.

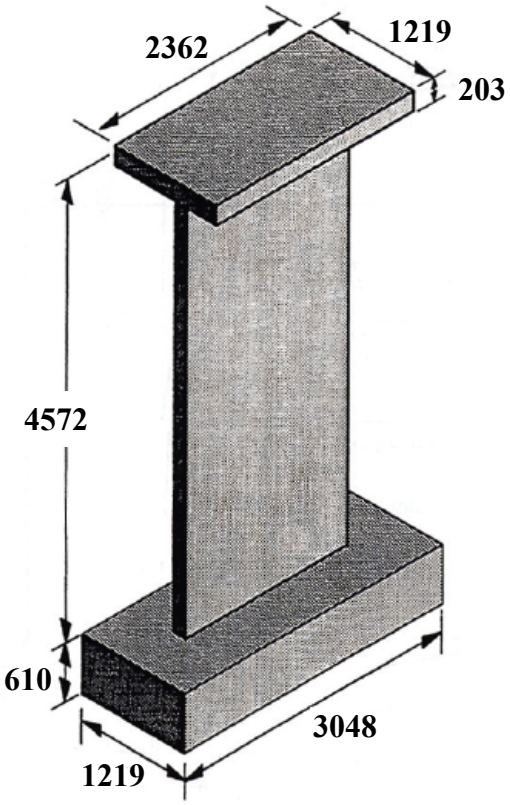


**Figure 6.27** Typical View of the PCA Walls (Kurama and Jiang, 2008)

**Table 6.8** Material Properties of the PCA Walls

| | | $d_b$ (mm) | $f_y$ (MPa) | $f_u$ (MPa) | $E_s$ (MPa) | $E_{sh}$ (MPa) | $\varepsilon_{sh}$ ($x10^{-3}$) | $\varepsilon_u$ ($x10^{-3}$) | $f'_c$ (MPa) | $\varepsilon_0$ ($x10^{-3}$) | $E_c$ (MPa) |
|---|---|---|---|---|---|---|---|---|---|---|---|
| B1 | #4 | 12.7 | 450 | 708 | 195130 | 2371 | 8.2 | 117 | 53 | 2.53* | 28130 |
| | #2 | 6.3 | 521 | 695 | 224087 | 2000 | 20 | 107 | | | |
| B2 | #6 | 19 | 410 | 695 | 208229 | 2258 | 6.8 | 133 | 53.6 | 2.48* | 28960 |
| | #2 | 6.3 | 532 | 701 | 221330 | 2061 | 20 | 102 | | | |
| B7 | #6 | 19 | 457 | 650 | 200000* | 2000* | 2.5* | 99* | 49.3 | 2.25* | 30100 |
| | #2 | 6.3 | 489 | 750 | 200000* | 2000* | 3* | 133* | | | |
| B8 | #6 | 19 | 447 | 650 | 200000* | 2000* | 2.5* | 104* | 42 | 2.36* | 25600 |
| | #2 | 6.3 | 454 | 750 | 200000* | 2000* | 3* | 151* | | | |
| R1 | #3 | 9.5 | 512 | 765 | 191681 | 2875 | 10 | 98 | 44.7 | 2.27* | 27787 |
| | #2 | 6.3 | 522 | 700 | 216503 | 1745 | 20 | 122 | | | |
| F1 | #4 | 12.7 | 445 | 707 | 193750 | 2451 | 8.1 | 115 | 38.4 | 2.24* | 25443 |
| | #2 | 6.3 | 525 | 705 | 215814 | 2143 | 20 | 104 | | | |

* estimated

The testing of the walls included the application of a lateral load to the top beam in a displacement-controlled mode to create reversed-cyclic loading conditions with displacement amplitude increments of 25.4 mm. In some of the walls (namely, Walls B7 and B8), a constant axial load of 1200 kN was applied to the top loading beam.

### 6.7.1 Analytical Modelling

The walls were modelled with member segments of varying lengths. A segment length of 175 mm (approximately 10% of the sectional-height) was used towards the base of the walls where a concentration of plastic deformation was expected. The segment lengths were gradually increased towards the top of the walls. The beam at the base of the walls was not modelled; rather, the walls were assumed to be fixed at the base (Figure 6.28(a)).

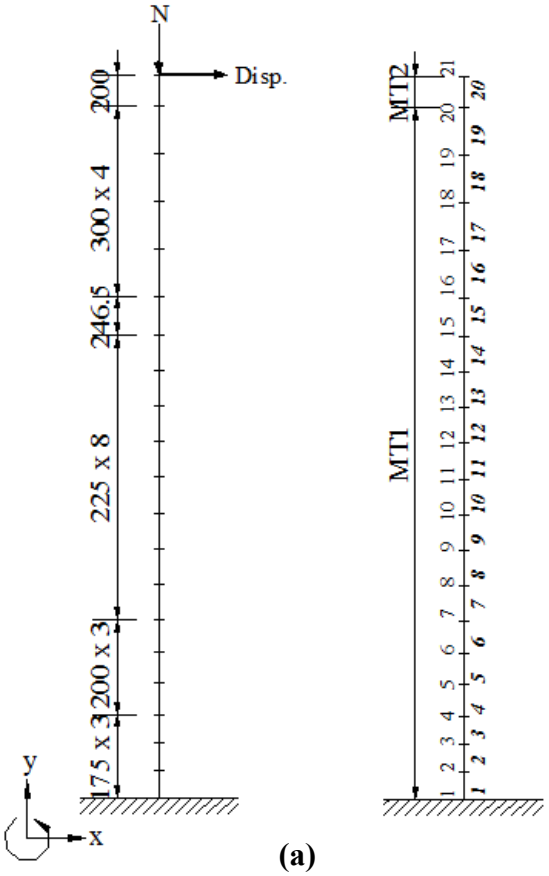


(a)

| | $\rho_t$ (%) | $\rho_{l,fl}$ (%) | $\rho_{l,web}$ (%) | $\rho_z$ (%) | N (kN) |
|---|---|---|---|---|---|
| **B1** | 0.31 | 1.11 | 0.29 | 0 | 0 |
| **B2** | 0.63 | 3.67 | 0.29 | 0 | 0 |
| **B7** | 0.63 | 3.67 | 0.29 | 1.35 | 1200 |
| **B8** | 1.38 | 3.67 | 0.29 | 1.35 | 1200 |
| **R1** | 0.31 | 1.47 | 0.25 | 0 | 0 |
| **F1** | 0.71 | 3.89 | 0.3 | 0 | 0 |

**(b)**

**Figure 6.28** Modelling of PCA Walls: **(a)** Frame Model; **(b)** Reinforcement Ratios

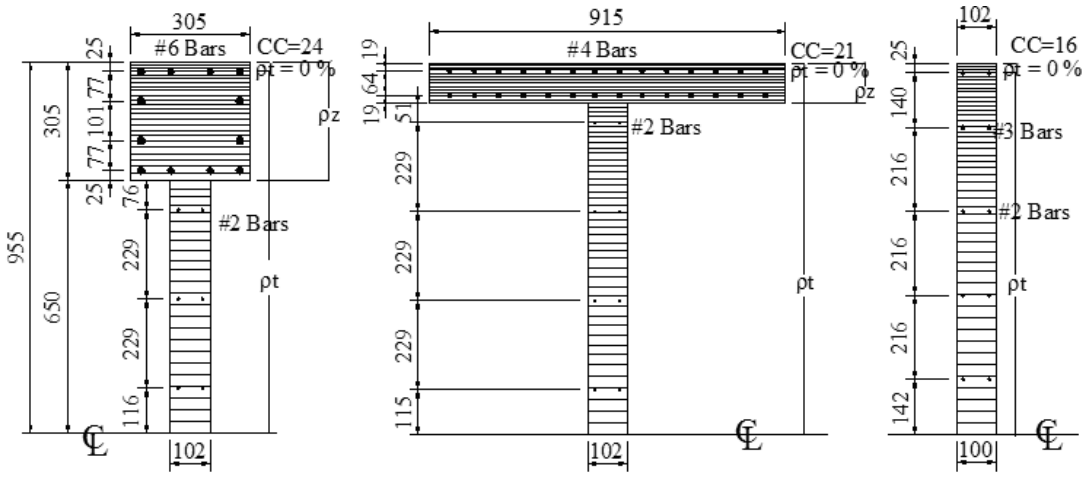


**Figure 6.29** Typical Sectional Models Used in the Analysis of PCA Walls

The smeared reinforcement reported for the walls is summarized in Figure 6.28(b), where $\rho_t$ is the transverse reinforcement ratio, $\rho_z$ is the out-of-plane reinforcement ratio, $\rho_{l,fl}$ is the longitudinal (along the y-axis) reinforcement ratio in the flanges, and $\rho_{l,web}$ is the longitudinal reinforcement ratio in the webs of the walls. Note that $\rho_{l,fl}$ and $\rho_{l,web}$ are not required for the analytical model; rather, the reinforcement areas and the distances from the top of the cross sections must be defined. The details of the longitudinal reinforcement configurations for each wall can be found in Oesterle et al. (1976).

One member type was used for the sectional models of the walls: MT1. To simulate the top loading beam, an artificial member type, MT2, was created by multiplying the reinforcement ratios of MT1 by a factor of 2.

Typical sectional models for MT1 for three different wall shapes is presented in Figure 6.29, 96 concrete layers were typically used for barbell-shaped walls (8.0 mm x 3 layers, 10 mm x 5 layers, 12.0 mm x 5 layers, 14.0 mm x 5 layers, 16.0 mm x 5 layers, 18.5 mm x 2 layers, 21 mm x 5 layers, 25 mm x 5 layers, 30 mm x 14 layers). A similar layer configuration was used for the flanged and rectangular walls. Transverse reinforcement was assigned to all layers except for the clear-cover (CC) layers, as defined in Figure 6.28(b).

Default material models were used except for the concrete base curve for which the Popovics (NSC) formulation was adopted as described in Section 6.3. Three load cases

were applied to the walls: a reversed-cyclic lateral displacement applied at Node 21, a constant axial load applied at Node 21, and an automatically calculated self-weight load case, which is a newly implemented algorithm.

### 6.7.2 Comparison of the Analytical and Experimental Responses

The analytical and experimental applied lateral load-deflection responses are compared in Figure 6.30 to Figure 6.36.

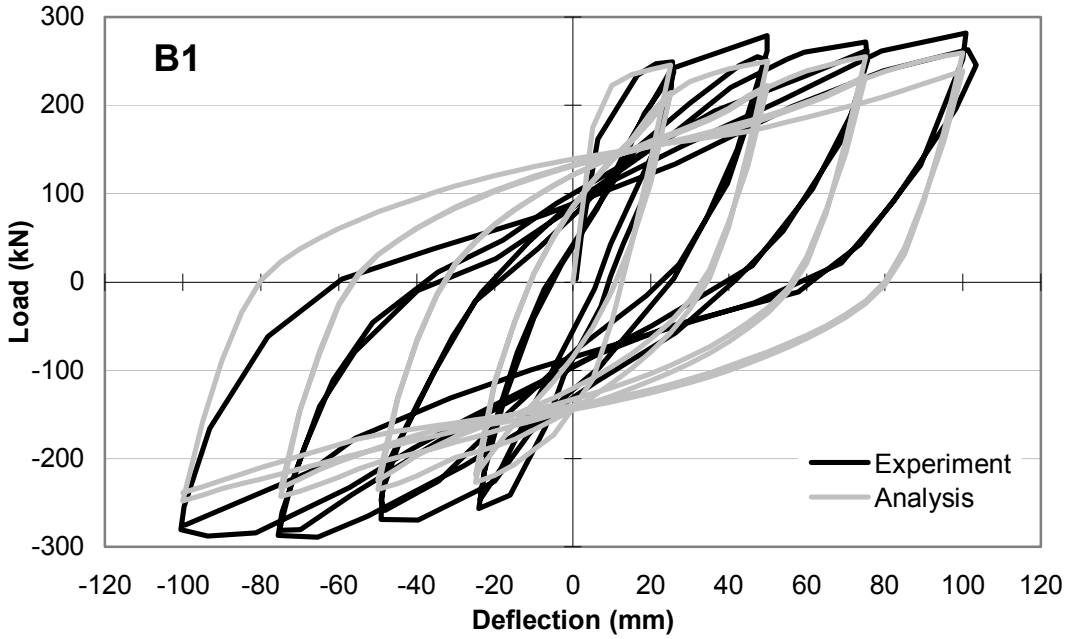


**Figure 6.30** Comparison of Load-Deflection Responses for PCA Wall B1

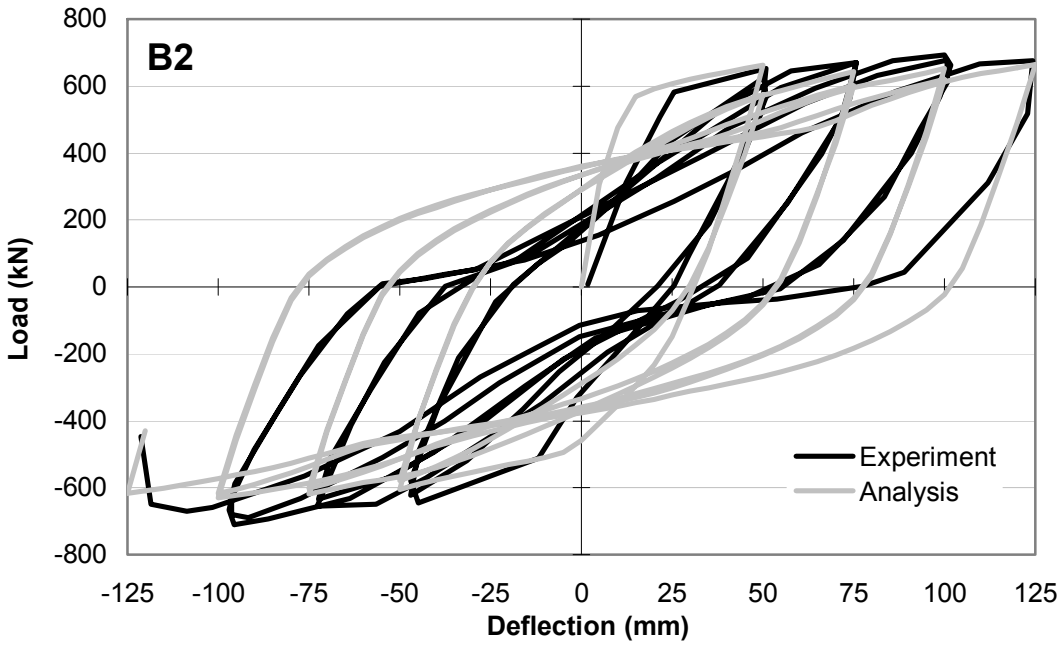


**Figure 6.31** Comparison of Load-Deflection Responses for PCA Wall B2

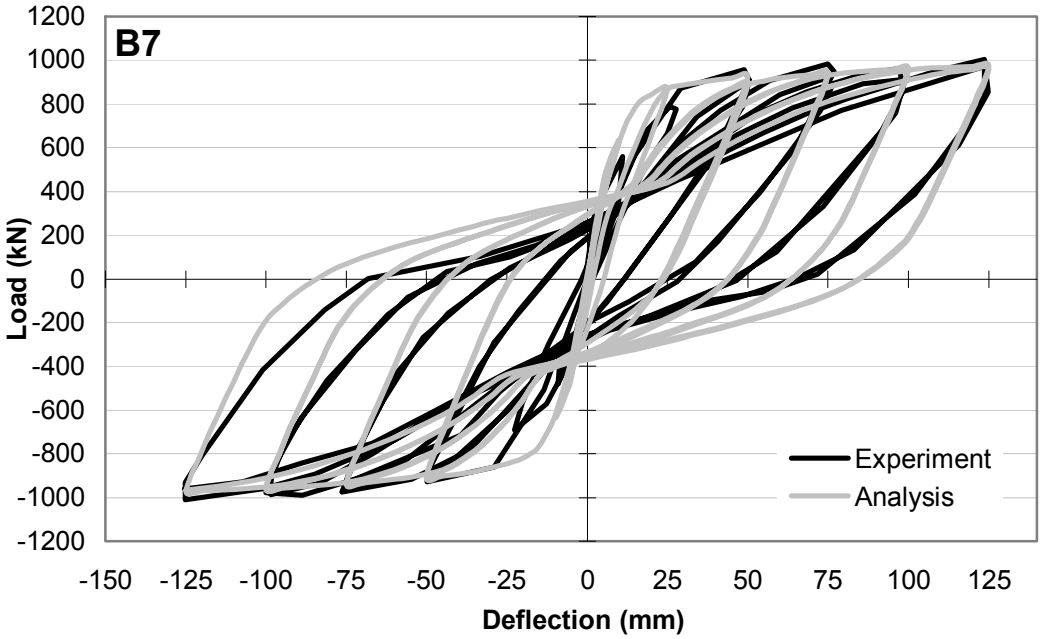


**Figure 6.32** Comparison of Load-Deflection Responses for PCA Wall B7

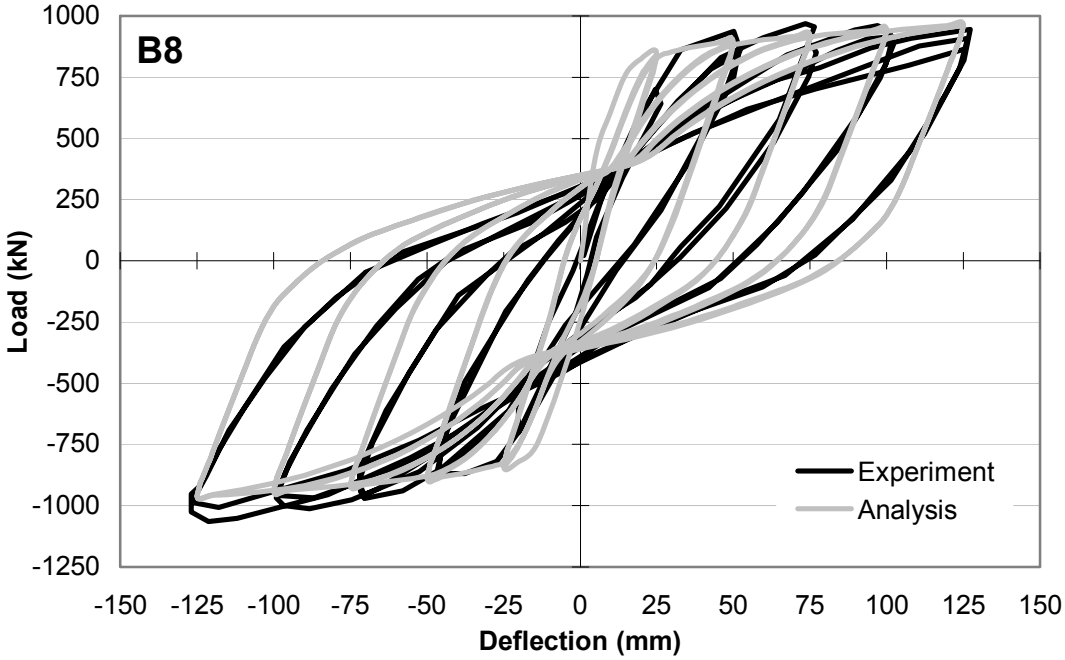


**Figure 6.33** Comparison of Load-Deflection Responses for PCA Wall B8

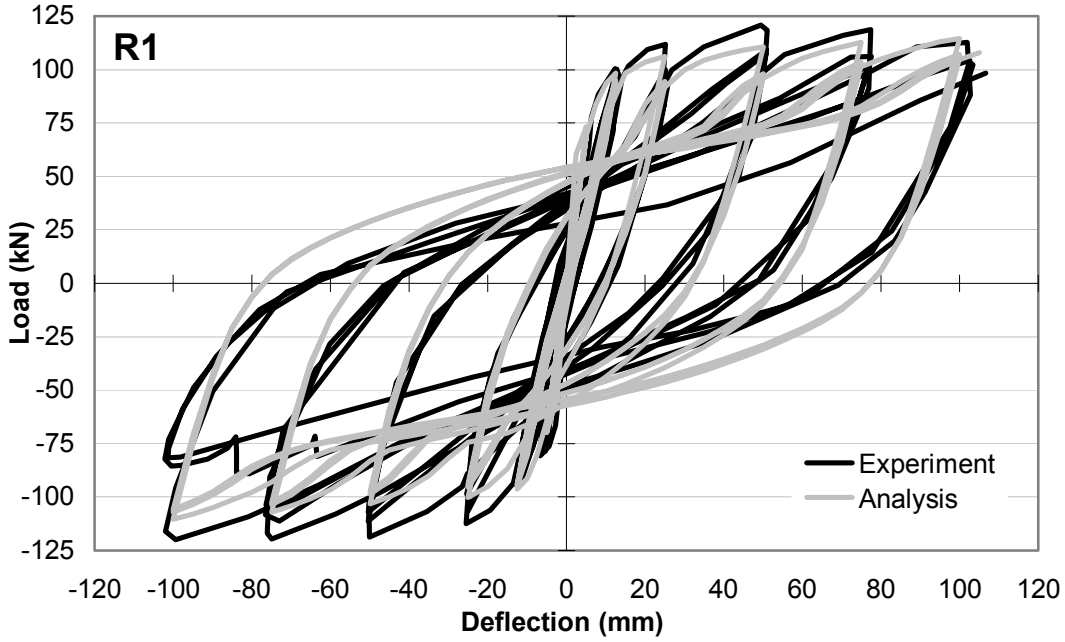


**Figure 6.34** Comparison of Load-Deflection Responses for PCA Wall R1

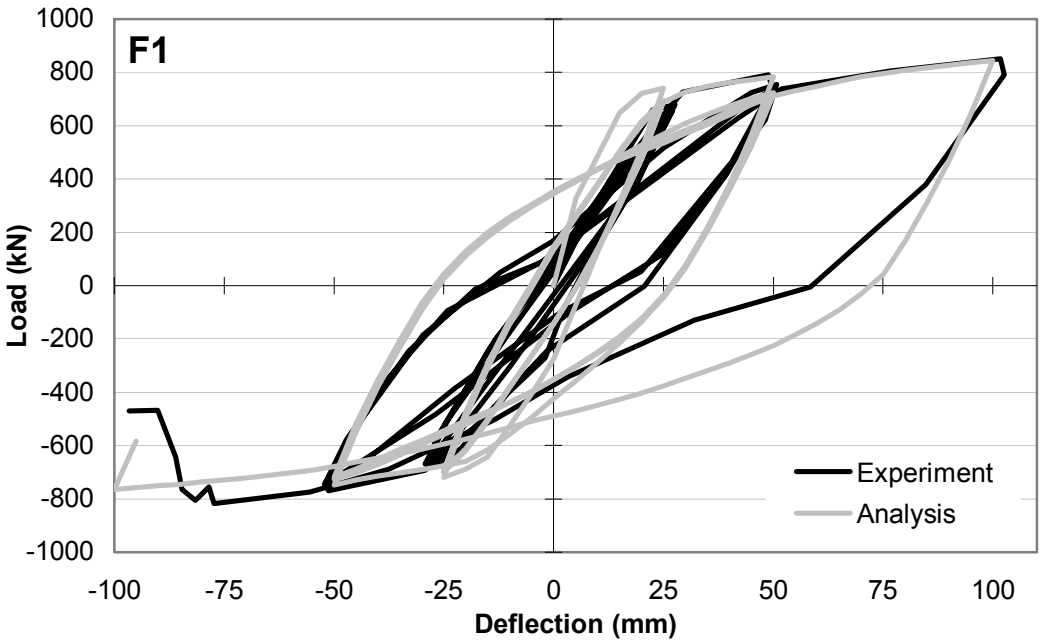


**Figure 6.35** Comparison of Load-Deflection Responses for PCA Wall F1

As seen from the graphs above, the overall behaviours of the walls were predicted with reasonable accuracy. In particular, the strength degradation under repeated cycles at the same displacement amplitude was estimated well. Note the decrease in the load capacity in the second cycle at each displacement amplitude. As explained previously, this decrease was primarily caused by excessive cracking and shear straining of, in particular, Member 1. Similar decreases in the reloading stiffnesses were observed experimentally.

The pinching behaviour of the experimental responses was underestimated in the analyses for four walls (i.e., B1, B2, R1 and F1), but estimated accurately for two walls (i.e., B7 and B8). The underestimation was particularly significant for Wall B2, which was not subjected to a constant axial load.

Similar underestimations of pinching behaviour were previously encountered in the analyses of the beam-column subassemblies in Sections 6.5 and 6.6, where it was attributed to the shear cracking of the joint panel zones and to possible bond-slip of the longitudinal reinforcement. A similar reasoning can be made in the analyses of these walls. As the main flexural reinforcement typically extended through the base beams, which were not incorporated into the analytical model, cracking of the base beams and

strain penetration in the base beams could have resulted in a more pinched response in the experiment. This reasoning is supported by the analytical responses of Walls B7 and B8, where the experimental pinching was simulated successfully. Walls B7 and B8 were the only walls tested under a constant axial force of 1200 kN. Due to the compression, less cracking in the base and less, if any, strain penetration is expected. Therefore, the analytical assumption of a perfectly fixed base and of perfect bond between the reinforcement and the concrete becomes more realistic, providing a better simulation of the pinching behaviour observed in the experiments.

Detailed comparisons of several parameters are compared in Table 6.9.

**Table 6.9** Comparison of Load and Deflection Results for PCA Walls

| | First Reinforcement Yielding | | | | | Max Story Shear | | | | |
|---|---|---|---|---|---|---|---|---|---|---|
| | VecTor5 | | Test | | Ratio | VecTor5 | | Test | | Ratio |
| | Disp (mm) | Shear (kN) | Disp | Shear | | Disp | Shear | Disp | Shear | |
| **B1 +** | 7.8 | **242** | 9.8 | **274** | **0.88** | 100 | **261** | 100 | **282** | **0.93** |
| **B1 -** | -14.3 | **-226** | -16.7 | **-256** | **0.88** | -100 | **-247** | -75 | **-289** | **0.85** |
| **B2 +** | 11.9 | **668** | 21.6 | **628** | **1.06** | 125 | **672** | 100 | **685** | **0.98** |
| **B2 -** | -8.5 | **-581** | -15.0 | **-593** | **0.98** | -100 | **-627** | -100 | **-713** | **0.88** |
| **B7 +** | 9.2 | **907** | 8.7 | **922** | **0.98** | 125 | **998** | 125 | **1010** | **0.99** |
| **B7 -** | -12.1 | **-880** | -16.0 | **-886** | **0.99** | -125 | **-988** | -125 | **-1010** | **0.98** |
| **B8 +** | 25.0 | **865** | 28.2 | **936** | **0.92** | 125 | **975** | 100 | **971** | **1.00** |
| **B8 -** | -14.7 | **-860** | -17.9 | **-841** | **1.02** | -125 | **-971** | -120 | **-1070** | **0.91** |
| **R1 +** | 6.0 | **1100** | 7.3 | **1190** | **0.92** | 100 | **1140** | 75 | **1190** | **0.96** |
| **R1 -** | -5.8 | **-9750** | -5.8 | **-11100** | **0.88** | -100 | **-1110** | -100 | **-1190** | **0.93** |
| **F1 +** | 13.5 | **760** | 21.0 | **750** | **1.01** | 150 | **831** | 100 | **852** | **0.98** |
| **F1 -** | -15.0 | **-720** | -17.0 | **-680** | **1.06** | -100 | **765** | -80 | **818** | **0.94** |
| **+** : Positive Loading Direction | | | | **Mean** | **0.97** | | | | **Mean** | **0.94** |
| | | | | **COV (%)** | **6.4** | | | | **COV (%)** | **5.0** |

As is apparent from Table 6.9, the strengths of the walls were predicted very well. The slight underestimation of strength can be attributed to the stockiness of the walls which, with a height-to-width ratio of 2.4, are at the transition point where direct strut action begins to play a prominent role.

**Table 6.10** Comparison of Ductility and Energy Dissipation Results for PCA Walls

| | Displacement Ductility | | | Energy Dissipation (kNm) | | |
|---|---|---|---|---|---|---|
| | VecTor5 | Test | Ratio | VecTor5 | Test | Ratio |
| B1 + | 12.9 | 10.2 | 1.26 | 113.7 | 102.8 | 1.11 |
| B1 - | 7.0 | 6.0 | 1.17 | 122.3 | 110.9 | 1.10 |
| B2 + | 10.5 | 5.8 | 1.82 | 349.6 | 287.7 | 1.22 |
| B2 - | 11.8 | 6.7 | 1.76 | 378.5 | 287.2 | 1.32 |
| B7 + | 13.6 | 14.3 | 0.95 | 576.6 | 501.3 | 1.15 |
| B7 - | 10.3 | 7.8 | 1.32 | 588.9 | 521.8 | 1.13 |
| B8 + | 5.0 | 4.4 | 1.13 | 677.1 | 573.8 | 1.18 |
| B8 - | 8.5 | 7.0 | 1.22 | 594.8 | 578.6 | 1.03 |
| R1 + | 16.7 | 13.7 | 1.22 | 81.6 | 74.5 | 1.10 |
| R1 - | 17.3 | 17.3 | 1.00 | 74.0 | 69.2 | 1.07 |
| F1 + | 7.4 | 4.8 | 1.55 | 202.3997 | 169.3 | 1.20 |
| F1 - | 8.3 | 4.7 | 1.77 | 202.3997 | 188.4 | 1.07 |
| | | Mean | 1.35 | | Mean | 1.14 |
| | | COV (%) | 29.0 | | COV (%) | 7.9 |

As presented in Table 6.10, the total energy dissipated by the walls was estimated with reasonable accuracy. Some discrepancies exist in the displacement ductility ratios of the walls. This is primarily caused by earlier yielding of the longitudinal reinforcement in the analyses. Base cracking and possible bond slip are most likely contributing to this phenomenon. It should be noted, however, that displacement ductilities were approximated from the load deflection curves, as described in Figure 6.14, due the lack of experimental information regarding the first yielding of reinforcement. Based on the assumed effective yielding approach, a small overestimation of the initial stiffness of the structure shifts the effective yielding point significantly, thereby affecting the estimated displacement ductilities greatly. Therefore, the displacement ductility comparisons should be used for information purposes, rather than for a detailed comparison.

All walls exhibited a flexure-dominated behaviour in both the analyses and the experiments, clear from the flat top of the load-deflection curves, except for Wall F1 which suffered a sudden web-crushing failure before reaching its flexural strength.

The experimentally observed damage mode of Walls B1 and B2 included significant main longitudinal reinforcement yielding, web concrete crushing and reinforcement buckling. The analysis results of Wall B1, at the end of the loading (second cycle -100 mm), indicated 9.2 mm flexural crack widths with $51.5 \times 10^{-3}$ longitudinal reinforcement

straining for Member 1. Some concrete crushing at the compression toe was predicted but to a lesser extent than experimentally observed. As for Wall B2, which included significantly more longitudinal reinforcement than Wall B1, a 5.1 mm maximum crack width with 48.2 x $10^{-3}$ longitudinal reinforcement strain was predicted for Member 1. Contrary to the experimental observations, no web crushing was predicted at the same experimental displacement level (i.e., -80 mm) for this wall.

In the experiments on Walls B1 and B2, web crushing and reinforcement buckling occurred almost simultaneously, contributing to each other. However, in the analytical procedure employed, such a mechanism is not taken into account. For concrete to crush in the analysis, a strain limit dependent on the concrete compression base curve and the confinement reinforcement present must be reached. Reinforcement buckling, on the other hand, is not currently considered in the analytical tool developed.

The damage modes of the walls B7 and B8 were reported by Palermo and Vecchio (2004) to include flexural mechanisms with significant web crushing. For Wall B7, very similar results were obtained analytically. The analysis results indicated a flexural crack width of 8.9 mm with 76.5 x $10^{-3}$ longitudinal reinforcement straining with crushing of the web concrete for Member 1. For Wall B8, which included more transverse reinforcement than Wall B7, a similar behaviour was obtained but no crushing of the web concrete was predicted at the same experimental displacement level (i.e., +150 mm).

The experimental failure mechanism of Wall R1 was initiated by two bars buckling at approximately +75 mm lateral displacement. Both buckled bars then fractured in the following negative cycle. The two drops in the load capacity in Figure 6.34, occurring at approximately -63 mm and -83 mm, correspond to these bar fractures. Such a mechanism is not accounted for in the analytical procedure. As a result, the damage mode is predicted to involve the plastic hinging of Member 1 with significant cracking and longitudinal straining as much as 55.0 x $10^{-3}$ at a lateral displacement of 100 mm.

The experimentally observed failure mechanism of Wall F1 included a sudden crushing of the web concrete at approximately -90 mm displacement, clear from Figure 6.35. The

analysis results corresponding to this displacement did not indicate such a failure. To determine the analytical failure mechanism of the wall, the analysis was continued to encounter the web crushing occurring at about -125 mm as shown in Figure 6.36.

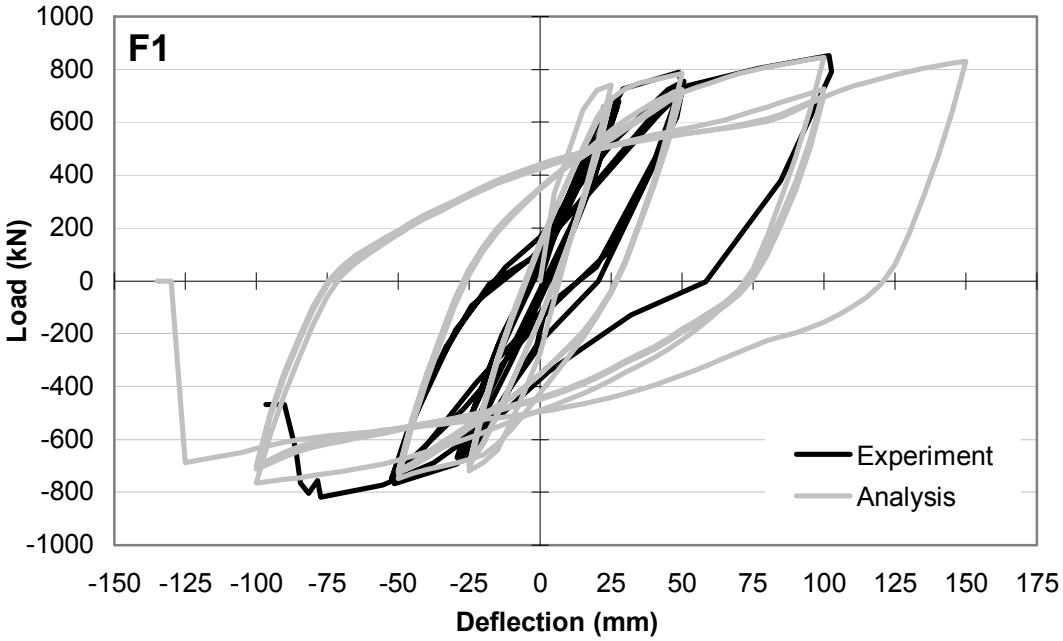


**Figure 6.36** Comparison of Load-Deflection Responses for PCA Wall F1

Of particular interest in the behaviour of these walls is the influence of the shear protection algorithm, which reduced the shear forces and strains in the first 6 members (i.e., within a height of 0.70 x d from the base). It is informative to investigate the influence of this reduction on the behaviour of the walls. For this purpose, the walls were analyzed twice under monotonically increasing load to failure: once using the shear protection algorithm and once considering the full shear effects without shear protection. Comparisons of the computed responses to the experimental backbone response for Wall B7 are presented in Figure 6.37.

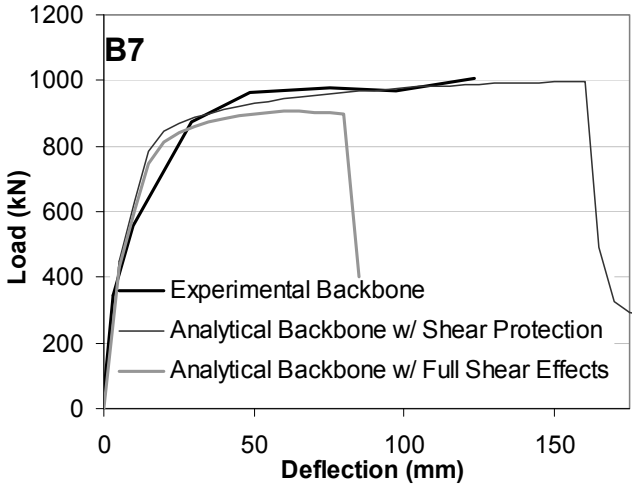


**Figure 6.37** Comparison of Responses for Two Different Shear Considerations (PCA Wall B7)

In the analysis considering the full shear effects, a premature *shear* failure of Member 1 was predicted, which did not occur experimentally. However, when the shear protection algorithm was invoked, a flexure-dominated response was obtained which is in strong agreement with the experimental response. In this case, the drop in the load capacity was caused by the fracture of reinforcement in tension in the analytical model.

Also of interest in the behaviour of these walls is the influence of the out-of-plane confinement effects in the concrete. As formulated in Section 3.13.5, out-of-plane reinforcement stresses were introduced into the sectional analyses to simulate confinement effects. In order to illustrate the influence of this effect, consider the response of concrete layer 4 of Wall B8 as shown in Figure 6.38; this layer was well confined with 1.35% out-of-plane reinforcement ratio.

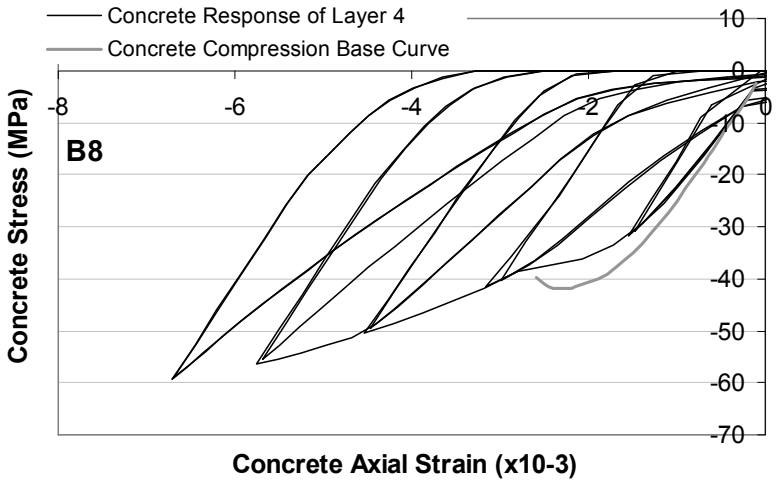


**Figure 6.38** Response of Concrete Layer 4 (PCA Wall B8)

As compared to the base curve, a strength enhancement of 43% was realized in this analysis. More importantly, the strain corresponding to the peak stress was enhanced by a factor of 2.8. It is significant that such important three-dimensional stress effects were successfully taken into account with a two dimensional analysis procedure.

## 6.8 Summary, Conclusions and Recommendations

In this chapter, the analytical procedure developed in Chapter 5 for general loading conditions was verified with one large-scale frame, four large-scale beam-column subassemblies and six 1/3-scale shear walls, all of which were previously tested. The experimental behaviours of the structures were compared to the analytical behaviours in terms of load-deflection responses, reinforcement strain responses and crack widths. The failure conditions of the structures, as obtained experimentally and analytically, were compared in terms of failure modes and failure displacements. Important in the seismic assessment of structures, the total energy dissipations and the displacement ductility ratios were also compared to the experimental results.

Considering all 11 structures examined in both the positive and negative loading directions, giving 22 values, a mean of 0.97 and a coefficient of variation (COV) of 6.0% were achieved for the predicted-to-observed strength ratio. For the displacements corresponding to the peak load capacities, a mean of 1.07 and a COV of 23.4% were realized. It should be noted that most of the load-deflection responses had a flat top, thus making them prone to large errors in estimating the displacements at the peak load. For the total energy dissipation, a mean of 1.18 with a COV of 14.6% was attained. The displacement ductilities were determined rather approximately using the load-deflection curves, based on the effective yielding approach, due to the lack of experimental data. As a result, a mean of 1.27 with a COV of 26.6% was obtained for the predicted-to-observed ductility ratio considering all 22 values. Considering the challenges involved in the simulation of behaviour of reinforced concrete structures under reversed-cyclic loading conditions, these ratios can be regarded as satisfactory. The failure modes of the structures were predicted accurately for the majority of the specimens. In addition, other

computed responses such as reinforcement strains, member elongations and crack widths showed strong correlations with the experimental results.

In conclusion, the nonlinear sectional analysis procedure implemented for the general loading condition provided reasonably accurate simulations of the responses of a variety of previously tested structures. Both shear- and flexure-related mechanisms were captured well.

Also notable is that all analyses were performed using the default material behaviour models and analysis options. In addition, all analyses concluded without any numerical stability problems and in a short period of time. A typical analysis of the PCA shear walls required a computation time of approximately 20 minutes*. This is significant considering the several hours required for such analyses using finite element procedures. Moreover, the highly irregular loading protocol of Specimen SP6 (Seckin, 1981) was successfully simulated through the use of seed files (i.e., binary input files).

The limitations of the analytical procedure were pointed out regarding the modelling of beam-column joints and the inability to consider longitudinal reinforcement bond-slip and buckling. It was emphasized that the analysis procedure should not be used for the detailed analysis and assessment of beam-column joints; rather, it is more suitable for global analyses of large frame structures. The need to include the reinforcement bond-slip and buckling mechanisms into the current computational algorithm for better simulations under large strain reversals was, however, borne out.

The newly implemented shear protection algorithm, which approximately takes into account the increased strengths of D-regions, performed well. Premature shear failures of the sections adjacent to the shear wall bases were effectively prevented.

---

*On a Laptop computer with an Intel ® Dual Core 2 Due® T7500 (2.2 GHz) Processor®, a 2 GB DDR2, 677MHz RAM and a 7200 RPM hard disk drive.

# CHAPTER 7

## DYNAMIC LOADING: THEORY AND IMPLEMENTATION

### 7.1 Chapter Layout

This chapter describes the theoretical principles needed for the nonlinear analysis of reinforced concrete frames subjected to dynamic loading conditions and their implementation into the analytical procedure developed for general loading conditions.

The chapter starts with a discussion of the need for nonlinear analysis capability under dynamic loading. Next, a discussion is presented on how a dynamic problem differs from a static problem and what is required to convert a nonlinear static analysis procedure into a nonlinear dynamic analysis procedure which also retains its nonlinear static analysis capabilities.

This is then followed by the theories and new algorithms implemented into the nonlinear analysis procedure, developed in Chapter 5, in order to consider dynamic loading conditions including time-varying base accelerations, time-varying impulse, impact and blast forces, initial mass velocities, and constant mass accelerations.

The chapter continues with a discussion on the selection of an appropriate time step length, the use of additional viscous damping for stability reasons in Newmark's average and linear acceleration methods, and the numerical damping present in Wilson's Theta method.

Finally, the chapter concludes with three verification examples analyzed under ground acceleration-time history loading, impulsive loading and initial velocity loading for corroboration purposes.

In addition, when necessary, the appropriate use of the different formulations and options implemented are discussed.

## 7.2 Need for Nonlinear Analysis Procedures for Dynamic Loading

For analyzing a structure subjected to seismic loading, two nonlinear procedures have generally gained acceptance in modern seismic design provisions such as IBC (2006). These are the nonlinear static analysis procedure, and the nonlinear dynamic analysis procedure.

The *nonlinear static analysis procedure* (NSP) can be performed through the use of static analysis techniques as developed for monotonic loads in Chapter 3. This analysis approach can provide some useful information on the nonlinear behaviour of frame structures under seismic excitations, as discussed in Section 5.2. The established procedure for such an analysis usually consists of the following steps. A nonlinear model of the frame structure is created, usually accounting for material and geometric nonlinearities such as P-Δ effects. The model is then analyzed under monotonically increasing lateral loads representing the inertia forces in an earthquake. The analysis is continued until a target displacement is met. The target displacement is intended to represent the maximum displacement likely to be experienced during the design earthquake. In this procedure, a control node, which usually corresponds to the mass centre of the building roof, must be selected to monitor the lateral displacement attained in order to check with the target displacement (Figure 7.1). The conditions of the members at the target displacement are then evaluated. If the members are capable of sustaining their loads at the target displacement, the structure is deemed to be adequate for the design earthquake considered. Otherwise, inadequate members are re-designed in the case of a structure not yet built or retrofitted in the case of an existing structure.

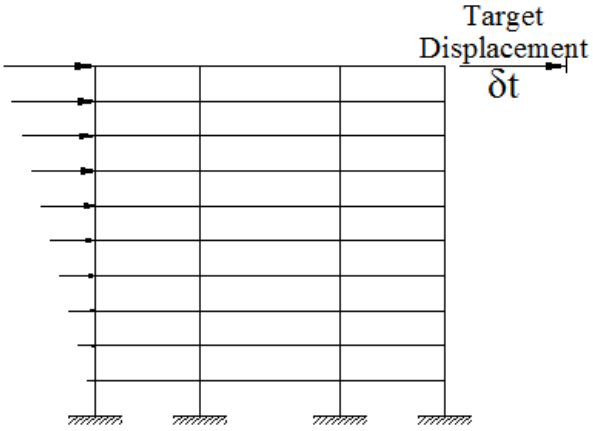


**Figure 7.1** Nonlinear Static Analysis Procedure for a Frame Structure

However, there are two difficulties involved in this approach that limits the use of nonlinear static analysis procedure. The first one is related to the use of a monotonically increasing lateral load distribution for the structure under consideration. In reality, due to material nonlinearities such as cracking of concrete and yielding of reinforcement, the stiffness characteristics of the structure can change drastically during a seismic event. This results in significant redistribution of the lateral loads induced by the ground motion. Therefore, the selection of a lateral load which increases monotonically with the same initial ratio is not appropriate for structures with highly nonlinear behaviour including significant yielding and force redistribution. The second difficulty is related to the effects of higher modes. The vibrational behaviour of a structure may change dramatically during a ground shaking if higher modes are contributing significantly to the structural response. Such behaviour is typical in tall and irregular buildings whose behaviour incorporates considerable torsional effects. However, the determination of both the monotonically increasing lateral load distribution and the target displacement is generally based on the first mode behaviour of the structure. As a result, the applicability of this procedure is limited. For example, the FEMA 356 (2000) prestandard, Clause 2.4.2.1 stipulates that "*nonlinear static analysis procedure shall be permitted in structures in which higher mode effects are not significant*" and requires a linear-elastic response spectrum analysis for determination of the effects of higher modes.

The second procedure is called the *nonlinear dynamic analysis procedure* (NDP), more commonly known as *nonlinear time-history analysis*. In this procedure, the establishment of neither a lateral load pattern nor a target displacement is required. Instead, the nonlinear analysis is carried out for a ground motion time-history which can be either a recorded or a synthetic motion. Because the numerical model accounts directly for material and geometric nonlinearities, the calculated response and internal forces are a reasonable approximation of those expected during the design earthquake (FEMA 356, 2000). However, the tools available for such an analysis require considerable judgement and experience, as indicated in Chapter 2. Acknowledging the difficulty involved, for example, FEMA 356 (2000) stipulates in Clause 2.4.2.2 that "*an analysis performed using the NDP shall be reviewed and approved by an independent third-party engineer with experience in seismic design and nonlinear procedures*". In addition, the intensive

time step calculations involved require significant computational power, which further constrains the use of this method.

Therefore, a nonlinear analysis tool for time-history analyses is much needed; one which is suitable for everyday office use by providing reasonably accurate responses with the use of default options, thereby not requiring previous knowledge of, for example, hinge behaviour, governing failure mechanism, and so on. This tool should also be executable by current computing power in a reasonable time.. For the reasons described above, in this chapter, several new dynamic analysis algorithms are developed and implemented into the calculation procedure, developed in Chapter 5, providing nonlinear time-history analysis capability for a given ground motion.

In addition to earthquakes, due to increased terror threats, nonlinear analysis of reinforced concrete structures under extreme loads, such as impact and blast, have recently gained added importance. Various analytical procedures have been reported in the literature to determine the global response of reinforced concrete structures under such loading conditions. However, as noted by Saatci (2007), the analysis methods reported are either over-simplified, such as the ones that treat reinforced concrete as a linearly-elastic or elastic-plastic material, or over-complicated, such as the ones that employ the sophisticated modelling techniques of a local response for a global structure. Moreover, the analytical tools available, even the highly sophisticated ones, commonly do not inherently consider shear-related influences. However, as was observed during the impact testing of reinforced concrete beams by Saatci (2007), even if a member is flexure-critical under static loads, shear damage under impact loads plays a major role in the overall behaviour of the member. Therefore, ignoring shear-related mechanisms with methods that assume flexural behaviour may lead to significant errors in the computed responses.

Therefore a nonlinear analysis tool is needed which is sufficiently practical for everyday use in an office design, yet sufficiently comprehensive to consider both flexure- and shear-related mechanisms at the global structural level. For these reasons, in this chapter, the implemented dynamic analysis procedure of VecTor5 is expanded to allow for an analysis capability under impact, impulse and blast loading conditions.

## 7.3 Essential Characteristics of a Dynamic Problem

A structural-dynamic problem is distinct from a structural-static problem in three fundamental aspects. First, a structural-dynamic problem is time dependent; therefore, contrary to the static problem, a dynamic problem does not have a single solution. Rather, it includes a succession of solutions corresponding to the response history. Second, dynamic loads are not only resisted by the stiffness of the structure, as with the static loads, but also by inertial forces resulting from accelerations of the structural mass. Inertial forces are the most important distinguishing characteristics of a structural-dynamics problem. In general, if the inertial forces represent a significant portion of the total load equilibrated by the internal forces of the structure, then the dynamic character of the problem must be considered (Clough and Penzien, 1993). Third, damping forces contribute to the load resistance of the structure by diminishing the amplitude of the free vibration of the structure. Particularly for the structures with various non-structural components, damping effects may be significant.

To illustrate the difference between structural-static and structural-dynamic problems, consider the simple model of a single degree-of-freedom system (SDOF) given in Figure 7.2. In a static system, the applied force, $p$, is resisted by one mechanism: the spring force $f_s$. Therefore, the static equilibrium equations becomes as follows:

$$p = k \times u \quad or \quad p = f_s \tag{7.1}$$

where $k$ is the stiffness of the spring, and $u$ is the displacement.

In a dynamic system, on the other hand, the applied force $p(t)$ is resisted by three mechanisms: the inertia force $f_I(t)$, the damping force $f_D(t)$, and the spring force $f_s(t)$. As a result, the *dynamic equation of motion* can be written as

$$f_I(t) + f_s(t) + f_D(t) = p(t) \qquad \text{or} \tag{7.2}$$

$$m \times \ddot{u}(t) + c \times \dot{u}(t) + k \times u(t) = p(t) \tag{7.3}$$

where m is the mass, c is the damping coefficient, k is the spring stiffness, $\ddot{u}(t)$ is the acceleration, $\dot{u}(t)$ is the velocity, and $u(t)$ is the displacement.

For a multi-degree-of-freedom system (MDOF), the matrix equivalent of the dynamic equation of motion can simply be written as follows:

$$[m]\times\{\ddot{u}(t)\}+[c]\times\{\dot{u}(t)\}+[k]\times\{u(t)\}=\{p(t)\} \tag{7.4}$$

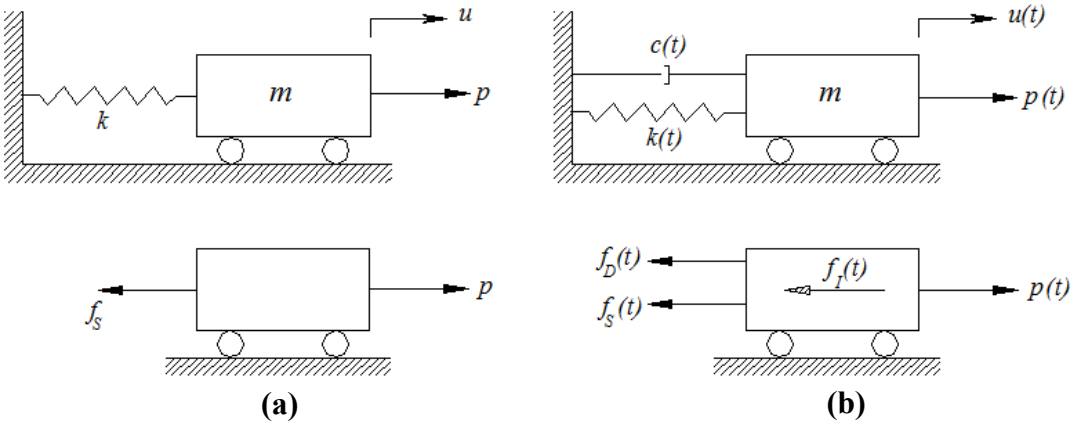


**Figure 7.2** Equilibrium of Forces: **(a)** Static System; **(b)** Dynamic System

## 7.4 Strategy Adopted for Inclusion of Dynamic Analysis Procedure into the Static Analysis Procedure of VecTor5

The construction of the dynamic equation of motion of Eq. 7.4 requires a mass matrix, a damping matrix, a stiffness matrix, and a time-varying load vector. After the determination of the required matrices or vectors, solution of the dynamic equation of motion is required. For complex excitations such as earthquake loading, an analytical solution of the dynamic equation of motion is usually not possible, requiring a numerical evaluation technique for the solution of the dynamic equation of motion.

In Chapter 5, VecTor5 was fully developed to perform a static nonlinear analysis under *general loading* conditions. In this formulation, as explained in Chapter 3, the solution of the static equilibrium equation of Eq. 7.1 is carried out by the global frame analysis algorithm by inversion of the stiffness matrix [$k$] to find the primary unknowns, displacements {$u$} as defined below.

$$[k] \times \{u\} = \{p\} \quad \text{and} \quad \{u\} = [k]^{-1} \times \{p\} \tag{7.5}$$

In order to be able to consider *dynamic loading* conditions, significant additions and modifications must be made to the existing calculation algorithm:

(1) An algorithm for the creation of a mass matrix, a damping matrix and a dynamic load vector must be implemented.

(2) A modal analysis algorithm should be implemented, which calculates vibration periods, mode shapes, damping coefficients and generalized masses, necessary for the creation of the damping matrix.

(3) At least one numerical time-stepping solution technique should be built into the existing solution procedure.

(4) An algorithm for the consideration of strain rate effects, which enhance the strength and stiffness of concrete and reinforcement under very high strain rates (up to 1000 $s^{-1}$), should be implemented. Consequently, concrete and reinforcement properties should be constantly modified in the sectional calculations based on the current strain rates.

It was desired to implement these calculations without radically changing the computation algorithm currently present in VecTor5 as nonlinear static analysis capability under the general loading conditions had to be completely retained. In other words, it was desired to condense the dynamic equation of motion of Eq. 7.4 so that it assumed the form of

$$[k^*] \times \{u\} = \{p^*\} \quad \text{and} \quad \{u\} = [k^*]^{-1} \times \{p^*\} \tag{7.6}$$

Through the adoption of such an approach, all the concepts described in Chapter 3, including the use of unbalanced forces, sectional calculations, second-order mechanisms and so on, were retained entirely.

## 7.5 Determination of Structural Property Matrices

In the following sections, the theoretical principles and formulations regarding the structural property matrices (i.e., mass matrix, damping matrix, stiffness matrix and load vectors) will be discussed.

### 7.5.1 Mass Matrix

The most important distinguishing characteristic of a structural dynamic problem, the inertial forces, result from time-varying acceleration of the structural mass. Because the mass of the structure is distributed continuously throughout the actual structure, the accelerations should be defined continuously throughout the structure; this would require a solution in terms of partial differential equations. However, if the mass of the structure is assumed to be concentrated at discrete points, the analytical problem becomes greatly simplified. This method, known as the *lumped-mass approach,* was employed in the formulation of the developed procedure for the mass matrix.

For clarification purposes, consider the frame model of a simply supported beam with five members shown in Figure 7.3(a). Based on the lumped-mass approach, the point masses are assumed to be concentrated at each end of the members as in Figure 7.3(b). From statics, half of the total mass of each member is assigned to each end. The total mass concentrated at any node of the complete structure is then determined as the sum of the nodal contributions from all members attached to that node as shown in Figure 7.3 (c). For example, the lumped mass for the Node 3 is calculated to be $m_3 = m_{2b} + m_{3a}$.

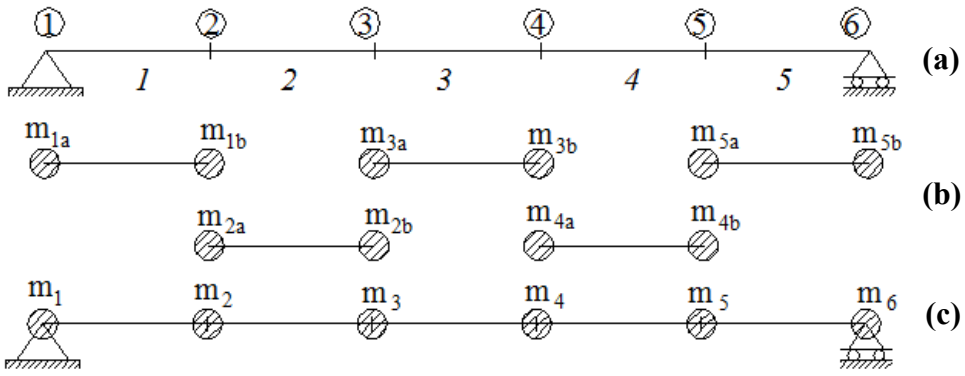


**Figure 7.3** A Simply Supported Beam: **(a)** Model; **(b)** Elemental Masses; **(c)** Nodal Masses

In the VecTor5 implementation, the masses due to the self-weight of the structure are calculated automatically based on the input density of the material and the geometry of the member. For each member, the total mass is calculated as follows:

$$m = \rho \times b \times h \times L \tag{7.7}$$

where $m$ is the mass of the member in kg, ρ is the density of concrete in kg/m$^3$, $b$ is the width of the cross section in mm, $h$ is the depth of the cross section in mm, and $L$ is the length of the member in mm. Modifiable by the user, the default value of density for normal weight reinforced concrete was assumed to be 2400 kg/m$^3$. In addition to the masses due to self weight, any other mass can be assigned to the desired nodes through the load data file.

Once the lumped masses at the nodes are calculated, the mass matrix for the structure can readily be formulated. As the rotational inertia of the mass has negligible influence on the dynamics of a plane frame structure, only two translational degrees-of-freedom are considered (Chopra, 2007). Therefore, for a lumped-mass idealization, the mass matrix is diagonal with

$$m_{ij} = 0 \quad if \quad i \neq j \quad and \quad m_{jj} = m_j \tag{7.8}$$

where $m_j$ is the lumped mass associated with the $j^{th}$ translational degree-of-freedom. Note that $m_j$ is zero for a rotational degree-of-freedom.

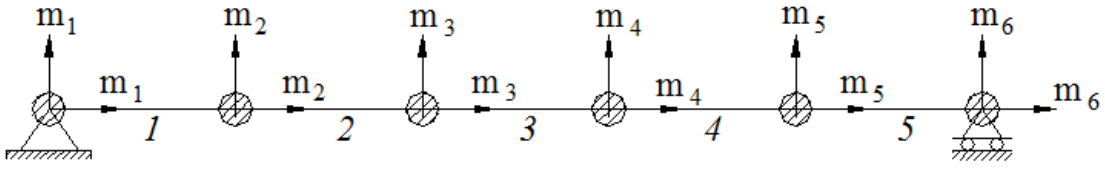


**Figure 7.4** Mass Degrees-of-Freedom of a Simply Supported Beam

Based on the approach described above, the degrees-of-freedom for the lumped masses of the simply supported beam are shown in Figure 7.4. During a dynamic event, the summation of the masses in the direction of the dynamic excitation equals the total mass

of the structure. If the mass of each member of Figure 7.4 is assumed to be equal to m, the resulting 12-by-12 diagonal mass matrix becomes as follows:

$$[m]=\begin{bmatrix} m/2 & 0 & 0 & 0 & 0 & 0 & 0 & 0 & 0 & 0 & 0 & 0 \\ 0 & m/2 & 0 & 0 & 0 & 0 & 0 & 0 & 0 & 0 & 0 & 0 \\ 0 & 0 & m & 0 & 0 & 0 & 0 & 0 & 0 & 0 & 0 & 0 \\ 0 & 0 & 0 & m & 0 & 0 & 0 & 0 & 0 & 0 & 0 & 0 \\ 0 & 0 & 0 & 0 & m & 0 & 0 & 0 & 0 & 0 & 0 & 0 \\ 0 & 0 & 0 & 0 & 0 & m & 0 & 0 & 0 & 0 & 0 & 0 \\ 0 & 0 & 0 & 0 & 0 & 0 & m & 0 & 0 & 0 & 0 & 0 \\ 0 & 0 & 0 & 0 & 0 & 0 & 0 & m & 0 & 0 & 0 & 0 \\ 0 & 0 & 0 & 0 & 0 & 0 & 0 & 0 & m & 0 & 0 & 0 \\ 0 & 0 & 0 & 0 & 0 & 0 & 0 & 0 & 0 & m & 0 & 0 \\ 0 & 0 & 0 & 0 & 0 & 0 & 0 & 0 & 0 & 0 & m/2 & 0 \\ 0 & 0 & 0 & 0 & 0 & 0 & 0 & 0 & 0 & 0 & 0 & m/2 \end{bmatrix} \tag{7.9}$$

Perhaps the biggest advantage of the lumped-mass matrix approach is the mathematical convenience in its determination and in the ensuing computations due to its *diagonal* characteristic.

A second approach is available in determining the mass matrix of the structure. In this approach, making use of the finite element concept, the mass influence coefficients are evaluated for each member by a procedure similar to the analysis of element stiffness coefficients. The resulting mass matrix is called the *consistent-mass matrix*. However, this procedure generally requires considerable more computational effort than does a lumped-mass system for two reasons: the resulting matrix has many off-diagonal terms leading to a mass coupling, and all rotational and translational degrees-of-freedom must be included in a consistent-matrix (Clough and Penzien, 1993). For these reasons, this approach is not implemented into the analysis procedure developed.

### 7.5.2 Damping Matrix

The process by which free vibration of a structure steadily diminishes in amplitude is called *damping* (Chopra, 2007). This decay results from the dissipation of energy of the vibrating system by various mechanisms. In a reinforced concrete structure, energy dissipation primarily occurs through the nonlinear hysteresis of concrete and

reinforcement. However, many other mechanisms contribute to the energy dissipation, including the opening, closing and sliding at cracks in the concrete, and the friction between structural and non-structural elements such as partition walls. In addition, the hysteretic behaviour of non-structural elements may be significant. Therefore, it seems impossible to identify or mathematically describe all of the energy dissipating mechanisms (Chopra, 2007). For this reason, the damping characteristics of a structure are determined in a *highly* idealized manner.

The damping of a MDOF system can conveniently be expressed in terms of modal damping ratios $\xi_n \ (n = 1, 2, ..., N)$ instead of an explicit damping matrix. However, when evaluating the nonlinear response of a structure under dynamic excitations, the response cannot be expressed by superposition of uncoupled modal responses because mode shapes are not fixed but are changing with changes in stiffness, requiring an explicit damping matrix. In such a situation, the most effective way to determine the required damping matrix is to first evaluate one or more proportional damping matrices and then to combine them through an assumed formulation to obtain the so-called *proportional damping matrix* [*c*].

There are a number of procedures available in the literature for constructing a proportional damping matrix. As they are already highly idealized representation of the damping properties of structures, further assumptions are usually included to make the resulting matrix easier to manipulate mathematically such as orthogonality with respect to the modes of vibration.

One of the most commonly used proportional damping formulations is called *Rayleigh damping*, after Lord Rayleigh (1878), which assumes that damping is proportional to a combination of the mass, $[m]$, and the stiffness, $[k]$, matrices as follows:

$$[c] = a_0 \times [m] + a_1 \times [k] \tag{7.10}$$

Rayleigh damping leads to the following relation between damping ratios and frequencies.

$$\xi_n = \frac{a_0}{2 \times \omega_n} + \frac{a_1 \times \omega_n}{2} \tag{7.11}$$

where $\xi_n$ is the modal damping ratio (ratio of the given damping to the critical damping), $a_0$ and $a_1$ are the proportionality constants of Rayleigh damping, and $\omega_n$ is the natural frequency of the $n^{th}$ mode.

As shown in Figure 7.5(a), the first term of Eq. 7.11 represents the mass proportional damping where the damping ratio is inversely proportional to the frequency, while the second term represents the stiffness proportional damping where the damping ratio is directly proportional to the stiffness. The combination of these two damping ratios creates the Rayleigh damping as shown in Figure 7.5(b).

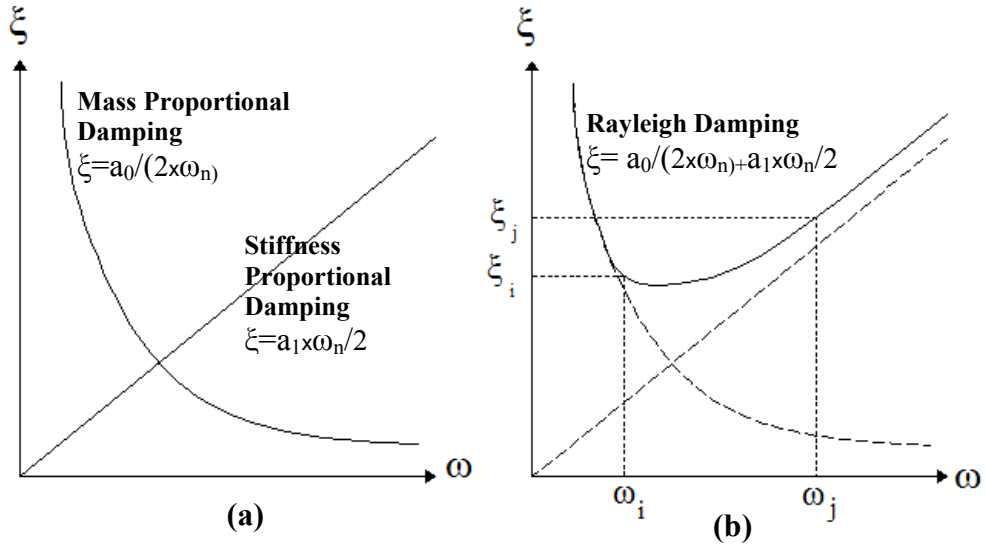


**Figure 7.5** Variation of Damping Ratios with Natural Frequency **(a)** Mass- and Stiffness-Proportional Damping; **(b)** Rayleigh Damping (Chopra, 2007)

The Rayleigh damping proportionality constants, $a_0$ and $a_1$, can be determined from specified damping ratios, $\xi_i$ and $\xi_j$, for the $i^{th}$ and $j^{th}$ modes, respectively. Expressing Eq. 7.11 in matrix form for these two modes leads to

$$\frac{1}{2} \times \begin{bmatrix} 1/\omega_i & \omega_i \\ 1/\omega_j & \omega_j \end{bmatrix} \begin{Bmatrix} a_0 \\ a_1 \end{Bmatrix} = \begin{Bmatrix} \xi_i \\ \xi_j \end{Bmatrix} \tag{7.12}$$

which can be solved to yield

$$a_0 = 2 \times \xi_i \times \omega_i - a_1 \times \omega_i^2 \tag{7.13}$$

$$a_1 = \frac{2 \times \xi_j \times \omega_j - 2 \times \xi_i \times \omega_i}{\omega_j^2 - \omega_i^2} \tag{7.14}$$

The damping matrix can then be calculated from Eq. 7.10 while the damping ratio for any other mode can be found from Eq. 7.11.

This procedure is implemented into the dynamic analysis algorithm developed requiring the selection of two vibration modes and the corresponding damping ratios at the beginning of an analysis. This selection should be made carefully to ensure reasonable damping ratios for the modes contributing significantly to the response. It is recommended that *mode i* be taken as the fundamental mode of the structure (the first mode), while *mode j* be one of the highest modes which contributes significantly to the response. The damping ratios of the modes between the two specified modes will be somewhat smaller than the specified damping ratios, while all modes higher than *mode j* will have damping ratios increasing monotonically with the frequency.

To illustrate this concept, consider a simply supported beam with 13 degrees of dynamic freedom and assume that the first five modes are contributing significantly to the dynamic response of the structure. Therefore, the first five modes are desired to have an assumed 5% damping ratio. To do this, the first and fifth modes were assigned the assumed 5% damping ratio and a dynamic analysis was carried out with VecTor5. The eigen analysis results output of the program indicated that the damping ratios for all modes are as follows:

**Table 7.1** Eigen Analysis Results of a Simply Supported Beam

| Mode | Period (s) | Natural Frequency (1/s) | Damping Ratio (%) |
|---|---|---|---|
| **1** | 0.019100 | 329.0 | **5.00** |
| 2 | 0.001480 | 4245.4 | 1.80 |
| 3 | 0.001260 | 4986.7 | 1.99 |
| 4 | 0.000618 | 10167.0 | 3.56 |
| **5** | 0.000430 | 14612.1 | **5.00** |
| 6 | 0.000366 | 17167.2 | 5.84 |
| 7 | 0.000271 | 23185.2 | 7.85 |
| 8 | 0.000210 | 29919.9 | 10.06 |
| 9 | 0.000208 | 30207.6 | 10.19 |
| 10 | 0.000178 | 35298.8 | 11.85 |
| 11 | 0.000166 | 37850.5 | 12.71 |
| 12 | 0.000147 | 42742.8 | 14.37 |
| 13 | 0.000064 | 97868.9 | 32.78 |

Inspection of Table 7.1 reveals that the damping ratios of the modes between the first and fifth have less than 5% damping ratios while the modes greater than the fifth have damping ratios increasing with the natural frequency. The end result of this situation is that the responses of high frequency modes are essentially eliminated by their high damping ratios (as much as 32.78% in this example).

Although mathematically convenient and numerically stable, it is not possible, as shown above, to exactly control the damping ratios in the Rayleigh damping formulation. Other than the two predefined modes, the damping ratios for the remaining modes are automatically determined by the procedure. However, in some situations, direct specification of the damping ratios for more than two modes may be desired.

In such a case, a more general formulation of the proportional damping matrix is needed. For this purpose, *Caughey damping*, after T. K. Caughey (1960), can be used. In this formulation, the damping ratios for all available modes can be exactly specified and the corresponding damping matrix is constructed as follows:

$$[c] = m \times \sum_{i=0}^{N-1} \left\{ a_i \times \left[ m^{-1} \times k \right]^i \right\} \tag{7.15}$$

where $N$ is the total number of modes, and $a_i$ are constants which can be determined by solving $N$ simultaneous equations as defined by Eq. 7.16.

$$\xi_n = \frac{1}{2} \times \sum_{i=0}^{N-1} \left( a_i \times \omega_n^{2i-1} \right) \tag{7.16}$$

It is also possible to specify the damping ratios for $J$ modes of an $N$-DOF system, where $J < N$. In this case, $N$ should be replaced with $J$ in Eq. 7.15 and Eq. 7.16.

While the Caughey damping matrix makes it possible to specify the damping ratios for any number of modes, some problems are reported in the literature. First, Eq. 7.16 is reported to be ill-conditioned (Chopra, 2007). Second, in the case of less than $N$ terms in Eq. 7.15, the creation of negatively damped modes, which would invalidate the analysis results, are reported by Clough and Penzien (1993). Moreover, the solution of $N$ simultaneous equations increases computation cost and analysis time. The resulting matrix becomes fully populated if more than two terms are included in Eq. 7.15, which further increases computational demand. For these reasons described, Caughey damping is not implemented into the dynamic analysis procedure developed.

When performing a dynamic analysis with the proposed procedure, most of the energy dissipation occurs through the nonlinear concrete and reinforcement stress-strain hystereses; therefore, the introduction of additional damping is not desired. In fact, in the application of the developed analysis tool to previously tested structures, discussed in Chapter 8, no additional damping was used. However, it was found, under specific circumstances, that a little additional damping may be necessary, for instance, for the fundamental mode of the structure when no viscous damping is needed for all of the remaining modes. Such a situation might arise especially when using the linear acceleration method, developed later in this chapter. However, with the implemented Rayleigh damping, such a specification of damping ratios is strictly not possible.

To address this issue, a second type of damping formulation is implemented into the analysis procedure developed. Known as *alternative damping,* this damping matrix is constructed through the superposition of modal damping matrices as follows (Clough and Penzien, 1993):

$$c = m \times \left[ \sum_{n=1}^{N} \frac{2 \times \xi_n \times \omega_n}{M_n} \times \phi_n \times \phi_n^T \right] \times m \tag{7.17}$$

where $M_n$ is the generalized mass, $\phi_n$ is the mode shape, $m$ is the mass matrix, and $N$ is the total dynamic degrees-of-freedom. The $n^{th}$ term in this summation is the contribution of the $n^{th}$ mode with its damping ratio $\xi_n$. If this term is not included, the resulting damping matrix $c$ will contain a zero damping ratio in the $n^{th}$ mode. It is reasonable to include only the first $J$ modes of an $N$-DOF system ($J < N$) in Eq. 7.17 that are expected to contribute significantly to the response. The lack of damping in modes $J$+1 to $N$ is reported to not create numerical problems (Chopra, 2007).

For use in Eq. 7.17, the generalized mass for the $n^{th}$ mode is obtained as follows:

$$M_n = \phi_n^T \times m \times \phi_n \tag{7.18}$$

The mode shapes, $\phi_n$, are determined by the modal analysis subroutine as discussed later in this chapter.

The above formulation was implemented into the dynamic analysis procedure developed, requiring the input of two damping ratios for the two specified modes. Consequently, this second damping option made it possible to consider viscous damping in up to two modes, while assuming zero damping for all of the remaining modes.

### 7.5.3 Stiffness Matrix

As explained in detail in Chapter 3, the stiffness matrix of the structure is determined by the global frame analysis algorithm, including the effects of geometric nonlinearity. Therefore, no additional calculations are necessary for the determination of the stiffness matrix for use in the dynamic equation of motion of Eq. 7.4.

### 7.5.4 Load Vector

In the formulation of the dynamic analysis procedure of VecTor5, four different dynamic loads are considered: time-varying base accelerations, time-varying forces (i.e., impulses) as defined by a tri-linear curve, initial velocities assigned to lumped masses, and constant accelerations assigned to lumped masses.

Time-varying base acceleration loads can be utilized when performing a *nonlinear dynamic time-history analysis*. A recorded or a synthetic ground motion time-history can be applied to the structure in the horizontal (x-direction) or in the vertical (y-direction) direction. In some situations, it may be necessary to consider simultaneously acting ground motions. For example, while applying a specific ground motion in the horizontal direction, it may be desired to consider a certain percentage of the same motion in the vertical direction. For this reason, in the implementation, two scaling factors are considered for the horizontal and vertical directions. Based on the input factors, the same ground motion can be scaled and applied to both directions simultaneously.

The load vector for the time-history analysis is created through the concept of *effective support excitation*, $p_{eff}(t)$. Based on this concept, equivalent static nodal forces are calculated for the particular time under consideration and the load vector is set up accordingly as follows:

$$\{p(t)\} = \{p_{eff}(t)\} = -[m] \times \{r\} \times \ddot{u}_g(t) \tag{7.19}$$

where $\ddot{u}_g(t)$ is the input ground acceleration, and $\{r\}$ is the influence coefficient vector which represents the displacements resulting from a unit support displacement. For example, consider the 6 DOF structure shown in Figure 7.6. If the ground motion is acting in the global x-direction, the influence coefficient vector will be $r = \{1 \quad 0 \quad 1 \quad 0 \quad 1 \quad 0\}^T$. For the consideration of two directions simultaneously, the r vector becomes fully populated with 1.

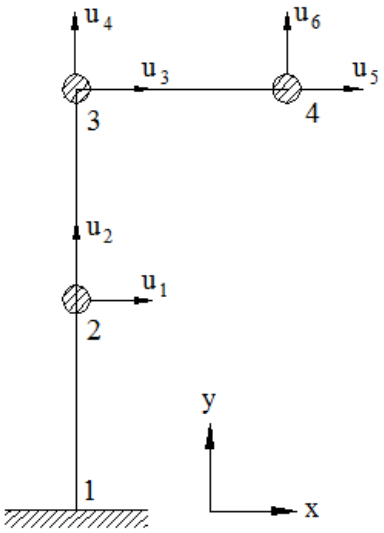


**Figure 7.6** A 6-DOF Structure with Mass Degrees-of-Freedom Shown

Time-varying forces can be utilized when performing a *nonlinear impulse, blast* or *impact analysis*. Pre-determined force-time histories can be applied to the desired nodes in either the global x- or y-direction. A tri-linear force-time history, as shown in Figure 7.7, is required as input for such a loading.

As the loads are the input values in this type of analysis, the load vector can easily be created considering the load application direction, the load value for the particular time under consideration and the node to which the load is applied. For example, assume that the load-time history below is applied to Node 4, in the global x-direction, of the structure shown in Figure 7.6. The load vector corresponding to time $t_1$ becomes $\{p(t)\} = \{0 \quad 0 \quad 0 \quad 0 \quad F_1 \quad 0\}^T$.

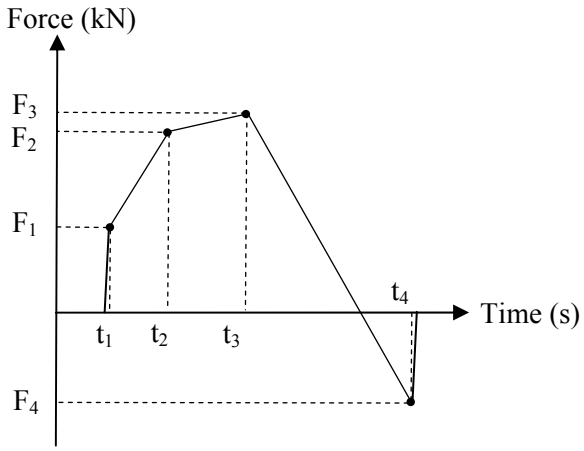


**Figure 7.7** Tri-Linear Force-Time History

Initial velocity loads can be utilized when performing a *nonlinear initial velocity problem* or, more importantly, a *nonlinear impact analysis,* as explained in detail in Section 8.3. Initial velocities can be assigned to the desired nodes in either the global x- or y-direction. The input initial velocities are directly used in the numerical solution of the dynamic equation of motion, as described in Section 7.7.3. As a result, no load vector is created for this type of loading.

Constant acceleration loads can be utilized when, for example, simulating the gravitational effects in *any type of nonlinear dynamic analyses.* They are used in this thesis when performing *nonlinear impact analyses* in Chapter 7. Constant accelerations can be assigned to the desired nodes in either the global x- or y-direction. Constant acceleration loads are taken into account through the use of the effective support excitation concept as explained above.

## 7.6 Numerical Evaluation of the Dynamic Equation of Motion

The dynamic equation of motion, for linearly elastic analyses, can conveniently be evaluated through a modal analysis technique which involves the evaluation of many independent response contributions combined to obtain the total response. However, when evaluating the *nonlinear* response of a structure under dynamic excitations, the response cannot be expressed by superposition of uncoupled modal responses because the mode shapes are not fixed but are changing with changes in stiffness.

The only generally applicable procedure for analysis of an arbitrary set of nonlinear response equations is numerical *step-by-step integration* (Clough and Penzien, 1993). According to this method, the response history is divided into a sequence of *short and equal* time intervals, during which the response is calculated, based on the physical properties existing at the beginning of the time interval. Thus, the nonlinear behaviour of a MDOF system is approximated as a sequence of linear analyses in which the physical properties of the system change progressively. In the numerical step-by-step integration, stepping from one time instance to another is usually not an exact procedure (Chopra, 2007). Many approximate procedures are available in the literature for this purpose. The

only generally applicable procedures for evaluation of the *nonlinear* dynamic response are based on the *variation of acceleration*.

Based on the assumed variation of acceleration, three numerical step-by-step integration methods were implemented into the dynamic analysis procedure developed. These are Newmark's average acceleration, Newmark's linear acceleration, and Wilson's Theta method. The formulations related to these methods are presented in the following sections.

### 7.6.1 Incremental Equation of Motion

When performing the step-by-step calculations for a *nonlinear* dynamic analysis, the physical properties of the structure are assumed to remain constant only for short increments of time. Accordingly, it is convenient to formulate the response in terms of an *incremental equation of motion*.

Consider the simplest model of a single degree-of-freedom system shown in Figure 7.2(b). The equilibrium of forces acting on the mass at time $t_i$ may be written as follows:

$$f_I(t) + f_D(t) + f_S(t) = p(t) \tag{7.20}$$

And a short time later, $\Delta t$, the equilibrium requirement becomes

$$f_I(t+\Delta t) + f_D(t+\Delta t) + f_S(t+\Delta t) = p(t+\Delta t) \tag{7.21}$$

Subtracting Eq. 7.20 from Eq. 7.21 yields the so-called incremental equation of motion

$$\Delta f_I(t) + \Delta f_D(t) + \Delta f_S(t) = \Delta p(t) \tag{7.22}$$

where the incremental forces may be expressed as follows:

$$\Delta f_I(t) = f_I(t+\Delta t) - f_I(t) = m \times \Delta \ddot{u} \tag{7.23}$$

$$\Delta f_D(t) = f_D(t+\Delta t) - f_D(t) = c(t) \times \Delta \dot{u} \tag{7.24}$$

$$\Delta f_S(t) = f_S(t+\Delta t) - f_S(t) = k(t) \times \Delta u \tag{7.25}$$

$$\Delta p(t) = p(t+\Delta t) - p(t) \tag{7.26}$$

In Eq. 7.24 and Eq. 7.25, $c(t)$ and $k(t)$ represent average values of the damping and stiffness which may vary during the time increment. However, the average values depend on the final values which are unknowns. This situation requires an iterative solution. However, in practice, it is common to use the initial tangent values instead, as shown in Figure 7.8 (Clough and Penzien, 1993).

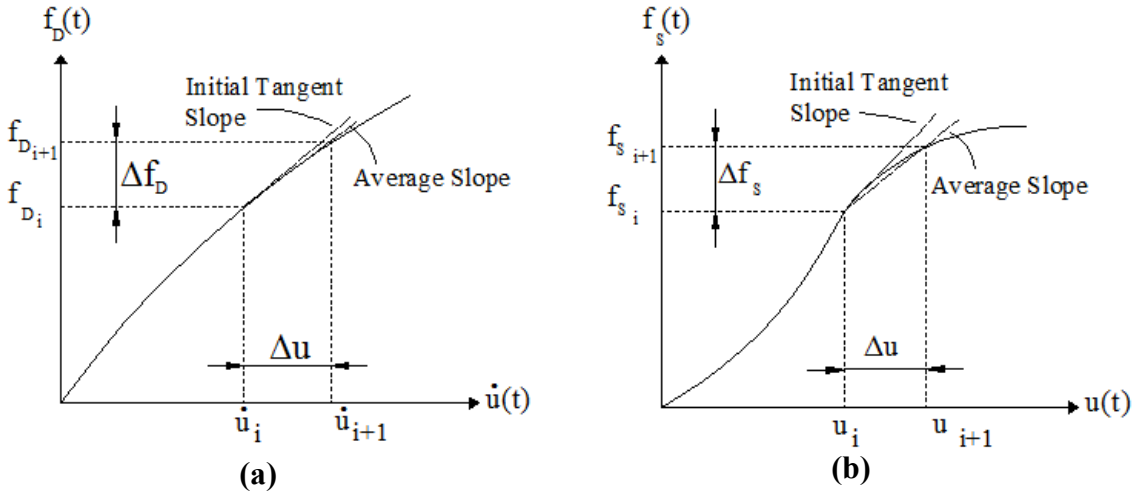


**Figure 7.8** Incremental Quantities: **(a)** Nonlinear Damping; **(b)** Nonlinear Stiffness (Clough and Penzien, 1993)

Substituting the force expressions of Eqs. 7.23 to 7.26 back into Eq. 7.22 leads to the final form of the incremental equilibrium equation, as follows:

$$m \times \Delta \ddot{u} + c(t) \times \Delta \dot{u} + k(t) \times \Delta u = \Delta p(t) \tag{7.27}$$

Denoting the values at the beginning of the time interval with *0* and at the end of time interval with *1,* the incremental acceleration, velocity and displacement can be written as

$$\Delta \ddot{u} = \ddot{u}_1 - \ddot{u}_0 \quad ; \quad \Delta \dot{u} = \dot{u}_1 - \dot{u}_0 \quad \text{and} \quad \Delta u = u_1 - u_0 \tag{7.28}$$

### 7.6.2 Newmark's Method

In 1959, Newmark suggested a family of time-stepping methods based on the following equations:

$$\dot{u}_1 = \dot{u}_0 + (1-\gamma)\times\Delta t\times\ddot{u}_0 + \gamma\times\Delta t\times\ddot{u}_1 \tag{7.29}$$

$$u_1 = u_0 + \Delta t\times\dot{u}_0 + \left(\frac{1}{2}-\beta\right)\times\Delta t^2\times\ddot{u}_0 + \beta\times\Delta t^2\times\ddot{u}_1 \tag{7.30}$$

where the parameters $\gamma$ and $\beta$ define the variation of acceleration over a time step and determine the stability and accuracy characteristics of the method. The typical values of $\gamma = \frac{1}{2}$ and $\frac{1}{6}\le\beta\le\frac{1}{4}$ are satisfactory from all points of view, including that of accuracy (Chopra, 2007). However, two special cases of Newmark's method are widely used in the literature; these are the well-known average acceleration and linear acceleration methods (Figure 7.9). In the average acceleration method $\beta$ is taken as $1/4$, while in the linear acceleration method $\beta = 1/6$.

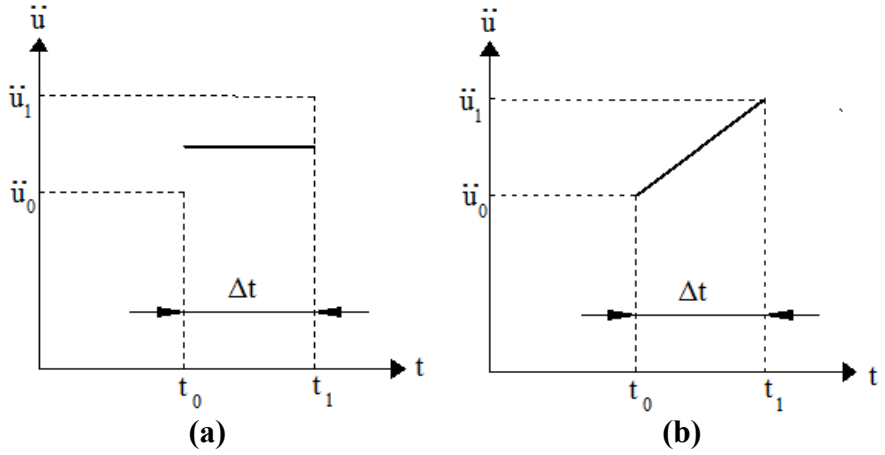


**Figure 7.9** Newmark's Method **(a)** Average Acceleration: γ=1/2 and β=1/4;
**(b)** Linear Acceleration: γ=1/2 and β=1/6

In the numerical solution of the incremental equation of motion with Newmark's method, two different formulations can be developed: implicit and explicit. In the *implicit* formulation, Eq. 7.29 and Eq. 7.30 are directly used in the numerical solution, giving way

to an iterative process because the unknown $\ddot{u}_1$ appears on the right-hand side of the Eq. 7.29 and Eq. 7.30. In the explicit formulation, Eq. 7.29 and Eq. 7.30 are modified so that the right-hand sides do not include any unknowns, enabling a non-iterative solution technique. Therefore, the explicit formulation is usually preferred over the implicit one (Clough and Penzien, 1993).

For implementation into the analytical tool developed, the explicit formulation was used to avoid a triple iterative calculation as the procedure is already based on a double iterative process (i.e., global and sectional calculation iterations).

### 7.6.3 Non-Iterative (Explicit) Solution of the Incremental Equation of Motion

Eq. 7.29 and Eq. 7.30 can simply be rewritten as

$$\Delta\dot{u} = \Delta t \times \ddot{u}_0 + \gamma \times \Delta t \times \Delta\ddot{u} \tag{7.31}$$

$$\Delta u = \Delta t \times \dot{u}_0 + \frac{\Delta t^2}{2} \times \ddot{u}_0 + \beta \times \Delta t^2 \times \Delta\ddot{u} \tag{7.32}$$

Conversion to an explicit formulation is performed by solving Eq. 7.32 to obtain

$$\Delta\ddot{u} = \frac{1}{\beta \times \Delta t^2} \times \Delta u - \frac{1}{\beta \times \Delta t} \times \dot{u}_0 - \frac{1}{2 \times \beta} \times \ddot{u}_0 \tag{7.33}$$

Substitution of Eq. 7.33 into Eq. 7.31 gives

$$\Delta\dot{u} = \frac{\gamma}{\beta \times \Delta t} \times \Delta u - \frac{\gamma}{\beta} \times \dot{u}_0 - \left( \frac{\gamma \times \Delta t}{2 \times \beta} - \Delta t \right) \times \ddot{u}_0 \tag{7.34}$$

In Eq. 7.33 and Eq. 7.34, all unknowns on the right-hand side are eliminated, enabling an explicit solution.

Substitution of Eq. 7.33 and Eq. 7.34 into Eq. 7.27 and rearrangement yields

$$\hat{k}_i \, \Delta u_i = \Delta \hat{p}_i \tag{7.35}$$

where

$$\hat{k} = k + \frac{\gamma}{\beta \times \Delta t} \times c + \frac{1}{\beta \times \Delta t^2} \times m \tag{7.36}$$

$$\Delta \hat{p} = \Delta p + \left( \frac{1}{\beta \times \Delta t} \times m + \frac{\gamma}{\beta} \times c \right) \times \dot{u}_0 + \left[ \frac{1}{2 \times \beta} \times m + \Delta t \times \left( \frac{\gamma}{2 \times \beta} - 1 \right) \times c \right] \times \ddot{u}_0 \tag{7.37}$$

In Eq. 7.36 and Eq. 7.37, the system properties *k* and *m* should be determined based on the assumption made (i.e., initial tangent slope or average slope in Figure 7.8).

As a result, using the system properties *m*, *k* and *c*, algorithm parameters $\gamma$ and $\beta$, velocities $\dot{u}_0$, and accelerations $\ddot{u}_0$ at the beginning of the time interval, the incremental displacement is found as follows:

$$\Delta u = \frac{\Delta \hat{p}}{\hat{k}} \tag{7.38}$$

The velocity at the end of time step can now be calculated using Eq. 7.34. It is recommended by Clough and Penzien (1993) to calculate the final acceleration from the equation of motion (rather than Eq. 7.31), to preserve the equilibrium equation, as follows:

$$\ddot{u}_1 = \frac{p_1 + c \times \dot{u}_1 - k \times u_1}{m} \tag{7.39}$$

### 7.6.4 Stability of Newmark's Method

The average acceleration method is an *unconditionally stable* procedure, which results in bounded solutions regardless of the time step length. The linear acceleration method, on

the other hand, is a *conditionally* stable procedure requiring a time-step length, $\Delta t$, less than $0.551 \times T_n$ where $T_n$ is the natural period of the highest mode. When evaluating the response of an MDOF system, this stability limit may impose severe restrictions on $\Delta t$ as the period of the highest mode usually corresponds to a very small number. For example, consider again the simply supported beam with 13 modes. The periods calculated are presented in Table 7.1 where the 13$^{th}$ mode has a period of 0.0000642 sec. For a stable solution, the linear acceleration method requires a time step length which is less than $0.551 \times 0.0000642 = 0.000035 \,\text{sec}$. This choice of $\Delta t$ requires approximately 28200 time steps to compute the response of the system for 1 second of the excitation. Due to the excessive computational demand required by the conditionally stable linear acceleration method, it is clear that the numerical procedure used should be an unconditionally stable one.

The average acceleration method is an unconditionally stable method suitable for the nonlinear analysis of MDOF systems. However, it has two drawbacks. The first is that a sequence of constant acceleration steps is a less accurate approximation of the true behaviour than a sequence of linear acceleration steps. Numerical experiments have demonstrated the superiority of the linear acceleration assumption as compared to the average acceleration assumption (Clough and Penzien, 1993). The second, and perhaps more important, drawback is that, similar to the linear acceleration, the average acceleration method does not provide any numerical damping in the solution. This is a disadvantage because it is desirable to filter out the response contributions of modes higher than the first $J$ significant modes ($J < N$) because these higher modes, which have been calculated from an idealization of structure, are usually not accurate relative to the actual properties of the structure (Chopra, 2007).

For the reasons explained above, a third procedure called *Wilson's Theta method* was implemented into the analytical procedure developed. This method is an unconditionally stable version of the linear acceleration procedure and provides numerical damping to the solution.

### 7.6.5 Wilson's Theta Method

Wilson's Theta method, after E. L. Wilson (1976), is a modification of the conditionally stable linear acceleration method to make it unconditionally stable. In this method, the acceleration is assumed to vary linearly over an *extended* time step length, $\delta t = \theta \times \Delta t$ as shown by Figure 7.10. The accuracy and stability of the method depends on the assumed value of the parameter $\theta$, which should be always greater than 1. However, for an unconditionally stable solution, $\theta \geq 1.37$ is required. A value of $\theta = 1.42$ is reported to give the optimal accuracy (Chopra, 2007).

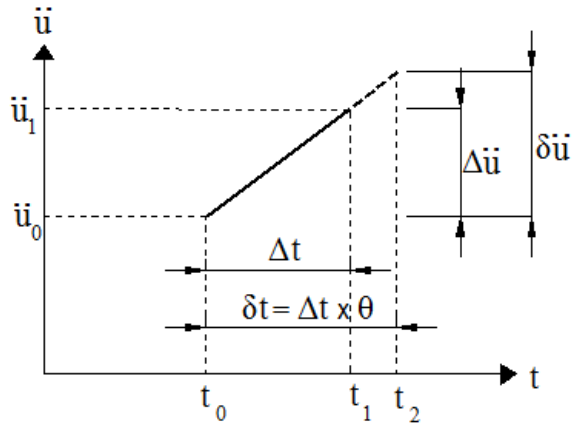


**Figure 7.10** Wilson's Theta Method: Variation of Acceleration with Time

The procedure can be formulated based on the incremental equation of motion, as described for the Newmark's Method in Section 7.6.3, by replacing $\Delta t$ with $\delta t$ and $\Delta p$ with $\delta p$, leading to the resulting equilibrium equation as follows:

$$\hat{k} \times \delta u = \delta \hat{p} \tag{7.40}$$

where

$$\hat{k} = k + \frac{\gamma}{\beta \times \delta t} \times c + \frac{1}{\beta \times \delta t^2} \times m \tag{7.41}$$

$$\delta \hat{p} = \delta p + \left( \frac{1}{\beta \times \delta t} \times m + \frac{\gamma}{\beta} \times c \right) \times \dot{u}_0 + \left[ \frac{1}{2 \times \beta} \times m + \delta t \times \left( \frac{\gamma}{2 \times \beta} - 1 \right) \times c \right] \times \ddot{u}_0 \tag{7.42}$$

$$\delta p = \theta \times \Delta p \quad \text{and} \quad \delta t = \theta \times \Delta t \tag{7.43}$$

Using the system properties m, k and c, algorithm parameters $\gamma = \frac{1}{2}$ and $\beta = \frac{1}{6}$, velocity $\dot{u}_0$, and acceleration $\ddot{u}_0$, at the beginning of the time interval, the incremental displacement $\delta u$ is found as follows:

$$\delta u = \frac{\delta \hat{p}}{\hat{k}} \tag{7.44}$$

The incremental acceleration $\delta \ddot{u}$ can now be calculated as follows:

$$\delta \ddot{u} = \frac{1}{\beta \times \delta t^2} \times \Delta u - \frac{1}{\beta \times \delta t} \times \dot{u}_0 - \frac{1}{2 \times \beta} \times \ddot{u}_0 \tag{7.45}$$

It should be noted that the calculated incremental values correspond to the *extended* time step; therefore, the final values corresponding to the *actual* time step must be determined as follows:

$$\Delta \ddot{u} = \frac{1}{\theta} \times \delta \ddot{u} \tag{7.46}$$

Once the incremental acceleration at the end of the actual time step is found, the resulting incremental velocity and displacement can be calculated through the same equations used for Newmark's Method (Eq. 7.31 and Eq. 7.32).

### 7.6.6 Solution Based on Total Loads and Secant Stiffness

As explained previously, the nonlinear frame analysis procedure employed in the developed analytical tool involves an iterative total-load secant-stiffness formulation. For

this reason, a total-load, secant stiffness based formulation for the numerical solution of the dynamic equation of motion, after Saatci (2007), is required for consistency. It was also desired to implement the three solution techniques defined above. For this reason, based on a total-load secant-stiffness approach, a three parameter formulation was derived in order to accommodate all three methods; namely, Newmark's average acceleration method, Newmark's linear acceleration method, and Wilson's Theta method. The summary of the derivations is presented below.

The dynamic equation of motion can be expressed in term of total loads as follows:

$$m \times \left( \ddot{u}_0 + \Delta \ddot{u} \right) + c \times \left( \dot{u}_0 + \Delta \dot{u} \right) + \bar{k}_1 \times u_1 = p_{stat} + p_1 \tag{7.47}$$

where the subscript *0* represents the values at the beginning of the time step, and the subscript *1* values at the end of the time step.

Substituting in Newmark's first equation (Eq. 7.29), and considering an extended time step $\delta t = \theta \times \Delta t$, Eq. 7.47 becomes

$$m \times \left( \ddot{u}_0 + \delta \ddot{u} \right) + c \times \left( \dot{u}_0 + \delta t \times \ddot{u}_0 + \gamma \times \delta t \times \delta \ddot{u} \right) + \bar{k}_1 \times u_1 = p_{stat} + p_1 * \tag{7.48}$$

The calculation of the equivalent load $p_1 *$ at the end of time step requires some additional manipulations as follows:

$$\delta p = \theta \times \Delta p \tag{7.43}$$

$$\text{where } \delta p = p_1 * - p_o \text{ and } \Delta p = p_1 - p_0 \tag{7.49}$$

Therefore,

$$p_1 * - p_o = \theta \times ( p_1 - p_0 ) \tag{7.50}$$

Rearrangement of Eq. 7.50 results in

$$p_1^* = p_1 \times \theta + p_0 \times (1-\theta) \tag{7.51}$$

When $\theta = 1$, the procedure reduces to the standard Newmark's method with $p_1^* = p_1$.

Substitution of Eq. 7.33 and Eq. 7.51 into Eq. 7.48 and rearrangement in the matrix format yields, (7.52)

$$\left[ [k_{stat}] + \frac{[m] + [c] \times \gamma \times (\theta \times \Delta t)}{\beta \times (\theta \times \Delta t)^2} \right] \times \{u_1\}$$
$$= \{p_{stat}\} + \{p_1^*\} + \frac{[m] + [c] \times \gamma \times (\theta \times \Delta t)}{\beta} \times \left[ \frac{\{u_0\}}{(\theta \times \Delta t)^2} + \frac{\{\dot{u}_0\}}{(\theta \times \Delta t)} + \frac{\{\ddot{u}_0\}}{2} \right]$$
$$- [c] \times \left\{ \{\dot{u}_0\} + (\theta \times \Delta t) \times \{\ddot{u}_0\} \right\} - [m] \times \{\ddot{u}_0\}$$

Further rearrangement of Eq. 7.52 leads to the *fundamental equation* of the dynamic analysis procedure implemented into the developed analysis procedure as follows:

$$\left[ [k_{stat}] + [k_{dyn}^{+}] \right] \times \{u_1\} = \{p_{stat}\} + \{p_{dyn}^{+}\} \tag{7.53}$$

where

$$[k_{dyn}^{+}] = \frac{[m] + [c] \times \gamma \times (\theta \times \Delta t)}{\beta \times (\theta \times \Delta t)^2} \tag{7.54}$$

$$\{p_{dyn}^{+}\} = \{p_1^*\} + \frac{[m] + [c] \times \gamma \times (\theta \times \Delta t)}{\beta} \times \left[ \frac{\{u_0\}}{(\theta \times \Delta t)^2} + \frac{\{\dot{u}_0\}}{(\theta \times \Delta t)} + \frac{\{\ddot{u}_0\}}{2} \right]$$
$$- [c] \times \left\{ \{\dot{u}_0\} + (\theta \times \Delta t) \times \{\ddot{u}_0\} \right\} - [m] \times \{\ddot{u}_0\} \tag{7.55}$$

Eq. 7.53 makes it possible to perform nonlinear dynamic analyses, based on a total-load secant-stiffness approach, without radically changing the computation algorithm currently present in VecTor5 as developed for general loading conditions.

Through the use of Eq. 7.53, it is possible to carry out a nonlinear dynamic analysis based on one of the three numerical analysis procedures:

(1) Newmark's average acceleration method: substitute $\gamma = \frac{1}{2}$ and $\beta = \frac{1}{4}$ and $\theta = 1$

(2) Newmark's linear acceleration method: substitute $\gamma = \frac{1}{2}$ and $\beta = \frac{1}{6}$ and $\theta = 1$

(3) Wilson's Theta method: substitute $\gamma = \frac{1}{2}$ and $\beta = \frac{1}{6}$ and $\theta = 1.42$

As mentioned previously, the value of $\theta$ governs the stability and accuracy of Wilson's Theta method. A value $\theta \geq 1$ is sufficient for this procedure to work. However, for an unconditionally stable solution $\theta \geq 1.37$ is required. A default value of $\theta = 1.42$ is used in VecTor5 calculations as it is reported to give the optimal accuracy (Chopra, 2007).

## 7.7 Dynamic Analysis Procedure Implemented

A flowchart indicating the dynamic analysis steps is presented in Figure 7.11, where the newly added steps are shown with bold type and the modified steps with dotted lines.

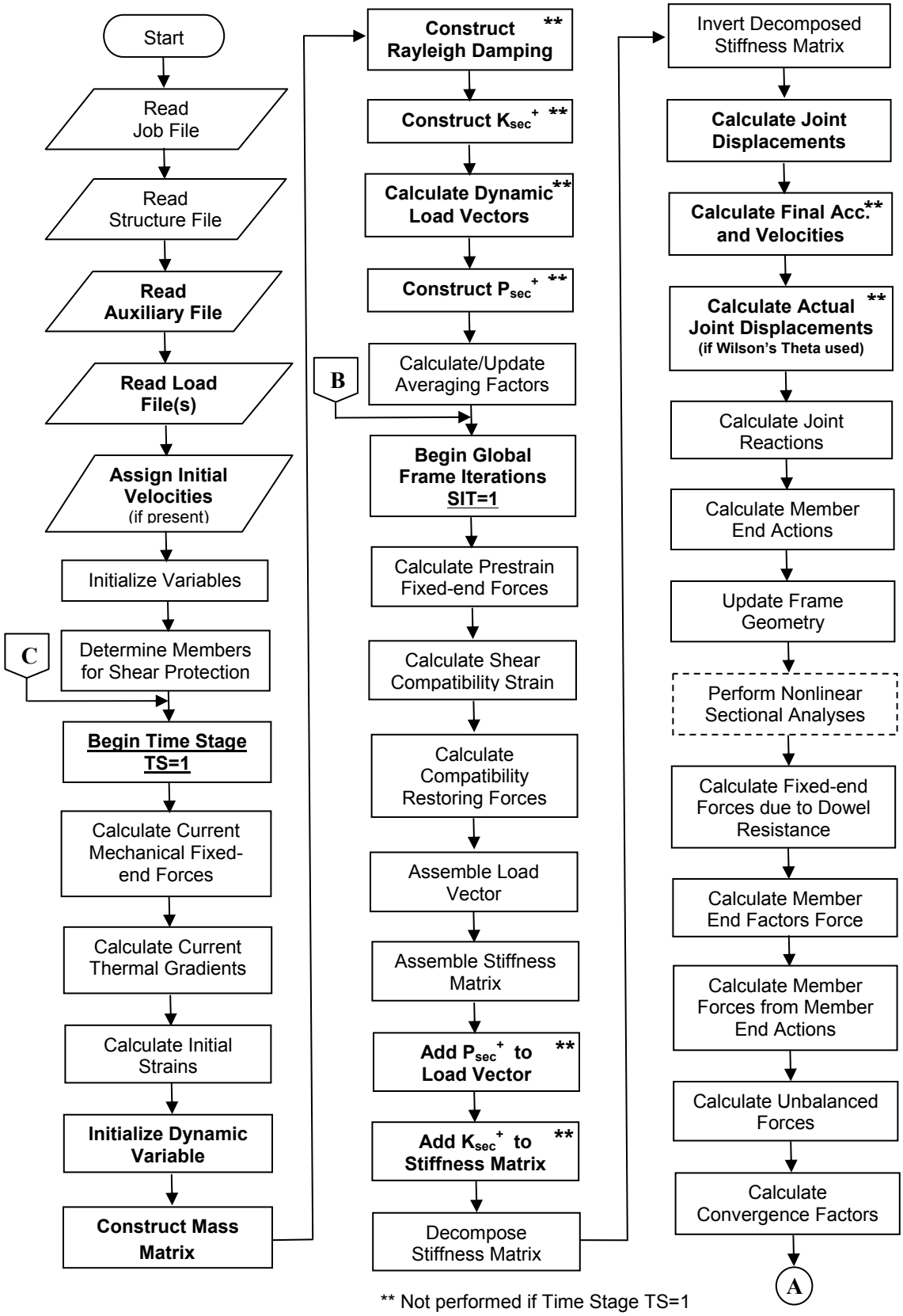


**Figure 7.11** Flow Chart for the Global Frame Analysis of VecTor5

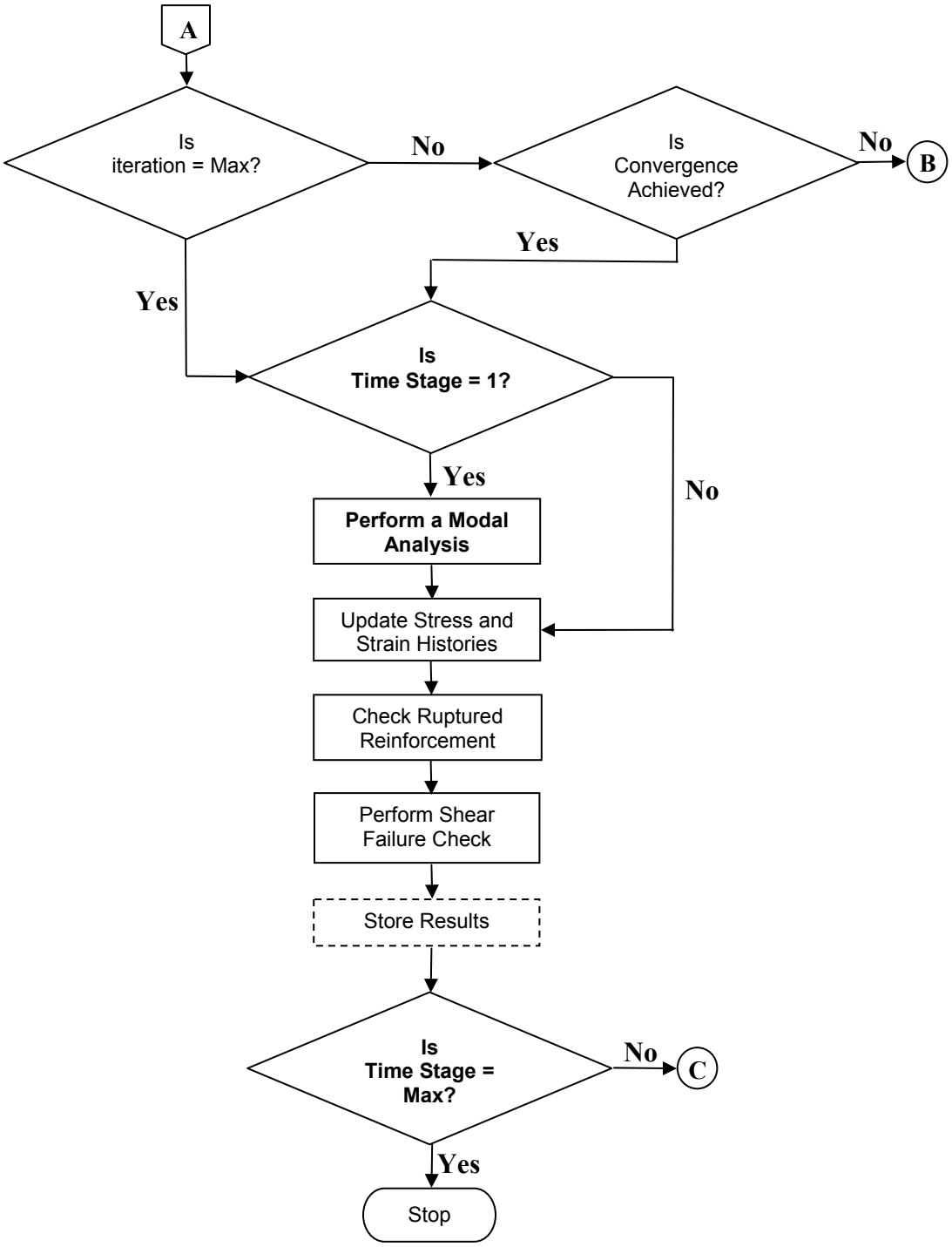


**Figure 7.11** Flow Chart for the Global Frame Analysis of VecTor5 (continued)

### 7.7.1 Read Auxiliary Data File

In addition to the parameters required for a static analysis, several dynamic analysis parameters are required in this file. These are: the selection of one of the three time-

integration methods, consideration of masses due to self-weight, input of up to two vibration modes and the corresponding damping ratios, and input of ground acceleration factors.

### 7.7.2 Read Load Data Files

Dynamic loads such as ground motion-time history, impulse/impact/blast load-time history as a tri-linear curve, initial velocities, and constant accelerations are input in this file. Additional dynamic masses can also be defined in this file.

### 7.7.3 Initialization of Dynamic Variables

Similar to the static degrees-of-freedom, three dynamic degrees-of-freedom are assumed for each node: two translational and one rotational as shown in Figure 7.12. Note that the rotational degrees-of-freedom will be active in the case of an analysis with additional viscous damping defined. As the rotational mass degrees-of-freedom are neglected (Figure 7.4), the rotational accelerations and velocities will be zero in the case of an analysis with no additional viscous damping defined.

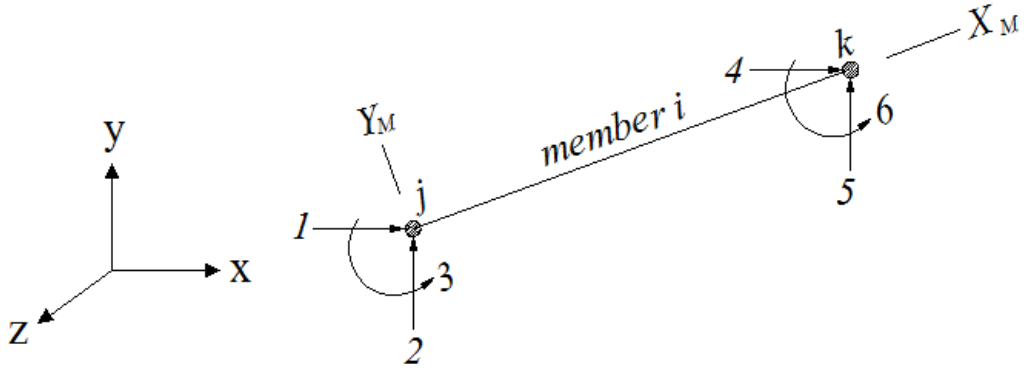


**Figure 7.12** Dynamic Degrees-of-Freedom of a Typical Member

In its most general form, each node has a total of 9 displacement, velocity and acceleration values associated with it. At the beginning of each time stage, the initial values of these variables should be updated using the final values at the end of previous time stage as defined below.

$$
\begin{aligned}
&u_{x_0} = u_{x_1}^{pre}, \quad u_{y_0} = u_{y_1}^{pre}, \quad u_{z_0} = u_{z_1}^{pre} \\
&\dot{u}_{x_0} = \dot{u}_{x_1}^{pre}, \quad \dot{u}_{y_0} = \dot{u}_{y_1}^{pre}, \quad \dot{u}_{z_0} = \dot{u}_{z_1}^{pre} \\
&\ddot{u}_{x_0} = \ddot{u}_{x_1}^{pre}, \quad \ddot{u}_{y_0} = \ddot{u}_{y_1}^{pre}, \quad \ddot{u}_{z_0} = \ddot{u}_{z_1}^{pre}
\end{aligned}
\tag{7.56}
$$

where subscript *0* refers to the value at the beginning of the time stage while subscript *1* is the value at the end of the time stage. The superscript *pre* signifies that the values are taken from the previous time stage.

In the first time stage, all values are taken as zero on the condition that no initial velocities or constant accelerations are defined in the load data files and that the analysis is not resumed from a previous analysis through the use of a seed file. In the presence of an initial velocity load, input initial velocities are assigned to the appropriate nodes in the relevant directions (x- or y-direction) in the first time stage only. In the presence of a constant acceleration load, *at all time stages*, input accelerations are assigned to the appropriate nodes in the relevant directions (x- or y-direction). In the case of resumption of a previous analysis by means of a seed file, the values at the end of previous analysis are taken as the initial values in the first time stage only.

### 7.7.4 Construction of Mass Matrix

As explained in Section 7.5.1, the masses due to self-weight are calculated and combined with any additional masses defined in the load data file to create the mass matrix.

### 7.7.5 Construction of Rayleigh Damping Matrix

In the case of an analysis requiring the use of Rayleigh damping, using the updated structural stiffness matrix and the mass matrix, the Rayleigh damping matrix is constructed as explained in Section 7.5.2.

In this calculation, the proportionality constants $a_0$ and $a_1$ are calculated at the beginning of the analysis ($t = 0$) and used throughout the analysis as constant values. In reality, however, those values may change due to the nonlinear behaviour of the structure such as the changes in stiffness and mode shapes.

In the formulation of VecTor5, nonlinear structural behaviour is taken into account by means of the *unbalanced forces approach*, and the initial stiffness matrix of the structure is used throughout the analysis. The only nonlinearity included in the stiffness matrix is the geometric nonlinearity due to P–Δ effects. In addition, the determination of $a_0$ and $a_1$ are performed through the static condensation of the stiffness matrix, which increases the computation time significantly if performed in each iteration or even in each load stage. For these reasons, the initial $a_0$ *and* $a_1$ values are used together with the updated stiffness matrix when evaluating the Rayleigh damping matrix as defined by Eq. 7.10.

This assumption is believed not to have a significant impact on the responses computed by VecTor5. As the energy dissipation primarily occurs through the nonlinear concrete and reinforcement hysteresis, usually no additional damping is required when performing a nonlinear dynamic analysis with VecTor5. In cases where additional viscous damping is desired, a ratio in the range of maximum 1% to 3% should suffice in most situations. As a result, consideration of viscous damping is not an essential part of the analyses performed with VecTor5; it is intended to be optional.

### 7.7.6 Construction of Additional Dynamic Stiffness Matrix

As mentioned before, the most important distinguishing dynamic characteristic of a structural-dynamics problem is the influence of the inertial forces. These forces are generated by the masses due to accelerations caused by fast and time-varying motions. As a result, inertial forces provide a significant portion of the structural resistance to the dynamic loads (Clough and Penzien, 1993). Therefore this additional resistance should be included in the structural stiffness matrix.

As derived in Section 7.6.6, at the beginning of each time stage, the additional dynamic stiffness matrix, $\left[k_{dyn}{}^{+}\right]$, can be conveniently determined by Eq. 7.54.

### 7.7.7 Construction of Dynamic Load Vectors

Dynamic load vectors are created at the beginning of each time stage as equivalent static nodal forces based on the *externally* applied dynamic loads which can be: time-varying

base accelerations, time-varying forces as defined by a tri-linear curve, initial velocities assigned to lumped masses, and constant accelerations assigned to lumped masses. The details of this calculation are presented in Section 7.5.4.

### 7.7.8 Construction of Additional Dynamic Load Vectors

Dynamic loads are not only created by the *externally* applied dynamic loads but also by the motion of the structure itself (i.e., structural displacements, velocities and accelerations) during a dynamic vibration. Therefore, all the external and internal dynamic forces should be assembled in a load vector, called herein the additional dynamic load vector $\left\{ p_{dyn}{}^{+} \right\}$ as defined by Eq. 7.55.

On the right-hand side of Eq. 7.55, the second term represents the load effects from the structural vibration itself. It includes nodal displacements, velocities and accelerations which are multiplied by a combination of the mass matrix and damping matrix to create forces. The third term includes the damping matrix with a negative sign to represent the resisting effects of the damping mechanism. The fourth term, with a negative sign, clearly denotes the creation of the inertial forces which resist the applied dynamic loads.

### 7.7.9 Calculation of Final Displacements (at end of extended time step)

In Section 7.6.6, the fundamental equation of the dynamic analysis procedure implemented was defined by Eq. 7.52. The final nodal displacements can thus be calculated as follows:

$$\left\{ u_1 \right\} = \left[ \left[ k_{stat} \right] + \left[ k_{dyn}{}^{+} \right] \right]^{-1} \times \left\{ \left\{ p_{stat} \right\} + \left\{ p_{dyn}{}^{+} \right\} \right\} \tag{7.57}$$

It should be noted that, if Wilson's Theta method is used, the calculated displacements correspond to the artificially extended time step and should be corrected as explained below.

### 7.7.10 Calculation of Final Accelerations, Velocities and Actual Displacements

The final acceleration values, three values for each node in the x-, y- and z-directions, as defined in Section 7.7.3, at the end of the *extended* time step length, are calculated by Eq. 7.58 which is based on Eq. 7.45.

$$\delta\ddot{u} = \frac{u_1 - u_0}{\beta \times (\theta \times \Delta t)^2} - \frac{\dot{u}_0}{\beta \times (\theta \times \Delta t)} - \frac{\ddot{u}_0}{2 \times \beta} \tag{7.58}$$

The final accelerations, three values for each node in the x-, y- and z- directions, for the *actual* time step are then found based on Eq. 7.46 as follows:

$$\ddot{u}_1 = \frac{\delta\ddot{u}}{\theta} + \ddot{u}_0 \tag{7.59}$$

The final velocities, three values for each node in the x-, y- and z-directions, for the *actual* time step are then found based on Eq. 7.31 as follows:

$$\dot{u}_1 = \Delta t \times \ddot{u}_0 + \gamma \times \Delta t \times (\ddot{u}_1 - \ddot{u}_0) + \dot{u}_0 \tag{7.60}$$

Finally, the actual displacements, three values for each node in the x-, y- and z-directions, for the *actual* time step are then found based on Eq. 7.32 as follows:

$$u_1 = \Delta t \times \dot{u}_0 + \frac{\Delta t^2}{2} \times \ddot{u}_0 + \beta \times \Delta t^2 \times (\ddot{u}_1 - \ddot{u}_0) + u_0 \tag{7.61}$$

### 7.7.11 Nonlinear Sectional Analyses

For the consideration of strain rate effects, a new subroutine is added into the sectional analysis subroutine. Based on this new addition, strain rates for each concrete layer, each longitudinal reinforcement layer and each smeared transverse reinforcement layer are first calculated. Dynamic increase factors are then determined and concrete and

reinforcement material properties are modified accordingly. The details of this calculation are presented in Section 7.8.

### 7.7.12 Modal Analysis

A modal analysis is performed at the first time stage (*t = 0 sec*) to determine the natural vibration characteristics of the structure to be analyzed under dynamic excitations. Using the initial linear-elastic stiffness matrix, the purpose of this analysis is to calculate: natural modal periods and frequencies, mode shapes, generalized masses if alternative damping is used, and Rayleigh damping proportionality constants, $a_0$ and $a_1$ if such a damping is used. A flowchart of the implemented algorithm is presented in Figure 7.13.

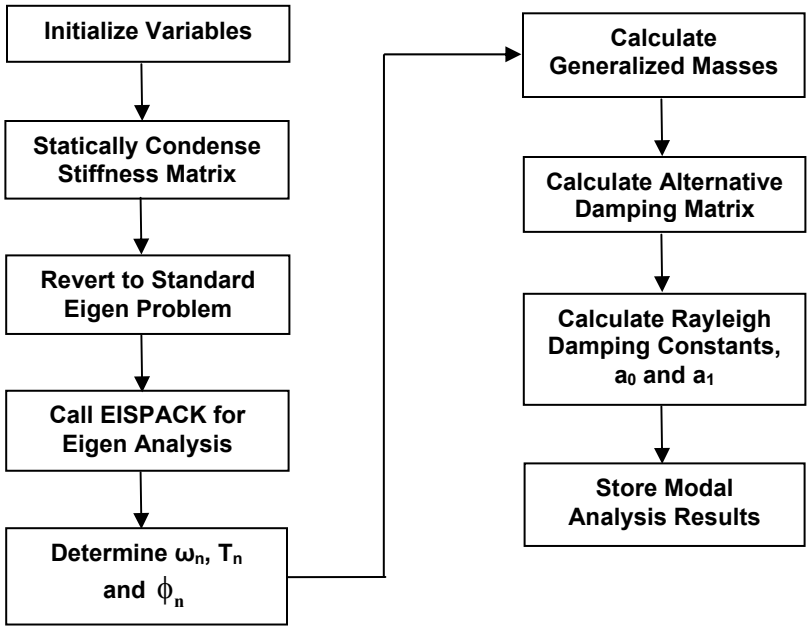


**Figure 7.13** Flow Chart for the Modal Analysis of VecTor5

#### 7.7.12.1 Calculation of Vibration Frequencies, Periods and Mode Shapes

The natural frequencies and mode shapes must satisfy the following algebraic equation:

$$[k] \times \{\phi_n\} = w_n^2 \times [m] \times \{\phi_n\} \tag{7.62}$$

Rearrangement of Eq. 7.62 leads to the so-called *frequency equation* as follows:

$$\left|[k] - w_n^{\,2} \times [m]\right| = 0 \tag{7.63}$$

Expanding the determinant results in an algebraic equation of the $N^{th}$ degree, the $N$ roots of which $(w_1^{\,2}, w_2^{\,2}, ..., w_N^{\,2})$ represent the frequencies that are possible in the system. Once these roots are found, the corresponding mode shapes $\{\phi_n\}$ can be obtained as follows:

$$\left[[k] - w_n^{\,2} \times [m]\right] \times \{\phi_n\} = 0 \tag{7.64}$$

Eq. 7.63 and Eq. 7.64 require positive definite mass $[m]$ and stiffness $[k]$ matrices; that is, non-zero diagonal terms are required in both matrices. For this reason, based on the mass degrees-of-freedom available, the stiffness matrix must be reduced to the same degrees-of-freedom. Such an operation requires a procedure called *static condensation*. The VecTor5 formulation of this procedure is based on the one formulated by Clough and Penzien (1993).

The standard eigenvalue problem, $[A] \times \{y\} = [\lambda] \times \{y\}$, arises frequently in mathematics; therefore, many solution algorithms are available in computer software libraries. However, to be able to use such an algorithm, Eq. 7.62 should be converted to the standard eigenvalue problem form. A method described by Chopra (2007) was used for this purpose. Based on this method, [$A$] is calculated as follows

$$[A] = [m]^{-1/2} \times [k] \times [m]^{-1/2} \tag{7.65}$$

and the eigenvalues and eigenvectors of $[A] \times \{y\} = [\lambda] \times \{y\}$ are then found using standard mathematical procedures. The resulting frequencies and mode shapes can then be found as

$$w_n = \sqrt{\lambda_n} \quad \text{and} \quad \{\phi_n\} = [m]^{-1/2} \times \{y_n\} \tag{7.66}$$

For the calculation of the standard eigenvalue problem, a FORTAN subroutine called EISPACK (Garbow, 1974) is used. Developed at the Argonne National Laboratory, this subroutine is freely available on the internet.

#### 7.7.12.2 Calculation of Alternative Damping Matrix

The construction of the alternative damping matrix is carried out based on Eq. 7.17, where the initial vibrational frequencies, mode shapes and generalized masses are utilized as calculated from initial transformed section properties. This matrix is used throughout the analysis.

#### 7.7.12.3 Calculation of Rayleigh Damping Constants

The proportionality constants $a_0$ and $a_1$ are determined through Eq. 7.13 and Eq. 7.14, and the damping ratios for the modes other than the two specified are calculated by Eq. 7.11, as explained in Section 7.5.2.

### 7.8 Consideration of Strain Rates

Transient dynamic loads typically result in high levels of *strain rates* (i.e., change in the strain per unit time) in the materials they applied to. Typical strain rates for various types of loading are given in Figure 7.14.

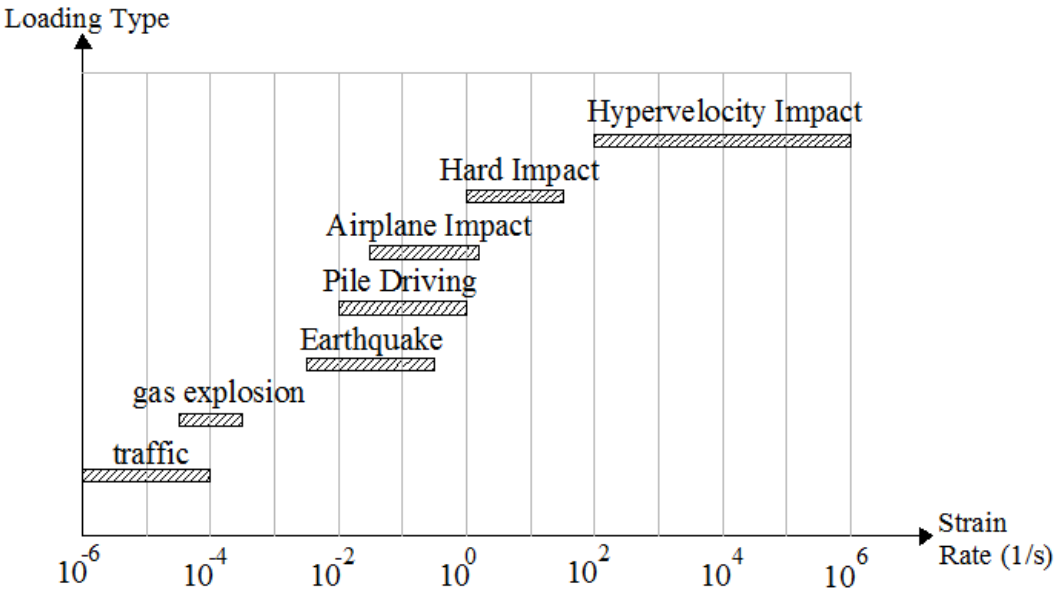


**Figure 7.14** Typical Strain Rates for Various Types of Loading (CEB-FIP, 1988)

Subjected to high strain rates, concrete and steel materials may exhibit significant strength increases. This increase is postulated to be related to the inertial effects (Ho, 2004). With concrete, for example, under high strain rates, expansion or contraction creates inertial resistance in the surrounding concrete, which may create effects similar to confinement. Many studies are available in the literature relating to strain rate-strength increase variations. Typically, the relationship between the dynamic increase factor (DIF) and the strain rates is presented graphically, where the DIF is the ratio of the dynamic to the static property of the material. The DIFs for concrete may relate to the peak stress $f_c'$, the peak strain $\varepsilon_0$, and the modulus of elasticity $E_c$. For the reinforcement, the DIFs are generally available for the yield stress $f_y$, and the ultimate stress $f_u$.

For the consideration of strain rates and the DIFs mentioned, a new subroutine was added into the sectional analysis procedure of VecTor5. In the newly implemented subroutine, the strain rates are calculated in each sectional iteration of each time stage based on the equation as follow:

$$\dot{\varepsilon} = \frac{\varepsilon - \varepsilon^{pre}}{\Delta t} \tag{7.67}$$

where $\dot{\varepsilon}$ is the strain rate, $\varepsilon$ is the total strain in the current time stage, $\varepsilon^{pre}$ is the total strain at the end of previous time stage, and $\Delta t$ is the time step length.

Two strain rates are calculated for concrete: one for the principal compressive strain and one for the principal tensile strain. In addition, strain rates are calculated for the reinforcement using the total strains: one for each of the longitudinal reinforcement components and one for the smeared transverse reinforcement in each concrete layer. These calculations require storing and updating the related total strains at all iterations performed. Once the strain rates are determined, the corresponding DIF is calculated according to the formulations presented below.

### 7.8.1 Concrete (CEB-FIB Model, 1990)

For concrete, the calculation of the DIF values is based on the formulation suggested by the CEB-FIP Model Code (1990) as follows:

Under Compression

$$DIF_{fc} = \left( \frac{\dot{\varepsilon}}{30 \times 10^{-6}} \right)^{1.026 \times \alpha} \qquad if \qquad \dot{\varepsilon} \le 30\ s^{-1} \tag{7.68}$$

$$DIF_{fc} = \gamma \times \dot{\varepsilon}^{1/3} \qquad if \qquad 300 \ge \dot{\varepsilon} > 30\ s^{-1} \tag{7.69}$$

$$\text{where } \alpha = \frac{1}{5 + 0.9 \times f_c'} \text{ and } \gamma = 10^{(6.156 \times \alpha - 0.492)} \tag{7.70}$$

$$DIF_{\varepsilon c} = \left( \frac{\dot{\varepsilon}}{30 \times 10^{-6}} \right)^{0.020} \qquad if \qquad \dot{\varepsilon} \le 300\ s^{-1} \tag{7.71}$$

$$DIF_{E_c} = \left( \frac{\dot{\varepsilon}}{30 \times 10^{-6}} \right)^{0.026} \qquad if \qquad \dot{\varepsilon} \le 300\ s^{-1} \tag{7.72}$$

At each iteration of the sectional analyses, the concrete compressive strength $f_c'$ is enhanced by $DIF_{fc}$, the peak strain $\varepsilon_0$ by $DIF_{\varepsilon c}$, and the modulus of elasticity $E_c$ by $DIF_{\mathrm{E}c}$. For strain rates greater than 300 $s^{-1}$, the DIFs corresponding $\dot{\varepsilon} = 300\ s^{-1}$ are assumed.

Under Tension

$$DIF_{ft} = \left( \frac{\dot{\varepsilon}}{3 \times 10^{-6}} \right)^{1.016 \times \delta} \qquad if \qquad \dot{\varepsilon} \le 30\ s^{-1} \tag{7.73}$$

$$DIF_{ft} = \eta \times \dot{\varepsilon}^{1/3} \qquad if \qquad 300 \ge \dot{\varepsilon} > 30\ s^{-1} \tag{7.74}$$

where $\delta = \dfrac{1}{10 + 0.6 \times f_c'}$ and $\eta = 10^{(6.933 \times \delta - 0.492)}$ (7.75)

$$DIF_{\varepsilon c} = \left( \frac{\dot{\varepsilon}}{3 \times 10^{-6}} \right)^{0.020} \qquad if \qquad \dot{\varepsilon} \le 300\, s^{-1} \tag{7.76}$$

$$DIF_{E_{ct}} = \left( \frac{\dot{\varepsilon}}{3 \times 10^{-6}} \right)^{0.016} \qquad if \qquad \dot{\varepsilon} \le 300\, s^{-1} \tag{7.77}$$

In the sectional analyses, the concrete tensile strength $f_t'$ is enhanced by $DIF_{ft}$, and the modulus of elasticity in tension $E_{ct}$ by $DIF_{\mathrm{Ect}}$. For strain rates greater than 300 $s^{-1}$, the DIFs corresponding $\dot{\varepsilon} = 300\, s^{-1}$ are assumed. The resulting relations are presented in Figure 7.15.

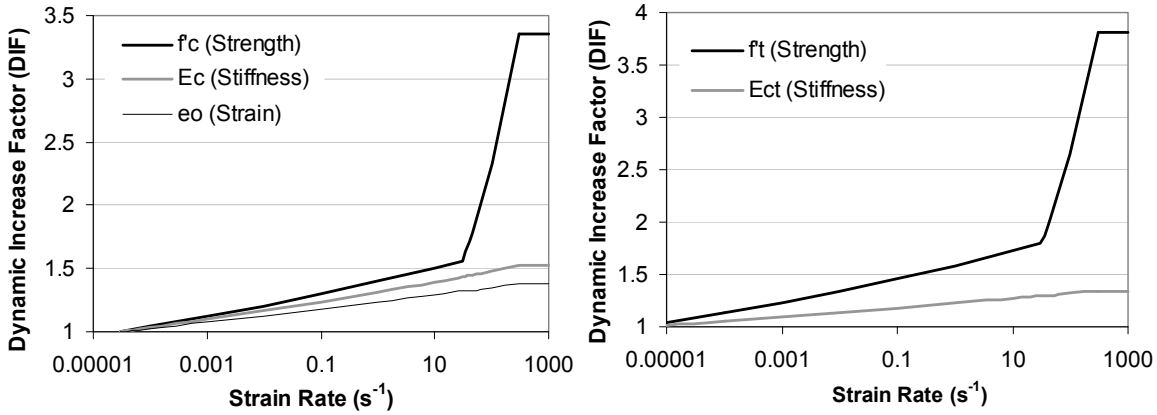


**Figure 7.15** Strain Rate - DIF Relationships: **(a)** Concrete in Compression: CEB-FIB Model (1990); **(b)** Concrete in Tension: CEB-FIB Model (1990)

### 7.8.2 Reinforcement

For both the longitudinal and transverse reinforcement, two different formulations are implemented. These are the Malvar and Crawford model (1998), and the CEB-FIB model (1988).

### 7.8.2.1 Malvar and Crawford (1998)

This model is selected as default as discussed in Section 8.8.5. According to this model,

$$DIF_{fy} = \left( \frac{\dot{\varepsilon}}{1 \times 10^{-4}} \right)^{\alpha_{fy}} \quad if \quad 1 \times 10^{-4} \le \dot{\varepsilon} \le 225\ s^{-1} \tag{7.78}$$

$$DIF_{fu} = \left( \frac{\dot{\varepsilon}}{1 \times 10^{-4}} \right)^{\alpha_{fu}} \quad if \quad 1 \times 10^{-4} \le \dot{\varepsilon} \le 225\ s^{-1} \tag{7.79}$$

where

$$\alpha_{fy} = 0.074 - 0.040 \times \frac{f_y}{414} \quad \text{where } f_y \text{ is in MPa} \tag{7.80}$$

$$\alpha_{fu} = 0.019 - 0.009 \times \frac{f_y}{414} \quad \text{where } f_y \text{ is in MPa} \tag{7.81}$$

At each iteration of the sectional analyses, the yield stress $f_y$ is enhanced by $DIF_{fy}$, and the ultimate stress $f_u$ by $DIF_{fu}$. The calculations are performed for both the longitudinal and transverse reinforcement. For strain rates greater than 225 $s^{-1}$, the DIFs corresponding to $\dot{\varepsilon} = 225\ s^{-1}$ are assumed. The resulting relations are presented in Figure 7.16(a).

### 7.8.2.2 CEB – FIP (1988)

The second option available is based on CEB-FIP Model Code (1990). According to this model,

$$DIF_{fy} = 1 + \left( \frac{6}{f_y} \right) \times \ln \left( \frac{\dot{\varepsilon}}{5 \times 10^{-5}} \right) \quad if \quad \dot{\varepsilon} \le 10\ s^{-1} \tag{7.82}$$

$$DIF_{fu} = 1 + \left( \frac{7}{f_u} \right) \times \ln \left( \frac{\dot{\varepsilon}}{5 \times 10^{-5}} \right) \quad if \quad \dot{\varepsilon} \le 10\ s^{-1} \tag{7.83}$$

For strain rates greater than 10 $s^{-1}$, the DIFs corresponding to $\dot{\varepsilon} = 10\, s^{-1}$ are assumed. The resulting relations are presented in Figure 7.16(b).

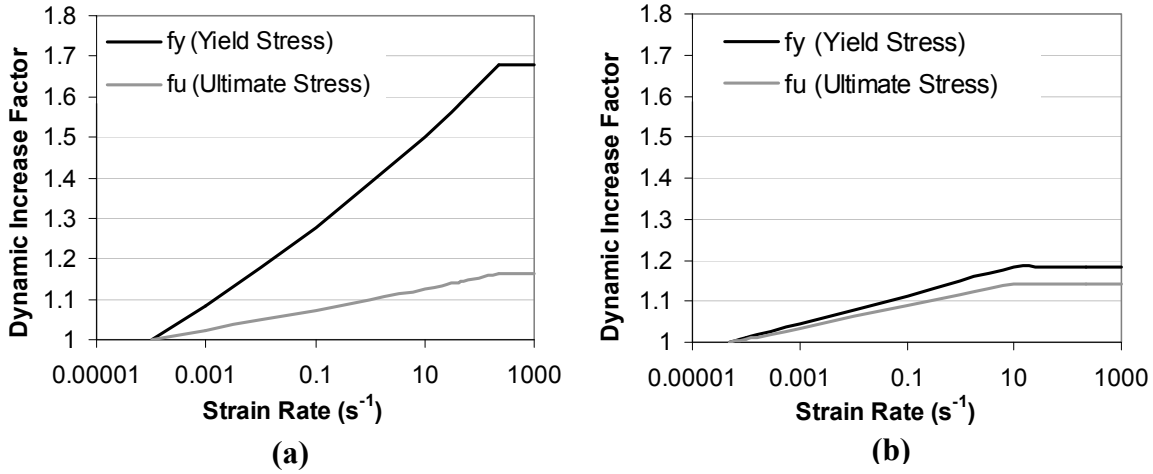


**Figure 7.16** Strain Rate - DIF Relationships for Reinforcement: **(a)** Malvar and Crawford Model (1998); **(b)** CEB-FIB Model (1988)

## 7.9 Selection of an Appropriate Time Step Length

Selection of the time step length has a significant impact on the accuracy of the analysis results. This is caused primarily by the fact that: the system properties are assumed to be constant throughout the length of the time step, an assumed variation of the accelerations is considered during the time step length, and an accumulation of errors may occur at the end of each time step. Therefore, a reasonably short time step length should be selected for the analysis. It is recommended by Chopra (2007) that the time step length should be approximately $T_j/10$ where $T_j$ is the period of the $J^{th}$ mode of an $N$ degree-of-freedom system where the first $J$ modes are expected to contribute significantly to the response. This suggestion can be taken as a starting point in the case of a nonlinear analysis. It is recommended to reduce the time step lengths until the response becomes acceptably consistent.

To illustrate this concept, consider a simple cantilever structure which consists of two columns and two assigned masses creating a 4 DOF system as shown in Figure 7.17. The

loading consists of an impulse force-time history applied at the top mass (Node 3) in the global x-direction as shown in Figure 7.18.

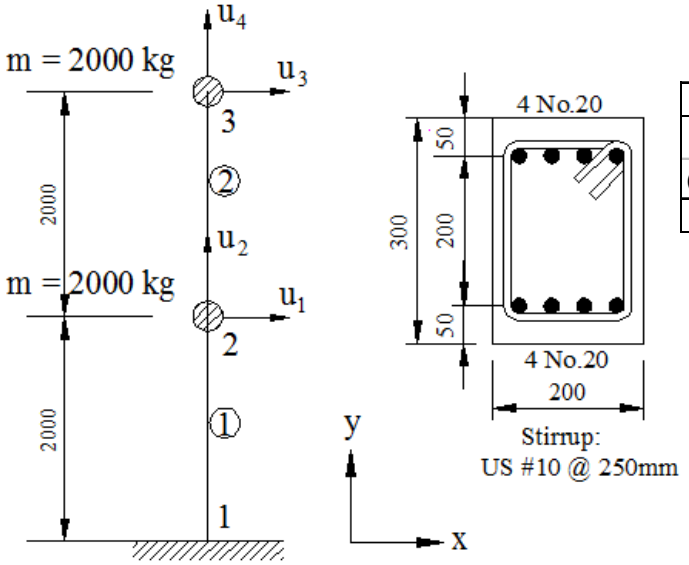


| Reinforcement | | | | |
|---|---|---|---|---|
| $f_y$ | $f_u$ | $E_s$ | $E_{sh}$ | $\varepsilon_{sh}$ |
| (MPa) | (MPa) | (MPa) | (MPa) | (x $10^{-3}$) |
| 400 | 550 | 200000 | 3000 | 4 |

| Concrete | | |
|---|---|---|
| $f'_c$ | $\varepsilon_0$ | $E_c$ |
| (MPa) | (x $10^{-3}$) | (MPa) |
| 32 | 2 | 32000 |

**Figure 7.17** Structural Details of a Simple Cantilever Structure

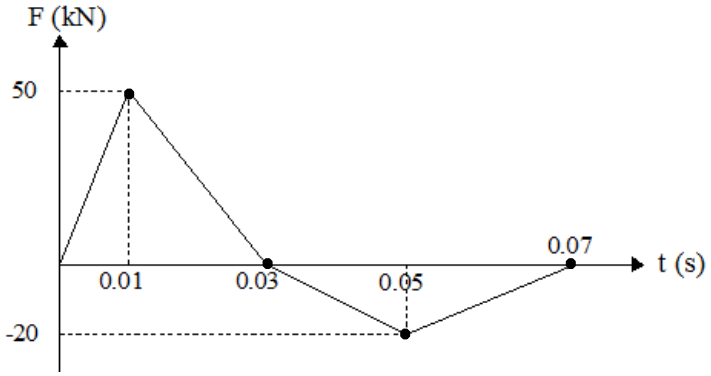


**Figure 7.18** Impulsive Loading Considered for the Simple Cantilever Structure

The analysis was first performed assuming linear-elastic behaviour. According to the eigen analysis results, the natural vibration periods are presented in Table 7.2.

**Table 7.2** Modal Periods for Linear-Elastic Analysis for the Simple Cantilever Structure

| Mode | Period (s) |
|---|---|
| 1 | 0.3590 |
| 2 | 0.0539 |

| Mode | Period (s) |
|---|---|
| 3 | 0.0147 |
| 4 | 0.0056 |

As all four modes should be included in the response, for optimal accuracy, an analysis with a time step length $\Delta t$ of $0.0056/10 = 0.0005\,\text{s}$ may be a reasonable starting point. For demonstrative purposes, the linear-elastic analysis was carried out considering various time steps using the average acceleration procedure. The resulting displacement-time responses are given in Figure 7.19.

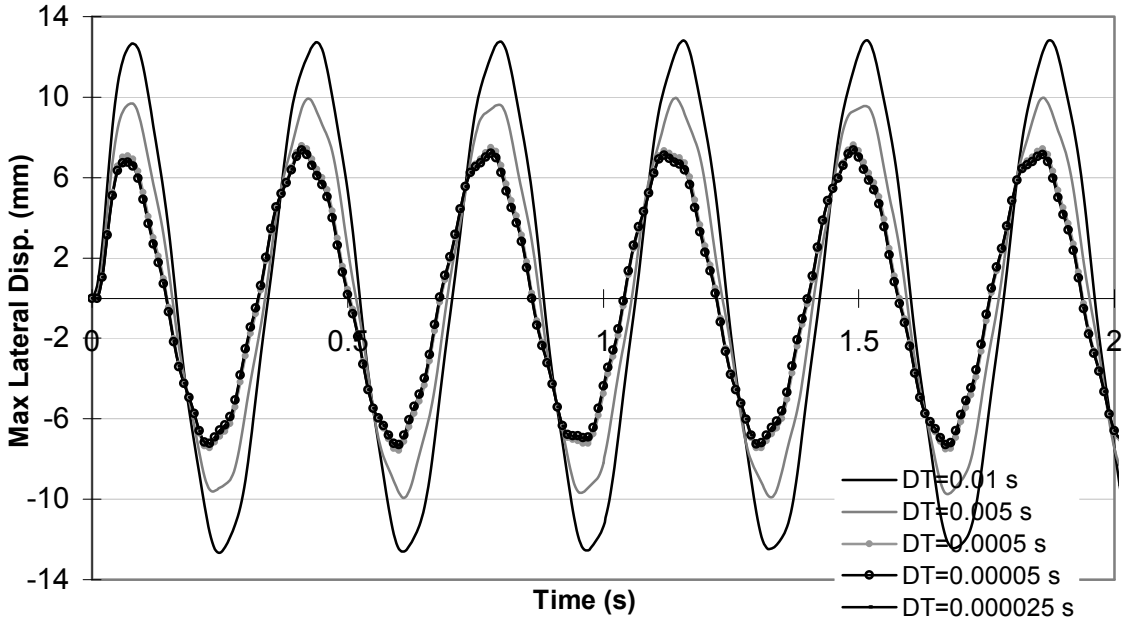


**Figure 7.19** Displacement Responses for the Simple Cantilever Structure (Linear-Elastic Analysis)

As seen in Figure 7.19, the use of time step lengths greater than 0.0005 s did not produce a reasonable approximation to the exact response (i.e., the response which does not change with the use of smaller time step lengths). A time step length of 0.01 s overestimated the exact peak displacement by 87%, while a time step length of 0.005 resulted in an overestimation of 43%. As the time step was reduced, the displacement response converged to the exact response (Figure 7.20(a)). In this study, the exact responses were approached from above with diminishing displacement responses by the use of smaller time steps.

It seems reasonable to assume a time step length of $T_N/10$ for the first analysis and then repeat the analysis with a reduced the time step length to decide whether the selected time step is appropriate. For this particular example, the response obtained using a time step of

0.00005 s improved the displacement response by only 2 percent as compared to the response obtained using a time step of $T_{N=4}/10$ =0.0005 s, suggesting that the selected time step is appropriate for the problem at hand. As for the reaction (base shear force) response, a similar pattern was observed but the gains attained by using smaller time step lengths were less than those of the displacement response.

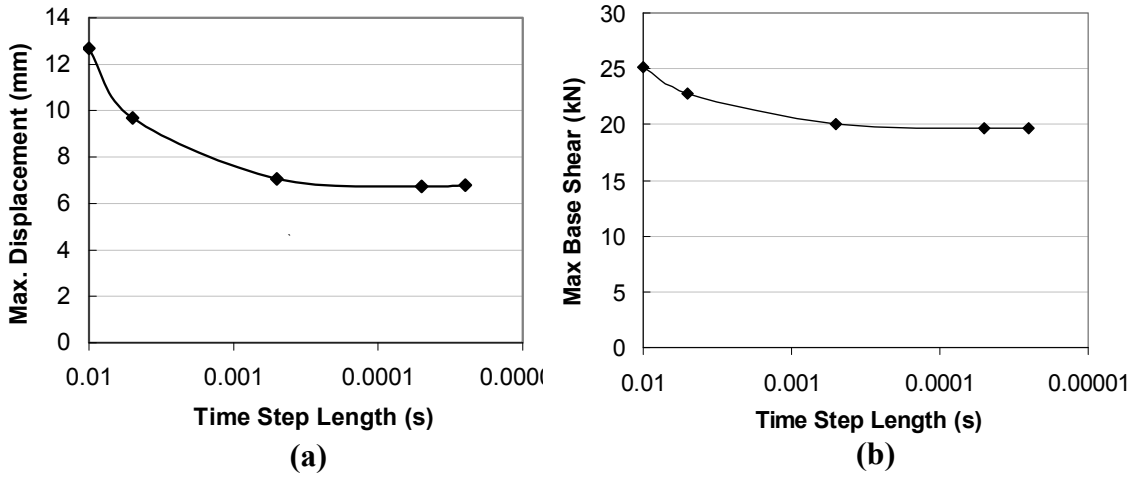


**Figure 7.20** Analysis Results for Different Time Step Lengths for the Simple Cantilever Structure (Linear-elastic Analysis): **(a)** Max. Displacement; **(b)** Max Base Shear

In order to investigate the effects of time step length in the case of a nonlinear analysis, the same structure under the same impulsive loading was analyzed considering nonlinear behaviour. Based on the eigen analysis results, the modal periods of the structure are listed in Table 7.3. The periods from the nonlinear analysis were found to be slightly less than those from the linear-elastic analysis. This is due to the use of transformed section properties which includes the stiffness of the reinforcement in the nonlinear analysis as opposed to the gross section properties used in the linear-elastic analysis. The resulting displacement-time response is given in Figure 7.21.

**Table 7.3** Modal Periods for Nonlinear Analysis for the Simple Cantilever Structure

| Mode | Period (s) |
|---|---|
| 1 | 0.3550 |
| 2 | 0.0534 |

| Mode | Period (s) |
|---|---|
| 3 | 0.0138 |
| 4 | 0.00528 |

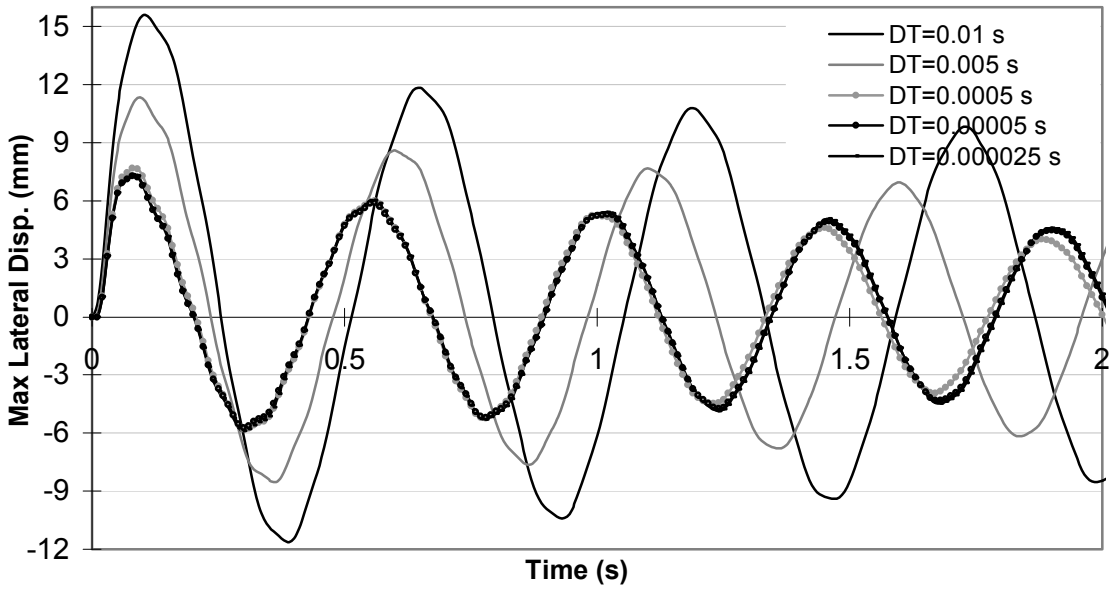


**Figure 7.21** Displacement Responses for the Simple Cantilever Structure (Nonlinear Analysis with No Yielding)

A similar relationship between the selected time step length and the displacement response accuracy was obtained (Figure 7.22). In addition, the elongation in the period was another variable in the nonlinear analysis results. The use of time steps larger than $T_N/10$ produced unacceptable responses in terms of not only the peak displacement but also the period of the oscillation.

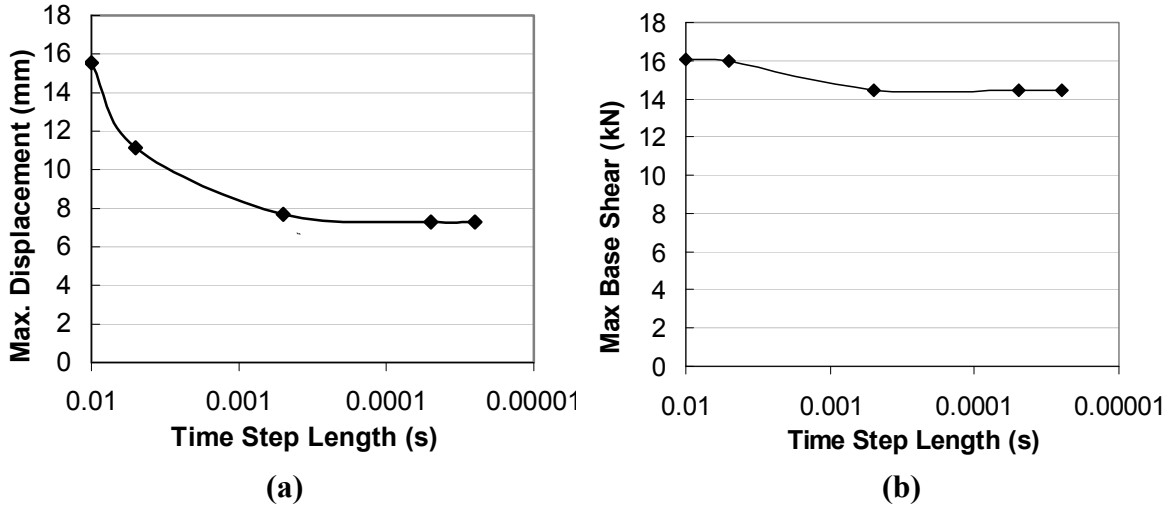


**Figure 7.22** Analysis Results for Different Time Step Lengths for the Simple Cantilever Structure (Nonlinear Analysis with No Yielding): **(a)** Max. Displacement; **(b)** Max Base Shear

In the nonlinear analysis above, the reinforcement stresses were well below the yield stresses (at a maximum of approximately 25 MPa). Thus, in a subsequent analysis, it was desired to obtain a response including plastic deformations. For this purpose, a scale factor of 10 was used for the impulse load, and the nonlinear analysis was repeated. Based on the analysis results, the initial modal periods were the same as the previous analysis (Table 7.3). The analysis results indicated that the longitudinal reinforcement attained a maximum strain of $4.2 \times 10^{-3}$ at the peak displacement. The resulting displacement response is given in Figure 7.23.

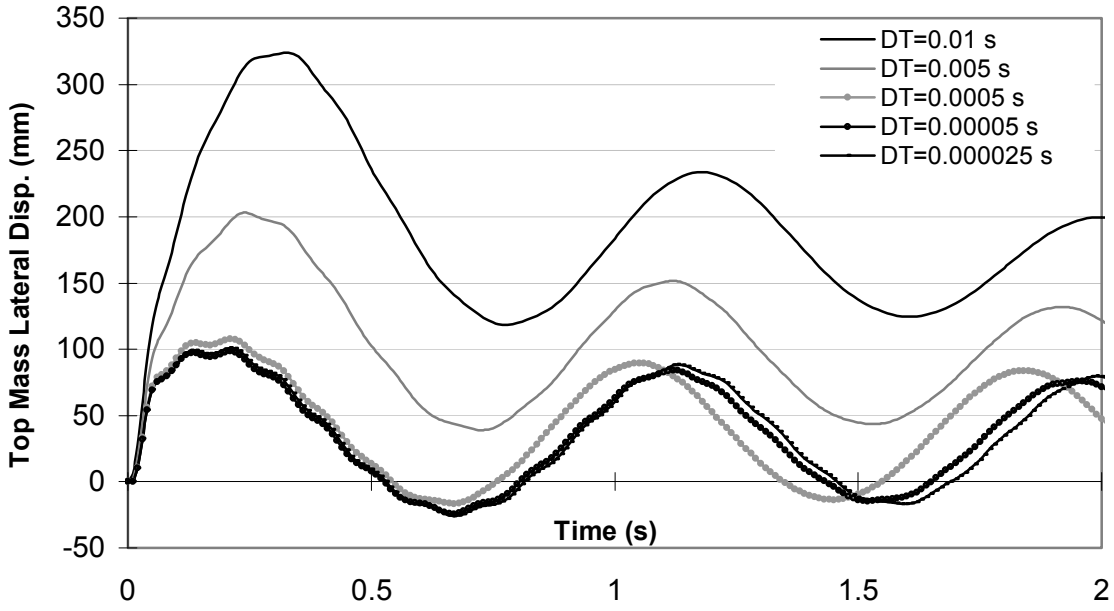


**Figure 7.23** Displacement Responses for the Simple Cantilever Structure (Nonlinear Analysis with Significant Yielding)

The selection of an appropriate time step length seems more important in nonlinear analyses involving plastic deformations. Figure 7.23 clearly demonstrates how an excessively coarse time step can lead to grossly inaccurate results. The analysis with a time step length of 0.01 s resulted in an overestimation of the peak deformation by 300% compared to the results from a time step of 0.0005 s. As recommended previously, the use of a time step length $\Delta t = T_N / 10$ provided a reasonable approximation to the peak displacement but underestimated the period of the oscillation slightly. In terms of the maximum base shear force, less gain was realized with the use of a smaller time step length compared to the displacement response (Figure 7.24).

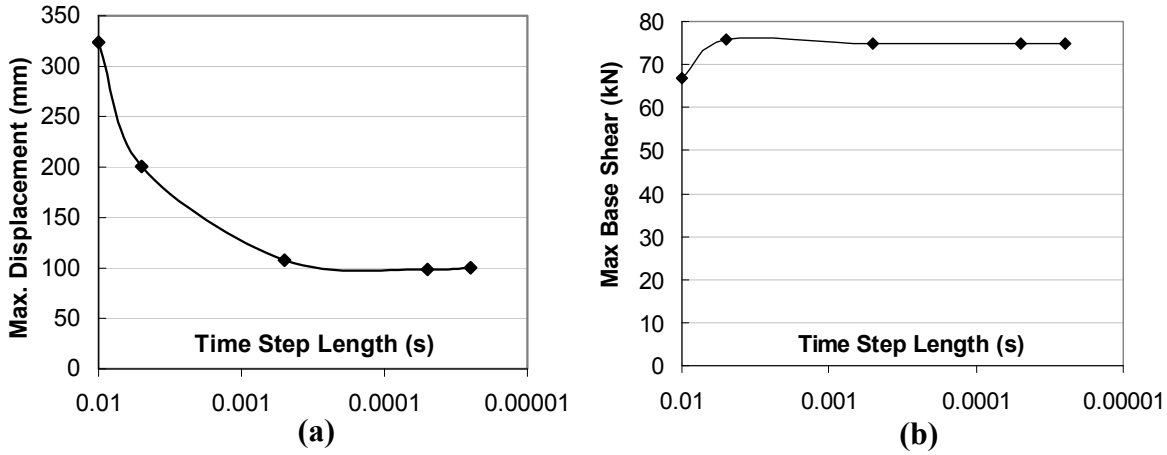


**Figure 7.24** Analysis Results for Different Time Step Lengths for the Simple Cantilever Structure (Nonlinear Analysis with Significant Yielding): **(a)** Maximum Displacement; **(b)** Maximum Base Shear

In conclusion, it is recommended performing an initial analysis with a time step length in the range of the smallest period of the structure, and then repeating the analysis with a smaller time step length to verify that the computed response does not change significantly.

## 7.10 Use of Additional Viscous Damping in Nonlinear Analysis for Stability Reasons

When performing a nonlinear dynamic analysis, one of the most important considerations is the *stability* of the analysis. The numerical analysis technique is expected to perform without a significant accumulation of errors and without loss of convergence in the course of the analysis.

In the case of the linear acceleration method, a time step less than $0.551 \times T_N$, where $T_N$ is the smallest modal period of the structure, is required. This stability limit necessitates the use of extremely small time step lengths as the period of the highest mode usually corresponds to an excessively small number. However, dynamic analysis experience with VecTor5 demonstrated that a small time step length is required regardless to obtain a reasonable simulation of the response. Therefore, the stability limit of the linear acceleration method did not cause a major difficulty in this study.

Rather than the use of small time step lengths, the need to introduce damping when using either the average or linear acceleration method was the main concern. It was observed that nonlinear analyses with these two procedures may lose stability if no viscous damping is introduced to the system. Consider the impact analysis performed for the Beam SS2a-1, analyzed in Chapter 8. The nonlinear analysis was performed using the average acceleration method and no viscous damping was defined. During the analysis, convergence was noticed to be inconsistent. Some time stages reached the maximum iteration limit with a poor convergence factor. The displacement and reaction responses obtained are given in Figure 7.25. Instability of the support reaction is clear with many fluctuating values. Some instability is also visible in the displacement response. There is also a noticeable amplification at the beginning of the second cycle in the displacement response. Such results obtained at the end of an analysis usually invalidate the entire analysis, raising grave concerns about the accuracy of the analytical procedure used.

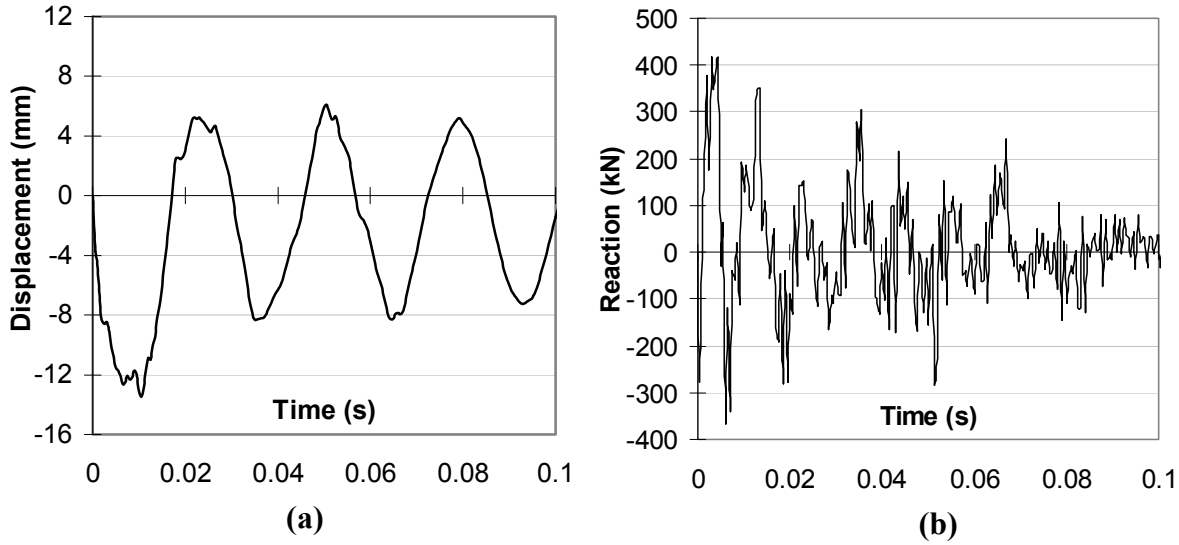


**Figure 7.25** Linear Acceleration Method with No Damping: **(a)** Displacement Response; **(b)** Reaction Response (Beam SS2a-1)

The same analysis was then repeated using Rayleigh damping with 0% and 1% damping assigned to the first and second modes, respectively. During this analysis, acceptable convergence was observed at all time stages. The results obtained are presented in Figure 7.26.

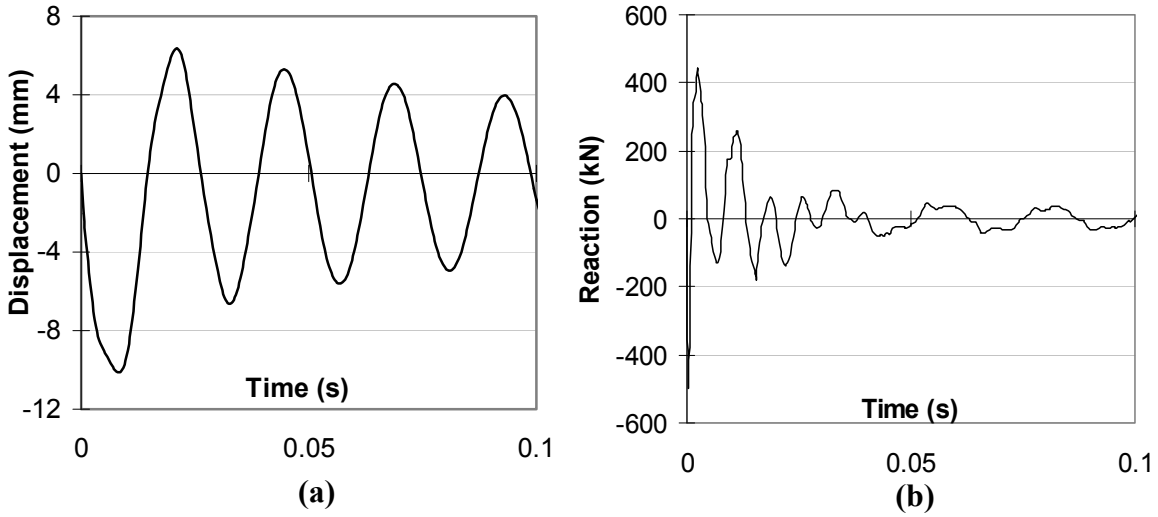


**Figure 7.26** Linear Acceleration Method with Damping: **(a)** Displacement Response; **(b)** Reaction Response (Beam SS2a-1)

As seen from the graphs above, the analysis with damping provided responses that were acceptable in terms of numerical stability. However, the selected damping ratio has a great influence on the computed response. Using more damping tends to reduce the displacement amplitudes and cause the vibration to diminish sooner. Therefore, an appropriate damping ratio should be selected, which is not a straightforward decision.

As mentioned previously, the nonlinear analysis procedure developed considers nonlinear material hysteresis through which most of the energy dissipation occurs; therefore, the additional viscous damping is not usually required. Accordingly, one approach that may be used is to determine the minimum damping ratios that will stabilize the analysis. According to this approach, with the use of, for example, Rayleigh damping, two vibration modes are to be determined to which the damping is assigned. A series of analyses are then performed to find the minimum amount of damping which would stabilize the response. Such an approach was successfully used by Saatci (2007) in the nonlinear impact analyses of reinforced concrete beams; these beams are also analyzed herein in Chapter 8.

There are two difficulties in such an approach. The first one involves the selection of the two vibrational modes to which the damping will be applied. Selection of the first two

modes may cause excessive damping in the higher modes participating in the dynamic response of the structure. For example, for the beam considered above, SS2a-1, if the damping ratios of 0% and 1% are assigned to the first and second modes, respectively, the damping ratios for the remaining modes assume the values as shown in Table 7.4. Note the excessive damping ratios of the higher modes.

**Table 7.4** Modal Damping Ratios Calculated for Rayleigh Damping (Beams SS2a-1)

| Mode | Damping Ratio (%) | Mode | Damping Ratio (%) | Mode | Damping Ratio (%) |
|---|---|---|---|---|---|
| 1 | 0 | 8 | 10.55 | 15 | 23.3 |
| 2 | 1 | 9 | 13.15 | 16 | 24.3 |
| 3 | 1.93 | 10 | 16.38 | 17 | 25.89 |
| 4 | 3.73 | 11 | 18.54 | 18 | 30.43 |
| 5 | 5.87 | 12 | 19.13 | 19 | 38.08 |
| 6 | 7.2 | 13 | 21.44 | 20 | 39.88 |
| 7 | 9.63 | 14 | 22 | 21 | 175.03 |

The second difficulty is that the multiple analyses required in determining the minimum damping ratios may take significant engineering time. This may eventually lead the analyst to use high damping ratios in the first analysis to avoid disappointment at the end of the analysis.

To specifically address these difficulties, a third procedure, Wilson's Theta method, was implemented into the dynamic analysis procedure of VecTor5. As mentioned previously, the biggest advantage of this procedure is the inherent numerical damping it provides which stabilizes the analyses. In the studies performed for this thesis, Wilson's Theta method was intensively used to analyze, linearly and nonlinearly, several structures under various dynamic loading conditions without the use of any additional viscous damping. No stability loss was observed regardless of the time step used. For example, for the Beam SS1a-1, the responses obtained for an undamped nonlinear analysis are given in Figure 7.27.

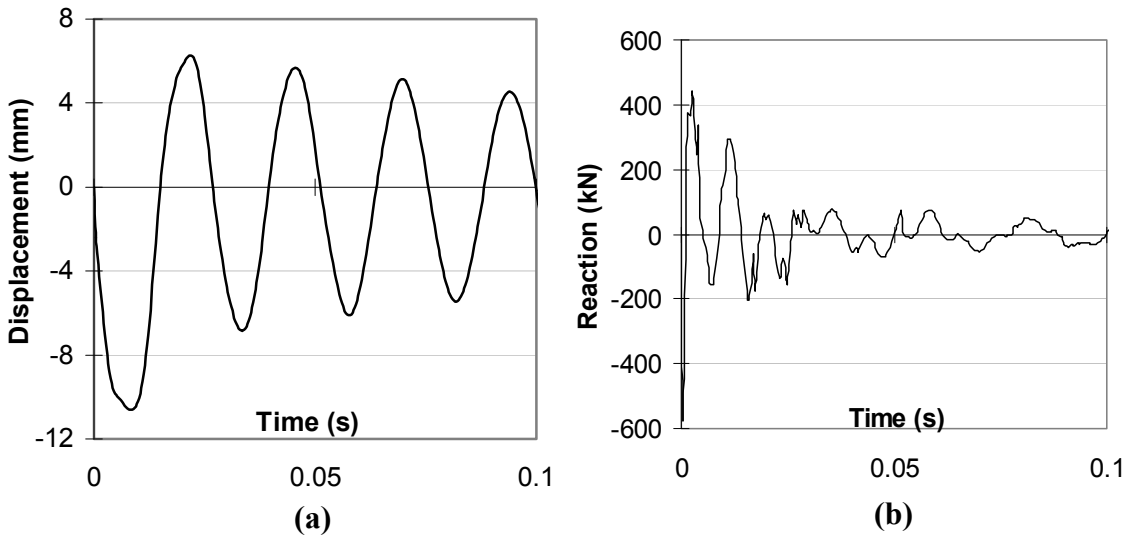


**Figure 7.27** Wilson's Theta Method with No Damping: **(a)** Displacement Response; **(b)** Reaction Response (Beam SS2a-1)

## 7.11 Discussion of the Numerical Damping Present in Wilson's Theta Method

Because the additional viscous damping is not desired in the nonlinear solution, the concept of numerical damping needs further examination. In other words, it is not desired to dampen out the actual structural response through the numerical damping present in the Wilson's Theta method; rather, it is desired that the solution be stabilized with no noticeable numerical damping in the response. To investigate this issue, it is more appropriate to consider a linear-elastic analysis. In a nonlinear analysis, the response diminishes due to material hysteresis; therefore, it is difficult to determine the contribution of the numerical damping to this decay. For this purpose, the analysis of the structure in Figure 7.17 was repeated using Wilson's Theta method with no damping defined. The displacement responses obtained for several different time step lengths are given in Figure 7.28. It is clear that the numerical damping present in the method did not cause any decay in the displacement response.

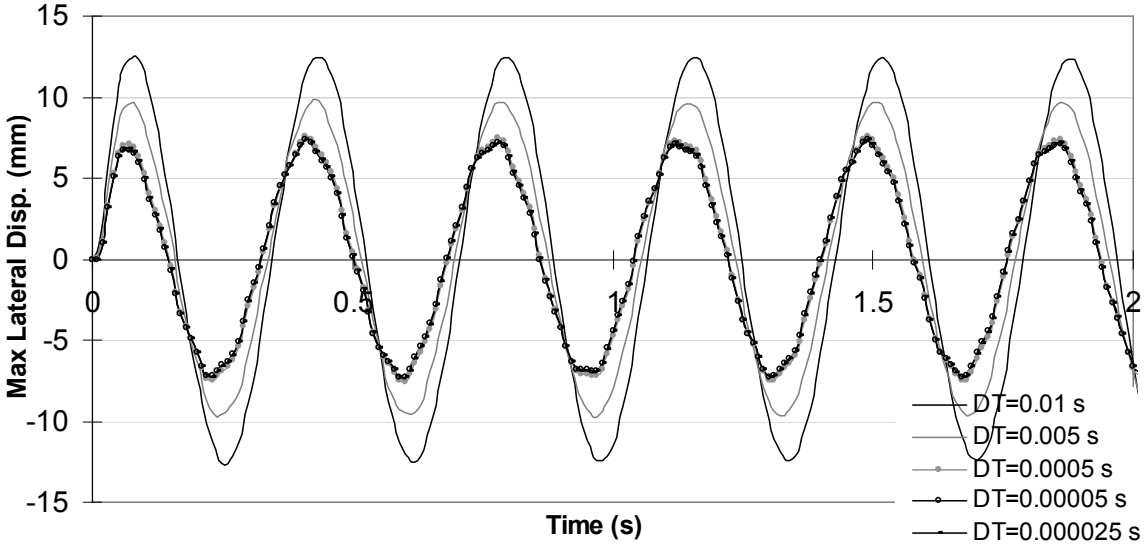


**Figure 7.28** Displacement Responses for Different Time Step Lengths for the Simple Cantilever Structure

The reaction response is presented in Figure 7.29. With time steps of 0.01 s and 0.005 s, some numerical damping effects are visible. The response, which initially includes higher mode contributions, dampens out somewhat and then retains the same amplitude of deformations. This is attributed to the process of filtering out the higher mode contributions from the reaction response and is deemed to be an advantage of this procedure. These higher modes, which have been calculated from an idealization of the structure, are usually not accurate relative to the actual properties of the structure (Chopra, 2007). When the time step is reduced, this filtering trend disappears as shown in Figure 7.30; the responses include several higher mode contributions. As discussed previously, a time step length less than or equal to 0.0005 s was needed for this analysis to be reasonably accurate. Therefore, no visible numerical damping will be present in the calculated reaction response of this structure. Similarly, in the analyses performed in this study, it was observed that no numerical filtering out of the reaction response occurred due to the small time step lengths needed.

Wilson's Theta method is reported by Chopra (2007) to provide numerical damping for modes with a shorter period than the time step length. Based on this statement, as the second modal period of the structure was 0.0539 s, the use of time steps of 0.05 s and 0.01 s provided numerical damping for the last two modes (i.e., third and fourth modes) (Figure 7.29). In accordance with the same statement, time steps of 0.0005 s and smaller

did not provide any numerical damping as the smallest period of the structure was 0.00056 s (Figure 7.30).

In conclusion, a time step length in the range of the smallest period of the structure (or smaller) is usually required for an acceptable accuracy in the analyses performed with the developed analysis tool. Therefore, numerical filtering of the reaction response in Wilson's Theta method is typically not an issue of practical concern, whether or not it is a desirable feature of the Wilson's Theta method.

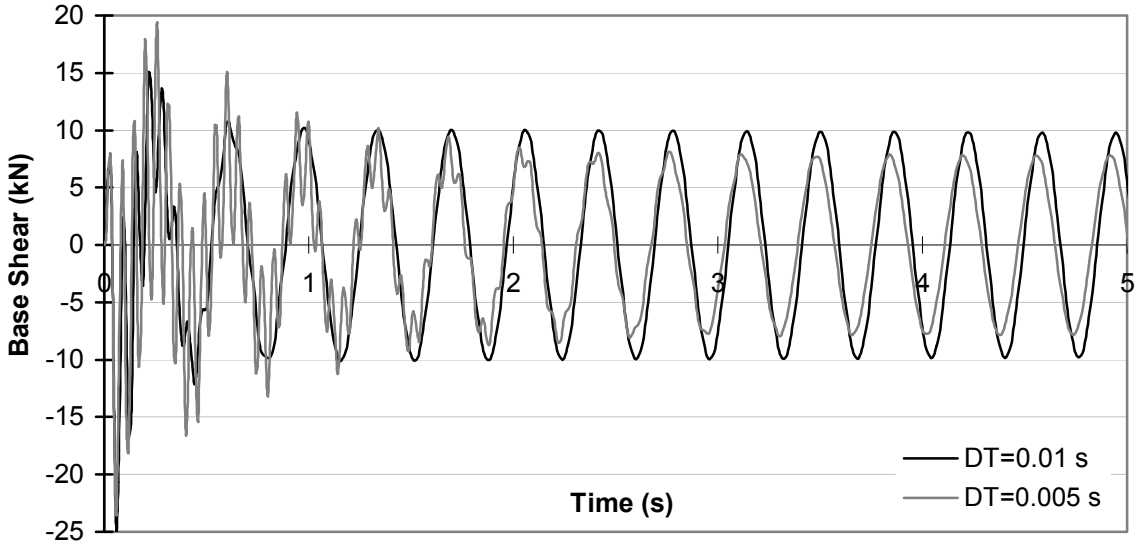


**Figure 7.29** Reaction Responses for Time Step Lengths of 0.01 s and 0.05 s for the Simple Cantilever Structure

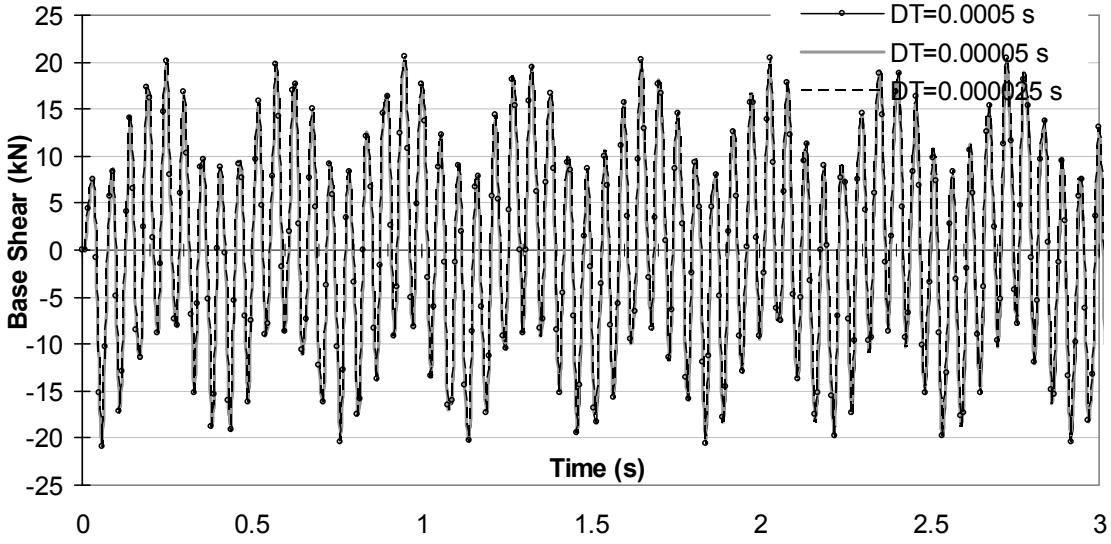


**Figure 7.30** Reaction Responses for Time Step Lengths of 0.0005 s, 0.00005 s and 0.000025 s for the Simple Cantilever Structure

## 7.12 Linear-Elastic Verification of the Analytical Procedure Developed

In order to validate the implemented dynamic analysis algorithms, a simple structure was analyzed linear-elastically. The structure under consideration is the simple cantilever structure with four dynamic degrees-of-freedom as shown in Figure 7.17. Two different types of dynamic loads were considered for this structure: a ground acceleration-time history loading, and an impulsive loading. The analyses were carried out with VecTor5 and SAP2000 and the results were compared. The verification of VecTor5 for an initial velocity loading was carried out by means of hand calculations. For this purpose, a one-dynamic-degree-of-freedom structure was analyzed and the results were compared.

In the verification analyses, the three time integration methods were used arbitrarily. In addition, viscous damping was included in some of the analyses for verification of the implemented Rayleigh damping algorithm. The details of the analyses are documented in the following sections.

### 7.12.1 Ground Accelerations

For the time-history analysis, the Northridge (Santa Monica, 1994) ground acceleration record was used. Obtained from the National Information Service for Earthquake Engineering (NISEE) at the University of California, Berkeley, the record includes 60 seconds of acceleration data recorded with a time interval of 0.02 seconds. The maximum acceleration observed was 8.66 m/s$^2$ (Figure 7.31).

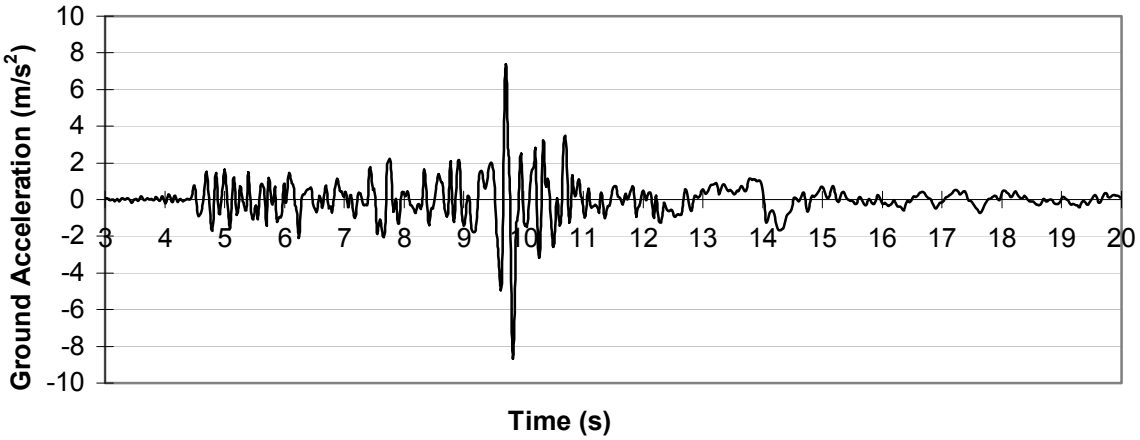


**Figure 7.31** Northridge Earthquake Accelerogram

The analyses were performed for the first 20 seconds of the record for demonstrative purposes. For the numerical analysis technique, the Wilson's Theta method with no viscous damping was employed. The resulting displacement and base shear force responses are shown in Figure 7.32 and 7.33.

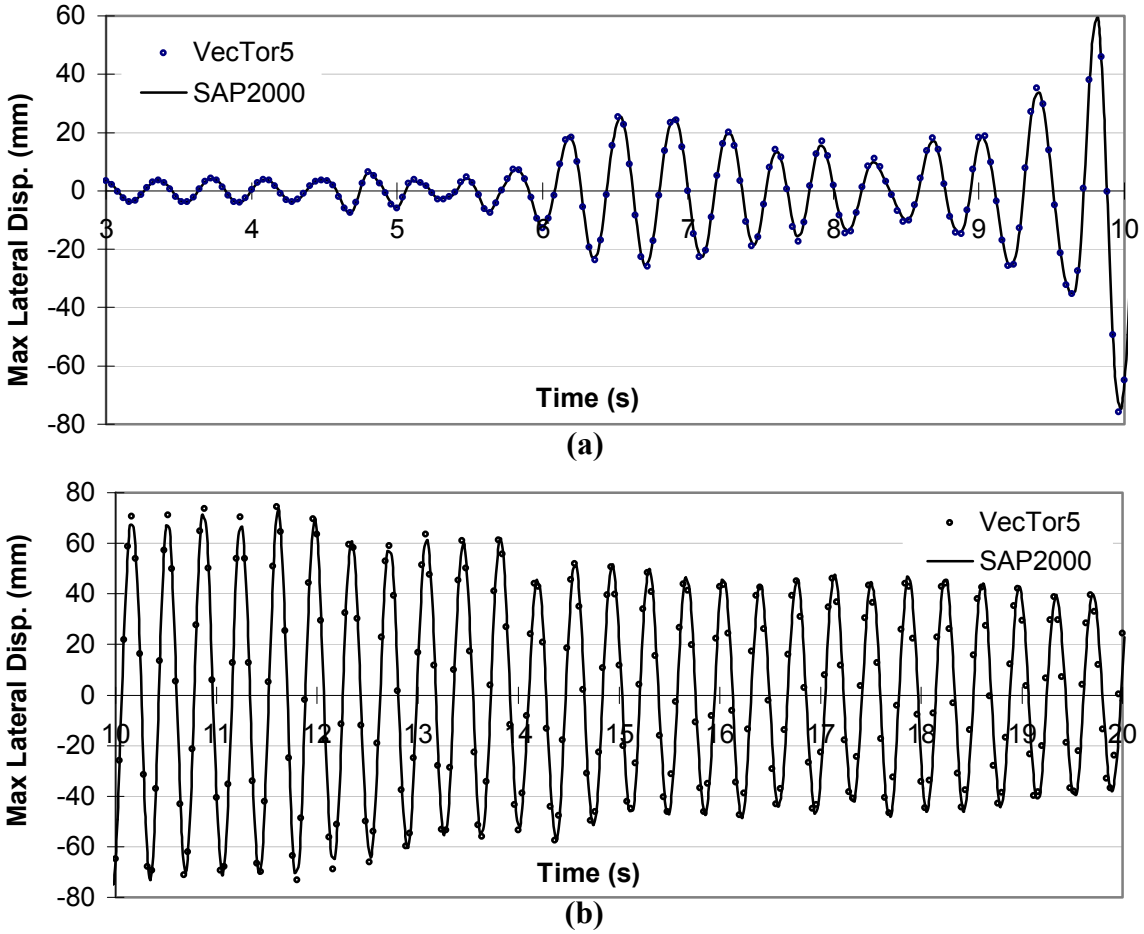


**(a)**




**(b)**

**Figure 7.32** Displacement Response for the Simple Cantilever Subjected to Northridge Earthquake (No Damping): **(a)** 3 s to 10 s; **(b)** 10 to 20 s

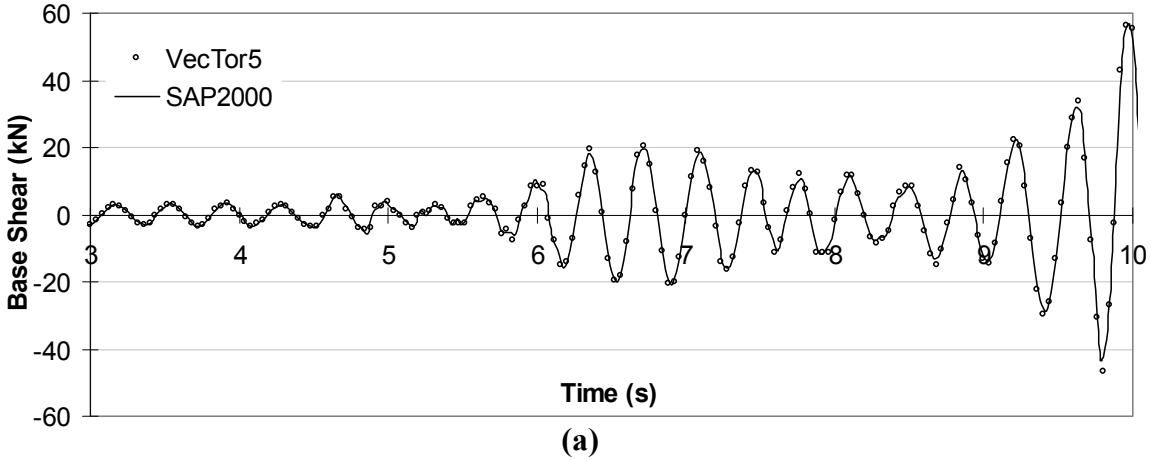


**(a)**

**Figure 7.33** Reaction Response for the Simple Cantilever Subjected to Northridge Earthquake (No Damping): **(a)** from 3 to 10 s

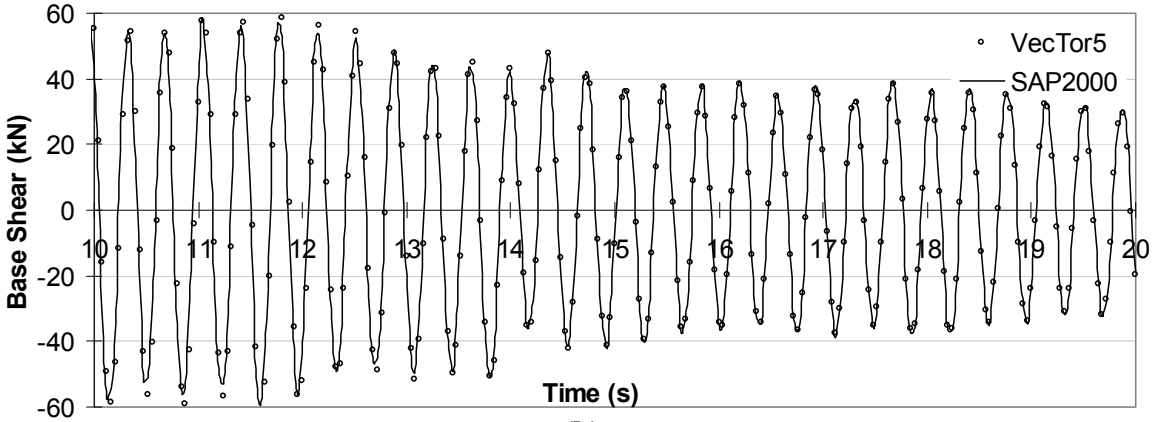


**(b)**

**Figure 7.33** Reaction Response for the Simple Cantilever Subjected to Northridge Earthquake (No Damping): **(b)** from 10 to 20 s

To verify the implemented Rayleigh damping algorithm, the analysis was repeated assigning a 5% damping ratio to the first and second vibration modes. The damping ratios for the remaining two modes were calculated by the programs automatically as explained in Section 7.5.2. The resulting responses are presented in Figure 7.34 and 7.35.

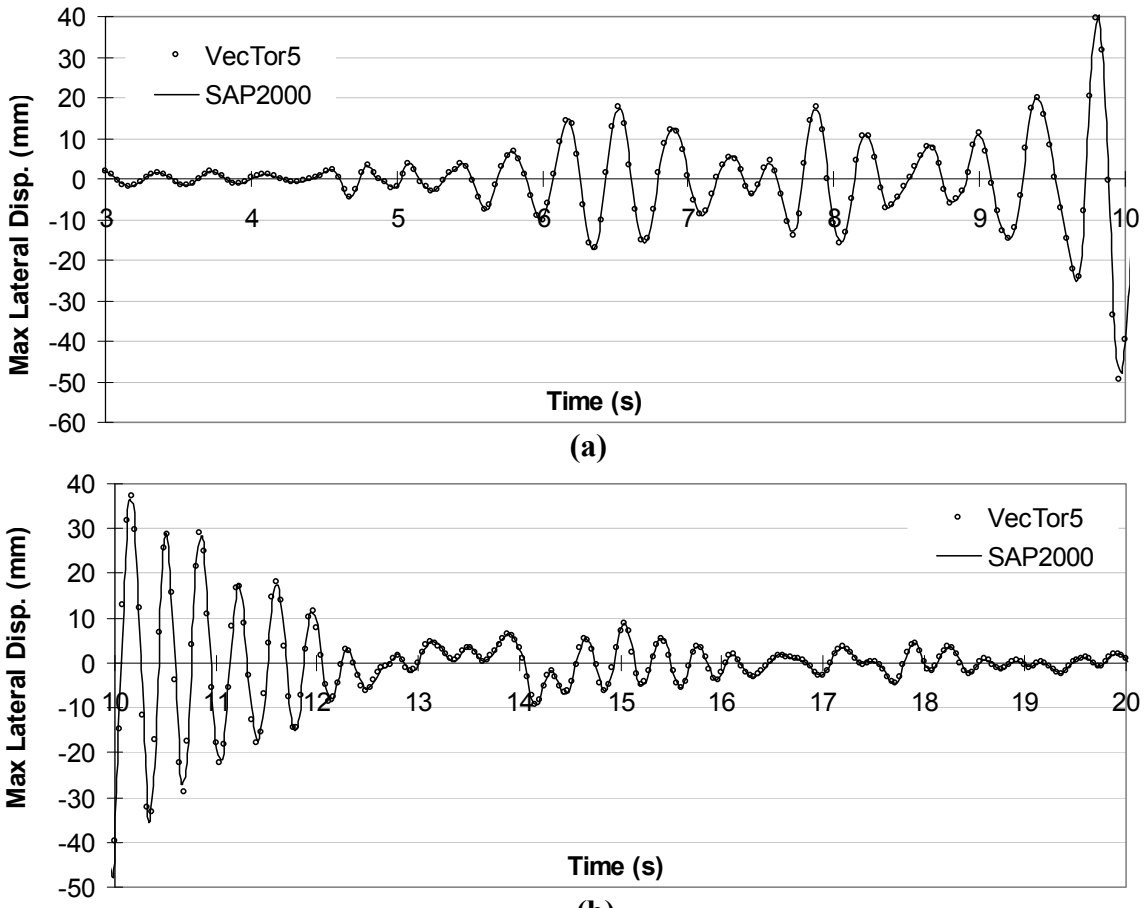


**(a)**

**(b)**

**Figure 7.34** Displacement Response for the Simple Cantilever Subjected to Northridge Earthquake (with Damping): **(a)** 3 to10 s; **(b)** 10 to 20 s

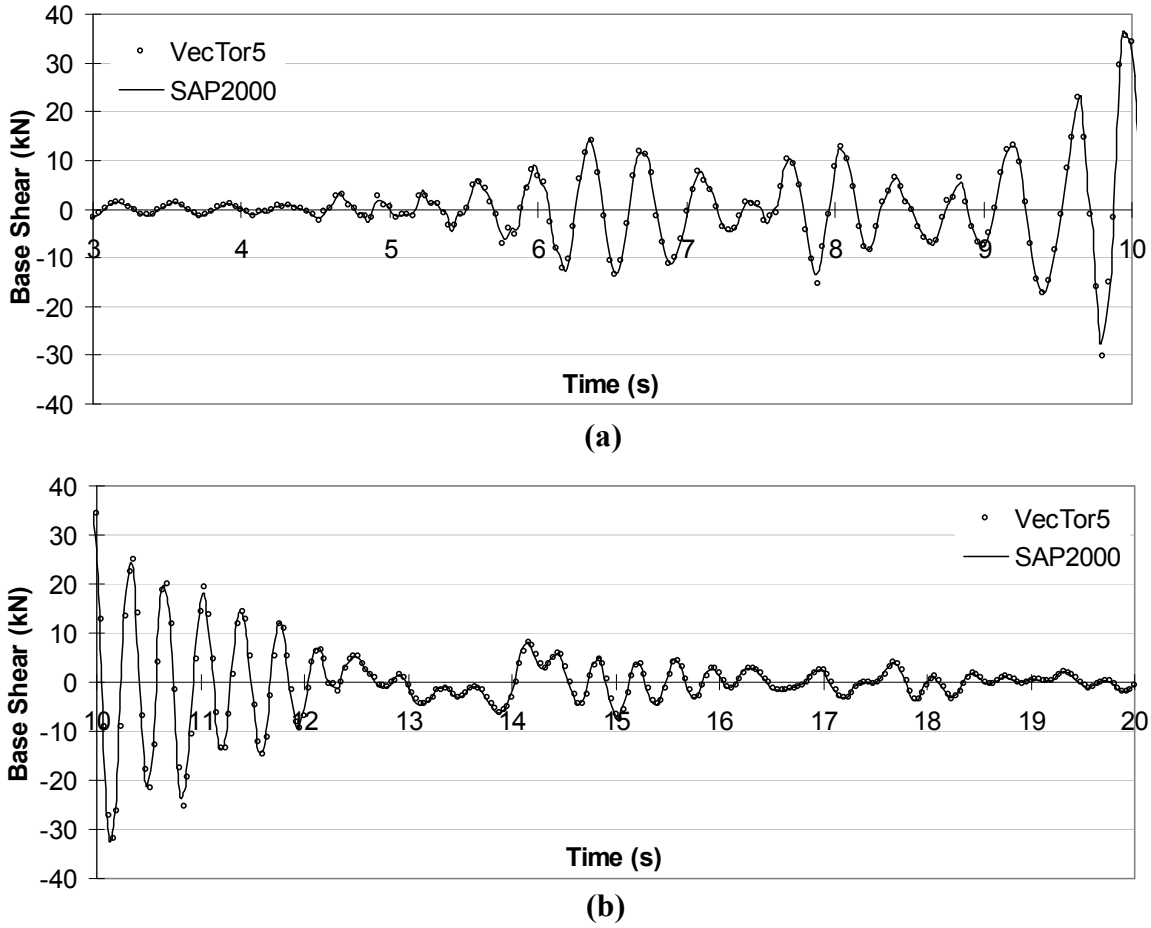


**Figure 7.35** Reaction Response for the Simple Cantilever Subjected to Northridge Earthquake (with Damping): **(a)** 3 to 10 s; **(b)** 10 to 20 s

### 7.12.2 Impulse Forces

The same structure was analyzed for the case where it is subjected to the impulse force-time history shown in Figure 7.18, applied to the top mass level (Node 3 in Figure 7.17). Analyses were performed for a time step length of 0.005 s using the Newmark's average acceleration procedure. Rayleigh damping was used with an assignment of 0% and 5% damping on the first and second modes of vibration, respectively. The displacement and reaction responses are presented in Figure 7.36 and 7.37.

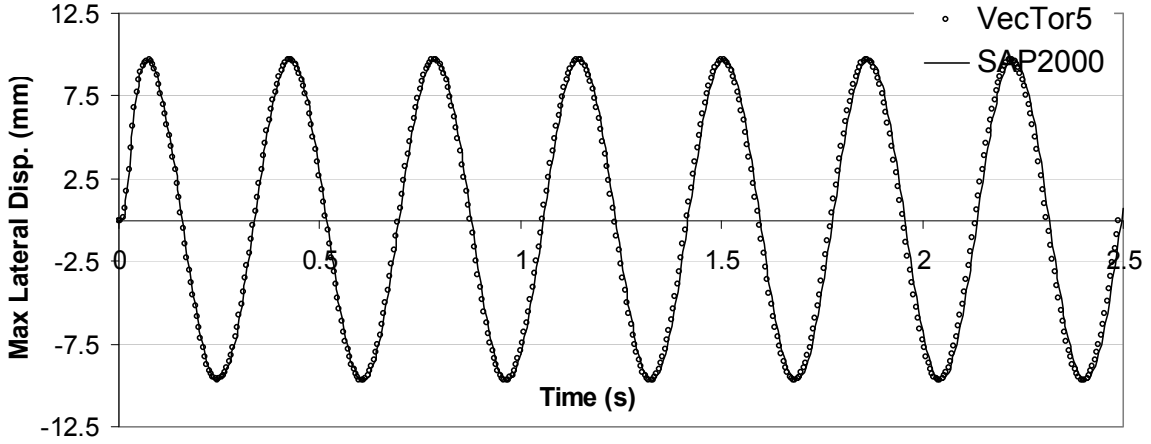


**Figure 7.36** Displacement Response for the Simple Cantilever Subjected to the Impulsive Loading (with Damping)

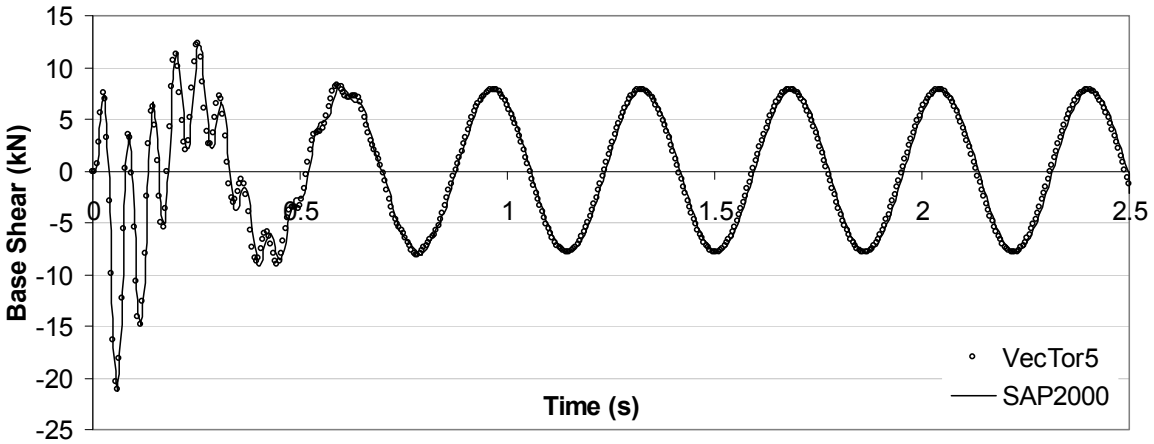


**Figure 7.37** Reaction Response for the Simple Cantilever Subjected to the Impulsive Loading (with Damping)

### 7.12.3 Initial Velocity

The initial velocity analysis capability of VecTor5 was verified with hand calculations. For this purpose, the structure used thus far was simplified to a one degree-of-freedom system as shown in Figure 7.38. Gross section properties were assumed with the modulus of elasticity of concrete taken as 32000 MPa.

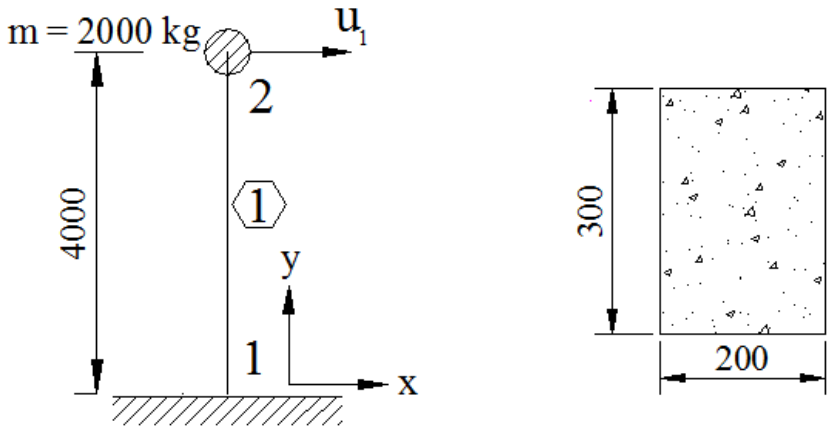


**Figure 7.38** Details of the 1-DOF Structure Subjected to Initial Velocity Loading

The structure was analyzed for the condition where an initial velocity of 8 m/s was applied to the top mass in the global x-direction (Node 2 in Figure 7.38). Analyses were performed for a time step length of 0.001 s, using Newmark's linear acceleration procedure.

The hand calculation procedure was performed according to the following steps. First, the structural stiffness matrix was created with reference to the global x- and y- axes as follows:

$$[k] = \begin{bmatrix} 2.7 & 0 & 5400 \\ 0 & 480 & 0 \\ 5400 & 0 & 14.4 \times 10^6 \end{bmatrix} \quad kN/mm$$

The lateral stiffness matrix corresponding to the dynamic degree-of-freedom $u_1$ was then calculated through the use of static condensation as $[k]_{lat} = [675]\ kN/m$.

The period of the system was calculated by means of Eq. 7.84 and verified with the VecTor5 calculated period of 0.342 s.

$$T = 2 \times \pi \times \sqrt{\frac{m}{k}} = 2 \times \pi \times \sqrt{\frac{2}{675}} = 0.342 \sec \qquad (7.84)$$

The free vibration response due to an initial acceleration was calculated through Eq. 7.85.

$$x(t) = \frac{\dot{x}_0}{w_n} \times \sin(w_n \times t) \tag{7.85}$$

where *x(t)* is the displacement, $\dot{x}_0$ is the initial velocity, $w_n$ is the natural frequency of the system calculated as $w_n = 2\pi / T_n$, and *t* is the elapsed time.

Finally, the base shear force was calculated as $k \times x(t) = 675\ ^{N/mm} \times x(t)$. The resulting displacement and reaction responses are presented in Figure 7.39 and 7.40.

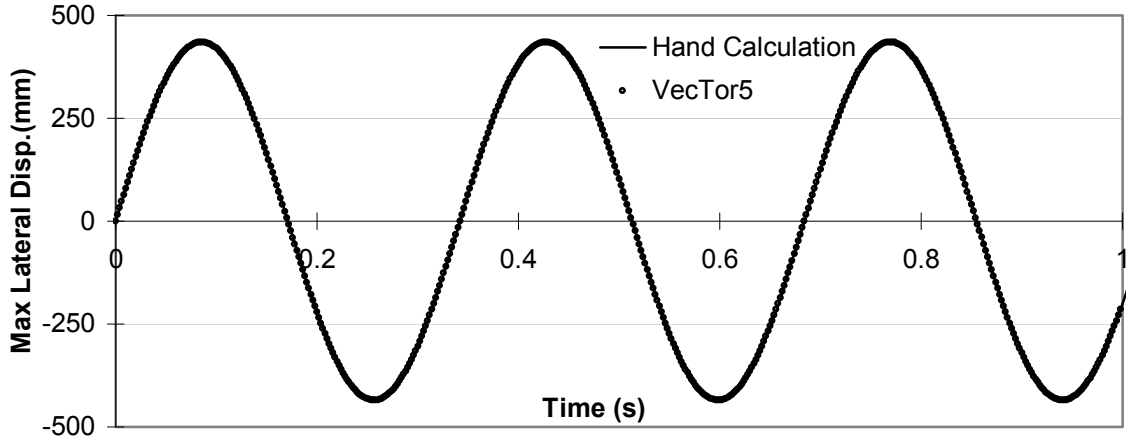


**Figure 7.39** Displacement Response for the 1-DOF Structure (No Damping)

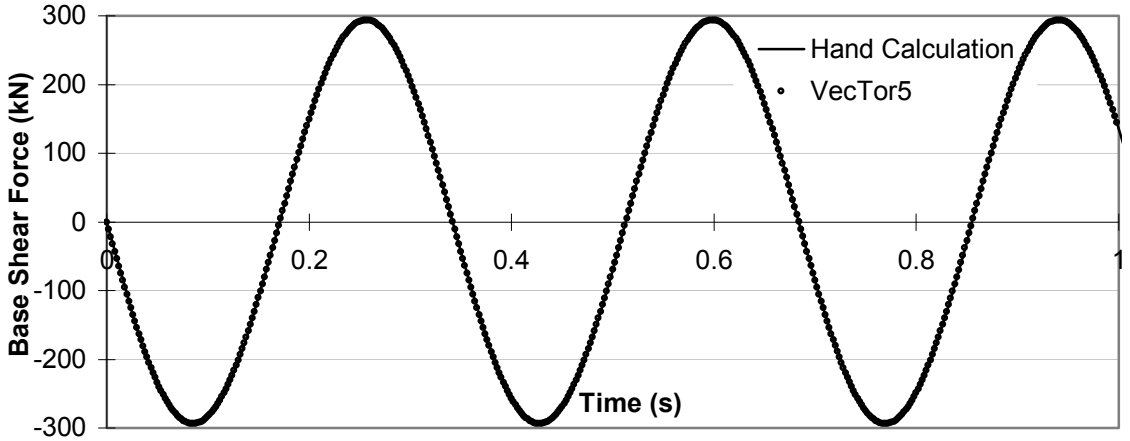


**Figure 7.40** Reaction Response for the 1-DOF Structure (No Damping)

For verification of the damping implementations, the analyses were repeated with an assigned 5% damping ratio. In the hand calculations, the displacement response for an initial velocity was calculated using Eq. 7.86.

$$x(t) = e^{-\xi \times w_n \times t} \times \left( \dot{x}_0 / w_D \right) \times \sin(w_D \times t) \tag{7.86}$$

where $\xi$ is the damping ratio and $w_D$ is the damped frequency of the system calculated as $w_D = w_n \times \sqrt{1-\xi^2}$ .

The resulting displacement and reaction responses are presented in Figure 7.41 and 7.42.

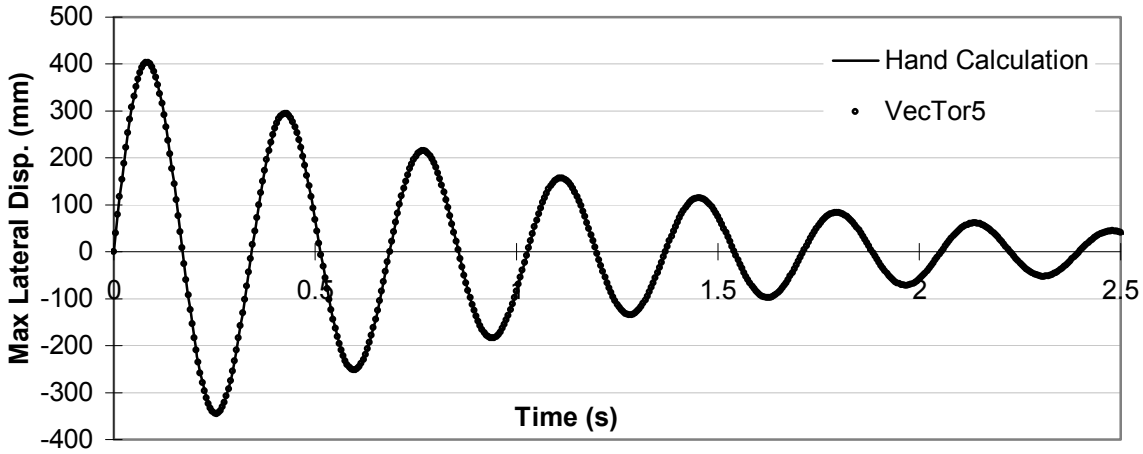


**Figure 7.41** Displacement Response for the 1-DOF Structure (with 5% Damping)

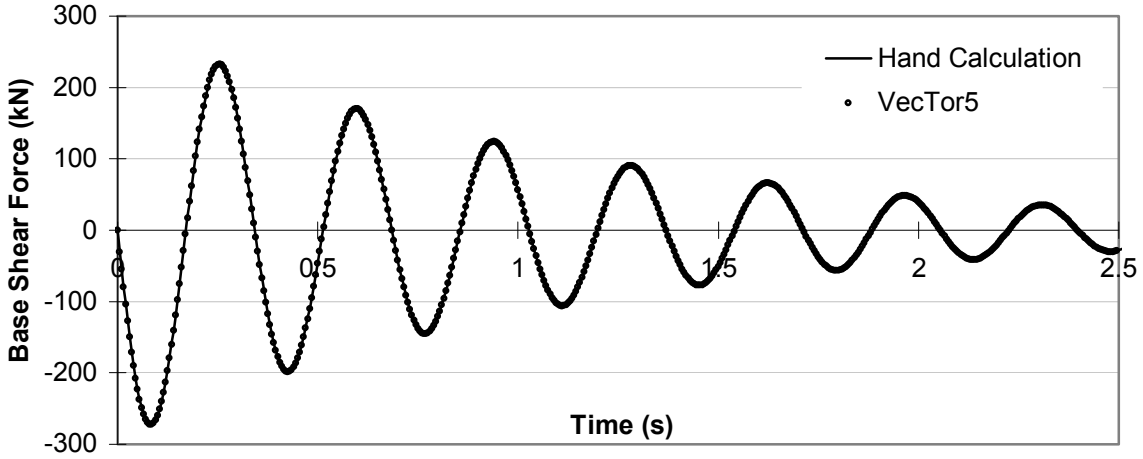


**Figure 7.42** Reaction Response for the 1-DOF Structure (with 5% Damping)

### 7.12.4 Conclusion

The linear-elastic dynamic analyses carried out with VecTor5 for the ground acceleration loading (Figure 7.32 to Figure 7.35), for the impulsive loading (Figure 7.36 and Figure 7.37) and for the initial velocity loading (Figure 7.39 to Figure 7.42) provided essentially the same responses as did SAP2000 and hand calculations in term of both displacements and reactions. The visible small variations in the responses can be attributed to numerical errors which are an inherent part of computerized analyses.

---

# CHAPTER 8

## DYNAMIC LOADING: VERIFICATION & APPLICATIONS

### 8.1 Chapter Layout

This chapter discusses the application of the newly implemented nonlinear dynamic analysis algorithms to previously tested structures. The purpose of this application is not only to verify the new algorithms but also to provide guidelines for modelling of reinforced concrete frame-related structures, particularly those subjected to impact loads.

The chapter starts with a summary of the comprehensive experimental program undertaken by Saatci (2007) involving twenty tests on simply-supported reinforced concrete beams under impact loads.

It is then followed by the analytical modelling of the beams tested in the experimental program. During the modelling process, a general guideline for modelling structures under impact loads when only the contact velocity and the impacting mass are known is provided. In addition, the selection of an appropriate time step length and the proper use of dynamic analysis parameters are discussed.

The chapter continues with the analyses of the beams using the procedures and formulations developed, and with comparisons of the analytical responses with the experimental results in terms of displacement and reaction responses, reinforcement strains, damage levels and failure modes when applicable.

Finally, the chapter concludes with a detailed discussion of the analytical predictions as compared to the experimental responses. Some deficiencies discovered in the formulations are also discussed. In addition, when necessary, the appropriate use of the different formulations and options implemented are discussed.

## 8.2 Saatci Beams

An experimental program was recently conducted at the structural testing laboratory of the University of Toronto to verify the dynamic analysis formulations implemented into a nonlinear finite element program, VecTor2, and to supply the literature with detailed and reliable test data pertaining to the impact response of shear-critical structures. The experimental program involved eight beams (four pairs) with varying shear reinforcement ratios tested under free-falling drop-weights. The beams were tested several times, providing a total number of 20 impact tests.

*Details of the Beams*

All eight beams were simply supported and spanned a clear distance of 3.0 m between two roller supports, leaving a 940 mm overhang on each side (Figure 8.1). All beams had a 250 x 410 mm cross section.

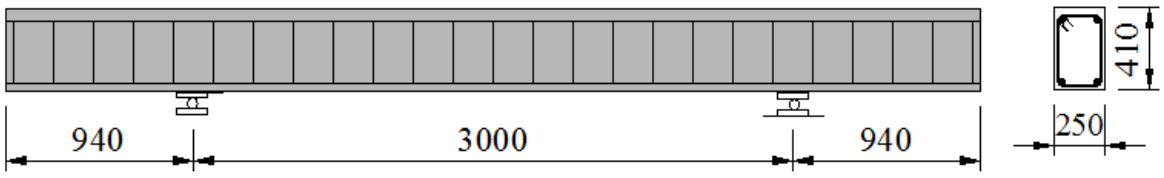


**Figure 8.1** Dimensions of Saatci Beams

The same amount of longitudinal reinforcement, with identical configuration, was used in all eight beams (Figure 8.2(a)). The main variable in the cross sections of the beams was the percentage of the transverse reinforcement. The four different ratios of shear reinforcement used were 0%, 0.1%, 0.2% and 0.4%. The concrete strengths were also varied slightly, ranging from 44.7 MPa to 50.1 MPa. All reinforcement and concrete material properties are documented in Table 8.1. The naming convention adopted for each beam was based on the transverse reinforcement ratio as shown in Figure 8.2(b).

**Table 8.1** Material Properties of Saatci Beams

| | Reinforcement | | | | | | | |
|---|---|---|---|---|---|---|---|---|
| | $A_s$ ($mm^2$) | $d_b$ (mm) | $f_y$ (MPa) | $f_u$ (MPa) | $E_s$ (MPa) | $E_{sh}$ (MPa) | $\varepsilon_{sh}$ ($x10^{-3}$) | $\varepsilon_u$ ($x10^{-3}$) |
| **No.30** | 700 | 29.9 | 464 | 630 | 195000 | 1088 | 12.5 | 165 |
| **D-6** | 38.7 | 7 | 605 | 652 | 190250 | 2794 | 3.2 | 20 |

| | Concrete | | |
|---|---|---|---|
| | $f'_c$ (MPa) | $\varepsilon_0$ ($x10^{-3}$) | $E_c$ (MPa) |
| **SS0** | 50.1 | 2.32 | 32000 |
| **SS1** | 44.7 | 2.36 | 27000 |
| **SS2** | 47 | 2,42 | 28000 |
| **SS3** | 46.7 | 2.51 | 27000 |

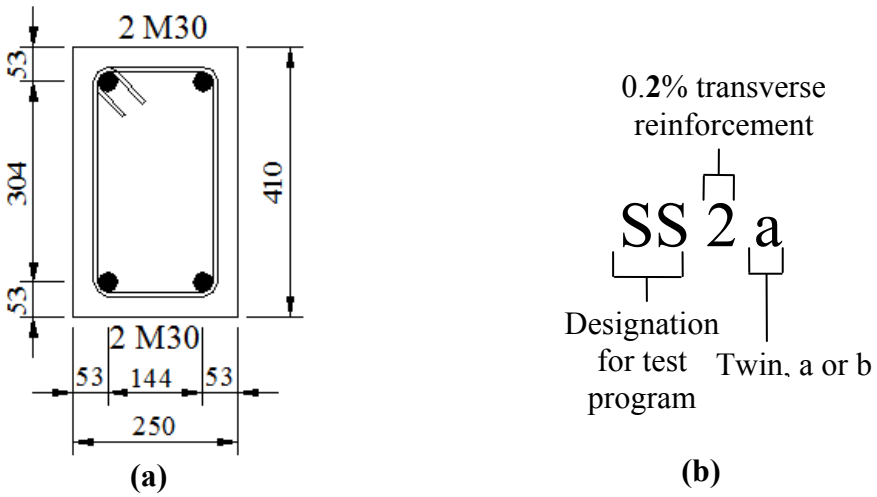


**Figure 8.2 (a)** Cross Section of Saatci Beams; **(b)** Name Convention Adopted (Saatci, 2007)

Thus, according to this convention, Beams SS0a, SS0b, SS1a, SS1b, SS2a, SS2b, SS3a and SS3b comprised the experimental program. Beam series-a and -b had identical details in all respects. They were subjected to a different loading program as described below.

*Loading Procedure*

All beams were tested under impact loads induced by free-falling drop-weights (Figure 8.3). For all tests, the weights were dropped from a clear height of 3.26 m above the specimen, resulting in an 8.0 m/s calculated impact velocity. All specimens, except SS0b, were tested more than once in order to investigate the effects of impact loads on previously damaged beams.

Two different loading programs were adopted in the experiment. The *a-series* beams were subjected to a drop-weight of 211 kg in the first impact test. A drop-weight of 600 kg was then used in second and third impact tests. The *b-series* beams, on the other hand, were subjected to a drop-weight of 600 kg in the first and second impact tests. A drop-weight of 211 kg was then used in the third impact test.

Taking into account the loading regime, the naming convention for a beam, for example SS2a, became as follows: SS2a-1, SS2a-2 and SS2a-3 where the numbers 1, 2 and 3 represented the first, second and third tests, respectively.

**(a)** **(b)** **(c)**

**Figure 8.3** Experiment Details of Saatci Beams **(a)** Light Drop-Weight (211 kg); **(b)** Heavy Drop-Weight (600 kg); **(c)** Test Setup (Saatci, 2007)

*Support Conditions*

All of the specimens were tested under the same simply-supported conditions. As uplift of the beams from the supports was expected during impact, a special arrangement of the supports was employed to prevent uplift of the specimens without creating any moments at the supports during vibration. For this purpose, the beams were held down with two No.30 reinforcement bars. The bars were threaded at both ends and bolted at the top end to a hollow structural steel (HSS) section which crossed the specimen (Figure 8.4(a)). At the bottom end, in order to enable free rotation, the bars were fitted to spherical bearings which were supported by steel floor beams bolted to the strong floor. A hinge was placed between the specimen and the HSS section at the top. With this setup, the specimens were able to rotate freely with minimal secondary moments at the supports (Figure 8.4(b)).

Although these support conditions rendered the system longitudinally unrestrained, they were chosen so as to prevent any possible axial load developing during the testing, which would have further complicated the analyses. As a result of this instability in the test setup, it was observed both by video records and displacement sensors that the specimens typically vibrated slightly in the longitudinal direction during the tests. The effects of this

movement on the vertical displacement measurements were found to be insignificant (Saatci, 2007).

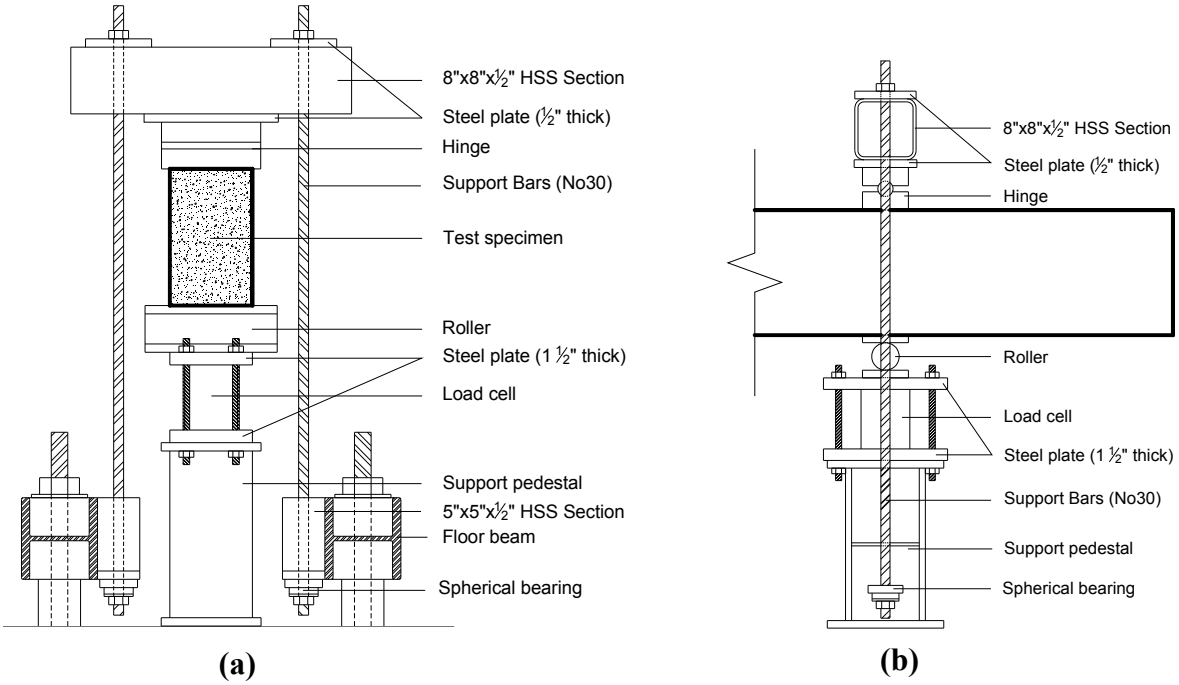


**Figure 8.4** Test Setup for Saatci Beams: **(a)** Cross Section at the Supports; **(b)** Side View of Support (Floor beams are not shown.) (Saatci, 2007)

## 8.3 Analytical Modelling

Taking advantage of the symmetry of the beams and the test setup, only one-half of each beam was modelled (Figure 8.5). In the model, half of the main span of the beam was divided into 6 segments with 250 mm segment lengths, each equalling approximately 0.6 times the cross section depth. For the overhangs, 4 segments with 235 mm lengths were used.

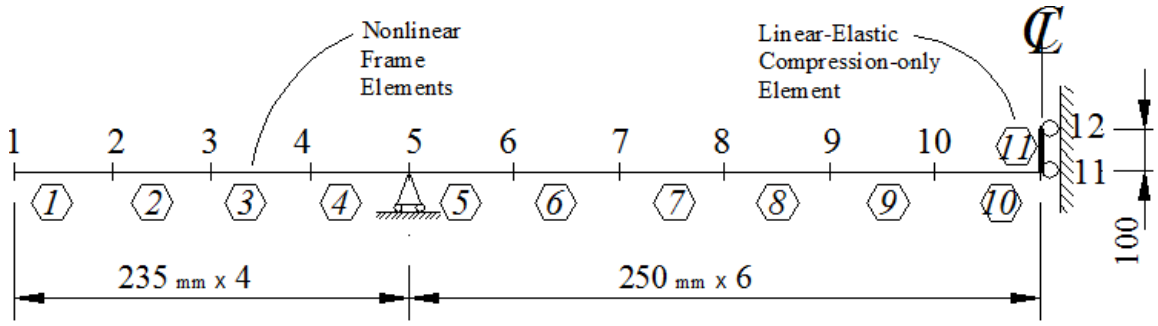


**Figure 8.5** Analytical Model for Saatci Beams

The cross section was modelled using 32 concrete layers and two steel layers (Figure 8.6(a)). As shown in Figure 8.6(b), transverse reinforcement ratios were assigned to all layers except the clear cover layers. Out-of-plane reinforcement was smeared into a tributary area of approximately 5 times the bar diameter (5 x 7.0 mm = 35mm) as shown in Figure 8.6 (c).

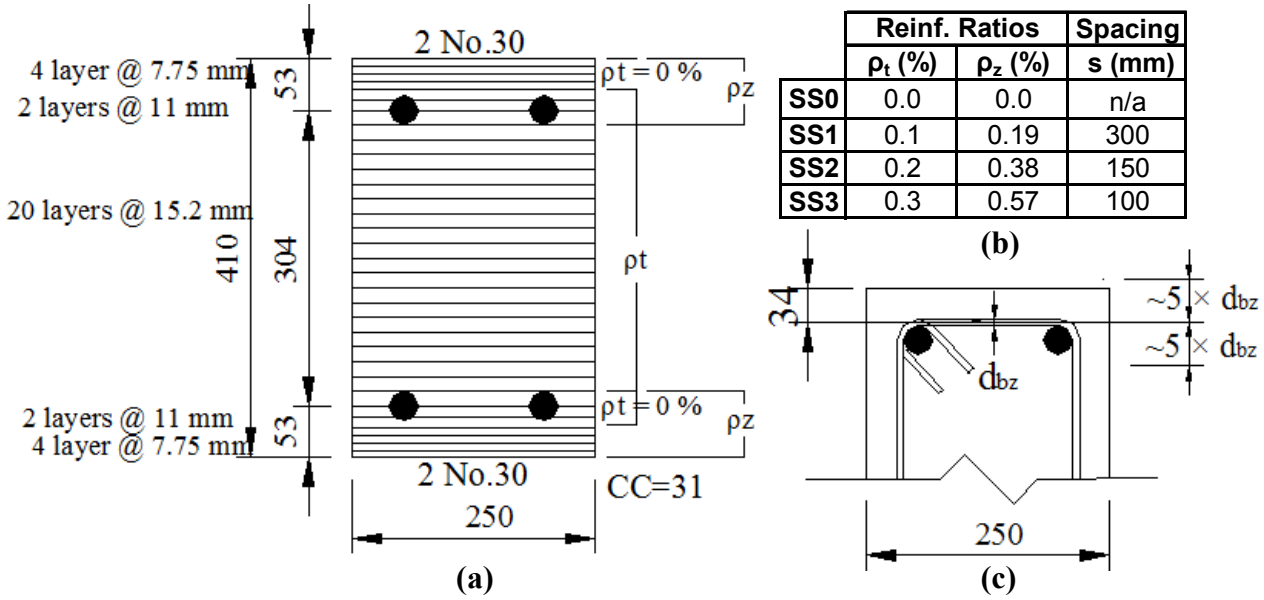


| | Reinf. Ratios | | Spacing |
|---|---|---|---|
| | $\rho_t$ (%) | $\rho_z$ (%) | s (mm) |
| SS0 | 0.0 | 0.0 | n/a |
| SS1 | 0.1 | 0.19 | 300 |
| SS2 | 0.2 | 0.38 | 150 |
| SS3 | 0.3 | 0.57 | 100 |

**Figure 8.6 (a)** Sectional Layers used in the Model of Saatci Beams; **(b)** Smeared Reinforcement Ratios; **(c)** Tributary Area for the Out-of-Plane Reinf.

The concrete properties used were as determined from standard cylinders; the longitudinal and transverse reinforcement properties were as determined by standard coupon tests (Table 8.1). The tensile strength of concrete was calculated through the formula $f_t^{'} = 0.33 \times \sqrt{f_c^{'}}$ as recommended by CSA A23.3-04.

*Support Restraints*

As mentioned in Section 8.2, to prevent any possible uplift, a special arrangement of the supports (Figure 8.4) was employed in the test setup through the use of a concrete pedestal under the beam and two support bars above the beam. If the support pedestal and support bars were included, the model of the beam would include two compression-only members at Node 5 as shown in Figure 8.7. The linear-elastic compression only members

would be used so that when Node 5, for example, displaced upwards, it did not cause tension force on the bottom support bar (Member 13) as was the case in the experimental setup.

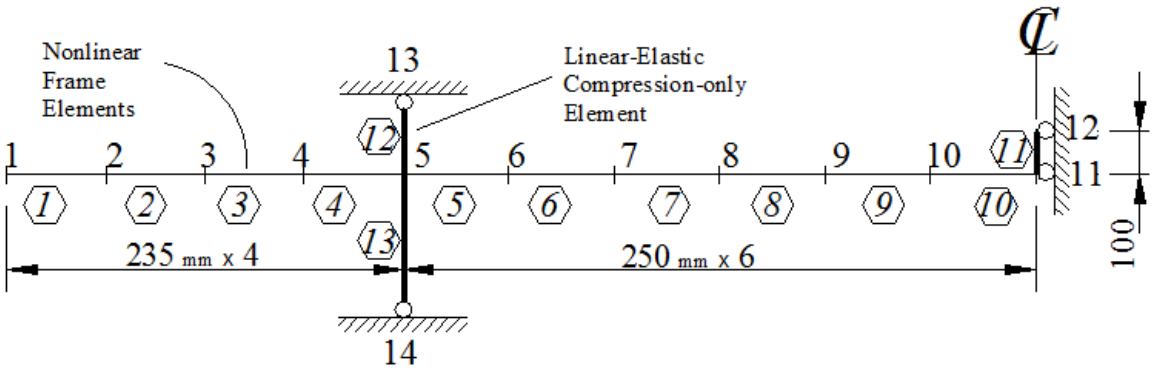


**Figure 8.7** Analytical Model of Saatci Beams including Special Supports (not used)

However, such an approach for representing the supports creates difficulties in term of modelling. One such difficulty is the uncertainty in the vibrational characteristics of the instrumentation used in the test setup as shown in Figure 8.4. During the impact and the ensuing oscillation, these parts are expected to vibrate which is difficult to model accurately. The other difficulty relates to the uncertainty in the calculation of the stiffness and inertial effects of the concrete pedestal and support bars including the HSS section.

As opposed to strut-and-tie models, the developed procedure is a sectional model that does not take into account the local support conditions. In other words, no transverse clamping stresses or concrete struts are created in the support regions. Therefore, a highly detailed representation of supports is not required.

For the reasons described above, the support was modelled as a simple roller by restraining the vertical degree-of-freedom of Node 5. The influence of this simplified support on the analytical predictions is discussed in Section 8.8.6. In addition to the roller support, to satisfy the condition of symmetry, both the horizontal and rotational degrees of freedom were restrained at Nodes 11 and 12 (Figure 8.5).

*Loading*

The main difficulty when modelling a structure under an impact load is the inclusion of the impact load itself. If the impact load-time history is known, the analyses can easily be carried out defining the impact load-time history as a load case similar to the impulse load-time history definition. However, the estimation of impact load-time history is a challenging task requiring several simplifications and assumptions which would limit the applicability of the procedures. Such an approach, for example, can be found in CEB-FIP (1988).

Therefore, the modelling of the impacting mass without the need to estimate the impact force-time history was much preferred in the formulation and application of VecTor5. The implementation of initial velocities and the development of compression-only members were carried out essentially for this reason.

Consequently, the impacting mass was simulated through the use of a special modelling technique similar to that used by Saatci (2007). Based on this technique, a *fictitious segment* (Member 11) was added to the model to simulate the load transfer from the drop-weight to the midspan of the beam. The following assumptions were made for this fictitious segment:

(1) A very high stiffness ($1 \times 10^9$ MPa modulus of elasticity with a 410 x 250 mm cross section) was assigned to this segment to create a hard impact condition.

(2) Linear-elastic behaviour was assumed for the fictitious segment to prevent any possible plastic deformations which would cause local energy dissipation. In reality, however, during the impact of the drop-weight on the beam, some energy dissipation occurred through such mechanisms as heat generation and local concrete spalling. However, a realistic consideration of such mechanisms in the analytical model is very difficult, if not impossible. Therefore, a linear-elastic assumption for the fictitious member was adopted, neglecting the local energy dissipation to avoid guess-work.

(3) The fictitious member was assumed to carry compression only in order to simulate the separation of the drop-weight from the beam immediately after the

impact occurs. Otherwise, the drop-weight would become attached to the beam after the impact, pulling it upwards due to the upward acceleration occurring during the bounce. Such behaviour would obviously render the model invalid.

The drop-weight was simulated by assigning a lumped mass to the top of the fictitious segment (Node 12). As Node 12 coincided with the axis of symmetry, only half of the mass was considered. Therefore, depending on the testing sequence, either a 105.5 kg or a 300 kg mass was assigned to Node 12. Only the y-degree-of freedom of this mass was included in the calculation as the x-degree-of-freedom of that node was restrained due to symmetry.

The impact load was simulated by assigning an initial velocity of *8.0 m/s* to the drop-weight (Node 12). In addition, a constant acceleration of 9.81 *m/s* was assigned to the drop-weight in order to simulate the gravitational effects once the separation occurred.

*Masses*

The nodal masses of the beam were calculated automatically by the program, assuming a material density of 2400 kg/m$^3$ (Figure 8.8).

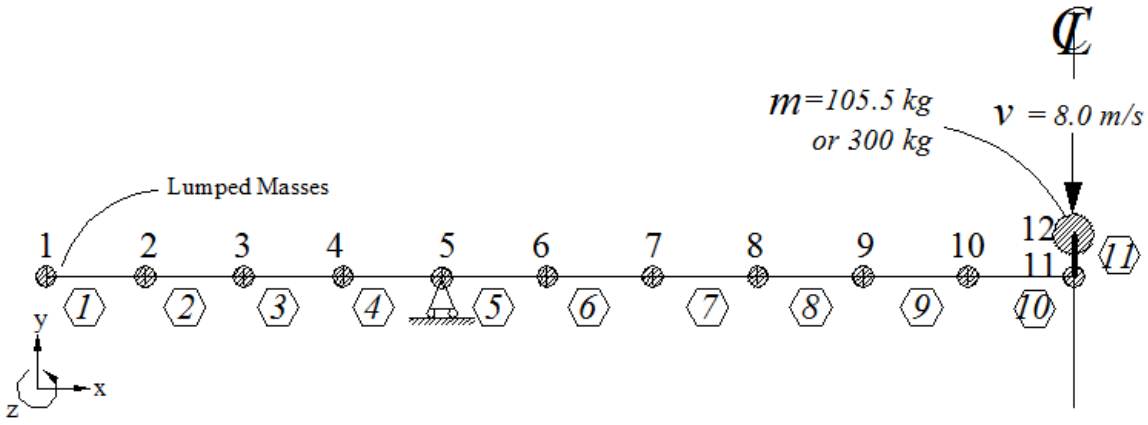


**Figure 8.8** Lumped Masses and Initial Velocity Loading Applied to Saatci Beams

As a result, the output file of the developed analytical procedure indicated the mass data as shown in Table 8.2.

**Table 8.2** Lumped Mass Data for Saatci Beams as Output by VecTor5

| Jnt | Mass-x self (kg) | Mass-x add. (kg) | Vel-x init. (m/s) | Acc-x const. ($m/s^2$) | Mass-y self (kg) | Mass-y add. (kg) | Vel-y init. (m/s) | Acc-y const. ($m/s^2$) |
|---|---|---|---|---|---|---|---|---|
| 1 | 28.9 | 0 | 0 | 0 | 28.9 | 0 | 0 | 0 |
| 2 | 57.8 | 0 | 0 | 0 | 57.8 | 0 | 0 | 0 |
| 3 | 57.8 | 0 | 0 | 0 | 57.8 | 0 | 0 | 0 |
| 4 | 57.8 | 0 | 0 | 0 | 57.8 | 0 | 0 | 0 |
| 5 | 59.7 | 0 | 0 | 0 | 0.00 | 0 | 0 | 0 |
| 6 | 61.5 | 0 | 0 | 0 | 61.5 | 0 | 0 | 0 |
| 7 | 61.5 | 0 | 0 | 0 | 61.5 | 0 | 0 | 0 |
| 8 | 61.5 | 0 | 0 | 0 | 61.5 | 0 | 0 | 0 |
| 9 | 61.5 | 0 | 0 | 0 | 61.5 | 0 | 0 | 0 |
| 10 | 61.5 | 0 | 0 | 0 | 61.5 | 0 | 0 | 0 |
| 11 | 0.00 | 0 | 0 | 0 | 30.8 | 0 | 0 | 0 |
| 12 | 0.00 | 0 | 0 | 0 | 0.00 | 105.5 | -8.00 | -9.81 |

*Seed Files*

As mentioned previously, after the first impact tests, the damaged beams were typically tested for a second and third time. The need to analyze the damaged beams for a second and third time required the use of seed files in which previous analysis results were stored in a binary format, allowing for future analysis of the damaged beams. Through the use of seed files, the damaged beam models were re-analyzed with the appropriate impacting mass depending on the testing sequence.

## 8.4 Analysis Parameters and Material Behaviour Models Used

As explained previously, one of the main focuses of this thesis is to perform analyses by using only default material models and analysis options common to all VecTor programs and predefined prior to this work. Therefore, the default analysis parameters and material behaviour models were used in the analyses of all beams with two exceptions.

As both the peak strain and the initial modulus of the elasticity of concrete were known from the cylinder tests, the Popovics formulation (1973) for normal strength concrete was selected for the concrete base curve under compression, rather than the default Hognestad (Parabola). As discussed in Section 4.2, depending on the known concrete properties, an appropriate selection of the concrete base curve in compression is recommended. However, if the analyses were performed with the default option of Hognestad (Parabola), the results did not change noticeably. A typical comparison of the responses

obtained using the default formulation and Popovics formulation is presented in Figure 8.9.

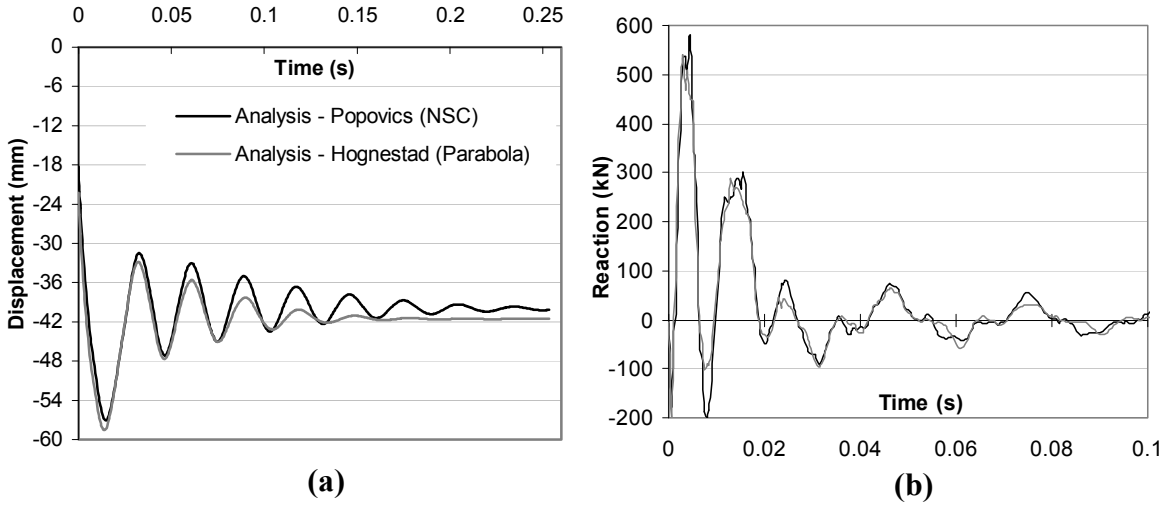


**Figure 8.9** Comparison of Experimental and Analytical Responses for Different Concrete Base Curve Models (SS3a-3): **(a)** Midspan Displacement; **(b)** Support Reaction

For the reinforcement hysteresis, the elastic-plastic model with strain hardening was selected rather than the default Seckin model with Bauschinger effect (Figure 5.15). The former model was selected after the observance of recovering reinforcement plastic offset strains under low strain reversals when using the Seckin Model.

It was noted during the impact analyses of Saatci Beams (Saatci, 2007) that the bottom longitudinal reinforcement typically yielded at the midspan in the first positive cycle, followed by low level strain reversals including both tension and compression excursions (Figure 8.10(a)). Shown in Figure 8.10(b) is the calculated plastic strain-time history for the reinforcement at the midspan of Beam SS2b-1. Note the recovery in the plastic offset strain. This behaviour analytically caused the residual midspan displacement to slightly recover, which was not observed experimentally. The top reinforcement typically behaved linear-elastically without yielding in the analytical model. Consequently, the Seckin model with Bauschinger effect was not used in the impact analyses performed in this chapter.

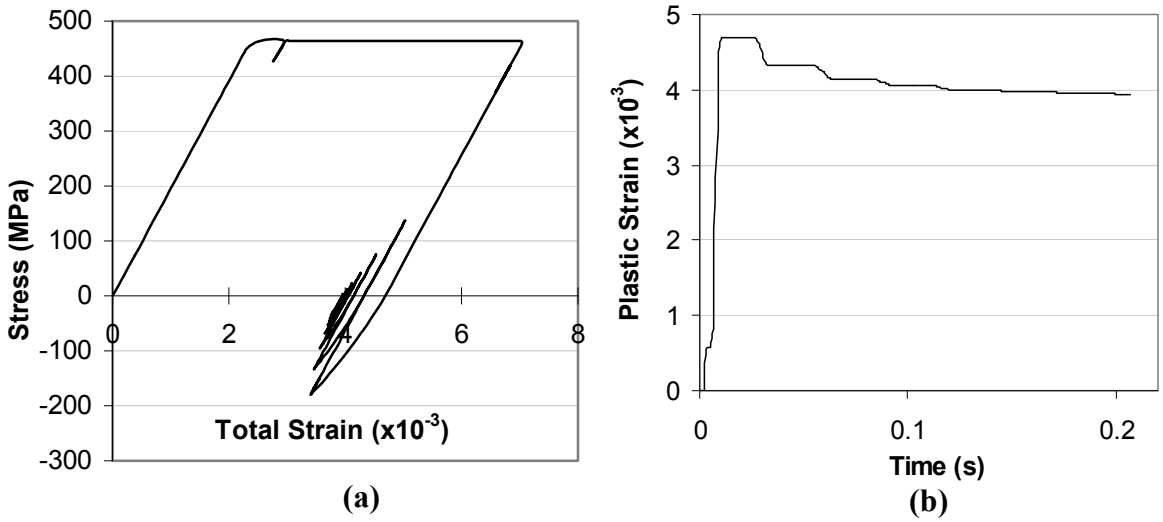


**Figure 8.10** Average Total Stains Calculated for the Bottom Longitudinal Reinforcement at the Midspan using Seckin Model with Bauschinger Effect (SS2b-1)

If the analyses were performed with the Seckin model, the only noticeable difference would be the residual displacements. A typical comparison of the responses obtained using the Seckin model and the elastic-plastic model with strain hardening is presented in Figure 8.11. Note how the residual displacement recovered somewhat during the vibration when the Seckin model was used.

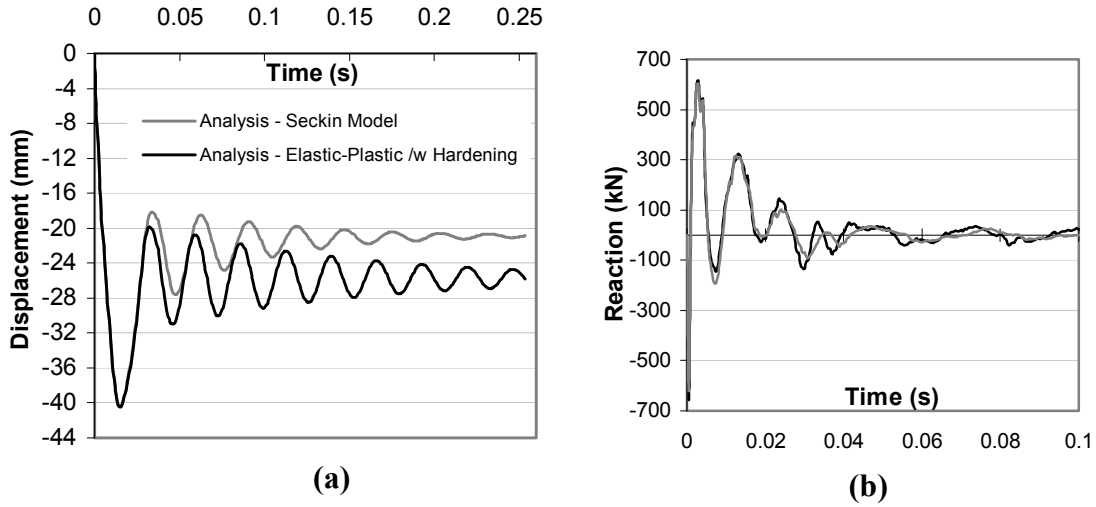


**Figure 8.11** Comparison of Experimental and Analytical Responses for Different Steel Hysteresis Models (SS2b-1): **(a)** Midspan Displacement; **(b)** Support Reaction

The material behaviour models for concrete and steel, as well as the general analysis options, used throughout all beam analyses are listed in Table 8.3.

**Table 8.3** Material Behaviour Models and General Analysis Options Used

| Concrete Behaviour | Model | Reinforcement Behaviour | Model |
|---|---|---|---|
| Compression Base Curve | Popovics (NSC)* | Hysteresis | El-Plastic w/ Hardening* |
| Compression Post-Peak | Modified Park-Kent | Dowel Action | Tassios (Crack Slip) |
| Compression Softening | Vecchio 1992-A | Strain Rate Effects | Malvar and Crawford |
| Tension Stiffening | Modified Bentz | | |
| Tension Softening | Linear | | |
| Tension Splitting | Not Considered | **Analysis Options** | **Model** |
| Confinement Strength | Kupfer / Richart | Geometric Nonlineartity | Considered |
| Dilatation | Variable - Kupfer | Shear Analysis Mode | Parabolic Shear Strain |
| Cracking Criterion | Mohr-Coulomb (Stress) | Shear Protection | On |
| Crack Width Check | Crack Limit (Agg/5) | Time Integration Method | Wilson's Theta |
| Hysteresis | NL (Vecchio) | Convergence Limit | 1.00001 |
| Slip Distortion | Vecchio-Lai | Maximum No of Iterations | 100 |
| Strain Rate Effects | CEB-FIB | | * non-default |

## 8.5 Damping

As discussed previously, the use of either the average or linear acceleration method requires some level of additional viscous damping for stability reasons. As most of the energy dissipation of concrete and reinforcement is already taken into account through the nonlinear material hysteretic behaviour, the use of additional viscous damping is not usually desired. For this reason, the Wilson Theta method with no additional damping was used. The damping characteristics of the analytical predictions are discussed in Section 8.8.3, and compared to the experimental responses.

## 8.6 Selection of an Appropriate Time-Step

The time step length selected has a major effect on the accuracy of the computed responses. Therefore, an appropriate value must be selected for the problem at hand. As explained previously, a dependable method for determining a suitable time step length is to assume a time step length and then progressively re-analyze the structure while reducing the assumed length, until a reasonably consistent response is obtained.

It was recommended in Chapter 7 that a time step length in the order of the smallest natural vibration period of the structure might provide optimal accuracy. For this reason, the eigen analysis results created at the beginning of the analysis were utilized. According

to the eigen analysis results, the modal periods of the beam with a 105.5 kg mass at Node 12 are presented in Table 8.4(a), and modal periods of the beam with a 300 kg mass at Node 12 are presented in Table 8.4(b). The smallest period of the beams (21$^{st}$ mode) is approximately 0.00003 s.

**Table 8.4** Natural Periods: **(a)** Model with 105.5 kg Mass; **(b)** Model with 300 kg Mass

**(a)**

| Mode | Period (s) |
|---|---|
| 1 | 0.0176 |
| 2 | 0.0048 |
| 3 | 0.00262 |
| 4 | 0.00138 |
| 5 | 8.81E-04 |
| 6 | 7.20E-04 |
| 7 | 5.37E-04 |
| 8 | 4.92E-04 |
| 9 | 3.94E-04 |
| 10 | 3.16E-04 |
| 11 | 2.80E-04 |

| Mode | Period (s) |
|---|---|
| 12 | 2.71E-04 |
| 13 | 2.42E-04 |
| 14 | 2.36E-04 |
| 15 | 2.22E-04 |
| 16 | 2.13E-04 |
| 17 | 2.00E-04 |
| 18 | 1.71E-04 |
| 19 | 1.36E-04 |
| 20 | 1.30E-04 |
| 21 | 3.01E-05 |

**(b)**

| Mode | Period (s) |
|---|---|
| 1 | 0.0217 |
| 2 | 0.00517 |
| 3 | 0.00262 |
| 4 | 0.00149 |
| 5 | 8.81E-04 |
| 6 | 7.28E-04 |
| 7 | 5.37E-04 |
| 8 | 5.09E-04 |
| 9 | 3.94E-04 |
| 10 | 3.16E-04 |
| 11 | 2.85E-04 |

| Mode | Period (s) |
|---|---|
| 12 | 2.71E-04 |
| 13 | 2.42E-04 |
| 14 | 2.38E-04 |
| 15 | 2.22E-04 |
| 16 | 2.13E-04 |
| 17 | 2.00E-04 |
| 18 | 1.73E-04 |
| 19 | 1.37E-04 |
| 20 | 1.31E-04 |
| 21 | 3.25E-05 |

As a result, a time step length in the order of 0.00001 s was anticipated. A series of analyses were then performed with varying time step lengths to determine the time step length to be used (Figure 8.12)

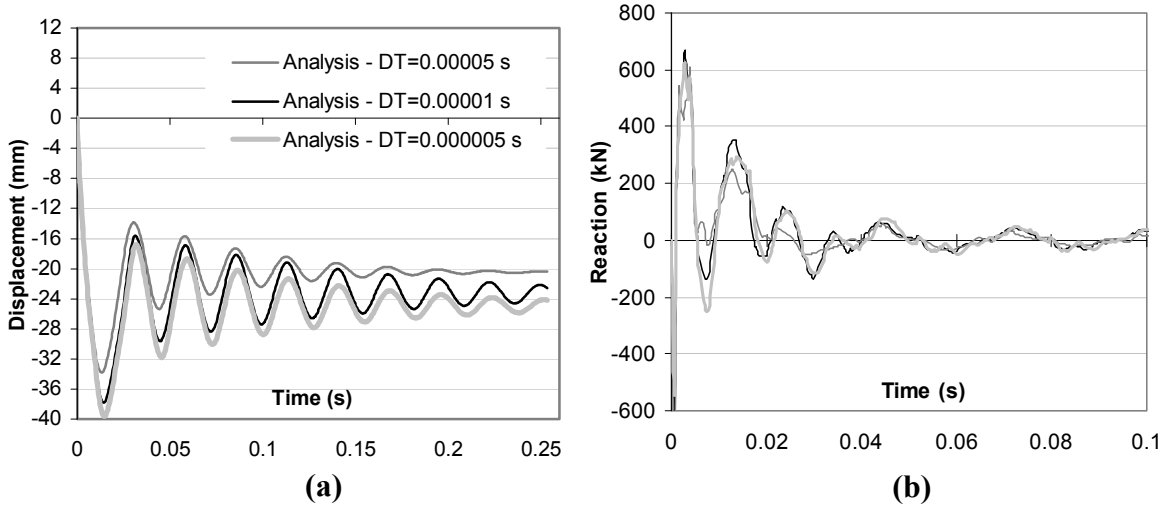


**Figure 8.12** Comparison of Experimental and Analytical Responses for Different Time Step Lengths (SS3b-1): **(a)** Midspan Displacement; **(b)** Support Reaction

As is apparent from the graphs above, the responses did not change significantly with time step lengths shorter than 0.00001 s. However, the computation time required increased significantly (Figure 8.13). Therefore, the selection of an appropriate time step length came down to the determination of an optimal balance between the accuracy and computation time. As a result, a time step length of 0.00001 s was selected and used for all impact analyses performed for the beams under consideration.

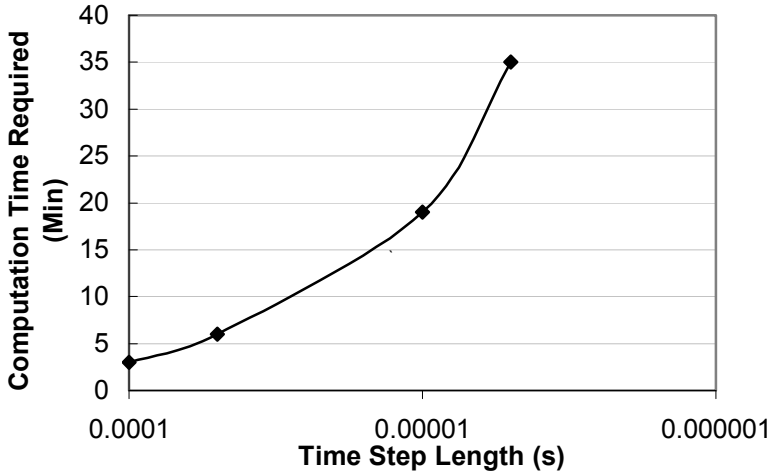


**Figure 8.13** Computation Time Required for Different Time Step Lengths (SS3b-1)

## 8.7 Comparison of the Analytical and Experimental Responses

The following section presents the comparisons of the analytically and experimentally obtained responses including midspan displacements and support reactions (Figure 8.14 to Figure 8.51). In addition, views of the beams at the end of each test are presented as taken from Saatci (2007). Comparisons of the longitudinal reinforcement strains, as calculated and experimentally reported at the midspan and at the support, can be found in Appendix A.

**Test SS0a - 1 (211 kg impacting mass)**

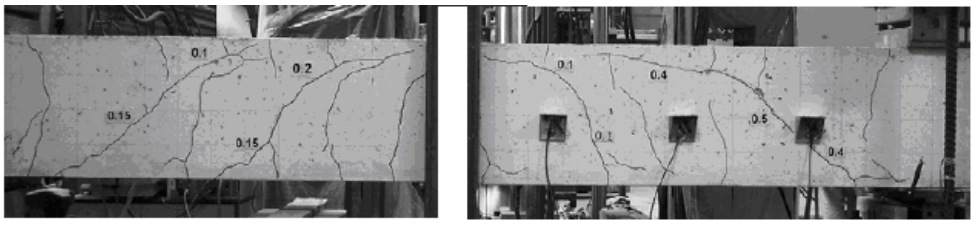

**(a)** **(b)**

**Figure 8.14** View of Beam SS0a-1 after Test: **(a)** North Half; **(b)** South Half

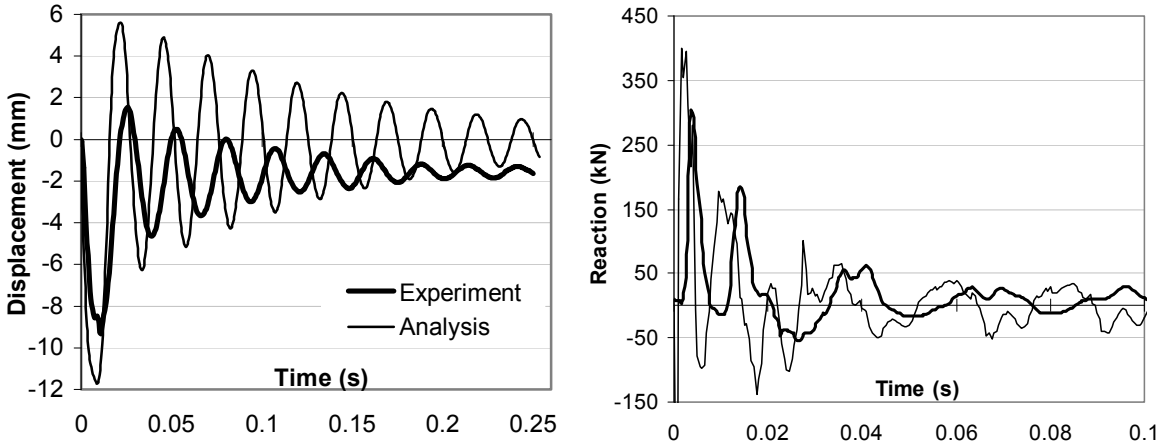


**(a)** **(b)**

**Figure 8.15** Comparison of Experimental and Analytical Responses for SS0a-1: **(a)** Midspan Displacement; **(b)** Support Reaction

**Test SS0a - 2 (600 kg impacting mass)**

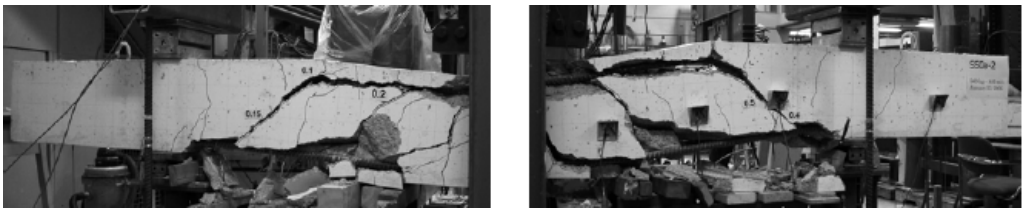

**(a)** **(b)**

**Figure 8.16** View of Beam SS0a-2 after Test: **(a)** North Half; **(b)** South Half

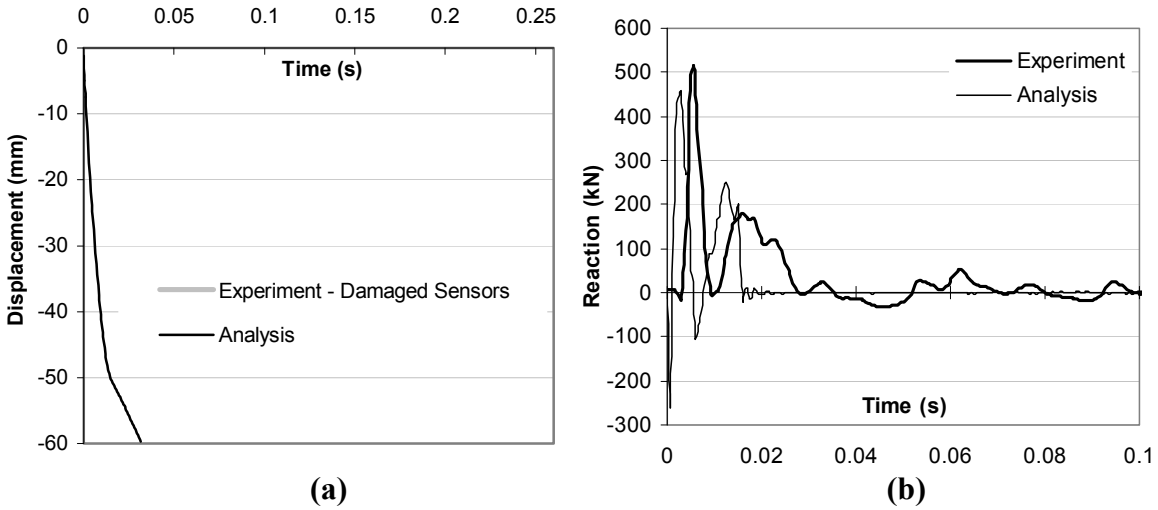


**Figure 8.17** Comparison of Experimental and Analytical Responses for SS0a-2: **(a)** Midspan Displacement; **(b)** Support Reaction

### Test SS0b-1 (600 kg impacting mass)

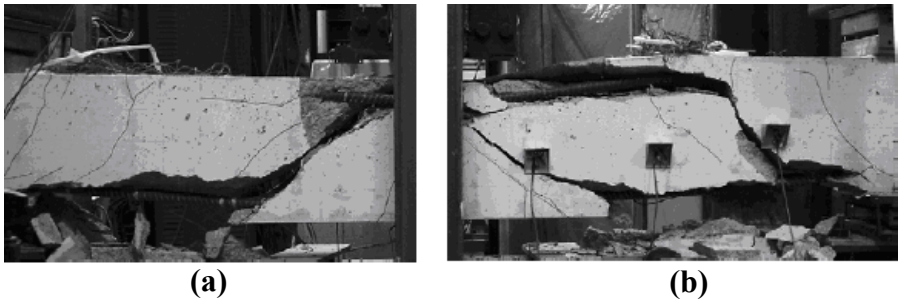


**Figure 8.18** View of Beam SS0b-1 after Test: **(a)** North Half; **(b)** South Half

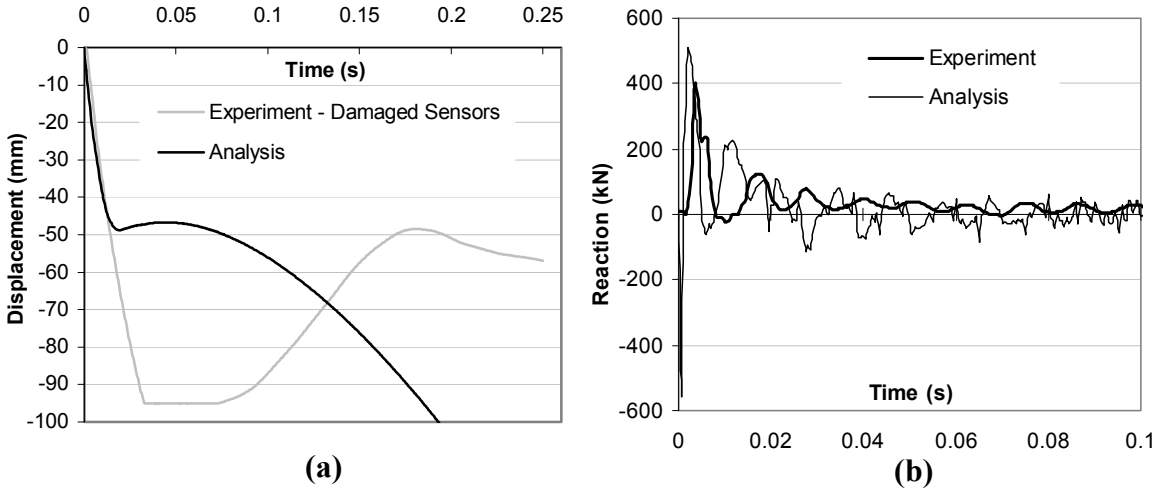


**Figure 8.19** Comparison of Experimental and Analytical Responses for SS0b-1: **(a)** Midspan Displacement; **(b)** Support Reaction

**Test SS1a - 1 (211 kg impacting mass)**

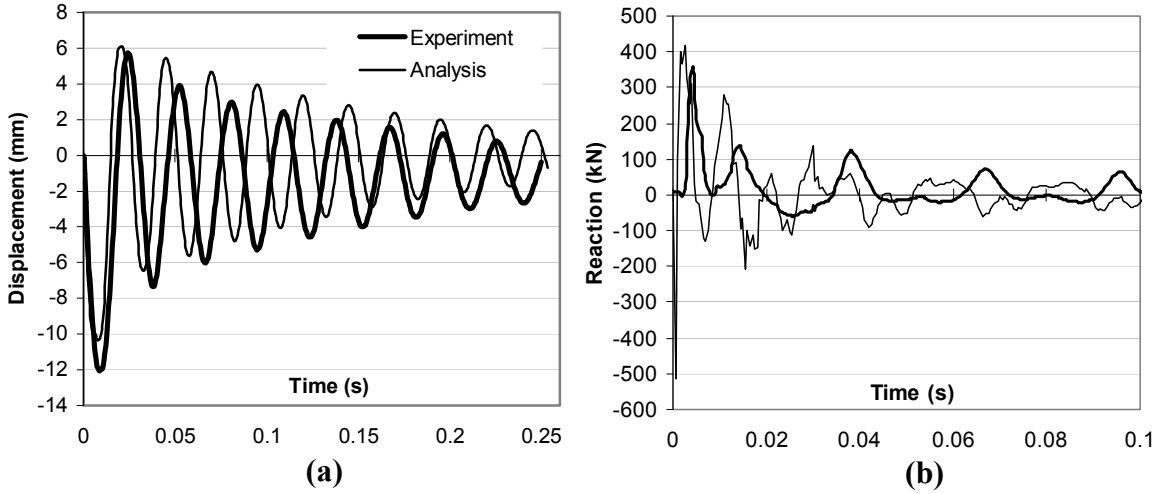


**Figure 8.20** Comparison of Experimental and Analytical Responses for SS1a-1: **(a)** Midspan Displacement; **(b)** Support Reaction

**Test SS1a - 2 (600 kg impacting mass)**

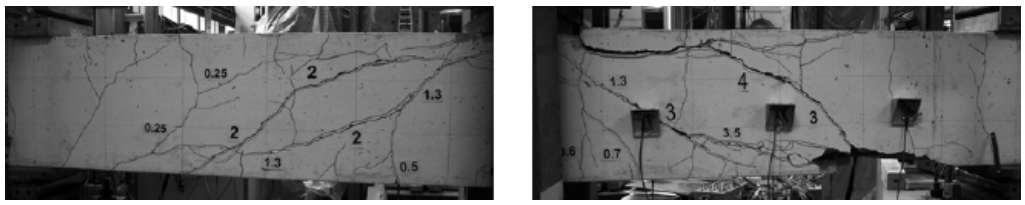


**Figure 8.21** View of Beam SS1a-2 after Test: **(a)** North Half; **(b)** South Half

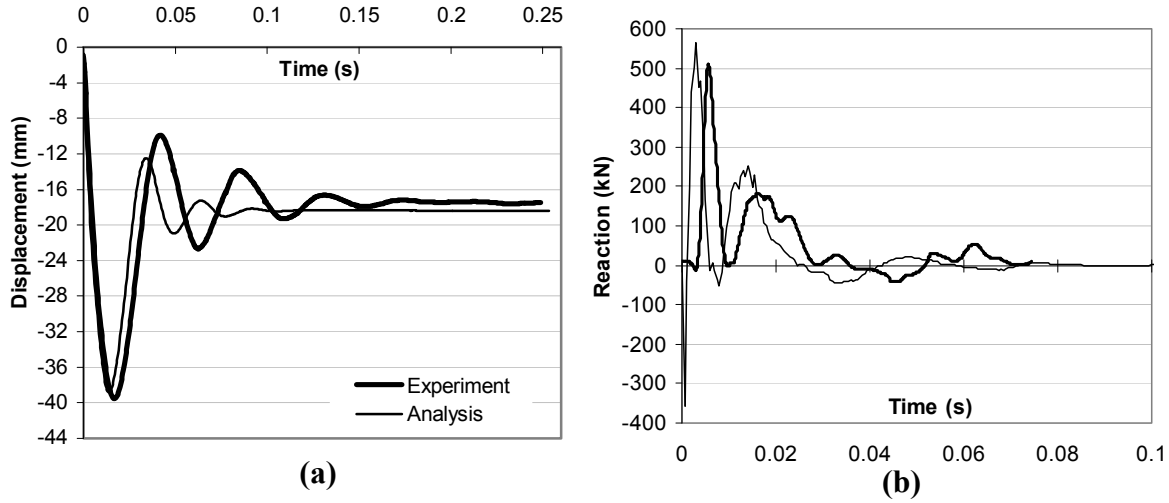


**Figure 8.22** Comparison of Experimental and Analytical Responses for SS1a-2: **(a)** Midspan Displacement; **(b)** Support Reaction

**Test SS1a - 3 (600 kg impacting mass)**

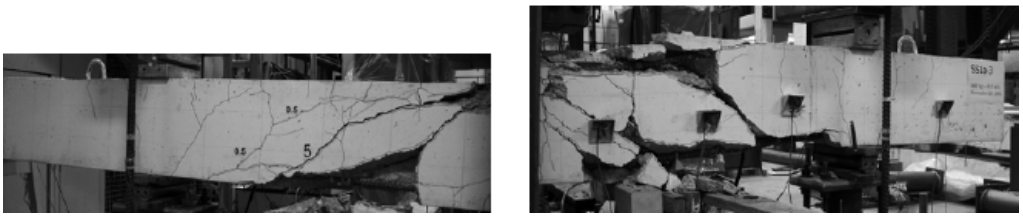

**(a)** **(b)**

**Figure 8.23** View of Beam SS1a-3 after Test: **(a)** North Half; **(b)** South Half

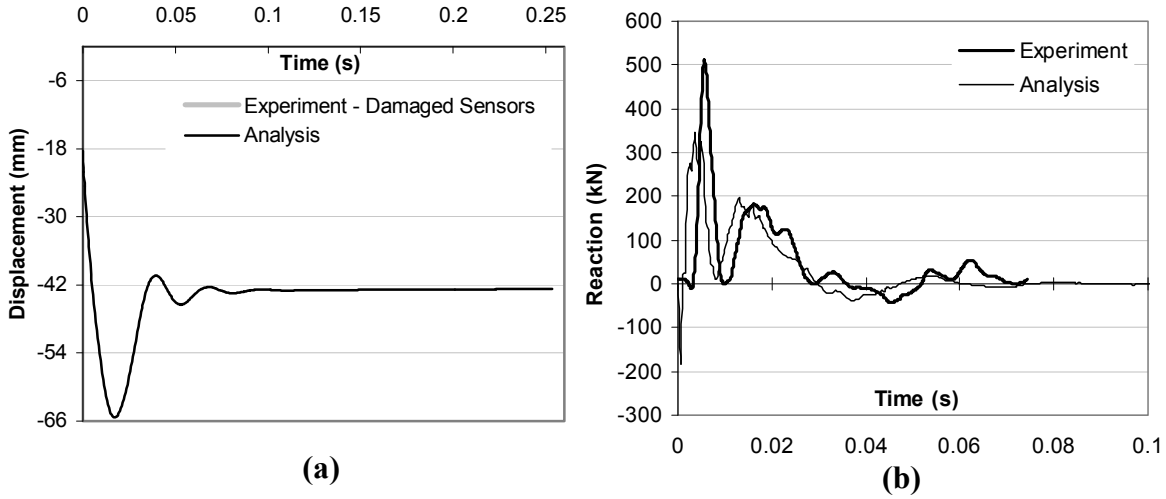


**(a)** **(b)**

**Figure 8.24** Comparison of Experimental and Analytical Responses for SS1a-3: **(a)** Midspan Displacement; **(b)** Support Reaction

**Test SS1b - 1 (600 kg impacting mass)**

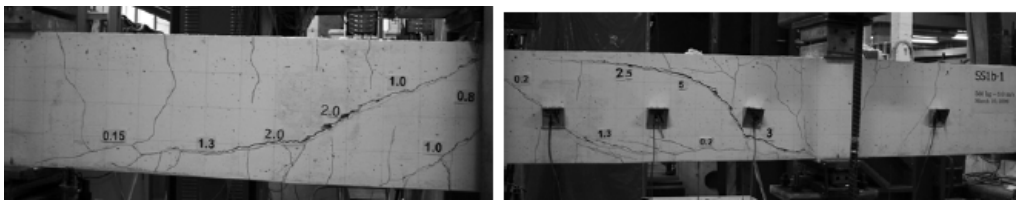

**(a)** **(b)**

**Figure 8.25** View of Beam SS1b-1 after Test: **(a)** North Half; **(b)** South Half

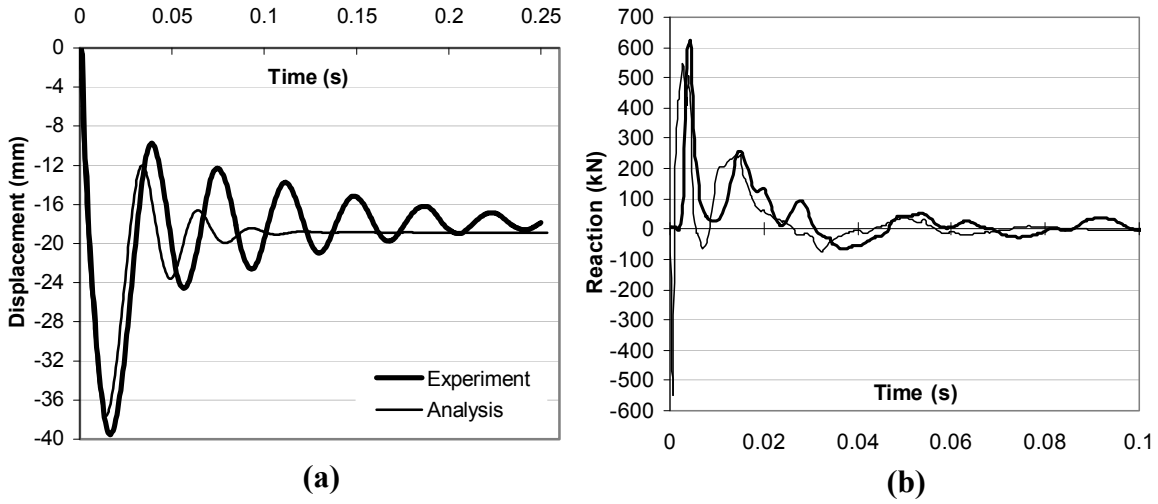


**Figure 8.26** Comparison of Experimental and Analytical Responses for SS1b-1: **(a)** Midspan Displacement; **(b)** Support Reaction

**Test SS1b - 2 (600 kg impacting mass)**

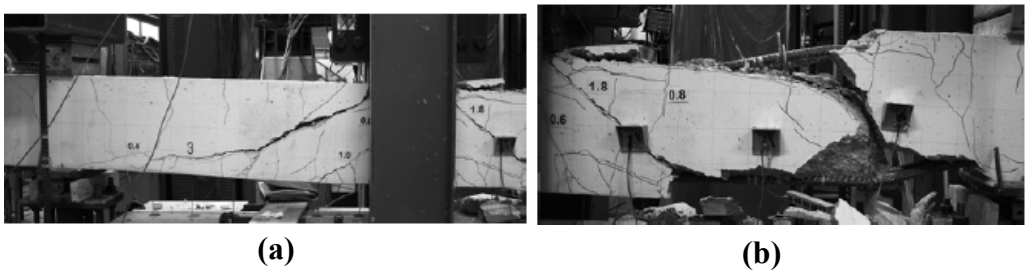


**Figure 8.27** View of Beam SS1b-2 after Test: **(a)** North Half; **(b)** South Half

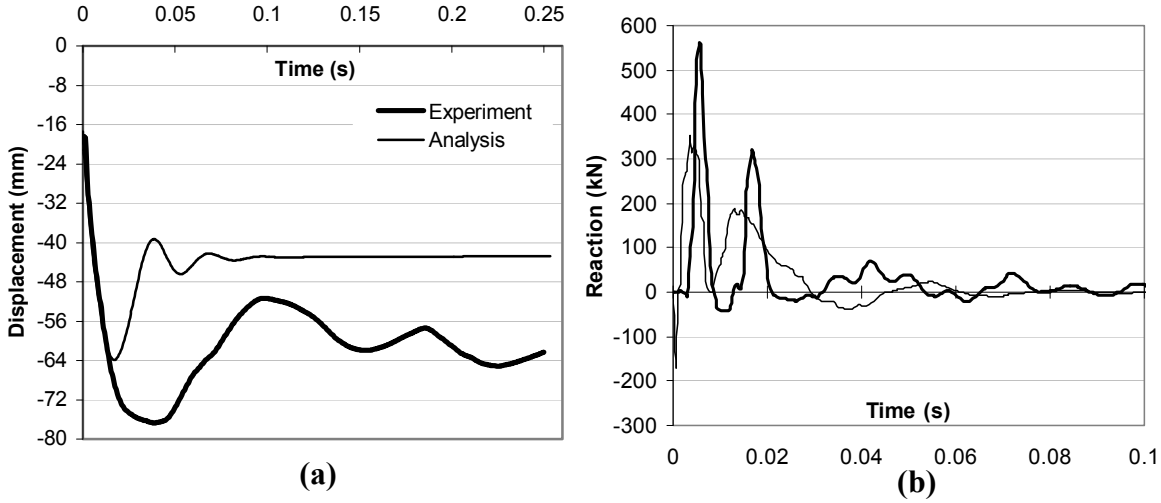


**Figure 8.28** Comparison of Experimental and Analytical Responses for SS1b-2: **(a)** Midspan Displacement; **(b)** Support Reaction

**Test SS2a – 1 (211 kg impacting mass)**

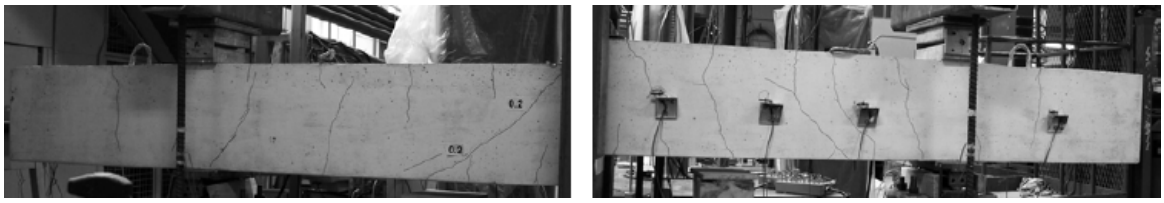

**(a)** **(b)**

**Figure 8.29** View of Beam SS2a-1 after Test: **(a)** North Half; **(b)** South Half

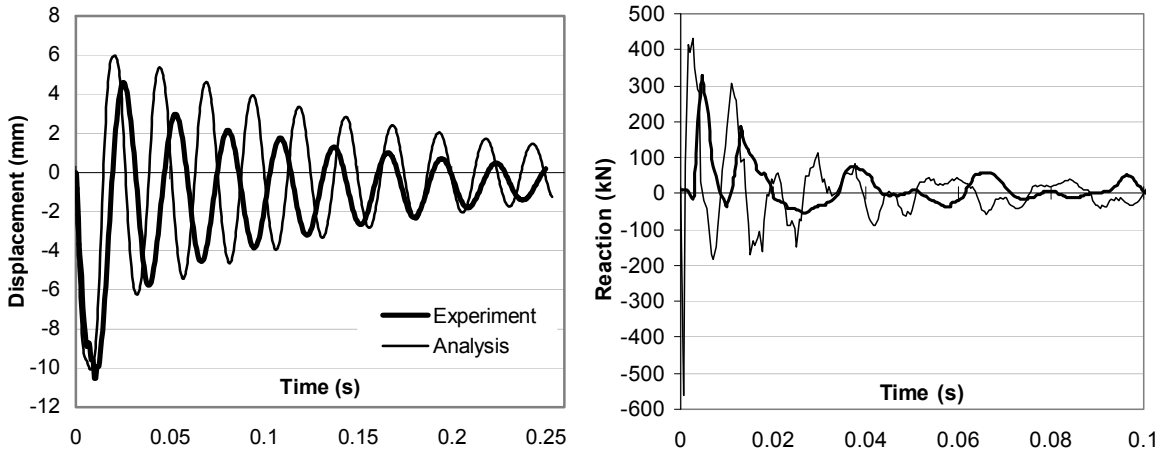


**(a)** **(b)**

**Figure 8.30** Comparison of Experimental and Analytical Responses for SS2a-1: **(a)** Midspan Displacement; **(b)** Support Reaction

**Test SS2a – 2 (600 kg impacting mass)**

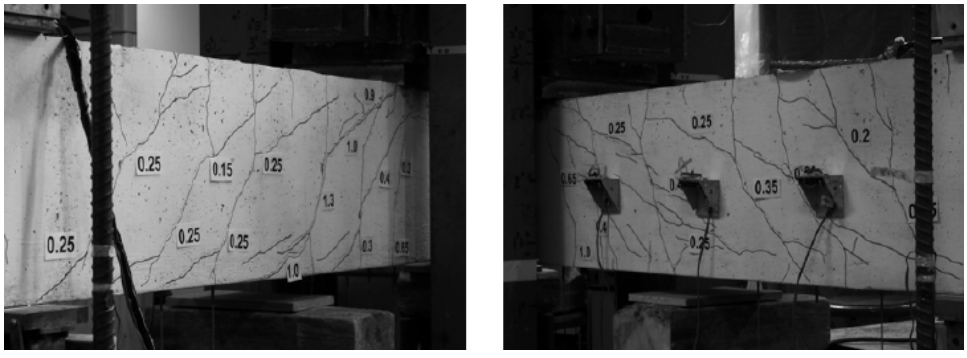

**(a)** **(b)**

**Figure 8.31** View of Beam SS2a-2 after Test: **(a)** North Half; **(b)** South Half

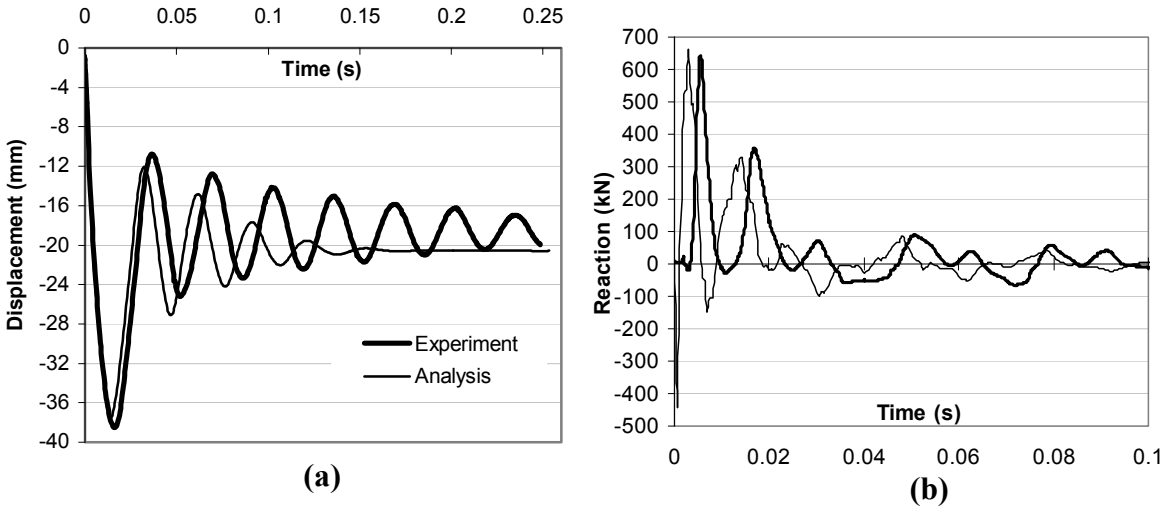


**Figure 8.32** Comparison of Experimental and Analytical Responses for SS2a-2: **(a)** Midspan Displacement; **(b)** Support Reaction

### Test SS2a - 3 (211 kg impacting mass)

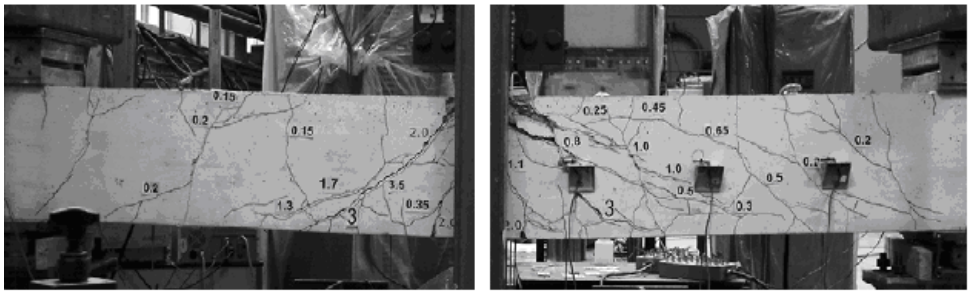


**Figure 8.33** View of Beam SS2a-3 after Test: **(a)** North Half; **(b)** South Half

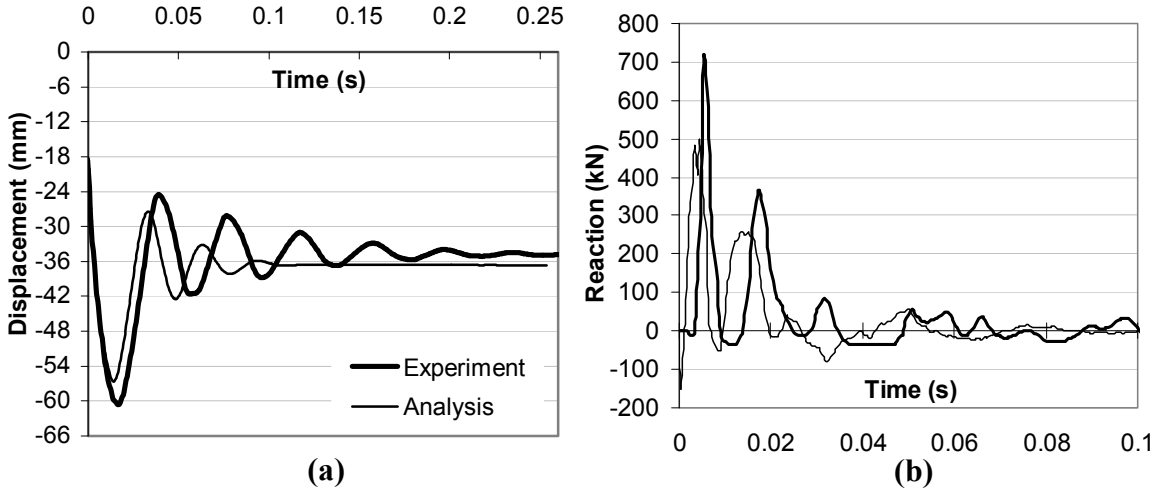


**Figure 8.34** Comparison of Experimental and Analytical Responses for SS2a-3: **(a)** Midspan Displacement; **(b)** Support Reaction

**Test SS2b – 1 (600 impacting mass)**

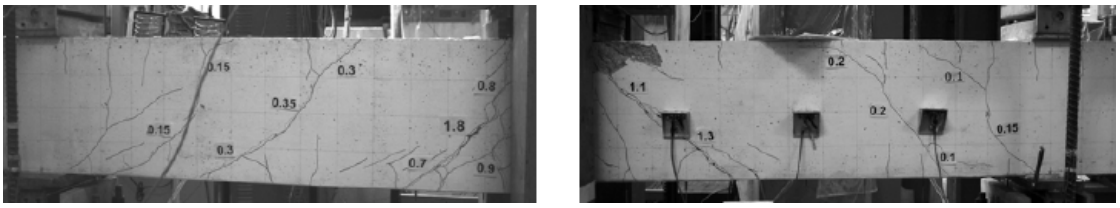

**(a)** **(b)**

**Figure 8.35** View of Beam SS2b-1 after Test: **(a)** North Half; **(b)** South Half

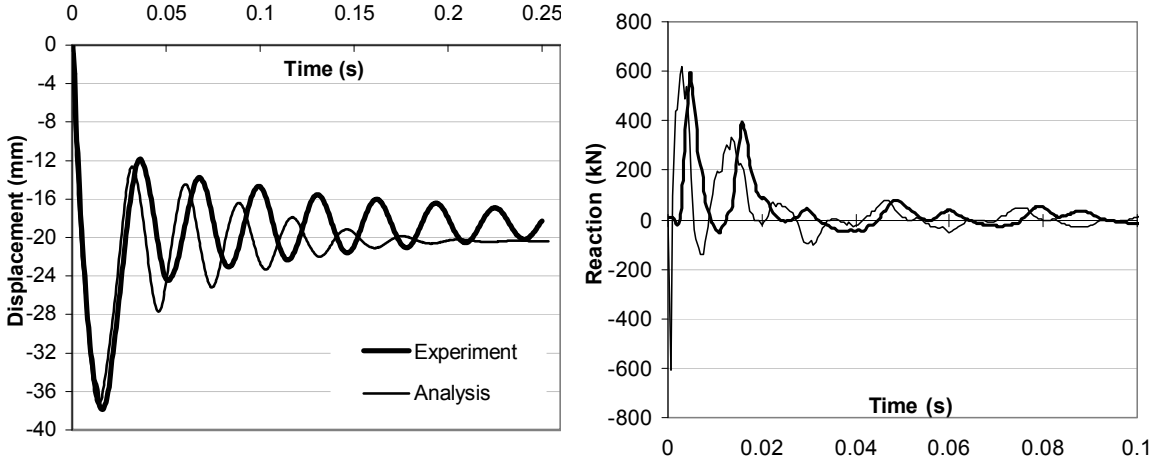


**(a)** **(b)**

**Figure 8.36** Comparison of Experimental and Analytical Responses for SS2b-1: **(a)** Midspan Displacement; **(b)** Support Reaction

**Test SS2b-2 (600 impacting mass)**

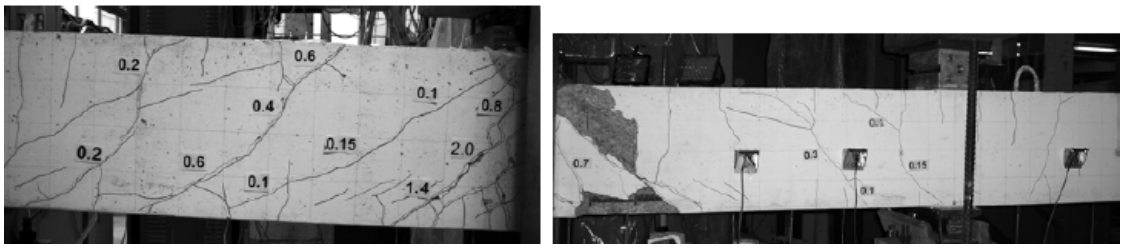

**(a)** **(b)**

**Figure 8.37** View of Beam SS2b-2 after Test: **(a)** North Half; **(b)** South Half

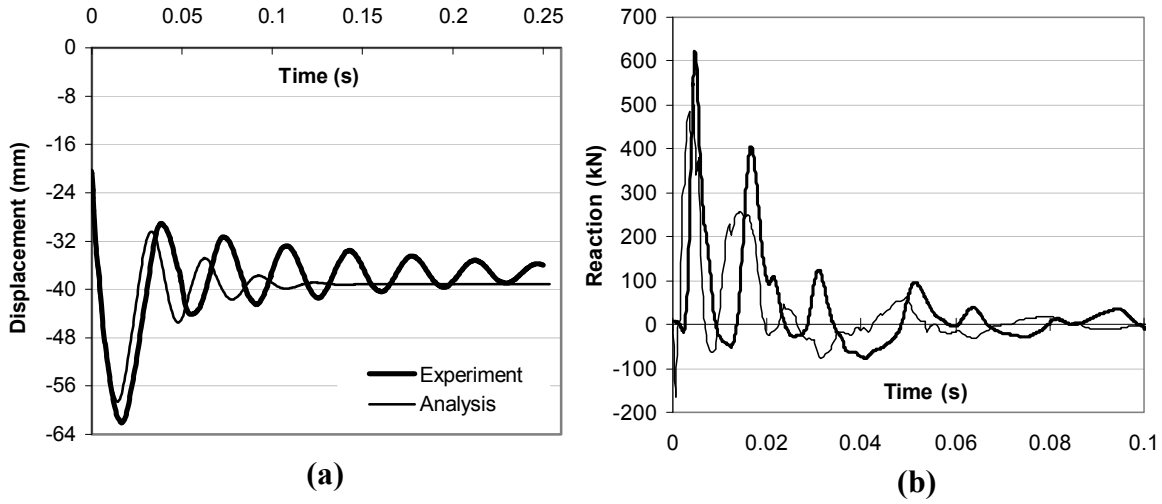


**Figure 8.38** Comparison of Experimental and Analytical Responses for SS2b-2: **(a)** Midspan Displacement; **(b)** Support Reaction

### Test SS2b – 3 (211 impacting mass)

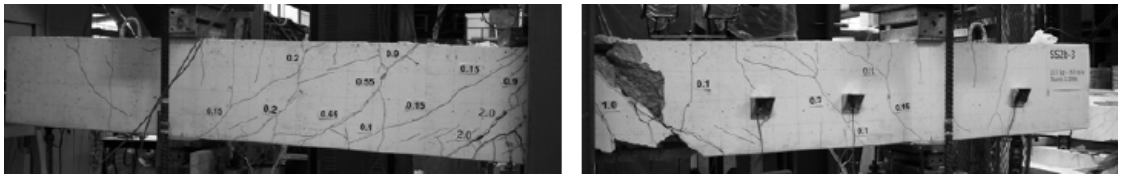


**Figure 8.39** View of Beam SS2b-3 after Test: **(a)** North Half; **(b)** South Half

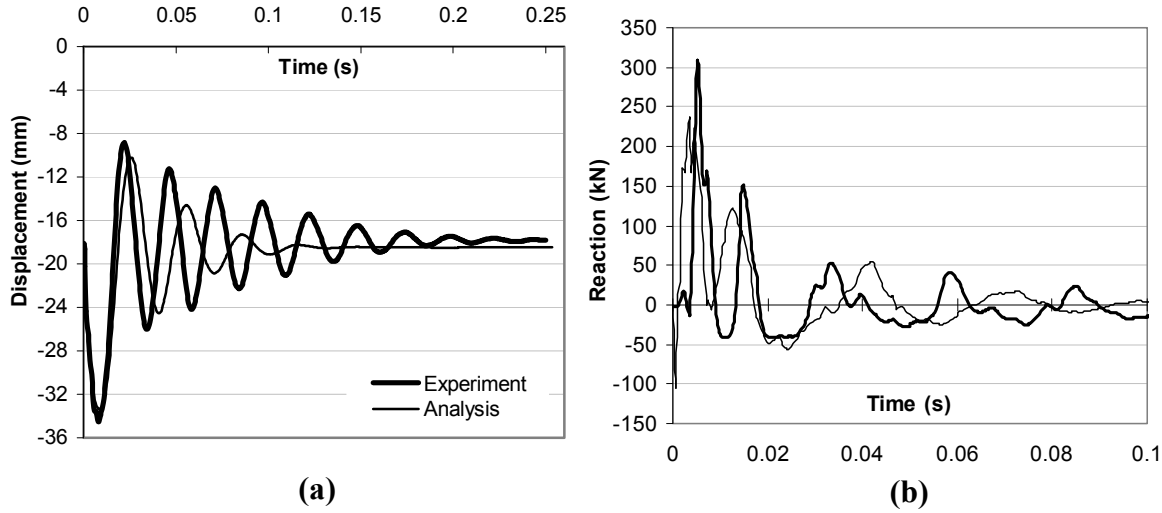


**Figure 8.40** Comparison of Experimental and Analytical Responses for SS2b-3: **(a)** Midspan Displacement; **(b)** Support Reaction

**Test SS3a – 1 (211 kg impacting mass)**

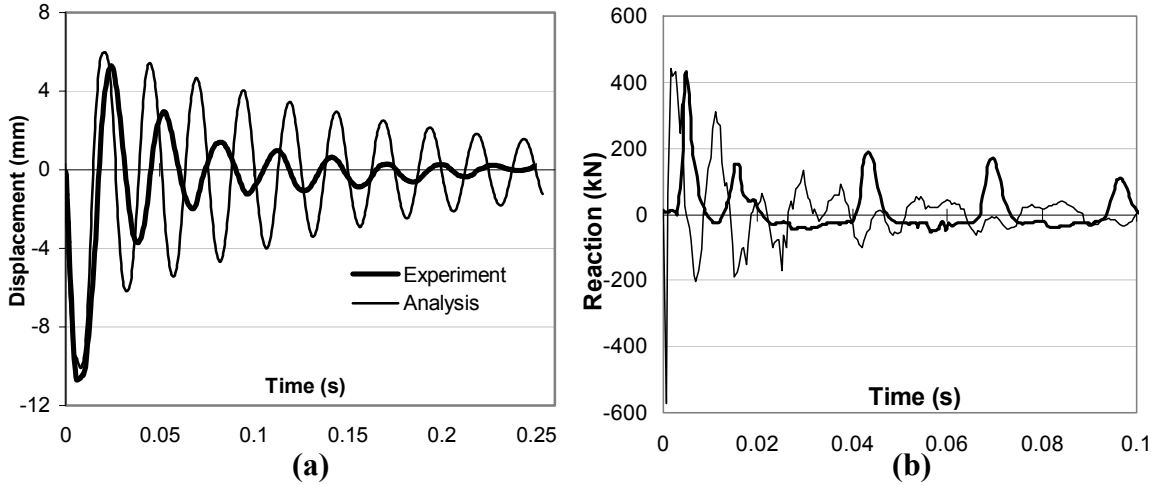


**Figure 8.41** Comparison of Experimental and Analytical Responses for SS3a-1: **(a)** Midspan Displacement; **(b)** Support Reaction

**Test SS3a – 2 (600 kg impacting mass)**

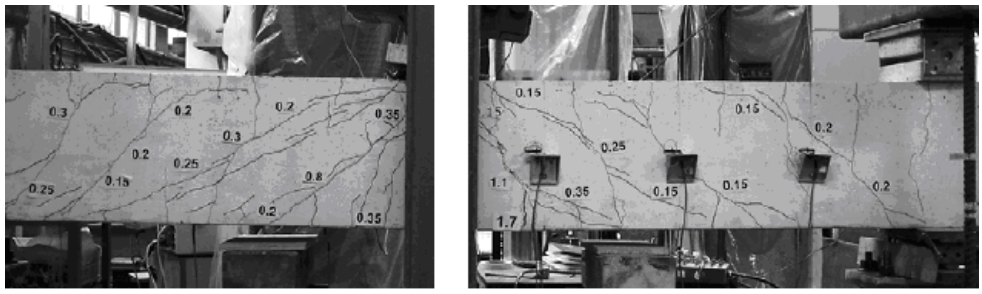


**Figure 8.42** View of Beam SS3a-2 after Test: **(a)** North Half; **(b)** South Half

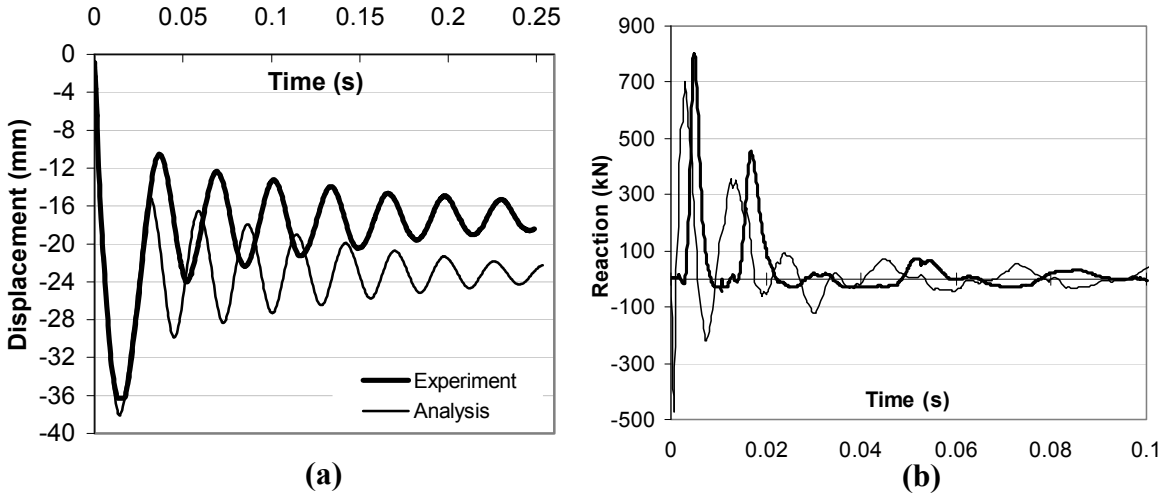


**Figure 8.43** Comparison of Experimental and Analytical Responses for SS3a-2: **(a)** Midspan Displacement; **(b)** Support Reaction

**Test SS3a – 3 (600 kg impacting mass)**

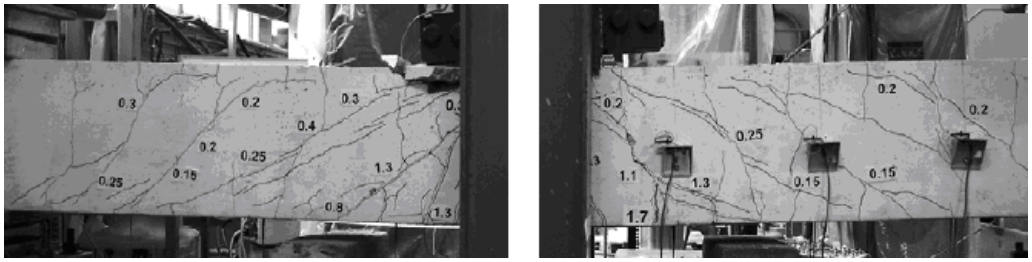

**(a)** **(b)**

**Figure 8.44** View of Beam SS3a-3 after Test: **(a)** North Half; **(b)** South Half

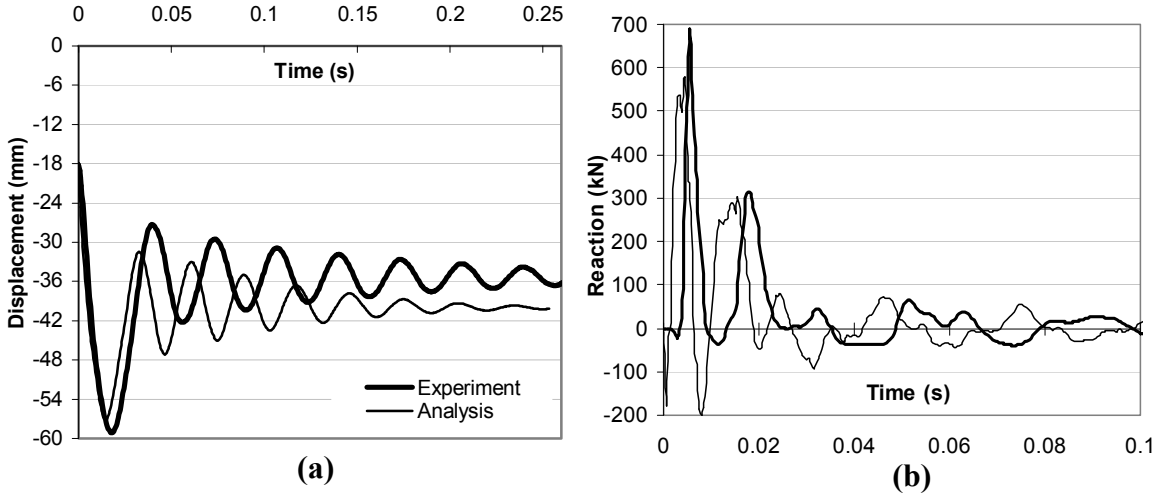


**(a)** **(b)**

**Figure 8.45** Comparison of Experimental and Analytical Responses for SS3a-3: **(a)** Midspan Displacement; **(b)** Support Reaction

**Test SS3b – 1 (600 kg impacting mass)**

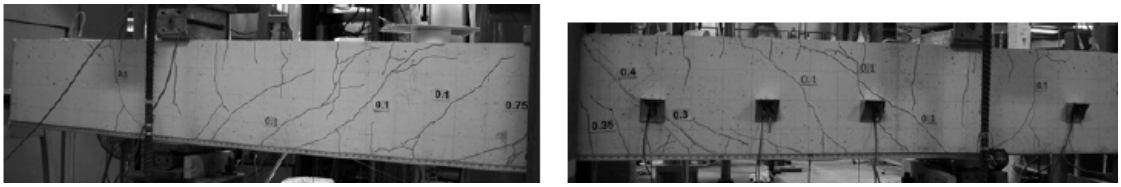

**(a)** **(b)**

**Figure 8.46** View of Beam SS3b-1 after Test: **(a)** North Half; **(b)** South Half

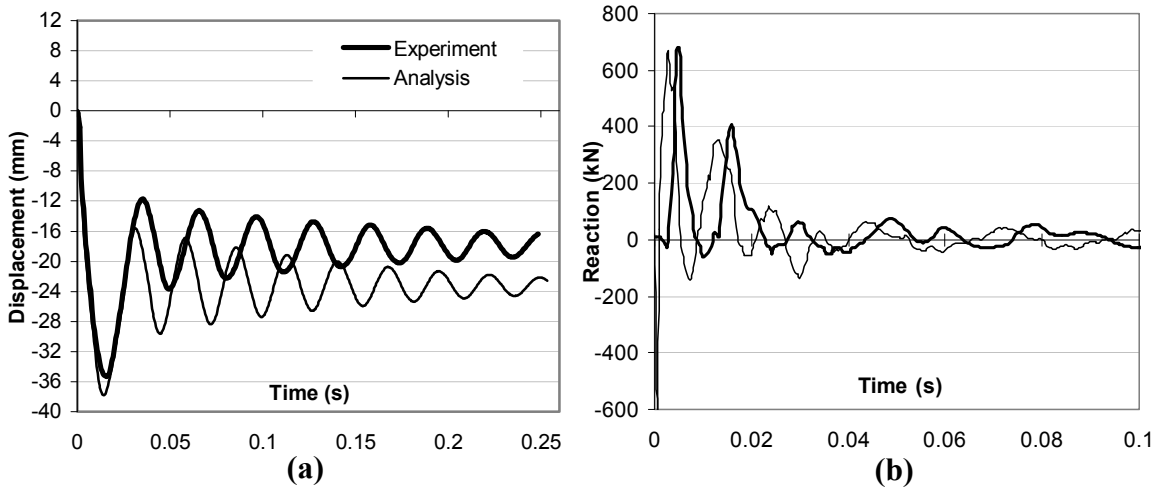


**Figure 8.47** Comparison of Experimental and Analytical Responses for SS3b-1: **(a)** Midspan Displacement; **(b)** Support Reaction

### Test SS3b – 2 (600 kg impacting mass)

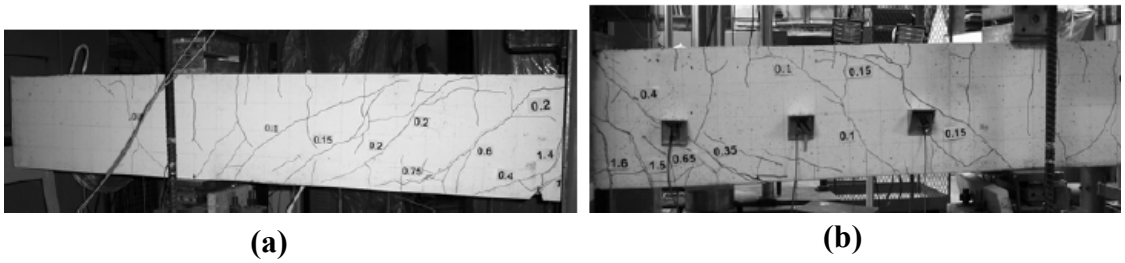


**Figure 8.48** View of Beam SS3b-2 after Test: **(a)** North Half; **(b)** South Half

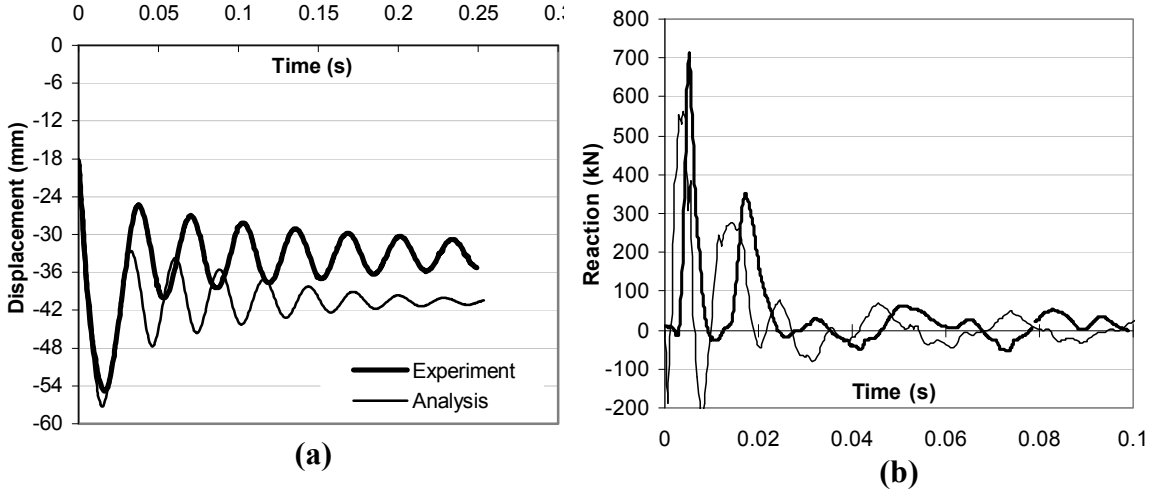


**Figure 8.49** Comparison of Experimental and Analytical Responses for SS3b-2: **(a)** Midspan Displacement; **(b)** Support Reaction

**Test SS3b – 3 (211 kg impacting mass)**

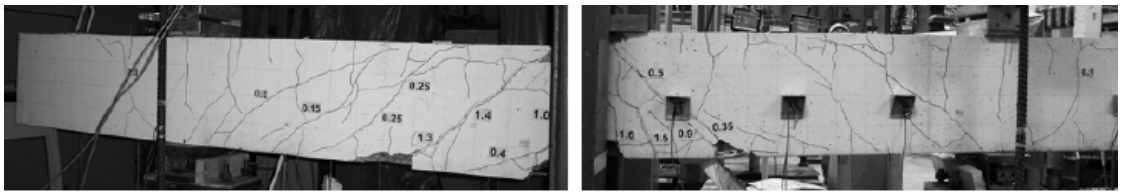

**(a)** **(b)**

**Figure 8.50** View of Beam SS3b-3 after Test: **(a)** North Half; **(b)** South Half

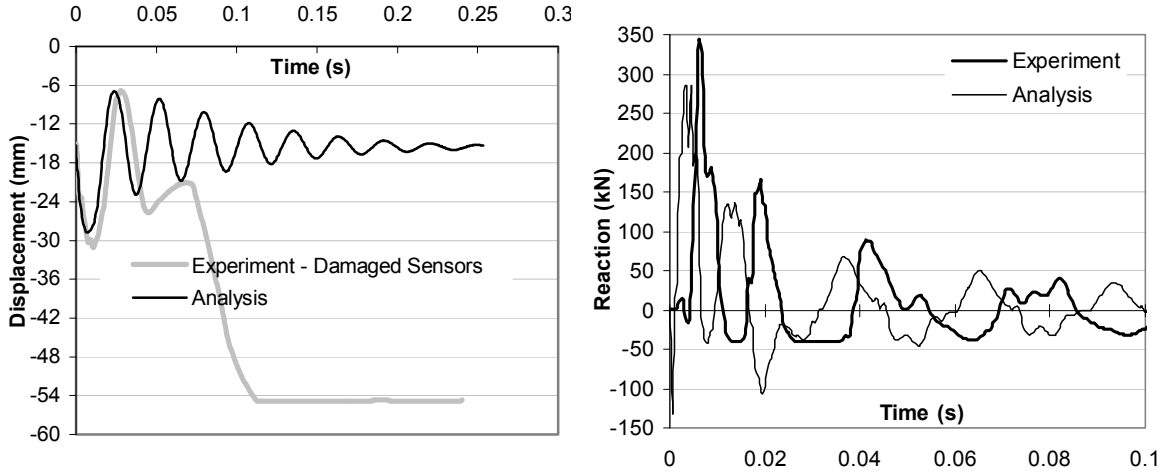


**(a)** **(b)**

**Figure 8.51** Comparison of Experimental and Analytical Responses for SS3b-3: **(a)** Midspan Displacement; **(b)** Support Reaction

## 8.8 Discussion of the Responses

The comparisons of the peak displacements, peak reactions and residual displacements, as obtained analytically and experimentally, are summarized in Table 8.5. Note that tests of SS0b-2, SS0a-3, SS0b-3 and SS1b-3 were not performed due to the complete failures sustained during the previous testing.

### 8.8.1 Peak Displacements

The peak displacements of the beams were predicted with very good accuracy, given the severity of the loading and the high degree of damage typically sustained. Considering the 17 tests for which the experimental peak displacement values were reported, a mean value of 0.99 and a coefficient of variation (COV) of 9.5% were achieved with respect to the predicted-to-observed peak displacement ratio.

The accuracy of the predictions improved considerably as the damage levels of the specimens increased. For the first impact analyses of the undamaged beams (7 tests), a mean ratio of 1.01 and a coefficient of variation of 12.7% were attained. For the second analyses of the damaged beams (6 tests) the values became 0.97 and 8.2%; for the third analyses of the damaged beams (4 tests), the values improved to 1.00 and 6.1%. Note the improvement in the COV which decreased by half from the first to third tests.

**Table 8.5** Comparison of Displacement and Reaction Results for Saatci Beams

| | Peak Displacement (mm) | | | Peak Reaction (kN) | | | Residual Disp. (mm) | | |
|---|---|---|---|---|---|---|---|---|---|
| | VecTor5 | Test | Ratio | VecTor5 | Test | Ratio | VecTor5 | Test | Ratio |
| **SS0a-1** | 11.7 | 9.3 | 1.26 | 400.0 | 300.0 | 1.33 | -0.2 | -1.6 | 0.13 |
| **SS1a-1** | 10.3 | 11.9 | 0.87 | 416.5 | 356.4 | 1.17 | -0.4 | -0.9 | 0.44 |
| **SS2a-1** | 10.1 | 10.5 | 0.96 | 430.0 | 326.8 | 1.32 | 0.0 | -0.5 | n/a |
| **SS3a-1** | 10.0 | 10.6 | 0.94 | 442.3 | 398.0 | 1.11 | 0.0 | 0.0 | n/a |
| **SS0b-1** | Shear Fail. | Shear Fail. | n/a | 504.3 | 399.8 | 1.26 | Shear Fail. | Shear Fail. | n/a |
| **SS1b-1** | 37.6 | 39.2 | 0.96 | 549.0 | 624.8 | 0.88 | -18.9 | -17.7 | 1.07 |
| **SS2b-1** | 37.4 | 37.6 | 0.99 | 621.6 | 592.5 | 1.05 | 20.4 | 19.0 | 1.07 |
| **SS3b-1** | 37.8 | 35.1 | 1.08 | 671.3 | 667.7 | 1.01 | 23.0 | 17.5 | 1.31 |
| | | Mean | 1.01 | | | 1.14 | | | 0.81 |
| | | COV (%) | 12.7 | | | 16.0 | | | 49.8 |

| | Peak Displacement (mm) | | | Peak Reaction (kN) | | | Residual Disp. (mm) | | |
|---|---|---|---|---|---|---|---|---|---|
| | VecTor5 | Test | Ratio | VecTor5 | Test | Ratio | VecTor5 | Test | Ratio |
| **SS0a-2** | Shear Fail. | Shear Fail. | n/a | 457.6 | 514.8 | 0.89 | Shear Fail. | Shear Fail. | n/a |
| **SS1a-2** | 38.8 | 39.3 | 0.99 | 564.0 | 510.0 | 1.11 | -18.4 | -17.5 | 1.05 |
| **SS2a-2** | 37.5 | 38.1 | 0.98 | 661.0 | 644.0 | 1.03 | 20.6 | 18.0 | 1.14 |
| **SS3a-2** | 38.1 | 36.8 | 1.04 | 703.0 | 802.0 | 0.88 | 23.2 | 17.0 | 1.36 |
| **SS1b-2** | 62.9 | 76.6 | 0.82 | 352.4 | 562.4 | 0.63 | -42.8 | -60.0 | 0.71 |
| **SS2b-2** | 58.6 | 61.5 | 0.95 | 498.0 | 621.0 | 0.80 | 37.5 | 39.1 | 0.96 |
| **SS3b-2** | 57.2 | 54.6 | 1.05 | 551.0 | 713.0 | 0.77 | 40.5 | 33.0 | 1.23 |
| | | Mean | 0.97 | | | 0.87 | | | 1.08 |
| | | COV (%) | 8.2 | | | 16.0 | | | 22.7 |

| | Peak Displacement (mm) | | | Peak Reaction (kN) | | | Residual Disp. (mm) | | |
|---|---|---|---|---|---|---|---|---|---|
| | VecTor5 | Test | Ratio | VecTor5 | Test | Ratio | VecTor5 | Test | Ratio |
| **SS1a-3** | 64.5 | n/a | n/a | 346.5 | 503.0 | 0.69 | -42.7 | n/a | n/a |
| **SS2a-3** | 60.2 | 56.6 | 1.06 | 499.3 | 718.0 | 0.70 | -36.6 | -34.8 | 1.05 |
| **SS3a-3** | 58.7 | 57.0 | 1.03 | 577.0 | 689.0 | 0.84 | 40.2 | 35.5 | 1.13 |
| **SS2b-3** | 32.4 | 34.3 | 0.94 | 237.8 | 308.5 | 0.77 | 18.5 | 17.8 | 1.04 |
| **SS3b-3** | 28.7 | 30.4 | 0.94 | 286.0 | 344.9 | 0.83 | 15.3 | n/a | n/a |
| | | Mean | 1.00 | | | 0.76 | | | 1.07 |
| | | COV (%) | 6.1 | | | 7.1 | | | 5.1 |

| | | | | | | | | |
|---|---|---|---|---|---|---|---|---|
| **All Tests** | **Mean** | **0.99** | | **AVG** | **0.95** | | **AVG** | **0.98** |
| | **COV (%)** | **9.5** | | **COV (%)** | **21.3** | | **COV (%)** | **33.9** |

n/a: data not available due to faulty sensors

The same conclusion is reached from another point of view; improved accuracy in the calculated peak displacements is observed for the beams subjected to heavier drop-weights which cause more damage than for the lighter drop-weights. Considering the 6 tests subjected to the lighter drop-weights, a mean value of 0.99 and a coefficient of variation (COV) of 13.7% were realized. However, for the 11 test with heavier drop-weights, the values improved to 1.00 and 7.1%. Again, in this case, the COV diminished by almost half. This better prediction of the peak displacements when the beams were subjected to greater damage levels can be attributed to several factors.

The first factor relates to the experimental setup. Certain deficiencies and irregularities in the test setup, such as the flexibility of the test apparatus, uneven contact of the support rollers with the specimens, uneven contact of the drop-weight with specimens, and vibrations in the longitudinal direction were reported by Saatci (2007). These mechanisms were inherently neglected in the analytical modelling of the beams. It can be postulated that when subjected to the heavier drop-weights, the specimens suffered more damage causing greater peak displacements in which the effects of the experimental deficiencies played a relatively smaller role. However, subjected to a lighter drop-weight causing less peak displacements, the experimental deficiencies may have contributed significantly to the overall displacement response of the beams.

Another factor may relate to the use of a fictitious member to simulate the load transfer from the drop-weight to the member. When using such a member, it was assumed that the member behaved linear-elastically, thereby neglecting the local energy dissipation. However, in the actual test, considerable local damage was reported to have taken place around the point where the impact load was applied. In addition, a special arrangement of steel plates was used at the impact point to create a well distributed impact force in the experimental setup. It is likely that some energy was dissipated by these plates through friction and heat generation. This energy dissipation was more likely significant in the overall response of the beams subjected to the lighter drop-weights compared to those subjected to the heavier drop-weights and sustaining more damage.

A third factor may relate to the effects of higher modes. As explained in Section 7.11, with the use of the Wilson's Theta method, the higher mode contributions are somewhat filtered out due to the numerical damping present in the method. It can be postulated that at more severe damage levels, the higher mode contributions to the overall response of the test beams diminish. This can result in behaviour more similar to the analytical solution, thereby providing a better displacement response for the beams that sustained greater damage. The use of Newmark's average or linear acceleration methods would create an even greater filtering of the higher modes due to the use of Rayleigh damping required for stability reasons, as discussed in detail in Section 7.5.2.

In terms of the peak displacement predictions, the least accuracy with a predicted-to-observed mean ratio of 1.26 was encountered in the specimen containing no stirrups; namely, SS0a-1. The behaviour of reinforced concrete elements which do not contain any shear reinforcement is intrinsically associated with mechanisms heavily dependent on concrete tensile strength (Vecchio, 2000). However, the tensile strength of concrete is not constant for a particular concrete but varies with a number of parameters such as the volume of concrete, gradient of longitudinal strain, and the presence of restrained shrinkage strains (Collins and Mitchell, 1991). As a result, due to the uncertainties regarding the tensile strength of concrete, a lower-bound value of $0.33\times\sqrt{f'c}$, recommended by CSA A23.3-04, is often used, as is the case throughout this study. Consequently, when analyzing a specimen with no shear reinforcement, more scattered predictions should typically be anticipated as experienced in the analysis of SS0 beams.

### 8.8.2 Residual Displacements

The residual displacements of the beams were predicted with reasonable accuracy. Considering all 14 tests for which the experimental residual displacement data were reported, a mean value of 0.98 and a coefficient of variation (COV) of 33.9% were achieved for the predicted-to-observed residual displacement ratio. The high scatter in the predictions was mainly caused by two tests involving undamaged specimens under the lighter drop-weights; namely, SS0a-1 and SS1a-1. However, although the discrepancies in the actual residual displacements of these two tests were quite negligible, they appear

to be high when considering their predicted-to-observed ratios of 0.13 and 0.44, respectively. The highest discrepancy between the analysis and test in terms of residual displacement in these two beams was a mere 1.4 mm. Such a discrepancy can rationally be associated with the deficiencies in the experimental setup as explained above. When those two tests are excluded, a mean value of 1.09 and a COV of 16.9% were achieved for the remaining 12 tests, which can be accepted as being of reasonable accuracy.

### 8.8.3 Damping Characteristics

The post-peak damping characteristics of the beams were predicted with reasonable accuracy when considering all 16 tests for which the post-peak responses were reported in the experimental study. The damping characteristics of three of the beams (SS1a-1, SS3a-2 and SS3b-1) were captured with excellent accuracy. The displacement responses for ten beams dampened out slightly faster than the experimental responses while the responses of 3 beams (SS0a-1, SS2a-1 and SS3a-1, three of the four first tests under the lighter drop-weights) damped out slower than the experimental responses. Especially for SS0a-1 and SS3a-1, the theoretical response diminished significantly slower than the experimental response. The reduced prediction accuracy of the damping characteristic of these beams under the *lighter* drop-weighs can be attributed to the three factors discussed in Section 8.8.1.

It should be noted that Wilson's Theta method was used in all analyses with no additional viscous damping; all damping resulted from the nonlinear concrete and reinforcement hystereses. When all 16 analyses were considered, the slight tendency in the analytical predictions was to dampen out more quickly than the experimental responses. In other words, the addition of viscous damping to the analyses would have caused deteriorated accuracy in terms of dampening of the displacement responses when all 16 tests were considered. This further justifies the use the unconditionally stable Wilson's Theta method with no additional damping, which was one of the focuses of the dynamic analysis procedure developed in this study. It should be noted, however, that when analyzing a structure having non-structural components, the use of additional viscous damping may be necessary due to the energy dissipation of non-structural elements as

discussed in Section 7.5.2. In this case, either Newmark's method or Wilson's Theta method can be employed with a proper additional viscous damping ratio.

### 8.8.4 Vibrational Periods

The vibrational periods of the beams were typically underestimated by 15 to 20 percent. For demonstrative purposes, a comparison of the analytically and experimentally determined vibrational periods of Beam SS2a is presented in Table 8.6.

**Table 8.6** Comparison of Experimental and Analytical Period of Vibrations (Beam SS2a): **(a)** First Test; **(b)** Second Test; **(c)** Third Test

**(a)**

| | SS2a-1 (211 kg) | | |
|---|---|---|---|
| | Period of Vibration (s) | | |
| Cycle | VecTor5 | Test | Ratio |
| 1st | 0.0263 | 0.0315 | 0.83 |
| 2nd | 0.0245 | 0.0269 | 0.91 |
| 3rd | 0.0245 | 0.0275 | 0.89 |
| 4th | 0.0245 | 0.0275 | 0.89 |
| 5th | 0.0245 | 0.0275 | 0.89 |
| | LE Period = 0.0176 | | |

**(b)**

| | SS2a-2 (600 kg) | | |
|---|---|---|---|
| | Period of Vibration (s) | | |
| | VecTor5 | Test | Ratio |
| | 0.0363 | 0.0413 | 0.88 |
| | 0.0295 | 0.0327 | 0.90 |
| | 0.0301 | 0.0331 | 0.91 |
| | 0.0307 | 0.0335 | 0.92 |
| | 0.0330 | 0.0337 | 0.98 |
| | LE Period = 0.0217 | | |

**(c)**

| | SS2a-3 (600 kg) | | |
|---|---|---|---|
| | Period of Vibration (s) | | |
| | VecTor5 | Test | Ratio |
| | 0.0382 | 0.0471 | 0.81 |
| | 0.0306 | 0.0388 | 0.79 |
| | 0.0318 | 0.0400 | 0.80 |
| | n/a | 0.0406 | n/a |
| | n/a | 0.0411 | n/a |
| | LE Period = 0.0217 | | |

LE: Linear-Elastic

In the first test under the drop weight of 211 kg, the period of the vibration remained constant after the second cycle in both the experiment and the analysis as indicated in Table 8.6(a). This is related to the damage levels sustained by the beam, which suffered little damage under the first drop weight with essentially zero residual displacement as shown in Table 8.5. Subjected to the second and the third impacts, the beam sustained significant damage and plastic deformation levels (i.e., experimental residual displacements of 18.0 and 34.8 mm, respectively), which resulted in an increase in the period of the vibrations in both the experiment and the analysis as shown in Table 8.6(b) and Table 8.6(c).

The fundamental periods of vibration calculated by the analytical tool developed, using the initial transformed section properties, are also presented in Table 8.6 as linear-elastic periods. It should be noted that these linear-elastic modal periods are used in the

nonlinear dynamic analyses only when using one of the implemented additional viscous damping schemes, as explained in Section 7.7.5 and Section 7.7.12.2. When using the Rayleigh damping formulation, these initial modal periods are used to calculate the proportionality constants as defined by Eq. 7.13 and Eq.7.14. When using the alternative damping formulation, the linear-elastically calculated modal periods, mode shapes and generalized masses are used in accordance with Eq. 7.17. When performing a nonlinear dynamic analysis with zero additional viscous damping, none of these linear-elastically calculated parameters are used. In all cases, the analyses are performed based on the principles outlined in Chapters 3, 5 and 7.

The analytical underestimation of periods of vibration with stiffer analytical behaviour can be associated with the nonlinear material behaviour models, such as the concrete hysteresis, reinforcement hysteresis and crack formulations. These models were typically developed for static loading conditions and do not take into account the dynamic nature of the impact loads. To illustrate the importance of, for example, the concrete hysteresis in the post-peak vibrational behaviour, the nonlinear analysis of Beam SS2a-1 was repeated using two different models: the Vecchio model with nonlinear unloading and the Palermo model. The comparison of the displacement responses are shown in Figure 8.52. Notice the elongation of the period when using the Palermo model. Because the focus of this study is to perform analyses by using only default material models and analysis options, the default concrete hysteresis rule, the Vecchio model with nonlinear unloading, was used throughout this thesis.

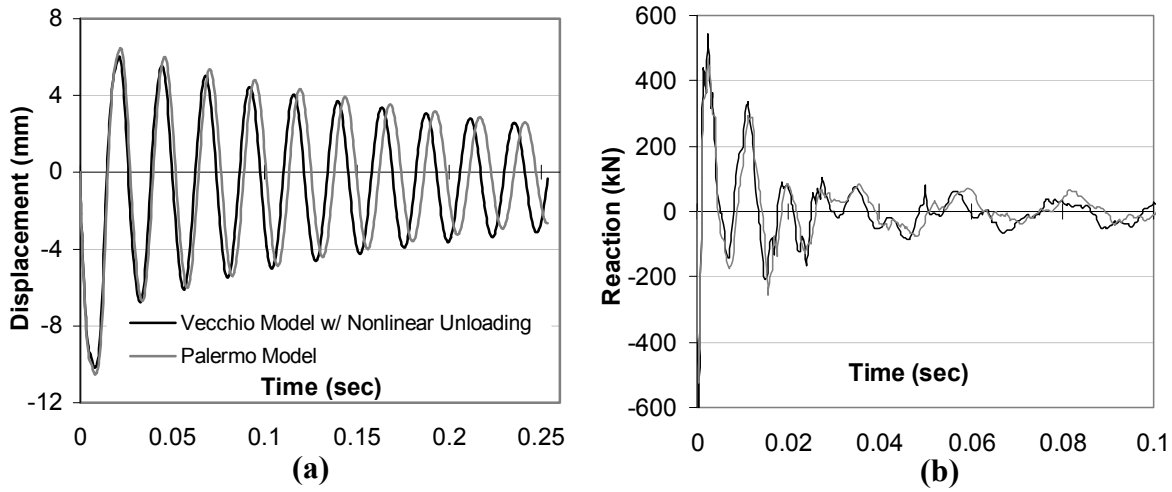


**Figure 8.52** Comparison of Responses for Different Concrete Hysteresis Models (SS2a-1): **(a)** Midspan Displacement; **(b)** Support Reaction

As an example of the influence of the strain rate formulations, Beam SS2a-1 was analyzed twice: first considering the strain rate effects and then neglecting them (i.e., using the input static material properties). In both analyses, the concrete hysteresis of the Vecchio Model with nonlinear unloading was used. The comparisons of the resulting responses are shown in Figure 8.53. Note the change in the vibrational period.

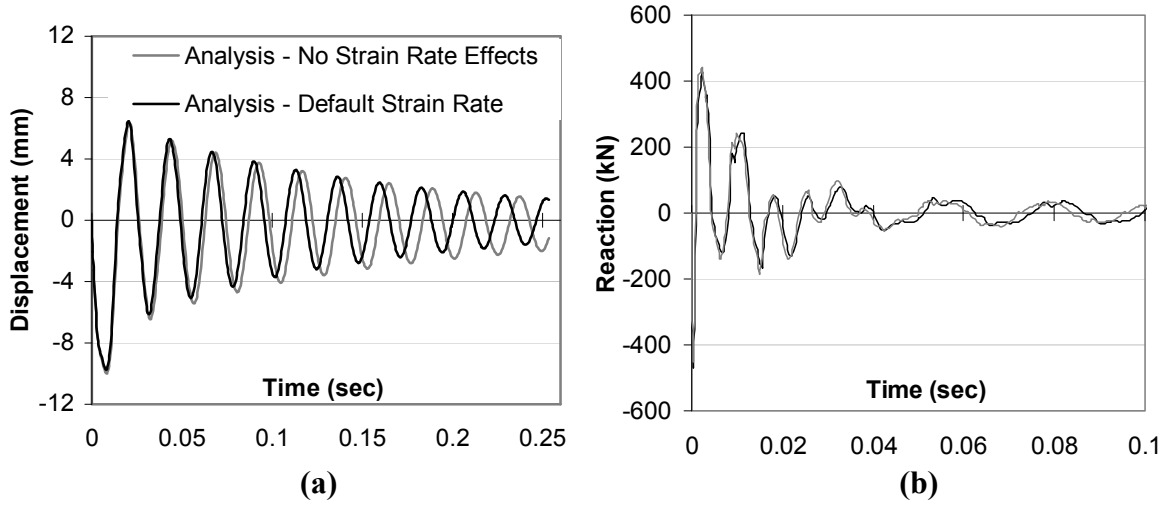


**Figure 8.53** Comparison of Responses with and without Strain Rate Effects (SS2a-1): **(a)** Midspan Displacement; **(b)** Support Reaction

The sensitivity of the vibrational periods to the material behaviour models used suggests the need for more comprehensive models that better represent behaviour under dynamic loading conditions. More experimental and analytical study is required in this realm to better understand and address these issues.

### 8.8.5 Strain Rate Effects

As formulated in Section 7.8, to account for the enhanced strength of concrete and steel materials at the high strain rates expected under an impact loading conditions, dynamic increase factors (DIF) were introduced into the sectional analysis calculations of the analytical procedure developed. Those formulations typically improve the static properties of concrete and reinforcement based on the strain rates calculated for the current time stage.

In the consideration of the DIFs for concrete (Figure 8.54), the CEB-FIP (1990) formulations, perhaps the most comprehensive among the few available models, were used as documented in Section 7.8. However, these formulations were derived mainly for plain concrete tested under almost *constant* rates of stress or strain. In other words, they are only valid for *constant* rates of loading (CEB-FIB, 1988), whereas strain rates change rapidly during an impact-induced vibration (Saatci, 2007). Moreover, these formulations were mainly derived based on the available experimental data. However, when there was insufficient information available, they were determined theoretically. For example, it is stated, for the DIF for concrete compressive strength, in CEB-FIP Synthesis Report (1988) Clause 3.3.1 that, *"It should be noted, however, that this steep increase* [in the strength of concrete] *has been determined theoretically and that experimental evidence is only attainable for natural rocks. Recent experimental results for concrete have not fully confirmed this prediction."*

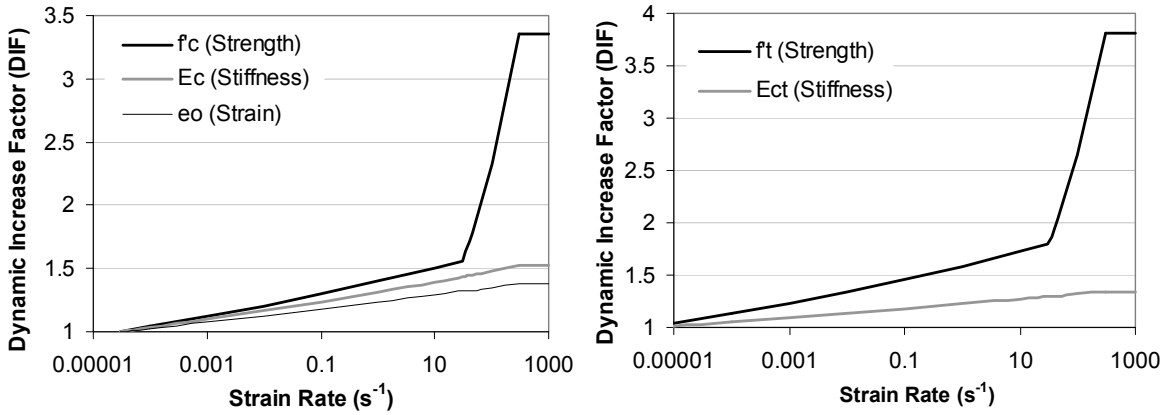


**Figure 8.54** DIFs for Concrete (CEB-FIP, 1990): **(a)** In Compression; **(b)** In Tension

For the DIFs of reinforcing steel, two formulations were implemented: the CEB-FIP (1988) and the Malvar and Crawford (1998) formulations. Although fewer assumptions were involved in the derivation of these formulations, there is a significant contradiction between the two models in terms of the DIF for the yield strength of the reinforcing steel. As shown in Figure 8.55, the yield strength is enhanced at a much greater rate in the Malvar and Crawford formulation.

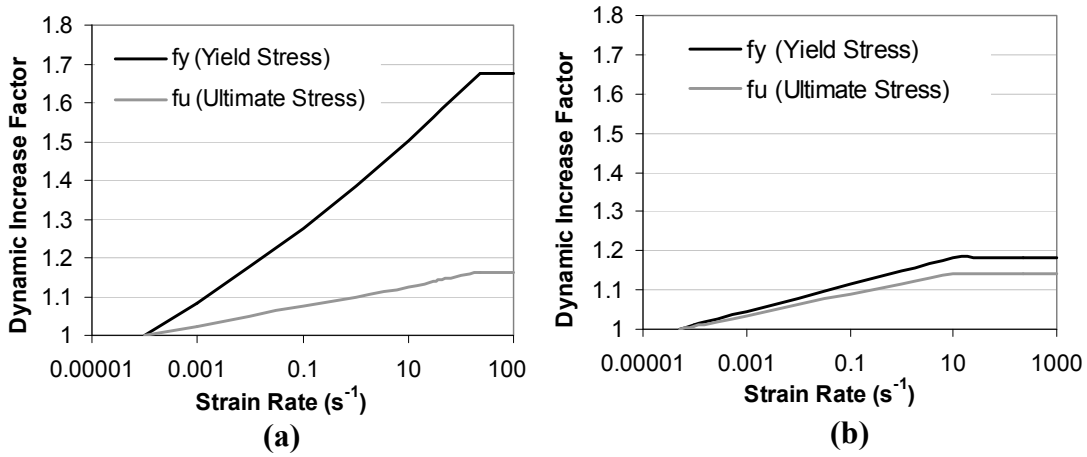


**Figure 8.55** DIFs for Reinforcement: **(a)** Malvar and Crawford; **(b)** CEB-FIP (1988)

Although both formulations were implemented and can be used as desired, a selection for the default set for use in dynamic analyses with VecTor5 was needed. For this purpose, a parametric analytical study was conducted including the impact tests of the Saatci beams. In this study, three sets of analyses were performed using: no strain rate effects, the Malvar and Crawford formulations (1998), and the CEB-FIP formulations (1988) for the reinforcing steel. In the analyses considering strain rate effects, the only available model implemented, the CEB-FIP (1990) formulations, was used for the concrete. It was observed that when strain rate effects were neglected in the analyses, the peak and, especially, the residual displacements were overestimated significantly. The use of the CEB-FIP (1988) formulations for the reinforcing steel typically improved the responses, resulting in less overestimation of the peak and residual displacements. The formulations proposed by Malvar and Crawford (1998) produced the best agreement with the experimental peak and residual displacements, although there was again a slight tendency to overestimate the peak and, particularly, the residual displacements as observed from the analytical results presented in Section 8.8.2. A typical comparison of the responses obtained from the all three analyses and the experiment is presented in Figure 8.56.

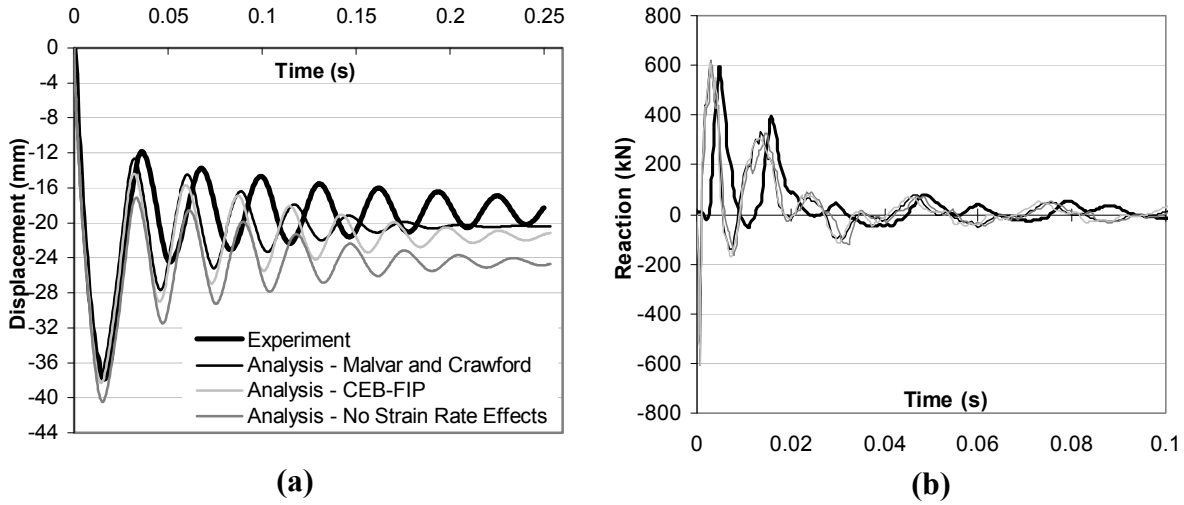


**Figure 8.56** Comparison of Responses for Different Strain Rate Formulations (SS2b-1): **(a)** Midspan Displacement; **(b)** Support Reaction

In conclusion, the implemented strain rate formulations were selected carefully from the available models which reflected current knowledge. However, there are significant contradictions and assumptions regarding these formulations. Therefore, improvements in these models for dynamic loading conditions are needed, requiring more experimental and analytical investigation.

### 8.8.6 Peak Reaction Forces

The peak support reactions of the beams were predicted with acceptable accuracy. Considering all 20 tests, a mean value of 0.95 and a coefficient of variation (COV) of 21.3% were achieved for the predicted-to-observed support reaction ratio. The general tendency in the analytical predictions was to overestimate the peak reaction forces in the first tests where a mean value of 1.14 and a COV of 16.0% were realized. In the second analyses, underestimation of the peak reaction forces was typical with a mean value of 0.87 and a COV of 16.0%. In the third tests, the peak support reactions were underestimated with a mean ratio of 0.76 and a COV of 7.1%.

The biggest inaccuracy in the peak support reaction predictions, however, was with the uplift forces which were typically observed in the experimental study immediately after the impact of the drop-weight. This behaviour is typically caused by sudden upward

inertial forces created by the structural masses as a resistance to the suddenly applied impact loads. In the experimental study, this force was reported to be typically in the range of 50 kN. However, the analyses predicted the uplift force in the range of 500 kN, which was unacceptable in all respects. Such high uplift forces resulted from the infinitely rigid roller support assumption.

As mentioned in Section 8.2, in the experimental setup a special arrangement for the supports was employed. It consisted of 1665 mm long two No.20 support bars and a bottom concrete pedestal. However, in the analytical model, the supports were modelled using infinitely rigid simple rollers due to the uncertainties in the modelling of the special support conditions, as explained in Section 8.3.

For demonstrative purposes, Beam SS2a-1 was re-modelled, approximately including the top support bars, with an estimated stiffness of 170 000 N / mm$^2$, and the bottom concrete pedestal using the model shown in Figure 8.7. The reaction responses obtained from this model and from the original model with the simple roller support are compared in Figure 8.57. Note how the uplift force decreased from 550 kN to a much more reasonable 55 kN. This modified model, however, was not used in the actual modelling, due to the difficulties and uncertainties explained in Section 8.3.

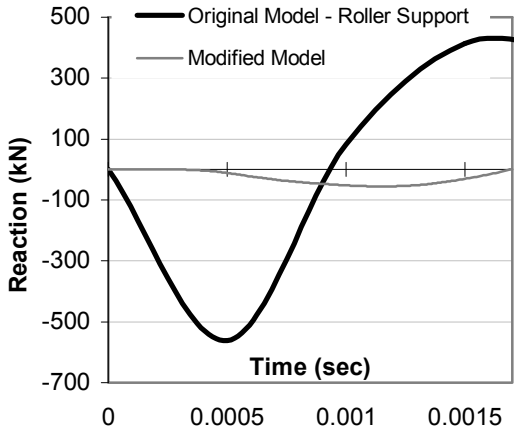


**Figure 8.57** Comparison of Support Reactions for Different Support Models (SS2a-1)

In conclusion, the uplift forces were highly dependent on the special support conditions employed in this particular experiment; consequently, their simulation was deemed to be

not an essential consideration in this study. Therefore, the extreme overestimation of uplift forces was accepted and the simpler model was used throughout this study.

### 8.8.7 Reinforcement Strains

Comparisons of the peak tensile longitudinal reinforcement strains at the midspan and at the support, as obtained analytically and experimentally, are summarized in Table 8.7. In the analytical determination of midspan strains, the average strain values calculated for the bottom reinforcement layer of Member 10 was used. Longitudinal reinforcement strains for the supports were determined as the average value of the top reinforcement layers of Member 4 and Member 5.

The peak longitudinal reinforcement strains, measured and calculated at the midspan of the beams, were calculated with reasonable accuracy in most cases. In the first test of the undamaged beams (7 tests), excellent accuracy was achieved with a mean value of 0.99 and a coefficient of variation of 6.9% for the predicted-to-observed peak reinforcement strain ratio. In the second tests, the values deteriorated to 1.57 and 85.9%. The unacceptably high scatter in the predictions was mainly caused by two tests: SS3a-2 and SS1b-2. Beam SS1b-2 was extensively damaged with crack widths reaching as high as 30 mm as shown in Figure 8.27. In the third tests, the values became 1.30 and 60.4%. This unacceptable scatter in the predictions of the third tests was mainly caused by SS1a-3 which was also extensively damaged as shown in Figure 8.23.

The accuracy of the experimental determination of the reinforcement strains is subject to several factors. First of all, local crack conditions in the vicinity of the strain gauges have a major effect on the strain readings. Especially at high deformation stages, with large width cracks near the gauge locations, the contact of the gauge with the bar may loosen causing strain readings to be typically smaller than the actual strains in the bar. This is most likely the case for SS1b-2 and SS1a-3. In addition, cracks near the gauges may cause significant local increases in the reinforcement strains. As a result, strain readings are closely related to the proximity of the gauge to the cracks. However, in the analytical predictions, average strain values were calculated and compared to the strain readings

which may correspond to the strains at the crack locations. In such a case, underestimation of the experimental strain readings should be expected.

**Table 8.7** Comparison of Experimental and Analytical Reinf. Strains for Saatci Beams

| | Peak Midspan Strain ($x10^{-3}$) | | | Peak Support Strain ($x10^{-3}$) | | |
|---|---|---|---|---|---|---|
| | VecTor5 | Test | Ratio | VecTor5 | Test | Ratio |
| **SS0a-1** | 2.4 | 2.3 | 1.06 | 1.3 | 0.8 | 1.59 |
| **SS1a-1** | 2.2 | 2.3 | 0.98 | 1.4 | 1.1 | 1.27 |
| **SS2a-1** | 2.2 | 2.1 | 1.05 | 1.5 | 0.9 | 1.60 |
| **SS3a-1** | 2.3 | 2.5 | 0.92 | 1.5 | 1.1 | 1.36 |
| **SS0b-1** | Shear Fail. | Shear Fail. | n/a | Shear Fail. | Shear Fail. | n/a |
| **SS1b-1** | 10.2 | 10.4 | 0.98 | 1.9 | 1.7 | 1.12 |
| **SS2b-1** | 15.4 | 17.3 | 0.89 | 2.0 | 1.6 | 1.25 |
| **SS3b-1** | 19.7 | 18.6 | 1.06 | 2.1 | 2.6 | 0.82 |
| | | Mean | 0.99 | | | 1.29 |
| | | COV (%) | 6.9 | | | 27.2 |

| | Peak Midspan Strain ($x10^{-3}$) | | | Peak Support Strain ($x10^{-3}$) | | |
|---|---|---|---|---|---|---|
| | VecTor5 | Test | Ratio | VecTor5 | Test | Ratio |
| **SS0a-2** | Shear Fail. | Shear Fail. | n/a | Shear Fail. | Shear Fail. | n/a |
| **SS1a-2** | 8.5 | 9.0 | 0.95 | 1.0 | 1.2 | 0.81 |
| **SS2a-2** | 14.2 | 14.3 | 1.00 | 2.0 | 1.6 | 1.24 |
| **SS3a-2** | 18.6 | 5.8 | 3.19 | 2.2 | 1.7 | 1.28 |
| **SS1b-2** | 6.8 | 3.6 | 1.87 | 1.0 | 1.5 | 0.65 |
| **SS2b-2** | 23.2 | 20.2 | 1.14 | 1.4 | 2.0 | 0.70 |
| **SS3b-2** | 29.6 | 22.9 | 1.29 | 1.6 | 2.7 | 0.61 |
| | | Mean | 1.57 | | | 0.88 |
| | | COV (%) | 85.9 | | | 30.1 |

| | Peak Midspan Strain ($x10^{-3}$) | | | Peak Support Strain ($x10^{-3}$) | | |
|---|---|---|---|---|---|---|
| | VecTor5 | Test | Ratio | VecTor5 | Test | Ratio |
| **SS1a-3** | 14.6 | 6.2 | 2.35 | 1.4 | 1.3 | 1.04 |
| **SS2a-3** | 2.0 | 1.6 | 1.24 | 1.6 | 1.9 | 0.87 |
| **SS3a-3** | 16.7 | 17.9 | 0.93 | 1.7 | 1.7 | 0.95 |
| **SS2b-3** | 17.6 | 18.0 | 0.98 | 1.0 | 1.4 | 0.66 |
| **SS3b-3** | 19.7 | 20.2 | 0.98 | 0.8 | 2.2 | 0.37 |
| | | Mean | 1.30 | | | 0.78 |
| | | COV (%) | 60.4 | | | 26.9 |

| | | | | | |
|---|---|---|---|---|---|
| **All Tests** | **AVG** | **1.27** | | **AVG** | **1.01** |
| | **COV (%)** | **60.7** | | **COV (%)** | **35.0** |

The peak longitudinal reinforcement strains, measured and calculated at the support of the beams, were predicted only marginally well. The general tendency in the predictions was to overestimate the strains in the first tests and to underestimate the strains in the second and third tests. Similar to the peak support reaction forces, this tendency can be associated with the simplified modelling of the beams. Nonetheless, considering the 18

tests with available experimental strain readings, a mean value of 1.01 and a coefficient of variation of 35.0% may be accepted as sufficient, considering the use of an overly simplified support.

### 8.8.8 Damage Levels and Failure Modes

Beam Series SS0 and SS1

The comparison of the beams' crack widths, damage levels and failure modes, when applicable, obtained analytically and experimentally, are presented in Table 8.8 for the beam series SS0 and SS1. All crack widths are the maximum crack widths measured or calculated at the final resting stage of the experiment or analysis.

**Table 8.8** Comparison Crack Widths and Damage Modes for SS0 and SS1 Beams

| | **$W_{cr}$ (mm) - Shear** | | **Dominant Behaviour or Failure Mode** | |
|---|---|---|---|---|
| | VecTor5 | Test | VecTor5 | Experiment |
| **SS0a-1** | 0.1 | 0.2 | Shear Cracking | |
| **SS0a-2** | Shear Fail. | Shear Fail. | Extensive Shear Failure | |
| **SS0b-1** | Shear Fail. | Shear Fail. | Shear Failure | |
| **SS1a-1** | 0.9 | 0.25 | Shear Cracking | |
| **SS1a-2** | 4.3 | 4.0 | Extensive Shear Cracking | |
| **SS1a-3** | 6.4 | 5.0 | Extensive Shear Damage | |
| **SS1b-1** | 4.3 | 5.0 | Extensive Shear Cracking | |
| **SS1b-2** | 6.3 | 30.0 | Extensive Shear Damage | Shear Failure |

Inspection of Table 8.8 suggests that very good correlation with the experimental behaviour was obtained analytically. Shear-related mechanisms were the major cause of the damage sustained by these beams in both the analytical and experimental cases. More notably, the failure mode of the beams SS0a-2 and SS0b-1 were predicted with excellent accuracy. In the analytical model, SS0a-2 experienced an extensive shear failure involving Members 6, 7, 8, and 9. A similar shear failure mechanism was observed experimentally as shown in Figure 8.16. On the other hand, the shear failure of SS0b-1 involved only Member 9 in the analytical model, also similar to the experimental observation as shown in Figure 8.18.

The least accuracy in the analytical predictions was encountered with SS1b-2. The level of shear damage was underestimated by the analysis. The model sustained extensive

shear damage but was able to retain its integrity and complete the analysis without a failure, whereas the beam sustained complete shear failure in the test.

The shear crack widths obtained analytically showed an excellent correlation with the experimental shear crack widths except for SS1b-2.

It is of interest to note that both beam series (SS0 and SS1) were shear-critical under static loading conditions. Similarly they exhibited shear-dominated behaviours under impact loads both in the experiments and in the analyses.

Beam Series SS2 and SS3

A similar comparison involving the beams series SS2 and SS3 is given in Table 8.9.

**Table 8.9** Comparison of Crack Widths and Damage Modes for SS2 and SS3 Beams

| | **$W_{cr}$ (mm) - Shear** | | **$W_{cr}$ (mm) - Flexure** | | **Dominant Behaviour or Failure Mode** | |
|---|---|---|---|---|---|---|
| | VecTor5 | Test | VecTor5 | Test | VecTor5 | Experiment |
| **SS2a-1** | 0.3 | 0.2 | 0.4 | n/a | Shear+Flexural Cracking | |
| **SS2a-2** | 2.0 | 3.0 | 3.4 | 1.8 | Shear Cracking | |
| **SS2a-3** | 2.9 | 5.0 | 5.3 | 1.8 | Extensive Shear Cracking | Extensive Shear Damage |
| **SS2b-1** | 2.2 | 1.8 | 3.4 | 1.3 | Shear+Flexural Cracking | |
| **SS2b-2** | 2.5 | 2.0 | 6.0 | n/a | Shear Cracking | |
| **SS2b-3** | 2.4 | 2.0 | 6.0 | n/a | No Significant Change | |
| **SS3a-1** | 0.0 | 0.2 | 0.1 | n/a | Flexure+Shear Cracking | Shear Cracking |
| **SS3a-2** | 1.2 | 1.1 | 4.6 | 0.8 | Shear Cracking | |
| **SS3a-3** | 1.5 | 1.3 | 8.0 | n/a | No Significant Change | |
| **SS3b-1** | 1.0 | 0.4 | 5.0 | 1.0 | Flexure+Shear | |
| **SS3b-2** | 1.3 | 2.0 | 9.0 | 2.0 | Shear Cracking | |
| **SS3b-3** | 1.8 | 2.0 | 9.0 | n/a | No Significant Change | |

n/r: value not reported

The dominant behaviour and the damage levels of the beams were predicted with remarkable accuracy. Similar to the experimental observations, the analytical behaviours of these beams were flexure-dominant for the first impact tests. The behaviour then shifted towards shear cracking in the second tests, analytically and experimentally. In the third impact tests, the experimental observation of 'no-significant-change' damage levels was also predicted with excellent accuracy by the analytical procedure.

The least accurately predicted response came from Beam SS3a subjected to the first impact test (the lighter drop-weight). The analytical prediction underestimated the shear

cracking and showed a predominantly-flexural behaviour, whereas shear cracking was the dominant behaviour in the experiment. Nonetheless, considering the analytical displacement and reaction responses of this beam, this result can be accepted as reasonable.

The analytical shear crack widths showed a very good correlation to the experimentally determined widths in almost all tests. However, the flexural crack widths calculated at the midspan systematically overestimated the experimental values significantly. This was likely caused by local effects which enhanced the strength of concrete. As discussed in Section 1.2.4, the sectional analyses do not consider how the loads are introduced into the member by neglecting, for example, the beneficial effects of the compressive clamping stresses and concrete strut actions. This may translate into more tensile straining of the concrete at the midspan, where the impact is applied, and may increase the flexural crack widths in turn.

It is of interest to note that both beam series (SS2 and SS3) were flexure-critical under static loading conditions. However, when subjected to impact loading, shear-related mechanisms played a significant role in their behaviour both in the experiment and in the analysis.

## 8.9 Summary, Conclusions and Recommendations

The analysis procedure developed in Chapter 5 for general loading conditions was significantly expanded and modified in Chapter 7 to allow for nonlinear analyses under dynamic loading conditions including time-varying base accelerations, time-varying impulse, impact and blast forces, initial mass velocities, and constant mass accelerations. Three time integration methods were implemented with the Wilson's Theta method being the most favoured one. The motivation for this was to avoid the need to introduce some additional viscous damping for stability reasons which arises when using the other two procedures, i.e., Newmark's average and linear acceleration methods. As was discussed in detail in Section 7.10, the selection of the vibration modes to which damping is assigned, and the selection of the appropriate damping ratios, is a major task involving

assumptions regarding several unknowns and requiring a series of repeated analyses which may take significant engineering time. It was also observed that the structural response changes significantly under different damping ratios, which makes the selection of an appropriate damping scheme more critical. Moreover, the nonlinear analysis procedure employed in VecTor5 considers nonlinear material hysteresis through which most of the energy dissipation occurs, thus not particularly requiring additional viscous damping. It should be, however, noted that when analyzing a real structure having non-structural components, the use of additional viscous damping may be necessary due to the energy dissipation of non-structural elements as discussed in Section 7.5.2. In this case, either Newmark's method or Wilson's Theta method can be employed with an appropriate additional viscous damping ratio.

In this chapter, the analytical procedure developed for dynamic loading condition was verified with a well-instrumented and well-documented experimental program (Saatci, 2007) involving 20 impact tests on eight reinforced concrete beams. The experimental behaviours of the beams were carefully compared to the analytical behaviours in terms of the displacement, support reaction and reinforcement strain responses. Damage levels, residual displacements, failure modes, and crack widths at the end of the loadings, as obtained experimentally and analytically, were also compared. Moreover, the analytical post-peak vibrational characteristics were compared to the experimental responses in terms of damping and vibrational periods. As well, guidelines for modelling reinforced concrete frame-related structures, particularly those subjected to impact loads, were provided.

Considering all 20 impact tests, a mean of 0.99 and a coefficient of variation (COV) of 9.5% were achieved for the predicted-to-observed peak displacement ratio. For the peak reaction forces, a mean of 0.95 and a COV of 21.3% were attained. For the residual displacements at the end of the loadings, a mean value of 0.98 and a COV of 33.9% were realized. The failure modes and damage levels sustained by the beams were predicted accurately. In addition, the computed post-peak characteristics showed reasonably strong correlations with the experimental results.

The damping characteristics of the test beams were captured reasonably well. The use of Wilson's Theta method *with no additional damping* provided stable analyses and proved to be a viable nonlinear dynamic analysis technique. Note that currently available nonlinear analyses programs generally require a certain percentage of viscous damping, sometimes up to 5%, even though they include other energy dissipating mechanisms such as the concrete hysteresis (Filippou et al., 1992). Therefore, the implementation of Wilson's Theta method with no additional damping was perhaps the most notable accomplishment among the dynamic implementations.

Also notable is that the displacement responses of previously damaged beams in second and third tests were predicted with high accuracy. The predicted-to-observed ratio of the peak displacements in the second and third impact tests had a mean of 0.98 with a COV of 7.1%. Since a very limited number of analytical tools are available for such an analysis, the capability of analyzing previously damaged structures proved to be a valuable feature of the analytical procedure developed.

The vibrational periods of the beams were predicted reasonably well with an underestimation of 15 to 20 percent. This was attributed to some of the material behaviour models used, which were primarily developed for static loading conditions. It was emphasized that more comprehensive models directly incorporating dynamic effects are required for improved analytical predictions.

The peak support reactions were predicted with acceptable accuracy even though an overly simplified roller support was used to simulate the special support condition employed in the experiment. However, unacceptably high uplift forces were predicted.

In conclusion, the newly implemented dynamic analysis algorithms of VecTor5 performed well. The behaviour of the beam specimens under impact loads were simulated with an accuracy which is acceptable in most engineering situations, let alone for elements that were subjected to very extreme levels of damage. Both shear- and flexure-related mechanisms were captured well.

Also notable is that the analyses were completed without any loss of computational stability and in a short period of time. A typical impact analysis of a beam in this study required a computation time of approximately 19 minutes*. This is significant considering that several hours were required for such analyses using finite element procedures with comparable computational power (Saatci, 2007).

To account for the strength gain of concrete and reinforcement materials under high strain rates, a number of formulations were implemented to calculate the dynamic increase factors. Although the implemented strain rate formulations were selected carefully from the available models which reflect current knowledge, significant assumptions and contradictions were noted regarding those formulations. The significant effects of these formulations on the calculated responses were pointed out with an emphasis on the need for more experimental and analytical studies to improve these formulations for more accurate simulations.

---

*On a Laptop computer with an Intel ® Dual Core 2 Due® T7500 (2.2 GHz) Processor®, a 2 GB DDR2, 677MHz RAM and a 7200 RPM hard disk drive.

# CHAPTER 9

## SUMMARY, CONCLUSIONS & RECOMMENDATIONS

### 9.1 Summary

In addition to providing a review of the previous studies and a critical look at the current state-of-the-art, this study was concerned with the development and verification of an analytical procedure for the nonlinear analysis of frame structures with the aim of capturing shear-related mechanisms as well as axial and flexural mechanisms. A frame analysis program, VecTor5, based on predecessor program TEMPEST (Vecchio, 1987; Vecchio and Collins, 1988), was further developed for this purpose. Originally developed in the early 1980s at the University of Toronto, TEMPEST was based on the Modified Compression Field Theory (MCFT) (Vecchio and Collins, 1986) and was capable of performing nonlinear frame analyses under temperature and monotonic loading conditions. Although providing generally satisfactory simulations, there were a number of deficiencies present in its computational algorithms.

This study consisted of three major parts: improvement of the original analysis procedure for monotonic loading conditions, further development of the procedure for general loading conditions, and further development of the procedure for dynamic loading conditions. Each part was supported by verification studies performed on a large number and variety of structures previously tested. In addition, considerations in nonlinear modelling were discussed with the aim of providing guidelines for general modelling applications.

In the first part, the original analytical procedure of VecTor5 was significantly improved and expanded to allow for improved simulations of the nonlinear behaviour of frame structures under monotonic loading conditions. The following modifications and additions were made to the original formulations of VecTor5 in this first part:

1. The sectional analyses algorithm was completely rewritten with an emphasis on improved representation of shear behaviour.

2. Refinements in the underlying theories that have occurred in the past two decades, such as the Disturbed Stress Field Model (DSFM) (Vecchio, 2000), were implemented.

3. The deficiencies previously reported were corrected.

4. Additional second-order effects such as reinforcement dowel action, concrete dilatation; concrete prestrains, concrete tension softening, and concrete crack slip check were implemented.

5. A new shear protection algorithm was implemented to approximately take into account the increased strengths of D-regions.

6. A new shear failure check algorithm was implemented to detect the shear failures of members which may have gone unnoticed with significant unbalanced shear forces in the cases where the specified maximum number of iterations turns out to be insufficient for the structure being analyzed.

7. The existing dynamic averaging scheme was improved to significantly reduce the unbalanced forces. This implementation was made a default feature of the analytical procedure.

8. A new variable crack spacing calculation algorithm was implemented to take into account the variable spacings of cracks depending on the longitudinal and transverse reinforcement configuration.

9. Stress calculations in the out-of-plane direction, strain hardening behaviour of transverse reinforcement and calculation of reinforcement local stresses and strains at a crack were included into the sectional analyses.

10. The total number of elements, concrete layers and steel layers, which can be handled by the program, were increased. A more comprehensive warning mechanism for input errors and a more detailed output for advanced users were provided.

11. The stability and convergence characteristics of the original program were improved significantly.

The resulting analytical procedure for monotonic loading condition was verified with a variety of structures including two sets of beams, three large-scale frames and six large-scale shear walls, all of which were previously tested. As the main focus of the analytical procedure developed was to accurately simulate shear-related mechanisms, two-thirds of the structures considered exhibited shear-dominated behaviour in the experiments. The experimental behaviours of the structures were compared to the analytical behaviours in terms of load-deflection responses, reinforcement strains, crack widths, failure modes and failure displacements. In addition, the analytical post-peak responses were compared to the experimental responses and the energy dissipation characteristics were discussed.

In the second part of this study, the analytical procedure developed was expanded to consider general loading conditions including the special cases of cyclic and reversed-cyclic loading. The following additions were made to the existing analytical procedure:

1. The concrete and reinforcement strain histories were included in the sectional analyses. Concrete strain histories were considered based on the incremental formulation proposed by Vecchio (1999).

2. Three concrete hysteresis models were implemented:
    i. The Vecchio model with linear unloading (Vecchio, 1999),
    ii. The Vecchio model with nonlinear unloading (Vecchio, 1999),
    iii. The Palermo model with decay (Palermo and Vecchio, 2003).

3. Three reinforcement hysteresis models were implemented:

i. The Seckin Model with Bauschinger effect (Seckin, 1981),

ii. The Elastic-Plastic model with strain hardening,

iii. The Elastic-Plastic model.

The resulting analytical procedure for general loading condition was verified with a variety of structures consisting of one large-scale frame, four large-scale beam-column subassemblies and six 1/3-scale shear walls, all of which were previously tested. The experimental behaviours of the structures were compared to the analytical behaviours in terms of load-deflection responses, reinforcement strains, crack widths, failure modes and failure displacements. Important in the seismic assessment of structures, the total energy dissipation and the displacement ductility ratios were also compared to the experimental results.

In the third part of this study, the analytical procedure developed was significantly expanded to consider dynamic loading conditions including time-varying base accelerations, impulse, impact and blast forces, initial mass velocities, and constant mass accelerations. The following additions and modifications were made to the existing analytical procedure:

1. Three time integration methods were implemented:
    i. Newmark's average acceleration method (1959),
    ii. Newmark's linear acceleration method (1959),
    iii. Wilson's Theta method (1976).

2. Two damping formulations were implemented to account for additional viscous damping mechanisms:
    i. Rayleigh damping (1878),
    ii. Alternative damping (Clough and Penzien, 1993).

3. Two dynamic increase factor formulations were implemented to account for the strength gain of concrete and the reinforcement under high strain rates:
    i. CEB-FIP (1988 and 1990) formulations,
    ii. Malvar and Crawford (1998) formulations.

4. A new modal analysis algorithm was implemented to calculate the vibration characteristic of the structure, such as the mode shapes and frequencies.

5. New algorithms were implemented to determine the lumped-mass matrix and dynamic load vectors.

The resulting analytical procedure developed for dynamic load conditions was verified with a well-instrumented and well-documented experimental program (Saatci, 2007) involving 20 impact tests on the eight reinforced concrete beams. The experimental behaviours of the beams were compared to the analytical behaviours in terms of the displacement, support reaction and reinforcement strain responses. Damage levels, residual displacements, failure modes, and crack widths at the end of the loadings, as obtained experimentally and analytically, were also compared. Moreover, the analytical post-peak vibrational characteristics were compared to the experimental responses in terms of damping and periods of vibration.

In all three parts, important considerations in the nonlinear modelling were discussed through the use of practical examples; details of the analytical models were presented with the aim of providing guidelines for the general modelling process. Moreover, the appropriate use of the newly implemented options and the appropriate selection of several parameters were discussed, including the selection of appropriate time steps, displacement steps and segment lengths, the use of additional viscous damping, and the selection of a time integration method.

## 9.2 Conclusions

- The following conclusions apply to the nonlinear static analyses of the three previously tested structures analyzed with some available software programs:

1. Strength predictions for flexure-critical structures are, in general, a straightforward calculation; reasonable estimations should be expected even when using the default models for flexural behaviour. On the other hand, caution should be exercised when calculating the ductility of flexure-critical structures; erroneous estimates may be obtained. Considering the two flexure-critical structures analyzed, using the default models for flexural behaviour, providing four values:

    i. The strengths of the structures were predicted successfully with a mean of 0.96 and a coefficient of variation (COV) of 5.6% for the predicted-to-observed ratio.

    ii. The ultimate displacements corresponding to the failure conditions of the structures were not predicted with reasonable accuracy. One of the software programs used did not indicate any failure displacements; the other typically predicted less than half of the experimental failure displacements.

2. Using generic or unknown models to simulate the behaviour of shear-critical structures can easily lead to grossly inaccurate results for both strength and ductility predictions. Considering the shear-critical frame analyzed, using the default models for shear behaviour, providing two values:

    i. The strength of the frame was poorly predicted with a mean of 0.79 and a COV of 67.6% for the predicted-to-observed ratio.

    ii. The failure displacement was not predicted with acceptable accuracy. One of the software programs used did not indicate any failure displacement; the other predicted less than one-tenth of the experimental failure displacement.

3. There is a need for advanced yet practical nonlinear analysis procedures which inherently include shear-related influences as well as flexure and axial related ones, thereby capturing all possible failure mechanisms.

4. The procedure needed for the nonlinear analysis of reinforced concrete frames should not require previous knowledge of the failure mechanism of the structure and should not require expert knowledge on the selection of material models and assumptions in the analysis.

- The following conclusions apply to all three parts of this study (i.e., monotonic, general and dynamic loading conditions):

1. The analytical procedure developed was shown to be successful in simulating the experimental responses of previously tested specimens with a high level of accuracy.

    i. For all the static analyses performed, comprising 55 simulations, a mean of 1.01 and a coefficient of variation (COV) of 10.4% were achieved for the predicted-to-observed strength ratio. The analyses covered a variety of structures, half of which were shear-critical, subjected to monotonic and reversed-cyclic loading conditions. For all the dynamic analyses performed under impact loading conditions, comprising 20 simulations, a mean of 0.99 and a COV of 9.5% were achieved for the predicted-to-observed peak reaction forces ratio. These analyses included the second and third impact tests on the damaged beams. Considering the challenges involved in the simulation of the behaviour of such structures under such loading conditions, these values can be regarded as excellent.

    ii. For all the analyses performed, the failure or damage modes were predicted with excellent accuracy for 90% of the structures. The failure modes of the remaining 10% structures were partially correctly captured. A failure mode which was contradictory to the experimental observations (e.g., shear failure rather than flexural failure or vice versa) was never predicted.

iii. The stiffnesses of the structures examined were captured reasonably well with slightly stiffer analytical responses than the experimental responses. This was attributed to the interference of the loading machine and irregularities in the experimental set-ups.

2. The implementations of the MCFT and DSFM theories into a sectional calculation procedure proved successful; the shear-dominated behaviours of the structures examined were predicted well.

3. The newly implemented shear protection algorithm performed well; premature shear failures of sections adjacent to beam-column panel zones, point load application areas, and support areas were prevented.

4. The newly implemented shear failure check algorithm performed well; sudden shear failures of several structures were detected that may have gone unnoticed otherwise.

5. Newly implemented algorithms for various second-order mechanisms performed well; improved simulations of the post-peak responses of the structures were achieved.

6. The aim of obtaining reasonable simulations with reasonable engineering effort was achieved.

    i. All analyses were performed with the use of default material behaviour models and analysis options. No decisions regarding the expected behaviour, failure mode or selection of appropriate parameters were made prior to the analyses. No additional calculations, such as interaction responses or moment-curvature responses of the cross sections, were performed in the modelling process.

    ii. The analyses typically required little computation time. Under monotonic loading, approximately one minute was required for the analysis of each of the beams examined; the longest analysis time of approximately 6 minutes was

required for the Duong frame*. Under general loading, approximately 20 minutes were required for the analysis of one of the PCA shear walls. Under dynamic loading, approximately 19 minutes were required for the impact analysis of one of the Saatci beams. These are remarkable considering the several hours required for such an analyses using finite element procedures as reported by Saatci using comparable computational power.

7. Optimum segment lengths to be used in the frame models were recommended as a result of a parametric study. A segment length in the range of 50% of the cross section depth was recommended for frame-related structures (i.e., beams, columns and frames); a segment length in the range of 10% of the cross section depth was suggested for shear walls (see Section 9.3, point 8).

- The following additional conclusions were reached in the first part of this study (i.e., monotonic loading conditions):

1. The developed analytical procedure for monotonic loading was shown to be successful in simulating the experimental responses of previously tested specimens with a high level of accuracy. For a variety of 33 structures examined, two-thirds of which were shear-critical:

    i. A mean of 1.03 and a coefficient of variation (COV) of 11.9% were achieved for the predicted-to-observed strength ratio. For displacements corresponding to complete failure, a mean of 0.85 with a COV of 20.7% was realized. Considering the challenges involved in the modelling of shear-critical structures, these ratios can be regarded as highly satisfactory.

    ii. The failure modes of the structures were predicted accurately. In addition, the computed reinforcement strain responses, member elongation responses and concrete crack widths showed reasonably strong correlations with the experimental results.

*On a Laptop computer with an Intel ® Dual Core 2 Due® T7500 (2.2 GHz) Processor®, a 2 GB DDR2, 677MHz RAM and a 7200 RPM hard disk drive.

2. The effective stiffness values for the three reinforced concrete frames examined were typically found, through the use of experimental load-deflection responses, to be approximately 0.25 times the uncracked gross stiffness values.

- The following additional conclusions were reached in the second part of this study (i.e., general loading conditions):

1. The analytical procedure developed for general loading was shown to be successful in simulating the experimental responses of previously tested specimens with a high level of accuracy. For a variety of 11 structures examined in the both positive and negative loading directions, comprising 22 simulations:

    i. A mean of 0.97 and a coefficient of variation (COV) of 6.0% were achieved for the predicted-to-observed strength ratio. For the displacements corresponding to the peak load capacities, a mean of 1.07 with a COV of 23.4% was realized.

    ii. The failure modes of the structures were predicted accurately for the majority of the specimens. In addition, the computed reinforcement strain responses, member elongation responses and crack widths showed reasonably strong correlations with the experimental results.

    iii. Important in the seismic assessment of structures, the total energy dissipated by the structures was predicted with reasonable accuracy, achieving a mean of 1.18 with a COV of 14.6% for the predicted-to-observed ratio. Considering the challenges involved in the simulation of behaviour of reinforced concrete under reversed-cyclic loading conditions, these ratios can be regarded as highly satisfactory.

    iv. The strength degradation characteristics of the structures, under repeated cycles at the same displacement amplitude, were simulated well. Also notable is that this degradation occurred despite the use of the default concrete hysteresis, which does not consider strength degradation. The computed

strength degradation was a result of increased shear straining and cracking. The crack width limit model was found to significantly contribute to the strength degradation.

v. The highly irregular loading protocol of SP6 specimen (Seckin, 1981) was successfully simulated through the use of implemented seed files (i.e., binary input files).

- The following additional conclusions were reached in the third part of this study (i.e., dynamic loading conditions):

1. The analytical procedure developed for dynamic loading was shown to be successful in simulating the experimental responses of 8 beam specimens previously tested under impact loading. Considering all 20 impact analyses:

   i. A mean of 0.99 and a coefficient of variation (COV) of 9.5% were achieved for the predicted-to-observed peak displacement ratio. For the predicted-to-observed peak reaction forces, a mean of 0.95 and a COV of 21.3% were attained. A mean value of 0.98 and a COV of 33.9% were realized for the predicted-to-observed residual displacements at the end of the loadings. These ratios can be regarded as highly satisfactory in most engineering situations, let alone for elements that were subjected to extreme levels of damage.

   ii. The failure modes and damage levels sustained by the beams were predicted accurately. Both shear- and flexure-related mechanisms were captured well.

   iii. The computed damping characteristics showed reasonably strong correlations with the experimental results.

   iv. The vibrational periods of the beams were captured reasonably well with typical underestimation of approximately 15 to 20 percent. This was attributed to some of the material behaviour models used, which were primarily developed for static loading conditions, and to the assumption of rigid supports.

2. The use of the Wilson's Theta method with no additional damping provided stable analyses and proved to be a viable nonlinear dynamic analysis technique. Note that other currently available nonlinear analyses programs generally require a certain percentage of viscous damping, sometimes up to 5%, even though they include energy dissipating mechanisms such as the concrete hysteresis (Filippou et al. 1992). Therefore, the implementation of Wilson's Theta method with no additional viscous damping was perhaps the most notable accomplishment among the dynamic implementations.

3. The displacement responses of previously damaged beams in second and third tests were predicted with high accuracy. The predicted-to-observed ratio of the peak displacements in second and third impact tests had a mean of 0.98 with a COV of 7.1%. Since a very limited number of analytical tools are available for such analyses, the capability of analyzing previously damaged structures proved to be a valuable feature of the analytical procedure developed.

4. The peak support reactions were predicted with acceptable accuracy, but unacceptably high uplift forces were predicted due to the use of overly simplified roller supports in the modelling of special support conditions employed in the experiment.

### 9.3 Current Limitations and Recommendations for Future Work

1. The analysis procedure developed should not be used for the detailed analysis and assessment of beam-column joints; rather, it should be used for global analyses of large frame structures.

2. New procedures (e.g. a new member type) should be developed for simulations of the behaviour of beam-column joint panel regions, capturing the joint distress.

3. Bond-slip mechanisms of the longitudinal reinforcement should be implemented into the current computation algorithm for better simulations of structural behaviour under large strain reversals.

4. The longitudinal bar buckling mechanism should be implemented into the current computation algorithm for better simulations of structural behaviour under large compressive strains.

5. A more general tension softening formulation should be developed for improved simulations of the behaviour of members containing very little amounts of shear reinforcement.

6. The concrete and reinforcement constitutive models, which were primarily developed for static loading conditions, should be further developed directly incorporating strain rate-related effects for improved analytical predictions in dynamic analyses.

7. More comprehensive strain rate formulations, which are developed specifically for the reinforced concrete, should be utilized. The implemented strain rate formulations were selected carefully from the available models which reflect current knowledge; more experimental and analytical studies are required to improve the formulations for more accurate simulations.

8. A more comprehensive study including shear-critical *shear walls* should be conducted to reach a conclusive recommendation for the optimum segment lengths to be used in the modelling of *shear walls*.

9. Introduction of a new algorithm for automatic member segmentation in which the frame members are automatically divided into smaller segments would reduce the effort required when modelling large frames.

# REFERENCES


Aguilera, C. K. (2003), "Long Term Structural Performance of Corroded RC Beams Repaired with Externally Bonded CFRP Reinforcement," M.A.Sc. Thesis, Department of Civil Engineering, University of Toronto, 331 pp.

Anagnostopoulos, S. (1981), "Inelastic Beams for Seismic Analysis of Structures," Journal of Structural Engineering, ASCE, 107(ST7), pp. 1297-1311.

Angelakos, D. (1999), "The Influence of Concrete Strength and Longitudinal Reinforcement Ratio on the Shear Strength of Large-Size Reinforced Concrete Beams with, and without, Transverse Reinforcement," M.A.Sc. Thesis, Department of Civil Engineering, University of Toronto, 181 pp.

Angelakos, D., Bentz, E. C., and Collins, M. P. (2001), "Effect of Concrete Strength and Minimum Stirrups on Shear Strength of Large Members," ACI Structural Journal, V.98, No.3, May-June, pp 290-300.

Arakawa, T. (1969), "Shear Reinforcement and Allowable Shear Stress of Reinforced Concrete Beams," Architectural Institute of Japan, Summaries of Technical Papers of Annual Meeting.

Balopoulou, S. (1988), "Nonlinear Response of a Reinforced Concrete Frame," M.A.Sc. Thesis, Department of Civil Engineering, University of Toronto, 170 pp.

Banon, H., Briggs, J. and Irvine, M. (1981), "Seismic Damage in Reinforced Concrete Frames," Journal of Structural Engineering, ASCE, 107(ST9), pp. 1713-1729.

Bathe, K. J. and Wilson, E. L. (1976), "Numerical Methods in Finite Element Analysis", Prentice-Hall, 528 pp.

Bayrak, O. (1998), "Seismic Performance of Rectilinearly Confined High Strength Concrete Columns," PhD. Thesis, Department of Civil Engineering, University of Toronto, 339 pp.

Bentz, E. C. (2000) "Sectional Analysis of Reinforced Concrete Members," PhD Thesis, Department of Civil Engineering, University of Toronto, 310 pp.

Bentz, E. C. (2005) "Explaining the Riddle of Tension Stiffening Models for Shear Panel Experiments," ASCE Journal of Structural Engineering, V. 131, No. 9, pp. 1422-1425.

Bentz, E. C., Collins, M. P. and Vecchio, F. J. (2006), "The Simplified MCFT for Calculating the Shear Strength of Reinforced Concrete Elements," ACI Structural Journal, V.103, No.4, pp. 614-624.

Bernoulli, J. (1705), "Histoire de l'Academie des Science de Paris." Paris.

Bertero, V. V., Aktan, A, Charney, F. and Sause, R. (1984), "Earthquake Simulator Tests and Associated Experimental, Analytical and Correctional Studies of One-Fifth Scale Model," in, Earthquake Effects on Reinforced Concrete Structures, American Concrete Institute, SP-84-13, Detroit, pp.375-424.

Blume, J. A., Newmark, N. M. and Corning, L. H. (1961), "Design of Multistory Reinforced Concrete Buildings for Earthquake Motions," Portland Cement Association, Illinois, 318 pp.

Brancaleoni, F., Ciampi, V., and Di Antonio, R. (1983), "Rate-Type Models for Non Linear Hysteresis Structural Behaviour," EUROMECH Colloquium, Palermo, Italy.

Bresler, B. and Scordelis, A. C. (1963), "Shear Strength of Reinforced Concrete Beams," Journal of American Concrete Institute, V.60, No.1, pp 51-72.

CAC (2006), "Concrete Design Handbook, Cement Association of Canada," 3rd Ed., Ottawa, Canada, 983 pp.

Carr, A. J. (2005), "User Manual for the 2-Dimensional Version Ruaumoko2D," University of Canterbury, Department of Civil Engineering, Computer Program Library, 87 pp.

Caughey, T. K. (1960), "Classical Normal Modes in Damped Linear Dynamic Systems," Journal of Applied Mechanics, ASME, 27, pp 269-271.

CEB-FIP (1990), "Model Code for Concrete Structures," Design Code, Comité EURO-International du Béton, 437 pp.

CEB-FIP (1978) "Model Code for Concrete Structures: CEB-FIB International Recommendations, " 3rd Ed., Comité EURO-International du Béton, Paris, 348 pp.

CEB-FIP (1988), "Concrete Structures under Impact and Impulsive Loading," Comité EURO-International du Béton, Bulletin D'Information, No. 187. 184 pp.

Cervenka, V. (2000), "Simulating a Response," Journal of Concrete Engineering International, V.4, No. 4, pp. 45-49.

Charney, F. and Bertero, V. V. (1982), "An Evaluation of the Design and Analytical Seismic Response of a Seven Story Reinforced Concrete Frame-Wall Structure," Earthquake Engineering Research Center, University of California, Berkeley, Report No. UCB/EERC–82/08, 196 pp.

Chopra, A. K. (2007), "Dynamics of Structures: Theory and Applications to Earthquake Engineering," 3rd Ed., Pearson Pretence Hall, New Jersey, 876 pp.

Christopoulos C. and Filiatrault, A. (2006), "Principles of Supplemental Damping and Seismic Isolation," IUSS Press, Milan, Italy, 500 pp.

Ciampi, V. and Nicoletti, M. (1986), "Parameter Identification for Cyclic Constitutive Models for Stiffness and Strength Degradation," 8th European Conference on Earthquake Engineering, Lisbon, Portugal, 7.1, pp 73-80

Clough, R. and Johnston, S. (1966), "Effect of Stiffness Degradation on Earthquake Ductility Requirements," Transaction of Japan Earthquake Engineering Symposium, Tokyo, pp. 195-198.

Clough, R. and Johnston, S. (1967), "Nonlinear Earthquake Behaviour of Tall Buildings," Journal of Mechanical Engineering, ASCE, 93(EM3), pp. 129-146

Clough, R. W. and Penzien, J. (1993), "Dynamics of Structures," McGraw-Hill, Inc, 2nd Ed., 648 pp.

Collins, M. P. and Mitchell, D. (1980), "Shear and Torsion Design of Prestressed and Non-Prestressed Concrete Beams," PCA Journal, V.25, No.25, pp 32-100; Discussion and Closure, PCI Journal, V.26, N.6, Nov-Dec 1981, pp 96-118.

Collins, M.P. and Mitchell, D. (1991), "Prestressed Concrete Structures," Response Publications, reprinted in 1997, Canada, 766 pp.

CSA A23.3-04 (2004) "Design of Concrete Structures", Canadian Standards Association, Mississauga, Ontario, Canada, 214 pp.

CSI (2005), "Analysis Reference Manual for SAP2000®, ETABS® and SAFE™," Computers and Structures, Inc., Berkeley, California, USA, 415 pp.

Duong, K. V. (2006), "Seismic Behaviour of Shear-Critical Reinforced Concrete Frame: An experimental and Numerical Investigation," M.A.Sc. Thesis, Department of Civil Engineering, University of Toronto, 296 pp.

Duong, K. V., Sheikh, S. A, Vecchio, F. J. (2007), "Seismic Behaviour of Shear-Critical Reinforced Concrete Frame: Experimental Investigation," ACI Structural Journal, V.104, No.3, May-June, pp 304-313.

El-Tawil, S. and Deierlein, G. G. (2001), "Nonlinear Analyses of Mixed Steel-Concrete Moment Frames. Part I – Beam-Column Formulation. Part II – Implementation and Verification.," ASCE, Journal of Structural Engineering, Vol. 127, No. 6, pp. 647-665.

Emara, M. B. (1990), "Shear Deformations in Reinforced Concrete Frames," M.A.Sc. Thesis, Department of Civil Engineering, University of Toronto, 193 pp.

Eurocode 2 (1992), "Design of Concrete Structures Part 1.2: General Rules – Structural Fire Design," European Standard, European Committee for Standardization, Brussels, 101 pp.

FEMA 356 (2000), "Prestandard and Commentary for the Seismic Rehabilitation of Buildings," Federal Emergency Management Agency, November, Washington, D. C., 518 pp.

Filippou, F. C., and Issa, A. (1988), "Nonlinear Analysis of Reinforced Concrete Reinforced Concrete Frames under Cyclic Load Reversals," Earthquake Engineering Research Center, University of California, Berkeley, Report No. UCB/EERC–88/12, 120 pp.

Filippou, F. C., D'Ambrisi, A., and Issa, A. (1992), "Nonlinear Static and Dynamic Analysis of Reinforced Concrete Subassemblages," Earthquake Engineering Research Center, University of California, Berkeley, Report No. UCB/EERC–92/08, 184 pp.

FIP (1998), Commission 3 on FIP 1996 Recommendations for "Practical Design of Structural Concrete," Federation Internationale de la Precontrainte, May, 113 pp.

FIB (2008), "Practitioners' Guide to Finite Element Modeling of Reinforced Concrete Structures," fib Bulletin No.45, 2008, (in publication).

Fulop, A. L. (1992), "Deformation Controlled Procedure for Nonlinear Analysis of Reinforced Concrete Frames," M.A.Sc. Thesis, Department of Civil Engineering, University of Toronto, 212 pp.

Garbow, B. S. (1974), "EISPACK – A Package of Matrix Eigensystem Routines.", Computer Physics Communications, V.7, pp.179-184.

Gere J. M. and Timoshenko, S. P. (1991), "Mechanics of Materials," 3rd Ed., Chapman and Hall Ltd., London, England, 807 pp.

Giberson M. F. (1967), "The Response of Nonlinear Multi-Storey Structures Subjected to Earthquake Excitations", PhD Thesis, California Institute of Technology, Pasadena, 232 pp.

He, X.G. and Kwan, A.K.H. (2001), "Modeling Dowel Action of Reinforcement Bars for Finite Element Analysis of Concrete Structures," Computers and Structures, V. 79, No.6, pp. 595-604.

Ho, D. (2004). "Impact Response of Reinforced Concrete: An Experimental and Numerical Investigation," M.A.Sc. Thesis, University of Toronto, Department of Civil Engineering, 267 pp.

Hooke, R. (1678), "Lectures De Potentia Restitutiva, or of Spring Explaining the Power of Springing Bodies," printed for John Martyn Printer to The Royal Society, at the Bell in St. Paul's Church-Yard, 24 pp.

Hoshikuma, J., Kawashima, K., Nagaya, K. and Taylor, A. W. (1997) "Stress-Strain Model for Confined Reinforced Concrete in Bridge Piers", ASCE Journal of Structural Engineering, V.123, No. 5, pp. 624-633.

IBC (2006), "International Building Code," International Building Code Council, USA, 679 pp.

Iwan, W. (1978), "Application of Nonlinear Analysis Techniques," Iwan W. ed., Applied Mechanics in Earthquake Engineering, ASME, AMD, 8, New York, pp. 135-161.

Kaba, S. and Mahin, S. A. (1984) 'Refined Modelling of Reinforced Concrete Columns for Seismic Analysis," Earthquake Engineering Research Center, University of California, Berkeley, Report No. UCB/EERC–84/03, 104 pp.

Kent, D.C., and Park, R. (1971), "Flexural Members with Confined Concrete," ASCE Journal of the Structural Division, V. 97, No. ST7, Proc. Paper 8243, pp. 1341-1360.

Kupfer, H., Hilsdorf, H.K. and Rusch, H. (1969), "Behavior of Concrete under Biaxial Stress", ACI Journal, V. 87, No. 2, pp. 656-666.

Kurama, Y. C. and Jiang, H. (2008), "Analytical Modeling of Monolithic Cast-in-Place RC Shear Walls," Journal of Structural Engineering, (in publication).

Lai, S., Will, G., Otani, S. (1984), 'Model for Inelastic Biaxial Bending of Concrete Members," Journal of Structural Engineering, ASCE, 110(ST11), pp. 2563-2584.

Lefas, I. D., Kotsovos, M. D. and Ambraseys, N. N. (1990), "Behaviour of Reinforced Concrete Structural Walls: Strength, Deformation Characteristics, and Failure Mechanism," ACI Structural Journal, V.87, No.1, January-February, pp 23-31.

Lubell, A., Sherwood, T., Bentz, E. C., Collins, M. P. (2004), "Safe Shear Design of Large, Wide Beams," Concrete International, January, pp 67-78.

Malvar, L. J. and Crawford, J. E. (1998), "Dynamic Increase Factors for Steel Reinforcing Bars," Twenty-Eight DDESB Seminar, Orlando, 16 pp.

Martino, R., Spacone, E., Kingsley, G. (2000), "Nonlinear Pushover Analysis of RC Structures." ASCE Conference Proceedings, Advanced Technology in Structural Engineering, M. Elgaaly, ed., ASCE, 8 pp.

Mörsh, E. (1902), "Der Eisenbetonbau, esine Theorie und Anwendung (Reinforced Concrete Theory and Application), Stuggart, Germany, 118 pp.

Mostafaei, H. (2006), "Axial-Shear-Flexure Interaction Approach for Displacement-Based Evaluation of Reinforced Concrete Elements," Ph.D Thesis, Architecture Department, University of Tokyo, Tokyo, Japan, 255 pp.

Navier, C-L. (1826), "Resume Des Lecons…De La Resistance Des Corps Solides," Paris.

NBCC (2005), "National Building Code of Canada", Institute for Research for Construction (IRC), National Research Council of Canada, Ottawa, 1167 pp.

Newmark, N. M. (1959), "A Method of Computation for Structural Dynamics," Journal of the Engineering Mechanics Division, ASCE, V.85, pp.67-94.

Oesterle, R. G., Fiorato, A. E., Johal, L. S., Carpenter, J. E., Russell, H. G. and Corley, W. G. (1976), "Earthquake Resistant Structural Walls – Tests of Isolated Walls," Construction Technology Laboratories, Portland Cement Association, Skokie, Illinois, 315 pp.

Okamura, H. and Maekawa, K. (1991) "Nonlinear Analysis and Constitutive Models of Reinforced Concrete," Giho-do Press, University of Tokyo, Tokyo, 182 pp.

Okamura, H., and Maekawa, K. (1991) "Nonlinear Analysis and Constitutive Models of Reinforced Concrete," Giho-do Press, University of Tokyo, Tokyo, 1991, 182 pp.

Otani, S. (1974), Inelastic Analysis of R/C Frame Structures", Journal of Structural Division, ASCE, 100 (ST7), pp 1433-1449.

Ozdemir, H. (1981), "Nonlinear Transient Dynamic Analysis of Yielding Structures", Ph.D Thesis, Department of Civil Engineering, University of California, Berkeley.

Palermo, D. and Vecchio, F. J. (2003), "Compression Field Modeling of Reinforced Concrete Subjected to Reversed Loading: Formulation," ACI Structural Journal, V.100, No.5, September-October, pp. 616-625.

Palermo, D. and Vecchio, F. J. (2004), "Compression Field Modeling of Reinforced Concrete Subjected to Reversed Loading: Verification," ACI Structural Journal, v.101, No.2, March-April, pp. 155-164.

Paulay, T., and Priestley, M. J. N. (1992), "Seismic Design of Reinforced Concrete and Masonry Buildings," Wiley Interscience Publications, New York, USA, 744 pp.

Petrangeli, M., Pinto, P. E., and Ciampi, V. (1999), "Fiber Element for Cyclic Bending and Shear of RC Structures. I: Theory," ASCE Journal of Engineering Mechanics, V. 125, No.9, pp.994-1001

Popovics, S. (1973), "A Numerical Approach to the Complete Stress-Strain Curve of Concrete", Cement and Concrete Research, Vol. 3, No.5, pp. 583-599.

Prakash, V. (1992), "Dynamic Response Analysis of Inelastic Building Structures: The DRAIN Series of Computer Programs," Ph.D. Thesis, University of California Berkeley, Department of Civil Engineering, 291 pp.

Rayleigh, Lord (1878), "Theory of Sound", V.1, Dover Publications (1945), 504 pp.

Richart, F.E., Brandtzaeg, A., and Brown, R.L. (1928), "A Study of the Failure of Concrete under Combined Compressive Stresses," Bulletin No.185, University of Illinois Engineering Experimental Station, Urbana, Illinois, 104 pp.

Ritter, W. (1899), Die Bauweise Hennebique (Construction Tecniques of Hennebique), Schweizerische Bauzeitung, 33 (7) Zurich, February, pp 41-43, 49-52, 59-61.

Saatci, S. (2007), "Behaviour and Modelling of Reinforced Concrete Structures Subjected to Impact Loading," PhD Thesis, Department of Civil Engineering, University of Toronto, 288 pp.

Sagbas, G. (2007), "Nonlinear Finite Element Analysis of Beam-Column Subassemblies," M.A.Sc. Thesis, Department of Civil Engineering, University of Toronto, 181 pp.

Schlaich, J., Schäfer, K. and Jennewein, M. (1987), "Toward a Consistent Design of Structural Concrete," PCI Journal, Issue 32, pp 74-150.

Seckin, M. (1981), "Hysteretic Behaviour of Cast-in-Place Exterior Beam-Column-Slab Subassemblies," PhD Thesis, Department of Civil Engineering, University of Toronto, 236 pp.

Shim, W. (2002), "Analysis of Beams with Low Shear Reinforcement," M.A.Sc. Thesis, Department of Civil Engineering, University of Toronto, 358 pp.

Shiohara, H., Kusuhara, F. (2006), "Benchmark Test for Validation of Mathematical Models for Non-linear and Cyclic Behaviour of R/C Beam-column Joints," Department of Architecture, School of Engineering, University of Tokyo, 37 pp, (online report).

Shirai N., Moriizumi, K., and Terasawa, K. (2001), "Cyclic Analysis of Reinforced Concrete Columns: Macro-Element Approach, Modeling of Inelastic Behavior of RC Structures under Seismic Load," American Society of Civil Engineers, Reston, Virginia, pp. 435-453.

Sittipunt, C., and Wood, S. L. (1995), "Influence of Web Reinforcement on the Cyclic Response of Structural Walls," ACI Structural Journal, V. 92, No.6, Nov.-Dec., pp. 745-756.

Spacone, E., Filippou, F. C. and Taucer, F. F. (1996), "Fiber Beam-Column Model for Nonlinear Analysis of R/C Frames. I: Formulation. II: Applications." Earthquake Engineering and Structural Dynamics, Vol. 7, pp. 1-22.

Takeda, T., Sozen, M. A. and Nielsen, N. (1970), 'Reinforced Concrete Response to Simulated Earthquakes," Journal of Structural Engineering, ASCE, 96(ST12), pp. 2557-2573.

Takizawa, H. (1976), "Notes on Some Problems in Inelastic Analysis of Planar RC Structures," Trans. Of Arch. Inst. Of Japan, 240, Part I in February, pp.51-62, Part II in March, pp. 65-77.

Taucer, F., Spacone, E, and Filippou F. C. (1991), "A Fiber Beam-Column Element for Seismic Response Analysis of Reinforced Concrete Structures," Earthquake Engineering Research Center, College of Engineering, University of California, Berkeley, Report No. UCB/EERC-91/17, 136 pp.

Vecchio, F. J. and Collins, M. P. (1986), "The Modified Compression-Field Theory for Reinforced Concrete Elements Subjected to Shear," ACI Journal, V.83, No.2, pp.219-231.

Vecchio, F. J. and Collins, M. P. (1988), "Predicting the Response of Reinforced Concrete Beams Subjected to Shear Using Modified Compression Field Theory," ACI Structural Journal, V.85, No.3, pp.258-268.

Vecchio, F. J. (1987), "Nonlinear Analysis of Reinforced Concrete Frames Subjected to Thermal and Mechanical Loads," ACI Structural Journal, V. 84, No.6, Nov. Dec., pp. 492-501.

Vecchio, F. J. (1992), "Finite Element Modeling of Concrete Expansion and Confinement," ASCE Journal of Structural Engineering, V. 118, No. 9, pp. 46-56.

Vecchio, F. J. (1999) "Towards Cyclic Load Modeling of Reinforced Concrete", ACI Structural Journal, V. 96, No.2, March-April., pp. 193-202.

Vecchio, F. J. (2000), "Analysis of Shear-Critical Reinforced Concrete Beams," ACI Structural Journal, V. 97, No. 1, pp. 102-110.

Vecchio, F. J. (2000), "Disturbed Stress Field Model for Reinforced Concrete: Formulation," Journal of Structural Engineering, V.126, No.9, pp. 1070-1077.

Vecchio, F. J. and Balopoulou, S. (1990), "On the Nonlinear Behaviour of Reinforced Concrete Frames," Canadian Journal of Civil Engineering, V.17, No.5, pp 698-704.

Vecchio, F. J. and Emara, M.B. (1992), "Shear Deformations in Reinforced Concrete Frames," ACI Structural Journal, V.89, No.1, pp 46-56.

Vecchio, F. J., Bentz, E.C., Collins, M.P. (2004), "Tools for Forensic Analysis of Concrete Structures," Computers and Concrete, V. 1, No. 1, pp 1-14

Vecchio, F. J., Shim, W. (2004), "Experimental and Analytical Reexamination of Classic Concrete Beam Tests," ASCE Journal of Structural Engineering, V. 130, No. 3, pp. 460-469.

Wagner, H. (1929), "Ebene Blechwandträger mit sehr dünnem Stegblech," (Metal Beams with Very Thin Webs), Zeitschrift für Flugtechnik und Motorluftschiffahr, V.20, Nos.8 to 12, Berlin, pp. 200.

Walraven, J. C. (1981), "Fundamental Analysis of Aggregate Interlock," Proceedings, ASCE, V. 107, STH, Nov., pp. 2245-2270.

Weaver, W. and Gere, J. M. (1990), "Matrix Analysis of Framed Structures," 3rd Ed., Van Nostrand Reinhold, New York, 546 pp.

Wong, P. S. and Vecchio, F. J. (2002), "VecTor2 and FormWorks User's Manual," Technical Report, Department of Civil Engineering, University of Toronto, 217 p.

Wood, S. L. (1990), "Shear Strength of Low-Rise Reinforced Concrete Walls," ACI Structural Journal, V.87, No.1, pp 99-107.

Yamamoto, T. (1999), "Nonlinear Finite Element Analysis of Transverse Shear and Torsional Problems in Reinforced Concrete Shells," M.A.Sc. Thesis, Department of Civil Engineering, University of Toronto, 112 pp.

Zeris, C. A. and Mahin, S. A. (1988), "Analysis of Reinforced Concrete Beam-Columns under Uniaxial Excitations," Journal of Structural Engineering, ASCE, 114(ST4), pp 804-820.

Zeris, C. A. and Mahin, S. A. (1991), "Behaviour of Reinforced Concrete Structures Subjected to Biaxial Excitations," Journal of Structural Engineering, ASCE, 117(ST9), pp 2657-2673.

# APPENDIX A

## COMPARISON OF ANALYTICALLY AND EXPERIMENTALLY OBTAINED LONGITIDUNAL REINFORCEMENT STRAINS FOR SAATCI BEAMS (Saatci, 2007)

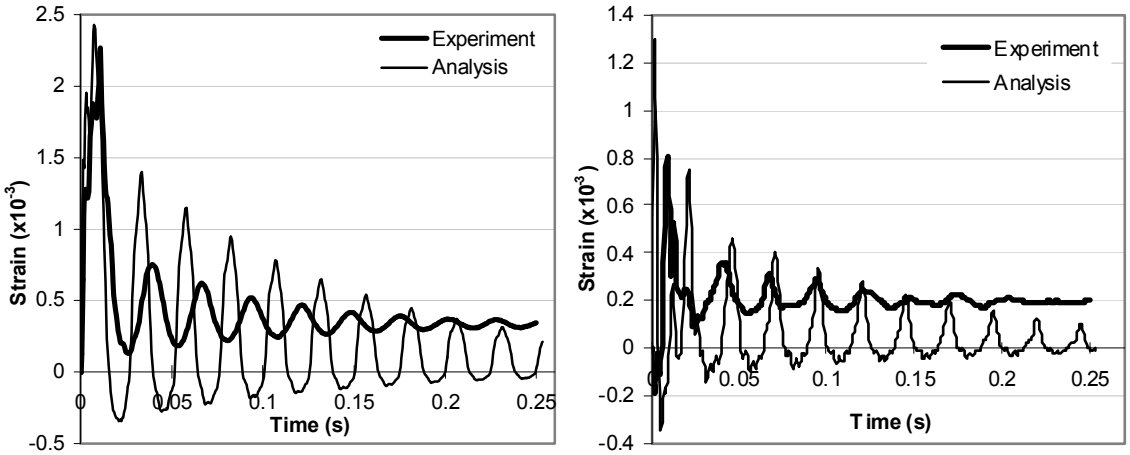


**Figure A.1** Comparison of Experimental and Analytical Responses for SS0a-1: **(a)** Midspan – Bottom Reinforcement Strain; **(b)** Support - Top Longitudinal Reinforcement Strain

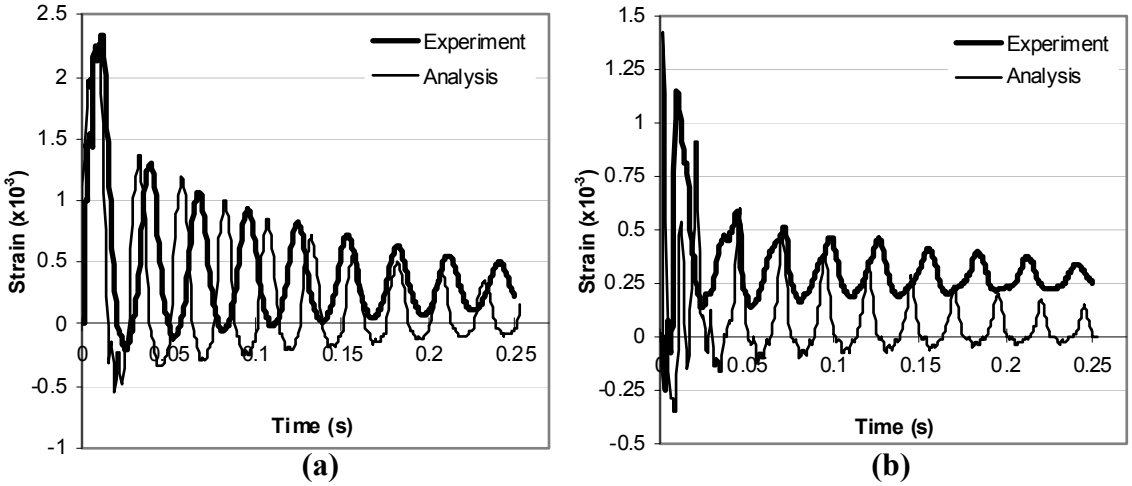


**Figure A.2** Comparison of Experimental and Analytical Responses for SS1a-1: **(a)** Midspan – Bottom Reinforcement Strain; **(b)** Support - Top Longitudinal Reinforcement Strain

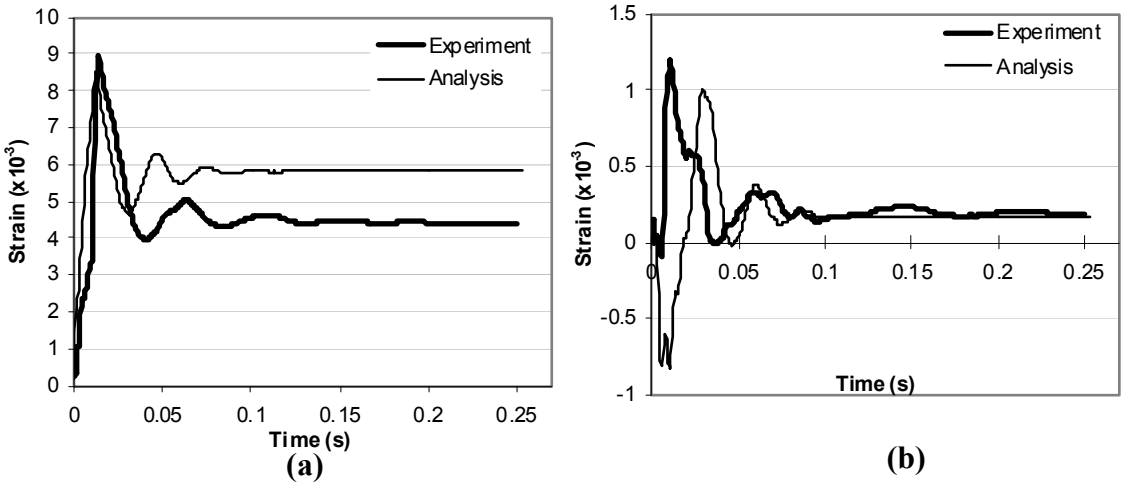


**Figure A.3** Comparison of Experimental and Analytical Responses for SS1a-2: **(a)** Midspan – Bottom Reinforcement Strain; **(b)** Support - Top Longitudinal Reinforcement Strain

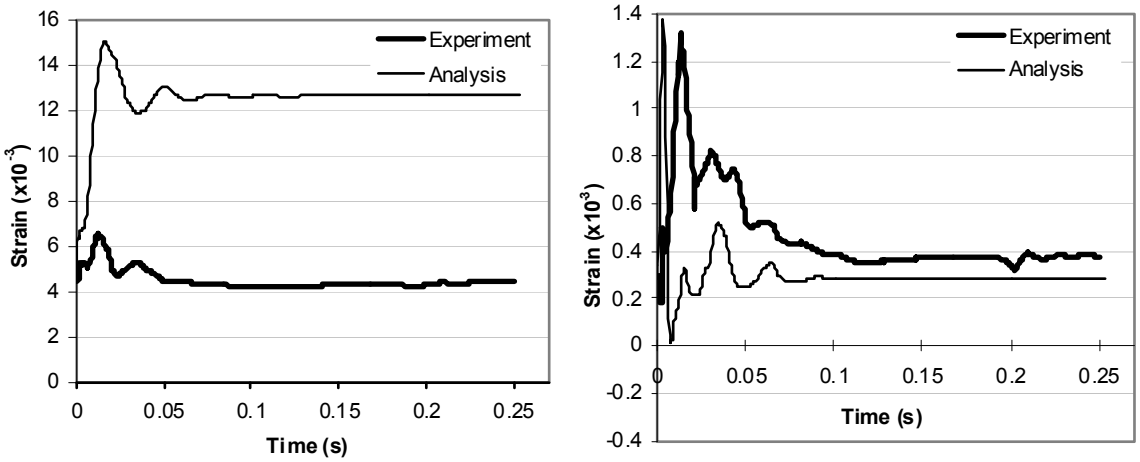


**(a)** **(b)**

**Figure A.4** Comparison of Experimental and Analytical Responses for SS1a-3: **(a)** Midspan – Bottom Reinforcement Strain; **(b)** Support - Top Longitudinal Reinforcement Strain

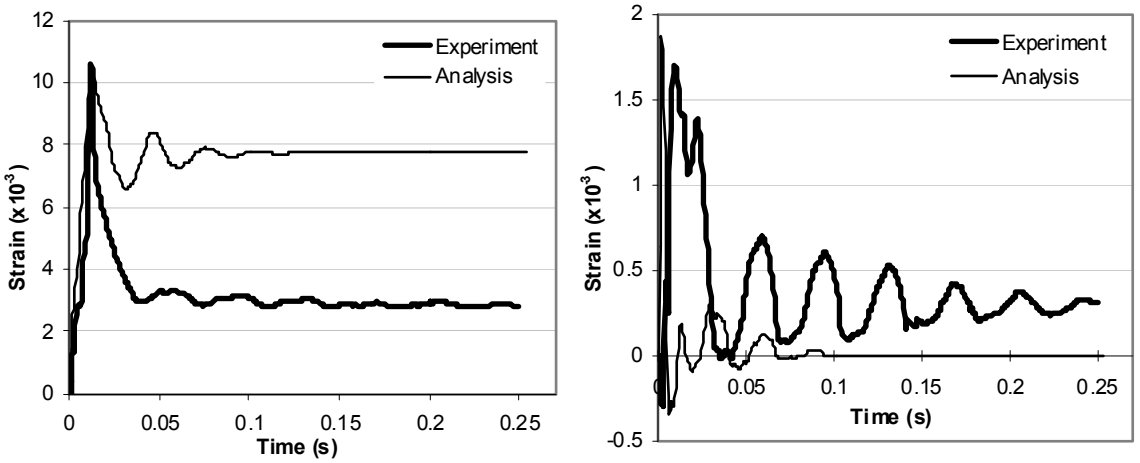


**(a)** **(b)**

**Figure A.5** Comparison of Experimental and Analytical Responses for SS1b-1: **(a)** Midspan – Bottom Reinforcement Strain; **(b)** Support - Top Longitudinal Reinforcement Strain

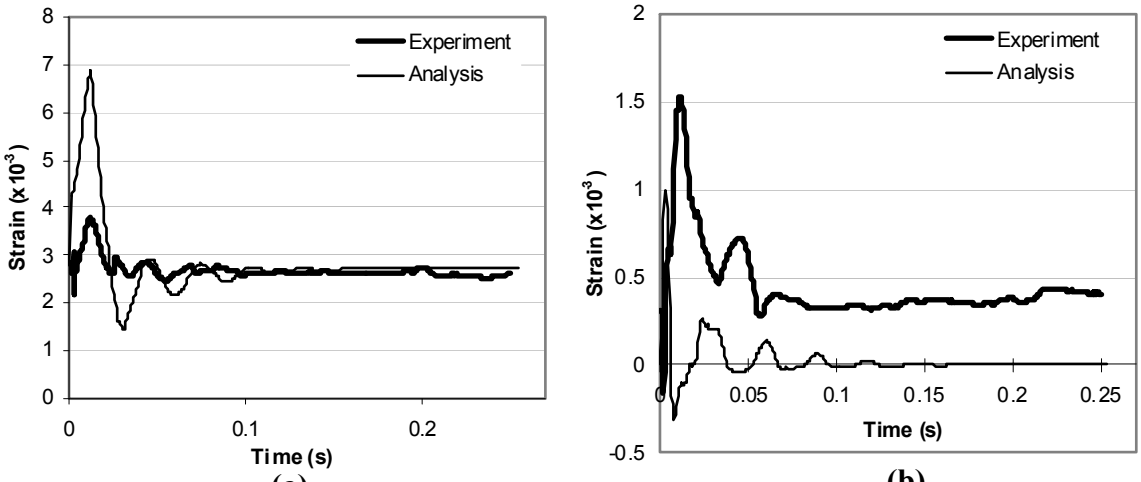


**(a)** **(b)**

**Figure A.6** Comparison of Experimental and Analytical Responses for SS1b-2: **(a)** Midspan – Bottom Reinforcement Strain; **(b)** Support - Top Longitudinal Reinforcement Strain

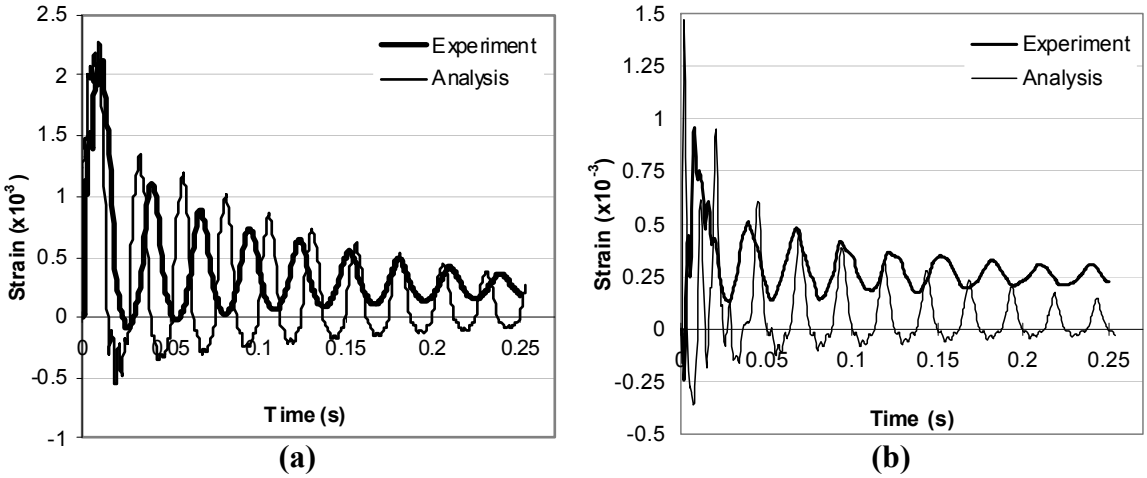


**Figure A.7** Comparison of Experimental and Analytical Responses for SS2a-1: **(a)** Midspan – Bottom Reinforcement Strain; **(b)** Support - Top Longitudinal Reinforcement Strain

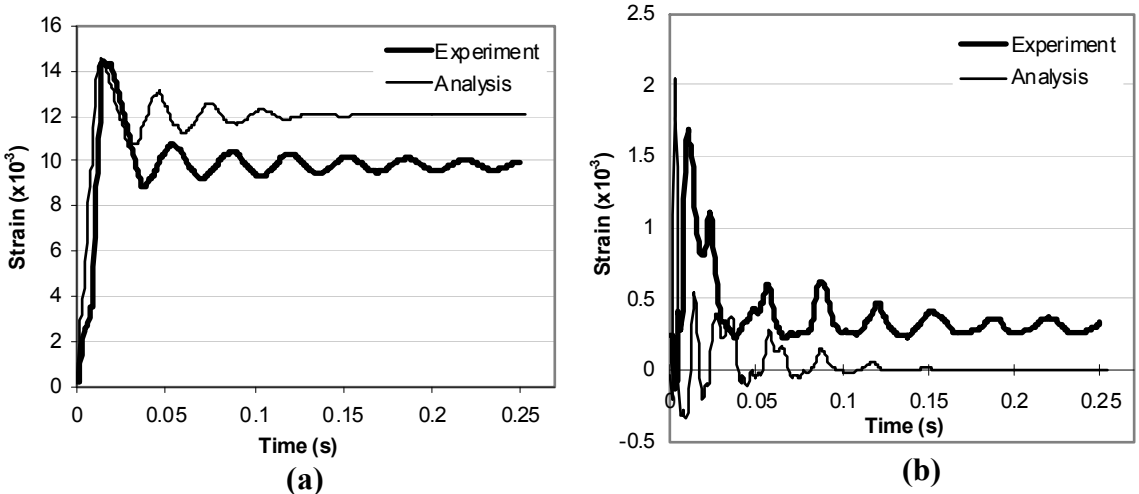


**Figure A.8** Comparison of Experimental and Analytical Responses for SS2a-2: **(a)** Midspan – Bottom Reinforcement Strain; **(b)** Support - Top Longitudinal Reinforcement Strain

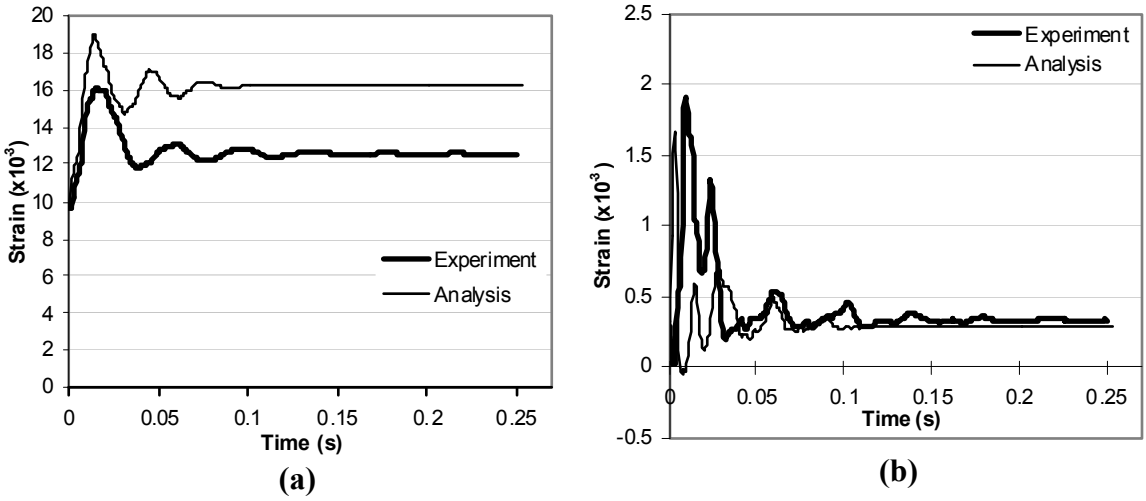


**Figure A.9** Comparison of Experimental and Analytical Responses for SS2a-3: **(a)** Midspan – Bottom Reinforcement Strain; **(b)** Support - Top Longitudinal Reinforcement Strain

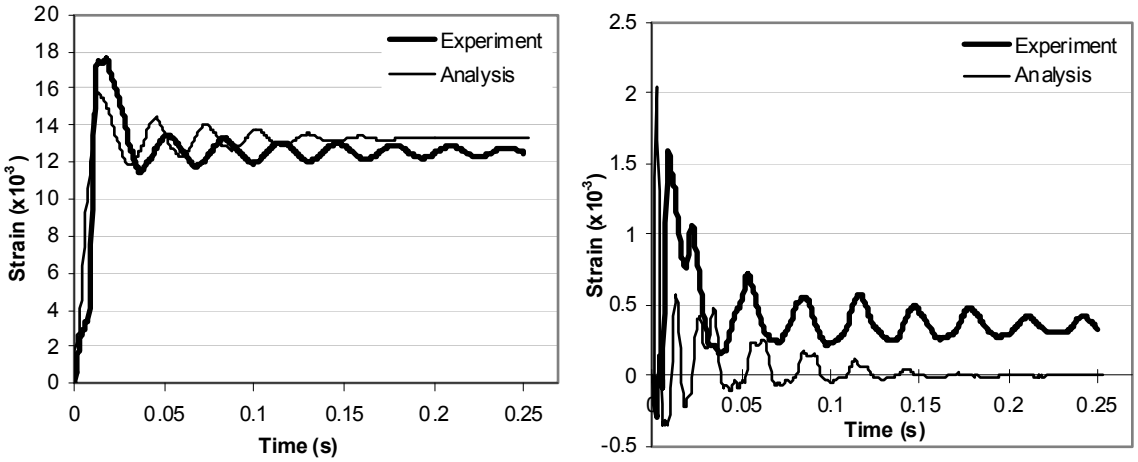


**Figure A.10** Comparison of Experimental and Analytical Responses for SS2b-1: **(a)** Midspan – Bottom Reinforcement Strain; **(b)** Support - Top Longitudinal Reinforcement Strain

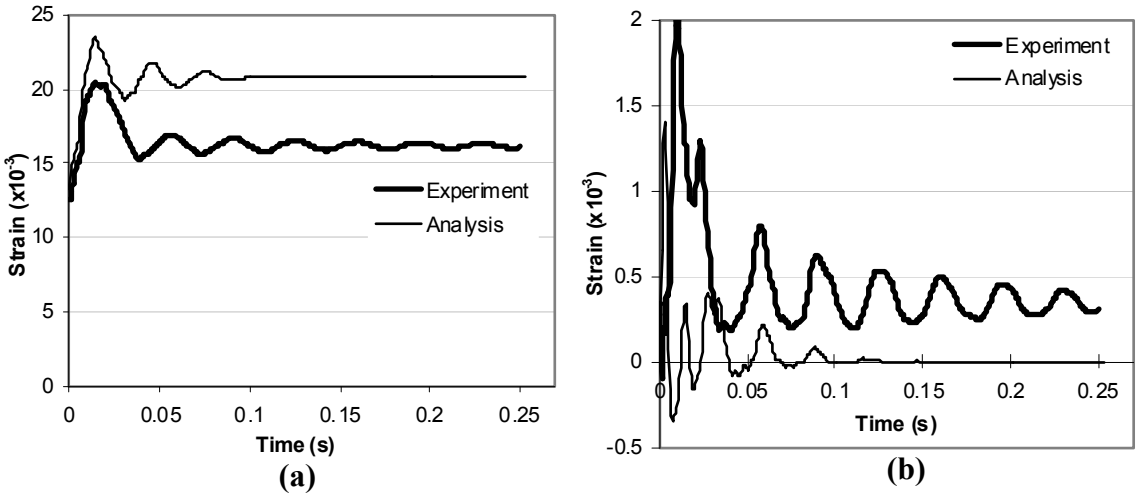


**Figure A.11** Comparison of Experimental and Analytical Responses for SS2b-2: **(a)** Midspan – Bottom Reinforcement Strain; **(b)** Support - Top Longitudinal Reinforcement Strain

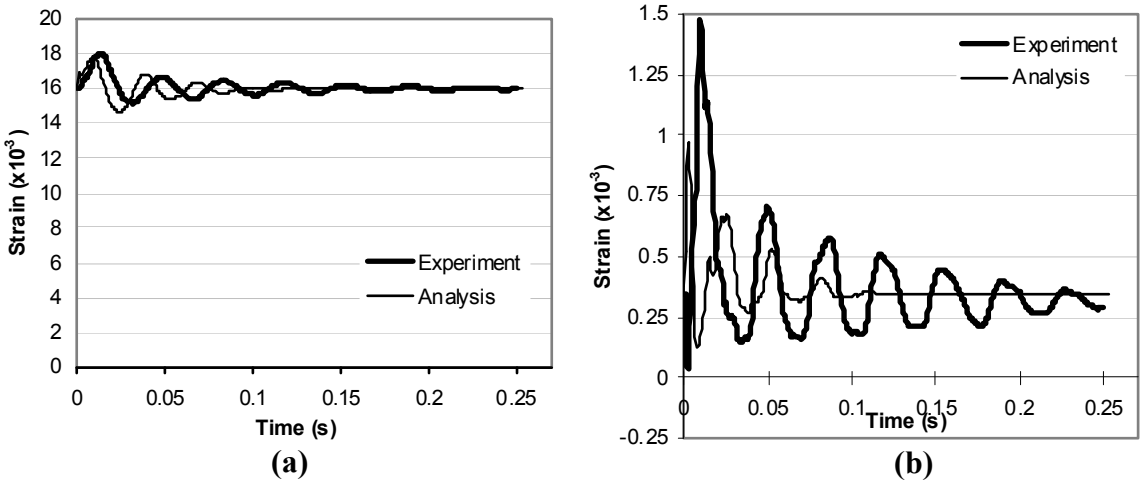


**Figure A.12** Comparison of Experimental and Analytical Responses for SS2b-3: **(a)** Midspan – Bottom Reinforcement Strain; **(b)** Support - Top Longitudinal Reinforcement Strain

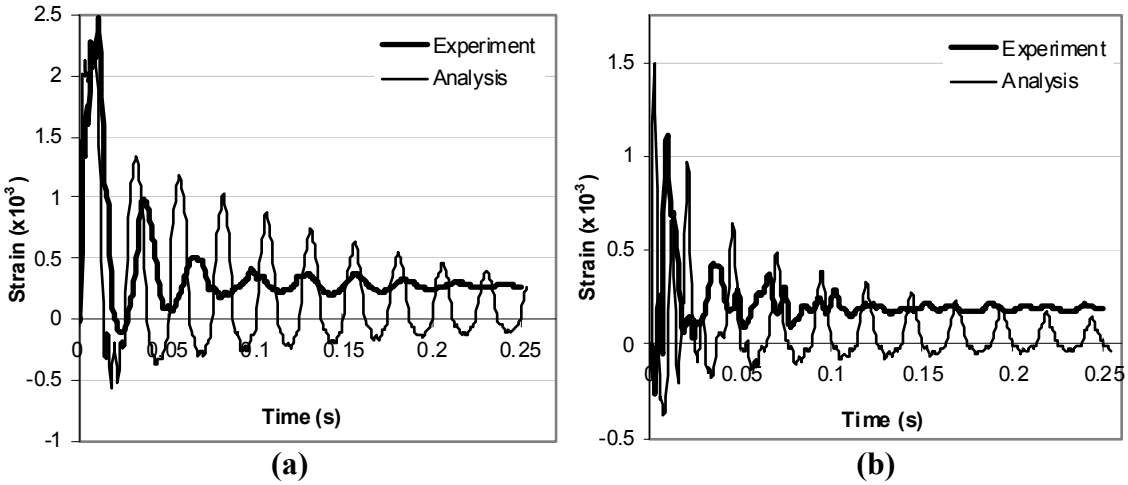


**Figure A.13** Comparison of Experimental and Analytical Responses for SS3a-1: **(a)** Midspan – Bottom Reinforcement Strain; **(b)** Support - Top Longitudinal Reinforcement Strain

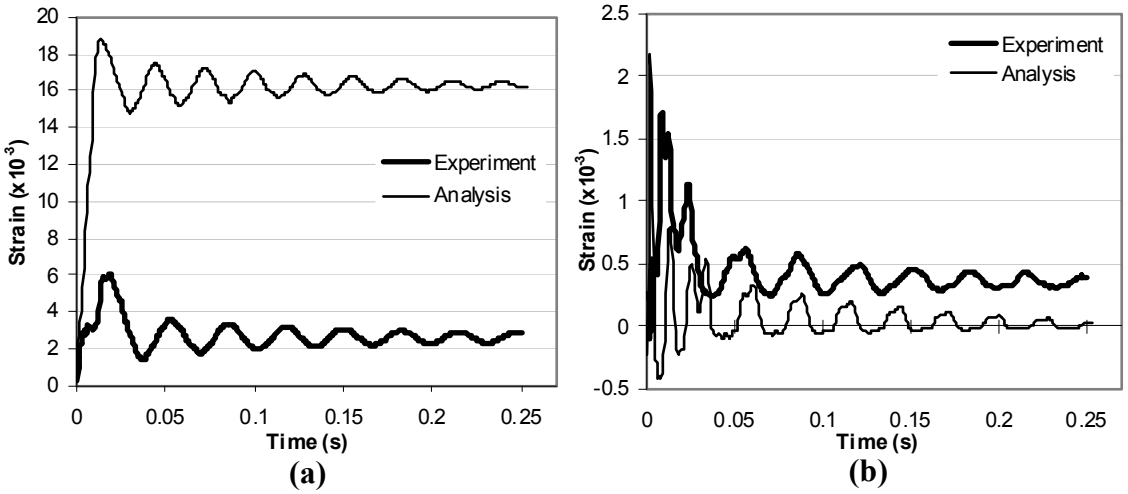


**Figure A.14** Comparison of Experimental and Analytical Responses for SS3a-2: **(a)** Midspan – Bottom Reinforcement Strain; **(b)** Support - Top Longitudinal Reinforcement Strain

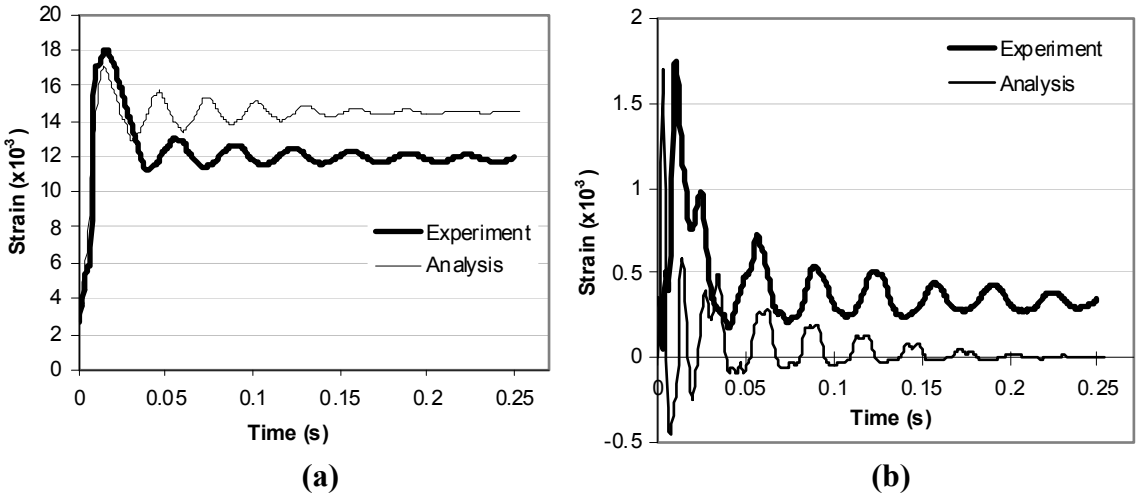


**Figure A.15** Comparison of Experimental and Analytical Responses for SS3a-3: **(a)** Midspan – Bottom Reinforcement Strain; **(b)** Support - Top Longitudinal Reinforcement Strain

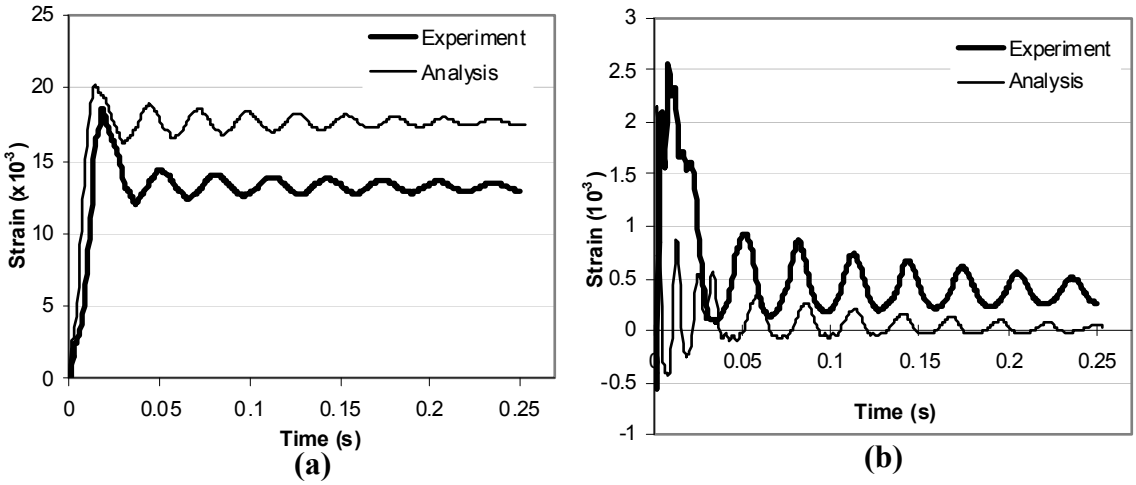


**Figure A.16** Comparison of Experimental and Analytical Responses for SS3b-1: **(a)** Midspan – Bottom Reinforcement Strain; **(b)** Support - Top Longitudinal Reinforcement Strain

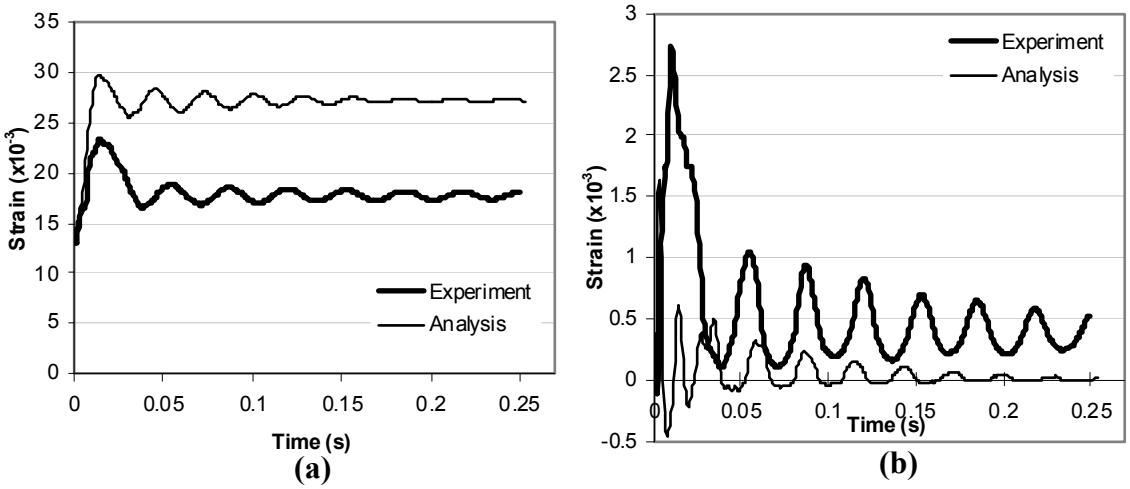


**Figure A.17** Comparison of Experimental and Analytical Responses for SS3b-2: **(a)** Midspan – Bottom Reinforcement Strain; **(b)** Support - Top Longitudinal Reinforcement Strain

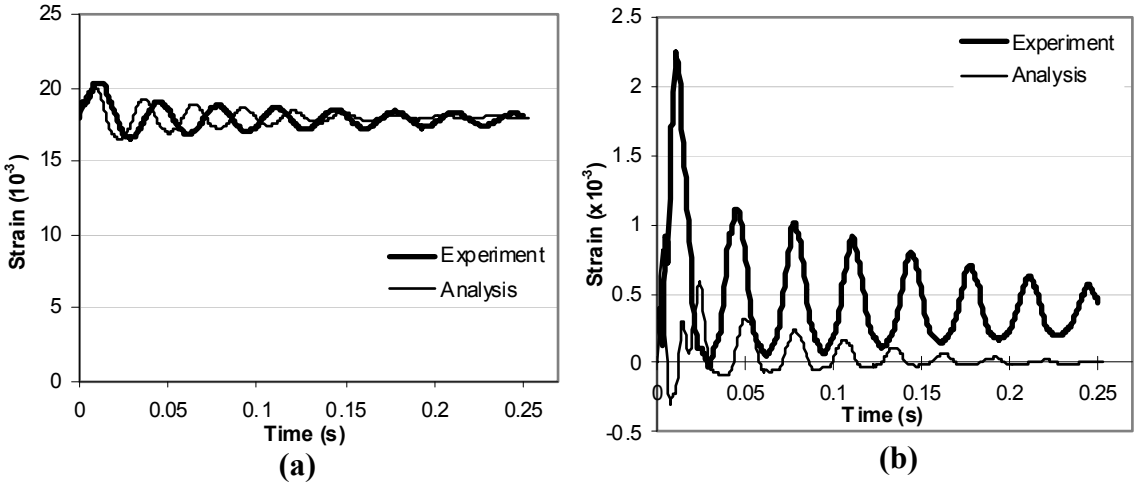


**Figure A.18** Comparison of Experimental and Analytical Responses for SS3b-3: **(a)** Midspan – Bottom Reinforcement Strain; **(b)** Support - Top Longitudinal Reinforcement Strain

# APPENDIX B

## INTRODUCTION TO THE USER'S MANUAL OF VECTOR5

# INTRODUCTION TO THE USER'S MANUAL OF VECTOR5

VecTor5 is a nonlinear sectional analysis program for two dimensional frame-related structures consisting of beams, columns and shear walls, subjected to temperature, static and dynamic loading conditions. Temperature loads include nonlinear thermal gradients; static loads include monotonic, cyclic and reversed-cyclic load cases; dynamic loads include base accelerations (time-history analysis under an input accelerogram), impulse, impact and blast loads, initial velocity and constant acceleration load cases. Based on the Modified Compression Field Theory (Vecchio and Collins, 1986) and the Disturbed Stress Field Model (Vecchio, 2000), VecTor5 uses a smeared, rotating crack approach for reinforced concrete using a total load, secant stiffness formulation.

The computational algorithm performs two interrelated analyses. Using a direct stiffness method, VecTor5 performs a global frame analysis first. Rigorous sectional analyses of concrete member cross sections are then performed at various sections along the lengths of the members, using a distributed nonlinearity fibre model approach. The computed responses are enforced with the use of an unbalanced force approach where the unbalanced forces are reduced to zero iteratively.

VecTor5 is capable of considering such second order effects as material and geometric nonlinearities, time- and temperature-related effects, membrane action, nonlinear degradation of concrete and reinforcement due to elevated temperatures, compression softening due to transverse cracking, tension stiffening due to load transfer between cracked concrete and reinforcement, tension softening due to fracture-associated mechanisms, shear slip along crack surfaces, nonlinear concrete expansion, confinement effects, previous loading history, effects of slip distortions on element compatibility relations and concrete prestrains. In addition, required for the dynamic analyses, VecTor5 considers strain rate effects on the concrete and reinforcement and damping effects on the structural response.

The complete user's manual and the basic version of VecTor5 can be found in the publications and the software sections of the VecTor Analysis Group website at 'www.civ.utoronto.ca/vector'.